Protocols and Methodologies in Basic Science and Clinical Cardiac MRI

Christakis Constantinides
Editor

Springer

Protocols and Methodologies in Basic Science and Clinical Cardiac MRI

Christakis Constantinides
Editor

Protocols and Methodologies in Basic Science and Clinical Cardiac MRI

Springer

Editor
Christakis Constantinides
Department of Cardiovascular Medicine
BMRU
Oxford
United Kingdom

ISBN 978-3-319-53000-0 ISBN 978-3-319-53001-7 (eBook)
https://doi.org/10.1007/978-3-319-53001-7

Library of Congress Control Number: 2017939941

Printed on acid-free paper

This Springer imprint is published by Springer Nature
The registered company is Springer International Publishing AG
The registered company address is: Gewerbestrasse 11, 6330 Cham, Switzerland

Foreword

Cardiovascular imaging is dynamic … not just in the literal sense as one follows cardiac contraction, but in a more global sense as this book highlights its continuing evolution. Cardiac imaging continues to undergo dramatic technical advances that spur new applications. The cycle of innovation, application, and innovation is seen repeatedly in this text. This book does a superb job of capturing the state of the art.

While there are many cardiac imaging methods, magnetic resonance provides by far the most comprehensive and diverse approach to understanding cardiovascular physiology and disease. The contributors to this book describe methods that cover the scale from molecular to macro. At the molecular level, hyperpolarized MRI (Chap. 4) and in vivo spectroscopy (Chaps. 5 and 6) probe cardiac metabolites in both endogenous and enhanced molecular species. At the cellular level, molecular-specific contrast agents yield insight into atherosclerosis (Chap. 8) through longitudinal studies that follow the evolution of plaques. At the cytoarchitectural scale, diffusion MRI and tractography (Chap. 3) illuminate details of the functional building units of the heart. At the meso- and macroscale, dynamic imaging methods (Chaps. 1, 2, and 9) simultaneously yield structure and function.

This book is comprehensive in a second important sense in that it covers cardiovascular disease in a truly interdisciplinary fashion. The fundamental physics of NMR is discussed in a comprehensible and relevant fashion. Engineering details of pulse sequences and novel strategies for measuring stress and strain are made clear. The chemistry underlying the metabolic pathways is accessible. Methods for quantitative measure of cardiovascular physiology and mechanics are included. Throughout, the many interdisciplinary threads are woven into the fabric of clinical cardiovascular disease. This book will find ready use by both basic scientists and clinicians seeking to use NMR/MRI to further understand cardiovascular disease.

Durham, NC, USA — G. Allan Johnson

Preface

Magnetic resonance imaging has been a short-lived, yet an exciting and a fast-progressing scientific field. Its early era spans the early technical development years through ground-breaking work at Aberdeen ('spin-warp' fundamentals) in the late 1970s, the introduction of the concept of the gradients by Paul Lauterbur, the subsequent parallel efforts and the early prototype tests at Nottingham (Sir Peter Mansfield, Raymond Andrew, Waldo Hinshaw, Neil Holland) in the late 1970s, and the first clinical work at Hammersmith in London in the early 1980s. Collective efforts of chemists, physicists, engineers, and mathematicians led to the clinical product that found its way into widespread use in the clinic, engaging radiologists, cardiologists, neuroscientists, and radiographers, in a truly multidisciplinary effort. Original scientific efforts in Europe were complemented, and were often rivalled, by parallel (or competitive) efforts across the Atlantic. International conferences were held as early as 1976 in Nottingham, followed by the well-known conference in Winston-Salem in North Carolina in 1981 (inspired by the Wright brothers who used to travel through the American mid-west states (Ohio to North Carolina) during summer breaks to run tests on their plane prototypes, marking the onset of the modern aviation era). Despite their limited attendance, both conferences were organized by leading scientific figures in NMR/MRI (Professors Hoult, Johnson, Mansfield, Edelstein, Bottomley, Lauterbur, etc.) later to become some of the scientific pillars that supported and led the MRI field. The International Society of Magnetic Resonance Imaging was formed soon thereafter (1982) that supports and steers this niche scientific area to this date.

While early imaging efforts focussed on brain imaging, there are documented cardiac NMR attempts that date back to the 1950s. Some of the first high-resolution cardiac imaging works are attributed to Professor G. Pohost and dates back to the early 1980s. Early strides targeted studies on T_1 and T_2 relaxation, and perfusion and metabolism in myocardial, while independent attempts in New York were steered towards novel, direct, multinuclear (^{23}Na, ^{31}P) MRI (Professors Hilal, Cannon). Professors Zerhouni and Axel introduced (independently) the fundamental ideas

behind myocardial tagging in the late 1980s, in an era that marked the onset of major, concerted efforts towards cardiac imaging, and the desire to establish cardiac MRI as a 'one-stop-shop' in the clinic.

Tremendous scientific progress was documented in the 1990s, including perfusion imaging (Professor N. Wilke), breathhold imaging (Professors McVeigh, Atalar), fast non-rectilinear imaging (Professor Glover), phase contrast imaging (Professor Pelc), cardiac functional imaging (Professors Higgins, Pettegrew, Raichek), and late gadolinium imaging (Professors Judd, Kim).

Strategic scientific planning in the early 2000s, concomitant with genomic mapping, opened new avenues in this area by introducing high-field, rodent cardiac imaging in the community. In association with major US funding program calls in nanomedicine, the introduction of stem cells to the scientific community during the same time period led to the emergence of the new subfield of molecular imaging, engaging molecular biology scientists, synthetic chemists, and geneticists (among others), marking the era of modern, personalized medicine.

This book focuses on the practical issues of the implementation of the state-of-the-art cardiac acquisition methodologies and protocols for both basic science and clinical practice. The motivation and philosophy behind its introduction is to serve as a practical guidebook for both beginners and advanced users for easy and practical implementation of acquisition protocols. It is relevant for a wide audience that ranges from students, residents, fellows, basic scientists, physicists, engineers, and medical practitioners.

The usefulness of this book relates to its intended practical use and focus on state-of-the-art cardiac MRI techniques that span both the clinical and basic science fields. In comparison and contrast to other similar, existing books, it is expected to distinguish itself for its practical usefulness and conciseness. Correspondingly, it may be used as a handbook (quick reference) for new starters, or people who would like to establish state-of-the-art cardiac MRI techniques at their institutions.

Given the historical evolution of the technical developments in MRI, the clinical and basic science topics are described separately. However, in instances where basic science development complements (or is envisaged to complement) clinical development, every effort has been made to ensure a comprehensive review, and associations of the clinical/basic science subfields.

Thirteen excellent contributions, which comprise this book, overview the current state of the art and describe relevant protocols and methodologies for implementation of basic science and clinical cardiac MRI techniques. Professor Young's opening chapter provides a superb overview of the role of MRI in preclinical and clinical functional quantification and modelling, while Professor Yu summarizes the current cardiac MRI techniques (tagging, DENSE, HARP, and SENC) for quantification of regional myocardial mechanics in the preclinical setting. Dr. Teh presents a comprehensive overview of ex- and in vivo diffusion MRI and tractography spanning the scales of the human to the animal hearts. On the forefront of metabolic and direct multinuclear imaging, Dr. Miller provides an excellent overview of the exciting new

advances in ^{13}C hyperpolarized MRI and their role in the study of cardiac energetics (Kreb's cycle, CK pathways). Complementary is the following chapter by Dr. Maguire who introduces the fundamentals of preclinical cardiac, in vivo spectroscopy, and recent efforts to accelerate imaging using chemical shift imaging. Dr. Constantinides completes this chapter trilogy with a discussion on direct, cardiac multinuclear imaging, emphasizing direct ^{23}Na, ^{31}P, and ^{39}K MRI.

The final three chapters in the first part of this book introduce novel and exciting new approaches in MRI, including cardiac elastography by Professor Kolipaka, molecular imaging of atherosclerosis by Dr. Plaza, and compressed sensing and fast imaging by Dr. Wech and Professor Schneider.

The second part overviews the current state of the art in clinical MRI, with excellent contributions by Dr. Francois on MR flow and quantification, myocardial viability in ischemic heart disease by Drs. Alkhalil and Dall'Armellina, congenital heart disease in paediatric cases by Dr. Muthurangu, and an excellent overview of cardiac MR angiography by Dr. Prieto.

I am honoured to have had the opportunity to edit these superb contributions from some of the most progressive MR scientists nowadays, a truly international effort. I am indebted to the support provided by the local Oxford environment, and Springer publications (Mr. Weston, Mr. Tournois), who have been extremely supportive of this effort since its early start.

I wish and foresee that this book will be welcomed by the International Society of Magnetic Resonance Imaging and the scientists in the field of MRI as a useful resource in addition to the plethora of other existing books currently used for teaching or other educational purposes.

With a sense of indebtedness, I sincerely thank Professor G. Allan Johnson who has graciously accepted to write the foreword of this book, a true gentleman, and one of the pillars of this field since its early inception. It has been a unique experience to have met and worked with him, and I am truly obliged by his genuine support over the years.

Oxford, UK Christakis Constantinides

Contents

Part II Clinical Cardiac Imaging

Editor's Bio Information

Dr. Christakis Constantinides completed his undergraduate studies at the Imperial College of Science, Technology and Medicine (Bachelors with First Class Honors in Electrical and Electronic Engineering, 1992) and his graduate (CASP/USIA scholar) and postgraduate (Whitaker Foundation scholar) studies at the Johns Hopkins University Whiting School of Engineering (M.S.E, 1994) and the Johns Hopkins University School of Medicine (Ph.D., 2000), in Biomedical Engineering. He held an appointment as a Visiting Research Fellow (Fogarty International Fellow) at the National Institutes of Health (2001–2003). He became an Assistant Professor in the Mechanical Engineering Department at the University of Cyprus (2005–2013). He was subsequently trained at the EU Institutions (DG-EAC) in Brussels (October 2013–February 2014). He is currently a Marie-Sklodowska Curie Research Fellow in the Department of Cardiovascular Medicine at University of Oxford (2015–2017). His specific research interests focus on the study of cardiac mechanical function, computational and tissue structural modeling and characterization, hardware design, and functional and cellular tracking methods using magnetic resonance imaging.

He has published over 80 papers in international peer-reviewed journals and conferences. He is the author of one book, four book chapters, and the editor of three books. He is a member of the American Physiological Society (APS), the International Society of Magnetic Resonance in Medicine (ISMRM), and serves as a reviewer (among others) for the journals of *JCMR*, *PLoS One*, *Magnetic Resonance in Medicine*, *Journal of Magnetic Resonance Imaging*, *Journal of Magnetic Resonance*, *NMR in Biomedicine*, and *Journal of Applied Physiology*. He is also a reviewer for ISMRM, IEEE-SBI, EMBS, and EU's COST-Action program.

Contributors

Mohammad Alkhalil RDM Cardiovascular Medicine University of Oxford, John Radcliffe Hospital, Oxford, UK

René M. Botnar Division of Imaging Sciences and Biomedical Engineering, King's College London, St. Thomas' Hospital, London, UK

The British Heart Foundation Centre of Excellence, Cardiovascular Division, King's College London, London, UK

Christakis Constantinides BHF Experimental Magnetic Resonance Unit, Radcliffe Department of Medicine, Division of Cardiovascular Medicine, Wellcome Trust Center of Human Genetics, University of Oxford, Oxford, UK

Erica D'Armellina Leeds Institute of Cardiovascular and Metabolic Medicine, Division of Biomedical Imaging, University of Leeds, Leeds, UK

Christopher Francois Department of Radiology, University of Winsonsin Madison, Madison, WI, USA

Pierre Gebhardt Division of Imaging Sciences and Biomedical Engineering, King's College London, St. Thomas' Hospital, London, UK

Department of Physics of Molecular Imaging, Institute of Experimental Molecular Imaging, RWTH Aachen University, Aachen, Germany

Kai Jiang Division of Nephrology and Hypertension, Mayo Clinic, Rochester, MN, USA

Arunark Kolipaka Department of Radiology, The Ohio State University, Columbus, OH, USA

Begoña Lavin Plaza Division of Imaging Sciences and Biomedical Engineering, King's College London, St. Thomas' Hospital, London, UK

Mahon L. Maguire BHF Experimental Magnetic Resonance Unit, Radcliffe Department of Medicine, Division of Cardiovascular Medicine, University of Oxford, Oxford, UK

Marcus R. Makowski Department of Radiology, Charité-University Medicine, Berlin, Germany

Warren J. Manning Division of Cardiology, Beth Israel Deaconess Medical Center, Boston, MA, USA

Jack Miller Department of Physiology, Anatomy and Genetics and Department of Physics, University of Oxford, Oxford, UK

Vivek Muthurangu UCL Centre for Cardiovascular Imaging, Institute of Cardiovascular Science, London, UK

Alkystis Phinikaridou Division of Imaging Sciences and Biomedical Engineering, King's College London, St. Thomas' Hospital, London, UK

Claudia Prieto Division of Imaging Sciences and Biomedical Engineering, King's College London, St. Thomas' Hospital, London, UK

Jürgen Ernst Schneider British Heart Foundation Magnetic Resonance Imaging Unit (BMRU), Cardiovascular Medicine, Wellcome Trust of Human Genetics, University of Oxford, Oxford, UK

Irvin Teh British Heart Foundation Magnetic Resonance Imaging Unit (BMRU), Cardiovascular Medicine, Wellcome Trust of Human Genetics, University of Oxford, Oxford, UK

Tobias Wech University of Wurzburg, Würzburg, Germany

W. Yong Kim Department of Cardiology, Aarhus University Hospital, Aarhus, Denmark

Alistair Young Auckland Bioengineering Institute, Auckland, New Zealand

Xin Yu Department of Biomedical Engineering Radiology, Physiology and Biophysics, Case Western Reserve University, Cleveland, OH, USA

Part I
Preclinical Cardiac Imaging

Chapter 1
The Role of MRI in Preclinical and Clinical Functional Quantification and Modelling

Alistair Young

Abbreviations

DENSE	Displacement encoding with stimulated echoes
GRE	Gradient-recalled echo
HARP	Harmonic phase
HFPEF	Heart failure with preserved ejection fraction
HFREF	Heart failure with reduced ejection fraction
LV	Left ventricle
NMR	Nuclear magnetic resonance
SPAMM	Spatial modulation of magnetization
SSFP	Steady-state free precession
TE	Echo time
TR	Repetition time

Introduction

Cardiovascular disease is the world's primary cause of death, and the highest burden on healthcare. However, effective diagnosis and treatment are hampered by a lack of knowledge of the pathophysiological mechanisms underlying disease development. Biomechanical factors are thought to play a significant role in many cardiac diseases. After myocardial infarction, for example, the heart adapts its shape and function (a process called remodelling) in response to signalling processes thought to be related to local tissue stretch and stress [1, 2]. In heart failure, patients can

A. Young, PhD
Auckland Bioengineering Institute, Auckland, New Zealand
e-mail: a.young@auckland.ac.nz

C. Constantinides (ed.), *Protocols and Methodologies in Basic Science and Clinical Cardiac MRI*, https://doi.org/10.1007/978-3-319-53001-7_1

present a spectrum of characteristics, loosely grouped into the categories of heart failure with reduced ejection fraction (HFREF), and heart failure with preserved ejection fraction (HFPEF) [3]. The prognosis after diagnosis of heart failure is very poor and treatments proven effective in HFREF have not been shown to be effective in HFPEF [4]. However, ejection fraction (the amount of blood pumped per beat, as a percentage of the end-diastolic volume) is a poor measure of tissue function. Patients with normal ejection fraction can have impaired muscle fiber shortening if the ventricle wall is thickened and the end-diastolic volume is small. Impaired filling characteristics are manifest in many patients, but whether this is due to an increased passive muscle stiffness, or a defect in the de-activation of sarcomeres, is unknown. Circulating biomarkers such as brain natriuretic peptide and troponin are now used routinely to evaluate patients, and these are thought to be affected by tissue mechanical factors [5, 6]. These show excellent negative predictive value, but specificity is not as high. Cardiac MRI may therefore have an important role in identifying different pathological mechanisms in patients with intermediate values of circulating biomarkers, and those requiring detailed characterization of structure and function.

This chapter will discuss the role of cardiac MRI in the evaluation of heart morphology, function, and mechanics. Attention will be given to geometry and motion, stress and strain, and also population analysis of remodelling between patient groups. Techniques will include cine imaging, myocardial tagging, displacement encoding, phase contrast velocity encoding in multiple dimensions, and associated analysis methods. Structural imaging, including diffusion tensor imaging for muscle fiber architecture, T_1 mapping, late gadolinium enhancement for scar imaging and extra-cellular volume quantification will be addressed in other chapters. The promising technique of MRI elastography for myocardial stiffness evaluation is also discussed in another chapter, although this should be seen as complimentary to the finite elasticity methods outlined here.

Imaging Physics- Fundamentals

Cardiac MRI relies on the fundamental property of some atomic nuclei (those with odd atomic number e.g., ^{1}H, ^{23}Na, and ^{19}F) to interact with magnetic fields and exhibit nuclear magnetic resonance (NMR). Most clinical imaging is done with ^{1}H nuclei (i.e., a single proton), because hydrogen is abundant in water and lipids, and has a strong signal relative to ^{23}Na or ^{19}F. Recently, hyperpolarized ^{13}C imaging has become possible for investigating metabolism and perfusion, since large signal can be achieved in a brief time period in a specially prepared contrast agent, but this not performed routinely. An NMR signal is obtained by placing the subject in a strong magnetic field (typically >1.0 Tesla), and transmitting a radio frequency excitation pulse tuned to the resonant frequency. This tilts the magnetic moment associated with the nuclei towards the transverse plane whereupon they precess in unison about the longitudinal direction and the evolved

signal is detected using coils placed on the chest. The frequency of precession is proportional to the field strength

$$\omega = \gamma B_0 \tag{1.1}$$

For hydrogen imaging (γ = 42.58 MHz/T) at 1.5 T, ω = 63.87 MHz. The signal depends on longitudinal and transverse relaxation time constants, termed T_1 and T_2. Typically, T_1 is approximately 800 ms and T_2 is 30 ms for healthy human myocardium. By changing the timing between excitations (TR or repetition time) and acquisitions (TE or echo time), the signal contrast can be made T_1 or T_2 weighted.

The transformation from NMR to MRI has been attributed mainly to Paul Lauterbur and Peter Mansfield, a chemist and physicist respectively, who jointly won the Nobel prize for Physiology and Medicine in 2003. Using mathematical methods derived from Computed Tomography, a tomographic image could be reconstructed from many signals, similar to filtered backprojection. By applying an imaging gradient (i.e., a spatial linear variation in the magnetic field strength) during signal acquisition, the frequency of precession is made dependent on spatial location. Today, the same method used in Lauterbur's original paper [7] (i.e., acquisition of radial projections) has become again very useful in rapid cardiac imaging using compressed sensing [8].

Gradient-recalled echo (GRE) imaging is often used in cardiac MRI since it can give T_1 or T_2 weighted images for imaging fibrosis and edema, as well as black blood imaging for vascular morphology. Blood oxygen level dependence is also possible in research settings [10]. However, morphological imaging with GRE is limited by the signal contrast between blood and muscle, particularly in long axis views, which have different inflow artifacts.

In the early 2000s, advances in the strength and linearity of imaging gradients made fast imaging possible using steady-state free precession (SSFP) [11]. This method uses balanced gradients and very short TR and TE to achieve a high signal which reflects the ratio of T_2 to (T_1+T_2) in the steady-state, thereby giving very good contrast between blood and muscle since this ratio is much higher in blood than muscle (Fig. 1.1). A retrospectively-gated SSFP acquisition of a short axis or long

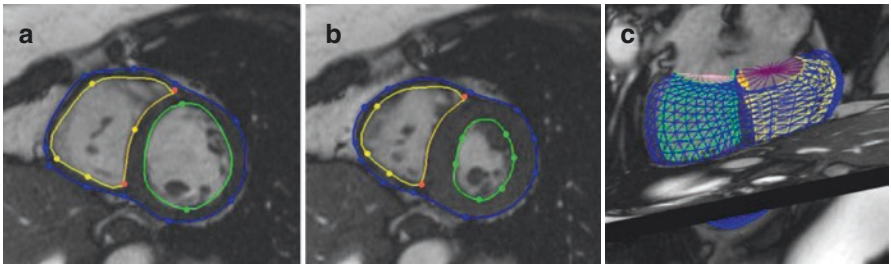

Fig. 1.1 SSFP cine short-axis images at end-diastole (**a**) and end-systole (**b**). (**c**) Finite element model customized to short and long axis images [9]

axis slice can routinely be performed in a breath-hold of under 10 s duration, in both short and long axis slices with minimal inflow artifacts. This now remains the workhorse of cardiac MRI at both 1.5 T and 3.0 T, although care must be taken at 3.0 T to avoid off-resonance effects (banding artifacts) by effective shimming and transmission of the excitation pulse. Safety concerns are also higher at higher field strengths, since energy disposition can heat the tissue, so typically the flip angle at 3 T is reduced relative to 1.5 T [12]. At higher field strengths (e.g., 7 T or 9.4 T) GRE is preferred to SSFP.

Methodology

This section gives an overview of the hardware and software parameters and settings used for morphology and function in cardiac MRI.

Hardware

The MRI scanner is essentially a large superconducting electromagnet. Current circulates around the superconducting wire at about 500 A, with no resistance if kept below the critical temperature (−264 °C for the niobium-titanium alloy used in most scanners). The temperature is maintained with a reservoir of liquid helium, which is continuously recycled by a cooling system. The homogeneity of the field must be better than 1 part per million, achieved using shimming, over the imaging volume (although larger imaging volumes can have up to 5 ppm). Gradient coils installed in the scanner chassis are meticulously designed to achieve linear variation in the main magnetic field, and can be switched on and off very rapidly (typical gradient strengths are 40–80 mT/m with a slew rate of approximately 200 T/m/s). The engineering requirements on the gradient power amplifiers are stringent with up to 2 kV and 500 A delivered on each of the x, y, and z, physical gradients. The signal detection system in clinical systems is typically made up of many small coil elements, arranged in an array and strapped onto the chest. Recent advances have been accomplished in parallel detection systems, enabling 64 or more channels to be acquired simultaneously. This speeds up imaging by requiring fewer excitations, using the coil geometry to encode spatial location. These methods are not common in preclinical imaging, where solenoid type coils are typically used. Finally the image reconstruction system needs to be capable to compute over 500 2D Fourier transforms per second. With the advent of iterative reconstruction methods, more powerful parallel processors are required. These avoid the Nyquist sampling requirement by assuming prior knowledge about the images acquired (e.g., they are sparse in a transform domain), but require nonlinear, computationally expensive processes [13].

Pulse Sequences

SSFP cine images are typically acquired with the following parameters (1.5 T): field of view 300–400 mm, TR = 3 ms, TE = 1.6 ms, flip angle = 60°, image matrix = 256·200, 25–50 cine frames per slice, breath-hold duration = 8–15 s, contiguous short axis slices 7 mm thick with an interslice gap of 3 mm [12]. Higher accelerated acquisitions are becoming more prevalent with temporal undersampling or iterative reconstruction, enabling more slices in a single breath-hold or higher temporal resolution [8]. Analysis of diastolic function typically requires higher temporal resolution, at least 50 cine frames per heartbeat.

Myocardial tissue tagging using spatial modulation of magnetization (SPAMM) has been for many years the reference standard for strain quantification in the heart in both clinical and preclinical studies [14]. The sequence is based around a magnetization preparation which, in its simplest form, produces a sinusoidal variation in magnetization across the field of view [15]. This is achieved with a 90° RF excitation pulse, a short gradient which wraps the phase of the signal according to spatial position, and a −90° RF pulse which stores the magnitude of the modulated signal in the longitudinal direction. The size and duration of the gradient encodes the spatial frequency of the tags. This modulated magnetization is then available for imaging, typically with GRE imaging [16], but also SSFP options are available [17]. The main limitation of SPAMM is that tags are typically spaced 6–8 mm apart, so that only one to three tags are possible across the wall, giving unreliable radial strain estimates in most cases [18].

Higher resolution strain imaging can be achieved with a phase contrast pulse sequence known as displacement encoded stimulated echo (DENSE) imaging [19]. This method can be thought of as similar to SPAMM, except that the tag pattern stored in the longitudinal direction is recalled as a phase angle in the acquired signal [20]. This encodes displacement in the phase of each pixel, giving higher resolution than tagging methods [21]. Radial strain is therefore better estimated with DENSE than tagging [18].

Phase contrast pulse sequences are also commonly used for quantifying blood velocity and flow. GRE images are acquired with an additional bipolar velocity encoding gradient. The size and duration of the gradient dictates the velocity encoding corresponding to a 2π phase wrap (typically 250 cm/s) [22]. There are many varieties of this sequence, which can be viewed as a spectrum of spatial and velocity encoding dimensions. At one end there is the 4D flow acquisition, which typically requires 10–20 min during gentle breathing, with respiratory as well as cardiac gating [23]. This results in high spatial resolution but limited temporal resolution. At the other end of the spectrum there is real time high temporal resolution 1D velocity encoded imaging, which gives information similar to M-mode Doppler ultrasound [24]. This method has been used to quantify pulse wave velocity in the descending aorta during exercise stress testing [25].

Image Processing

Left and right ventricular mass and volume is commonly calculated from short axis cine slices, by contouring each frame and summing areas [26]. Simpson's rule is often quoted, however this specific quadratic integration formula is not commonly employed. Care must be taken at the base to avoid inclusion of the atrial volume and tissue in the ventricular sum [27, 28]. This is best done using long axis images to determine the position and angulation of the valves. The large motion of the base through the plane of the short axis image is particularly problematic for RV analysis, where the ventricle is more complex, and where large through-plane motions occur [29]. Information from short and long axis slices can be integrated to achieve interactive assessment of pump function [30, 31]. The debate on whether to include trabeculation and papillary muscles in the blood pool or in the myocardial mass is still ongoing. Quantification of trabeculation and papillary muscle is currently difficult with standard 2D imaging, due to partial voluming, but 3D cine methods are now becoming available. In the near future automatic methods may be able to accurately quantify these structures [32, 33].

Standard conventions have been written for guiding the analysis and reporting of cardiac MRI [34]. Training must be given for manually-guided methods, to reduce variability in the estimate [35], however, bias between centers is more difficult to remove. A recent study showed that subtle biases in the demarcation of inner and outer boundaries can lead to integrated differences in the overall mass and volume, and care should therefore be exercised when comparing results between centers [36].

Regional analysis is typically performed using the 17 standard segments defined for the left ventricle (LV) [37]. A qualitative scoring system is often used for wall motion and wall thickening (0: normal; 1: mildly dyskinetic; 2: severely dyskinetic; 3: akinetic; 4: dyskinetic), and differences between rest and stress are indicative of myocardial ischemia [38]. However, these are somewhat subjective. Automated motion analysis methods are now becoming available for quantification of regional wall motion abnormalities [39, 40], with good agreement with human scoring.

Recently, fully automated analysis methods are becoming available [41]. Multi-atlas segmentation techniques are very promising [42]. Furthermore, advances in machine learning algorithms are showing impressive results [43, 44]. Progress in this field is greatly facilitated by the availability of open benchmarking datasets [45].

Diastolic function can be evaluated using parameters derived from M-mode echocardiography, e.g., peak inflow velocity (E) and peak tissue velocity at the mitral annulus (E′). Phase contrast velocity imaging has been used to quantify inflow and tissue velocity [46]. Diastolic function can also be evaluated from a volume-time graph derived from the LV volume measured in each frame of the SSFP cine (Fig. 1.2c). The rate of ejection and filling gives analogous values (note that E is a flow rate rather than a velocity), and mitral valve points can be tracked using texture tracking methods to give E′ [47, 48]. Texture tracking methods can

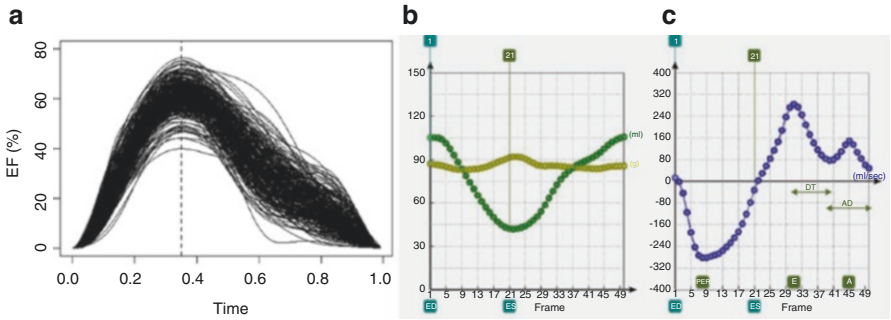

Fig. 1.2 Temporal analysis of ventricular function: (**a**) a collection of regional ejection fraction time curves from 300 patients, which have been registered in time to end-diastole (0) and end-systole (0.38) within a normalized cycle duration of 1.0 unit. (**b**) Left ventricular volume (*green*) and mass (*gold*) with respect to frame number for a single case. (**c**) Rate of change in left ventricular volume in ml/s for the same case, showing peak ejection rate (PER), peak early filling rate (E) peak late filling rate (A), deceleration time (DT) and A-wave duration (AD)

also be incorporated to track the boundaries throughout the cardiac cycle, giving greater reproducibility in mass and volume [49].

There has been a lot of work done on analyzing tagged MRI data for strain and deformation [50]. Recent methods have used texture tracking methods, which are not so dependent on the actual tag pattern used [18, 51]. The harmonic phase (HARP) method gives a fast analysis method for MR tagged images [52, 53]. This filters the image data in frequency space to isolate the harmonic peak generated by tagging. However, the resolution of this method is limited by the size of the filter used. The sinmod algorithm extends the filter by modelling the local texture as a sine wave with a local frequency and amplitude, selected using a tuned bandpass filter [54, 55]. Myocardial strain can be quantified directly from DENSE displacement data at each pixel [56]. Simplified analysis methods are now available [57], and 3D analysis is a straightforward extension [58], which is enhanced with interactive guide-point modeling [59].

One problem with strain quantification is that, being a numerical derivative of displacement, strain is very sensitive to noise in the displacement. A generalized model-based strain analysis method has been proposed [18] in which tagged and DENSE data could be analyzed using the same pipeline. This was validated in a deforming phantom with known analytic strain field, showing excellent agreement provided there are no discontinuities in strain [18].

Texture tracking methods are now popular for the estimation of displacement and deformation from untagged cine images. Diastolic strain can be quantified from retrospectively gated SSFP cine images, and good agreement has also been found compared with tagging [60]. However, regional results can show large differences with respect to tagging [61]. A recent study investigated which SSFP image features are the most important in the estimation of regional strain [62]. SSFP untagged cine images were masked in three ways, firstly by replacing the pixel values between the epicardial and endocardial contours with representative value (Myo), secondly by

replacing the image outside the epicardium and endocardial contours with representative values (Ex-Myo), and thirdly by using representative values both within and outside the contours (Contour, see Fig. 1.3). Circumferential strains were then quantified using texture tracking, and the results compared to tagging in the same mid-ventricular slice for 85 patients with cardiovascular disease. Averaged over the whole slice, all three masked images gave similar results to tagging. However, regional strain estimates were different from tagging in all cine SSFP images. This shows that global strain estimates are derived from the overall length changes of the contours, and that features outside the myocardium have a large effect on regional strain estimates.

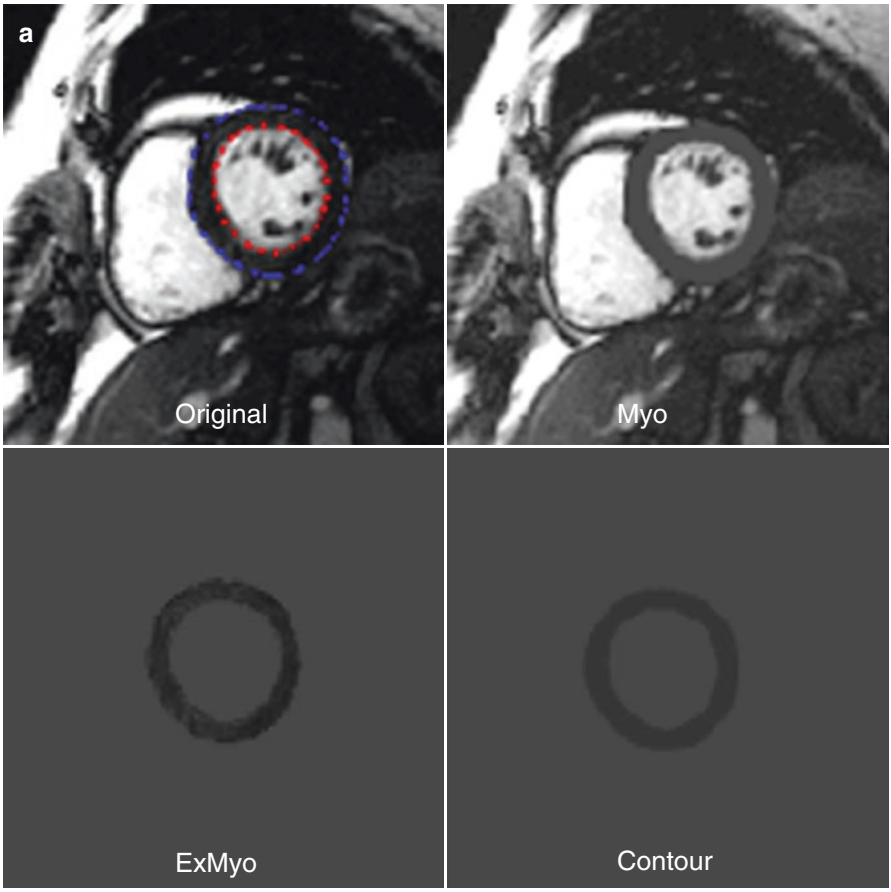

Fig. 1.3 (**a**) Original image with epicardial (*blue*) and endocardial (*red*) contours (Original), and masked images for myocardium (Myo), extra-myocardium (ExMyo), and both (Contour). (**b**) Mean differences between tagging and SSFP circumferential segmental strain were greater for ExMyo and Contour, than Original or Myo. *GLOBAL* average over the whole slice, *AS* anterior septum, *A* anterior, *AL* anterior lateral, *IL* inferior lateral, *I* inferior, *IS* inferior septum

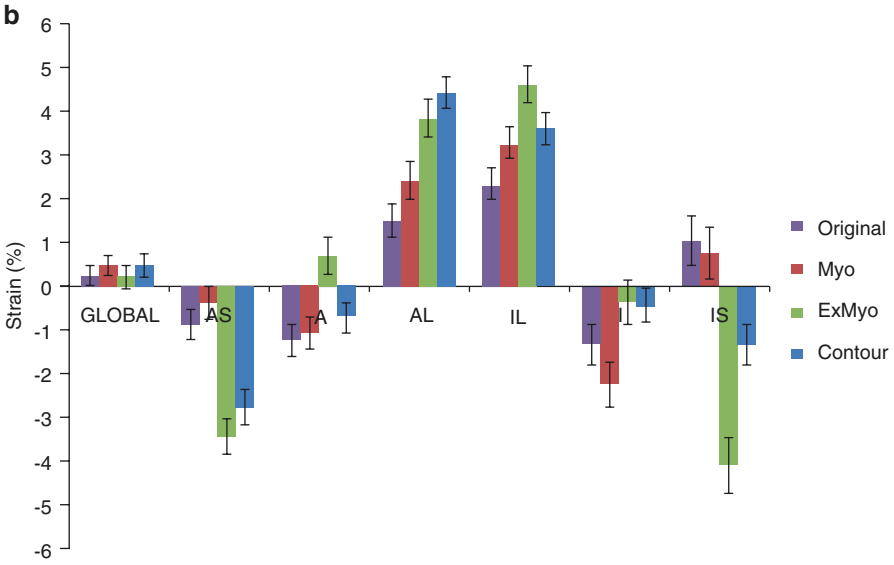

Fig. 1.3 (continued)

Typically torsion is computed from the relative rotation of apical and basal short axis slices, and is best calculated from tagging or DENSE acquisitions. Torsion should be quantified by the circumferential-longitudinal shear angle, which can be approximated by the difference in rotation between apical and basal slices, multiplied by the average radius and divided by the distance between slices [63]. The scaling using the radius is required to normalize the size of the heart, giving similar values of torsion across most mammalian species [63]. Torsion can be divided by shortening strain to give the torsion-to-shortening ratio, which is an index of subendocardial dysfunction [63]. The characteristic distribution of myofiber orientation in the healthy heart equilibrates fiber contraction and fiber stress across the wall, so that myocytes contract uniformly from epicardium to endocardium [64, 65].

More recently, atlas-based methods have been used to obtain finer resolution of regional differences in shape and function [66]. In one popular method, atlas-based shape indices can be derived from principal component analysis [66]. This unsupervised dimension reduction technique finds the modes of variation that explain the most covariance in the shapes. The first mode explains the most covariance, the next mode explains the most remaining covariance, and so on. Linear discriminant analysis is a common statistical method that can combine principal components in an optimal way, for example to determine the dependence on traditional risk factors [67]. Information maximizing component analysis is an extension of linear discriminant analysis, which does not depend on assumptions that the underlying distributions are Gaussian [68]. Such atlas-based analysis measures can be readily used to calculate asynchrony measures, such as the tissue synchrony index which

quantifies the disparity in the timing of contraction and predicts the response to cardiac resynchronization therapy [69].

The remodeling processes by which the heart adapts to disease are thought to be triggered by changes in local stress and strain experienced by the myocytes and/or extracellular matrix. The quantification of local tissue strain is now possible using MRI tagging or DENSE techniques. However the estimation of stress (force per unit area) is problematic. Direct measurement is currently impossible, since this involves disruption of the tissue itself. Mathematical models offer the only method of stress estimation at present [70]. Biophysical simulations of cardiac mechanics and electrical activation can provide patient-specific biophysical parameters optimized to imaging data [71–73]. Muscle stiffness and sarcomere contraction and relaxation are simulated by adjusting the biophysical parameters to match the simulated motion to the imaged motion. Finite element analysis of electromechanical processes can simulate realistic propagation of the activation wavefront and represent non-linear, anisotropic material properties. Calcium transients and sensitivity are simulated by model parameters related to sarcomere activation and de-activation. Multi-scale modelling of cellular processes may be customized using imaging data, resulting in patient specific models [74]. In patients with congenital heart disease, such customized models are being used to predict outcomes of surgical interventions [75].

Cardiac Applications

Longitudinal strain has been shown be a sensitive marker for dysfunction, before other changes, e.g., in ejection fraction, are manifest [76]. Fiber strain is depressed in hypertrophic cardiomyopathy [77] despite preserved ejection fraction. Strain is also impaired in aortic stenosis [78], hypertension [79], ischemia [80], infarction [81], diastolic dysfunction [82, 83] and asymptomatic pre-clinical pathology [84]. In stress pharmacological stress studies, tagging has shown greater sensitivity than untagged wall motion for the detection of coronary artery disease and outcomes [80]. In the Losartan Intervention for Endpoint Reduction in Hypertension trial, patients with hypertensive LV hypertrophy had markedly heterogeneous strain patterns [85]. Heterogeneity of function was also found in patients with idiopathic dilated cardiomyopathy, which was alleviated in some patients by ventricular reduction surgery [86].

In asymptomatic volunteers taking part in the Multi-ethnic Study of Atherosclerosis (MESA), myocardial tissue tagging showed subclinical dysfunction in those with subclinical atherosclerosis [87]. Strain relaxation was also shown to be a better predictor of future heart failure and atrial fibrillation events than traditional diastolic parameters [88]. Greater systolic dysfunction has been associated with lower post-contrast T_1, an index of fibrosis, using the modified look-locker inversion-recovery sequence [89]. Both lower myocardial perfusion reserve [90] and LV hypertrophy [91] have been associated with reduced systolic circumferential myocardial strain.

Torsion has been used to study diseases in which the myofiber architecture is disrupted. For example, in situs inversus totalis, the apical and epicardial basal fiber orientation is normal but the deeper basal fibers have an inverted fiber orientation, leading to a change in sign in torsion from apex to base [92]. The torsion-to-shortening ratio [78], an index of regional function, is increased in patients with aortic stenosis [78] and also increases with age [93] and hypertension [94]. One mechanism for increased torsion-to-shortening ratio is reduced sub-endocardial fiber shortening. Increased torsion and torsion to shortening ratio was found in hypertrophic cardiomyopathy mutation carriers with normal wall thickness, indicating preclinical subendocardial dysfunction [95].

Feature tracking estimation of strain in SSFP untagged cine images has proven useful in characterizing the status of tissue function independent of chamber geometry. This method has elucidated ventricular strain abnormalities in Duchenne's muscular dystrophy [96], hypertrophic cardiomyopathy [97], coarctation repair [98], tetralogy of Fallot [99], Churg-Strauss syndrome [100], single ventricle [101], and myocardial infarction [102]. More recently, local feature tracking strain estimates have been used in patients with marked regional abnormalities, for example in detecting local functional reserve in patients with ischemic cardiomyopathy [103].

Cardiac MRI is also being used in several large prospective population studies, to investigate imaging-based biomarkers of incipient disease. The MESA study used cardiac MRI to examine the progression of disease in asymptomatic volunteers [104], to augment the traditional risk factors established by previous population-based studies, including the Framingham study [105]. For example, reduced long axis strain from cine MRI has been shown to be associated with higher risk of future heart failure and other adverse events [106]. The UK Biobank is also using imaging in a large population study. Over 500,000 participants are enrolled in the main study, and 100,000 participants will be studied with brain, heart and abdominal MRI over the next 5 years [107, 108].

Principal component analysis shape modelling has been applied in the MESA study, showing significant differences between groups with different risk factors, including alcohol and smoking [66]. Combining component scores with linear discriminant analysis showed how these components could be used to determine subtle differences in shape due to traditional risk factors, and are more sensitive than the standard clinical indices of mass and volume [67]. Dimension reduction methods can also be applied in a supervised way to learn shape components that change between patient groups [68]. As shown in Fig. 1.4, an information-maximizing discriminant analysis resulted in a single shape mode able to distinguish patients with myocardial infarction with 95% accuracy [68]. These methods can be extended to the analysis of both left and right ventricle, which has particular application in children with congenital heart disease. An extension to biventricular analysis, modelling both left and right ventricles along with the four inlet and outlet valves has been developed for rapid analysis of patients with congenital heart disease [109]. This method incorporated a fast real-time solution in response to interactive edits, using a preconditioned iterative solver with polar predicted points and a regularisation

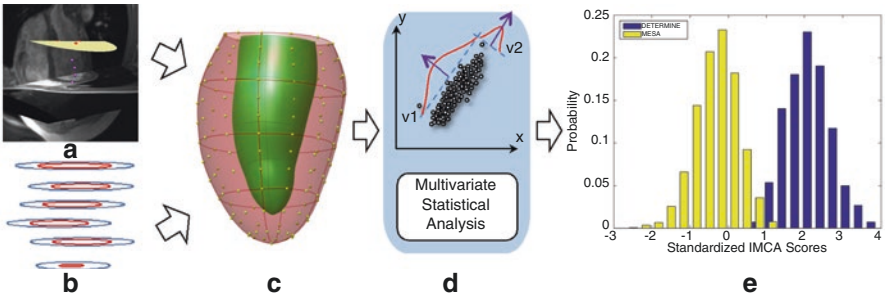

Fig. 1.4 Flow chart of the shape analysis: (**a**) fiducial landmarks defined on the images (3D view from anterior). (**b**) Contours drawn manually. (**c**) 3D finite element model after correction for breath-hold misregistration, showing shape control points (*yellow*). (**d**) Calculation of remodelling indices. (**e**) Variation in one remodelling component (information maximizing component analysis or IMCA) showing z-score distributions in asymptomatic (MESA) vs myocardial infarction patients (DETERMINE) [68]

method which penalized non-affine deformations [110]. Several templates have been constructed to describe characteristic congenital pathologies, such as congenitally corrected transposition of the great arteries, so that different shapes and configurations can be interactively customised to MRI data [9].

Discussion and Future Directions

Cardiac MRI methods enable detailed and extensive examination of the underlying pathophysiological changes and adaptations due to cardiovascular disease. Atlas-based methods show considerable promise for quantifying these changes in healthy and diseased regional wall motion. These methods enable quantitative evaluation of shape and function against population norms derived from the MESA study or the UK Biobank. Advances in imaging are also occurring, and 3D cine SSFP acquisitions using advanced reconstruction methods are now becoming more widely available.

References

1. Kerckhoffs RC. Computational modeling of cardiac growth in the post-natal rat with a strain-based growth law. J Biomech. 2012;45(5):865–71.
2. Kerckhoffs RC, Omens J, McCulloch AD. A single strain-based growth law predicts concentric and eccentric cardiac growth during pressure and volume overload. Mech Res Commun. 2012;42:40–50.
3. Reddy YN, Borlaug BA. Heart failure with preserved ejection fraction. Curr Probl Cardiol. 2016;41(4):145–88.
4. Owan TE, Hodge DO, Herges RM, Jacobsen SJ, Roger VL, Redfield MM. Trends in prevalence and outcome of heart failure with preserved ejection fraction. N Engl J Med. 2006;355(3):251–9.
5. Iwanaga Y, Nishi I, Furuichi S, Noguchi T, Sase K, Kihara Y, Goto Y, Nonogi H. B-type natriuretic peptide strongly reflects diastolic wall stress in patients with chronic heart failure: comparison between systolic and diastolic heart failure. J Am Coll Cardiol. 2006; 47(4):742–8.
6. White HD. Pathobiology of troponin elevations: do elevations occur with myocardial ischemia as well as necrosis? J Am Coll Cardiol. 2011;57(24):2406–8.
7. Lauterbur PC. Image formation by induced local interactions. Examples employing nuclear magnetic resonance. Nature. 1973;242:190–1.
8. Feng L, Axel L, Chandarana H, Block KT, Sodickson DK, Otazo R. XD-GRASP: golden-angle radial MRI with reconstruction of extra motion-state dimensions using compressed sensing. Magn Reson Med. 2016;75(2):775–88.
9. Gilbert K, Farrar G, Cowan BR, Suinesiaputra A, Occleshaw C, Pontre B, Perry J, Hegde S, Marsden A, Omens J, McCulloch A, Young AA. Creating shape templates for patient specific biventricular modeling in congenital heart disease. Conf Proc IEEE Eng Med Biol Soc. 2015;2015:679–82.
10. Arnold JR, Karamitsos TD, Bhamra-Ariza P, Francis JM, Searle N, Robson MD, Howells RK, Choudhury RP, Rimoldi OE, Camici PG, Banning AP, Neubauer S, Jerosch-Herold M, Selvanayagam JB. Myocardial oxygenation in coronary artery disease: insights from blood oxygen level-dependent magnetic resonance imaging at 3 Tesla. J Am Coll Cardiol. 2012;59(22):1954–64.
11. Carr JC, Simonetti O, Bundy J, Li D, Pereles S, Finn JP. Cine MR angiography of the heart with segmented true fast imaging with steady-state precession. Radiology. 2001;219(3):828–34.
12. Kramer CM, Barkhausen J, Flamm SD, Kim RJ, Nagel E. Standardized cardiovascular magnetic resonance (CMR) protocols 2013 update. J Cardiovasc Magn Reson. 2013;15:91.
13. Lustig M, Donoho D, Pauly JM. Sparse MRI: the application of compressed sensing for rapid MR imaging. Magn Reson Med. 2007;58(6):1182–95.
14. Simpson RM, Keegan J, Firmin DN. MR assessment of regional myocardial mechanics. J Magn Reson Imaging. 2013;37(3):576–99.
15. Axel L, Dougherty L. MR imaging of motion with spatial modulation of magnetization. Radiology. 1989;171(3):841–5.
16. Axel L, Dougherty L. Heart wall motion: improved method of spatial modulation of magnetization for MR imaging. Radiology. 1989;172(2):349–50.
17. Zwanenburg JJ, Kuijer JP, Marcus JT, Heethaar RM. Steady-state free precession with myocardial tagging: CSPAMM in a single breathhold. Magn Reson Med. 2003;49(4):722–30.
18. Young AA, Li B, Kirton RS, Cowan BR. Generalized spatiotemporal myocardial strain analysis for DENSE and SPAMM imaging. Magn Reson Med. 2012;67(6):1590–9.
19. Aletras AH, Ding S, Balaban RS, Wen H. DENSE: displacement encoding with stimulated echoes in cardiac functional MRI. J Magn Reson. 1999;137(1):247–52.

20. Kim D, Gilson WD, Kramer CM, Epstein FH. Myocardial tissue tracking with two-dimensional cine displacement-encoded MR imaging: development and initial evaluation. Radiology. 2004;230(3):862–71.
21. Kuijer JP, Hofman MB, Zwanenburg JJ, Marcus JT, van Rossum AC, Heethaar RM. DENSE and HARP: two views on the same technique of phase-based strain imaging. J Magn Reson Imaging. 2006;24(6):1432–8.
22. Pelc NJ, Sommer FG, Li KC, Brosnan TJ, Herfkens RJ, Enzmann DR. Quantitative magnetic resonance flow imaging. Magn Reson Q. 1994;10(3):125–47.
23. Bock J, Frydrychowicz A, Stalder AF, Bley TA, Burkhardt H, Hennig J, Markl M. 4D phase contrast MRI at 3 T: effect of standard and blood-pool contrast agents on SNR, PC-MRA, and blood flow visualization. Magn Reson Med. 2009;63(2):330–8.
24. Bock M, Schad LR, Muller E, Lorenz WJ. Pulsewave velocity measurement using a new real-time MR-method. Magn Reson Imaging. 1995;13(1):21–9.
25. Roberts PA, Cowan BR, Liu Y, Lin AC, Nielsen PM, Taberner AJ, Stewart RA, Lam HI, Young AA. Real-time aortic pulse wave velocity measurement during exercise stress testing. J Cardiovasc Magn Reson. 2015;17(1):86.
26. Longmore DB, Klipstein RH, Underwood SR, Bland C, Poole-Wilson PA, Denison D, Klipstein RH, Firmin DN, Watanabe M, Fox K, Rees RSO, Mcneilly AM, Burman ED. Dimensional accuracy of magnetic resonance in studies of the heart. Lancet. 1985;1:1360–2.
27. Bloomer TN, Plein S, Radjenovic A, Higgins DM, Jones TR, Ridgway JP, Sivananthan MU. Cine MRI using steady state free precession in the radial long axis orientation is a fast accurate method for obtaining volumetric data of the left ventricle. J Magn Reson Imaging. 2001;14(6):685–92.
28. Rogers Jr WJ, Shapiro EP, Weiss JL, Buchalter MB, Rademakers FE, Weisfeldt ML, Zerhouni EA. Quantification of and correction for left ventricular systolic long-axis shortening by magnetic resonance tissue tagging and slice isolation. Circulation. 1991;84(2):721–31.
29. Hudsmith LE, Petersen SE, Francis JM, Robson MD, Neubauer S. Normal human left and right ventricular and left atrial dimensions using steady state free precession magnetic resonance imaging. J Cardiovasc Magn Reson. 2005;7(5):775–82.
30. Hung J, Francois C, Nelson NA, Young A, Cowan BR, Jerecic R, Carr J. Cardiac image modeling tool for quantitative analysis of global and regional cardiac wall motion. Investig Radiol. 2009;44(5):271–8.
31. Young AA, Cowan BR, Thrupp SF, Hedley WJ, Dell'Italia LJ. Left ventricular mass and volume: fast calculation with guide-point modeling on MR images. Radiology. 2000;216(2):597–602.
32. Captur G, Muthurangu V, Cook C, Flett AS, Wilson R, Barison A, Sado DM, Anderson S, McKenna WJ, Mohun TJ, Elliott PM, Moon JC. Quantification of left ventricular trabeculae using fractal analysis. J Cardiovasc Magn Reson. 2013;15:36.
33. Sievers B, Schrader S, Rehwald W, Hunold P, Barkhausen J, Erbel R. Left ventricular function assessment using a fast 3D gradient echo pulse sequence: comparison to standard multi-breath hold 2D steady state free precession imaging and accounting for papillary muscles and trabeculations. Acta Cardiol. 2011;66(3):349–57.
34. Schulz-Menger J, Bluemke DA, Bremerich J, Flamm SD, Fogel MA, Friedrich MG, Kim RJ, von Knobelsdorff-Brenkenhoff F, Kramer CM, Pennell DJ, Plein S, Nagel E. Standardized image interpretation and post processing in cardiovascular magnetic resonance: Society for Cardiovascular Magnetic Resonance (SCMR) board of trustees task force on standardized post processing. J Cardiovasc Magn Reson. 2013;15:35.
35. Karamitsos TD, Hudsmith LE, Selvanayagam JB, Neubauer S, Francis JM. Operator induced variability in left ventricular measurements with cardiovascular magnetic resonance is improved after training. J Cardiovasc Magn Reson. 2007;9(5):777–83.
36. Suinesiaputra A, Bluemke DA, Cowan BR, Friedrich MG, Kramer CM, Kwong R, Plein S, Schulz-Menger J, Westenberg JJ, Young AA, Nagel E. Quantification of LV function and

mass by cardiovascular magnetic resonance: multi-center variability and consensus contours. J Cardiovasc Magn Reson. 2015;17(1):63.
37. Cerqueira MD, Weissman NJ, Dilsizian V, Jacobs AK, Kaul S, Laskey WK, Pennell DJ, Rumberger JA, Ryan T, Verani MS. Standardized myocardial segmentation and nomenclature for tomographic imaging of the heart. A statement for healthcare professionals from the Cardiac Imaging Committee of the Council on Clinical Cardiology of the American Heart Association. Circulation. 2002;105(4):539–42.
38. Jahnke C, Nagel E, Gebker R, Kokocinski T, Kelle S, Manka R, Fleck E, Paetsch I. Prognostic value of cardiac magnetic resonance stress tests: adenosine stress perfusion and dobutamine stress wall motion imaging. Circulation. 2007;115(13):1769–76.
39. Medrano-Gracia P, Suinesiaputra A, Cowan B, Bluemke D, Frangi A, Lee DC, Lima J, Young AA. An atlas for cardiac MRI regional wall motion and infarct scoring. In: Camara O, Mansi T, Pop M, Rhode K, Sermesant M, Young AA (eds) Statistical atlases and computational models of the heart. Imaging and modelling challenges. Lecture Notes in Computer Science. Spinger, Berlin; 2013. p. 188–97.
40. Duchateau N, De Craene M, Allain P, Saloux E, Sermesant M. Infarct localization from myocardial deformation: prediction and uncertainty quantification by regression from a low-dimensional space. IEEE Trans Med Imaging. 2016;35:2340–52.
41. Petitjean C, Dacher JN. A review of segmentation methods in short axis cardiac MR images. Med Image Anal. 2011;15(2):169–84.
42. Bai W, Shi W, Ledig C, Rueckert D. Multi-atlas segmentation with augmented features for cardiac MR images. Med Image Anal. 2015;19(1):98–109.
43. Tran PV (2016) A fully convolutional neural network for cardiac segmentation in short-axis MRI. arXiv 1604.00494.
44. Avendi MR, Kheradvar A, Jafarkhani H. A combined deep-learning and deformable-model approach to fully automatic segmentation of the left ventricle in cardiac MRI. Med Image Anal. 2016;30:108–19.
45. Suinesiaputra A, Cowan BR, Al-Agamy AO, AlAttar MA, Ayache N, Fahmy AS, Khalifa AM, Medrano-Gracia P, Jolly MP, Kadish AH, Lee DC, Margeta J, Warfield SK, Young AA. A collaborative resource to build consensus for automated left ventricular segmentation of cardiac MR images. Med Image Anal. 2014;18(1):50–62.
46. Bollache ERA, Clément-Guinaudeau S, Defrance C, Perdrix L, Ladouceur M, Lefort M, De Cesare A, Herment A, Diebold B, Mousseaux E, Kachenoura N. Automated left ventricular diastolic function evaluation from phase-contrast cardiovascular magnetic resonance and comparison with Doppler echocardiography. J Cardiovasc Magn Reson. 2010;12:63.
47. Maceira AM, Prasad SK, Khan M, Pennell DJ. Normalized left ventricular systolic and diastolic function by steady state free precession cardiovascular magnetic resonance. J Cardiovasc Magn Reson. 2006;8(3):417–26.
48. Maceira AM, Prasad SK, Khan M, Pennell DJ. Reference right ventricular systolic and diastolic function normalized to age, gender and body surface area from steady-state free precession cardiovascular magnetic resonance. Eur Heart J. 2006;27:2879–88.
49. Li B, Liu Y, Occleshaw CJ, Cowan BR, Young AA. In-line automated tracking for ventricular function with magnetic resonance imaging. JACC Cardiovasc Imaging. 2010;3(8):860–6.
50. Ibrahim E-SH. Myocardial tagging by cardiovascular magnetic resonance: evolution of techniques – pulse sequences, analysis algorithms, and applications. J Cardiovasc Magn Reson. 2011;13:36.
51. Dougherty L, Asmuth JC, Blom AS, Axel L, Kumar R. Validation of an optical flow method for tag displacement estimation. IEEE Trans Med Imaging. 1999;18(4):359–63.
52. Osman NF, Kerwin WS, McVeigh ER, Prince JL. Cardiac motion tracking using CINE harmonic phase (HARP) magnetic resonance imaging. Magn Reson Med. 1999;42(6): 1048–60.
53. Osman NF, McVeigh ER, Prince JL. Imaging heart motion using harmonic phase MRI. IEEE Trans Med Imaging. 2000;19(3):186–202.

54. Arts T, Prinzen FW, Delhaas T, Milles JR, Rossi AC, Clarysse P. Mapping displacement and deformation of the heart with local sine-wave modeling. IEEE Trans Med Imaging. 2010;29(5):1114–23.
55. Miller CA, Borg A, Clark D, Steadman CD, McCann GP, Clarysse P, Croisille P, Schmitt M. Comparison of local sine wave modeling with harmonic phase analysis for the assessment of myocardial strain. J Magn Reson Imaging. 2013;38(2):320–8.
56. Spottiswoode BS, Zhong X, Hess AT, Kramer CM, Meintjes EM, Mayosi BM, Epstein FH. Tracking myocardial motion from cine DENSE images using spatiotemporal phase unwrapping and temporal fitting. IEEE Trans Med Imaging. 2007;26(1):15–30.
57. Suever JD, Wehner GJ, Haggerty CM, Jing L, Hamlet SM, Binkley CM, Kramer SP, Mattingly AC, Powell DK, Bilchick KC, Epstein FH, Fornwalt BK. Simplified post processing of cine DENSE cardiovascular magnetic resonance for quantification of cardiac mechanics. J Cardiovasc Magn Reson. 2014;16:94.
58. Wehner GJ, Suever JD, Haggerty CM, Jing L, Powell DK, Hamlet SM, Grabau JD, Mojsejenko WD, Zhong X, Epstein FH, Fornwalt BK. Validation of in vivo 2D displacements from spiral cine DENSE at 3 T. J Cardiovasc Magn Reson. 2015;17(1):5.
59. Auger DA, Zhong X, Epstein FH, Meintjes EM, Spottiswoode BS. Semi-automated left ventricular segmentation based on a guide point model approach for 3D cine DENSE cardiovascular magnetic resonance. J Cardiovasc Magn Reson. 2014;16:8.
60. Moody WE, Taylor RJ, Edwards NC, Chue CD, Umar F, Taylor TJ, Ferro CJ, Young AA, Townend JN, Leyva F, Steeds RP. Comparison of magnetic resonance feature tracking for systolic and diastolic strain and strain rate calculation with spatial modulation of magnetization imaging analysis. J Magn Reson Imaging. 2015;41(4):1000–12.
61. Augustine D, Lewandowski AJ, Lazdam M, Rai A, Francis J, Myerson S, Noble A, Becher H, Neubauer S, Petersen SE, Leeson P. Global and regional left ventricular myocardial deformation measures by magnetic resonance feature tracking in healthy volunteers: comparison with tagging and relevance of gender. J Cardiovasc Magn Reson. 2013;15(1):8.
62. Cowan BR, Peereboom SM, Greiser A, Guehring J, Young AA. Image feature determinants of global and segmental circumferential ventricular strain from cine CMR. JACC Cardiovasc Imaging. 2015;8(12):1465–6. doi:10.1016/j.jcmg.2014.10.005.
63. Young AA, Cowan BR. Evaluation of left ventricular torsion by cardiovascular magnetic resonance. J Cardiovasc Magn Reson. 2012;14:49.
64. Arts T, Reneman RS, Veenstra PC. A model of the mechanics of the left ventricle. Ann Biomed Eng. 1979;7(3–4):299–318.
65. Rijcken J, Bovendeerd PH, Schoofs AJ, van Campen DH, Arts T. Optimization of cardiac fiber orientation for homogeneous fiber strain during ejection. Ann Biomed Eng. 1999;27(3):289–97.
66. Medrano-Gracia P, Cowan BR, Ambale-Venkatesh B, Bluemke DA, Eng J, Finn JP, Fonseca CG, Lima JAC, Suinesiaputra A, Young AA. Left ventricular shape variation in asymptomatic populations: the Multi-Ethnic Study of Atherosclerosis. J Cardiovasc Magn Reson. 2014;16:56.
67. Zhang X, Cowan BR, Bluemcke DA, Finn JP, Fonseca CG, Kadish AH, Lee DC, Lima JAC, Suinesiaputra A, Young AA, Medrano-Gracia P. Atlas-based quantification of cardiac remodeling due to myocardial infarction. PLoS One. 2014;9(10):e110243.
68. Zhang X, Ambale-Venkatesh B, Bluemcke DA, Cowan BR, Finn JP, Fonseca CG, Kadish AH, Lee DC, Lima JAC, Hundley WG, Suinesiaputra A, Young AA, Medrano-Gracia P. Information maximizing component analysis of left ventricular remodeling due to myocardial infarction. J Transl Med. 2015;3(13):343.
69. Chalil S, Stegemann B, Muhyaldeen S, Khadjooi K, Smith RE, Jordan PJ, Leyva F. Intraventricular dyssynchrony predicts mortality and morbidity after cardiac resynchronization therapy: a study using cardiovascular magnetic resonance tissue synchronization imaging. J Am Coll Cardiol. 2007;50(3):243–52.
70. Wang VY, Nielsen PM, Nash MP. Image-based predictive modeling of heart mechanics. Annu Rev Biomed Eng. 2015;17:351–83.

71. Marchesseau S, Delingette H, Sermesant M, Cabrera-Lozoya R, Tobon-Gomez C, Moireau P, Figueras i Ventura RM, Lekadir K, Hernandez A, Garreau M, Donal E, Leclercq C, Duckett SG, Rhode K, Rinaldi CA, Frangi AF, Razavi R, Chapelle D, Ayache N. Personalization of a cardiac electromechanical model using reduced order unscented Kalman filtering from regional volumes. Med Image Anal. 2013;17(7):816–29.
72. Chabiniok R, Wang VY, Hadjicharalambous M, Asner L, Lee J, Sermesant M, Kuhl E, Young AA, Moireau P, Nash MP, Chapelle D, Nordsletten DA. Multiphysics and multiscale modelling, data–model fusion and integration of organ physiology in the clinic: ventricular cardiac mechanics. Interface Focus. 2016;6:20150083.
73. Wang VY, Lam HI, Ennis DB, Cowan BR, Young AA, Nash MP. Modelling passive diastolic mechanics with quantitative MRI of cardiac structure and function. Med Image Anal. 2009;13(5):773–84.
74. Krishnamurthy A, Villongco CT, Chuang J, Frank LR, Nigam V, Belezzuoli E, Stark P, Krummen DE, Narayan S, Omens JH, McCulloch AD, Kerckhoffs RC. Patient-specific models of cardiac biomechanics. J Comput Phys. 2013;244:4–21.
75. Meoli A, Cutri E, Krishnamurthy A, Dubini G, Migliavacca F, Hsia TY, Pennati G, Modeling of Congenital Hearts Alliance G, Taylor A, Giardini A, Khambadkone S, Schievano S, de Leval M, Hsia TY, Bove E, Dorfman A, Baker GH, Hlavacek A, Migliavacca F, Pennati G, Dubini G, Marsden A, Feinstein J, Vignon-Clementel I, Figliola R, McGregor J. A multiscale model for the study of cardiac biomechanics in single-ventricle surgeries: a clinical case. Interface Focus. 2015;5(2):20140079.
76. Fallah-Rad N, Walker JR, Wassef A, Lytwyn M, Bohonis S, Fang T, Tian G, Kirkpatrick ID, Singal PK, Krahn M, Grenier D, Jassal DS. The utility of cardiac biomarkers, tissue velocity and strain imaging, and cardiac magnetic resonance imaging in predicting early left ventricular dysfunction in patients with human epidermal growth factor receptor II-positive breast cancer treated with adjuvant trastuzumab therapy. J Am Coll Cardiol. 2011;57(22):2263–70.
77. Young AA, Kramer CM, Ferrari VA, Axel L, Reichek N. Three-dimensional left ventricular deformation in hypertrophic cardiomyopathy. Circulation. 1994;90(2):854–67.
78. Delhaas T, Kotte J, van der Toorn A, Snoep G, Prinzen FW, Arts T. Increase in left ventricular torsion-to-shortening ratio in children with valvular aortic stenosis. Magn Reson Med. 2004;51(1):135–9.
79. Biederman RW, Doyle M, Young AA, Devereux RB, Kortright E, Perry G, Bella JN, Oparil S, Calhoun D, Pohost GM, Dell'Italia LJ. Marked regional left ventricular heterogeneity in hypertensive left ventricular hypertrophy patients: a losartan intervention for endpoint reduction in hypertension (LIFE) cardiovascular magnetic resonance and echocardiographic substudy. Hypertension. 2008;52(2):279–86.
80. Kuijpers D, Ho KY, van Dijkman PR, Vliegenthart R, Oudkerk M. Dobutamine cardiovascular magnetic resonance for the detection of myocardial ischemia with the use of myocardial tagging. Circulation. 2003;107(12):1592–7.
81. Bove CM, DiMaria JM, Voros S, Conaway MR, Kramer CM. Dobutamine response and myocardial infarct transmurality: functional improvement after coronary artery bypass grafting-initial experience. Radiology. 2006;240(3):835–41.
82. Fogel MA, Weinberg PM, Hubbard A, Haselgrove J. Diastolic biomechanics in normal infants utilizing MRI tissue tagging. Circulation. 2000;102(2):218–24.
83. Rosen BD, Gerber BL, Edvardsen T, Castillo E, Amado LC, Nasir K, Kraitchman DL, Osman NF, Bluemke DA, Lima JA. Late systolic onset of regional LV relaxation demonstrated in three-dimensional space by MRI tissue tagging. Am J Physiol Heart Circ Physiol. 2004;287(4):H1740–6.
84. Rosen BD, Edvardsen T, Lai S, Castillo E, Pan L, Jerosch-Herold M, Sinha S, Kronmal R, Arnett D, Crouse 3rd JR, Heckbert SR, Bluemke DA, Lima JA. Left ventricular concentric remodeling is associated with decreased global and regional systolic function: the Multi-Ethnic Study of Atherosclerosis. Circulation. 2005;112(7):984–91.
85. Biederman RW, Young AA, Doyle M, Devereux RB, Kortright E, Perry G, Bella JN, Oparil S, Calhoun D, Pohost GM, Dell'Italia LJ. Regional heterogeneity in 3D myocardial shorten-

ing in hypertensive left ventricular hypertrophy: a cardiovascular CMR tagging substudy to the life study. J Biomed Sci Eng. 2015;8(3):213–25.
86. Young AA, Dokos S, Powell KA, Sturm B, McCulloch AD, Starling RC, McCarthy PM, White RD. Regional heterogeneity of function in nonischemic dilated cardiomyopathy. Cardiovasc Res. 2001;49(2):308–18.
87. Fernandes VR, Polak JF, Edvardsen T, Carvalho B, Gomes A, Bluemke DA, Nasir K, O'Leary DH, Lima JA. Subclinical atherosclerosis and incipient regional myocardial dysfunction in asymptomatic individuals: the Multi-Ethnic Study of Atherosclerosis (MESA). J Am Coll Cardiol. 2006;47(12):2420–8.
88. Ambale-Venkatesh B, Armstrong AC, Liu CY, Donekal S, Yoneyama K, Wu CO, Gomes AS, Hundley GW, Bluemke DA, Lima JA. Diastolic function assessed from tagged MRI predicts heart failure and atrial fibrillation over an 8-year follow-up period: the Multi-Ethnic Study of Atherosclerosis. Eur Heart J Cardiovasc Imaging. 2014;15(4):442–9.
89. Donekal S, Venkatesh BA, Liu YC, Liu CY, Yoneyama K, Wu CO, Nacif M, Gomes AS, Hundley WG, Bluemke DA, Lima JA. Interstitial fibrosis, left ventricular remodeling, and myocardial mechanical behavior in a population-based multiethnic cohort: the Multi-Ethnic Study of Atherosclerosis (MESA) study. Circ Cardiovasc Imaging. 2014;7(2):292–302.
90. Rosen BD, Lima JA, Nasir K, Edvardsen T, Folsom AR, Lai S, Bluemke DA, Jerosch-Herold M. Lower myocardial perfusion reserve is associated with decreased regional left ventricular function in asymptomatic participants of the multi-ethnic study of atherosclerosis. Circulation. 2006;114(4):289–97.
91. Rosen BD, Saad MF, Shea S, Nasir K, Edvardsen T, Burke G, Jerosch-Herold M, Arnett DK, Lai S, Bluemke DA, Lima JA. Hypertension and smoking are associated with reduced regional left ventricular function in asymptomatic: individuals the Multi-Ethnic Study of Atherosclerosis. J Am Coll Cardiol. 2006;47(6):1150–8.
92. Delhaas T, Kroon W, Bovendeerd P, Arts T. Left ventricular apical torsion and architecture are not inverted in situs inversus totalis. Prog Biophys Mol Biol. 2008;97(2–3):513–9.
93. Lumens J, Delhaas T, Arts T, Cowan BR, Young AA. Impaired subendocardial contractile myofiber function in asymptomatic aged humans, as detected using MRI. Am J Physiol Heart Circ Physiol. 2006;291(4):H1573–9.
94. Yoneyama K, Gjesdal O, Choi EY, Wu CO, Hundley WG, Gomes AS, Liu CY, McClelland RL, Bluemke DA, Lima JA. Age, sex, and hypertension-related remodeling influences left ventricular torsion assessed by tagged cardiac magnetic resonance in asymptomatic individuals: the multi-ethnic study of atherosclerosis. Circulation. 2012;126(21):2481–90.
95. Russel IK, Brouwer WP, Germans T, Knaapen P, Marcus JT, van der Velden J, Gotte MJ, van Rossum AC. Increased left ventricular torsion in hypertrophic cardiomyopathy mutation carriers with normal wall thickness. J Cardiovasc Magn Reson. 2011;13:3.
96. Hor KN, Gottliebson WM, Carson C, Wash E, Cnota J, Fleck R, Wansapura J, Klimeczek P, Al-Khalidi HR, Chung ES, Benson DW, Mazur W. Comparison of magnetic resonance feature tracking for strain calculation with harmonic phase imaging analysis. JACC Cardiovasc Imaging. 2010;3(2):144–51.
97. Harrild DM, Han Y, Geva T, Zhou J, Marcus E, Powell AJ. Comparison of cardiac MRI tissue tracking and myocardial tagging for assessment of regional ventricular strain. Int J Card Imaging. 2012;28(8):2009–18. doi:10.1007/s10554-012-0035-3.
98. Kutty S, Rangamani S, Venkataraman J, Li L, Schuster A, Fletcher SE, Danford DA, Beerbaum P. Reduced global longitudinal and radial strain with normal left ventricular ejection fraction late after effective repair of aortic coarctation: a CMR feature tracking study. Int J Card Imaging. 2013;29(1):141–50.
99. Kempny A, Fernandez-Jimenez R, Orwat S, Schuler P, Bunck AC, Maintz D, Baumgartner H, Diller GP. Quantification of biventricular myocardial function using cardiac magnetic resonance feature tracking, endocardial border delineation and echocardiographic speckle tracking in patients with repaired tetralogy of Fallot and healthy controls. J Cardiovasc Magn Reson. 2012;14:32.

100. Szczeklik W, Miszalski-Jamka T, Mastalerz L, Sokolowska B, Dropinski J, Banys R, Hor KN, Mazur W, Musial J. Multimodality assessment of cardiac involvement in Churg-Strauss syndrome patients in clinical remission. Circ J. 2011;75(3):649–55.
101. Truong UT, Li X, Broberg CS, Houle H, Schaal M, Ashraf M, Kilner P, Sheehan FH, Sable CA, Ge S, Sahn DJ. Significance of mechanical alterations in single ventricle patients on twisting and circumferential strain as determined by analysis of strain from gradient cine magnetic resonance imaging sequences. Am J Cardiol. 2010;105(10):1465–9.
102. Maret E, Todt T, Brudin L, Nylander E, Swahn E, Ohlsson JL, Engvall JE. Functional measurements based on feature tracking of cine magnetic resonance images identify left ventricular segments with myocardial scar. Cardiovasc Ultrasound. 2009;7:53.
103. Schuster A, Paul M, Bettencourt N, Morton G, Chiribiri A, Ishida M, Hussain S, Jogiya R, Kutty S, Bigalke B, Perera D, Nagel E. Cardiovascular magnetic resonance myocardial feature tracking for quantitative viability assessment in ischemic cardiomyopathy. Int J Cardiol. 2011;166:413–20.
104. Bild DE, Bluemke DA, Burke GL, Detrano R, Diez Roux AV, Folsom AR, Greenland P, Jacob Jr DR, Kronmal R, Liu K, Nelson JC, O'Leary D, Saad MF, Shea S, Szklo M, Tracy RP. Multi-ethnic study of atherosclerosis: objectives and design. Am J Epidemiol. 2002; 156(9):871–81.
105. Bluemke DA, Kronmal RA, Lima JA, Liu K, Olson J, Burke GL, Folsom AR. The relationship of left ventricular mass and geometry to incident cardiovascular events: the MESA (Multi-Ethnic Study of Atherosclerosis) study. J Am Coll Cardiol. 2008;52(25):2148–55.
106. Gjesdal O, Yoneyama K, Mewton N, Wu C, Gomes AS, Hundley G, Prince M, Shea S, Liu K, Bluemke DA, Lima JA. Reduced long axis strain is associated with heart failure and cardiovascular events in the multi-ethnic study of Atherosclerosis. J Magn Reson Imaging. 2016;44(1):178–85.
107. Petersen SE, Matthews PM, Bamberg F, Bluemke DA, Francis JM, Friedrich MG, Leeson P, Nagel E, Plein S, Rademakers FE, Young AA, Garratt S, Peakman T, Sellors J, Collins R, Neubauer S. Imaging in population science: cardiovascular magnetic resonance in 100,000 participants of UK Biobank – rationale, challenges and approaches. J Cardiovasc Magn Reson. 2013;15(1):46.
108. Petersen SE, Matthews PM, Francis JM, Robson MD, Zemrak F, Boubertakh R, Young AA, Hudson S, Weale P, Garratt S, Collins R, Piechnik S, Neubauer S. UK Biobank's cardiovascular magnetic resonance protocol. J Cardiovasc Magn Reson. 2016;18:8.
109. Gilbert K, Lam HI, Pontre B, Cowan BR, Occleshaw CJ, Liu JY, Young AA. An interactive tool for rapid biventricular analysis of congenital heart disease. Clin Physiol Funct Imaging. 2015. doi:10.1111/cpf.12319.
110. Gilbert K, Cowan BR, Suinesiaputra A, Occleshaw C, Young AA. Rapid D-affine biventricular cardiac function with polar prediction. Paper presented at the Medical Image Computing and Computer-Assisted Intervention Boston. 2014.

Chapter 2
Quantification of Regional Ventricular Wall Motion in Laboratory Animals

Kai Jiang and Xin Yu

Abbreviations

2D	Two-dimensional
3D	Three-dimensional
ADC	Analog-to-digital converter
CANSEL	Cosine and sine modulation to eliminate
CF	Cystic fibrosis
CFTR	Cystic fibrosis transmembrane conductance regulator
CMR	Cardiac magnetic resonance
cMyBPC	Cardiac myosin binding protein C
CNR	Contrast-to-noise ratio
CSPAMM	Complementary spatial modulation of magnetization
DANTE	Delay alternating with nutations for tailored excitation
DENSE	Displacement encoding with stimulated echoes
ECG	Electrocardiogram
FE	Frequency-encoding
HARP	Harmonic phase
HCM	Hypertrophic cardiomyopathy
LAD	Left anterior descending
LV	Left-ventricular
MI	Myocardial infarction
MRI	Magnetic resonance imaging

K. Jiang, PhD
Division of Nephrology and Hypertension, Mayo Clinic, Rochester, MN, USA

X. Yu, ScD (✉)
Departments of Biomedical Engineering, Case Western Reserve University, Cleveland, OH, USA
e-mail: Xin.Yu@case.edu

C. Constantinides (ed.), *Protocols and Methodologies in Basic Science and Clinical Cardiac MRI*, https://doi.org/10.1007/978-3-319-53001-7_2

PE	Phase-encoding
PKC-ε	Cardiac specific protein kinase C-ε
RF	Radio-frequency
SENC	Strain-encoded
SNR	Signal-to-noise ratio
SPAMM	Spatial modulation of magnetization
SS	Slice-selection

Introduction

Assessment of ventricular function remains an important part of clinical cardiology. To date, clinical practice has largely focused on the quantification of the global functional parameters such as ejection fraction and cardiac output. However, with the development of cardiac magnetic resonance (CMR) imaging techniques and speckle tracking echocardiography, parameters that describe regional myocardial wall motion have been recognized as more sensitive indicators of early-stage functional alterations.

CMR offers the possibility for high-resolution and accurate delineation of cardiac anatomy and function without ionizing radiation. Over the past three decades, several CMR imaging techniques have been developed for the measurement of regional myocardial wall motion, including myocardial tissue tagging [1–3], displacement encoding with stimulated echoes (DENSE) [4], phase contrast [5], and strain encoded imaging [6]. These techniques have enabled a better understanding of cardiac wall motion mechanics, as well as the development of ventricular dysfunction in disease progression.

Laboratory animals, especially rodents such as mice and rats, play an important role in our understanding of heart mechanics and investigation of cardiovascular diseases. The development of genetic engineering technology has brought forth a wide variety of genetically manipulated mouse models, which have gained increasing popularity as a prominent tool for the understanding of human cardiac diseases in the past two decades or so. The translation of CMR technology to the characterization of these mouse models has enabled the understanding of the molecular mechanisms responsible for altered cardiac function.

Cardiac imaging of small laboratory animals faces challenges that are different from those in imaging human patients. First, owing to the small size of a rodent heart, the requirement for spatial resolution is an order of magnitude higher. Second, the heart rate of a mouse is also about an order of magnitude higher than that of a human patient. A conscious adult mouse typically has a heart rate of about 600 beats per minute [7]. Finally, the animals are usually kept under anesthesia during MRI scan, which can induce significant changes in hemodynamics, body temperature, heart rate, etc. Hence, care must be taken to maintain the normal physiological conditions such that functional measurements by CMR are physiologically relevant [8].

In this chapter, we will mainly focus on the two extensively used and closely related CMR techniques, i.e., tissue tagging and DENSE, and their applications to

the characterization of small animals. An important post-processing technique for tagged images, the harmonic phase (HARP) analysis method, will also be discussed. Other techniques, such as phase velocity imaging and strain encoding, will be briefly introduced. In the last section, the applications of these techniques to several laboratory animal models of cardiovascular diseases will be discussed.

Myocardial Wall Mechanics

The pumping of the blood in mammalian hearts is facilitated by the unique organization of the myocardial fibers. These fibers change gradually from a right-handed helix in the subendocardial region, to a circumferential arrangement in the mid wall, then to a left-handed helix in the subepicardial region [9, 10]. This intricate fiber architecture gives rise to a complex pattern of myocardial deformation during contraction. The synchronized shortening of the oblique and circumferentially oriented fibers leads to the shortening of the left-ventricle in both the longitudinal and circumferential directions, and the thickening of myocardial wall in the radial direction. In addition, the left-ventricle also undergoes a torsional motion due to the obliquely oriented fibers in the subendocardial and subepicardial regions [11]. This torsional motion allows efficient ejection of blood during systole, and the untwisting at early diastole allows rapid filling of the left-ventricle. Perturbation of the torsional motion has also been shown to be a sensitive marker for functional alterations at the early stage of the disease [12–14]. In this section, methods and parameters for quantitative description of myocardial wall deformation and torsional motion will be introduced.

The Coordinate Systems

Two coordinate systems have been commonly used to describe myocardial wall motion: the imaging coordinate system and the myocardial coordinate system (Fig. 2.1a). In the imaging coordinate system, the three orthogonal axes (X-Y-Z) align with the short- and long-axes of the heart. Typically, the Z-axis is defined as parallel to the long-axis of the heart, and the X-Y plane forms the short-axis plane. In the myocardial coordinate system, the radial, circumferential, and longitudinal directions (R-C-L) form the three orthogonal axes. While the L-axis is parallel to the Z-axis in the imaging coordinate system, the directions of R- and C-axes are perpendicular and tangential to the circumference of the heart at any specific location. Hence, the myocardial coordinate system changes orientation along the circumferential direction, with the R-axis always pointing to the center of the ventricular cavity.

The use of the imaging coordinate system allows straightforward analysis of the imaging data. However, transforming the results to the myocardial coordinate system enables the correlation of functional parameters with the anatomy and structure of the ventricle, and it is preferred for studies on the structure-function relationship in the heart.

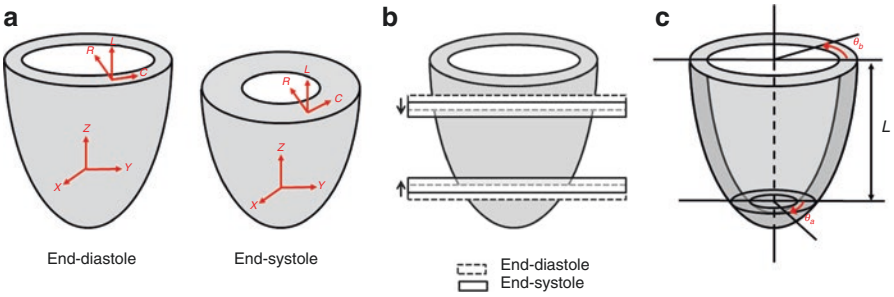

Fig. 2.1 Myocardial wall motion during contraction. (**a**) Description of myocardial wall strains in the imaging (*X-Y-Z*) and myocardial (*R-C-L*) coordinate systems. (**b**) Schematic representation of through-plane motion due to fiber shortening in longitudinal direction. (**c**) The torsional motion during contraction

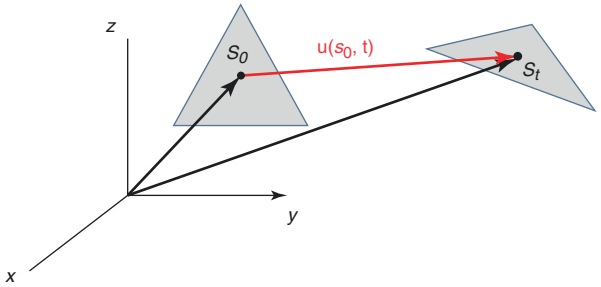

Fig. 2.2 Deformation of a continuum body. The displacement vector, $u(s_0, t)$, describes the deformation of a material point in the continuum body

Strain and Strain Rate

The deformation of the myocardium can be described by a three-dimensional (3D) strain tensor. Each element in a strain tensor is, in a simple sense, a measurement of the relative change of length in a specific direction, i.e., $\Delta L/L$, where L is the original length before deformation and ΔL is the net change in length when deformation occurs. A positive strain value indicates lengthening, while a negative strain value represents shortening. During myocardial contraction, the lengthening in the radial direction gives rise to wall thickening.

In continuum mechanics, the strain tensor is calculated from the displacement field, which describes the motion of each material point in a continuum body (Fig. 2.2). For a specific point at position s_0 in the undeformed state, it moves to a new position s_t at time t. The displacement vector is defined as

$$\boldsymbol{u}\left(s_0, t\right) = \boldsymbol{s}_t - \boldsymbol{s}_0 \tag{2.1}$$

The displacement field completely describes the change in the shape of the myocardium, from which the deformation gradient ($\boldsymbol{F}$) and Lagrangian strain tensor ($\boldsymbol{E}$) can be calculated as

$$\boldsymbol{F} = \boldsymbol{I} + \nabla \boldsymbol{u} \tag{2.2}$$

and

$$\boldsymbol{E} = \frac{1}{2}\left(\boldsymbol{F}^{T}\boldsymbol{F} - \boldsymbol{I}\right) \tag{2.3}$$

Under a specific basis set, a 3D strain tensor can be represented by a 3 × 3 symmetric matrix with six independent elements. In the imaging coordinate system, the strain tensor is described as

$$\boldsymbol{E} = \begin{bmatrix} E_{XX} & E_{XY} & E_{XZ} \\ E_{XY} & E_{YY} & E_{YZ} \\ E_{XZ} & E_{YZ} & E_{ZZ} \end{bmatrix} \tag{2.4}$$

where E_{XX}, E_{YY}, and E_{ZZ} represent length changes in the X-, Y-, and Z-directions, respectively. E_{XY}, E_{XZ}, and E_{YZ} are the shear strain in the X-Y, X-Z, and Y-Z planes, respectively. Diagonalization of this strain tensor gives rises to three principal strains (E_1, E_2, and E_3) and three eigenvectors along the directions of the greatest length changes. Typically, the greatest length increase is associated with the wall thickening, and the greatest length decrease is associated with shortening in either circumferential or longitudinal directions. The use of principal strains has the advantage of quantifying tissue deformation independent of the ventricular geometry [15].

In the myocardial coordinate system, the strain tensor is described as

$$\boldsymbol{E} = \begin{bmatrix} E_{RR} & E_{RC} & E_{RL} \\ E_{RC} & E_{CC} & E_{CL} \\ E_{RL} & E_{CL} & E_{LL} \end{bmatrix} \tag{2.5}$$

where the three diagonal elements represent the radial (E_{RR}), circumferential (E_{CC}), and longitudinal (E_{LL}) strains, respectively. They respectively describe myocardial wall thickening, circumferential and longitudinal shortening. The three off-diagonal elements, E_{RC}, E_{RL}, and E_{CL}, represent shear strains within the radial-circumferential, radial-longitudinal, and circumferential-longitudinal planes, respectively.

As a result of the longitudinal shortening, through-plane motion occurs when acquiring short-axis images, especially at the base and apex (Fig. 2.1b). The through-plane motion can be a source of error in the quantification of myocardial wall strain. Several techniques have been developed to reduce the inaccuracy, which will be discussed later in this chapter.

Strain rate, which is calculated as the time derivative of strain, describes how fast the shortening of myofibers or thickening of myocardial wall occurs. It has been extensively used in the evaluation of diastolic function. Decreased diastolic strain rate has been observed in patients with asymptomatic left-ventricular (LV) hypertrophy [16].

Ventricular Twist and Torsion

The twist or torsional motion of the left-ventricle arises from contraction of the obliquely oriented fibers in the subendocardial and subepicardial regions. When viewed from the apex of the heart, the base rotates in a clockwise direction, whereas the apex rotates in a counterclockwise direction (Fig. 2.1c). During diastole, the relaxation of myocardial fibers gives rise to the untwisting of the left-ventricle.

The twist angle at a short-axis plane is calculated as the angle of rotation from the undeformed state to a deformed state. Ventricular torsion is then quantified by normalizing the net twist by the distance between base and apex, i.e.

$$\text{Torsion} = \frac{\theta_b - \theta_a}{L} \tag{2.6}$$

where θ_b and θ_a are basal and apical twist angles, respectively, and L is the distance between base and apex. Finally, the twist and torsion rate can also be calculated by taking the time derivatives of twist and torsion.

Evaluation of Ventricular Wall Motion by Cardiac Magnetic Resonance Tagging

Tagging by magnetization saturation was the first CMR technique that allowed regional quantification of myocardial wall motion [1]. The technique used a combination of slice-selective radio-frequency (RF) pulses and saturation gradients to create a saturation band, or taglines, at the intersection of the excited slices and the imaging plane. Because each tagline is created sequentially, RF energy deposition is high and the number of taglines created can be quite limited. Techniques developed later on, such as spatial modulation of magnetization (SPAMM) [2, 3] and delay alternating with nutations for tailored excitation (DANTE) [17], showed much more favorable features, such as higher tagging resolution, thinner taglines, and improved tagging efficiency. Among these methods, SPAMM has been extensively adopted for its low RF energy deposition and shorter implementation time.

Myocardial Tagging by SPAMM

The simplest SPAMM sequence, referred to as SPAMM11 [3], uses two 90° RF pulses and a tagging gradient to generate a sinusoidal modulation of the magnetization across the imaging plane (Fig. 2.3a). The evolution of longitudinal and transverse magnetization during the tagging module is shown in Fig. 2.3b. After the first RF pulse, longitudinal magnetization is rotated to the transverse plane. Following the RF pulse, the tagging gradient (G_{tag}) induces spin dephasing in the transverse plane. The amount of dephasing is dependent on the location of spins, as well as the strength and duration of the gradient, i.e.,

$$\theta = \gamma \int_0^{\tau} G_{\text{tag}} \cdot y \, dt = k_{\text{tag}} y \tag{2.7}$$

where γ is the gyromagnetic ratio, y is the location of the spins, and G_{tag} and τ are the strength and duration of the modulation gradient, respectively. K_{tag}, which is defined as $k_{\text{tag}} = \gamma \int_0^{\tau} G_{\text{tag}}$, represents the spatial modulation of magnetization. The second 90° hard pulse rotates the magnetization back to the longitudinal axis. However, due to the spin dephasing, the longitudinal magnetization is now modulated by a sinusoidal function according to

$$M_z(y) = M_0 \cos\left(k_{\text{tag}} y\right) \tag{2.8}$$

where M_0 is the longitudinal magnetization at thermal equilibrium. This sinusoidal modulation of the magnetization gives rise to a set of parallel taglines in the direction along which the tagging gradient is applied. Finally, a crusher gradient is applied to eliminate the transverse magnetization before imaging.

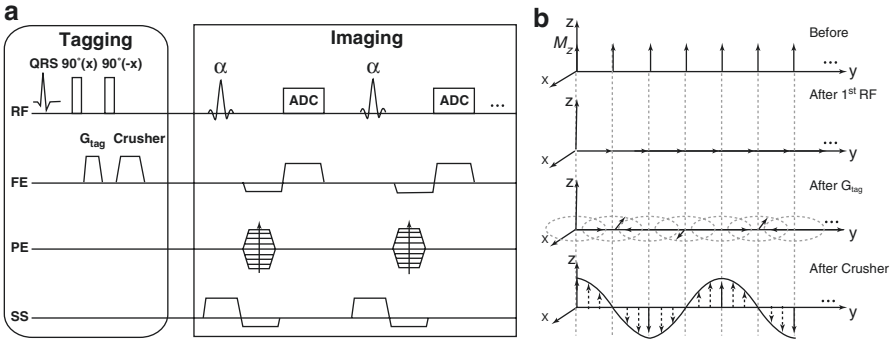

Fig. 2.3 (**a**) Schematics of a SPAMM11 sequence. (**b**) The evolution of magnetization. *RF* radio-frequency pulse, *FE* frequency-encoding, *PE* phase-encoding, *SS* slice-selection, *ADC* analog-to-digital converter

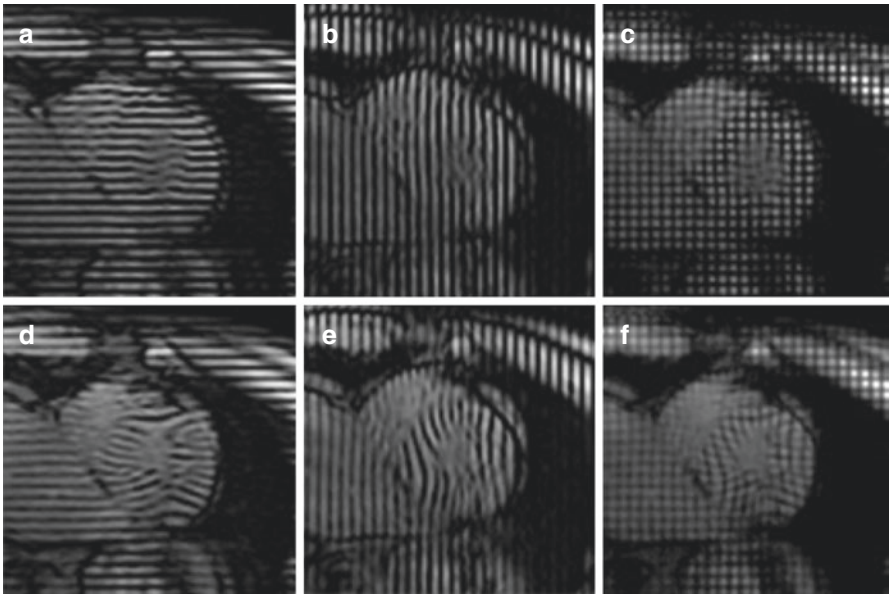

Fig. 2.4 Representative tagged images at end-diastole (**a**–**c**) and end-systole (**d**–**f**). Horizontal and vertical taglines are generated with two orthogonal tagging gradients. Multiplication of the two images gives rise to the tagging grids in (**c**) and (**f**)

Based on Eq. 2.8, the tagging frequency (k_{tag}), which is inversely proportional to the distance between two adjacent taglines, is governed by the strength and duration of the modulation gradient. A larger and longer modulation gradient gives rise to a higher tagging frequency. Practically, the tagging frequency should be chosen such that there are a minimal of four imaging pixels between two adjacent taglines to allow the identification of taglines throughout the entire cardiac cycle.

Shown in Fig. 2.4 are representative tagged images of a short-axis slice at end-diastole and end-systole. The horizontal and vertical taglines are generated by applying the tagging gradient in two perpendicular directions. Multiplication of the images tagged horizontally and vertically gives rise to the tagging grids shown in Fig. 2.4c, f. Alternatively, the tagging grid can also be generated by applying two sequential tagging modules with orthogonal tagging gradients. However, this will cause a reduction in signal-to-noise ratio (SNR) as a result of the additional modulation of the magnetization. Furthermore, it will double the time for generation of taglines which may not be practical for small animals such as mice.

High-order SPAMM sequence that uses a binomial combination of RF pulses can be used to generate thinner taglines [3]. However, adding more RF pulses and tagging gradients inevitably increases the time of the tagging module. Long tagging time can be problematic for imaging small animals, especially for mice. Since the first tagged frame is frequently used as the undeformed reference frame, it is important that the tagging module is implemented within the QRS complex prior to rapid

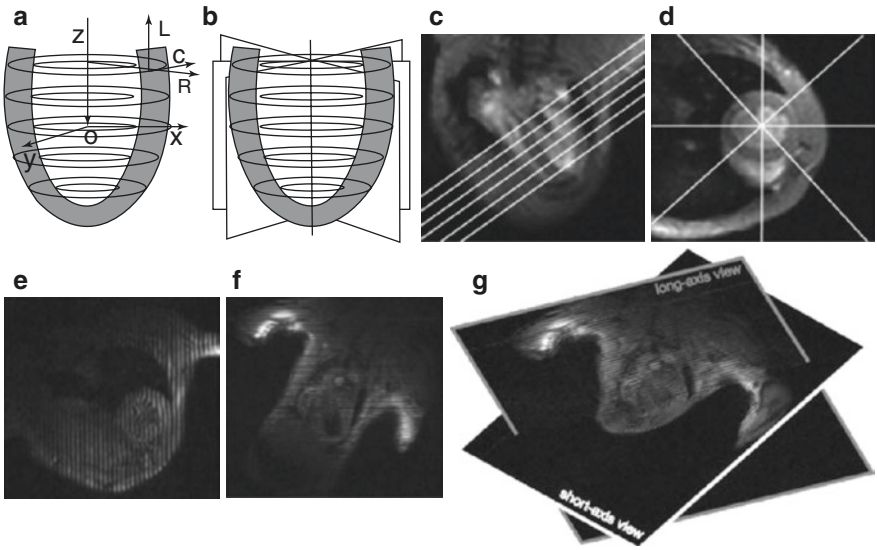

Fig. 2.5 3D CMR tagging. Short-axis planes (**a**) are prescribed from long-axis scout image (**c**). Radially distributed long-axis planes (**b**) are prescribed from short-axis image (**d**). Tagged short-axis (**e**) and long-axis (**f**) images are registered in a 3D imaging coordinate system (*x*-*y*-*z*) shown in (**a**). The registration of (**e**) and (**f**) is shown in (**g**). The calculated strain is converted to the myocardial coordinate system (*R*-*C*-*L*) (Images reproduced with permission from Zhong et al. [20])

myocardial contraction. The duration of the QRS complex in a mouse heart is typically less than 30 ms [18]. SPAMM121 and SPAMM1331 provide a good compromise between tagline profile and implementation time, and they are typically used in mouse imaging.

For quantification of 3D myocardial wall motion, data acquisition is typically comprised of a set of short-axis images with tagging grids, and another set of long-axis images with horizontal taglines [19]. Figure 2.5 shows the planning and coordinate systems used for 3D motion reconstruction [20]. Typically, short-axis slices that cover the entire ventricle from base to apex are acquired, while long-axis slices are distributed radially around the LV long-axis.

Analysis of Tagged Images

Major steps in the analysis of tagged images are shown in Fig. 2.6. The analysis of tagged images involves two steps: tracking of the taglines and calculation of wall motion parameters. Several techniques have been developed for extracting and tracking myocardial tags. Software packages such as SPAMMVU [21], FindTags [22], and TAGASIST [23] typically use manual or semi-automatic methods to identify the location of taglines and their intersecting points. Figure 2.6a shows an

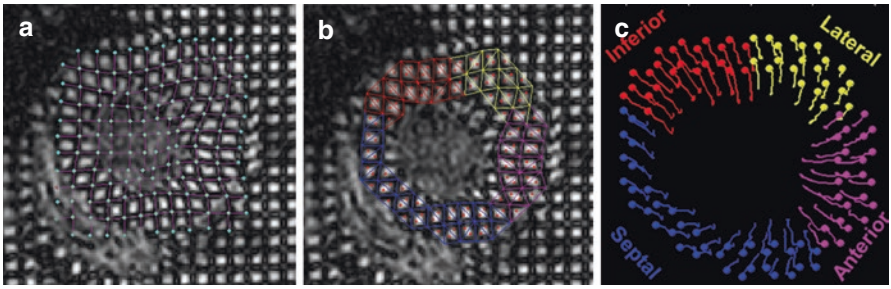

Fig. 2.6 Tagging image analysis. (**a**) Short-axis tagged image overlaid with the tagging mesh. (**b**) Triangulation of the myocardium in homogeneous strain analysis. (**c**) Visualization of myocardial wall motion from end diastole to end systole (Images reproduced with permission from Liu et al. [24])

example of a tagged short-axis image overlaid with the tagging mesh tracked interactively using coupled cubic spline snakes [24]. Based on the tracked taglines, the myocardium is divided into non-overlapping triangles using sets of adjacent tag points as the vertices (Fig. 2.6b), and regional myocardial wall motion can be visualized by tracking the displacement of the centroid of each triangle from diastole to systole (Fig. 2.6c).

To reconstruct the 3D motion of the heart, short-axis and long-axis images are registered in the imaging coordinate system illustrated in Fig. 2.5a. Displacement of those material points that are initially located at the intersections of the three undeformed orthogonal tagging planes (P_1 to P_5) can be calculated using iterative point-tracking techniques, as illustrated in Fig. 2.7 [20, 25]. Specifically, P_1 to P_5 are the material points located at the intersection of three orthogonal tag planes at end-diastole (Fig. 2.7a), and tag planes 1 and 2 are the two tagging planes orthogonal to the short-axis imaging planes. In a deformed state, the displaced material points $\left(P_1^{'} \text{to} P_5^{'}\right)$ are determined by finding the intersecting points of the long-axis tag planes with the intersecting line of deformed tag planes (Fig. 2.7b).

Once all the tagging points are identified throughout the cardiac cycle, more quantitative analysis can be performed by calculating the Lagrangian strain tensor. A homogenous strain analysis method is typically used to calculate the strain in each triangular element [26]. Modeling approaches, including finite element analysis [27, 28], the volumetric modeling [29–31], the statistical modeling [28, 32], and the 3D active contour modeling [33–36], have also been developed for strain quantification. In addition to strain quantification, the twist angle in each triangular element can be calculated as the rotation of the centroid of the triangle around the ventricular cavity. Finally, ventricular torsion can be calculated by subtracting the apical and basal twist and normalizing the net twist by the distance between the apical and basal slices.

A major challenge in the analysis of tagged images is the extensive user interaction for tagline tracking, which can be laborious and time consuming. The harmonic

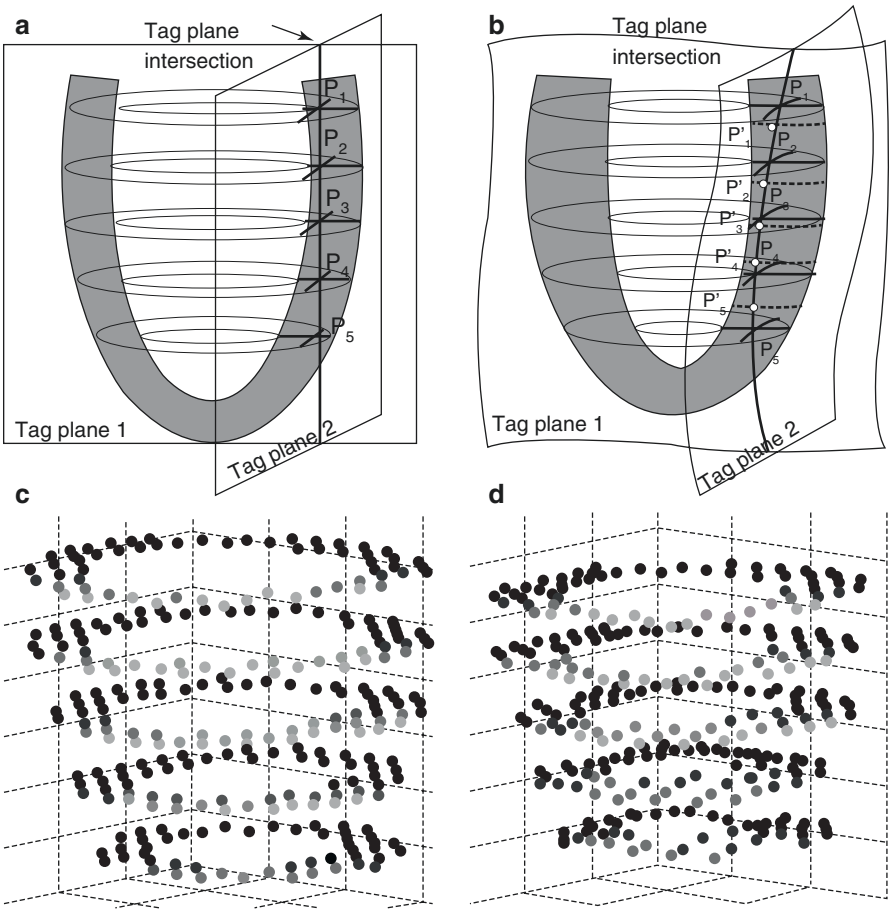

Fig. 2.7 Reconstruction of 3D tagging data. Reconstruction of tagging markers at end-diastole (**a**) and in a deformed state in cardiac cycle (**b**). (**c**, **d**) Reconstructed tagging markers at end-diastole and end-systole (Images reproduced with permission from Zhong et al. [20])

phase (HARP) analysis method was developed for automated processing of SPAMM tagged images [37, 38]. Since the SPAMM modulation of an MR image takes the form of a sinusoidal dependence of the longitudinal magnetization, it produces an array of spectral peaks (harmonic peaks) in the k-space (Fig. 2.8a). The inverse Fourier transform of a harmonic peak has two parts: the magnitude and the phase. HARP image refers to the phase image of a harmonic peak (Fig. 2.8b). The phase angle is a material property of the tagged tissue. It remains invariant throughout the cardiac cycle for a particular material point. Hence, the phase angle can be used to track the motion of the underlying tissue (Fig. 2.8c). Besides allowing automatic tracking of the taglines, HARP images also encode directly the displacement field and thus can be used for direct strain calculation [37, 39–41].

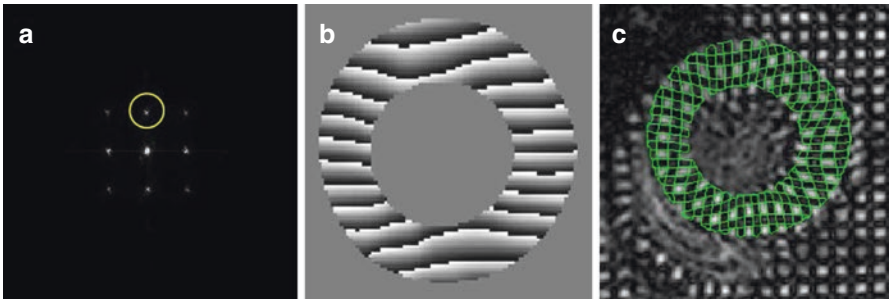

Fig. 2.8 HARP analysis. (**a**) SPAMM-tagged image in k-space. The yellow circle represents one of the filters used for extracting the harmonic peak. (**b**) The corresponding HARP image masked using myocardial contours. (**c**) Synthetic tag lines generated from the isophase contours of $\pi/2$ (Images reproduced with permission from Liu et al. [41])

Improvements on SPAMM Tagging

SPAMM suffers from the fading of taglines due to T_1 relaxation. Typically, the tagging module is applied at the beginning of systole after the detection of the R-wave. The fading of taglines thereafter will diminish the contrast between the taglines and myocardium, leading to inaccurate quantification of myocardial wall motion during late diastole. Using high field scanners will allow taglines to persist for a longer period of time as T_1 relaxation time increases with the magnetic field strength [42]. Alternatively, using balanced steady-state free precession readout also allows longer persistence of tagline contrast [43].

For small animal imaging, since the heart rate is much faster and the R-R interval is much shorter, tagline fading usually is not a concern. However, due to the shortening of the myocardium in the longitudinal direction, tagged images acquired at different phases of a cardiac cycle do not always represent the same slice of the myocardium [44]. Consequently, quantification of regional functional parameters, especially torsion, suffers from inaccuracies due to such through-plane motion. Brotman et al. reported a 19% overestimation in torsion without correction of the through-plane motion in human hearts [45].

The complementary SPAMM (CSPAMM) method was initially developed to improve the tagging contrast at a later stage into the cardiac cycle [46]. CSPAMM separates the component of magnetization with the tagging information from the relaxation component by subtraction of two acquisitions, with the tagging modules in the two acquisitions differ by a phase shift of π in the second RF pulse. In both acquisitions, the restored magnetization due to T_1 relaxation is the same. However, the sinusoidal modulation of the two acquisitions differs by a phase shift of π. Hence, the subtraction of the two datasets can effectively eliminate the T_1 relaxation component of the magnetization, and increase the SNR in the final tagged images by approximately 40%. Furthermore, by using slice-selective RF pulses in the tagging module, the through-plane motion artifact can also be effectively reduce with

CSPAMM [47]. To further improve the contrast-to-noise ratio (CNR) at later cardiac phases, a variable flip angle scheme can be used in the imaging sequence.

Displacement Encoding with Stimulated Echoes (DENSE)

DENSE was developed in 1999 by Aletras et al. [4]. In DENSE, tissue displacement is encoded directly in the phase of each imaging pixel. It thus has the advantage of automated data processing. DENSE shares many similarities with HARP in terms of displacement encoding and image analysis. The major difference is that the displacement-encoding peak in HARP is located off-center in the k-space, while a displacement-decoding gradient applied prior to readout is used to shift the displacement-encoding peak to the center of the k-space in DENSE MRI.

Multi-phase DENSE Sequence

A multi-phase DENSE sequence is based on SPAMM11 tagging as shown in Fig. 2.9. Displacement encoding is achieved by the SPAMM11 sequence in combination with the additional decoding gradient in the subsequent imaging sequence. Same as in the tagging sequence, the SPAMM11 module gives rise to the spatial modulation of the longitudinal magnetization that can be described as

$$M_z(y) = M_0 \cos(k_{\mathrm{ENC}} y) \tag{2.9}$$

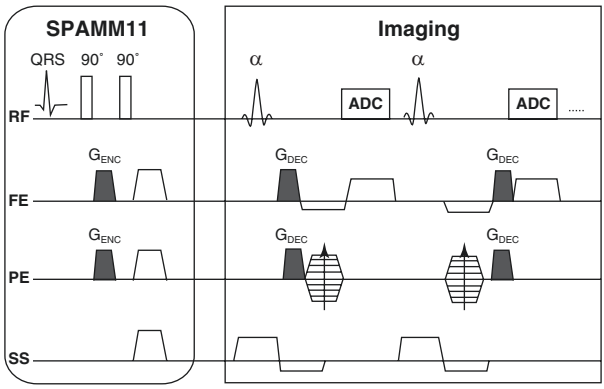

Fig. 2.9 Schematics of a multi-phase DENSE sequence. Two encoding gradients (G_{ENC}), one in SPAMM11 module and one in imaging module, are used to enable displacement encoding. *RF*, radio-frequency; *FE*, frequency-encoding; *PE*, phase-encoding; *SS*, slice-selection; *ADC*, analog-to-digital converter

where $k_{\mathrm{ENC}} = \gamma \int_0^{\tau} G_{\mathrm{ENC}}\, dt$ represents the modulation of magnetization due to the encoding gradient G_{ENC}. Between the SPAMM11 module and the imaging sequence is a mixing period (T_M) during which T_1 relaxation occurs. At the end of the mixing period, the longitudinal magnetization becomes [48]

$$M_z\left(y, T_M\right) = M_0 \cos\left(k_{\mathrm{ENC}} y\right) E_M + M_0\left(1 - E_M\right) \tag{2.10}$$

or

$$M_z\left(y, T_M\right) = \frac{M_0}{2}\left(e^{jk_{\mathrm{ENC}} y} + e^{-jk_{\mathrm{ENC}} y}\right) E_M + M_0\left(1 - E_M\right) \tag{2.11}$$

where $E_M = e^{-T_M / T_1}$. In the imaging sequence, a unencoding gradient with the same area as G_{ENC} is applied prior to data acquisition, which will induce a location-dependent phase change. If the displacement Δy occurs during the mixing period, the transverse magnetization becomes:

$$M_{\perp}\left(y\right) = M_z\left(y, T_M\right) e^{-jk_{\mathrm{ENC}}\left(y + \Delta y\right)} \sin\alpha \tag{2.12}$$

where α is the flip angle of the RF pulse in imaging module. Using $M_z\,(y, T_M)$ shown in Eq. 2.11, the transverse magnetization can be expressed as

$$M_{\perp}\left(y\right) = \left[\frac{1}{2} E_M e^{-jk_{\mathrm{ENC}}\Delta y} + \frac{1}{2} E_M e^{-jk_{\mathrm{ENC}}\left(2y + \Delta y\right)} + \left(1 - E_M\right) e^{-jk_{\mathrm{ENC}}\left(y + \Delta y\right)}\right] M_0 \sin\alpha \tag{2.13}$$

The three terms in Eq. 2.13 describe three echoes that are phase-modulated by 0, $2k_{\mathrm{ENC}}$ and k_{ENC}, respectively. As can be seen, the phase of the first echo is linearly proportional to the displacement Δy, it is thus called the displacement-encoding echo, or DENSE echo. The second and third echoes are referred to as the complex conjugate echo and the T_1-relaxation echo, respectively. A low-pass filter in the k-space can be applied to extract the DENSE echo for the calculation of myocardial displacement. Alternatively, the displacement-encoding gradient can be applied in the phase encoding direction, and only data from the central k-space where the DENSE echo is located needs to be acquired. With the acquisition of less than half of the k-space lines, the second approach has the benefit of significantly shortening the acquisition time.

Background phase errors caused by B_0 field inhomogeneity needs to be corrected in DENSE MRI. The correction can be achieved by either acquiring another set of images without displacement encoding [49], or acquiring a second set of DENSE images using displacement encoding/unencoding gradients with the same magnitude but opposite polarity as the first data set [50]. Comparing to the phase-error correction

using a phase reference image without displacement encoding, the subtraction of two scans with opposite displacement-encoding gradients has the benefit of doubling the sensitivity of displacement encoding. However, it requires the acquisition of two sets of DENSE images in two-dimensional (2D) displacement encoding, while the same phase reference image without displacement encoding can be used for phase correction of images with displacement encoding applied to any directions.

For a more comprehensive assessment of myocardial wall motion by DENSE, Gilson et al. developed a multi-slice DENSE sequence which allowed 3D displacement encoding with high spatial resolution in mouse hearts [49]. In this method, the CSPAMM module is used in the sequence on three slices located at the basal, midventricular, and apical levels. In this technique, a total of three DENSE datasets are acquired, with two datasets for in-plane displacement encoding in two orthogonal directions and a third dataset for through-plane displacement encoding along the slice-selection direction. Using this technique, DENSE images containing the 3D myocardial displacement in basal, midventricular, and apical slices can be acquired within approximately 50 min.

Analysis of DENSE Images

Similar to HARP, myocardial displacement is calculated from the phase image in the DENSE echo, which can be obtained after taking the inverse Fourier transform of the DENSE peak. A representative phase image from a DENSE echo acquired at end-systole is shown in Fig. 2.10a, with the displacement encoding in

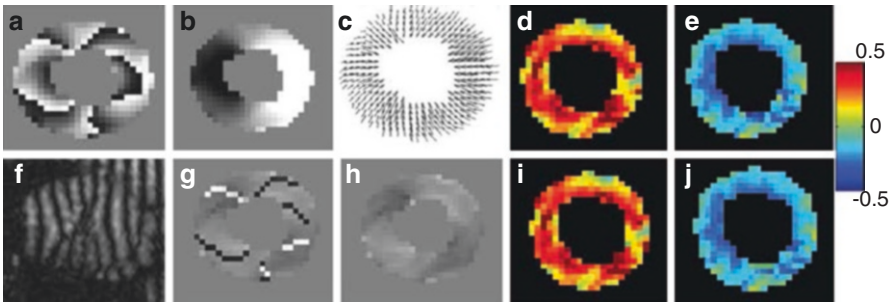

Fig. 2.10 Representative end-systolic DENSE images and the corresponding displacement and strain maps. (**a**) A representative phase image at end-systolic. (**b**) The unwrapped phase image. (**c**) 2D displacement map. (**d**, **e**) Radial and circumferential strain maps. (**f**) Magnitude image with vertical taglines. (**g**, **h**) Phase gradient maps in the horizontal direction before (**g**) and after (**h**) removal of discontinuity. (**i**, **j**) Radial and circumferential strain maps calculated directly from the phase gradient maps (Figure reproduced with permission from Zhong et al. [50])

the horizontal direction. The magnitude image of the DENSE echo is similar to a tagging image (Fig. 2.10f). It can be appreciated from the phase image that phase wrapping occurs at locations where the phase changes between adjacent pixels exceed π. Correct calculation of the displacement field requires phase unwrapping. Numerous phase unwrapping methods have been developed and evaluated. We have used an algorithm similar to the quality-guided path following method [51]. Following the unwrapping of the original phase image (Fig. 2.10b), the 2D displacement map can be calculated from vector addition of two individual 1D displacement maps in two orthogonal directions (Fig. 2.10c). Subsequently, the radial and circumferential strain maps are calculated from the displacement field (Fig. 2.10d, e). From the displacement map, ventricular twist and torsion can also be quantified.

Alternatively, the Lagrangian strain tensor can be directly calculated from the deformation gradient tensor, which is linearly related to the gradient of the phase image (Fig. 2.10g). When calculating the gradient of the phase image, discontinuities appear at locations with phase wrapping. These discontinuities can be readily removed by adding a phase shift π to the original phase image before calculating the gradient (Fig. 2.10h) [50]. Strains calculated using this method should be equivalent to that calculated from the displacement (Fig. 2.10i, j). However, quantification of twist and torsion is not feasible using this method.

Improvements on DENSE MRI

Because of the overlap between the DENSE echo and the T_1 relaxation echo, peak extraction using a simple low-pass filter not only reduces image resolution, but also introduces inaccuracies in the quantification of the displacement field. While using a larger displacement-encoding gradient can further separate the two echoes and thus reduce the overlap, it also introduces more phase wrapping which can be problematic in post-processing. Alternatively, the T_1 relaxation echo can be suppressed physically. The inversion recovery technique has been used to suppress the T_1 relaxation echo by nulling the signal for a particular T_1 [52]. However, this technique cannot suppress the T_1 relaxation echo from diseased hearts or tissues with other T_1 values. In addition, it is not suitable for multi-phase DENSE since images at different cardiac phases need to be acquired. Alternatively, the complementary DENSE method, which is similar to CSPAMM, acquires two datasets with the second RF pulse in the SPAMM module phase shifted by π. The subtraction of these two datasets can effectively remove the T_1 relaxation echo [48].

Besides complementary DENSE, the T_1-relaxation and the complex conjugate echoes can also be removed through the use of cosine and sine modulation (CANSEL) [53]. Specifically, four DENSE datasets, including two cosine- and two

sine-modulated sets, are acquired by alternating the phase of both RF pulses in the 1–1 SPAMM tagging module. The elimination of the T_1 relaxation and the complex conjugate echoes is achieved by addition and subtraction of these four datasets. Although the data acquisition time is prolonged, CANSEL has the advantage of improved SNR and accuracy. Furthermore, imaging acceleration can be achieved through parallel imaging and other fast imaging methods [54].

Other CMR Methods of Functional Assessment

In addition to MR tissue tagging and DENSE, phase velocity mapping and strain encoded (SENC) imaging have also been developed to quantify regional myocardial wall motion. Phase velocity mapping, also known as phase contrast imaging or phase mapping, employs a bipolar gradient to encode tissue velocity in the phase of the acquired image such that the phase shift in each imaging pixel is proportional to the velocity along the direction of the encoding gradient [55, 56]. Phase velocity mapping has the advantage of fast post-processing. In addition to the quantification of myocardial tissue velocity [56–60], it can also be used to measure blood flow [56, 61].

Strain-encoded (SENC) imaging is a relatively new technique for myocardial strain quantification [6]. Similar to tagging, the strain information is encoded in the magnitude of the acquired images in SENC imaging. However, the tagging planes in SENC are orientated parallel rather than perpendicular to the imaging plane. Therefore, SENC enables the measurement of the through-plane motion, and myocardial longitudinal and circumferential strains can be quantified in short- and long-axis images, respectively. A limitation of the SENC method is that radial strain cannot be readily measured. The utility of SENC has been demonstrated in detecting alterations in myocardial wall motion in myocardial infarction [62], coronary stenosis [63], and ischemia, at low dobutamine doses [64].

CMR in Laboratory Animals

CMR techniques, especially MR tissue tagging and DENSE, have been extensively used in preclinical studies on laboratory animals [65]. The combination of these methods with an animal model of human cardiac diseases has become a powerful tool in the investigation of various aspects of disease progression, from the structural-functional to the energy-functional relationships. With genetically manipulated mouse models playing an increasingly important role in the exploration of cardiovascular diseases, CMR can also provide an important tool for the investigation of the molecular mechanisms of a spectrum of cardiovascular diseases.

Experimental Settings and Animal Preparation

High-field MR scanners are typically used to achieve high spatial resolution with satisfactory SNR. Volume coils can be used for both transmission and reception, although a small surface coil placed against the chest wall can give rise to higher SNR. If a preclinical high-field MR scanner is not available, clinical scanners with lower field strength can also be used with the appropriate coil setup. Typically, the body coil is used for uniform RF transmission and a multi-channel coil can be used for reception.

Isoflurane is typically used in conjunction with air or pure oxygen for the induction and maintenance of anesthesia [8]. Typically, 1–2% isoflurane is sufficient to maintain the anesthesia level. If not maintained properly, the body temperature of mice under anesthesia can decrease significantly, which may consequently cause substantial fluctuation in heart rate and mean arterial pressure. A recent study suggested that an isoflurane level of 1.5% yielded the most stable heart rate and mean arterial pressure [8]. In addition to changes in heart rate and mean arterial pressure, anesthesia will also induce a downregulation of basal metabolism, which will lead to rapid decrease in body temperature due to the heat loss via a relatively large body surface area for a small rodent. To keep the body temperature at the physiological level, feedback control systems have been developed to blow warm air onto the mice. Alternatively, the animals can also be kept warm with a circulating water bed. These systems can effectively maintain the body temperature at approximately 35–37 °C. With a good control over mouse body temperature and isoflurane level, the normal physiological conditions can be maintained during the functional measurements by CMR.

Similar to clinical CMR, imaging acquisition for functional assessment is frequently performed with electrocardiogram (ECG) gating. Both subcutaneous and surface electrodes can be used for the acquisition of the ECG signal. Electrodes are typically attached to the forelimbs and the right leg. The maintenance of a physiological and stable heart rate is important for imaging quality, especially when multiple averages and scans are acquired over a period of time. An acceptable heart rate for a mouse under anesthesia is between 400 and 600 beats per minute, and is approximately 300 beats per minute for a rat. Besides ECG gating, respiratory triggering may also be needed if severe respiratory motion artifacts are observed. A detailed layout of the experimental procedures is listed in Fig. 2.11.

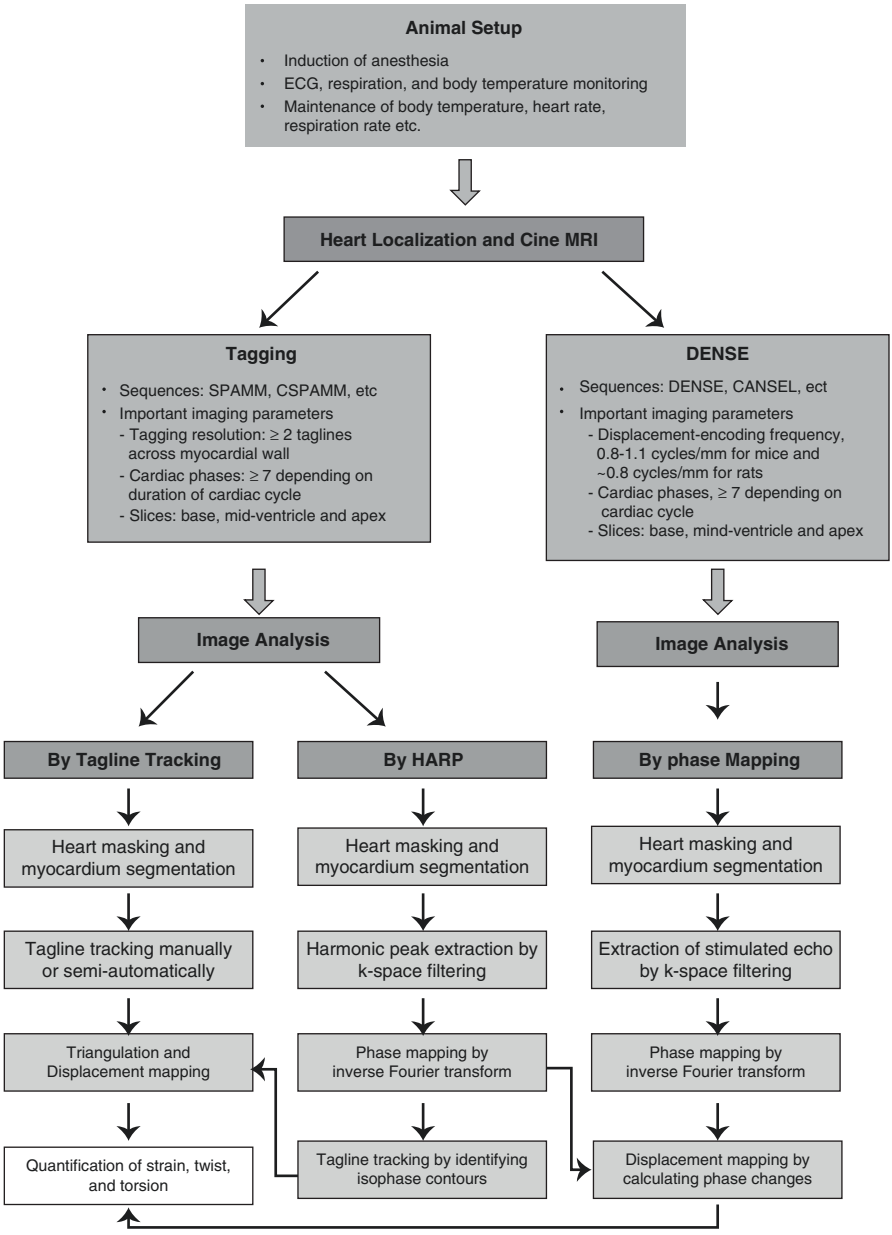

Fig. 2.11 Experimental procedures for measurement of myocardial regional mechanics in rodents using MR tagging and DENSE

Regional Wall Motion in Normal Hearts

The myofiber orientation of the left ventricle changes gradually from a right-handed helix in the subendocardium to a left-handed helix in the subepicardium [66], giving rise to an intricate motion pattern that facilitates efficient blood pumping. Several studies have reported transmural heterogeneity of myocardial wall motion in both humans and animals. It has been shown that circumferential (E_{CC}), longitudinal (E_{LL}), and radial (E_{RR}) strains all increase from epicardium to endocardium in humans [19, 67, 68], dogs [69–71], rats [72], and mice [50, 73]. In addition, maximum twist angle has also been shown to increase transmurally from the epicardium towards the endocardium. Studies using phase velocity mapping also demonstrated such transmural gradient in myocardial velocities in mice [74, 75] and rabbits [75].

While the intramural heterogeneity in wall strain is similar between humans and rodents, there are also distinct differences in myocardial wall motion patterns among different species. Liu et al. [24] observed conserved ventricular twist in humans as compared to mice and rats, leading to a significantly smaller torsion in humans. However, both circumferential strain and normalized radial shortening were the largest in human subjects. In another study using phase velocity mapping, Jung et al. reported a slower radial velocity in apex compared to the base in humans and rabbits, which was found the opposite in mice [75]. Differences in the patterns of longitudinal shortening have also been observed: while contraction velocities along the long-axis were fairly homogeneous in mice, they appeared more dominant in the lateral wall of human heart and in the base of the rabbit heart. In addition, a marked difference in rotational behavior during early-systole was found in mice, which exhibited clockwise rotation in all slice locations compared to counter-clockwise rotation in rabbits and humans [75].

Insights Gained from Surgical Animal Models of Cardiac Diseases

Myocardial Ischemia and Infarction

Myocardial infarction (MI) results in altered myocardial wall motion in both the infarcted region and the border zones. These functional alterations trigger the onset of prolonged remodeling, which, if left untreated, can lead to further functional deterioration and eventually heart failure. A thorough understanding of post-infarct remodeling may aid in the clinical diagnosis and novel therapeutic interventions. The impact of acute and chronic MI on regional myocardial function in infarcted, border zones, and remote myocardium has been extensively investigated using animal models, in which myocardial infarction was typically induced by temporary or permanent ligation of the left anterior descending (LAD) coronary artery.

Numerous animal studies have demonstrated the utility of MR tagging in the delineation of infarcted myocardium, as well as in the evaluation of post-infarct ventricular remodeling. Azevedo et al. observed significant systolic and diastolic dysfunction in infarcted regions of canine hearts, whereas risk regions only showed diastolic but not systolic dysfunction [76]. Also in canine hearts, Croisille et al. applied 3D MR tagging to differentiate viable but stunned myocardium from nonviable myocardium [77]. A study by Kraitchman et al. combined tagging with perfusion assessment by contrast-enhanced MRI to distinguish myocardial infarction from functionally compromised myocardium [78]. Using MR tagging in a longitudinal study, Thomas et al. observed diminished strain and more circumferentially oriented strain in infarcted rat hearts [79]. Furthermore, MR tagging has been employed to evaluate myocardial function in infarcted, adjacent, and remote zones in mouse hearts [80, 81].

DENSE CMR has also been used to evaluate myocardial wall motion in post-infarct hearts. Aletras et al. reported partially improved regional radial strain in risk myocardium over 2 months in dogs with ischemia/reperfusion [70], while Ashikaga et al. observed further functional deterioration such as abnormal stretch and loss of the transmural gradient of radial, circumferential, and longitudinal strains in both infarcted and remote regions in dogs with chronic infarction [82]. Furthermore, Gilson et al. measured myocardial wall motion in mice before and after infarction using multi-slice DENSE [49]. Later, they developed a modified DENSE sequence that could also detect contrast-enhanced infarcted myocardium from the magnitude images of the same DENSE dataset [48].

Hypertrophy and Heart Failure

Hypertrophic cardiomyopathy (HCM) is one of the most common genetic heart disorders, with an occurring rate of more than 1 in 500 people according to a recent report [83]. Compensated hypertrophy describes the process of sustained ventricular wall thickening with compromised blood pumping capacity. The most common cause of LV hypertrophy is pressure overload due to obstruction of the aortic valve, aortic stenosis, or chronic hypertension [84]. Upon an increase in ventricular workload, the heart undergoes maladaptive processes in structure and metabolism, which will lead to myocardial fibrosis and eventually heart failure [85].

Animal studies have been performed to investigate the mechanisms responsible for the transition from compensated hypertrophy to heart failure. In these studies, aortic constriction at ascending [86], transverse [87, 88], or descending [89] locations has been commonly used to induce elevated blood pressure, which mimics symptoms in patients with aortic stenosis or systemic hypertension. After surgery, follow-up monitoring of cardiac function can be performed to characterize the progression of myocardial hypertrophy to heart failure. Nierop et al. employed MR tagging in the longitudinal measurement of ventricular function in mice with mild and severe transverse aortic constrictions [88]. At 10 weeks after surgery, mice with severe constriction showed compromised radial and circumferential strains, while no significant changes was observed in mice with mild constriction.

Assessing Therapeutic Efficacies

In addition to the delineation of regional functional changes in diseased hearts, CMR can also play an important role in the evaluation of therapeutic outcomes. In recent years, a variety of new treatment strategies have been developed for various cardiac diseases, including surgical intervention, stem cell transplantation, and gene therapy. While surgical intervention has been shown to preserve regional myocardial function in the post-infarct hearts, most of the studies were performed in large animals such as swine [90], canine [91], and ovine [92]. On the contrary, stem cell transplantation and gene therapy have been evaluated extensively in small animal models.

Stem cell transplantation and cell therapy have been proposed as promising therapeutic interventions for myocardial repair in recent years. However, they have not been in wide clinical use because of the modest effects on global cardiac function observed in preclinical studies [93]. Assessment of local myocardial biomechanics with more detailed measurements of regional cardiac function has been proposed to facilitate the development of improved strategies [94]. Using MR tagging, Karantalis et al. reported improved diastolic function in swine hearts treated with both mesenchymal stem cells and c-kit^{+} cardiac stem cells [95]. More mechanistic understanding can be gained by combine regional functional assessment with the delineation of cardiac structure. In a recent study, Chen et al. used DENSE MRI and diffusion tensor MRI to evaluate the effects of human umbilical cord blood stem cells on myocardial function and structure in infarcted rat hearts [96]. They observed not only improved ventricular function, but also preserved fiber organization in stem cell-treated rats. These results suggest that stem cell treatment may prevent or delay the adverse structural remodeling in post-infarct hearts, which provides the structural basis for the observed functional improvement.

Although still at experimental stage, gene therapy in cardiovascular applications is aiming at treating heart failure from both ischemic and non-ischemic causes. Molecular targets include the adrenergic system, proteins involved in calcium cycling, and the angiogenic pathway [97]. Regional functional assessment with CMR allows the evaluation of the end-point of the therapy, i.e., the functional improvement. Using MR tagging, Carlsson et al. reported improved radial and circumferential strains in remote, peri-infarcted, and infarcted myocardium in post-infarct swine hearts treated with a hepatocyte growth factor gene [98]. In a more comprehensive study, Saeed et al. also observed improved myocardial perfusion and reduced infarct size in swine hearts treated with the hepatocyte growth factor gene, which provided the structural and physiological bases for the functional improvement [99]. In a similar study, Dicks et al. also observed improved radial, circumferential, and longitudinal strains in canine hearts treated with vascular endothelial growth factor gene [100]. While these studies were all performed in large animals, similar studies performed on small rodents have the advantage of allowing the evaluation of regional functional changes to be correlated to in vivo assessment of gene expression by an optical imaging method.

Genetically Manipulated Mouse Models of Cardiovascular Diseases

Hypertrophic Cardiomyopathy

Mutations in the gene encoding cardiac myosin binding protein C (cMyBPC) have been recognized as one of the most common causes of inherited hypertrophic cardiomyopathy [101]. A recent study by Desjardins et al. investigated the impact of cMyBPC expression on the development of hypertrophic cardiomyopathy in mice lacking cMyBPC alleles using DENSE [102]. Along with accelerations in stretch activation cross-bridge kinetics, decreased ventricular torsion and circumferential strain, as well as circumferential strain rates in early systole and diastole were reported in mice with both homogeneous and heterogeneous knockout of cMyBPC, suggesting that a modest decrease in cMyBPC expression in the mouse heart could lead to decreased contractile function that might contribute to the development of hypertrophic cardiomyopathy later in life.

Dilated Cardiomyopathy

Dilated cardiomyopathy is anatomically characterized by the enlargement of the left ventricle and myocardial wall thinning, which are usually accompanied by systolic dysfunction. The prevalence of asymptomatic idiopathic dilated cardiomyopathy is larger than hypertrophic cardiomyopathy, affecting ≥1 in 250 individuals according to a recent report [103]. Hankiewicz et al. investigated the temporal changes in wall thickness and principal strains in a mouse model with cardiac specific protein kinase C-ε (PKC-ε) overexpression [104]. They observed that the average principal strain E_1 in PKC-ε TG mice decreased starting at the age of 7 months. In contrast, no appreciable wall thinning occurred until 9 months, suggesting that the principal strain E_1 could provide a prognostic indicator of dilated cardiomyopathy.

Dunchenne Muscular Dystrophy

Dunchenne muscular dystrophy is an inherited X-linked genetic disease characterized by early onset of skeletal muscle degeneration and progressive weakness, which affects approximately 1 in 3,500 male birth [105]. However, early cardiac dysfunction is frequently undetected due to physical inactivity and generalized debilitation. Li et al. performed 3D CMR tagging in dystrophin-deficient mdx mice, a mouse model of Duchenne muscular dystrophy, and reported a biphasic change in myocardial wall strain and torsion. Specifically, they observed an initial increase in myocardial wall strain and torsion at young age, followed by a progressive decrease at older ages [106]. In contrast, global contractile indices, such as ejection fraction, were found unchanged. Hence, this study demonstrated that CMR tagging could

provide more sensitive detection of functional alterations than global functional indices in dystrophin-related cardiomyopathies.

Cystic Fibrosis

Cystic fibrosis (CF) is the most common life-shortening autosomal recessive disorder in Caucasians [107]. CF results from mutations in the gene encoding the cystic fibrosis transmembrane conductance regulator (CFTR), which functions primarily as a cAMP-activated and ATP-gated chloride channel. Systemic disorders occurs in CF patients, among which pulmonary diseases are the leading cause of morbidity and mortality. CFTR has been most notably studied in epithelial cells but has also been identified in cardiac myocytes [108]. Previous studies suggest that CFTR may play a role in maintaining the resting membrane potential and regulating the action potential duration, as well as in minimizing the depolarizing effect of Ca^{2+} entry upon β-adrenergic stimulation [109]. Clinical studies on CF patients have reported abnormalities in both left and right ventricles. However, due to the presence of lung disease, it remains unknown whether these observed changes in ventricular function are secondary to pulmonary dysfunction or a direct impact from CFTR disruption in the heart.

In contrast, CFTR knockout mice do not develop CF-like pulmonary disease [110] and provide an ideal model for investigation of the direct impact of CFTR disruption on cardiac function. Jiang et al. evaluated the impact of CFTR disruption on cardiac function in two mouse models with either muscle-specific or global knockout of CFTR. DENSE MRI was employed to quantify myocardial wall motion at baseline and under β-adrenergic stimulation [111]. They reported increased twist and torsion in both CFTR knockout models at baseline. While muscle-specific knockout mice showed unaltered response to β-stimulation, the response in mice with global CFTR knockout was found diminished. In addition, a significant decrease in aortic diameter was observed in both CF mouse models. However, in vitro characterization of myocyte contractility and calcium transients revealed no difference between the CFTR-knockout and wildtype mice. These results suggest that CFTR disruption leads to increased myocardial contractility at baseline, which may trigger myocardial remodeling in CF patients that is independent of lung diseases.

Discussion and Future Work

The advent of MR tagging opened the door for comprehensive and accurate measurement of myocardial wall motion. Although the initial implementation of the MR tagging technique based on magnetization saturation suffered from tagging inefficiency and low tagging resolution, the SPAMM technique that was developed later successfully addressed these limitations and remains among the most widely used CMR techniques to-date. However, post-processing of tagged images remains to be the bottleneck in the application of tagging CMR, despite significant efforts in

developing automated tagline tracking algorithms and motion estimation models. In addition, the accurate measurement of myocardial transmural wall motion is limited by the tagging resolution.

The development of advanced CMR techniques, such as HARP and DENSE, provides the opportunity for rapid and accurate measurement of myocardial wall motion. Although developed independently, HARP and DENSE share more similarities than differences. In HARP analysis, the first-order harmonic peaks in the k-space is extracted to create the HARP images, in which tissue motion can be tracked by following the pixels of constant phases. In contrast, DENSE shifts the displacement-encoded spectral peak to the center of k-space by adding a displacement unencoding gradient prior to data acquisition. Despite these differences, similar techniques during image processing including k-space filtering, suppression of artifact generating echoes, and phase unwrapping, can be applied in both HARP and DENSE.

Although HARP and DENSE have the advantages of fast post-processing and myocardial motion tracking on a pixel by pixel basis, they both suffer from low SNR due to the fact that only a fraction of k-space information is utilized. To compensate for such loss in SNR, an increase in signal averages is usually employed, which inevitably increases the imaging time. Usage of high-field MR scanners can improve SNR, while fast imaging readout techniques, such as spiral sampling, may also aid in reducing scan time.

The extensive applications of CMR techniques in preclinical studies have demonstrated their potential in the evaluation of normal myocardial mechanics, the detection of abnormal cardiac function, and the elucidation of the underlying mechanisms of disease development in laboratory animals. These phenotypic characterization and mechanistic investigation can benefit from large-scale CMR studies and the establishment of a database that documents regional myocardial mechanics in various cardiovascular diseases. Finally, with the advancement in imaging techniques and post-processing tools, the capabilities of these CMR techniques will be largely improved and their applications will also further enhance our understanding of the mechanical complexities underlying the function of the normal and pathological hearts.

Graphical Summary: Quantification of Regional Ventricular Wall Motion in Laboratory Animals

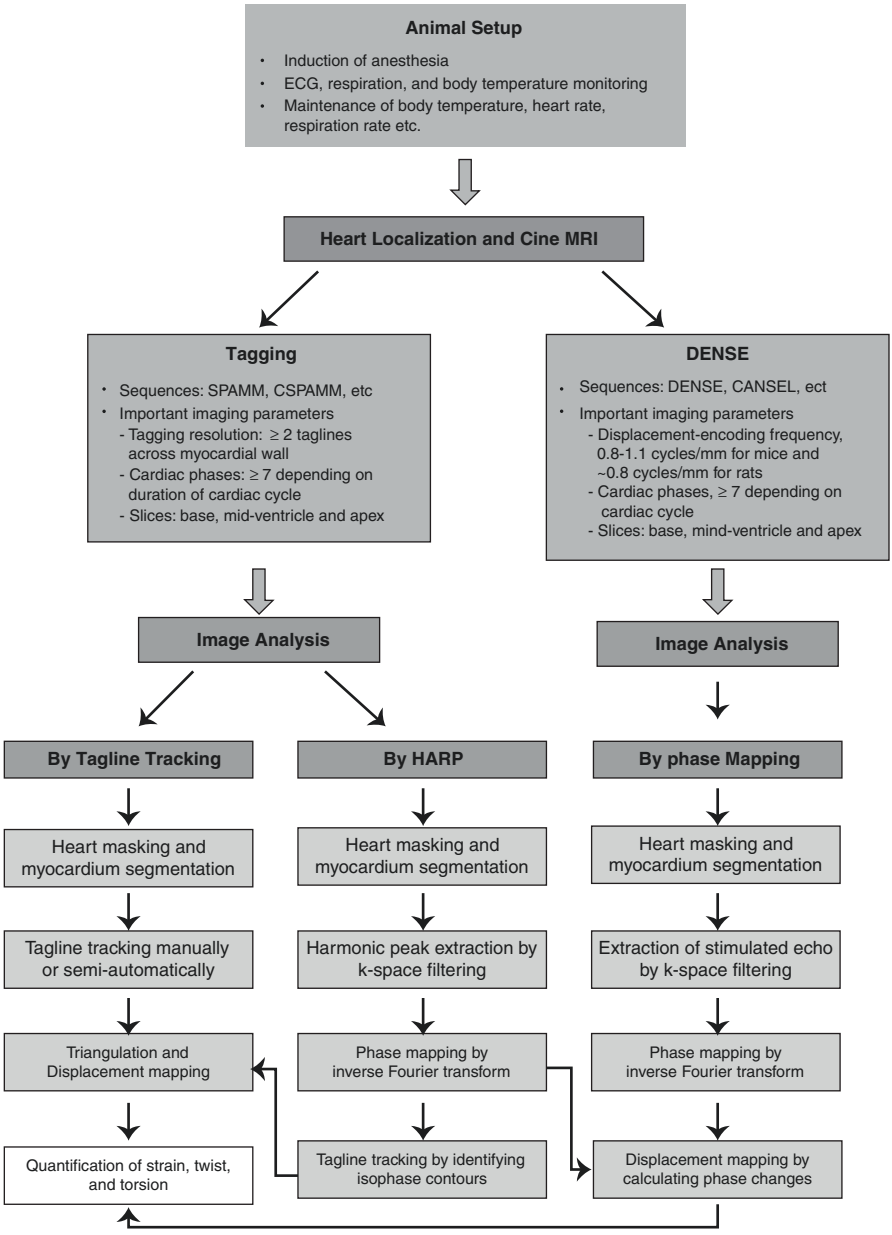

References

1. Zerhouni EA, Parish DM, Rogers WJ, Yang A, Shapiro EP. Human heart: tagging with MR imaging – a method for noninvasive assessment of myocardial motion. Radiology. 1988;169:59–63.
2. Axel L, Dougherty L. MR imaging of motion with spatial modulation of magnetization. Radiology. 1989;171:841–5.
3. Axel L, Dougherty L. Heart wall motion: improved method of spatial modulation of magnetization for MR imaging. Radiology. 1989;172:349–50.
4. Aletras AH, Ding S, Balaban RS, Wen H. DENSE: displacement encoding with stimulated echoes in cardiac functional MRI. J Magn Reson. 1999;137:247–52.
5. Reese TG, Feinberg DA, Dou J, Wedeen VJ. Phase contrast MRI of myocardial 3D strain by encoding contiguous slices in a single shot. Magn Reson Med. 2002;47:665–76.
6. Osman NF, Sampath S, Atalar E, Prince JL. Imaging longitudinal cardiac strain on short-axis images using strain-encoded MRI. Magn Reson Med. 2001;46:324–34.
7. Butz GM, Davisson RL. Long-term telemetric measurement of cardiovascular parameters in awake mice: a physiological genomics tool. Physiol Genomics. 2001;5:89–97.
8. Constantinides C, Mean R, Janssen BJ. Effects of isoflurane anesthesia on the cardiovascular function of the C57BL/6 mouse. ILAR J. 2011;52:e21–31.
9. Streeter DD, Spotnitz HM, Patel DP, Ross J, Sonnenblick EH. Fiber orientation in the canine left ventricle during diastole and systole. Circ Res. 1969;24:339–47.
10. Armour JA, Randall WC. Structural basis for cardiac function. Am J Phys. 1970;218: 1517–23.
11. Taber LA, Yang M, Podszus WW. Mechanics of ventricular torsion. J Biomech. 1996;29: 745–52.
12. Ashford MW, Liu W, Lin SJ, Abraszewski P, Caruthers SD, Connolly AM, Yu X, Wickline SA. Occult cardiac contractile dysfunction in dystrophin-deficient children revealed by cardiac magnetic resonance strain imaging. Circulation. 2005;112:2462–7.
13. Chung J, Abraszewski P, Yu X, Liu W, Krainik AJ, Ashford M, Caruthers SD, McGill JB, Wickline SA. Paradoxical increase in ventricular torsion and systolic torsion rate in type I diabetic patients under tight glycemic control. J Am Coll Cardiol. 2006;47: 384–90.
14. Burns AT, McDonald IG, Thomas JD, Macisaac A, Prior D. Doin' the twist: new tools for an old concept of myocardial function. Heart. 2008;94:978–83.
15. Shehata ML, Cheng S, Osman NF, Bluemke DA, Lima JA. Myocardial tissue tagging with cardiovascular magnetic resonance. J Cardiovasc Magn Reson. 2009;11:55.
16. Edvardsen T, Rosen BD, Pan L, Jerosch-Herold M, Lai S, Hundley WG, Sinha S, Kronmal RA, Bluemke DA, Lima JAC. Regional diastolic dysfunction in individuals with left ventricular hypertrophy measured by tagged magnetic resonance imaging – the Multi-Ethnic Study of Atherosclerosis (MESA). Am Heart J. 2006;151:109–14.
17. Mosher TJ, Smith MB. A DANTE tagging sequence for the evaluation of translational sample motion. Magn Reson Med. 1990;15:334–9.
18. Wehrens XHT, Kirchhoff S, Doevendans PA. Mouse electrocardiography: an interval of thirty years. Cardiovasc Res. 2000;45:231–7.
19. Moore CC, Lugo-Olivieri CH, McVeigh ER, Zerhouni EA. Three-dimensional systolic strain patterns in the normal human left ventricle: characterization with tagged MR imaging. Radiology. 2000;214:453–66.
20. Zhong J, Liu W, Yu X. Characterization of three-dimensional myocardial deformation in the mouse heart: an MR tagging study. J Magn Reson Imaging. 2008;27:1263–70.
21. Axel L, Gonçalves RC, Bloomgarden D. Regional heart wall motion: two-dimensional analysis and functional imaging with MR imaging. Radiology. 1992;183:745–50.
22. Guttman MA, Prince JL, McVeigh ER. Tag and contour detection in tagged MR images of the left ventricle. IEEE Trans Med Imaging. 1994;13:74–88.

23. Bundy JM, Lorenz CH. Tagasist: a post-processing and analysis tools package for tagged magnetic resonance imaging. Comput Med Imaging Graph. 1997;21:225–32.
24. Liu W, Ashford MW, Chen J, Watkins MP, Williams TA, Wickline SA, Yu X. MR tagging demonstrates quantitative differences in regional ventricular wall motion in mice, rats, and men. Am J Physiol Heart Circ Physiol. 2006;291:H2515–21.
25. Moore CC, O'Dell WG, McVeigh ER, Zerhouni EA. Calculation of three-dimensional left ventricular strains from biplanar tagged MR images. J Magn Reson Imaging. 1992;2: 165–75.
26. Fogel MA, Gupta KB, Weinberg PM, Hoffman EA. Regional wall motion and strain analysis across stages of Fontan reconstruction by magnetic resonance tagging. Am J Phys. 1995;269:H1132–52.
27. Young AA. Model tags: direct three-dimensional tracking of heart wall motion from tagged magnetic resonance images. Med Image Anal. 1999;3:361–72.
28. Hu Z, Metaxas D, Axel L. In vivo strain and stress estimation of the heart left and right ventricles from MRI images. Med Image Anal. 2003;7:435–44.
29. Pipe JG, Boes JL, Chenevert TL. Method for measuring three-dimensional motion with tagged MR imaging. Radiology. 1991;181:591–5.
30. O'Dell WG, Moore CC, Hunter WC, Zerhouni EA, McVeigh ER. Three-dimensional myocardial deformations: calculation with displacement field fitting to tagged MR images. Radiology. 1995;195:829–35.
31. Kuijer JP, Marcus JT, Götte MJ, van Rossum AC, Heethaar RM. Three-dimensional myocardial strain analysis based on short- and long-axis magnetic resonance tagged images using a 1D displacement field. Magn Reson Imaging. 2000;18:553–64.
32. Chen Y, Amini AA. A MAP framework for tag line detection in SPAMM data using Markov random fields on the B-spline solid. IEEE Trans Med Imaging. 2002;21:1110–22.
33. Huang J, Abendschein D, Dávila-Román VG, Amini AA. Spatio-temporal tracking of myocardial deformations with a 4-D B-spline model from tagged MRI. IEEE Trans Med Imaging. 1999;18:957–72.
34. Wang YP, Chen Y, Amini AA. Fast LV motion estimation using subspace approximation techniques. IEEE Trans Med Imaging. 2001;20:499–513.
35. Amini AA, Chen Y, Elayyadi M, Radeva P. Tag surface reconstruction and tracking of myocardial beads from SPAMM-MRI with parametric B-spline surfaces. IEEE Trans Med Imaging. 2001;20:94–103.
36. Tustison NJ, Dávila-Román VG, Amini AA. Myocardial kinematics from tagged MRI based on a 4-D B-spline model. IEEE Trans Biomed Eng. 2003;50:1038–40.
37. Osman NF, Kerwin WS, McVeigh ER, Prince JL. Cardiac motion tracking using CINE harmonic phase (HARP) magnetic resonance imaging. Magn Reson Med. 1999;42:1048–60.
38. Osman NF, Prince JL. Regenerating MR tagged images using harmonic phase (HARP) methods. IEEE Trans Biomed Eng. 2004;51:1428–33.
39. Osman NF, McVeigh ER, Prince JL. Imaging heart motion using harmonic phase MRI. IEEE Trans Med Imaging. 2000;19:186–202.
40. Osman NF, Prince JL. Visualizing myocardial function using HARP MRI. Phys Med Biol. 2000;45:1665–82.
41. Liu W, Chen J, Ji S, Allen JS, Bayly PV, Wickline SA, Yu X. Harmonic phase MR tagging for direct quantification of Lagrangian strain in rat hearts after myocardial infarction. Magn Reson Med. 2004;52:1282–90.
42. Valeti VU, Chun W, Potter DD, Araoz PA, McGee KP, Glockner JF, Christian TF. Myocardial tagging and strain analysis at 3 Tesla: comparison with 1.5 Tesla imaging. J Magn Reson Imaging. 2006;23:477–80.
43. Herzka DA, Guttman MA, McVeigh ER. Myocardial tagging with SSFP. Magn Reson Med. 2003;49:329–40.
44. Pattynama PM, Doornbos J, Hermans J, van der Wall EE, de Roos A. Magnetic resonance evaluation of regional left ventricular function. Effect of through-plane motion. Invest. Radiology. 1992;27:681–5.

45. Brotman D, Zhang Z, Sampath S. Effect of through-plane motion on left ventricular rotation: a study using slice-following harmonic phase imaging. Magn Reson Med. 2013;69:1421–9.
46. Fischer SE, McKinnon GC, Maier SE, Boesiger P. Improved myocardial tagging contrast. Magn Reson Med. 1993;30:191–200.
47. Fischer SE, McKinnon GC, Scheidegger MB, Prins W, Meier D, Boesiger P. True myocardial motion tracking. Magn Reson Med. 1994;31:401–13.
48. Gilson WD, Yang Z, French BA, Epstein FH. Complementary displacement-encoded MRI for contrast-enhanced infarct detection and quantification of myocardial function in mice. Magn Reson Med. 2004;51:744–52.
49. Gilson WD, Yang Z, French BA, Epstein FH. Measurement of myocardial mechanics in mice before and after infarction using multislice displacement-encoded MRI with 3D motion encoding. Am J Physiol Heart Circ Physiol. 2005;288:H1491–7.
50. Zhong J, Yu X. Strain and torsion quantification in mouse hearts under dobutamine stimulation using 2D multiphase MR DENSE. Magn Reson Med. 2010;64:1315–22.
51. Ghiglia DC, Pritt MD. Two-dimensional phase unwrapping: theory, algorithms, and software. New York: Wiley; 1998.
52. Aletras AH, Wen H. Mixed echo train acquisition displacement encoding with stimulated echoes: an optimized DENSE method for in vivo functional imaging of the human heart. Magn Reson Med. 2001;46:523–34.
53. Epstein FH, Gilson WD. Displacement-encoded cardiac MRI using cosine and sine modulation to eliminate (CANSEL) artifact-generating echoes. Magn Reson Med. 2004; 52:774–81.
54. Aletras AH, Ingkanisorn WP, Mancini C, Arai AE. DENSE with SENSE. J Magn Reson. 2005;176:99–106.
55. Bryant DJ, Payne JA, Firmin DN, Longmore DB. Measurement of flow with NMR imaging using a gradient pulse and phase difference technique. J Comput Assist Tomogr. 1984;8: 588–93.
56. van Dijk P. Direct cardiac NMR imaging of heart wall and blood flow velocity. J Comput Assist Tomogr. 1984;8:429–36.
57. Arai AE, Gaither CC, Epstein FH, Balaban RS, Wolff SD. Myocardial velocity gradient imaging by phase contrast MRI with application to regional function in myocardial ischemia. Magn Reson Med. 1999;42:98–109.
58. Delfino JG, Johnson KR, Eisner RL, Eder S, Leon AR, Oshinski JN. Three-directional myocardial phase-contrast tissue velocity MR imaging with navigator-echo gating: in vivo and in vitro study. Radiology. 2008;246:917–25.
59. Jung BA, Kreher BW, Markl M, Hennig J. Visualization of tissue velocity data from cardiac wall motion measurements with myocardial fiber tracking: principles and implications for cardiac fiber structures. Eur J Cardiothorac Surg. 2006;29(Suppl 1):S158–64.
60. Beache GM, Wedeen VJ, Weisskoff RM, O'Gara PT, Poncelet BP, Chesler DA, Brady TJ, Rosen BR, Dinsmore RE. Intramural mechanics in hypertrophic cardiomyopathy: functional mapping with strain-rate MR imaging. Radiology. 1995;197:117–24.
61. Nayler GL, Firmin DN, Longmore DB. Blood flow imaging by cine magnetic resonance. J Comput Assist Tomogr. J Comput Assist Tomogr.1986;10:715–22.
62. Neizel M, Korosoglou G, Lossnitzer D, Kühl H, Hoffmann R, Ocklenburg C, Giannitsis E, Osman NF, Katus HA, Steen H. Impact of systolic and diastolic deformation indexes assessed by strain-encoded imaging to predict persistent severe myocardial dysfunction in patients after acute myocardial infarction at follow-up. J Am Coll Cardiol. 2010;56:1056–62.
63. Korosoglou G, Lossnitzer D, Schellberg D, et al. Strain-encoded cardiac MRI as an adjunct for dobutamine stress testing: incremental value to conventional wall motion analysis. Circ Cardiovasc Imaging. 2009;2:132–40.
64. Korosoglou G, Lehrke S, Wochele A, Hoerig B, Lossnitzer D, Steen H, Giannitsis E, Osman NF, Katus HA. Strain-encoded CMR for the detection of inducible ischemia during intermediate stress. JACC Cardiovasc Imaging. 2010;3:361–71.
65. Epstein FH. MR in mouse models of cardiac disease. NMR Biomed. 2007;20:238–55.

66. Sengupta PP, Korinek J, Belohlavek M, Narula J, Vannan MA, Jahangir A, Khandheria BK. Left ventricular structure and function: basic science for cardiac imaging. J Am Coll Cardiol. 2006;48:1988–2001.
67. Kuijer JPA, Marcus JT, Götte MJW, van Rossum AC, Heethaar RM. Three-dimensional myocardial strains at end-systole and during diastole in the left ventricle of normal humans. J Cardiovasc Magn Reson. 2002;4:341–51.
68. Young AA, Kramer CM, Ferrari VA, Axel L, Reichek N. Three-dimensional left ventricular deformation in hypertrophic cardiomyopathy. Circulation. 1994;90:854–67.
69. Rademakers FE, Rogers WJ, Guier WH, Hutchins GM, Siu CO, Weisfeldt ML, Weiss JL, Shapiro EP. Relation of regional cross-fiber shortening to wall thickening in the intact heart. Three-dimensional strain analysis by NMR tagging. Circulation. 1994;89:1174–82.
70. Aletras AH, Tilak GS, Natanzon A, Hsu LY, Gonzalez FM, Hoyt RF, Arai AE. Retrospective determination of the area at risk for reperfused acute myocardial infarction with T2-weighted cardiac magnetic resonance imaging: histopathological and displacement encoding with stimulated echoes (DENSE) functional validations. Circulation. 2006;113:1865–70.
71. McVeigh ER, Zerhouni EA. Noninvasive measurement of transmural gradients in myocardial strain with MR imaging. Radiology. 1991;180:677–83.
72. Daire JL, Jacob JP, Hyacinthe JN, Croisille P, Montet-Abou K, Richter S, Botsikas D, Lepetit-Coiffé M, Morel D, Vallée JP. Cine and tagged cardiovascular magnetic resonance imaging in normal rat at 1.5 T: a rest and stress study. J Cardiovasc Magn Reson. 2008;10:48.
73. Zhong J, Liu W, Yu X. Transmural myocardial strain in mouse: quantification of high-resolution MR tagging using harmonic phase (HARP) analysis. Magn Reson Med. 2009;61:1368–73.
74. Dall'Armellina E, Jung BA, Lygate CA, Neubauer S, Markl M, Schneider JE. Improved method for quantification of regional cardiac function in mice using phase-contrast MRI. Magn Reson Med. 2012;67:541–51.
75. Jung B, Odening KE, Dall'Armellina E, Föll D, Menza M, Markl M, Schneider JE. A quantitative comparison of regional myocardial motion in mice, rabbits and humans using in-vivo phase contrast CMR. J Cardiovasc Magn Reson. 2012;14:87.
76. Azevedo CF, Amado LC, Kraitchman DL, Gerber BL, Osman NF, Rochitte CE, Edvardsen T, Lima JAC. Persistent diastolic dysfunction despite complete systolic functional recovery after reperfused acute myocardial infarction demonstrated by tagged magnetic resonance imaging. Eur Heart J. 2004;25:1419–27.
77. Croisille P, Moore CC, Judd RM, JAC L, Arai M, ER MV, Becker LC, Zerhouni EA. Differentiation of viable and nonviable myocardium by the use of three-dimensional tagged MRI in 2-day-old reperfused canine infarcts. Circulation. 1999;99:284–91.
78. Kraitchman DL, Young AA, Bloomgarden DC, Fayad ZA, Dougherty L, Ferrari VA, Boston RC, Axel L. Integrated MRI assessment of regional function and perfusion in canine myocardial infarction. Magn Reson Med. 1998;40:311–26.
79. Thomas D, Ferrari VA, Janik M, Kim DH, Pickup S, Glickson JD, Zhou R. Quantitative assessment of regional myocardial function in a rat model of myocardial infarction using tagged MRI. MAGMA. 2004;17:179–87.
80. Zhou R, Pickup S, Glickson JD, Scott CH, Ferrari VA. Assessment of global and regional myocardial function in the mouse using cine and tagged MRI. Magn Reson Med. 2003;49:760–4.
81. Epstein FH, Yang Z, Gilson WD, Berr SS, Kramer CM, French BA. MR tagging early after myocardial infarction in mice demonstrates contractile dysfunction in adjacent and remote regions. Magn Reson Med. 2002;48:399–403.
82. Ashikaga H, Mickelsen SR, Ennis DB, Rodriguez I, Kellman P, Wen H, McVeigh ER. Electromechanical analysis of infarct border zone in chronic myocardial infarction. Am J Physiol Heart Circ Physiol. 2005;289:H1099–105.
83. Semsarian C, Ingles J, Maron MS, Maron BJ. New perspectives on the prevalence of hypertrophic cardiomyopathy. J Am Coll Cardiol. 2015;65:1249–54.
84. McMurray JJ, Stewart S. Epidemiology, aetiology, and prognosis of heart failure. Heart. 2000;83:596–602.
85. Neubauer S. The failing heart – an engine out of fuel. N Engl J Med. 2007;356:1140–51.

86. Litwin SE, Katz SE, Weinberg EO, Lorell BH, Aurigemma GP, Douglas PS. Serial echocardiographic-doppler assessment of left ventricular geometry and function in rats with pressure-overload hypertrophy. Chronic angiotensin-converting enzyme inhibition attenuates the transition to heart failure. Circulation. 1995;91:2642–54.
87. Songstad NT, Johansen D, How OJ, Kaaresen PI, Ytrehus K, Acharya G. Effect of transverse aortic constriction on cardiac structure, function and gene expression in pregnant rats. PLoS One. 2014;9:e89559.
88. van Nierop BJ, van Assen HC, van Deel ED, Niesen LBP, Duncker DJ, Strijkers GJ, Nicolay K. Phenotyping of left and right ventricular function in mouse models of compensated hypertrophy and heart failure with cardiac MRI. PLoS One. 2013;8:1–9.
89. Cantor EJF, Babick AP, Vasanji Z, Dhalla NS, Netticadan T. A comparative serial echocardiographic analysis of cardiac structure and function in rats subjected to pressure or volume overload. J Mol Cell Cardiol. 2005;38:777–86.
90. Blom AS, Pilla JJ, Arkles J, Dougherty L, Ryan LP, Iii JHG, Acker MA, Gorman RC. Ventricular restraint prevents infarct expansion and improves borderzone function after myocardial infarction: a study using magnetic resonance imaging, three-dimensional surface modeling, and myocardial tagging. Ann Thorac Surg. 2007;84:2004–10.
91. Azevedo CF, Amado LC, Kraitchman DL, Gerber BL, Edvardsen T, Osman NF, Rochitte CE, Wu KC, Lima JAC. The effect of intra-aortic balloon counterpulsation on left ventricular functional recovery early after acute myocardial infarction: a randomized experimental magnetic resonance imaging study. Eur Heart J. 2005;26:1235–41.
92. Guccione JM, Walker JC, Beitler JR, et al. The effect of anteroapical aneurysm plication on end-systolic three-dimensional strain in the sheep: a magnetic resonance imaging tagging study. J Thorac Cardiovasc Surg. 2006;131:579–86.
93. Traverse JH, Henry TD, Moye' LA. Is the measurement of left ventricular ejection fraction the proper end point for cell therapy trials? An analysis of the effect of bone marrow mononuclear stem cell administration on left ventricular ejection fraction after ST-segment elevation myocardia. Am Heart J. 2011;162:671–7.
94. Van Slochteren FJ, Teske AJ, Van Der Spoel TIG, Koudstaal S, Doevendans PA, Sluijter JPG, Cramer MJM, Chamuleau SAJ. Advanced measurement techniques of regional myocardial function to assess the effects of cardiac regenerative therapy in different models of ischaemic cardiomyopathy. Eur Heart J Cardiovasc Imaging. 2012;13:808–18.
95. Wolf A, Sanina C, Premer C, et al. Synergistic effects of combined cell therapy for chronic ischemic cardiomyopathy. J Am Coll Cardiol. 2015;66(18):1990–9.
96. Chen Y, Ye L, Zhong J, et al. The structural basis of functional improvement in response to human umbilical cord blood stem cell transplantation. Cell Transplant. 2015;24:971–83.
97. Scimia MC, Gumpert AM, Koch WJ. Cardiovascular gene therapy for myocardial infarction. Expert Opin Biol Ther. 2014;14:183–95.
98. Carlsson M, Osman NF, Ursell PC, Martin AJ, Saeed M. Quantitative MR measurements of regional and global left ventricular function and strain after intramyocardial transfer of VM202 into infarcted swine myocardium. Am J Physiol Heart Circ Physiol. 2008;295:H522–32.
99. Saeed M, Saloner D, Do L, Wilson M, Martin A. Cardiovascular magnetic resonance imaging in delivering and evaluating the efficacy of hepatocyte growth factor gene in chronic infarct scar. Cardiovasc Revascularization Med. 2011;12:111–22.
100. Dicks D, Saloner D, Martin A, Carlsson M, Saeed M. Percutaneous transendocardial VEGF gene therapy: MRI guided delivery and characterization of 3D myocardial strain. Int J Cardiol. 2010;143:255–63.
101. Harris SP, Lyons RG, Bezold KL. In the thick of it: HCM-causing mutations in myosin binding proteins of the thick filament. Circ Res. 2011;108:751–64.
102. Desjardins CL, Chen Y, Coult AT, Hoit BD, Yu X, Stelzer JE. Cardiac myosin binding protein C insufficiency leads to early onset of mechanical dysfunction. Circ Cardiovasc Imaging. 2012;5:127–36.
103. Hershberger RE, Hedges DJ, Morales A. Dilated cardiomyopathy: the complexity of a diverse genetic architecture. Nat Rev Cardiol. 2013;10:531–47.

104. Hankiewicz JH, Goldspink PH, Buttrick PM, Lewandowski ED. Principal strain changes precede ventricular wall thinning during transition to heart failure in a mouse model of dilated cardiomyopathy. Am J Physiol Heart Circ Physiol. 2008;294:H330–6.
105. Biggar WD, Klamut HJ, Demacio PC, Stevens DJ, Ray PN. Duchenne muscular dystrophy: current knowledge, treatment, and future prospects. Clin Orthop Relat Res. 2002;88–106
106. Li W, Liu W, Zhong J, Yu X. Early manifestation of alteration in cardiac function in dystrophin deficient mdx mouse using 3D CMR tagging. J Cardiovasc Magn Reson. 2009;11:40.
107. Lubamba B, Dhooghe B, Noel S, Leal T. Cystic fibrosis: insight into CFTR pathophysiology and pharmacotherapy. Clin Biochem. 2012;45:1132–44.
108. Nagel G, Hwang TC, Nastiuk KL, Nairn AC, Gadsby DC. The protein kinase A-regulated cardiac Cl^- channel resembles the cystic fibrosis transmembrane conductance regulator. Nature. 1992;360:81–4.
109. Fomby P, Cherlin AJ. Family instability and child well-being. Am Sociol Rev. 2007;72:181–204.
110. Hodges CA, Cotton CU, Palmert MR, Drumm ML. Generation of a conditional null allele for Cftr in mice. Genesis. 2008;46:546–52.
111. Jiang K, Jiao S, Vitko M, Darrah R, Flask CA, Hodges CA, Yu X. The impact of cystic fibrosis transmembrane regulator disruption on cardiac function and stress response. J Cyst Fibros. 2016;15:34–42.

Chapter 3
Cardiac Diffusion MRI

Irvin Teh

Abbreviations

1D	One-dimensional
3D	Three-dimensional
ADC	Apparent diffusion coefficient
bSSFP	Balanced steady-state free precession
CODE	Convex optimised diffusion encoding
CPMG	Carr-Purcell-Meiboom-Gill
DKI	Diffusion kurtosis imaging
DSI	Diffusion spectrum imaging
DTI	Diffusion tensor imaging
DW	Diffusion-weighted
EPI	Echo planar imaging
FA	Fractional anisotropy
FACT	Fibre assignment by continuous tracking
FSE	Fast spin echo
GMN	Gradient moment-nulling
HA	Helix angle
HARDI	High angular resolution diffusion imaging
HCM	Hypertrophic cardiomyopathy
IVIM	Intra-voxel incoherent motion
LAD	Left anterior descending artery
LGE	Late gadolinium enhanced

I. Teh, PhD
British Heart Foundation Experimental Magnetic Resonance Unit (BMRU),
Division of Cardiovascular Medicine, University of Oxford,
Wellcome Trust Centre for Human Genetics, Old Road Campus, Roosevelt Drive,
Oxford OX3 7BN, UK
e-mail: Irvin.teh@cardiov.ox.ac.uk

C. Constantinides (ed.), *Protocols and Methodologies in Basic Science and Clinical Cardiac MRI*, https://doi.org/10.1007/978-3-319-53001-7_3

LV	Left ventricle
MD	Mean diffusivity
MI	Myocardial infarction
MRI	Magnetic resonance imaging
ODF	Orientation distribution function
PCATMIP	Principal component analysis and temporal maximum intensity projection
PGSE	Pulsed gradient spin echo
PMI	Post-mortem intervals to fixation
QBI	Q-ball imaging
RF	Radiofrequency
ROI	Region-of-interest
RV	Right ventricle
SE	Spin echo
SNR	Signal-to-noise ratio
SRI	Synchrotron radiation imaging
STEAM	Stimulated echo acquisition mode
TA	Transverse angle
TD	Trigger-delay
TMIP	Temporal maximum intensity projection
VF	Vascular volume fraction

Introduction

The objective of this chapter is to introduce the application of diffusion MRI in structural imaging of the heart. It begins with an introduction to the underlying biological structure of the heart, and a brief history of the evolution of cardiac diffusion MRI. The concept and methodology of diffusion MRI is introduced, and followed by a description of the state-of-the-art in acquisition, reconstruction and application of cardiac diffusion MRI. Key challenges and solutions specific to in vivo and ex vivo cardiac diffusion MRI are reviewed. Quality assurance and validation of diffusion MRI methods are presented. The chapter concludes with an overview of current gaps in knowledge and potential research opportunities.

Cardiac Structure

The cardiac microstructure is comprised primarily of locally-aligned cardiomyocytes that are connected in a branching network or syncytium via intercalated discs. The length and width of cardiomyocytes in human heart are in the range of 141 ± 9 μm and 19 ± 1.7 μm respectively [59]. Around each myocardial cell and group of cells are nerves, vessels, and a supporting matrix of collagenous fibrous tissue that forms the endomysium and perimysium. The cardiomyocytes are organised into

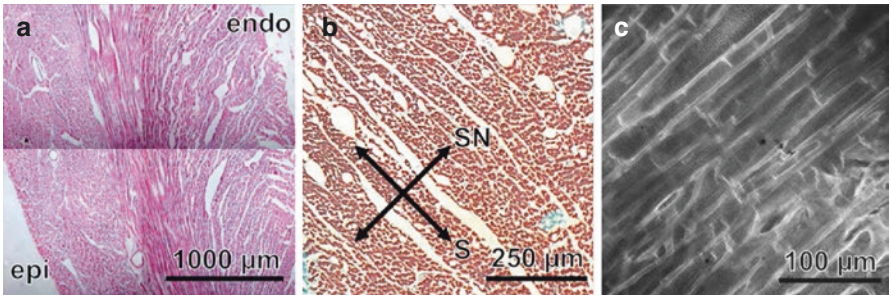

Fig. 3.1 (**a**) 2 × 2 histological montage in the LV septal wall in a rabbit heart shows the left to right helical fibre orientation from the subepicardium to the subendocardium (Haemotoxylin and Eosin, 5× objective). (**b**) Histological image of mid-ventricular LV myocardium in a rabbit heart illustrates organisation of cells into sheetlet structures. Sheetlet (S) and sheetlet-normal (SN) directions are shown, with cells oriented perpendicular to the image plane (Massons Trichrome Stain, 10× objective). (**c**) Two-photon microscopy of a rat dye-loaded heart shows highly coherent organisation of cardiomyocytes and capillaries (Di-4-ANEPPS) (Histology images courtesy of Dr. Rebecca Burton (Peter Kohl Lab, Oxford) and 2-photon image courtesy of Dr. Rebecca Burton and Dr. Alex Corbett, University of Oxford)

laterally interconnected layers or laminae, known as sheets or sheetlets, several cells thick and long, and separated by small cleft-like spaces [35, 70, 107]. Others have emphasised that these laminar structures are highly discontinuous and extend over short length scales [10, 36], and the term *sheetlets* is therefore adopted here. Despite the fact that cardiomyocytes are branching and do not form discrete, single fibres in the anatomical sense, their voxel-averaged long-axis orientation is often referred to, for convenience, as the *fibre direction* or *fibre orientation* in the context of diffusion MRI. The sheetlet direction corresponds to the direction normal to the fibre direction within the plane of the sheetlets. The sheetlet-normal is the direction orthogonal to the fibre and sheetlet directions (Fig. 3.1).

The helical arrangement of cardiomyocytes across the heart is well known [111]. Quantitative assessment by histological methods showed that the fibre orientation changes from a left- to right-handed helix progressing from the subepicardium to subendocardium [178], while alternating herringbone-like arrangements of sheetlets have been observed in the left ventricle (LV) myocardium [70]. There is ongoing debate regarding the higher order organisation of cardiomyocytes and excellent reviews are available [10, 61]. The reader is also referred to more detailed descriptions of heart architecture and microstructure [73, 95].

Evolution of Cardiac Diffusion MRI

The advent of diffusion MRI dates back to 1950 when Hahn observed that spin motion in the presence of a heterogeneous magnetic field resulted in a decreased signal intensity [68]. In 1955, Anderson, et al. demonstrated that spin echoes and pulsed field gradients can be used to store information [9], while in 1956, Torrey established the

Bloch-Torrey equation describing the magnetisation of spins in the presence of diffusion that governs diffusion MRI [187]. Stejskal and Tanner pioneered the use of the pulsed gradient spin echo (PGSE) sequence that remains the most widely used method to date for acquiring diffusion-weighted (DW) data [175]. Callaghan subsequently described the framework of q-space imaging that relates the measured signal with the diffusion propagator [25]. In 1994, Basser et al. conceptualised use of a tensor to fit the DW signal, thereby enabling measurement of rotationally invariant indices of anisotropic diffusion [16]. The approach known as diffusion tensor imaging (DTI) continues to drive many structural imaging applications in the heart and other organs.

The application of diffusion MRI in the heart is a more recent phenomenon, mainly due to the technical difficulties associated with imaging a beating organ with an imaging sequence that is highly sensitive to motion. Major milestones in cardiac diffusion MRI are summarised in Table 3.1.

Table 3.1 Major milestones in development of cardiac diffusion MRI

Year	Description	Authors
1994	Observation of anisotropy in isolated rat myocardium	Garrido et al. [57]
1994	First diffusion MRI of human heart in vivo, with stimulated echo echo planar imaging	Edelman et al. [44]
1995	Imaging of cardiac cell architecture in vivo and in vitro	Reese et al. [155]
1998	Histological validation of DTI and correspondence to fibre direction	Hsu et al. [77], Scollan et al. [160]
1999	Identification of sweet spots for strain-free DTI in vivo	Tseng et al. [190]
2001	Use of bi-exponential fit to quantify perfusion component of the diffusion signal	Hsu et al. [76]
2003	Histological validation of DTI and correspondence to sheetlet structures	Tseng et al. [191]
2005	Investigation of roles of fibre and sheetlet structure in ventricular wall thickening	Chen et al. [29]
2006	Mapping of structure-function relationship in hypertrophic human heart	Tseng et al. [189]
2006	Mapping DTI changes in infarct and remodelling in human patients	Wu et al. [207]
2007	Spin echo diffusion MRI in vivo for reduced motion sensitivity	Gamper et al. [56]
2009	Diffusion spectrum imaging of the heart	Sosnovik et al. [171]
2009	Investigation of development in heart with DTI and histological correlation	Wu and Wu [208]
2012	DTI atlas of ex vivo human hearts	Lombaert et al. [110]
2014	Diffusion MRI in vivo with 3D balanced steady-state free precession	Nguyen et al. [136]
2014	Strain correction for stimulated echo DTI in vivo	Stoeck et al. [176]
2014	First DTI of mouse heart in vivo and assessment of cell therapy in vivo	Sosnovik et al. [169]
2015	Quantitative assessment and validation of myocardial perfusion in isolated hearts	Abdullah et al. [2]
2015	Use of higher order motion-nulled diffusion gradients for improved motion insensitivity; first DTI of rat heart in vivo	Welsh et al. [203]

Table 3.1 (continued)

Year	Description	Authors
2016	Systematic comparison of methods for assessing non-Gaussian diffusion	McClymont et al. [118]
2017	Validation of DTI in whole rat myocardium with structure tensor synchrotron radiation imaging	Teh et al. [185]
2017	Assessment of myocardial microstructural dynamics by in vivo DTI	Nielles-Vallespin et al. [139]

Theory

Origin of Signal

In 1827, the botanist Robert Brown observed the random motion of pollen grains in water using microscopy [22]. Einstein subsequently showed that such macroscopic random or Brownian motion is related to the thermal energy of particles, and formalised the description of Brownian motion as a stochastic process [47]. Taking into consideration the Gaussian conditional probability of self-diffusion, he derived an expression for the mean-square displacement of free diffusion in three dimensions (Eq. 3.1) from which the diffusion coefficient can be determined.

$$\left\langle \left(\mathbf{r}' - \mathbf{r}\right)^2 \right\rangle = 6Dt \tag{3.1}$$

where $\mathbf{r}'$ is the particle or spin displacement after time t, $\mathbf{r}$ is its displacement at time zero, and D is the diffusion coefficient.

In biological tissues, diffusion (of water, as is referred to throughout this chapter) is affected by the presence of cells, organelles, membranes, vessels, and other structures, and can be said to be both *hindered* and *restricted* [19]. In anisotropic structures such as cardiac tissue, diffusion occurs preferentially along the fibre direction, resulting in anisotropic diffusion. The measured DW signal can therefore be used to infer structural features such as cell and sheetlet orientation. Furthermore, the presence of multiple compartments such as the intracellular, extracellular and vascular spaces, and restrictions to diffusion due to membranes and other structures, means that the diffusion profile is generally non-Gaussian [118].

Measuring Diffusion

In a spatially varying magnetic field, the Larmor frequency of spins is governed by the main magnetic field, $\mathbf{B_0}$, the proton gyromagnetic ratio, γ, the gradient of the pulsed field gradient component parallel to $\mathbf{B_0}$, $\mathbf{g}$ and the nuclear spin coordinates, $\mathbf{r}$. The transverse magnetisation in the rotating frame, M_+, can be expressed with the Bloch-Torrey equation (Eq. 3.2).

$$\frac{\partial M_+(\mathbf{r},t)}{\partial t} = -i\gamma \mathbf{g}\cdot\mathbf{r} - \frac{M_+(\mathbf{r},t)}{T_2} + D\nabla^2 M_+(\mathbf{r},t) - \mathbf{v}\cdot\nabla M_+(\mathbf{r},t) \tag{3.2}$$

where D is the diffusion coefficient, $\mathbf{v}$ is flow, t is time and T_2 is relaxation time.

Diffusion is typically measured by sensitising a pulse sequence to diffusion through the application of diffusion gradients. Figure 3.2 illustrates a commonly used pulse sequence known as a PGSE or Stejskal-Tanner sequence including diffusion gradients G_1 and G_2 [175]. Immediately following the radiofrequency (RF) excitation pulse, spins within a given voxel are in phase. The application of G_1 results in a spatially varying distribution of Larmor frequencies, which in turn results in dephasing of spins along the direction of G_1. Application of the RF refocusing pulse reverses the magnetisation vectors and, in the idealised case without diffusion or motion, G_2 perfectly rephases the spins and the magnitude of the net magnetisation is recovered, less that due to spin-spin or T_2 relaxation. Where diffusion along the direction of G_1 and G_2 occurs during the diffusion-weighting period, individual spins are not perfectly rephased. This phase dispersion results in a decrease in net signal magnitude that forms the basis of diffusion contrast. Ignoring imaging gradients, the accrued phase in a given spin at the time of the spin echo is given by Eq. 3.3. In the case of coherent motion such as bulk flow, there is a net phase shift but no loss of signal. In contrast, incoherent motion leads to phase dispersion akin to that occurring as a result of diffusion.

$$\phi(t) = \gamma \int_0^t \mathbf{G}(t)\cdot\mathbf{r}(t)\,dt \tag{3.3}$$

where ϕ is the phase of a given spin, γ is the proton gyromagnetic ratio, $\mathbf{G}$ is the gradient waveform, $\mathbf{r}$ is the spin displacement vector and t is time.

In a homogeneous system free of restrictions, the net signal magnitude decreases exponentially with diffusion-sensitising factor known as the b-value or b, and Eq. 3.2 can be reformulated as Eq. 3.4. By acquiring identical measurements with at least two different b-values, usually with at least one non-DW measurement, the apparent diffusion coefficient (ADC) can be determined. The ADC is sometimes referred to as the tissue diffusivity. However, the term *apparent* is used to highlight that in practice, the measured diffusivity depends on measurement parameters, as contrasted with tissue intrinsic diffusivity that is independent of the acquisition.

$$S_i = S_0 \cdot e^{-b_i D} \tag{3.4}$$

where S_i is the measured signal intensity, S_0 is the signal intensity in the absence of diffusion-weighting, b_i is the b-value and D is the apparent diffusion coefficient.

The effective b-value includes contributions from the diffusion gradients, imaging gradients and interactions between the diffusion and imaging gradients, or cross-terms. For simplicity, imaging gradients are sometimes neglected as they tend to be small, and the non-DW data are loosely referred to as $b = 0$ data despite having

non-zero b-value. However, the effect of cross-terms on the effective b-value can be significant, and a more accurate calculation of b may be needed. In a spin echo sequence, the b-matrix is given generally by Eq. 3.5 [105]. Comprehensive detail on deriving b-values may be found elsewhere [65, 94].

$$\mathbf{b}(t) = \gamma^2 \int_0^{TE} \left| \int_0^t \mathbf{G}(t')\, dt' \right|^2 dt \tag{3.5}$$

where $\mathbf{b}$ is the b-matrix, γ is the proton gyromagnetic ratio, TE is the echo time, $\mathbf{G}$ are gradient vectors, and $\mathbf{G}(t') = -\mathbf{G}(t')$ after the refocusing pulse.

For the simplified case of trapezoidal diffusion gradients (Fig. 3.2), the b-value contribution by the diffusion gradients in the direction of $\mathbf{G}$ incorporating and ignoring diffusion gradient ramp times are given by Eqs. 3.6 and 3.7 respectively.

$$b = \gamma^2 G^2 \left[\delta^2 \left(\Delta - \frac{\delta}{3} \right) + \frac{\varepsilon^2}{30} - \frac{\delta \varepsilon^2}{6} \right] \tag{3.6}$$

$$b = \gamma^2 G^2 \delta^2 \left(\Delta - \frac{\delta}{3} \right) \tag{3.7}$$

where G is the diffusion gradient magnitude, δ is the diffusion duration, Δ is the diffusion time and ε is the diffusion gradient ramp time.

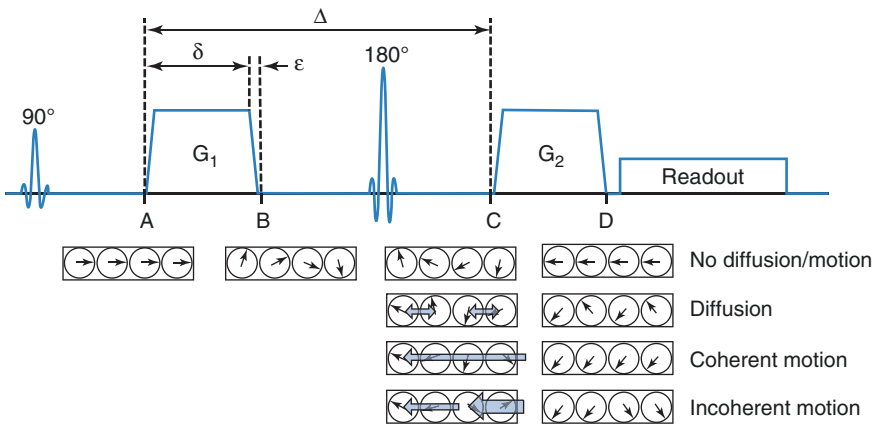

Fig. 3.2 Simplified diffusion-weighted spin echo sequence illustrates phase accrual as a result of identical diffusion gradients, G_1 and G_2. (**a**) After excitation, the magnetisation of spins in a given voxel are in phase; (**b**) G_1 results in dephasing of spins, which are (**c**) inverted by the refocusing pulse. In the absence of diffusion and bulk motion, (**d**) spins are rephased by G_2, and the signal is recovered. When diffusion occurs along the direction of the diffusion encoding, the spins are incompletely rephased, and there is a net signal loss due to phase dispersion. This is distinct from the effect of coherent motion or flow, which results in a phase shift rather than dispersion. Incoherent motion additionally leads to diffusion-like phase dispersion. For clarity, imaging gradients and T_2 relaxation are ignored

Signal Behaviour

In the myocardium, the diffusion signal arises from multiple compartments, primarily the intracellular, extracellular and vascular space, and is restricted by the presence of cellular structures such as membranes. Approximation of the diffusion signal with a mono-exponential function therefore works well only over a limited range of b-values. Figure 3.3 depicts the signal attenuation with b-value in a small region in the myocardium of an ex vivo rat heart, and in the buffer filling the LV cavity. The data illustrate that the signal intensity, S in the buffer is the same with different DW directions, with minor variations due to noise, and the diffusion in the buffer can be said to be isotropic. In the myocardium, S depends on the direction of diffusion weighting, and therefore diffusion in the myocardium is described as anisotropic. Based on prior knowledge, we find in this particular region at the midline of the LV septal wall, that the signal attenuation is greatest when the diffusion-weighting corresponds to the putative fibre direction (red line), intermediate in the putative sheetlet direction (yellow line), and least in the putative sheetlet-normal direction (blue line). In the myocardium, the signal attenuation is near mono-exponential up to b-values of about 1600 s/mm^2, above which the apparent diffusion is underestimated relative to the hypothetical unrestricted case due to restrictions by structures such as cell membranes [118]. In the buffer, deviation from mono-exponential decay at higher b-values is observed as a result of the noise floor rather than structural features.

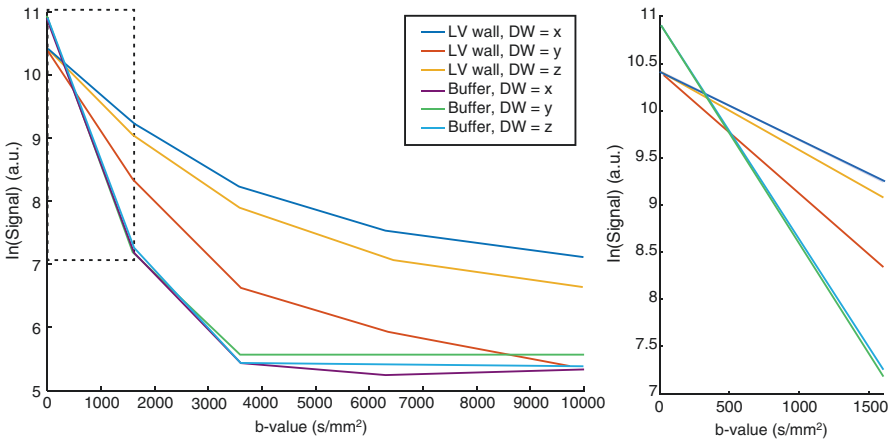

Fig. 3.3 Signal attenuation against b-value in a representative 3×3×3 voxel region at the midline of the LV septal wall in an ex vivo rat heart and at the buffer in the LV cavity. Data with diffusion-weighting in x, y and z, and b = 12, 400, 1600, 3600, 6400 and 10,000 s/mm^2 in an ex vivo rat heart are presented. Magnified region highlighting low b-value regime where signal attenuation is largely mono-exponential, contrasts with the non-mono-exponential decay at higher b-values

Acquisition and Reconstruction Strategies

Diffusion in the heart is a complex three-dimensional (3D) process and its behaviour can be described by a displacement distribution, also known as the *diffusion propagator*, e*nsemble average propagator* or *diffusion probability density function*. The diffusion propagator, $P(\mathbf{R})$ is the Fourier transform of q-space, a 3D space containing the DW signal intensities (Eq. 3.8). Details on q-space formalism can be found [15, 25].

$$P(\mathbf{R}) = \int_{\mathbf{q}\in\Re^3} E(\mathbf{q}) e^{-2\pi i \mathbf{q}.\mathbf{R}} d\mathbf{q} \tag{3.8}$$

where $E(\mathbf{q})$is the DW signal intensity at position $\mathbf{q}$ in q-space normalised by the non-DW signal intensity, $\mathbf{R}$ is the spin dynamic displacement, and $\mathbf{q} = \gamma\delta\mathbf{G}/2\pi$ where γ is the gyromagnetic ratio, δ is the diffusion duration and $\mathbf{G}$ is the diffusion gradient vector, assuming infinitesimally short δ, and $\delta << \Delta$ [128].

Various diffusion acquisition strategies exist to assess diffusion by sampling q-space in different ways [67], and tradeoffs are often made between scan time and accuracy (Fig. 3.4). In each of the following methods, at least one non-DW reference image is typically acquired along with a defined set of DW images, where each DW image corresponds to one point in q-space ($\mathbf{q} \neq \mathbf{0}$), resulting in a six-dimensional dataset.

In trace-weighted imaging, images are acquired with diffusion-weighting in three orthogonal directions. Measures of average diffusivity can be obtained by taking either the sum or the mean of the ADCs in three directions, calculated using Eq. 3.4, to yield the trace and mean ADC respectively. DTI is widely used as it provides rotationally invariant measures of orientation and anisotropy while maintaining relative low data requirements and reconstruction complexity. Here, a minimum of six images with non-collinear diffusion-weighting are acquired and diffusion is approximated with a second order tensor that can be represented as a 3D ellipsoid [16, 17, 93]. In order to minimise orientation bias in the acquisition,

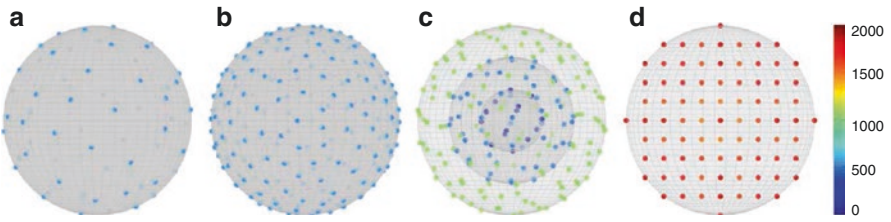

Fig. 3.4 Examples of q-space sampling schemes for (**a**) DTI, (**b**) high angular resolution diffusion imaging (HARDI), (**c**) diffusion kurtosis imaging (DKI) and (**d**) diffusion spectrum imaging (DSI) with 30, 100, 100 and 514 samples in q-space. Points are coloured by q-value (cm^{-1})

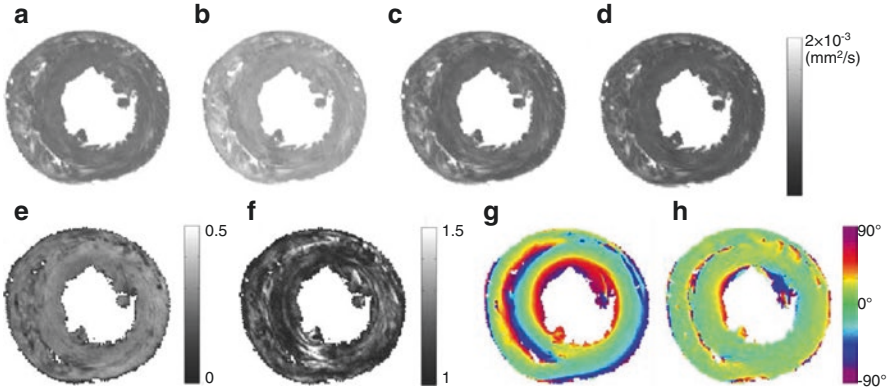

Fig. 3.5 Commonly reported DTI parameter maps (from **a**–**h**): mean diffusivity, λ_1, λ_2, λ_3, fractional anisotropy, transverse anisotropy, helix angle, transverse angle

q-samples are distributed evenly over a sphere, for instance, using electrostatic repulsion theory [33, 87]. Parametric maps representing various diffusion properties can readily be extracted from the tensors on a voxel-wise basis (Fig. 3.5).

For instance, the lengths and orientations of the three orthogonal major axes of the diffusion tensor correspond to the directions of greatest, intermediate and least diffusion, and are described by the primary, secondary and tertiary eigenvalues (λ_1, λ_2, λ_3) and eigenvectors ($\mathbf{v_1}$, $\mathbf{v_2}$, $\mathbf{v_3}$) respectively. Common metrics reported include the mean diffusivity (MD; Eq. 3.9), fractional anisotropy (FA; Eq. 3.10) [145], transverse anisotropy that is the ratio between λ_2 and λ_3, and transverse diffusivity that is the mean of λ_2 and λ_3. Since the trace is rotationally invariant, then the MD and mean ADC are equivalent, ignoring the effects of imaging gradients. Measures such as the relative anisotropy and volume ratio are also available [6], and the tensor can be further decomposed into basis sets to yield linear, planar and spherical components of the tensor [205].

$$MD = \frac{\lambda_1 + \lambda_2 + \lambda_3}{3} \tag{3.9}$$

$$FA = \sqrt{\frac{3\left[\left(\lambda_1 - \langle\lambda\rangle\right)^2 + \left(\lambda_2 - \langle\lambda\rangle\right)^2 + \left(\lambda_3 - \langle\lambda\rangle\right)^2\right]}{2\left(\lambda_1^2 + \lambda_2^2 + \lambda_3^2\right)}} \tag{3.10}$$

where λ_1, λ_2, λ_3 are the primary, secondary and tertiary eigenvalues of the diffusion tensor.

Based on ex vivo DTI studies in the heart, $\mathbf{v_1}$, $\mathbf{v_2}$ and $\mathbf{v_3}$ have collectively been shown to generally correspond to the myocardial fibre, sheetlet and sheetlet-normal directions [72, 74, 77, 97, 160, 191]. Here, superquadric glyphs offer an appealing visual representation of the tensor that better reflects sheetlet structures than ellipsoids [48, 159]. The predominant cell and sheetlet orientations can then be characterised in terms of helix angle (HA), transverse angle (TA), sheetlet elevation

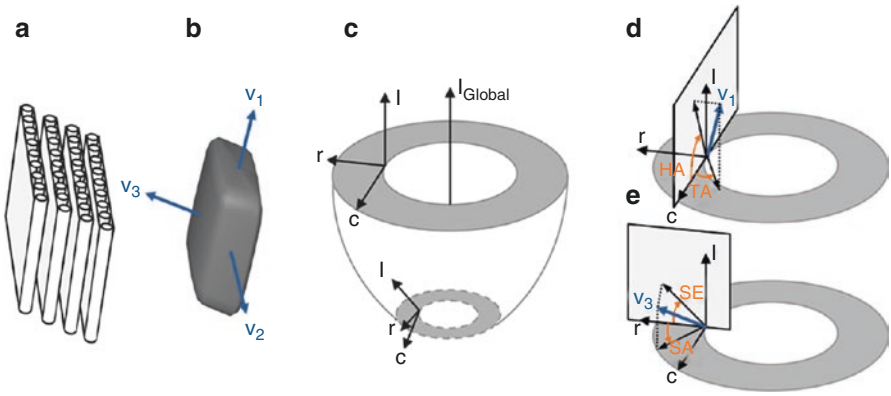

Fig. 3.6 (**a**) Schematic of cardiomyocytes arranged in four sheetlet layers. (**b**) Superquadric glyph describing the diffusion tensor and principal eigenvectors $\mathbf{v}_1$, $\mathbf{v}_2$ and $\mathbf{v}_3$ in a volume containing cardiomyocytes in (**a**). (**c**) Orientations of the longitudinal, radial and circumferential axes (**l**, **r**, and **c**) in the local coordinate system depend on the surface curvature of the heart, shown here in a basal and an apical slice. (**d**) Helix angle (HA) is the angle subtended by the projection of $\mathbf{v}_1$ onto the c-l plane and the short-axis plane. Transverse angle (TA) is the angle subtended by the projection of $\mathbf{v}_1$ onto the short-axis plane and the local circumferential axis. (**e**) Sheetlet elevation (SE) is the angle subtended by the projection of $\mathbf{v}_3$ onto the l-r plane and the short-axis plane. Sheetlet azimuth (SA) is the angle subtended by the projection of $\mathbf{v}_3$ onto the short-axis plane and the local radial axis (Figure by Teh et al. licenced under CC BY [184])

and sheetlet azimuth as described in Fig. 3.6 [184]. By convention, a negative HA describes a left-handed helix, and a positive HA describes a right-handed helix. The TA is also known as the intruding angle [158] or imbrication angle [126], and the sheetlet elevation has been referred to as the sheet angle [12], tertiary eigenvector inclination angle [161] and intersection angle ($+\pi/2$) [72]. In generating angle maps, it is important to take into account that the heart tapers towards the apex. Local coordinate systems are therefore computed based on the surface curvature of the heart, for instance using Laplace's method [88, 184], and used instead of global coordinate systems in the calculation of angle maps.

A major limitation of DTI is that it approximates P (Eq. 3.8) with a single Gaussian distribution, and thereby does not account for cell restrictions and can be ambiguous or misleading in the presence of multiply oriented cell and sheetlet populations. High angular resolution diffusion imaging (HARDI) provides a more accurate estimate of the diffusion orientation distribution function (ODF), that represents the probability that a water molecule diffuses in a given direction, and enables identification of multiply-oriented cell populations. HARDI data are acquired at a single q-shell as in DTI, but with more DW directions, typically exceeding 60, and higher b-values. Reconstruction of HARDI data using analytical q-ball imaging (QBI) [40, 192] and constrained spherical deconvolution [188] has shown that diffusion and fibre ODFs in the myocardium can be complex, and may be indicative of regions containing multiply oriented cell populations [180]. Deviation of P from Gaussian behaviour has also been assessed using QBI and observed at the intersection of the LV and right ventricle (RV) [41].

Tissue restrictions and compartmentalisation give rise to P that is non-Gaussian (Fig. 3.3) and can be assessed with multiple q-shell approaches. In diffusion kurtosis imaging (DKI), for example, DW data are acquired in multiple directions and with a minimum of two q-shells. The diffusion kurtosis, a measure of the deviation of the diffusion signal from Gaussian behaviour, can be determined from a Taylor series expansion of the DW signal up to the second-order term [78]. DKI in ex vivo porcine heart showed that kurtosis is greater perpendicular to $\mathbf{v_1}$ than along $\mathbf{v_1}$, consistent with greater restrictions across rather than along the long-axis of the cells [117]. However, as higher order terms are neglected, fitting of the kurtosis tensor is only appropriate up to a limiting b-value, and an informed choice of tissue-specific b-values is needed. Acquisition of data with multiple b-values also expands the choice of fitting methods available. Bi-exponential fitting facilitates characterisation of fast and slow diffusing components. This has been used to describe non-Gaussian diffusion relating to cell restrictions ex vivo [23, 118] and pseudo-diffusion relating to blood perfusion in vivo [2, 26, 76]. While the fast diffusing component has been shown to primarily correspond to the perfusion fraction in vivo, further work is needed to understand the biophysical origin of the fast and slow diffusion components ex vivo. It is known that the fast and slow components do not directly correspond with extra- and intra-cellular volume fractions [140], and it has been hypothesised that a short intracellular T_2 and longer extracellular T_2 could explain the high volume fraction of the fast diffusing component [51].

In contrast to the previous methods, P can be measured directly and free of assumptions using diffusion spectrum imaging (DSI) [201]. Here, images are acquired with different b-values and diffusion gradient orientations, and q-space is sampled in a cartesian grid circumscribed by a sphere. The Fourier transform of the complex MR signal yields P (Eq. 3.8), a weighted radial summation of which gives the ODF. In the heart, DSI enables identification of multiple cell populations per voxel and estimation of diffusion kurtosis [109, 170]. Additional parameters describing properties of P, including the full-width-at-half-maximum and the probability at zero displacement, are readily available [101]. Further parameters describing non-Gaussian diffusion, including kurtosis and skewness, arising from heterogeneous myocardial tissue can be extracted by fitting stretched exponential, bi-exponential, kurtosis and statistical models to the information-rich DSI data [118]. A comprehensive review of techniques in diffusion MRI, with a focus on the brain, is available elsewhere [84].

While methods such as QBI and DSI are used in the brain to distinguish multiple white matter fibre populations, these require a minimum crossing angle of at least 25° for distinguishing these fibre populations [37]. This calls into question the suitability of existing methods in assessing myocardial structure where cardiomyocytes tend to be characterised by a smooth transmural transition in HA and sheetlets by discontinuous arrangements. The transmural progression of HA gives rise to intra-voxel cell dispersion that reduces FA. Here microscopic FA based on double diffusion encoding methods reflect intrinsic pore anisotropy independent of dispersion [79, 182]. Moreover, extensive sampling of q-space requires high signal-to-noise ratio (SNR) and long acquisition times, and these methods are currently tractable only in ex vivo cardiac applications. DTI remains the workhorse of cardiac diffusion MRI in general, achieving a practical balance between information obtained and acquisition time.

Cardiac Applications

Diffusion of water is affected by many factors including cell morphology and organisation, membrane permeability and metabolic processes. These are implicated in a broad range of healthy and pathological processes.

Healthy State

Studies in healthy hearts serve to establish baseline parameters, clarify normal inter-subject and inter-species variation, and aid understanding of physiological phenomena such as contraction, development and perfusion (See *Perfusion* section). DTI studies in healthy mouse [11, 71, 81], rat [123, 184], rabbit [71, 181], dog [72, 144, 206], pig [116], goat [58], sheep [30, 71, 123], monkey [198] and human hearts [110, 121, 123, 202] show that the transmural progression from left to right helical fibre orientation from the subepicardium to subendocardium is highly preserved across species (Fig. 3.7) consistent with early histological findings [178], although specific measurements of transmural range and linearity of HA can differ. Sheetlet orientation is more difficult to measure reliably, due to more stringent acquisition requirements and ambiguity of the diffusion tensor in describing complex structures. Studies have reported that myocardial sheetlets exhibit sharp discontinuities as well as pleated, accordion-like, and V-, N- and herringbone-shaped arrangements [30, 72, 148, 184]. However, measurements of sheetlet orientation have been found to be less precise compared to the fibre orientation [11, 110].

Cardiac contraction is intimately linked to morphology and the orientation of cells and sheetlets. DTI experiments in ex vivo isolated living rat hearts in different simulated states of contracture showed that there was a right-ward shift in fibre orientation, that is a decreased voxel proportion with left-handed helical fibre orientation ($-90°<$ HA $<-30°$) and an increased voxel proportion with right-helical orientation ($+30°<$ HA$< +90°$). Sheetlet reorientation was observed to play a prominent role in myocardial wall thickening [108]. In particular, sheetlets tend to align more closely with the

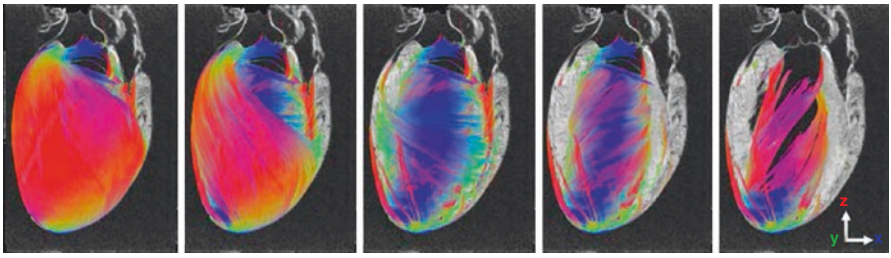

Fig. 3.7 Tracks based on $\mathbf{v}_1$ in ex vivo rat heart DTI data illustrate the transmural progression of left to right helical fibre orientation from the subepicardium to subendocardium (*left to right*). Tracks were reconstructed based on $\mathbf{v}_1$ and colour-coded by orientation: apico-basal (*red*), anterior-posterior (*green*) and lateral-septal (*blue*)

short-axis plane during contraction [29, 69]. Assuming 15% isovolumic shortening, contraction of cardiomyocytes can only account for about 8% in wall thickening [13]. The shear deformation and slippage of sheetlet layers is therefore understood to be a major contributor to the >25% LV wall thickening observed in healthy hearts [13, 108, 174]. Concurrently, torsion of the ventricles by rotation of the apex relative to the base of the heart may serve to redistribute stresses in the myocardium [13].

DTI can also be used to assess structural changes during development, therefore potentially allowing for identification of abnormal developmental processes. Ex vivo DTI studies have reported changes in DTI metrics over gestation time and post-natal age correlated with histology. These show that diffusion anisotropy can be detected at early time points, subject to inter-species variation. In pig hearts, it was found that the helical cardiomyocyte architecture was observed as early as 60 days mid-gestation [210]. FA increased from mid-gestation and decreased after birth. Another study found that λ_2 and λ_3 increased by 54% and 85% in the LV of 5-month old sheep hearts compared to third trimester foetal hearts [3]. This led to a decrease in FA of 41%. Over this time course, histology showed that cardiac development was associated first with hyperplasia then with myocyte growth. Correlations were shown between the λ_1 and myocyte length, and transverse diffusivity and myocyte width. In rat heart, the helical myocardial structure was observed at post-natal day 2 [208]. Mean ADC and FA increased up to day 4 and decreased thereafter, reflecting the transition from hyperplasia to hypertrophy. In human foetal heart, it was found that anisotropy starts to develop between 14 and 19 weeks gestation, whereas sheetlet structure only begins to develop late in gestation and matures after birth [124].

Diseased State

Diffusion is implicated in disease processes including inflammation, oedema, remodelling and scar formation. These are in turn associated with a number of cardiac pathologies including ischaemia, infarct, hypertrophy and fibrosis. Broadly speaking, a compromise in tissue integrity and the ordered arrangement of cells following disease leads to an increase in mean ADC and a reduction in FA. Similarly, angular measures are seen to vary with changes in gross morphology and contractility. In addition, the diffusion signal has poor specificity, and different pathologies may lead to similar changes in DTI measurements. Pseudo-normalisation of diffusion values depending on the time course of disease progression constitutes another potential confound. However, the potential for structural imaging without use of contrast agents is appealing.

Diffusion MRI has been used to assess remodelling in human heart in vivo following myocardial infarction (MI). In one study in patients with acute MI, the infarcted zone exhibited higher mean ADC, lower FA and a leftward shift in fibre orientation compared to the remote zone [207]. Similarly, in live pigs with chronic MI following occlusion of the left anterior descending artery (LAD), the mean ADC in MI territories was significantly higher than the remote myocardium: $2.4 \pm 0.3 \times 10^{-3}$ mm^2/s versus $2.2 \pm 1.4 \times 10^{-3}$ mm^2/s. Infarct volumes derived from the mean ADC map and

late gadolinium enhanced (LGE) imaging were in good agreement [135]. DTI in fixed rat hearts with chronic MI, following LAD occlusion of 4 weeks, showed that infarcted myocardium exhibited 41% higher MD and 37% lower relative anisotropy relative to healthy myocardium [28]. Ex vivo DTI of fixed rhesus monkey hearts with sub-acute MI following LAD occlusion of 7 days showed a significant reduction in FA and transmural range of HA and increase in ADC in infarcted hearts relative to healthy controls [198]. The results are non-uniform however, one study in patients with MI reported significant differences between sub-acute, chronic and remote myocardium with mean ADC of $6.39 \pm 0.35 \times 10^{-3}$ mm^2/s, $7.43 \pm 0.56 \times 10^{-3}$ mm^2/s and $8.95 \pm 0.19 \times 10^{-3}$ mm^2/s respectively [98]. Another study reported a significant reduction in mean ADC and increase in FA in ex vivo mouse hearts excised up to 14 days post-infarction relative to controls [179]. This was attributed to formation of collagen fibres in scar tissue.

Regional disorder, in terms of less ordered fiber orientation and reduced FA, was observed in a study of patients with hypertrophic cardiomyopathy (HCM). By comparison with strain data in the same patients, it was shown that regions with reduced strain, particularly cross-fibre strain, correlated with regions with reduced FA [189]. Concurrently, marked disorder was found in the angle between principal shortening and fibre orientation, suggesting that normal patterns of cell contraction and wall thickening are disrupted in HCM. In a separate in vivo study of healthy controls and patients with HCM, no significant differences were found in HA. However, E2A, a measure of sheetlet angulation, was higher in HCM hearts than control hearts in both systole and diastole [49]. This contrasts with the results from an ex vivo mouse study where ventricular hypertrophy was induced by infusion of angiotensin II. Here, DTI revealed significantly smaller HA and higher TA in mice with hypertrophied myocardium [158]. DSI of ex vivo mouse heart with HCM induced by ablation of MyBP-C gene also showed loss of predicted transmural HA configuration and inter-voxel orientational coherence [197]. A DTI study observed that MD, FA and HA were reproducible in a cohort of HCM patients, supporting the role of diffusion MRI in the clinical setting [120]. Whereas an ex vivo study of hypertrophied rat heart following transverse aortic constriction showed that there was considerable overlap in diffusion tensor eigenvalues, mean ADC and FA, between hypertrophied and control hearts. In contrast, diffusion kurtosis and skewness were more than 20% higher in $\mathbf{v_2}$ and $\mathbf{v_3}$ relative to control hearts, reflecting higher sensitivity of non-Gaussian diffusion methods in detecting hypertrophy [118].

Other applications of diffusion MRI include characterisation of fibrosis, oedema associated with acute myocarditis and idiopathic dilated cardiomyopathy. In one study, the mean ADC in fibrotic regions, as defined by extracellular volume maps from LGE imaging, was $2.2 \pm 0.3 \times 10^{-3}$ mm^2/s and significantly higher than $1.6 \pm 0.3 \times 10^{-3}$ mm^2/s observed in non-fibrotic regions [137]. In myocarditis, significantly higher DW signal intensity was observed in the myocardium of patients than controls, and sensitivity and diagnostic accuracy were higher compared to T_2-weighted imaging, at 92% versus 54% and 95% versus 70% respectively [152]. LV specimens collected from patients with idiopathic dilated cardiomyopathy showed 22% lower FA, 12% higher MD, 14% higher λ_2 and 24% higher λ_3 compared to those from normal donors [1].

Computational Modelling

Diffusion MRI, particularly ex vivo, provides opportunities to acquire high quality data for tractography, atlas building and electro-mechanical modelling [72, 161, 184]. Tracking of diffusion eigenvectors is a valuable method for estimation and visualisation of long-range connections across the whole heart, which can in turn be used to inform computational models. In the brain, the primary objective is to track white matter fibres and the terms *tractography* and *fibre tracking* are interchangeably used. Here, the term *fibre tracking* is avoided as cardiomyocytes form a branching syncytium rather than fibres. There are two main approaches to tractography – deterministic and probabilistic. In deterministic algorithms, such as *fiber assignment by continuous tracking* (FACT) [129], tracks originate from seed voxels which may comprise a small region-of-interest (ROI) or even the whole heart. These tracks are propagated from voxel to voxel based on the local orientation of the diffusion tensor, subject to constraints on the maximum turning angle, and terminated when the local FA is lower than a minimum threshold (Fig. 3.8). Euler and Runge-Kutta methods can be used for sub-voxel interpolation of tracks [18]. However, the accuracy of reconstructed tracks is influenced by the presence of sample motion, image noise and distortion. A useful reference quantitatively evaluates ten state-of-the-art tractography methods in a standardised brain phantom [50]. Probabilistic methods additionally incorporate an uncertainty estimate that can be represented as a probability density function of tissue orientation, and describes the confidence of connections [143]. This offers a quality metric for understanding the data, and may be better able to cope with branching and dispersion as observed throughout the heart.

Recent technical developments have made it possible to visualise structural details within fine anatomical features, such as valves and vessels, in ex vivo rat hearts [184] (Fig. 3.9). In the wall of the aorta and other major vessels, for instance, tracks based on $\mathbf{v_1}$ are circumferentially oriented. In the valves, tracks are oriented roughly parallel to the free edge of each valve leaflet. Tracks are seen extending from the apical myocardium along the LV endocardium, and these appear to reflect free-running Purkinje fibres. Tracks are not restricted to cardiomyocytes, and are also observed in the chordae tendinae comprised of well-aligned collagen, elastin and endothelial cells.

Tracking along $\mathbf{v_2}$ and $\mathbf{v_3}$ additionally provides information about sheetlets and other laminar structures (Fig. 3.10). In the papillary muscles, they point to a concentric arrangement of cell layers and a twisting of the papillary muscles along their length. Sharp discontinuities were observed in sheetlet orientation across the myocardial wall, which were reproducible across five hearts. Tracks based on $\mathbf{v_3}$ are radially oriented in the aorta, whereas they are generally aligned normal to the local surface within the atria.

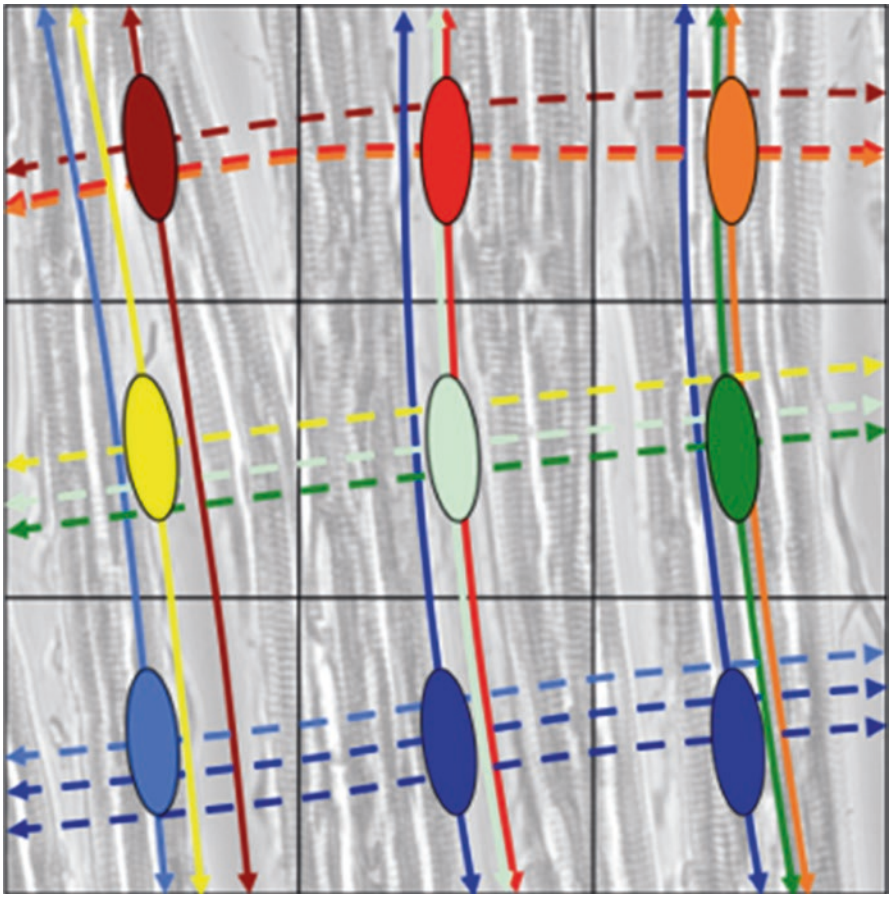

Fig. 3.8 Exemplar tensors overlaid on a bright-field microscopy image of ex vivo rat myocardium in a 3×3 voxel neighbourhood. Each of nine tensors is represented in a different colour. Tracks are propagated in matching colours from individual seed voxels, based on $\mathbf{v}_1$ (*solid lines*) and $\mathbf{v}_3$ (*dashed lines*) (Figure by Teh et al. licenced under CC BY [184])

Initial results in hearts from healthy volunteers demonstrates that in vivo tractography is feasible [202]. Motion-induced signal loss was addressed through the use of principal component analysis and temporal maximum intensity projection (PCATMIP) [153] or wavelet-based image fusion, however further work is needed to improve scan efficiency and validate track estimates.

To date, cardiac tractography has largely relied on methods developed for the brain, where cylindrical geometry of fibres is assumed. The concept of tracking and

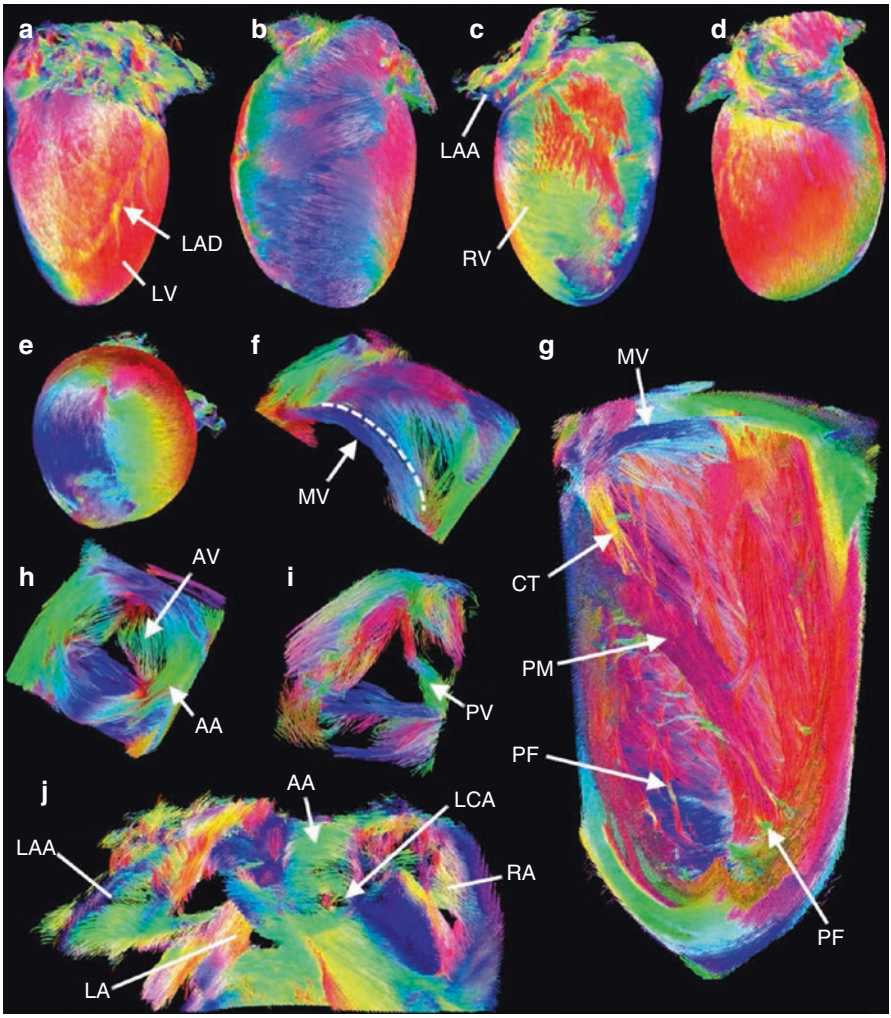

Fig. 3.9 Tracking based on $\mathbf{v}_1$ in the ex vivo rat heart based on DW data acquired at 100 μm isotropic resolution. Tracks were colour-coded by orientation: apico-basal (*red*), anterior-posterior (*green*) and lateral-septal (*blue*). Tracks in the heart from (**a**) lateral, (**b**) anterior, (**c**) septal, (**d**) posterior and (**e**) apical views. (**f**) Tracks in the leaflets of the mitral valve (MV), (**g**) aorta (AA) and aortic valve (AV) (**h**) and pulmonary valve (PV). (**i**) Tracks in the left and right atria (LA and RA), left atrial appendage (LAA) and left coronary artery (LCA). (**j**) Tracks in a 13×5×5 mm section in the LV reveal chordae tendinae (CT), oriented longitudinally between their connections to the MV and papillary muscle (PM), and networks of Purkinje fibres (PF) (Figure by Teh et al. licenced under CC BY [184])

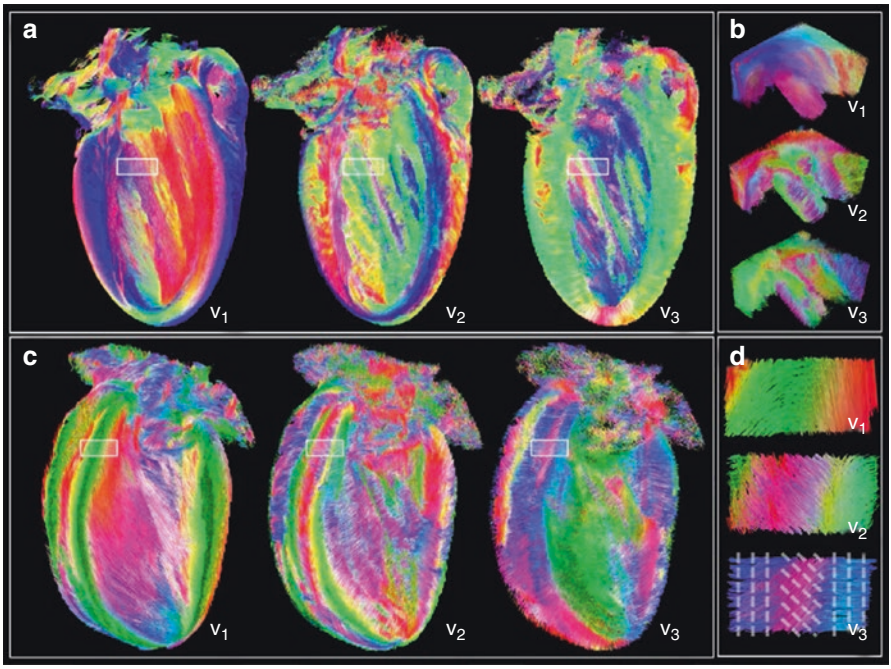

Fig. 3.10 Tracking of myocardial cell and sheetlet structures based on $\mathbf{v}_1$, $\mathbf{v}_2$ and $\mathbf{v}_3$, colour-coded by orientation: apico-basal (*red*), anterior-posterior (*green*) and lateral-septal (*blue*). (**a**) Digitally bisected heart viewed from the LV septal wall. (**b**) Magnified isometric view of tracks in a $4 \times 3.5 \times 2$ mm section in the papillary muscles. (**c**) Digitally bisected heart viewed from the LV anterior wall. (**d**) Magnified view of tracks in a $2.5 \times 1 \times 1$ mm section in the LV septal wall. Dashed lines overlaid on $\mathbf{v}_3$ tracks approximate the underlying sheetlet laminae (Figure by Teh et al. licenced under CC BY [184])

clustering of sheetlets in the heart offers an additional dimension for assessing the contraction of the heart, in particular, its shear and torsion characteristics [184]. Further work is needed to disambiguate tracks in regions with multiply oriented cell and sheetlet populations. Existing methods that assume one-to-one connections in tracks across neighbouring voxels or use a minimum FA threshold based on the transition between grey and white matter may not be appropriate in the highly branching and interconnected myocardium without obvious termination points. It is worthwhile to remember that tracks are streamlines connecting diffusion tensor eigenvectors, and are not anatomical features of the heart. Semi-quantitative methods, such as track counting and track length, are highly dependent on track reconstruction parameters and more quantitative, statistical methods of assessment are needed, together with careful validation using reproducibility studies, phantoms and simulations.

Atlases play an important role in defining an average heart and understanding inter-subject and inter-species variation. One study in ex vivo canine hearts proposed a framework for building a statistical atlas of the heart based on DTI data, involving group-wise registration of anatomical MRI data, transformation of diffusion tensor fields, and computation of average tensors and corresponding covariance matrices [144]. Good stability in fibre orientations was established, with higher variability in sheetlet orientations across subjects. The statistical model was shown to be more complete and accurate than a synthetic model of fibre orientation. A study in ex vivo human hearts showed, using a similar approach, that HA is highly correlated to transmural depth, and recapitulated that there is higher dispersion in sheetlet orientations than fibre orientations [110].

Cardiac structure is a key determinant of electrical propagation [75] and mechanical function [34] in the heart. Tractography and atlas construction therefore contribute directly to the development of electro-mechanical models of the heart. Such models have been used in extrapolation of high-resolution structural information across species [144], planning of ablation sites in radio-frequency ablation [156] and optimisation of electrode placement for cardiac resynchronisation therapy [166]. Computational models have also been used in the estimation of ventricular pressures, myocardial stiffness, and cardiac geometry, kinematics and function [31, 63, 96, 141], which can be used to augment clinical diagnosis and treatment with patient-specific tissue mechanical properties.

Methodology

Diffusion MRI is influenced by the choice of pulse sequence and imaging parameters. It is especially challenging in vivo due to its sensitivity to microscopic motion and the presence of heart wall motion on the scale of millimetres in the beating heart. Other major challenges that affect the diffusion signal include tissue deformation, or strain, and myocardial perfusion. Ex vivo diffusion MRI avoids these issues, but introduces others including sample fixation, preparation, embedding and temperature control. In this section, specific issues pertaining to cardiac diffusion MRI in the general, in vivo and ex vivo settings are discussed together with current methods for addressing these issues. All the considerations in diffusion MRI that are non-specific to cardiac applications apply, for instance the influence of eddy currents and magnetic susceptibility, and the following review articles are recommended [86, 104].

General

Pulse Sequences

There are three main pulse sequences that are used for in vivo cardiac diffusion MRI: stimulated echo acquisition mode (STEAM), spin echo (SE) and balanced steady-state free precession (bSSFP) (Fig. 3.11). The former two are typically coupled with

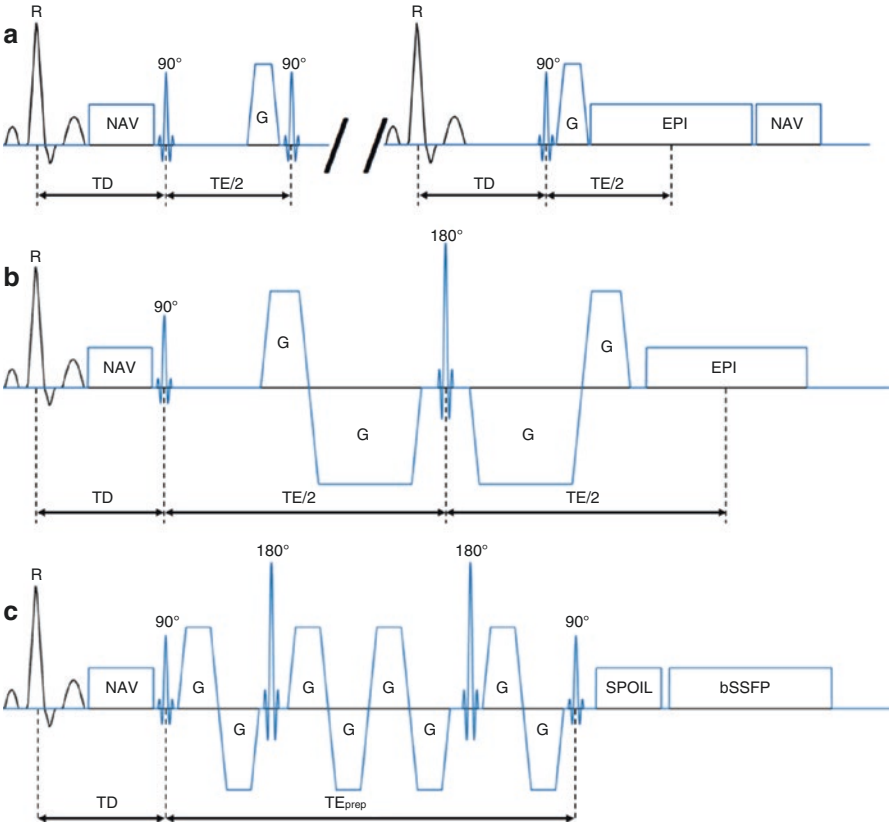

Fig. 3.11 Pulse sequences used for in vivo cardiac diffusion MRI include (**a**) stimulated echo acquisition mode (STEAM), (**b**) spin echo (SE) and (**c**) diffusion-prepared balanced steady state free precession (bSSFP). QRS complexes (*black*), 90° and 180° RF pulses, diffusion gradients (G), navigators (NAV), spoilers (SPOIL) and echo planar imaging (EPI) readouts are shown. Timings include trigger-delays (TD), echo times (TE) and preparation times (TE_{prep}). For clarity, imaging gradients are omitted

single-shot echo planar imaging (EPI) readouts [115], and all are fast imaging techniques to mitigate motion effects.

In STEAM [52], diffusion is encoded over two consecutive heart beats. This relies on the heart being in identical positions across the two cardiac cycles. One benefit of using STEAM, given the long diffusion time corresponding to the interval between heart beats or *RR-interval*, is the relatively low maximum gradient strength, G_{max} required for adequate diffusion-weighting. This is readily achieved on clinical MRI scanners. However, there are a number of drawbacks. In STEAM, SNR is reduced by half compared to SE methods and each readout is acquired over two heart beats, reducing SNR efficiency. Breath holding, navigator gating or other strategies are required to ensure the diffusion gradients over two cardiac cycles are appropriately timed, further reducing scan efficiency. Even with such methods, the heart may not be in precisely the same position between beats particularly

in patients with arrhythmias, leading to reduced accuracy in measurements. When RR-intervals are not uniform, Δ is variable, necessitating recalculation of b and leading to variation in the microscopic length scales to which the diffusion sequence is sensitive to. While this may not affect estimates of $\mathbf{v_1}$ which tend be robust, it is likely to have a significant impact in the assessment of $\mathbf{v_2}$, $\mathbf{v_3}$ and non-Gaussian diffusion. STEAM is also sensitive to myocardial strain that needs to be addressed. While STEAM-EPI has been the mainstay of cardiac diffusion MRI [42, 44, 102, 138, 155, 176, 190, 207], newer techniques offer many advantages.

In SE-EPI, diffusion-weighting and the readout are performed within a single RR-interval. The major benefits of this approach are the higher SNR efficiency and relative insensitivity to strain compared to STEAM [7, 54, 56, 169, 177, 202]. At a heart rate of 60 min^{-1} and physiological T_1 and T_2, the theoretical SNR is 3.5× that of STEAM. In practice, the SNR ranged from 2.9 to 2.3× as b increased from 50 to 450 s/mm^2. This can be attributed to the longer diffusion times in STEAM, leading to reduced signal attenuation for a given b in the presence of cell restrictions. Indeed, the differences in diffusion times give rise to significant differences in DTI measurements. For instance, MD in the healthy human myocardium was $1.43 \pm 0.06 \times 10^{-3}$ mm^2/s in SE and $1.05 \pm 0.08 \times 10^{-3}$ mm^2/s in STEAM. The transmural HA variation was found to be more linear, and the TA more homogeneous across subjects and myocardial sectors, in SE compared to STEAM [196]. As the diffusion encoding occurs over a much shorter time scale than in STEAM, strain is less detrimental in SE. However, residual motion within the diffusion encoding period requires use of gradient moment-nulling (GMN) for suppressing sensitivity to bulk tissue motion (Fig. 3.12). SE methods require higher G_{max} to achieve suffi-

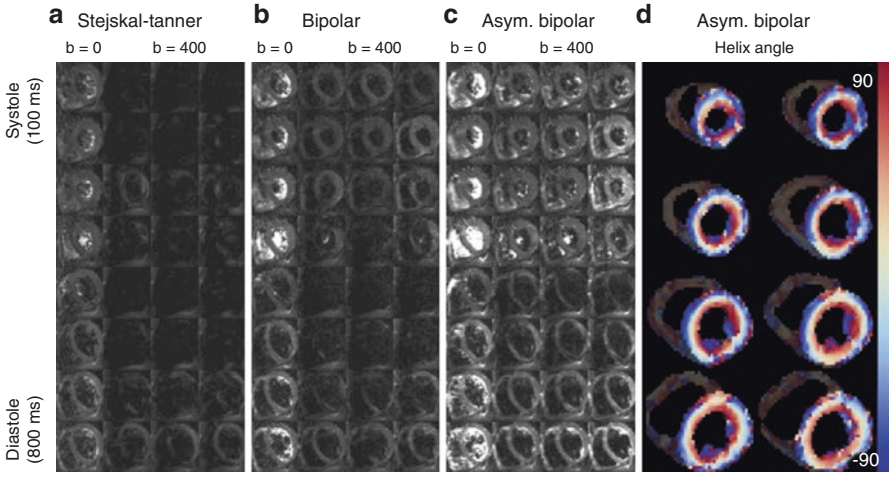

Fig. 3.12 In vivo SE-EPI DTI in human heart using (**a**) M_0-nulled, (**b**) M_1-nulled and (**c**) M_2-nulled diffusion encoding gradients in different cardiac phases linearly spaced from 100 to 800 ms. For each sub-figure the left column shows the non-DW images and the right three columns show the images (b = 400 s/mm^2) DW in x, y and z directions. Signal dropouts are mitigated by use of higher order gradient moment nulling. (**d**) HA maps calculated based on M_2-nulled DTI data (Figure by Froeling et al. licensed under CC BY [55])

cient *b* and adequate diffusion contrast given the shorter diffusion times. This is feasible in clinical scanners with strong gradient systems with $G_{max} \geq 80$ mT/m, and will be increasingly tractable with ongoing improvements in gradient hardware.

Single-shot EPI in the heart is subject to magnetic susceptibility artefacts, T_2* relaxation and motion occurring during long readouts. A 3D segmented free-breathing bSSFP approach with diffusion preparation and second order GMN has been proposed to address these issues [136]. Diffusion-preparation allows separation of diffusion encoding from imaging readout via crushing of residual transverse magnetisation. A multi-shot acquisition with short echo train length then mitigates magnetic susceptibility and T_2* relaxation, and adds flexibility to use higher resolution and 3D sequences subject to scan time availability. To maintain diffusion-weighting, optimised catalyst pulses are required to rapidly bring the sample into a stable steady-state. The drawbacks of DW-bSSFP are that (i) multi-shot methods are prone to signal amplitude variation between shots, and (ii) a long quiescent period is needed for diffusion-preparation limiting the technique to acquisition at end-diastole.

The constraints on ex vivo diffusion MRI are less severe as sample motion, strain and perfusion are generally absent. SE methods can be used without navigator echoes, gating, GMN and EPI readouts, thus reducing TE, minimising scan redundancy, improving SNR efficiency and/or avoiding T_2* blurring [11, 81]. Fast spin echo (FSE) methods can also be used to further reduce scan times by a factor equal to the echo train length, at the cost of T_2 blurring [69, 184]. It is important to note that FSE requires that the phase of the transverse magnetisation be stable across echoes. This requirement known as the Carr-Purcell-Meiboom-Gill (CPMG) condition [27], is generally not met following application of diffusion-weighting gradients. Methods to address this include alternating the phase of the refocusing pulses [147], eliminating unwanted signal pathways [8], splitting the signal into two pathways [157] and using twin navigators [130].

Signal-to-Noise Ratio and Sequence Parameters

Contrast in diffusion MRI is dependent on signal attenuation. SNR is therefore a key determinant that limits the imaging resolution and maximum b-value. Insufficient SNR leads to an underestimation of the diffusivity as the signal attenuation at higher b-values is curtailed by the noise floor. This leads to 'squashing' of the ADC preferentially in the direction of greatest diffusion and an underestimation of FA [85] that depends on SNR, b-value, and tissue diffusivity and anisotropy. Neglecting T_2, it has been recommended for DTI in the brain that the optimal b-value is approximately $1.1 \times 3/\text{Trace}(\mathbf{D})$, and the ratio of b_{high} to b_{low} experiments is approximately 7.5:1 [87]. This maximises diffusion contrast while minimising noise floor effects.

The maximum b-value used in cardiac diffusion MRI in vivo is often low (<500 s/mm^2) and potentially sub-optimal. One study in healthy volunteers investigated the effect of b-values on the reconstructed DTI parameters using STEAM-EPI [164]. By recombination of various non-DW and DW data with b-values denoted by b_{low} and b_{high} respectively, it was demonstrated that the diffusion signal is heavily influenced by a fast diffusing component at low b_{low}, that is putatively associated with

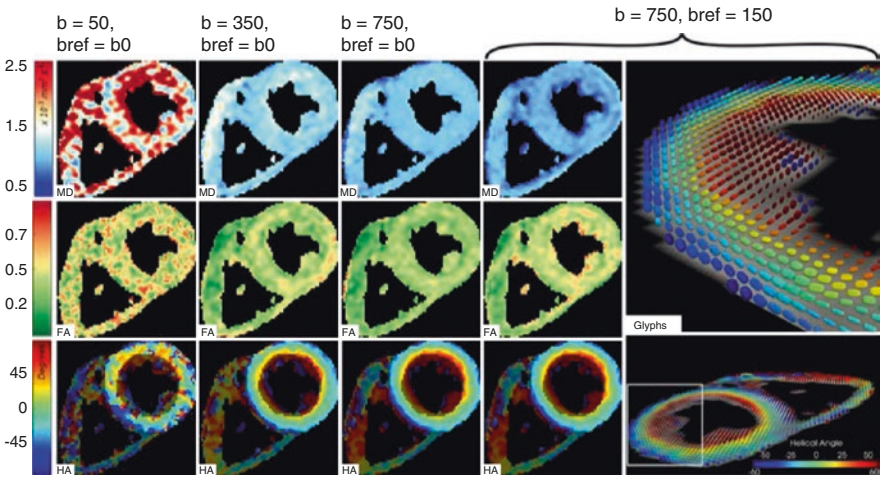

Fig. 3.13 MD (in mm²/s; *top*), FA (dimensionless; *middle*) and HA (in°; *bottom*) maps for 4 pairs of diffusion weightings. In data with optimal b-values (b_{ref} = 150 s/mm², b = 750 s/mm²), superquadric glyphs describing the diffusion tensors are shown in the anterolateral wall of the LV (*top right*) and whole short axis slice (*bottom right*) (Figure by Scott et al. licenced under CC BY [162])

microvascular perfusion, and increasing b_{high} significantly decreased MD and FA (Fig. 3.13). It was recommended in this instance that b_{low} = 150 s/mm², high enough to suppress the fast component, while low enough to minimise voxels with negative eigenvalues, and that b_{high} = 750 s/mm², for maximising contrast while avoiding noise floor effects. These principles are informative, however, specific values of b_{low} and b_{high} would depend on the specific hardware, pulse sequence and sample. In a recent ex vivo study, it was found that the diffusion signal was best fit with a tensor up to b_{high} = 2000 s/mm² based on the Akaike Information Criterion [118]. Given that the MD was similar to the study by Scott et al. it would suggest that higher b-values may improve contrast in DTI, and that b-values used in vivo are routinely limited by SNR. This has important implications on the accuracy of DTI metrics. Simulations show that where the SNR of the non-DW data are lower than about 20, as is often the case in cardiac DTI in vivo, λ_1 is overestimated and λ_3 is underestimated, leading to overestimation of FA [145]. Simulations show a transition from over to underestimation of FA from low to high b-values in the presence of limited SNR [85]. A similar inverse relation of FA and b-value was observed in an ex vivo DTI study of pig hearts [53]. However, as the transition also depends on tissue diffusion properties, it is difficult to define an optimal b-value for low SNR cases, as bias is likely to be heterogeneous, particularly in pathology. Experimental verification of potential bias in vivo requires higher SNR than is generally available.

Common strategies for improving SNR include signal averaging, minimising TE, reducing receiver bandwidth, decreasing spatial resolution and using gadolinium-based contrast agents to shorten T_1. As the signal intensity varies widely with b-value, dynamic gain adjustment to maximise receiver gain as a function of b-value has been shown to improve the precision of DTI principal eigenvalues by 41% [184]. In DTI, SNR can also be improved by increasing the number of DW directions. Monte Carlo

simulations showed that a minimum of 20 and 30 unique DW directions is recommended for robust estimation of anisotropy and tensor orientation respectively, and that acquiring additional DW directions was preferable to averaging of multiple data with identical DW [83]. The benefit of acquiring additional DW directions over averages in the heart in vivo given a fixed acquisition time remains to be verified [163]. Magnitude images in MRI are characterised by a Rician noise distribution [64], and low signals are biased by the noise floor. To mitigate this bias, the phase can be removed [46] or complex averaging can be performed [165], bearing in mind that averaging of STEAM-EPI data assumes consistent RR-intervals which may be variable particularly in patients. Spatial averaging and smoothing can also reduce FA and the transmural range of angular measurements such as HA due to dispersion of cell orientations.

Δ defines the diffusion time and therefore the length scale of diffusion to which the pulse sequence is sensitive. In the heart, Δ may vary from 5 ms in SE-based preclinical DTI ex vivo to 1000 ms in STEAM-EPI-based clinical DTI in vivo. Longer Δ increases the interaction of water molecules with cellular restrictions, reducing ADC preferentially in the directions of $\mathbf{v_2}$ and $\mathbf{v_3}$ where restrictions are most prevalent, thereby increasing FA. It was observed in ex vivo calf heart that λ_2 and λ_3 decreased by 29–36% as Δ increased from 32 to 400 ms, whilst λ_1 remained the same [91]. In ex vivo pig hearts, all three principal eigenvalues decreased as Δ increased from 52 to 322 ms [53].

Gradient Calibration

Diffusion MRI is particularly sensitive to the calibration of the gradient system as ADC depends on the square of the applied gradient strength, G [32]. For example, an error of ±2% in G translates to an error of ±4% in ADC. Different errors in each of the x-, y- and z-gradients can lead to over or underestimation of the FA depending on the alignment of the diffusion tensor with respect to the scanner axes. This effect was demonstrated in ex vivo rat heart [184].

Calibration is usually performed by the vendor during routine servicing using anatomical scans of a phantom of known dimensions. It is also possible to exploit the sensitivity of diffusion MRI for calibrating the gradient system, by comparing the measured diffusivity at a measured temperature against a known independent reference. Studies have used phantoms filled with cyclooctane [183], polyvinylpyrolidone [146], ethylene glycol [173], n-undecane [209], dodecane [38] or water [114, 133, 151] for this purpose. While water is readily available and its temperature can be controlled via ice water bath, its high diffusivity and low viscosity renders it susceptible to vibration, convection and flow. This problem is mitigated with use of the more viscous compounds listed above. Cyclooctane is particularly useful for gradient calibration as it exhibits mono-exponential behaviour up to at least b = 10,000 s/mm^2, and has a single proton resonance, thus avoiding signal cancellation from J-coupling and chemical shift artefacts. Correction maps, α can be generated along the scanner orthogonal axes and used both to prospectively correct the linear gradient scaling and retrospectively correct for gradient non-linearity in a model-free manner [183]. The improvement in calibration was validated using a structured phantom and high-resolution anatomical imaging. Numerical calculation

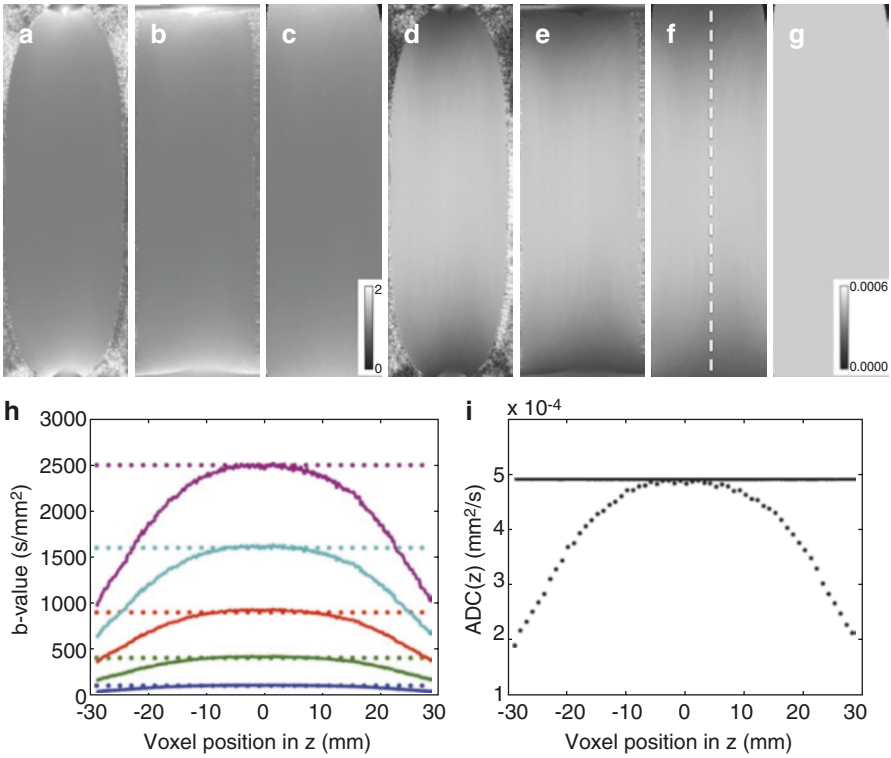

Fig. 3.14 α correction maps in a phantom filled with cyclooctane, with diffusion along the readout direction (z) and in coronal view (**a**) without correction for gradient non-linearity, (**b**) with correction in the phase encoding direction (x) only, (**c**) with correction in the phase encoding and readout directions. (**d**–**f**) Corresponding apparent diffusion coefficient (ADC) maps (mm^2/s). The cylindrical geometry of the tube is recovered post-correction. The estimated α increases and ADC decreases towards either end of the coil, where the gradient profile becomes increasingly non-linear. (**g**) Corrected ADC map (mm^2/s) is more homogeneous after correction. (**h**) Nominal (*dotted*) and corrected (*solid*) b-values across a profile in z as indicated by the dashed line in (**f**). Nominal b = 100, 400, 900, 1600 and 2500 s/mm^2 are shown in blue, green, red, cyan and magenta respectively. (**i**) Nominal (*dotted*) and corrected (*solid*) ADC in z across the same profile along z. The nominal ADC was subsampled by a factor of ten for display purposes, to distinguish it from the corrected data (Figure by Teh et al. licenced under CC BY [183])

of actual b-values applied based on the actual rather than nominal gradients used, enables voxel-wise correction of the measured ADC over large FOVs (Fig. 3.14).

Cross-Terms and Imaging Gradients

Besides diffusion gradients, imaging gradients and their interaction with diffusion gradients known as cross-terms contribute to the b-matrix (Eq. 3.5). In a PGSE sequence, the contributions of the imaging gradients are usually negligible ($b_{imaging}$

<5 s/mm^2). However, in one example, the contribution of cross-terms depends on the sequence in which the gradients are played out, and $b_{cross\text{-}terms}$ can range from $0.013b$ to $0.33b$ [105]. The significant contribution to b by the cross-terms is exacerbated by the use of crusher gradients for crushing unwanted signal following the RF refocusing pulse. In an extreme case with nominal b = 1000 s/mm^2 and fixed crushers where $b_{imaging}$ = 61 s/mm^2, the effective b ranged from 666 to 1320 s/mm^2 depending on the direction of the diffusion gradient [184]. Fitting the diffusion tensor to data acquired at different b would lead to bias as P is non-Gaussian in biological tissues. Cross-terms are enhanced further when crushers interact with diffusion gradients over long mixing times as in STEAM imaging.

The issue of cross-terms can be ameliorated in several ways. The first is to minimise interactions between imaging and diffusion gradients, for example, by playing the readout dephasing gradient immediately prior to the readout rather than prior to the first diffusion gradient. Depending on the imaging resolution and b-values desired, the diffusion gradients may be adequate to crush unwanted FIDs, and crusher gradients can be removed when acquiring DW data [176]. Alternatively, the crusher and diffusion encoding gradients can be orthogonalised [132]. Second, the diffusion gradients can be adjusted based on DW direction such that the effective b-value matches the nominal b-value [112]. Third, the crusher gradients can be inverted with respect to the slice refocusing gradient such that $b_{imaging}$ = 0 s/mm^2 during the mixing time [92]. Fourth, a second DW dataset can be acquired with reversed diffusion gradient polarity. Taking the geometric mean of data with diffusion gradients in opposite directions eliminates $b_{cross\text{-}terms}$ at the cost of doubling of scan time [134].

Eigenvector Sorting

The relative magnitudes of λ_1, λ_2 and λ_3 define the eigenvector orientations $\mathbf{v_1}$, $\mathbf{v_2}$ and $\mathbf{v_3}$. While λ_1 tends to be much higher than λ_2 and λ_3, the ratio of λ_2/λ_3 or transverse anisotropy is relatively low, at 1.16 in ex vivo human heart data [110]. In the case of transverse isotropy, $\lambda_2/\lambda_3 = 1$ and $\mathbf{v_2}$ and $\mathbf{v_3}$ should rotate randomly about $\mathbf{v_1}$, This results in inaccurate sorting of eigenvectors, and invalidates estimates of sheetlet and sheetlet-orientation. However, a statistical analysis showed that sorting was robust in spite of the low transverse anisotropy, providing justification for sheetlet structures [72]. Random assignation of $\mathbf{v_2}$ and $\mathbf{v_3}$ should also dramatically compromise their precision. However, this was not the case in ex vivo rat hearts (N = 5) where the 95% cones-of-uncertainty [82], a measure of the angular confidence interval, in $\mathbf{v_1}$, $\mathbf{v_2}$ and $\mathbf{v_3}$, averaged across the global myocardium, were $3.7° \pm 0.2°$, $10.9° \pm 0.4°$ and $10.6° \pm 0.5°$ respectively [184]. While the evidence from ex vivo data suggests that the eigenvectors are correctly ordered, it has been shown in STEAM-EPI in vivo that material strain leads to stretching and compression of the diffusion tensor, and ignoring strain can lead to swapping of second and third eigenvectors [176]. In both cases, further investigation is required to inform the interpretation of DTI data in the presence of cell and sheetlet co-dominance and merging.

In Vivo MRI

Assessing diffusion in the beating heart is highly challenging due to motion, strain, perfusion and limited scan times. Wide variability in DTI metrics, such as MD and FA, has been reported even in healthy subjects (Table 3.2). We continue to discuss methodological considerations that could give rise to these differences.

Table 3.2 Diffusion MRI measurements in healthy subjects in vivo

Sequence	F (T)	b_{max} (s/mm^2)	DW	Species	N	MD ($\times 10^{-3}$ mm^2/s)	FA	Authors
SE-EPI	3	350	3	Human	10	1.9 ± 0.6		Aliotta et al. [7]
STEAM-EPI		456	3	Human	15	1.17 ± 0.18		Edelman et al. [44]
STEAM-EPI	3	350	6	Human	10	1.19 ± 0.16	0.48 ± 0.08	Lau et al. [102]
SE-EPI	1.5	350	12	Human	10	1.72 ± 0.09	0.36 ± 0.02	Moulin et al. [131]
3D bSSFP	1.5	500	3	Human	10	1.5 ± 0.4		Nguyen et al. [136]
STEAM-EPI	3	350	6	Human	10	0.9 ± 0.2	0.60 ± 0.203	Nielles-Vallespin et al. [138]
STEAM-EPI	1.5	300	6	Human	3	0.87 ± 0.13		Reese et al. [155]
STEAM-EPI	3	750	6	Human	10	0.87 ± 0.06	0.419 ± 0.036	Scott et al. [164]
STEAM-EPI	3	500	6	Human	10	1.07 ± 0.06	0.409 ± 0.027	Scott et al. [165]
SE-EPI	9.4	650	24	Mouse	6	1.20 ± 0.06	0.29 ± 0.02	Sosnovik et al. [169]
STEAM-EPI	1.5	500	10	Human	10	0.87 ± 0.11	0.61 ± 0.04	Stoeck et al. [176]
STEAM-EPI	3	350	6	Human	10	1.17 ± 0.14	0.54 ± 0.04	Tunnicliffe et al. [193]
STEAM-EPI	1.5	450	12	Human	7	1.14 ± 0.13	0.53 ± 0.11	von Deuster et al. [196]
SE-EPI	1.5	450	12	Human	7	1.58 ± 0.10	0.29 ± 0.07	von Deuster et al. [196]
SE-EPI	1.5	200	12	Human	6	0.75 ± 0.12	0.43 ± 0.05	Wei et al. [202]
SE-EPI	7	350	12	Rat	12	1.44 ± 0.08	0.41 ± 0.05	Welsh et al. [203]

Abbreviations include field strength (F), number of DW directions (DW), sample size (N), mean diffusivity or mean apparent diffusion coefficient as reported by study (MD) and fractional anisotropy (FA). Where available, measurements given here are reported in LV, mid-ventricular LV or the lateral wall of the LV, in diastole. Studies with data acquired with different pulse sequences are listed twice. Data were acquired in two-dimensions unless otherwise specified

Motion

Motion is a major confound in diffusion MRI, as the scale of motion in the beating human heart is three orders of magnitude greater than the scale of diffusion that the acquisition is sensitive to. In the preclinical setting, high heart rates of up to 300 min^{-1} in rats and 600 min^{-1} in mice present additional challenges. Respiratory motion is a further confound. When unaccounted for, bulk non-rigid motion of the heart leads to artefactual phase accumulation, and severe and unrecoverable signal attenuation (Fig. 3.12).

There are several complementary strategies to deal with cardiac and respiratory motion, several of which are often applied in tandem. These involve minimising motion during the acquisition window, synchronising the sequence to cardiac and respiratory motion, encoding the position of the heart, rejecting or down-weighting corrupted data, and nulling higher order gradient moments.

The first approach makes use of fast single-shot readouts such as EPI. Rapid acquisition of k-space in a single-shot avoids ghosting that arises from having variable phase across k-space as a result of non-reproducible motion between shots. However, single-shot methods are limited in spatial resolution and hampered by distortion and blurring. Reduced FOV and multi-shot techniques with appropriate phase correction can be used to improve the imaging resolution, while parallel imaging and partial Fourier can be used to reduce echo train lengths and distortion. Data are often acquired within specific time windows coinciding with more quiescent periods during the cardiac cycle such as during diastole [153, 155], precluding acquisition of data in multiple contraction states across the full cardiac cycle. Breath-holding is an effective way to mitigate respiratory motion [44]. In healthy volunteers, breath-hold times of up to 15 s are typically used. However, the use of breath-holding is limited in patients with severe prognosis and in preclinical imaging.

Cardiac and respiratory gating or triggering is extensively used in cardiac MRI to synchronise the imaging sequence to the cardiac and respiratory cycles respectively. Cardiac gating is usually achieved via placement of ECG electrodes and detection of the R-peak. The excitation pulse is then played following a prescribed trigger delay (TD) after the R-peak, so that the heart is imaged in the desired cardiac phase. Respiratory movements can be monitored via respiratory belt, pressure transducer or navigator echoes. Imaging sequences can then be prospectively gated to acquire data only when respiratory motion is minimised, such as towards end-expiration, or retrospectively gated where data are continually acquired with repetition, and data outside the acceptance window are rejected. The drawbacks of respiratory gating are reduced scan efficiency either through reduced sampling rate or rejection of data, and prospectively gated methods are incompatible with steady-state imaging sequences. Dual gating approaches combining both cardiac and respiratory gating are routinely used.

Navigator echoes are readouts that encode motion information and can be used for phase correction of the imaging data and/or estimation of sample positioning. These echoes are typically acquired before or after the imaging echo train. In a SE-EPI study, a one-dimensional (1D) pencil-beam navigator was used to measure cardiac and liver position, enabling real-time slice tracking and repositioning with high scan

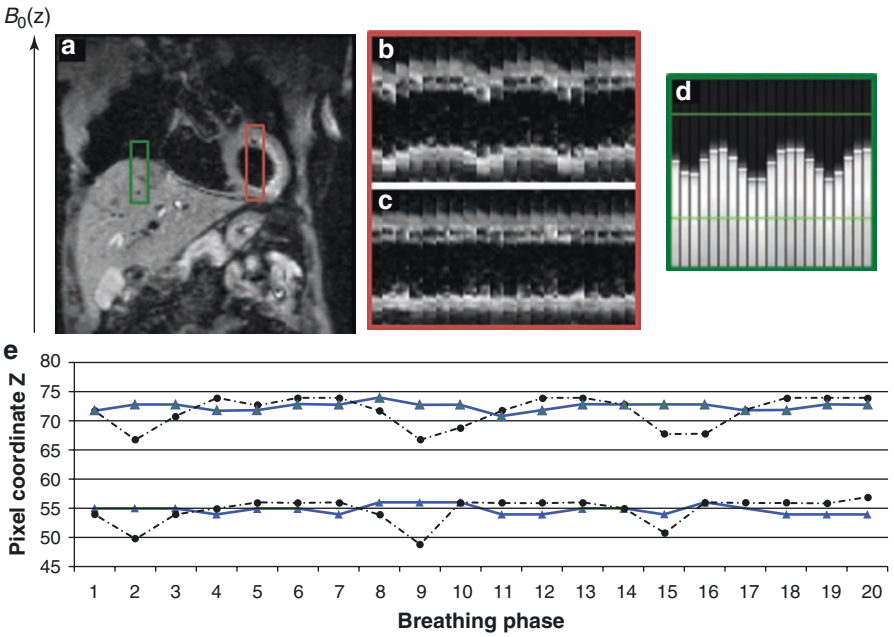

Fig. 3.15 Motion correction in SE-EPI free-breathing diffusion MRI with slice following. (**a**) Coronal image with $b = 30$ s/mm^2. Signal intensity evolution over time in a vertical ROI crossing the left ventricle (**b**) without and (**c**) with slice following. (**d**) Navigator information (**e**) myocardial edges extracted from coronal images (*red rectangular* ROI) with (*blue line*) and without (*black line*) slice following over three breathing cycles (Figure by Moulin et al. reproduced with permission [131], Copyright 2015 Wiley Periodicals, Inc.)

efficiency (Fig. 3.15) [131]. In STEAM-EPI, employment of two 1D navigators over the diaphragm, one prior to excitation and one post-readout, has been used for data rejection when motion between excitation and readout is deemed excessive [138]. A complementary method provides subjects with visual feedback from the navigator signal, helping them regulate their breathing to optimise data acceptance. In combination with data averaging, no significant differences were found in MD and FA between breath-holding and free-breathing navigated experiments. The free-breathing approach showed good reproducibility in patients with HCM [120].

Despite the abovementioned methods, residual motion-induced phase often leads to individual DW images being corrupted in an unpredictable manner. One correction method involves acquiring data at multiple closely-spaced TDs spaced across a time window with minimal motion, and applying a temporal maximum intensity projection (TMIP) on a voxel-basis [153]. The final reconstructed DW image is then a composite of voxels with the highest signal intensity across the images. Further filtering with principal component analysis (PCA) can be used to improve SNR. The downside of a TMIP approach is high data redundancy of up to tenfold, as the SNR for the reconstructed image is no greater than that of a single image. Another method

involves performing intensity-based correlation between images and a reference image, coupled with image rejection and modulus averaging of unrejected data [56].

Recent studies combine several methods to achieve good motion insensitivity. In one study for instance, a pencil-beam navigator was used for real-time slice tracking and repositioning in free-breathing healthy volunteers [131]. ECG-triggering was used, together with multiple trigger delays and sequential sliding of the acquisition window located in the quiescent phase at end diastole. Non-rigid supervised diffeomorphic registration [194], PCATMIP [153] and additional registration for correction of eddy current effects and in-plane motion were used.

Spins moving through a magnetic field gradient acquire a net phase shift (Eq. 3.3). The motion of spins can be expressed as a Taylor series expansion in terms of gradient waveform time moments, where displacement, velocity, acceleration and jerk of spins are given by the 0th, 1st, 2nd and 3rd order terms respectively [168]. Nulling of higher order moments via insertion of additional gradient waveforms results in insensitivity of phase to higher order motion, and have been used in non-DW motion-compensated imaging sequences [66]. PGSE sequences are inherently 0th order or M_0-nulled and bipolar DW sequeces are M_1-nulled. Here, nulling to the n^{th} moment implies nulling also of lower-order moments. M_1-nulling has been used to reduce motion sensitivity [42, 56], but the results can be suboptimal as illustrated in Fig. 3.12.

Recent developments in M_2-nulled DW show great promise for motion-robust cardiac diffusion MRI in vivo [7, 54, 136, 177, 196, 203]. M_2-nulling was shown to increase the range of viable trigger delays and broaden the acquisition window by 2.5× compared to an M_1-nulled sequence [177], reduce the mean ADC in healthy human myocardium from $3.8 \pm 0.6 \times 10^{-3}$ mm^2/s in PGSE to $1.9 \pm 0.3 \times 10^{-3}$ mm^2/s reflecting lower artefactual signal loss [7], and be capable of acquiring free-breathing DTI data for estimation of HA in whole human heart within 10 min [55]. Gradient system performance may be a limiting factor, and lower G_{max} and gradient slew rates lead to prolonged gradient duration and TE. Higher order GMN limits b-value, increases TE and reduces SNR. A study using M_0 to M_3-nulled DW in rat hearts in vivo found that the M_2-nulled approach provided the optimal combination in terms of b-value, SNR and motion insensitivity [203].

There are various ways to achieve higher order GMN. In M_2-nulled DW, the maximum diffusion gradients strength can be fixed and the diffusion duration varied, or vice versa, with the former method enabling potentially shorter TE. The diffusion gradients can also be calculated via numerical optimisation. Convex optimised diffusion encoding (CODE) minimises TE in SE-EPI sequences by eliminating dead time between the excitation and refocusing pulses (Fig. 3.16) [7]. Subject to constraints on the timings of the RF pulses and EPI readouts, b-value, order of GMN desired, and hardware constraints, CODE finds the minimum TE by iterative convex optimisation. An SNR of 9.1 ± 3.9 was reported in the human LV myocardium (N = 10) in vivo using CODE, and this compared favourably with SNR = 7.0 ± 2.6 from a conventional M_2-nulled sequence, whilst mean ADCs were similar with both methods. Current limitations are that δ and Δ are not defined by

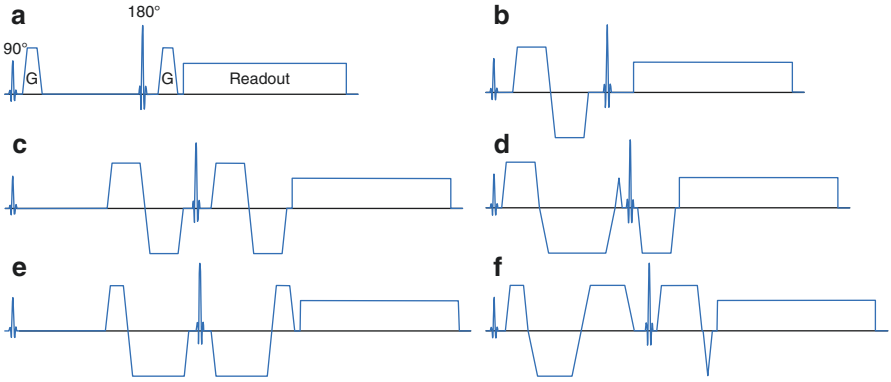

Fig. 3.16 SE-EPI sequences with conventional (**a**) M_0, (**c**) M_1 and (**e**) M_2-nulling diffusion gradients with typical echo times of 67, 97 and 99 ms respectively, and CODE-optimised (**b**) M_0, (**d**) M_1 and (**f**) M_2-nulling diffusion gradients exhibiting echo times of 60, 72 and 82 ms respectively. In all sequences, b = 500 s/mm^2 and EPI readout time = 52.8 ms. Gradient waveforms (**G**), RF pulses and EPI readouts are shown. Imaging gradients are omitted for clarity

single values and the diffusion gradients on either side of the refocusing pulse are non-identical, leading to a need for concomitant magnetic fields correction [122].

Strain

The effect of material strain or deformation that occurs during a diffusion encoding period is to modulate the effective phase distribution [154, 155]. A compression along the DW direction leads to an increase in effective diffusion-weighting, whereas stretching leads to a decrease in diffusion-weighting. The observed diffusion tensor, $\mathbf{D}^{\mathbf{obs}}$ can be described by Eq. 3.11.

$$\mathbf{D}^{\mathbf{obs}} = \frac{1}{\Delta}\int_0^{\Delta} \mathbf{U}(t)^{-1}\,\mathbf{D}\mathbf{U}(t)^{-1}\,dt \tag{3.11}$$

where Δ is the diffusion time, **U** is the right stretch tensor which describes material compression/extension in 3D, **D** is the diffusion tensor in the absence of strain and assuming zero net displacement between 0 and Δ.

U can be estimated from measured strain maps assuming small-strain approximation [113]. Strain can in turn be encoded by the phase evolution during a STEAM sequence [154] that forms the basis of displacement encoding with stimulated echoes or DENSE imaging [5], or reconstructed from 3D tagging data [176]. Alternatively, strain rate can be measured with 3D velocity-sensitive methods with bipolar gradient pulses [155]. From Eq. 3.11, it is observed that the diffusion tensor is modulated not just by strain, but also the strain that occurs over the cardiac cycle,

or strain history. Although the heart returns to its initial configuration after a full cardiac cycle, in general $\mathbf{D}^{\text{obs}} \neq \mathbf{D}$. Exceptions are at the effective mid-points of the motion cycle, corresponding to mid-systole and mid-diastole, when the contraction and dilation of the heart serve to minimise the net effect of strain. These time points are known as *sweet spots*, where diffusion can be measured without strain correction [190], and are consistent with numerical simulations [125].

Figure 3.17 illustrates the substantial deformation that occurs in the myocardium in the radial, circumferential and longitudinal orientations over the course of the cardiac cycle [176]. During systole and without strain correction, radial diffusion components are overestimated and longitudinal and circumferential components are underestimated. This leads to stretching of the diffusion tensor in the radial direction and compression in the longitudinal and circumferential directions. Strain correction leads to changes in transverse and sheet angle distributions during systole, where sheet angle here is equal to $\pi/2$ minus the sheetlet elevation as previously described. Differences in HA and during diastole were small. The marked effect on sheetlet orientation and flattening of sheetlets was consistent with previous findings [42, 190]. Strain correction also led to a significant increase and decrease in MD during systole and diastole respectively, as well as an increase in FA during systole. The strain correction method was validated against data measured at the cardiac sweet spots.

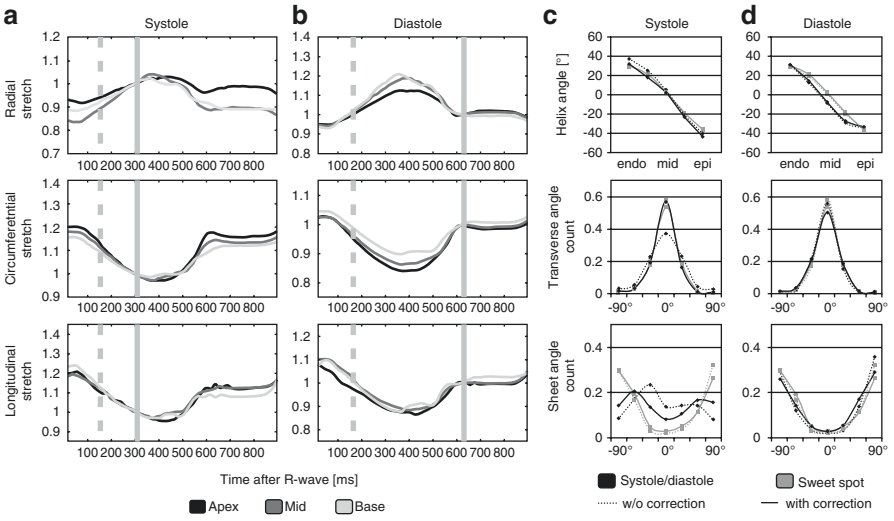

Fig. 3.17 Time course of the measured stretch tensor. Radial, circumferential and longitudinal components of the right stretch tensors are plotted as a function of time after the R-wave. (**a**) Systolic and (**b**) diastolic timings of the DTI sequence (*vertical solid line*) and systolic sweet spot (*vertical dashed line*) are shown. Transmural course of the helix angles, and transverse and sheet angle histograms at a medial/basal level are presented in (**c**) systole and (**d**) diastole. Systolic and diastolic (*black*) and sweet-spot (*gray*) data are shown before (*dotted line*) and after (*solid line*) strain correction (Figure by Stoeck et al. licensed under CC BY [176])

Uncompensated strain leads to errors in estimation of the diffusion tensor that depends both on the diffusion tensor and the local 3D strain history. The complex myocardial arrangement of cells and sheetlets coupled with the 3D contraction of the heart means that errors in DTI metrics will be spatially heterogeneous. These errors are manifested most prominently in the characterisation of sheetlets due to modest transverse anisotropy, leading to errors in eigenvector sorting and 90° offsets in estimates of sheetlet orientation. Furthermore, the complex contraction of the heart involving compression, shear and torsion obviates simple modelling of strain. STEAM-EPI can be desensitised to strain through the use of bipolar diffusion gradients at the cost of reducing maximum b-value or increasing TE [42]. These findings strongly motivate the use of strain correction methods in STEAM-EPI, or SE-EPI methods that are less sensitive to strain due to short diffusion times.

Perfusion

Measurement of perfusion is valuable in studies of ischaemia and oxygen delivery, while isolation of its contribution to the diffusion signal will improve accuracy in characterisation of both the intra- and extravascular environment. Failure to account for perfusion may, for example, lead to overestimation of FA where vessels and cardiomyocytes are aligned, which can mask small FA changes in disease. The myocardium is well perfused, and the vascular fraction ranges from about 8% to 27% [21, 142]. Capillary diameters range from 4 to 9 μm in humans [172]. Blood flow through the microvasculature can be described by a distribution of flow velocities. This results in a distribution of spin displacements resulting in signal attenuation in the presence of diffusion encoding gradients (Fig. 3.2), which can be measured using bi-exponential fitting methods such as the intra-voxel incoherent motion (IVIM) technique. IVIM was first used to describe the contribution of the microcirculation to the diffusion signal in the brain [106]. As the scale of spin displacements due to flow generally exceeds diffusion, the resultant diffusion signal can be modelled with a bi-exponential function with fast and slow components representing vascular and non-vascular compartments (Eq. 3.12).

$$\frac{S}{S_0} = (1-f)e^{-bD} + fe^{-b(D^*+D)} \tag{3.12}$$

where S is the DW signal intensity, S_0 is the non-DW signal intensity, f is the vascular volume fraction, D is the tissue diffusivity and D^* is the pseudo-diffusion coefficient.

One study in isolated, perfused hearts from healthy rats found that $D_{1,fast} = 2.16 \pm 0.04 \times 10^{-3}$ mm²/s in the myocardium corresponded well to $D_{mean} = 2.15 \pm 0.04 \times 10^{-3}$ mm²/s in the surrounding perfusate and $D_{mean} \sim 2.0 \times 10^{-3}$ mm²/s in free water at 19 °C [127] suggesting that perfusion contributes to the fast component. However, $f = 0.76 \pm 0.01$ and exceeds the vascular volume fraction (VF) of 14–22% estimated

from histological studies [199]. Other factors besides perfusion are therefore likely to contribute to the fast component. It has been hypothesised that the longer T_2 in vascular and interstitial water and a decreased apparent T_1 due to perfusion may contribute to the apparent elevation in *f*. In contrast, diffusion due to Brownian motion is expected to primarily contribute to the slow component.

Quantitation of pseudo-diffusion was performed in canine [26] and human heart in vivo [39, 131, 164]. In the former study, both the tissue diffusivity and vascular volume fraction were found to be anisotropic: $D_c = 1.64 \pm 0.18 \times 10^{-3}$ mm²/s, $D_r = 0.99 \pm 0.14 \times 10^{-3}$ mm²/s, $D_l = 1.17 \pm 0.18 \times 10^{-3}$ mm²/s, $f_c = 11.14 \pm 2.20\%$, $f_r = 8.25 \pm 2.58\%$ and $f_l = 5.35 \pm 1.71\%$. in the circumferential (c), radial (r) and longitudinal (l) directions. In contrast, D^* was not significantly different across the three orthogonal directions and $D^*_{mean} = 12.87 \pm 2.56 \times 10^{-3} mm^2/s$. These observations were attributed to the presence of two groups of capillaries, one parallel to the cardiomyocytes, the other forming bridges interconnecting the first group. Mean blood velocities in both parallel and bridging capillaries are similar leading to similar D^* across DW directions. The anisotropic orientation distribution of capillaries leads to increased *f* when their dominant orientation coincides with the DW direction, in this case, the circumferential direction. However, direct correlation between f_c, f_r, f_l and the single physical capillary volume fraction is not straightforward. Separate administration of the vasodilating agent adenosine led to statistically significant increase in *f* and D^* in all three directions. However, there was a two to threefold increase in perfusion following adenosine measured by first-pass gadolinium-enhanced imaging, whereas the increase in product fD^* was only 44%. One explanation could be the moderating effect of water exchange between the intra- and extravascular compartments. In human studies, measurements of mean D^* varied widely, from 17×10^{-3} mm²/s [164], to 43.6×10^{-3} mm²/s [131], and 74.5×10^{-3} mm²/s [39]. These marked differences may be attributed to, among others, differences in pulse sequence, diffusion timings, ROI selection and relaxation effects.

The IVIM technique was originally designed for imaging in the brain where capillaries are poorly aligned. In the heart, capillaries are known to generally run parallel to the cardiomyocytes [150], in violation of a key assumption in IVIM. The dependence of IVIM-based measurements on the orientation of capillaries was investigated in isolated, perfused guinea pig hearts [2]. In numerical simulations of laminar flow in aligned capillaries along the x-direction, D_{tissue} and D^*_{app} exhibited the expected half-cosine behaviour with rotation of diffusion encoding from the x-direction (relative encoding angle, $\theta = 0°$) to the y-direction ($\theta = 90°$) where D_{tissue} is the tissue diffusivity and D^*_{app} is the apparent pseudo-diffusion coefficient combining diffusion and flow effects in the blood (Fig. 3.18).

D^*_{app} was non-linear and increased markedly with flow rate and coherence of capillary and DW orientations, whereas D_{tissue} appeared unrelated to flow. The simulated VF = 15% was accurately estimated in cases of moderate and high flow when capillaries and DW were aligned, and underestimated when they were poorly

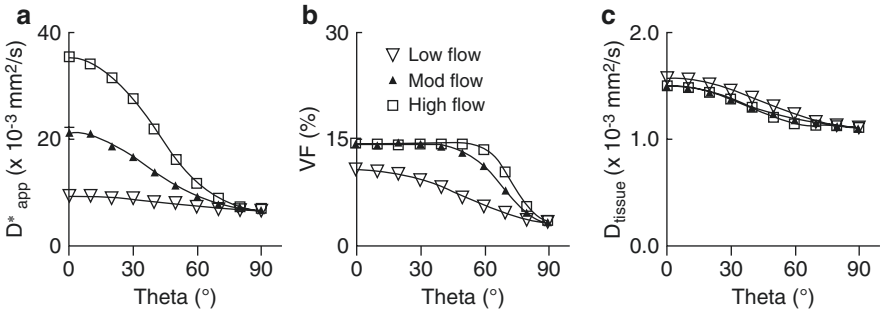

Fig. 3.18 (**a–c**) Anisotropy of IVIM parameters in a noise-free simulated perfectly aligned capillary network as a function of flow speed and encoding angle, θ. Capillary radii were Gaussian-distributed and flow was laminar. Low, moderate, and high flow settings corresponded to mean speeds of 0.32 ± 0.13, 0.64 ± 0.25 and 0.86 ± 0.34 mm/s respectively (Figure by Abdullah et al. reproduced with permission [2], Copyright 2015 Wiley Periodicals, Inc.)

aligned or when there was low flow. These findings were reproduced elegantly in vivo and validated against myocardial blood flow maps derived from arterial spin labelling data, in situations of low and normal flow, and with θ = 0°, 30°, 60° and 90°. Collectively, the simulations and experiments confirmed the signal dependence on flow speed, microvascular anisotropy and relative encoding angle. In this framework, the signal anisotropy is reflected in D^*_{app} and not VF, which may be more intuitive as D^*_{app} reflects spin translational dispersion which is generally anisotropic in the myocardium, and VF is a scalar reflecting compartment sizes. Further work is needed to better understand the mismatch between D^* and perfusion values derived from arterial spin labelling and first-pass contrast enhanced imaging.

Ex Vivo MRI

Ex vivo MRI facilitates high resolution scans free of artefacts associated with in vivo imaging, and is particularly important for development of computational models. However, the heart is by definition in a different physiological state that depends on the sample preparation, and scan times are long leading to concerns over sample stability. Table 3.3 presents a range of technical and sample preparation parameters that have been used in ex vivo studies. Mean myocardial values of MD and FA vary widely: mouse (0.89×10^{-3} mm^2/s, 0.25) [11], rat (1.07×10^{-3} mm^2/s, 0.26) [119], rabbit (1.34×10^{-3} mm^2/s, 0.29) [181], dog (1.66×10^{-3} mm^2/s, 0.33) [206], pig (0.52×10^{-3} mm^2/s, 0.42) [116], sheep (0.70×10^{-3} mm^2/s, 0.33) [97], monkey (0.46×10^{-3} mm^2/s, 0.65) [198] and human (0.68×10^{-3} mm^2/s, 0.27) [1]. Here, we discuss relevant factors that contribute to diffusion MRI measurements ex vivo, over and above inter-species variation. Careful control of these factors is important to avoid misinterpretation of observations.

Table 3.3 Variation in ex vivo DTI protocols in the preparation and imaging of isolated healthy hearts

D	Seq	F(T)	b_{max} (s/mm^2)	DW	Species	N	Fixative	Embedding medium	Authors
2D	SE	7	1500	12	Human	14	Formalin 10%	Fomblin	Abdullah et al. [1]
3D	SE	9.4	1852	6	Mouse	5	Formalin 10%	Fomblin	Angeli et al. [11]
2D	SE	4.7	764	6	Rat	7	Formalin 10%	Water	Chen et al. [28]
2D	SE	9.4		6	Rat	6	None	None	Garrido et al. [57]
2D	SE	4.7	1763	10	Goat	5	None	Gel	Geerts et al. [58]
3D	SE	7	1000	12	Rat	8	Formalin 10%	Fomblin	Giannakidis et al. [60]
3D	SE	9.4	1130	12	Mouse	10	Formalin		Healy et al. [71]
3D	SE	7.1	748	12	Rabbit	6	Formalin		Healy et al. [71]
3D	SE	2	1175	12	Sheep	5	Formalin		Healy et al. [71]
3D	FSE	1.5	1500	16	Dog	7	Formalin 7%	Fomblin	Helm et al. [72]
3D	SE	9.4	1130	12	Mouse	2	PFA 4%	Fomblin	Jiang et al. [81]
3D	SE	2	1175	12	Sheep	4	Formalin		Jiang et al. [80]
2D	SE-EPI	1.5	1500	55	Sheep	6	Formalin 10%	Fomblin	Kung et al. [97]
3D	SE-EPI	1.5	1000	12	Human	10	None	Gel	Lombaert et al. [110]
2D	SE-EPI	3	1000	256	Pig	8	None	None	Mazumder et al. [116]
2D	SE-EPI	3	1000	256	Pig	8	Formalin 10%	None	Mazumder et al. [116]
3D	FSE	9.4	1000	61	Rat	5	Karnovsky's	Gel	McClymont et al. [119]
2D	SE-EPI	3	2000	6	Human	5	PFA 4%	Fomblin	Mekkaoui et al. [123]
2D	SE-EPI	3	2000	6	Sheep	5	PFA 4%	Fomblin	Mekkaoui et al. [123]
3D	SE-EPI	4.7	1866	24	Rat	5	PFA 4%	Fomblin	Mekkaoui et al. [123]
3D	SE	9.4	1000	12	Rabbit	1	Karnovsky's	Gel	Teh et al. [181]
2D	EPI	7	1300	30	Monkey	8	PFA 1%	Fomblin	Wang et al. [198]
2D	SE-EPI	3	800	15	Dog	6	Formalin	Formalin	Wu et al. [206]

Abbreviations include number of dimensions (D), pulse sequence (Seq), field strength (F), number of DW directions (DW), and paraformaldehyde (PFA). Karnovsky's fixative where specified were low concentration 300 mOsm formulations. Studies with data acquired with different species and fixation are listed multiple times

Tissue Fixation

Freshly excised biological tissues degrade rapidly. Over post-mortem intervals to fixation (PMI) of 0–27 days, it was found that MD and principal eigenvalues increased non-linearly, while FA decreased non-linearly [45]. Freezing and thawing causes rupture of cell membranes and has similarly deleterious effects on the diffusion parameters [4].

Formalin operates by cross-linking proteins which stops cellular activity, and is widely used for fixing the heart [204]. Pre-mortem perfusion fixation is important for rapid and homogeneous distribution of fixative [43] and is particularly important in larger organs since diffusion of fixative occurs at a rate of about 1 mm/h. Without perfusion, diffusion through the full myocardium could take many hours, leading to heterogeneous PMI and tissue decomposition. Tissues are then immersed in fixative to continue fixation. Studies suggest that a minimum fixation time of 2 days is required after which initial changes to MD and FA stabilise [200]. However, prolonged fixation of 6–8 weeks led to increased MD, decreased FA and more longitudinal fibre orientations [60], suggesting that cell membrane degradation may continue over prolonged fixation. This may be exacerbated by high osmotic gradients between concentrated formalin and isosmotic tissue.

Although studies have shown that formalin fixation does not substantially affect fibre orientation [74, 160], it has been found to increase mean ADC and reduce FA [116]. Formalin fixation also causes shrinkage of sarcomeres on the scale of 4.2% in the myocardium [63]. Finally, formalin reduces tissue T_1 and T_2, the latter leading to reduced SNR [167]. This shortening of relaxation times is reversible through rinsing with PBS to remove free formalin.

Besides formalin, Karnovsky's fixative [89], comprised of paraformaldehyde, glutaraldehyde and sodium cacodylate, is another commonly used option for tissue fixation. The addition of glutaraldehyde fixes proteins irreversibly and more rapidly than formalin despite slower penetration [90]. Slices of brain tissue fixed in Karnovsky's fixative and washed in PBS had similar T_2 but higher mean ADC than unfixed, viable tissue [167]. Dilute, isosmotic fixatives can further be used to minimise osmotic gradients [69, 184]. In brief, tissue fixation is a necessary for all except the shortest ex vivo imaging protocols. Its effects are variable depending on the fixative type and concentration, PMI, fixation time, and parameter of interest. It is therefore essential to minimise the within-study variation of the fixation protocol.

Physiological State

The physiological state of the heart can be modulated prior to fixation, enabling simulation of different perfusion states and time points in the cardiac cycle. Often, hearts are excised and immediately perfused in Langendorff mode [99] with normal Tyrode or Krebs-Henseleit buffer equilibriated to a pH of 7.4 with 95% O_2–5% CO_2. This flushes out blood that causes signal dropouts due to paramagnetic effects of deoxyhaemoglobin. Hearts can then be arrested in specific, reproducible states

before fixation. For example, using high potassium buffer such as St Thomas' solution to simulate diastole, or lithium or barium chloride to simulate systole. As far as possible, solutions used should mimic physiological conditions, including pH of 7.4, osmolality of 300 mOsm, and temperature of 37 °C [69].

Imaging of isolated, living hearts are particularly useful in the investigation of cardiac perfusion and contraction as the confounds of motion and strain are largely removed [2, 29, 69, 76, 109, 149]. After excision, hearts are perfused retrogradely via the aorta with oxygenated buffer such as Tyrode solution, and can be arrested as above or paced via electrodes placed on the RV. All solutions should be oxygen-enriched and at body temperature via insulated fluid lines. However, residual heat loss along the perfusion line alters solubility of gases, and a bubble trap is needed to avoid ingress of bubbles into the heart. Addition of bovine serum albumin reduces interstitial oedema, and susceptibility artefacts and sample temperature gradients are minimised by completely immersing the heart in perfusate. Depending on the study, aortic perfusion can be modulated with a pump [2] or enhanced by infusion of adenosine [100]. Contraction state can also be altered by switching between (i) Tyrode solution simulating slack state in diastole, (ii) inflating a balloon inserted in the LV simulating volume-loaded venous return and (iii) lithium-Tyrode solution simulating contracture in end-systole.

Embedding Medium

Ex vivo samples need to be held securely over typically long imaging times. This can be achieved by mechanical localisation with a sample holder or by embedding in gel. Samples held in place and surrounded by air are prone to dehydration, and the images to susceptibility artefacts. Securing of the sample in water reduces susceptibility issues, but potentially leads to osmotic gradients and cell swelling. Common embedding mediums include Fomblin or agarose gel.

Fomblin is a perfluoropolyether mineral oil that is susceptibility-matched to biological tissue. In contrast to gel, Fomblin contributes no MR signal maximising the potential to use higher receiver gain settings for improving SNR, does not need to be heated, and is hydrophobic and therefore interacts minimally with the sample. As a liquid however, a custom rig is needed to hold the sample in place, potentially compressing or distorting the sample. In some cases, residual motion causes sample misregistration requiring post-hoc correction [11].

The benefits of gel embedding are that the samples are held firmly in place, reducing artefacts due to convection and flow of the surrounding media, and held in a neutral state, thus avoiding physical compression or other distortion. The samples are kept hydrated, thus maintaining sample integrity and geometry, are amenable to further processing such as for histology, and susceptibility artefacts arising from air-tissue interfaces are minimised. One consideration is that the liquid gel should be cooled to approximately body temperature in a water bath prior to embedding the sample. Exceeding approximately 40 °C should be avoided as protein denaturation can rapidly compromise tissue integrity. Second, air bubbles should be excluded at all times

to avoid introducing susceptibility artefacts. Third, diffusion occurs between the sample and gel over the course of the experiment. It is therefore important that the gel be prepared with the same or similar solution that the heart had last been prepared in. This minimises gradients in solutes, osmolality and pH that could lead to heterogeneity in the local tissue environment. A common approach is to rinse the heart of fixative with saline or PBS, and follow with embedding in gel made with the same buffer.

Temperature

Ex vivo samples are prone to temperature fluctuations due to a lack of homeostatic capacity, heat transfer from the gradient system and absorption of RF energy. Sample temperature in turn affects water diffusion, where a 1 °C increase in temperature leads to a 2.4% increase in apparent diffusion coefficient [103]. Higher temperatures can also shorten T_2, resulting in reduced SNR [195]. In DTI experiments in rat heart ex vivo, sample temperature increased from an ambient 20.2 °C to a thermal equilibrium of 23.8 °C during scanning [184]. This increase in temperature translated to a 10% reduction in mean myocardial non-DW signal intensity. Gradient system heating may also affect the magnetic field and lead to errors as demonstrated in phase contrast MRI [24].
Heating can be mitigated by using fewer RF refocusing pulses, longer repetition times, and lower b-values, at the cost of acquisition time and diffusion contrast. Temperature variation can also be minimised by application of warm-up DW scans, interleaving non-DW and DW scans, randomising scans with different b-values, and applying dummy diffusion gradients during sequence dead time. Good ambient temperature control is important either by way of the room air handling unit, temperature blanket, hot air blower or similar mechanism.

Quality Assurance

The proliferation of cardiac diffusion MRI studies is increasing demand for quantitative evaluation of sequence performance and validation of diffusion MRI measurements using independent means. Various methods are explored for improving quality assurance of data and informing the interpretation of the diffusion signal.

Reproducibility

Good reproducibility of data is important for improving sensitivity to pathology and reducing study sample sizes. In one study, breath-hold and free-breathing STEAM-EPI DTI were performed and repeated in healthy volunteers. No significant differences were reported in MD and FA across the two measurements, as determined by two-tailed paired *t* tests [138]. Inter-centre reproducibility was

assessed in DTI of healthy volunteers also using STEAM-EPI. Here, no significant differences were detected in systolic mean ADC and FA, and diastolic FA across measurements, however a difference was found in the mean ADC in diastole that was attributed to differences in image segmentation [193]. The inter-centre, intra-subject coefficients of variation for systolic mean ADC and FA, and diastolic mean ADC and FA were 7%, 6%, 7% and 3% respectively. In this respect, methods for automating data acquisition and reconstruction may be important for reducing operator bias or error in multi-centre studies. In a SE-EPI study of healthy volunteers, reproducibility of the MD, in terms of the Lin concordance correlation coefficient, was good with high accuracy and precision, but poorer in FA where accuracy was good but precision was limited [131]. Repeated analysis-of-variance showed no significant differences between repeated measurements of MD, FA and HA. Reproducibility of MD, FA and HA were also demonstrated in a cohort of patients with HCM [120]. This is important as patients often have irregular heart rates, and poor tolerance for breath-holding and long scan times. These studies suggest that DTI data are reproducible in volunteers and patients across centres. As diffusion MRI in vivo continues to develop, further studies incorporating the latest technical developments, are essential for establishing wider acceptance of diffusion MRI in the clinic.

Phantom Development

Phantoms are widely used in MRI for development of novel pulse sequences and diffusion models. These objects that are aimed to mimic the sample of interest, can be characterised in high-resolution by independent means such as scanning electron microscopy, and therefore serve as a reference for MRI measurements. They are typically designed to be stable and reproducible in manufacture, and can be used to validate reproducibility of data acquisition over time and across multiple centres, thereby enhancing quality control. Perhaps most important, is the ability to isolate different components that contribute to the diffusion signal, for instance the effects of motion, thereby enabling development of strategies for avoiding or correcting for such confounds.

Diffusion phantoms are commonly based on bundles of polymer fibres to simulate the anisotropic structure in biological tissues. One promising method uses co-electrospinning to create hollow polymer fibres with pore sizes that can be customised to match cellular dimensions [211]. Based on this method, a biomimetic cardiac diffusion phantom was fabricated with concentric helical fibre strips mimicking the transmural progression of fibre orientation in the myocardium [186]. Measurements of mean ADC and FA were similar to those from ex vivo rat heart studies, and were found to be stable over 4 months. The principal eigenvectors recapitulated the cell and sheetlet orientations found in the myocardium, albeit in a static and simplified manner with discrete layers. A different phantom was designed to investigate the sensitivity of diffusion sequences to motion. The phantom

comprised a custom-built fixture for holding the sample of interest, in this case, a section of fixed pig spinal cord. The fixture was coupled to a stepper motor by an MR-compatible rotating shaft, that enabled arbitrary control of rotational motion. The study showed that single-sided bipolar spin echo sequence (Fig. 3.16b) was more robust to motion that either conventional PGSE or bipolar DW sequences. The limitations of the phantom were the use of biological tissue that limits longitudinal stability, and the lack of contractile motion. Future developments in phantoms that simulate realistic structure, motion, strain and other parameters will catalyse pulse sequence development, and provide quality control metrics for wider adoption of diffusion MRI in the clinical setting.

Validation

The voxel sizes in diffusion MRI far exceed the scale of the underlying microstructure whose properties we aim to measure. Therefore, accurate validation is needed to inform our interpretation of simplified metrics such as the diffusion tensor. Several microscopy methods are available for this purpose, including optical microscopy, scanning electron microscopy, confocal microscopy, polarised light microscopy, and light sheet fluorescent microscopy. Of these, histological methods coupled with optical microscopy have served as the preferred validation method due to their availability, high spatial resolution and cell specificity.

Based on histology in fixed hearts ex vivo, fibre orientations have been found to generally correspond to $\mathbf{v_1}$ [74, 77, 123, 160]. Correspondence of sheetlet and sheetlet-normal orientations to $\mathbf{v_2}$ and $\mathbf{v_3}$ has also been shown [97, 191], subject to lower precision in their estimation and criticism that cleavage planes in between sheetlets could be an artefact of sample preparation – it has been observed for instance that ethanol dehydration can result in up to 33% tissue volume shrinkage [14]. However, these findings assume a single population of cells and sheetlets within a given voxel. This conflicts with the known dispersion in cell orientation and discontinuity in sheetlet structures. In voxels containing multiply oriented cell and sheetlets, the principal eigenvectors are liable to be inaccurate and misleading. Besides orientations, positive correlations have been observed in developing sheep hearts between the longitudinal diffusivity and myocyte length, and between transverse diffusivity and myocyte width [3]. Positive correlations have also been detected in human excised myocardium between collagen content and MD, λ_2 and λ_3, while collagen content and FA were negatively correlated [1]. In infarcted rat hearts, relative anisotropy was negatively correlated with histological measures of fibre disarray [28]. Significant limitations of histological methods are that they are labour-intensive and therefore routinely limited in FOV, destructive and prone to distortion and cell shrinkage during sample preparation that typically involves dehydration and wax embedding. As an inherently two-dimensional approach, reconstruction of 3D volumes of 3D tensors based on variably distorted slices is challenging and highly dependent on the reconstruction method.

In contrast to histology, structure tensor orientations calculated based on 3D anatomical MRI data have been shown to correlate with diffusion tensor orientations in the rat heart. The downside of anatomical MRI is insufficient resolution to resolve individual cells and sheetlets, resulting in voxel averaging of structures with different relaxation times [20]. An emerging technique that promises to address these issues is synchrotron radiation imaging (SRI). The high brilliance of SRI combines with phase retrieval to yield excellent resolution and contrast over a relatively large 3D FOV, without need for additional sample preparation following DTI. Orientations of structure tensors based on SRI data were found to correspond well with orientations of diffusion tensors across the rat heart [185].

Summary of Methods

Field strength is not generally a limitation in diffusion MRI, with studies having been performed from 1.5 to 9.4 T. Instead, gradient performance is often a critical factor. Here, G_{max} and the maximum slew rate govern the maximum b-value and flexibility of diffusion waveforms. These in turn influence the diffusion contrast available and minimum echo times. In the clinic, gradient systems with $G_{max} = 80$ mT/m are seen to be a requirement for second-order GMN nulling SE-EPI methods. In contrast, STEAM-EPI is compatible with more widely available gradient systems with $G_{max} = 45$ mT/m. In preclinical systems, maximum gradient strengths of 1 T/m are not uncommon, and provide opportunities to assess non-Gaussian diffusion and diffusion over shorter length scales.

Reconstruction of diffusion MRI data typically involves image registration and segmentation, tensor or other fitting, and calculation of diffusion parameters and angle maps. Rejection of motion-corrupted scans, denoising, b-matrix rotation and eddy current correction may further aid image reconstruction. Many of these individual operations are performed using in-house developed code or specialised tools. Ongoing developments in comprehensive open-source cardiac data analysis packages will improve ease and standardisation of data analysis and reporting.

Future Directions

Diffusion MRI is a valuable and unique method for acquiring micro-structural information in the whole heart both in vivo and ex vivo. Major advances over the past two decades have made it feasible to acquire information on tissue diffusivity, cell and sheetlet orientations in the beating heart in health and disease. However, many challenges remain in its adoption in the clinical setting. These include addressing the confounds of motion, strain, perfusion and relaxation times in an integrated and robust manner, and improving the scan efficiency such that adequate spatial and

temporal coverage is obtained within a clinically feasible scan time. Examples of accelerating image acquisition are the use of dual slice encoding [176], simultaneous multi-slice imaging [102] and compressed sensing [119]. While tensor fitting is commonly used, its limitations are well-known. This is driving the use of non-Gaussian diffusion imaging and tissue modelling for estimation of biophysical parameters of interest.

Diffusion measurements vary considerably in the literature, and retrospective evaluation of studies is confounded by a host of variables to which the diffusion parameters are sensitive to. These include biological factors such as species, disease and progression, contractility, tissue viability, temperature, use of chemical agents and location in the heart, as well as technical factors such as pulse sequence, SNR, b-value, diffusion timings, reconstruction method and presence of artefacts. Harmonisation and establishment of best practices in sample preparation, data acquisition and reconstruction, and reported metrics will be invaluable to improving inter-study comparison and accelerating the development of robust imaging methods. Underlying this is the need for rigorous optimisation of protocols that are theoretically supported by numerical simulations and experimentally validated by phantom studies and independent imaging modalities.

References

1. Abdullah OM, Drakos SG, Diakos NA, Wever-Pinzon O, Kfoury AG, Stehlik J, Selzman CH, Reid BB, Brunisholz K, Verma DR, Myrick C, Sachse FB, Li DY, Hsu EW. Characterization of diffuse fibrosis in the failing human heart via diffusion tensor imaging and quantitative histological validation. NMR Biomed. 2014;27:1378–86.
2. Abdullah OM, Gomez AD, Merchant S, Heidinger M, Poelzing S, Hsu EW. Orientation dependence of microcirculation-induced diffusion signal in anisotropic tissues. Magn Reson Med. 2015;76:1252.
3. Abdullah OM, Seidel T, Dahl M, Gomez AD, Yiep G, Cortino J, Sachse FB, Albertine KH, Hsu EW. Diffusion tensor imaging and histology of developing hearts. NMR Biomed. 2016;29:1338.
4. Agger P, Lass T, Smerup M, Frandsen J, Pedersen M. Optimal preservation of porcine cardiac tissue prior to diffusion tensor magnetic resonance imaging. J Anat. 2015;227:695–701.
5. Aletras AH, Ding S, Balaban RS, Wen H. Dense: displacement encoding with stimulated echoes in cardiac functional MRI. J Magn Reson. 1999;137:247–52.
6. Alexander AL, Hasan K, Kindlmann G, Parker DL, Tsuruda JS. A geometric analysis of diffusion tensor measurements of the human brain. Magn Reson Med. 2000;44:283–91.
7. Aliotta E, Wu HH, Ennis DB. Convex optimized diffusion encoding (CODE) gradient waveforms for minimum echo time and bulk motion-compensated diffusion-weighted MRI. Magn Reson Med. 2016;77:717–29.
8. Alsop DC. Phase insensitive preparation of single-shot rare: application to diffusion imaging in humans. Magn Reson Med. 1997;38:527–33.
9. Anderson AG, Garwin RL, Hahn EL, Horton JW, Tucker GL, Walker RM. Spin echo serial storage memory. J Appl Phys. 1955;26:1324–38.
10. Anderson RH, Ho SY, Redmann K, Sanchez-Quintana D, Lunkenheimer PP. The anatomical arrangement of the myocardial cells making up the ventricular mass. Eur J Cardiothorac Surg. 2005;28:517–25.
11. Angeli S, Befera N, Peyrat JM, Calabrese E, Johnson GA, Constantinides C. A high-resolution cardiovascular magnetic resonance diffusion tensor map from ex-vivo C57BL/6 murine hearts. J Cardiovasc Magn Reson. 2014;16:77.
12. Arts T, Costa KD, Covell JW, McCulloch AD. Relating myocardial laminar architecture to shear strain and muscle fiber orientation. Am J Physiol Heart Circ Physiol. 2001;280:H2222–9.
13. Axel L, Wedeen VJ, Ennis DB. Probing dynamic myocardial microstructure with cardiac magnetic resonance diffusion tensor imaging. J Cardiovasc Magn Reson. 2014;16:89.
14. Bahr GF, Bloom G, Friberg U. Volume changes of tissues in physiological fluids during fixation in osmium tetroxide or formaldehyde and during subsequent treatment. Exp Cell Res. 1957;12:342–55.
15. Basser PJ. Relationships between diffusion tensor and q-space MRI. Magn Reson Med. 2002;47:392–7.
16. Basser PJ, Mattiello J, Le Bihan D. Estimation of the effective self-diffusion tensor from the Nmr spin-echo. J Magn Reson Ser B. 1994;103:247–54.
17. Basser PJ, Mattiello J, Le Bihan D. MR diffusion tensor spectroscopy and imaging. Biophys J. 1994;66:259–67.
18. Basser PJ, Pajevic S, Pierpaoli C, Duda J, Aldroubi A. In vivo fiber tractography using DT-MRI data. Magn Reson Med. 2000;44:625–32.
19. Beaulieu C. The basis of anisotropic water diffusion in the nervous system – a technical review. NMR Biomed. 2002;15:435–55.
20. Bernus O, Radjenovic A, Trew ML, LeGrice IJ, Sands GB, Magee DR, Smaill BH, Gilbert SH. Comparison of diffusion tensor imaging by cardiovascular magnetic resonance and gadolinium enhanced 3D image intensity approaches to investigation of structural anisotropy in explanted rat hearts. J Cardiovasc Magn Reson. 2015;17:31.

21. Binotto MA, Higuchi Mde L, Aiello VD. Left ventricular remodeling in hearts with tricuspid atresia: morphologic observations and possible basis for ventricular dysfunction after surgery. J Thorac Cardiovasc Surg. 2003;126:1026–32.
22. Brown R. A brief account of microscopical observations made in the months of June, July and August, 1827, on the particles contained in the pollen of plants; and on the general existence of active molecules in organic and inorganic bodies. Phil Mag. 1828;4:161–73.
23. Bueno-Orovio A, Teh I, Schneider JE, Burrage K, Grau V. Anomalous diffusion in cardiac tissue as an index of myocardial microstructure. IEEE Trans Med Imaging. 2016;35:2200–7.
24. Busch J, Vannesjo SJ, Barmet C, Pruessmann KP, Kozerke S. Analysis of temperature dependence of background phase errors in phase-contrast cardiovascular magnetic resonance. J Cardiovasc Magn Reson. 2014;16:97.
25. Callaghan PT. Principles of nuclear magnetic resonance microscopy. Oxford: Oxford University Press; 1991.
26. Callot V, Bennett E, Decking UK, Balaban RS, Wen H. In vivo study of microcirculation in canine myocardium using the IVIM method. Magn Reson Med. 2003;50:531–40.
27. Carr HY, Purcell EM. Effects of diffusion on free precession in nuclear magnetic resonance experiments. Phys Rev. 1954;94:630–8.
28. Chen J, Song SK, Liu W, McLean M, Allen JS, Tan J, Wickline SA, Yu X. Remodeling of cardiac fiber structure after infarction in rats quantified with diffusion tensor MRI. Am J Physiol Heart Circ Physiol. 2003;285:H946–54.
29. Chen JJ, Liu W, Zhang HY, Lacy L, Yang XX, Song SK, Wickline SA, Yu X. Regional ventricular wall thickening reflects changes in cardiac fiber and sheet structure during contraction: quantification with diffusion tensor MRI. Am J Physiol Heart Circ Phys. 2005;289: H1898–907.
30. Cheng A, Langer F, Rodriguez F, Criscione JC, Daughters GT, Miller DC, Ingels Jr NB. Transmural sheet strains in the lateral wall of the ovine left ventricle. Am J Physiol Heart Circ Physiol. 2005;289:H1234–41.
31. Choi YJ, Constantino J, Vedula V, Trayanova N, Mittal R. A new MRI-based model of heart function with coupled hemodynamics and application to normal and diseased canine left ventricles. Front Bioeng Biotechnol. 2015;3:140.
32. Conturo TE, McKinstry RC, Aronovitz JA, Neil JJ. Diffusion MRI: precision, accuracy and flow effects. NMR Biomed. 1995;8:307–32.
33. Cook PA, Symms M, Boulby PA, Alexander DC. Optimal acquisition orders of diffusion-weighted MRI measurements. J Magn Reson Imaging. 2007;25:1051–8.
34. Costa KD, Holmes JW, McCulloch AD. Modelling cardiac mechanical properties in three dimensions. Philos Trans R Soc Lond Ser A-Math Phys Eng Sci. 2001;359:1233–50.
35. Costa KD, Takayama Y, McCulloch AD, Covell JW. Laminar fiber architecture and three-dimensional systolic mechanics in canine ventricular myocardium. Am J Physiol Heart Circ Physiol. 1999;276:H595–607.
36. Criscione JC, Rodriguez F, Miller DC. The myocardial band: simplicity can be a weakness. Eur J Cardiothorac Surg. 2005; 28: 363–4. Author Reply 364–7.
37. Daducci A, Canales-Rodriguez EJ, Descoteaux M, Garyfallidis E, Gur Y, Lin YC, Mani M, Merlet S, Paquette M, Ramirez-Manzanares A, Reisert M, Reis Rodrigues P, Sepehrband F, Caruyer E, Choupan J, Deriche R, Jacob M, Menegaz G, Prckovska V, Rivera M, Wiaux Y, Thiran JP. Quantitative comparison of reconstruction methods for intra-voxel fiber recovery from diffusion MRI. IEEE Trans Med Imaging. 2014;33:384–99.
38. De Santis S, Evans CJ, Jones DK. Rapid: a routine assurance pipeline for imaging of diffusion. Magn Reson Med. 2013;70:490–6.
39. Delattre BM, Viallon M, Wei H, Zhu YM, Feiweier T, Pai VM, Wen H, Croisille P. In vivo cardiac diffusion-weighted magnetic resonance imaging: quantification of normal perfusion and diffusion coefficients with intravoxel incoherent motion imaging. Investig Radiol. 2012;47:662–70.
40. Descoteaux M, Angelino E, Fitzgibbons S, Deriche R. Regularized, fast, and robust analytical Q-ball imaging. Magn Reson Med. 2007;58:497–510.

41. Dierckx H, Benson AP, Gilbert SH, Ries ME, Holden AV, Verschelde H, Bernus O. Intravoxel fibre structure of the left ventricular free wall and posterior left-right ventricular insertion site in canine myocardium using Q-ball imaging. Funct Imaging Model Heart Proc. 2009;5528:495–504.
42. Dou JG, Reese TG, Tseng WYI, Wedeen VJ. Cardiac diffusion MRI without motion effects. Magn Reson Med. 2002;48:105–14.
43. Dyrby TB, Baare WF, Alexander DC, Jelsing J, Garde E, Sogaard LV. An ex vivo imaging pipeline for producing high-quality and high-resolution diffusion-weighted imaging datasets. Hum Brain Mapp. 2011;32:544–63.
44. Edelman RR, Gaa J, Wedeen VJ, Loh E, Hare JM, Prasad P, Li W. In vivo measurement of water diffusion in the human heart. Magn Reson Med. 1994;32:423–8.
45. Eggen MD, Swingen CM, Iaizzo PA. Ex vivo diffusion tensor MRI of human hearts: relative effects of specimen decomposition. Magn Reson Med. 2012;67:1703–9.
46. Eichner C, Cauley SF, Cohen-Adad J, Moller HE, Turner R, Setsompop K, Wald LL. Real diffusion-weighted MRI enabling true signal averaging and increased diffusion contrast. NeuroImage. 2015;122:373–84.
47. Einstein A. Über Die Von Der Molekularkinetischen Theorie Der Wärme Geforderte Bewegung Von In Ruhenden Flüssigkeiten Suspendierten Teilchen. Ann Phys. 1905;322:549–60.
48. Ennis DB, Kindlman G, Rodriguez I, Helm PA, McVeigh ER. Visualization of tensor fields using superquadric glyphs. Magn Reson Med. 2005;53:169–76.
49. Ferreira PF, Kilner PJ, McGill LA, Nielles-Vallespin S, Scott AD, Ho SY, McCarthy KP, Haba MM, Ismail TF, Gatehouse PD, De Silva R, Lyon AR, Prasad SK, Firmin DN, Pennell DJ. In vivo cardiovascular magnetic resonance diffusion tensor imaging shows evidence of abnormal myocardial laminar orientations and mobility in hypertrophic cardiomyopathy. J Cardiovasc Magn Reson. 2014;16:87.
50. Fillard P, Descoteaux M, Goh A, Gouttard S, Jeurissen B, Malcolm J, Ramirez-Manzanares A, Reisert M, Sakaie K, Tensaouti F, Yo T, Mangin JF, Poupon C. Quantitative evaluation of 10 tractography algorithms on a realistic diffusion MR phantom. NeuroImage. 2011;56: 220–34.
51. Forder JR, Bui JD, Buckley DL, Blackband SJ. MR imaging measurement of compartmental water diffusion in perfused heart slices. Am J Physiol Heart Circ Physiol. 2001;281: H1280–5.
52. Frahm J, Merboldt KD, Hanicke W, Haase A. Stimulated echo imaging. J Magn Reson. 1969;64:81–93.
53. Froeling M, Mazzoli V, Nederveen AJ, Luijten PR, Strijkers GJ. Ex vivo cardiac DTI: on the effects of diffusion time and B-value. J Cardiovasc Magn Reson. 2014;16(Suppl 1):P77.
54. Froeling M, Strijkers GJ, Nederveen AJ, Chamuleau SA, Luijten P R. Diffusion tensor MRI of the heart – in vivo imaging of myocardial fiber architecture. Curr Cardiovasc Imag Rep. 2014;7(7):1–11.
55. Froeling M, Strijkers GJ, Nederveen AJ, Luijten PR. Whole heart DTI using asymmetric bipolar diffusion gradients. J Cardiovasc Magn Reson. 2015;17(Suppl 1):P15.
56. Gamper U, Boesiger P, Kozerke S. Diffusion imaging of the in vivo heart using spin echoes – considerations on bulk motion sensitivity. Magn Reson Med. 2007;57:331–7.
57. Garrido L, Wedeen VJ, Kwong KK, Spencer UM, Kantor HL. Anisotropy of water diffusion in the myocardium of the rat. Circ Res. 1994;74:789–93.
58. Geerts L, Bovendeerd P, Nicolay K, Arts T. Characterization of the normal cardiac myofiber field in goat measured with MR-diffusion tensor imaging. Am J Physiol Heart Circ Physiol. 2002;283:H139–45.
59. Gerdes AM, Kellerman SE, Moore JA, Muffly KE, Clark LC, Reaves PY, Malec KB, McKeown PP, Schocken DD. Structural remodeling of cardiac myocytes in patients with ischemic cardiomyopathy. Circulation. 1992;86:426–30.
60. Giannakidis A, Gullberg GT, Pennell DJ, Firmin DN. Value of formalin fixation for the prolonged preservation of rodent myocardial microanatomical organization: evidence by MR diffusion tensor imaging. Anat Rec (Hoboken). 2016;299:878–87.

61. Gilbert SH, Benson AP, Li P, Holden AV. Regional localisation of left ventricular sheet structure: integration with current models of cardiac fibre, sheet and band structure. Eur J Cardiothorac Surg. 2007;32:231–49.
62. Gomez AD, Bull DA, Hsu EW. Finite-element extrapolation of myocardial structure alterations across the cardiac cycle in rats. J Biomech Eng-Trans Asme. 2015;137:101010.
63. Grimm AF, Wohlfart B. Sarcomere Lengths at the Peak of the Length-Tension Curve in Living and Fixed Rat Papillary Muscle. Acta Physiologica Scandinavica. 1974;92:575–77.
64. Gudbjartsson H, Patz S. The rician distribution of noisy MRI data. Magn Reson Med. 1995;34:910–4.
65. Gullmar D, Haueisen J, Reichenbach JR. Analysis of B-value calculations in diffusion weighted and diffusion tensor imaging. Concepts Magn Reson Part A. 2005;25a:53–66.
66. Haacke EM, Lenz GW. Improving MR image quality in the presence of motion by using rephasing gradients. Am J Roentgenol. 1987;148:1251–8.
67. Hagmann P, Jonasson L, Maeder P, Thiran JP, Wedeen VJ, Meuli R. Understanding diffusion MR imaging techniques: from scalar diffusion-weighted imaging to diffusion tensor imaging and beyond. Radiographics. 2006;26(Suppl 1):S205–23.
68. Hahn EL. Spin echoes. Phys Rev. 1950;80:580–94.
69. Hales PW, Schneider JE, Burton RA, Wright BJ, Bollensdorff C, Kohl P. Histo-anatomical structure of the living isolated rat heart in two contraction states assessed by diffusion tensor MRI. Prog Biophys Mol Biol. 2012;110:319–30.
70. Harrington KB, Rodriguez F, Cheng A, Langer F, Ashikaga H, Daughters GT, Criscione JC, Ingels NB, Miller DC. Direct measurement of transmural laminar architecture in the anterolateral wall of the ovine left ventricle: new implications for wall thickening mechanics. Am J Physiol Heart Circ Physiol. 2005;288:H1324–30.
71. Healy LJ, Jiang Y, Hsu EW. Quantitative comparison of myocardial fiber structure between mice, rabbit, and sheep using diffusion tensor cardiovascular magnetic resonance. J Cardiovasc Magn Reson. 2011;13:74.
72. Helm PA, Tseng HJ, Younes L, McVeigh ER, Winslow RL. Ex vivo 3D diffusion tensor imaging and quantification of cardiac laminar structure. Magn Reson Med. 2005;54:850–9.
73. Ho SY. Anatomy and myoarchitecture of the left ventricular wall in normal and in disease. Eur J Echocardiogr. 2009;10:iii3–7.
74. Holmes AA, Scollan DF, Winslow RL. Direct histological validation of diffusion tensor MRI in formaldehyde-fixed myocardium. Magn Reson Med. 2000;44:157–61.
75. Hooks DA, Tomlinson KA, Marsden SG, LeGrice IJ, Smaill BH, Pullan AJ, Hunter PJ. Cardiac microstructure – implications for electrical, propagation and defibrillation in the heart. Circ Res. 2002;91:331–8.
76. Hsu EW, Buckley DL, Bui JD, Blackband SJ, Forder JR. Two-component diffusion tensor MRI of isolated perfused hearts. Magn Reson Med. 2001;45:1039–45.
77. Hsu EW, Muzikant AL, Matulevicius SA, Penland RC, Henriquez CS. Magnetic resonance myocardial fiber-orientation mapping with direct histological correlation. Am J Phys. 1998;274:H1627–34.
78. Jensen JH, Helpern JA, Ramani A, Lu H, Kaczynski K. Diffusional kurtosis imaging: the quantification of non-gaussian water diffusion by means of magnetic resonance imaging. Magn Reson Med. 2005;53:1432–40.
79. Jespersen SN, Lundell H, Sonderby CK, Dyrby TB. Orientationally invariant metrics of apparent compartment eccentricity from double pulsed field gradient diffusion experiments. NMR Biomed. 2013;26:1647–62.
80. Jiang Y, Guccione JM, Ratcliffe MB, Hsu EW. Transmural heterogeneity of diffusion anisotropy in the sheep myocardium characterized by MR diffusion tensor imaging. Am J Physiol Heart Circ Physiol. 2007;293:H2377–84.
81. Jiang Y, Pandya K, Smithies O, Hsu EW. Three-dimensional diffusion tensor microscopy of fixed mouse hearts. Magn Reson Med. 2004;52:453–60.
82. Jones DK. Determining and visualizing uncertainty in estimates of fiber orientation from diffusion tensor MRI. Magn Reson Med. 2003;49:7–12.

83. Jones DK. The effect of gradient sampling schemes on measures derived from diffusion tensor MRI: a Monte Carlo study. Magn Reson Med. 2004;51:807–15.
84. Jones DK. Diffusion MRI. Oxford: Oxford University Press; 2010.
85. Jones DK, Basser PJ. "Squashing peanuts and smashing pumpkins": how noise distorts diffusion-weighted MR data. Magn Reson Med. 2004;52:979–93.
86. Jones DK, Cercignani M. Twenty-five pitfalls in the analysis of diffusion MRI data. NMR Biomed. 2010;23:803–20.
87. Jones DK, Horsfield MA, Simmons A. Optimal strategies for measuring diffusion in anisotropic systems by magnetic resonance imaging. Magn Reson Med. 1999;42:515–25.
88. Jones SE, Buchbinder BR, Aharon I. Three-dimensional mapping of cortical thickness using Laplace's equation. Hum Brain Mapp. 2000;11:12–32.
89. Karnovsky MJ. A formaldehyde-glutaraldehyde fixative of high osmolarity for use in electron microscopy. J Cell Biol. 1965;27:137a–8a.
90. Kiernan JA. Histological and histochemical methods: theory and practice. Boston: Butterworth And Heinenmann; 1999.
91. Kim S, Chi-Fishman G, Barnett AS, Pierpaoli C. Dependence on diffusion time of apparent diffusion tensor of ex vivo calf tongue and heart. Magn Reson Med. 2005;54:1387–96.
92. Kinchesh P, Kleinnijenhuis M, Miller K L, Smart S. Minimizing diffusion encoding of slice selection in stimulated echo imaging In: Proceedings of the 23rd annual meeting of ISMRM, Toronto. 2015; 2791.
93. Kingsley PB. Introduction to diffusion tensor imaging mathematics: part I. Tensors, rotations, and eigenvectors. Concepts Magn Reson Part A. 2006;28A:101–22.
94. Kingsley PB. Introduction to diffusion tensor imaging mathematics: part II. Anisotropy, diffusion-weighting factors, and gradient encoding schemes. Concepts Magn Reson Part A. 2006;28a:123–54.
95. Kohl P. Heterogeneous cell coupling in the heart: an electrophysiological role for fibroblasts. Circ Res. 2003;93:381–3.
96. Krishnamurthy A, Villongco CT, Chuang J, Frank LR, Nigam V, Belezzuoli E, Stark P, Krummen DE, Narayan S, Omens JH, McCulloch AD, Kerckhoffs RC. Patient-specific models of cardiac biomechanics. J Comput Phys. 2013;244:4–21.
97. Kung GL, Nguyen TC, Itoh A, Skare S, Ingels Jr NB, Miller DC, Ennis DB. The presence of two local myocardial sheet populations confirmed by diffusion tensor MRI and histological validation. J Magn Reson Imaging. 2011;34:1080–91.
98. Laissy JP, Gaxotte V, Ironde-Laissy E, Klein I, Ribet A, Bendriss A, Chillon S, Schouman-Claeys E, Steg PG, Serfaty JM. Cardiac diffusion-weighted MR imaging in recent, subacute, and chronic myocardial infarction: a pilot study. J Magn Reson Imaging. 2013;38:1377–87.
99. Langendorff O. Untersuchungen Am Überlebenden Saugetierherzen. Pflügers Arch Für Gesamte Physiol Menschen Tiere. 1987;66:355–400.
100. Lasley RD, Mentzer Jr RM. Dose-dependent effects of adenosine on interstitial fluid adenosine and postischemic function in the isolated rat heart. J Pharmacol Exp Ther. 1998;286:806–11.
101. Latt J, Nilsson M, Wirestam R, Johansson E, Larsson EM, Stahlberg F, Brockstedt S. In vivo visualization of displacement-distribution-derived parameters in q-space imaging. Magn Reson Imaging. 2008;26:77–87.
102. Lau AZ, Tunnicliffe EM, Frost R, Koopmans PJ, Tyler DJ, Robson MD. Accelerated human cardiac diffusion tensor imaging using simultaneous multislice imaging. Magn Reson Med. 2015;73:995–1004.
103. Le Bihan D, Delannoy J, Levin RL. Temperature mapping with MR imaging of molecular diffusion: application to hyperthermia. Radiology. 1989;171:853–7.
104. Le Bihan D, Poupon C, Amadon A, Lethimonnier F. Artifacts and pitfalls in diffusion MRI. J Magn Reson Imaging. 2006;24:478–88.
105. Le Bihan D, Turner R, Moonen CT, Pekar J. Imaging of diffusion and microcirculation with gradient sensitization: design, strategy, and significance. J Magn Reson Imaging. 1991;1:7–28.

106. Le Bihan D, Breton E, Lallemand D, Grenier P, Cabanis E, Lavaljeantet M. Mr imaging of intravoxel incoherent motions – application to diffusion and perfusion in neurologic disorders. Radiology. 1986;161:401–7.
107. LeGrice IJ, Smaill BH, Chai LZ, Edgar SG, Gavin JB, Hunter PJ. Laminar structure of the heart: ventricular myocyte arrangement and connective tissue architecture in the dog. Am J Phys. 1995;269:H571–82.
108. LeGrice IJ, Takayama Y, Covell JW. Transverse shear along myocardial cleavage planes provides a mechanism for normal systolic wall thickening. Circ Res. 1995;77:182–93.
109. Lohezic M, Teh I, Bollensdorff C, Peyronnet R, Hales PW, Grau V, Kohl P, Schneider JE. Interrogation of living myocardium in multiple static deformation states with diffusion tensor and diffusion spectrum imaging. Prog Biophys Mol Biol. 2014;115:213–25.
110. Lombaert H, Peyrat JM, Croisille P, Rapacchi S, Fanton L, Cheriet F, Clarysse P, Magnin I, Delingette H, Ayache N. Human atlas of the cardiac fiber architecture: study on a healthy population. IEEE Trans Med Imaging. 2012;31:1436–47.
111. Lower R. Tractatus De Corde. Item De Motu & Colore Sanguinis Et Chyli In Eum Transitu. Duck Lane: Jo. Redmayne; 1669.
112. Lundell H, Alexander DC, Dyrby TB. High angular resolution diffusion imaging with stimulated echoes: compensation and correction in experiment design and analysis. NMR Biomed. 2014;27:918–25.
113. Malvern LE. Introduction to the mechanics of continuous media [online]. Englewood Cliffs: Prentice-Hall; 1989.
114. Malyarenko D, Galban CJ, Londy FJ, Meyer CR, Johnson TD, Rehemtulla A, Ross BD, Chenevert TL. Multi-system repeatability and reproducibility of apparent diffusion coefficient measurement using an ice-water phantom. J Magn Reson Imaging. 2013;37:1238–46.
115. Mansfield P. Multi-planar image-formation using NMR spin echoes. J Phys C-Solid State Phys. 1977;10:L55–8.
116. Mazumder R, Choi S, Clymer BD, White RD, Kolipaka A. Diffusion tensor imaging of healthy and infarcted porcine hearts: study on the impact of formalin fixation. J Med Imaging Radiat Sci. 2016;47:74–85.
117. Mazzoli V, Froeling M, Nederveen AJ, Nicolay K, Strijkers GJ. Cardiac diffusion MRI beyond DTI. In: Proceedings of the 22nd annual meeting of ISMRM, Milan. 2014; 2434.
118. McClymont D, Teh I, Carruth E, Omens JH, McCulloch AD, Whittington HJ, Kohl P, Grau V, Schneider JE. Evaluation of non-Gaussian diffusion in cardiac MRI. Magn Reson Med. 2016; doi:10.1002/mrm.26466.
119. McClymont D, Teh I, Whittington HJ, Grau V, Schneider JE. Prospective acceleration of diffusion tensor imaging with compressed sensing using adaptive dictionaries. Magn Reson Med. 2016;76:248–58.
120. McGill LA, Ismail TF, Nielles-Vallespin S, Ferreira P, Scott AD, Roughton M, Kilner PJ, Ho SY, McCarthy KP, Gatehouse PD, De Silva R, Speier P, Feiweier T, Mekkaoui C, Sosnovik DE, Prasad SK, Firmin DN, Pennell DJ. Reproducibility of in-vivo diffusion tensor cardiovascular magnetic resonance in hypertrophic cardiomyopathy. J Cardiovasc Magn Reson. 2012;14:86.
121. McGill LA, Scott AD, Ferreira PF, Nielles-Vallespin S, Ismail T, Kilner PJ, Gatehouse PD, De Silva R, Prasad SK, Giannakidis A, Firmin DN, Pennell DJ. Heterogeneity of fractional anisotropy and mean diffusivity measurements by in vivo diffusion tensor imaging in normal human hearts. Plos One. 2015;10:E0132360.
122. Meier C, Zwanger M, Feiweier T, Porter D. Concomitant field terms for asymmetric gradient coils: consequences for diffusion, flow, and echo-planar imaging. Magn Reson Med. 2008;60:128–34.
123. Mekkaoui C, Huang S, Chen HH, Dai G, Reese TG, Kostis WJ, Thiagalingam A, Maurovich-Horvat P, Ruskin JN, Hoffmann U, Jackowski MP, Sosnovik DE. Fiber architecture in remodeled myocardium revealed with a quantitative diffusion cmr tractography framework and histological validation. J Cardiovasc Magn Reson. 2012;14:70.
124. Mekkaoui C, Porayette P, Jackowski MP, Kostis WJ, Dai G, Sanders S, Sosnovik DE. Diffusion MRI tractography of the developing human fetal heart. Plos One. 2013;8:E72795.

125. Mekkaoui I, Moulin K, Croisille P, Pousin J, Viallon M. Quantifying the effect of tissue deformation on diffusion-weighted MRI: a mathematical model and an efficient simulation framework applied to cardiac diffusion imaging. Phys Med Biol. 2016;61:5662–86.
126. Merchant SS, Gomez AD, Morgan JL, Hsu EW. Parametric modeling of the mouse left ventricular myocardial fiber structure. Ann Biomed Eng. 2016;44:2661–73.
127. Mills R. Self-diffusion in normal and heavy-water in range 1–45 degrees. J Phys Chem. 1973;77:685–8.
128. Mitra PP, Halperin BI. Effects of finite gradient-pulse widths in pulsed-field-gradient diffusion measurements. J Mag Reson Series A. 1995;113:94–101.
129. Mori S, Crain BJ, Chacko VP, Van Zijl PC. Three-dimensional tracking of axonal projections in the brain by magnetic resonance imaging. Ann Neurol. 1999;45:265–9.
130. Mori S, Van Zijl PC. A motion correction scheme by twin-echo navigation for diffusion-weighted magnetic resonance imaging with multiple RF echo acquisition. Magn Reson Med. 1998;40:511–6.
131. Moulin K, Croisille P, Feiweier T, Delattre BM, Wei H, Robert B, Beuf O, Viallon M. In vivo free-breathing DTI and IVIM of the whole human heart using a real-time slice-followed SE-EPI navigator-based sequence: a reproducibility study in healthy volunteers. Magn Reson Med. 2016;76:70–82.
132. Nagy Z, Thomas DL, Weiskopf N. Orthogonalizing crusher and diffusion-encoding gradients to suppress undesired echo pathways in the twice-refocused spin echo diffusion sequence. Magn Reson Med. 2014;71:506–15.
133. Nagy Z, Weiskopf N, Alexander DC, Deichmann R. A method for improving the performance of gradient systems for diffusion-weighted MRI. Magn Reson Med. 2007;58:763–8.
134. Neeman M, Freyer JP, Sillerud LO. A simple method for obtaining cross-term-free images for diffusion anisotropy studies in NMR microimaging. Magn Reson Med. 1991;21:138–43.
135. Nguyen C, Fan Z, Xie Y, Dawkins J, Tseliou E, Bi X, Sharif B, Dharmakumar R, Marban E, Li D. In vivo contrast free chronic myocardial infarction characterization using diffusion-weighted cardiovascular magnetic resonance. J Cardiovasc Magn Reson. 2014;16:68.
136. Nguyen C, Fan ZY, Sharif B, He Y, Dharmakumar R, Berman DS, Li DB. In vivo three-dimensional high resolution cardiac diffusion-weighted MRI: a motion compensated diffusion-prepared balanced steady-state free precession approach. Magn Reson Med. 2014;72:1257–67.
137. Nguyen C, Lu M, Fan Z, Bi X, Kellman P, Zhao S, Li D. Contrast-free detection of myocardial fibrosis in hypertrophic cardiomyopathy patients with diffusion-weighted cardiovascular magnetic resonance. J Cardiovasc Magn Reson. 2015;17:107.
138. Nielles-Vallespin S, Mekkaoui C, Gatehouse P, Reese TG, Keegan J, Ferreira PF, Collins S, Speier P, Feiweier T, De Silva R, Jackowski MP, Pennell DJ, Sosnovik DE, Firmin D. In vivo diffusion tensor MRI of the human heart: reproducibility of breath-hold and navigator-based approaches. Magn Reson Med. 2013;70:454–65.
139. Nielles-Vallespin S, Khalique Z, Ferreira PF, de Silva R, Scott AD, Kilner P, McGill LA, Giannakidis A, Gatehouse PD, Ennis D, Aliotta E, Al-Khalil M, Kellman P, Mazilu D, Balaban RS, Firmin DN, Arai AE, Pennell DJ. Assessment of myocardial microstructural dynamics by in vivo diffusion tensor cardiac magnetic resonance. J Am Coll Cardiol. 2017;69:661–676.
140. Niendorf T, Dijkhuizen RM, Norris DG, Van Lookeren Campagne M, Nicolay K. Biexponential diffusion attenuation in various states of brain tissue: implications for diffusion-weighted imaging. Magn Reson Med. 1996;36:847–57.
141. Nordbo O, Lamata P, Land S, Niederer S, Aronsen JM, Louch WE, Sjaastad I, Martens H, Gjuvsland AB, Tondel K, Torp H, Lohezic M, Schneider JE, Remme EW, Smith N, Omholt SW, Vik JO. A computational pipeline for quantification of mouse myocardial stiffness parameters. Comput Biol Med. 2014;53:65–75.
142. O'Keefe DD, Hoffman JI, Cheitlin R, O'Neill MJ, Allard JR, Shapkin E. Coronary blood flow in experimental canine left ventricular hypertrophy. Circ Res. 1978;43:43–51.

143. Parker GJ, Haroon HA, Wheeler-Kingshott CA. A framework for a streamline-based probabilistic index of connectivity (PICo) using a structural interpretation of MRI diffusion measurements. J Magn Reson Imaging. 2003;18:242–54.
144. Peyrat JM, Sermesant M, Pennec X, Delingette H, Xu C, McVeigh ER, Ayache N. A computational framework for the statistical analysis of cardiac diffusion tensors: application to a small database of canine hearts. IEEE Trans Med Imaging. 2007;26:1500–14.
145. Pierpaoli C, Basser PJ. Toward a quantitative assessment of diffusion anisotropy. Magn Reson Med. 1996;36:893–906.
146. Pierpaoli C, Sarlls J, Nevo U, Basser PJ, F Horkay. Polyvinylpyrrolidone (PVP) water solutions as isotropic phantoms for diffusion MRI studies. In: Proceedings of the 17th annual meeting of ISMRM, Honolulu. 2009; 1414.
147. Pipe JG, Farthing VG, Forbes KP. Multishot diffusion-weighted FSE using PROPELLER MRI. Magn Reson Med. 2002;47:42–52.
148. Plank G, Burton RA, Hales P, Bishop M, Mansoori T, Bernabeu MO, Garny A, Prassl AJ, Bollensdorff C, Mason F, Mahmood F, Rodriguez B, Grau V, Schneider JE, Gavaghan D, Kohl P. Generation of histo-anatomically representative models of the individual heart: tools and application. Philos Trans Math Phys Eng Sci. 2009;367:2257–92.
149. Poelzing S, Veeraraghavan R. Heterogeneous ventricular chamber response to hypokalemia and inward rectifier potassium channel blockade underlies bifurcated t wave in guinea pig. Am J Physiol Heart Circ Physiol. 2007;292:H3043–51.
150. Poole DC, Batra S, Mathieucostello O, Rakusan K. Capillary geometrical changes with fiber shortening in rat myocardium. Circ Res. 1992;70:697–706.
151. Posnansky O, Kupriyanova Y, Shah NJ. On the problem of gradient calibration in diffusion weighted imaging. Int J Imaging Syst Technol. 2011;21:271–9.
152. Potet J, Rahmouni A, Mayer J, Vignaud A, Lim P, Luciani A, Dubois-Rande JL, Kobeiter H, Deux JF. Detection of myocardial edema with low-b-value diffusion-weighted echo-planar imaging sequence in patients with acute myocarditis. Radiology. 2013;269: 362–9.
153. Rapacchi S, Wen H, Viallon M, Grenier D, Kellman P, Croisille P, Pai VM. Low b-value diffusion-weighted cardiac magnetic resonance imaging: initial results in humans using an optimal time-window imaging approach. Investig Radiol. 2011;46:751–8.
154. Reese TG, Wedeen VJ, Weisskoff RM. Measuring diffusion in the presence of material strain. J Magn Reson B. 1996;112:253–8.
155. Reese TG, Weisskoff RM, Smith RN, Rosen BR, Dinsmore RE, Wedeen VJ. Imaging myocardial fiber architecture in-vivo with magnetic-resonance. Magn Reson Med. 1995;34:786–91.
156. Relan J, Chinchapatnam P, Sermesant M, Rhode K, Ginks M, Delingette H, Rinaldi CA, Razavi R, Ayache N. Coupled personalization of cardiac electrophysiology models for prediction of ischaemic ventricular tachycardia. Interface Focus. 2011;1:396–407.
157. Schick F. Splice: sub-second diffusion-sensitive MR imaging using a modified fast spin-echo acquisition mode. Magn Reson Med. 1997;38:638–44.
158. Schmitt B, Fedarava K, Falkenberg J, Rothaus K, Bodhey NK, Reischauer C, Kozerke S, Schnackenburg B, Westermann D, Lunkenheimer PP, Anderson RH, Berger F, Kuehne T. Three-dimensional alignment of the aggregated myocytes in the normal and hypertrophic murine heart. J Appl Physiol (1985). 2009;107:921–7.
159. Schultz T, Kindlmann GL. Superquadric glyphs for symmetric second-order tensors. IEEE Trans Vis Comput Graph. 2010;16:1595–604.
160. Scollan DF, Holmes A, Winslow R, Forder J. Histological validation of myocardial microstructure obtained from diffusion tensor magnetic resonance imaging. Am J Phys. 1998;275:H2308–18.
161. Scollan DF, Holmes A, Zhang J, Winslow RL. Reconstruction of cardiac ventricular geometry and fiber orientation using magnetic resonance imaging. Ann Biomed Eng. 2000;28:934–44.
162. Scott AD, Ferreira P, Nielles-Vallespin S, McGill LA, Kilner PJ, Pennell DJ, Firmin D. Improved in-vivo cardiac DTI using optimal B-values. J Cardiovasc Magn Reson. 2015;16(Suppl 1):O27.

163. Scott AD, Ferreira P, Nielles-Vallespin S, McGill LA, Pennell DJ, Firmin D. Directions vs. averages: an in-vivo comparison for cardiac DTI. J Cardiovasc Magn Reson. 2015;17(Suppl 1):P25.
164. Scott AD, Ferreira PF, Nielles-Vallespin S, Gatehouse P, McGill LA, Kilner P, Pennell DJ, Firmin DN. Optimal diffusion weighting for in vivo cardiac diffusion tensor imaging. Magn Reson Med. 2015;74:420–30.
165. Scott AD, Nielles-Vallespin S, Ferreira PF, McGill LA, Pennell DJ, Firmin DN. The effects of noise in cardiac diffusion tensor imaging and the benefits of averaging complex data. NMR Biomed. 2016;29:588–99.
166. Sermesant M, Chabiniok R, Chinchapatnam P, Mansi T, Billet F, Moireau P, Peyrat JM, Wong K, Relan J, Rhode K, Ginks M, Lambiase P, Delingette H, Sorine M, Rinaldi CA, Chapelle D, Razavi R, Ayache N. Patient-specific electromechanical models of the heart for the prediction of pacing acute effects in CRT: a preliminary clinical validation. Med Image Anal. 2012;16:201–15.
167. Shepherd TM, Thelwall PE, Stanisz GJ, Blackband SJ. Aldehyde fixative solutions alter the water relaxation and diffusion properties of nervous tissue. Magn Reson Med. 2009;62: 26–34.
168. Simonetti OP, Wendt 3rd RE, Duerk JL. Significance of the point of expansion in interpretation of gradient moments and motion sensitivity. J Magn Reson Imaging. 1991;1:569–77.
169. Sosnovik DE, Mekkaoui C, Huang S, Chen HH, Dai G, Stoeck CT, Ngoy S, Guan J, Wang R, Kostis WJ, Jackowski MP, Wedeen VJ, Kozerke S, Liao R. Microstructural impact of ischemia and bone marrow-derived cell therapy revealed with diffusion tensor magnetic resonance imaging tractography of the heart in vivo. Circulation. 2014;129:1731–41.
170. Sosnovik DE, Wang R, Dai G, Reese TG, Wedeen VJ. Diffusion MR tractography of the heart. J Cardiovasc Magn Reson. 2009;11:47.
171. Sosnovik DE, Wang R, Dai G, Wang T, Aikawa E, Novikov M, Rosenzweig A, Gilbert RJ, Wedeen VJ. Diffusion spectrum MRI tractography reveals the presence of a complex network of residual myofibers in infarcted myocardium. Circ Cardiovasc Imaging. 2009;2:206–12.
172. Spaan J. Coronary blood flow: mechanics, distribution, and control. Springer Netherlands; 1991.
173. Spees WM, Song SK, Garbow JR, Neil JJ, Ackerman JJ. Use of ethylene glycol to evaluate gradient performance in gradient-intensive diffusion MR sequences. Magn Reson Med. 2012;68:319–24.
174. Spotnitz HM, Spotnitz WD, Cottrell TS, Spiro D, Sonnenblick EH. Cellular basis for volume related wall thickness changes in the rat left ventricle. J Mol Cell Cardiol. 1974;6: 317–31.
175. Stejskal EO, Tanner JE. Spin diffusion measurements: spin echoes in the presence of a time-dependent field gradient. J Chem Phys. 1965;42:288.
176. Stoeck CT, Kalinowska A, Von Deuster C, Harmer J, Chan RW, Niemann M, Manka R, Atkinson D, Sosnovik DE, Mekkaoui C, Kozerke S. Dual-phase cardiac diffusion tensor imaging with strain correction. Plos One. 2014;9:E107159.
177. Stoeck CT, Von Deuster C, Genet M, Atkinson D, Kozerke S. Second-order motion-compensated spin echo diffusion tensor imaging of the human heart. Magn Reson Med. 2016;75:1669–76.
178. Streeter Jr DD, Spotnitz HM, Patel DP, Ross Jr J, Sonnenblick EH. Fiber orientation in the canine left ventricle during diastole and systole. Circ Res. 1969;24:339–47.
179. Strijkers GJ, Bouts A, Blankesteijn WM, Peeters TH, Vilanova A, Van Prooijen MC, Sanders HM, Heijman E, Nicolay K. Diffusion tensor imaging of left ventricular remodeling in response to myocardial infarction in the mouse. NMR Biomed. 2009;22:182–90.
180. Sun CY, Wang LH, Yang F, Zhu YM. Investigation of intravoxel fiber configuration complexity in the human heart. In: Proceedings of the 24th annual meeting of ISMRM, Singapore. 2016; 3451.
181. Teh I, Burton RA, McClymont D, Capel RA, Aston D, Kohl P, Schneider JE. Mapping cardiac microstructure of rabbit heart in different mechanical states by high resolu-

tion diffusion tensor imaging: a proof-of-principle study. Prog Biophys Mol Biol. 2016; 121:85.
182. Teh I, Lundell H, Whittington HJ, Dyrby TB, Schneider JE. Resolving microscopic fractional anisotropy in the heart. In: Proceedings of the 24th annual meeting of ISMRM, Singapore. 2016; 800.
183. Teh I, Maguire ML, Schneider JE. Efficient gradient calibration based on diffusion MRI. Magn Reson Med. 2017;77:170–9.
184. Teh I, McClymont D, Burton RA, Maguire ML, Whittington HJ, Lygate CA, Kohl P, Schneider JE. Resolving fine cardiac structures in rats with high-resolution diffusion tensor imaging. Sci Rep. 2016;6:30573.
185. Teh I, McClymont D, Zdora MC, Whittington HJ, Davidoiu V, Lee J, Lygate CA, Rau C, Zanette I, Schneider JE. Validation of Diffusion Tensor MRI Measurements of Cardiac Microstructure with Structure Tensor Synchrotron Radiation Imaging. J Cardiovasc Magn Reson. 2017; In Press.
186. Teh I, Zhou FL, Hubbard Cristinacce PL, Parker GJM, Schneider JE. Biomimetic phantom for cardiac diffusion magnetic resonance imaging. J Magn Reson Imaging. 2016;43: 594–600.
187. Torrey HC. Bloch equations with diffusion terms. Phys Rev. 1956;104:563–5.
188. Tournier JD, Yeh CH, Calamante F, Cho KH, Connelly A, Lin CP. Resolving crossing fibres using constrained spherical deconvolution: validation using diffusion-weighted imaging phantom data. NeuroImage. 2008;42:617–25.
189. Tseng WY, Dou J, Reese TG, Wedeen VJ. Imaging myocardial fiber disarray and intramural strain hypokinesis in hypertrophic cardiomyopathy with MRI. J Magn Reson Imaging. 2006;23:1–8.
190. Tseng WY, Reese TG, Weisskoff RM, Wedeen VJ. Cardiac diffusion tensor MRI in vivo without strain correction. Magn Reson Med. 1999;42:393–403.
191. Tseng WY, Wedeen VJ, Reese TG, Smith RN, Halpern EF. Diffusion tensor MRI of myocardial fibers and sheets: correspondence with visible cut-face texture. J Magn Reson Imaging. 2003;17:31–42.
192. Tuch DS. Q-ball imaging. Magn Reson Med. 2004;52:1358–72.
193. Tunnicliffe EM, Scott AD, Ferreira P, Ariga R, McGill LA, Nielles-Vallespin S, Neubauer S, Pennell DJ, Robson MD, Firmin DN. Intercentre reproducibility of cardiac apparent diffusion coefficient and fractional anisotropy in healthy volunteers. J Cardiovasc Magn Reson. 2014;16:31.
194. Vercauteren T, Pennec X, Perchant A, Ayache N. Diffeomorphic demons: efficient non-parametric image registration. NeuroImage. 2009;45:S61–72.
195. Vesanen PT, Zevenhoven KC, Nieminen JO, Dabek J, Parkkonen LT, Ilmoniemi RJ. Temperature dependence of relaxation times and temperature mapping in ultra-low-field MRI. J Magn Reson. 2013;235:50–7.
196. Von Deuster C, Stoeck CT, Genet M, Atkinson D, Kozerke S. Spin echo versus stimulated echo diffusion tensor imaging of the in vivo human heart. Magn Reson Med. 2016;76:862–72.
197. Wang TT, Kwon HS, Dai G, Wang R, Mijailovich SM, Moss RL, So PT, Wedeen VJ, Gilbert RJ. Resolving myoarchitectural disarray in the mouse ventricular wall with diffusion spectrum magnetic resonance imaging. Ann Biomed Eng. 2010;38:2841–50.
198. Wang Y, Cai W, Wang L, Xia R. Evaluate the early changes of myocardial fibers in rhesus monkey during sub-acute stage of myocardial infarction using diffusion tensor magnetic resonance imaging. Magn Reson Imaging. 2016;34:391–6.
199. Warley A. Changes in sodium concentration in cardiac myocytes from diabetic rats. Scanning Microsc. 1991;5:239–44. Discussion 244-5.
200. Watson BR, Hsu EW. Effects of formalin fixation on diffusion tensor imaging of myocardial tissues. In: Proceedings of the 20th annual meeting of ISMRM, Melbourne. 2012; 1114.

201. Wedeen VJ, Hagmann P, Tseng WY, Reese TG, Weisskoff RM. Mapping complex tissue architecture with diffusion spectrum magnetic resonance imaging. Magn Reson Med. 2005;54:1377–86.
202. Wei H, Viallon M, Delattre BM, Moulin K, Yang F, Croisille P, Zhu Y. Free-breathing diffusion tensor imaging and tractography of the human heart in healthy volunteers using wavelet-based image fusion. IEEE Trans Med Imaging. 2015;34:306–16.
203. Welsh CL, DiBella EV, Hsu EW. Higher-order motion-compensation for in vivo cardiac diffusion tensor imaging in rats. IEEE Trans Med Imaging. 2015;34:1843–53.
204. Werner M, Chott A, Fabiano A, Battifora H. Effect of formalin tissue fixation and processing on immunohistochemistry. Am J Surg Pathol. 2000;24:1016–9.
205. Westin CF, Maier SE, Khidhir B, Everett P, Jolesz FA, Kikinis R. Image processing for diffusion tensor magnetic resonance imaging. Med Image Comput Comput-Assis Interv, Miccai'99, Proc. 1999;1679:441–52.
206. Wu EX, Wu Y, Tang H, Wang J, Yang J, Ng MC, Yang ES, Chan CW, Zhu S, Lau CP, Tse HF. Study of myocardial fiber pathway using magnetic resonance diffusion tensor imaging. Magn Reson Imaging. 2007;25:1048–57.
207. Wu MT, Tseng WY, Su MY, Liu CP, Chiou KR, Wedeen VJ, Reese TG, Yang CF. Diffusion tensor magnetic resonance imaging mapping the fiber architecture remodeling in human myocardium after infarction: correlation with viability and wall motion. Circulation. 2006;114:1036–45.
208. Wu Y, Wu EX. MR study of postnatal development of myocardial structure and left ventricular function. J Magn Reson Imaging. 2009;30:47–53.
209. Wu YC, Alexander AL. A method for calibrating diffusion gradients in diffusion tensor imaging. J Comput Assist Tomogr. 2007;31:984–93.
210. Zhang L, Allen J, Hu LZ, Caruthers SD, Wickline SA, Chen JJ. Cardiomyocyte architectural plasticity in fetal, neonatal, and adult pig hearts delineated with diffusion tensor MRI. Am J Phys Heart Circ Phys. 2013;304:H246–52.
211. Zhou FL, Hubbard PL, Eichhorn SJ, Parker GJM. Coaxially electrospun axon-mimicking fibers for diffusion magnetic resonance imaging. ACS Appl Mater Interfaces. 2012;4:6311–6.

Chapter 4
Myocyte Metabolic Imaging with Hyperpolarised MRI

Jack J. Miller

Introduction

The Challenges and Rewards of Non-proton Magnetic Resonance

In every magnetic resonance experiment the ultimate signal-to-noise ratio (SNR) obtained is directly proportional to M_0, the initial magnetisation of the sample [1]. Under the experimental circumstances usually encountered in magnetic resonance, this magnetisation itself originates due to the weak paramagnetism of the sample being investigated, and is typically extraordinarily small in absolute terms. The fact that M_0 is small is a fundamental consequence of the basic physics of magnetic resonance, and the hyperpolarisation methods which are the subject of this chapter fundamentally aim to side-step this limitation in order to temporarily increase M_0 by several orders of magnitude. As a consequence, they directly increase the signal-to-noise ratio of magnetic resonance experiments, and open new fields of study for hyperpolarised research.

A Brief Refresher on Thermodynamics and Magnetic Resonance

Within our universe, it is an experimental fact that fundamental particles possess an intrinsic form of angular momentum known as spin. Systems containing more than one particle with spin (such as a nucleus) have a resulting intrinsic angular momentum that is not simply the sum of its constituents, but rather a set of possible

J.J. Miller
University of Oxford, Oxford, UK
e-mail: Jack.Miller@physics.org

C. Constantinides (ed.), *Protocols and Methodologies in Basic Science and Clinical Cardiac MRI*, https://doi.org/10.1007/978-3-319-53001-7_4

Table 4.1 A summary of the net effect of the constraints imposed by the quantum-mechanical addition of angular momenta that aid the determination of the possible nuclear spin, I, for the isotope ${}^{A}_{Z}\mathrm{X}_{N}$, where A is the atomic mass number, Z the atomic number, and N the neutron number

A	Z	N	I	Example
Even	Even	Even	0	${}^{12}_{6}\mathrm{C}_{6}$
	Odd	Odd	Integer	${}^{2}_{1}\mathrm{H}_{1}$
Odd	Even	Odd	Half-integer	${}^{13}_{6}\mathrm{C}_{7}$
	Odd	Even	Half-integer	${}^{15}_{7}\mathrm{N}_{8}$

quantised values that can be derived from considering the commutation relations of the angular momentum operators [2]. For a system as complex as a nucleus the resulting total nuclear spin I is usually considered an intrinsic property of a given isotope. However, the fundamental quantum mechanical constraints placed on the behaviour of spins manifest themselves as a set of apparent "rules" that determine whether a nucleus will have zero spin (and hence be of no use to magnetic resonance experiments), which are summarised in Table 4.1.

It can also be shown that, provided it is not zero, this intrinsic spin of a nucleus is associated with an intrinsic nuclear magnetic moment μ. The maximum magnitude of μ can be found [3] to be

$$\begin{aligned}\mu &= \frac{e}{2m_p} g_N \hbar I \\ &\equiv \gamma \hbar I\end{aligned} \tag{4.1}$$

where e is elementary charge, m_p the mass of a proton, $\hbar$ reduced Planck's constant, and g_N in (4.1) is the Landé g-factor, a number specific to a given particle that famously is about two for an electron, and notoriously difficult to calculates. For these reasons, as stated in Eq. (4.2) the quantity γ is defined in terms of these fundamental constants, measured experimentally, and is known as the gyromagnetic (or magnetogyric) ratio. It is constant for a given nucleus. Table 4.2 lists γ for several nuclei commonly encountered in magnetic resonance; note that no other nucleus possesses a γ as high as that as the proton.

Assuming that individual spins can only interact with each other relatively weakly, and are not strongly coupled as may be found in, e.g., a ferro- or ferrimagnetic sample, the net behaviour of a sample consisting of N spins placed in an external magnetic field of strength B is well understood. The Zeeman interaction between the spin I sample and the external field results in the evolution of $2I + 1$ available energy levels, each of magnitude

$$E = -\gamma \hbar B m, \quad \text{where } m = -I, -(I-1), ..., I. \tag{4.2}$$

Table 4.2 Gyromagnetic ratios and nuclear spin for several commonly encountered nuclei in magnetic resonance. Values for γ are computed based on published values of g adapted from Lide [4]

Isotope	Spin	$\gamma/(2\pi)$ (MHz T^{-1})	Relative sensitivity $\lvert\gamma/\gamma_{^1H}\rvert$
Electron	$S = 1/2$	28024.9540	658
^{1}H	$I = 1/2$	42.5775	1
^{2}H	1	6.5359	0.15
^{3}He	1/2	−32.4341	0.76
^{7}Li	1/2	16.5483	0.38
^{13}C	3/2	10.7084	0.25
^{14}N	1	3.0777	0.07
^{19}F	1/2	40.0776	0.94
^{23}Na	3/2	11.2688	0.26
^{29}Si	1/2	−8.4655	0.20
^{31}P	1/2	17.2515	0.41

Thermodynamic considerations mean that, at thermal equilibrium, the expected occupancy of each level follows a Boltzmann distribution, and, hence, the number N_m of spins *at thermal equilibrium* in a state m is given by

$$N_m = N \frac{\exp\left(-\dfrac{E_m}{k_B T}\right)}{\displaystyle\sum_{i=1}^{I} e^{\frac{-E_i}{k_B T}}}, \tag{4.3}$$

where k_B is Boltzmann's constant, and the sample is assumed to contain N spins in total.

It is customary to define P as the nuclear polarisation, the appropriately normalised population difference between available spin states. As a consequence, *for a sample at thermal equilibrium* containing a total number N of spin I nucleons at a temperature T, M_0 can be explicitly evaluated as

$$\begin{aligned} M_0 &= N\left(\frac{\hbar\gamma}{2}\right)P \\ &= N\left(\frac{\hbar\gamma}{2}\right)\tanh\left(\frac{\hbar\gamma B}{2k_B T}\right) \text{ for an } I = \frac{1}{2} \text{ nucleus.} \end{aligned} \tag{4.4}$$

For temperatures compatible with life, and magnetic fields achievable on Earth, P is exceptionally small; at 3 T and room temperature, $P \approx 3 \times 10^{-6}$, indicating that three spins in a million are in excess in the ground state, as graphically illustrated in Fig. 4.1. It is therefore entirely appropriate to obtain a series of expansion of Eq. (4.4), and observe that M_0 scales approximately linearly with both B and γ.

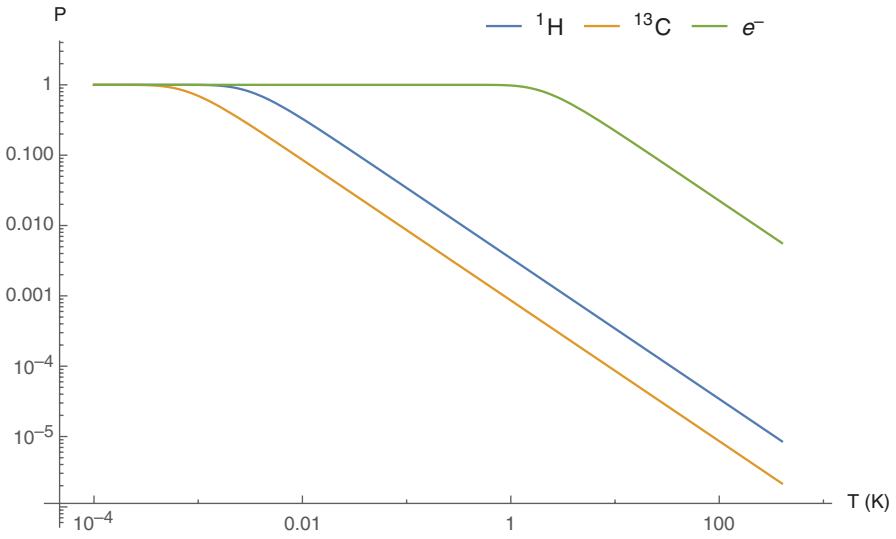

Fig. 4.1 Nuclear polarisation, *P*, as described by the Botlzmann equation, plotted as a function of temperature at 3 T for both electrons, protons, and ^{13}C. It is apparent that, for nucleons, temperatures on the order of millikelvin are required before *P* is close to unity

Sensitivity

As a direct consequence of Eq. (4.4), magnetic resonance is usually considered to be an inherently insensitive technique. Magnetic Resonance Imaging as used as a clinical imaging modality sidesteps this problem by predominantly imaging anatomy by exciting ^{1}H alone, predominantly chemically found either in water or fat, both of which are commonly present at high concentrations in biological samples: for reference, the concentration of protons in water is approximately 110 M (as the concentration of pure water is approximately 55 M under standard conditions).

Spectroscopy, "even" proton spectroscopy, is therefore always challenging *in vivo*: in comparison to free water, many specific metabolites of biological interest are present physiologically in millimolar concentrations or below. One of the great challenges of proton spectroscopy is therefore acquiring spectra with a sufficient dynamic range to be able to detect metabolites which may be four orders of magnitude or more lower in amplitude than the water peak, and, due to the relatively coarse spectral linewidths available *in vivo*, potentially superimposed underneath it. It should be noted that magnetic resonance techniques are essentially unique in their ability to potentially report, non-invasively, on the relative concentrations and chemical identity of particular molecular species within a living organism. Such information is obviously of potentially vital consequence in clinical practice, as well as of interest for basic science.

Therefore, in order to obtain functional information about cellular biochemistry there are three main methods that are commonly used to overcome this problem, and obtain information from biologically interesting compounds that are inherently present at low concentrations.

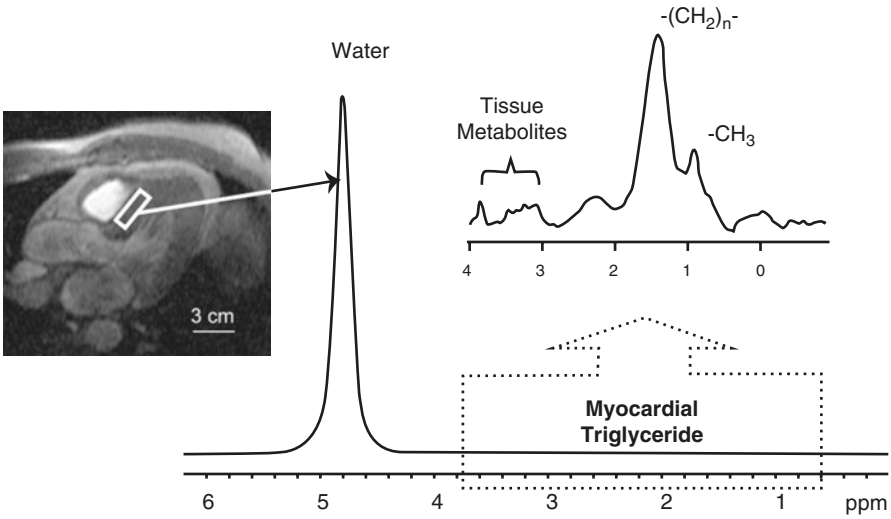

Fig. 4.2 An example *in vivo* ^{1}H spectrum obtained from a 6 ml voxel of interest in the human interventricular septum without water suppression by a localised spectroscopy sequence known as PRESS. The fact that the myocardium is approximately 73% water by mass serves to render the quantification of other metabolites, particularly those with chemical shifts near $\delta = 4.8$ ppm, exceptionally difficult, with a factor of ~ 10^3 between the maximum amplitude of the water peak and that of the CH_2 peak (Figure ©2003 John Wiley and Sons, adapted from Szczepaniak et al. [7] with permission)

Firstly, modern proton spectroscopy techniques rely upon sophisticated water suppression schemes to avoid acquiring the large, spectrally contaminating water peak. Saturation methods are commonly used to suppress the water signal in *in vivo* proton spectroscopy to a large degree [5], or spectral editing techniques such as quantum filtering can be used to avoid acquiring it in the first place, albeit at the cost of SNR [6]. As illustrated in Fig. 4.2, in contrast to the ability of modern conventional anatomical imaging techniques which can produce high resolution functional and anatomical views of most organs relatively quickly in essentially any species, proton spectroscopy remains comparatively slow, and low resolution. The concentration difference between water and compounds of biological interest remains a significant, and unavoidable, limitation.

Secondly, by exploiting the fact that protons in many aqueous molecules of biological interest are in rapid exchange with those of water, it is possible to saturate proton spins whilst they are bound to another molecule with a small bandwidth saturation pulse, and observe the resulting change in the intensity of the water peak as a function of the frequency of irradiation. This technique, Chemical Shift Exchange Saturation Transfer, or CEST [8], forms an attractive method to detect, quantify, and image protons in exchange with water. As a consequence of chemical shift selectivity, the method can preferrentially distinguish protons from a variety of different biological sources, such as those ordinarily bound to amides, glycogen, or glycosaminoglycan. However, CEST is unable to probe protons that are *not* freely in exchange with water, and the accurate quantitation of the CEST effect is far from straightforward.

Thirdly, non-proton spectroscopy offers the ability to obtain information from other nuclei directly, without the confounding effects of a high water signal, as well as typically a broader range of chemical shift. However, as illustrated Table 4.2, no stable nucleus possesses a gyromagnetic ratio as high as that as the proton, and that the nucleus with the second highest gyromagnetic ratio, ^{19}F, is not endogenous to any living system [9]. Most molecules probed by *in vivo* non-proton spectroscopy are those with ^{13}C, ^{23}Na or ^{31}P nuclei, all of whom possess γ less than half that of the proton.

As the initial magnetisation present for MR experiments scales approximately linearly with both B and γ (c.f. Eq. (4.4) as well as the number of nuclei present, each of these three methods is limited in initial M^0 and, consequently, SNR. As a direct consequence, the MR experiment in question is usually repeated several times, and the acquired data summed to improve SNR, a process referred to as signal averaging. Performing this operation n times increases the total received signal by a factor of n; however, the distribution of noise is such that it also increases, but only by a factor of $\sqrt{n}$ [10]. Therefore, averaging results in a net increase by $\sqrt{n}$ in the SNR of a reconstructed image or spectrum, which is inefficient. Therefore, the reduction in M_0 obtained by observing a different nucleus in a particular molecule of interest can have dire implications for the time required to perform a particular magnetic resonance experiment. For example, detecting urea (CH_4N_2O) by carbon MRS as opposed to proton MRS would entail a reduction of sensitivity by at least a factor of approximately 16 – four from the ratio $\gamma_{^1\mathrm{H}}/\gamma_{^{13}\mathrm{C}}$, and four from the fact that urea has four identical protons and one carbon nucleus. Ignoring the difference in relaxation times (the carbon T_1 of urea is far longer than that of the proton T_1), one can therefore expect the carbon experiment to take 256 times longer than an equivalent proton one, albeit with a spectral background greatly reduced in complexity and without the potentially contaminating presence of a large water peak. It is arguably for this reason that the use of non-proton spectroscopy has historically been confined to the research environment, as opposed to clinical practice, despite the surfeit of relevant biochemical information that could be obtained by simple spectroscopic methods.

Breaking the Boltzmann Barrier: Signal Enhancement Methods

As outlined above, the fact that magnetic resonance is an inherently insensitive technique frustrates many of its potential applications. Whilst P increases approximately linearly with B under physiological conditions, the cost of a given spectrometer does not, and, due to engineering constraints it is not possible to build an arbitrarily high-field spectrometer. Additionally, due to the fact that T_1 and T_2 are themselves functions of B, it is not necessarily clear *a priori* that increasing B arbitrarily is advantageous for the study of living systems, although the issue has been studied extensively historically [11–13]. Consequently, numerous methods have been proposed to try and independently increase M_0 without increasing B, outside of the magnetic resonance system used, by several orders of magnitude. Such signal

enhancement methods generate enhanced nuclear polarisation (referred to as hyperpolarisation) in a specific nuclei in a given molecule of interest, typically at cryogenic temperatures. The molecule of interest is chosen to be biologically significant, and is usually biochemically active within the timescale of the experiment. When removed (rapidly) from the polariser, its nuclear polarisation returns to thermal equilibrium exponentially, with a characteristic time T_1. Typically, non-proton nuclei are used, both to enable the detection of the large, hyperpolarised signal without any effective background signal, and also because the T_1 of other nuclei is often longer than that of nearby protons. Additionally, the wider range of chemical shift experienced by most nuclei compared to protons results in an enhanced spectral separation that often serves to be advantageous in probing the subsequent *in vivo* biochemistry of the particular probe.

The "Brute Force" Method

Arguably the most immediate method to increase the nuclear polarisation of a particular sample is by "brute force", increasing B or reducing T such that P become closer to unity. Owing to the fact that the critical field for most known superconductors is on the order of ~23 T, and that electrical power dissipation scales with the square of current, it is only feasible to pursue this approach by reducing T close to 0 K, and not increasing B without limit. As illustrated in Fig. 4.1, it is necessary to cool a particular sample to millikelvin temperatures in order to have $P \approx 1$ for nuclei (in contrast to electrons, where $P = 0.90$ at $T \approx 1.5$ K and 3 T, for comparison). Practically this has to be obtained via the use of ^{3}He–^{4}He dilution refrigerators, which exploit the enthalpy of mixing between the two isotopes of helium to provide a close cryogenic cycle that can obtain temperatures on the order of 10 mK in superconducting B fields up to 15 T [14]. In order to be used as a signal enhancement method, a particular molecular probe has to be labelled with an appropriate nucleus of choice (typically ^{13}C or ^{31}P), introduced to the dilution refrigerator, allowed to reach the new thermodynamic equilibrium at greatly enhanced P, removed, and rapidly brought to physiological temperatures before injection into the biological system under test.

Every one of these steps represents a significant challenge. ^{3}He is extremely limited in supply and exceptionally expensive owing to its use in neutron detectors, the large number of neutron detectors installed in ports worldwide as a result of anti-terrorism and and anti-nuclear proliferation activity [15]. Additionally, as a matter of necessity, the low temperature region of the brute force polariser has to be isolated from the outside world, and it is not trivial to introduce samples to it without disrupting its efficacy. By far the biggest challenge to the method, however, is the fact that without intervention the T_1 for most molecules of biological interest at mK temperatures is on the order of several 100 h [16]. Waiting naïvely for a frozen sample to reach the new, polarised, thermodynamic equilibrium would therefore take several months. Lanthanide relaxation agents (such as dysprosyium-diethylenetriaminepentacetate [DPTA] and holmium-DPTA) combined with ^{1}H–^{13}C

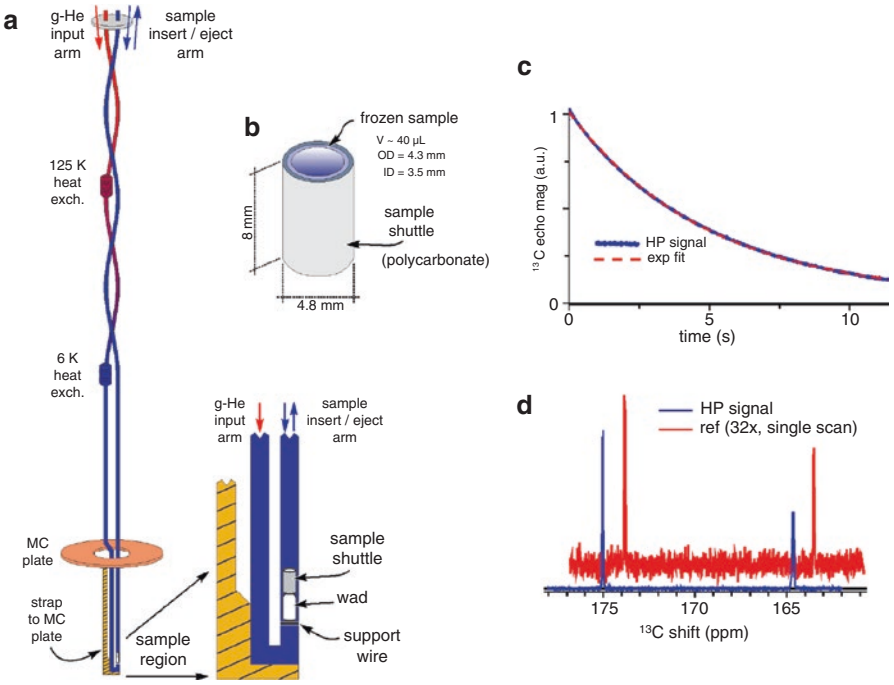

Fig. 4.3 The "brute force" method for preparing hyperpolarised (HP) samples. (**a**) A pair of heat-exchanging pneumatic tubes allow a polycarbonate "shuttle" to be introduced into a mixing chamber within a 14 T dilution refrigerator. The helical coiling of the heat exchanging tubes is required in order to reduce radiative losses. In order to avoid ice formation from stray contaminant gasses, a 99.999% pure ^{4}He source is required for pneumatically removing the sample from the chamber. (**b**) Illustrative schematic of the polycarbonate sample holder, which is required to be 'wadded' in with a teflon disc to facilitate efficient, rapid, removal. (**c**, **d**) After rapid removal from the MC, the sample is melted and rapidly injected to a nearby MR system, a process which takes approximately 60 s. The polarisation method generates an initial signal enhancement factor on the order of ~150 compared to a thermal equilibrium reference ("ref", **d**), which decays exponentially with characteristic time T_1 (Figure ©2015 by the American Chemical Society, reprinted (adapted) with permission from Hirsch et al. [16])

polarisation transfer schemes have therefore been proposed to reduce the time taken for polarisation, by reducing T_1 only at low temperatures, and, due to the correlation time of the relaxation agent, not once a sample has been melted. At present, [1-^{13}C] pyruvic acid, sodium [1-^{13}C]lactate, and [1-^{13}C]acetic acid have been polarised by brute force methods, prior to rapid subsequent melting and introduction to a nearby MR system. The enhancement factor of the initial signal intensity compared to that expected at thermal equilibrium was reported to be approximately 1600 [16].

Figure 4.3 illustrates a cartoon design for the insert of a brute-force hyperpolariser, in which samples are contained in a polycarbonate "shuttle", pneumatically moved into place in a 14 T dilution refrigerator, before being left to polarise for

between 10 and 70 h. The thermal coupling of the sample to the cold region of the dilution refrigerator is a requirement for the efficient cooling of the sample, but an ingenious counter-current heat exchanger is required to prevent the introduction of heat necessarily used to remove the sample from quenching the superconducting magnet (Fig. 4.3a, b). The technique enhances M_0 by a factor of several hundred depending on the polarisation time; after removal from the polariser and subsequent melting its exponential return to the new thermal equilibrium with characteristic time T_1 can be observed (Fig. 4.3c, d).

Whilst the brute force approach is technically difficult, it has the advantage that, in principle, essentially *any* nuclear spin can be enhanced by it. The technique also potentially parallelises well, in the sense that large dilution refrigerators containing numerous samples at the bottom have been proposed. Such devices could produce a large number of hyperpolarised molecular probes without consumable costs beyond that of the probe itself.

Parahydrogen Induced Polarisation (PHIP)

Background

Parahydrogen induced polarisation is a novel way of exploiting the thermal behaviour of the two different nuclear spin isomers of molecular hydrogen to provide a supply of molecular hydrogen in a known spin configuration, again at low temperatures. This supply of hydrogen gas is then rapidly chemically bound onto a molecule of interest, and the polarisation transferred between the proton spins and, owing to their longer T_1, that of a nucleus of interest (typically ^{13}C). The technique is chemically somewhat versatile, and has the advantage that it is comparatively easy to prepare a large quantity of hydrogen in a known spin configuration which can then be stored for a long period of time.

Diatomic molecular hydrogen, H_2, possesses two spin isomeric states, known as orthohydrogen and parahydrogen. This experimental fact arises from the singlet triplet splitting of energy levels of a hydrogen molecule, which itself is a consequence of a fundamental physical theorem, known as the spin statistics theorem [2]. Briefly, the proton is a spin-half particle, and therefore must have a wavefunction that is anti-symmetric under exchange of labels. Applying the rules for the addition of spin, the resulting molecule can therefore be spin 1 or 0 overall, corresponding to the symmetric or antisymmetric alignment of proton spins respectively. This is of significance when the overall wavefunction for the molecule is considered, as a factored product of vibrational, rotational, and spin components, i.e. $\psi_{\text{total}} = \psi_{\text{Vib.}}\psi_{\text{Rot.}}\psi_{\text{Spin}}$. It can be shown [17] that the vibrational component is always symmetric under exchange, reflecting the linear-diatomic nature of hydrogen. Allowing for the two possible cases of the spin wavefunction, and noting that the overall wavefunction is required to be antisymmetric under exchange, there are two resulting possible combinations of all parts:

$$\psi_{\text{Total, antisymmetric}} = \psi_{\text{Vib., symmetric}}\psi_{\text{Rot., symmetric}}\psi_{\text{Spin, antisymmetric}} \tag{4.5}$$

$$\psi_{\text{Total, antisymmetric}} = \psi_{\text{Vib., symmetric}}\psi_{\text{Rot., antisymmetric}}\psi_{\text{Spin, symmetric}}. \tag{4.6}$$

Further microscopic considerations lead to the realisation that these two forms correspond to even (Eq. (4.5)) and odd (Eq. (4.6)) numbered energy levels in their rotational wavefunction, and additionally have a different number of degenerate nuclear spin substates, corresponding to the "orientation" (spin eigenvalues) of the individual protons in the diatomic molecule. For Eq. (4.6), there are three possible combinations of individual spin wavefunctions that are symmetric under exchange of labels, all corresponding to a net $I = 1$ state: (a), the parallel state $|\uparrow\uparrow\rangle$, (b) the anti-parallel state $|\downarrow\downarrow\rangle$ and (c), the superposition $\frac{1}{\sqrt{2}}(|\downarrow\uparrow\rangle + |\uparrow\downarrow\rangle)$, where $|\uparrow\uparrow\rangle$ denotes the state of both atoms in the molecule having the same spin state. This spin configuration is called **orthohydrogen**[1] and, owing to the three different possible combinations involved in producing it, is known as the triplet state. Likewise, the requirement for the spin wavefunction for the overall hydrogen molecule in Eq. (4.5) to be antisymmetric under exchange ensures that it must be given by the combination $\frac{1}{\sqrt{2}}(|\downarrow\uparrow\rangle - |\downarrow\uparrow\rangle)$, with $I = 0$ [18]. As a result, Eq. (4.5) is referred to as **parahydrogen**.[2]

At high temperatures, the thermal energy is large enough to populate all available substates, and the distribution over nuclear spin states is such that approximately 75% of room-temperature hydrogen gas is orthohydrogen, and 25% parahydrogen, reflecting the 3:1 degeneracy discussed above. However, the lowest parahydrogen level is lower than the lowest orthohydrogen one, and is therefore favoured as $T \to 0$. As the temperature of the gas is decreased, conversion between the 3:1 high-energy equilibrium states and a pure parahydrogen state is relatively slow in the absence of catalysts or other mechanisms due to the fact that, although it is thermodynamically favoured, the conversion is first-order forbidden by symmetry considerations. Therefore, a weakly paramagnetic catalyst is required, such as activated charcoal or iron oxide, and commercial gas handling systems exist to cool hydrogen to 20 K (where, thermodynamically, it is expected to be 99.98% parahydrogen), pass it over an ortho-parahydrogen catalyst, and then store it prior to subsequent use. Advantageously, the fact that the ortho-para reaction occurs at a slow rate, even if it is thermodynamically favoured, enables the gas to be stored at higher temperatures; its half-life at room temperature is several hours.

[1] This name has little to do with hydrogen itself. One explanation for it is that, if one imagines arrows drawn on a piece of paper to represent nuclear spins operators, then "ortho" -hydrogen consists of the states where most of the arrows would be parallel, and hence the use of *óρθ o*–denotes them as "upright".

[2] Similarly, another "folk etymology" that is commonly shared is that the anti-parallel nature of parahydrogen is that the opposing arrows commonly used to denote its spins are *παρα*–denoting their opposing orientation.

Exploitation

After production of a pure (or nearly pure) supply of hydrogengas in the parahydrogen state, the next step towards the use of the technique for signal enhancement is the rapid chemical hydrogenation of a molecule of interest with parahydrogen. Such reactions are not necessarily straightforward to design; thermodynamic considerations ensure that it is desirable to keep the hydrogenation reaction as cool as possible to preserve the prepared spin state of the para-hydrogen gas,although typical industrial schemes operate at ~ 450 °C [19]. However, owing to the short nuclear T_1 of the majority of protons in small molecules, it is desirable to transfer the enhanced polarisation that the parahydrogen technique generates to nearby nuclei, typically carbonyl ones. There are a number of NMR schemes that are able to do this effectively: **P**arahydrogen **A**nd **S**ynthesis **A**llow **D**ramatically **E**nhanced **N**uclear **A**lignment (PASADENA) was the first, in which the parahy-drogen was originally introduced directly to the sample (and spontaneous hydrogenation occurred) within the detection spectrometer itself; weak nuclear contact between the protons and ^{13}C nuclei nearby served to provide polarisation transfer mechanisms, in a fashion that is highly dependent on the magnetic field in which the reaction occurs. ALTADENA, **A**diabatic **L**ongitudinal **T**ransport **A**fter **D**issociation **E**ngenders **N**et **A**lignment, represents a complimentary technique that exploits mechanistically different pathways by performing the hydrogenation reaction *outside* the main magnetic field, in a low (but necessarily non-zero) magnetic field [20, 21]. Likewise, more advanced field-cycling and direct polarisation transfer NMR schemes have been proposed to take advantage of the prepared para-hydrogen spin structure and transform it into usable net magnetisation on a labelled carbonyl group; of these approaches, Parahydrogen-INEPT sequences (which transfer magnetisation with a modified INEPT pulse sequence) and **S**ignal **A**mplification **B**y **R**eversible **E**xchange (SABRE), in which a transient interaction with a metal ion catalyst are exploited are probably the best well known [22–24]. Therefore, the overall process for most biological PHIP experiments schematically proceeds as illustrated in Fig. 4.4. Parahydrogen is produced, rapidly chemically attached to a probe of interest, subject to a polarisation transfer scheme, and the resulting hyperpolarised molecule is then injected into the system under study.

In terms of biological application, this requirement for in-situ or nearly in-situ hydrogenation marks a substantial limitation, although several ingenious schemes have been devised to work around it, such as the production of hyperpolarised succinate, with reported polarisation levels on the order of 15% to 20% by PASADENA (c.f. Fig. 4.5), and the *in vivo* detection of downstream metabolic products following its intravenous (IV) injection into a mouse [26]. Likewise, the ability (and requirement) to flexibly exploit novel chemical synthesis has led to unexpected novel probes, such as the use of PHIP-polarised maleic acid dimethyl ester as an angiographic contrast agent that can be used with sub-second temporal resolution and no signal background [27]; or the reported production of a highly lipophilic compound (tetrafluropropyl [1-^{13}C]propionate-D3) that effectively binds to lipid bilayers and is of interest as a future probe of arterial disease and atheromatous plaque [28]. In contrast to the single-shot nature of the brute force method, parahydrogen can be

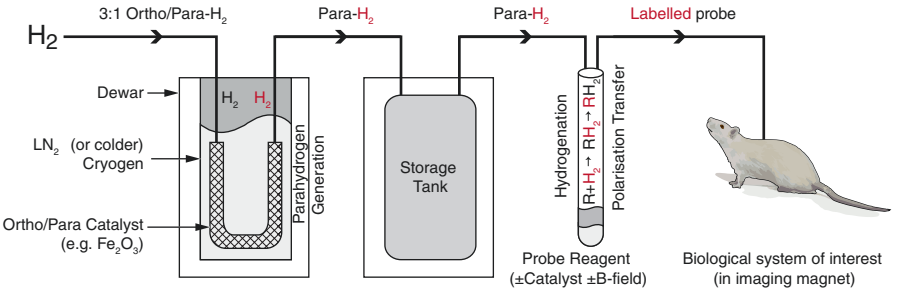

Fig. 4.4 A schematic overview for the process of using parahydrogen induced polarisation to probe living systems. A 50% pure parahydrogen state can be readily produced by bubbling H_2 gas over a charcoal catalyst at 77 K (the boiling point of liquid nitrogen, LN_2). This increases to 99.98% by ~20 K. In a suitably controlled environment, this spin structure (denoted *red*) is very long lived: it is possible to generate parahydrogen at low temperatures and keep it in a storage tank for an appreciable period of time. It is then necessary to chemically react the generated hydrogen with the probe of choice, and then rapidly use a polarisation transfer scheme, such as PASADENA, ALTADENA, or SABRE (discussed in the body of the text) to exploit the longer T_1 of most ^{13}C nuclei compared to ^{1}H, which may involve the use of a catalyst. After preparation, the probe can be injected into the biological system of interest, located in a nearby magnetic resonance system

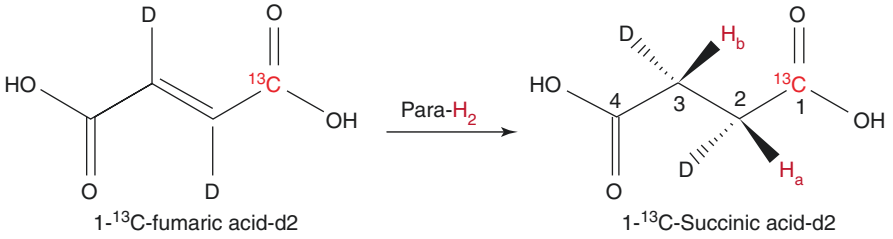

Fig. 4.5 Parahydrogen and PASADENA production of hyperpolarised [1-^{13}C]succinic acid-D2, showing the hydrogenation route for polarisation transfer to the pre-existing ^{13}C label, with a reported liquid-state succinate polarisation level on the order of 15–20% (Figure ©2008 American Chemical Society, reprinted (adapted) with permission [25])

produced continuously, and is therefore more amenable to more traditional MR pulse sequence paradigms, where acquisitions can be repeated during a continuous infusion of the hyperpolarised contrast agent. However, it is worth noting that, as of 2015, no identifiable "key application" has been found for parahydrogen produced probes in a cardiac imaging context, although this remains an active area of research.

Dissolution Dynamic Nuclear Polarisation

Dynamic Nuclear Polarisation (DNP) represents an ingenious method for the direct spin-pumping of nuclei of interest into a given state, under cryogenic conditions in a strong magnetic field. In contrast to the optical pumping of spin isomers of

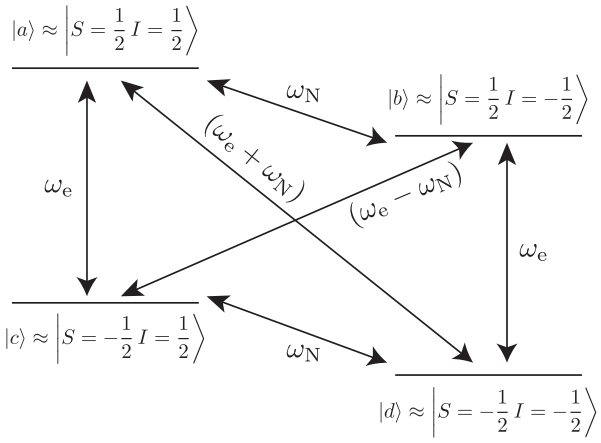

Fig. 4.6 Energy levels and possible transitions in an isolated spin-½ electron-nucleon system. The four states $|a\rangle$ to $|d\rangle$ are approximately pure spin-states, weakly mixed by the dipolar interaction. Hence, the 'forbidden' transitions at $\omega_{\mathrm{e}} \pm \omega_{\mathrm{N}}$ can occur

hydrogen above, DNP occurs when a source of free electrons (chemically provided by a stable electronic free radical, typically trityl or nitroxide) is introduced to the sample of interest, and irradiated close to its Larmor frequency, which typically is at microwave frequencies. Under the conditions commonly experimentally chosen, B (3.35 T or higher) and T (typically ~ 1 K, i.e. the lowest temperature that can be obtained by vacuum pumping liquid helium without isotopic enrichment) are such that the vast majority of the $S = \frac{1}{2}$ electrons are thermally expected to be in their ground state. Even at ~ 1 K, the distribution over nuclear spins is still thermally approximately 50/50, although the nuclear T_1 is very long. To ensure that the electrons are thermally in the ground state, the electronic T_1, denoted T_{1e}, is required to be "sufficiently short" compared to the lifetime of the thermal introduction of the sample to the cryostat, and relaxation agents such as gadolinium are typically added in small quantities before the mixture is frozen to ensure that this is the case. Irradiation with microwaves close to the Larmor frequency of the electron can cause two main classes of microscopic processes to occur: (1) it can directly elicit zero- or double-quantum transitions between the weakly interacting electronic and nuclear spins through a mechanism referred to as the solid effect (shown in Fig. 4.6), and (2) it can pump electrons into their excited state, effectively inverting the electronic spin population and creating an 'electronic bath' with a negative spin temperature[3]. Such systems are thermodynamically driven to relax, and the weak coupling of the electronic spin system to that of the nuclei produces the net effect of a cooling of the nuclei, and hence increasing their P. This contact occurs through

[3] Spin temperature is the concept that the Boltzmann equation is sufficient to provide an effective *definition* of temperature given a particular P. Such definitions are common in low temperature systems when quantum effects dominate and the thermal motion of the system is small in absolute terms.

a variety of microscopic mechanisms, and the net process is collectively referred to as thermal mixing.

The Solid Effect: A Detailed Picture

The Solid Effect refers to a precise mechanism of DNP that occurs solely due to the electrodynamic interaction between anucleus and free electron, which are treated as being isolated from other spin species. As such, it is analytically very tractable in the Schrödinger equation formulation of quantum mechanics, as it is possible to write down appropriate Hamiltonians describing the interaction of the two spins with both each other and the magnetic field, and hence obtain quantitative predictions for their dynamics [29]. Such predictions match well with experiments in 'uncomplicated' systems, such as lithium salts at low temperature, but do not explain the complete dynamics of the behaviour of the spin systems commonly used in biological research. A brief description of the physical basis of the solid effect is below, which can safely be skipped by those not interested in quantum mechanics.

Consider the two-spin (*IS*) system described above in the experimentally feasible regions of B and T where the majority of electronic spins will sit in the ground state, that is $P_e \approx 1$, and there is still no great nuclear polarisation, so that $P_N \approx 0$ (this occurs at e.g. $B = 3$ T, $T = 1$ K). The comparatively weak electromagnetic dipolar interaction permits two-quantum or zero-quantum transitions between nuclear and electronic spin states, in addition to optical transitions within the nuclear or electronic spin structures. As shown in Fig. 4.6, there are hence four permissible transitions: first-order optical transitions between the spin states of the nucleus and electron occurring separately, with energy $\hbar\omega_e$ and $\hbar\omega_N$, and two-quantum dipolar interactions at $\hbar(\omega_e - \omega_N)$ and $\hbar(\omega_e + \omega_N)$. These transitions can occur because the dipolar interaction mixes the states of S and I into states which are not pure eigenstates of S and I. Specifically, it can be shown that the canonical dipolar interaction between spins i and j a distance r_{ij} apart

$$\mathcal{H}_D = \frac{1}{2}\sum_{i,j}\frac{\gamma_i\gamma_j\hbar}{r_{ij}^3}\left(\mathbf{I}_i\cdot\mathbf{I}_j - 3\right)\left(\mathbf{I}_i\cdot\hat{\mathbf{r}}_{ij}\right)\left(\mathbf{I}_i\cdot\hat{\mathbf{r}}_{ij}\right) \tag{4.7}$$

mixes the four pure states $|a_0\rangle = |S = \tfrac{1}{2}\ I = \tfrac{1}{2}\rangle \equiv |{+}{+}\rangle$, $|b_0\rangle = |{+}{-}\rangle$, $|c_0\rangle = |{-}{+}\rangle$ and $|d_0\rangle = |{-}{-}\rangle$ into the superpositions.

$$\begin{aligned}
|a\rangle &= p|a_0\rangle - q^*|b_0\rangle \\
|b\rangle &= p|b_0\rangle + q|a_0\rangle \\
|c\rangle &= p|c_0\rangle + q^*|d_0\rangle \\
|d\rangle &= p|d_0\rangle - q|c_0\rangle.
\end{aligned} \tag{4.8}$$

The superposition coefficients p and q can be approximated analytically through first-order perturbation theory, and it is found that $p \approx 1$, $q \ll 1$ [29]. By considering transitions between these states and sources of relaxation (i.e. transitions towards thermal equilibrium) in an isolated electron-nucleus pair, it is possible to derive rate equations for the system as a whole, when irradiated with microwaves at $\omega_e - \omega_N$.

Additionally, the characteristic time for relaxation, T_1, can be estimated as a function of temperature, magnetic field strength, and polarisation. Analytic expressions for the resulting maximum nuclear polarisation (known as the "maximum solid state enhancement") can subsequently be derived, and this enhancement is found to scale approximately linearly with temperature, decreasing as T increases.

If the nuclear-electronic system is found in a glass, promoted electronic spins are typically able to relax quickly ($T_{1e} \approx 10^{-3}$ s), whereas nuclear spins at low temperature have a longer spin-lattice relaxation time (T_{1N}) on the order of hours; the presence of a well-defined crystal structure for the nuclei in bulk can serve to reduce T_{1N} dramatically. Under these circumstances, an appreciable fraction of nuclear spins can be pumped into one of the two eigenstates by irradiation at $\omega_e \pm \omega_N$. The process is analogous to a three-state laser: irradiation at $\omega_e - \omega_N$, for example, will flip promote transitions between the $|c\rangle$ state and the $|b\rangle$ state. As the electronic T_1 is short, this quickly decays to the state $|d\rangle$, emitting a photon of frequency ω_e. An analogous process occurs for irradiation at $\omega_e + \omega_N$, pumping into the state $|c\rangle$ from $|d\rangle$.

Provided that the electronic linewidth is small in comparison to the nuclear frequency (ω_N), irradiation at $\omega_e + \omega_N$ can only promote one transition, as the other is off-resonance with the driving frequency. This situation is known as the 'well-resolved solid effect', and usually requires considerable microwave power (on the order of Watts) due to the two-quantum transition. The NMR peak amplitude as a function of irradiation frequency, known as a 'microwave sweep', is predicted to be symmetric for a purely solid effect process, and have two Lorentzian peaks [29, 30].

Thermal Mixing

Most real materials feature an ensemble of electronic spins in different environments, broadening the effective electronic and nuclear linewidths. In most cases, the electronic linewidth is not small in comparison to ω_N, and the concentration of electrons is such that spins can interact with each other. This leads to a second, complementary mechanism through which DNP can occur. Essentially, in a complex system numerous nuclear processes serve to mix the spin populations, and this mixing occurs primarily due to thermodynamic considerations. It is therefore known as thermal mixing. Owing to the fact that an inverted electronic spin population is produced by irradiation with microwaves, the system has a negative spin temperature and therefore is driven to cool. This cooling is realised by the pumping of nuclear spins into an unfavourable entropic configuration, resulting in enhancement

and increasing P_N. As the first of these steps ('dynamic cooling') involves a single quantum transition this effect usually dominates if it can occur [30].

Consider irradiating a sample in a magnetic field with photons close to, but distinct from, the electronic Larmor frequency, at a frequency ω, where $\Delta \equiv \omega - \omega_e$ is small. It can be shown that the effective Zeeman Hamiltonian in this situation is time-independent in a frame of reference that is rotating at the frequency of the applied irradiation. This implies that the system can be characterised in this frame, and that the concept of a 'spin temperature' in a frame of reference rotating at ω, T_R is well defined. Due to the broad electronic linewidth, it is possible to change the energy of the system by an amount $\hbar\,\Delta$, flipping a spin in a particular environment. So, if $\Delta < 0$, then such a decrease of the electron spin system's energy leads to a lowering of the system's temperature. If $\Delta > 0$, then T_R can become negative, as the spin population inverts. Sources of relaxation between the electronic spin system and the lattice couple the lattice temperature and T_R, leading to the relation

$$T_R = \frac{\Delta^2 + aD^2}{\omega_e \Delta} T \tag{4.9}$$

where T is the temperature of the lattice (i.e. cryostat), a is a model-dependent parameter on the order of 2, and D the dipolar second moment of the electronic linewidth [29].

The second step, 'thermal mixing in the strict sense', is the coupling of this electronic spin temperature to the nuclei of interest in the laboratory frame of reference.

This is a thermodynamically favoured relaxation process involving the simultaneous transition of two electron spins and one nuclear spin ($\delta m_{S1} = \pm 1$, $\delta m_{S2} = \mp 1$, $\delta m_I = \mp 1$), which proceeds through the Hartmann-Hahn mechanism, which requires a broad electronic linewidth so that the difference in energy between the two electrons from the distribution is equal to $\hbar\,\omega_N$. Such transitions can only occur if there is a mutual interaction between electron spins, and between an electron spin and a nuclear spin. The rate of this transition therefore increases with electron concentration. From thermodynamic considerations, one can see that this step will equalise the spin temperatures of the polarised nuclei and the electron system [30–33].

Recent progress in understanding thermal mixing has been made by assuming that only the five nuclear processes shown in Fig. 4.7 contribute to the process [34, 35]. Briefly, these are electronic spin pumping due to the applied microwave irradiation (**A**) with a rate $1/T_{1\mathrm{MW}}$; spectral diffusion between neighbouring electrons at a rate $1/T_{1e}$ (**B**); the Hartmann-Hahn ISS process (**C** with rate $1/T_{\mathrm{ISS}}$), and longitudinal relaxation for both nuclei and electrons (**D** and **E**, relaxing at a rate $1/T_1$). Each of these rate constants can be measured or approximated analytically, and the rate equations for the system are first order in these processes, conserving spin and energy. As reported by Serra et al. [34, 35], derived quantities from these equations match experimental values. However, it might be argued that this approach does not fundamentally improve understanding, as calculating rate

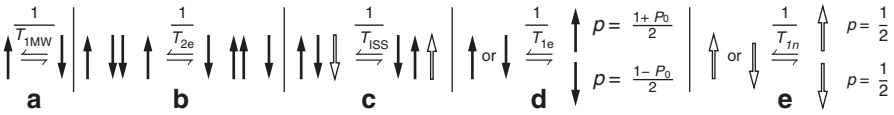

Fig. 4.7 The five electronic (*black arrow*) and nuclear (*white arrow*) processes that predominantly contribute to thermal mixing. (**a**): Electronic spin pumping due to microwave irradiation; (**b**): Spectral diffusion between electrons through the glass; (**c**): the Hartmann-Hahn *ISS* process; (**d**, **e**): Electronic and nuclear relaxation processes back towards thermal equilibrium. It is assumed that, at the temperature considered, the nuclear thermal equilibrium polarisation is still very close to zero, but that of the electrons is not; here it is denoted P_0

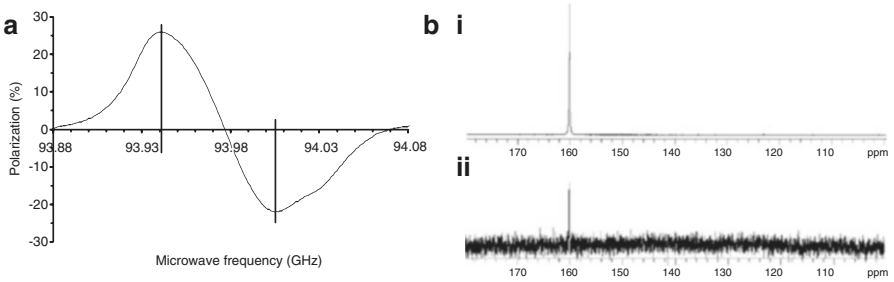

Fig. 4.8 (**a**) A 'microwave sweep', obtained by recording the solid-state (i.e. ~ 1 K) NMR amplitude of the labelled probe of interest whilst iterating over microwave irradiation frequencies. The vertical lines denote the maximum enhancement, obtained by irradiation with a relatively narrowband microwave source at $\omega_e \pm \omega_N$ respectively. (**bi**, **ii**) After dissolution, the corresponding liquid state NMR amplitude (a single shot pulse and acquire ^{13}C-urea spectrum of hyperpolarised urea is shown in i) is enhanced by several orders of magnitude compared to the thermal equilibrium signal (**ii**, 232,128 averages) (Figure ©2003 National Academy of Sciences, reprinted with permission [36])

constants *a priori* is not straightforward, and depends on parameters such as the exact geometry of the experimental apparatus and its dielectric properties. This approach is therefore likely to be most profitable if it is at least quasi-phenomenological, using experimentally determined rate constants to identify experimental regions where the maximal enhancement given by an experiment is higher.

In practice, thermal mixing remains a difficult example of mesoscopic physics, in which thermodynamic considerations drive a large disordered ensemble through a variety of processes. It manifests itself experimentally in two main ways; (1) the power required to provide enhancement is dramatically reduced compared to the solid effect, as the overall process is thermodynamically favoured, and (2) the microwave sweep lineshape – the enhancement as a function of irradiation – is not symmetrical. Experimentally, most labelled biological molecules are found to be polarised predominantly by thermal mixing under conditions commonly used. Figure 4.8a illustrates both the microwave irradiation frequency corresponding to $\omega_e \pm \omega_N$ (solid vertical lines), and also the corresponding asymmetric lineshape found on the microwave sweep that indicates thermal mixing is occurring. Maximum

enhancement is also found to be reached with irradiation powers on the order of ~100 mW, rather than the ~W required for the well-resolved solid effect [30].

Dissolution DNP

DNP, mechanistically occurring primarily through the solid effect, was historically extensively investigated by Abgragam and others for the purpose of creating solid, spin-polarised lithium targets for use in particle physics at cryogenic temperatures [29, 37]. Its application to living systems came with the landmark realisation, by Ardenkjaer-Larssen and others [36], that a solid sample could be hyperpolarised by DNP and then rapidly melted by the introduction of a hot neutralising solvent at ~ 450 K and 10 bar onto the ~ 1 K frozen sample. After melting, the resulting hyperpolarised liquid could then be introduced into a nearby MR system for subsequent NMR or MRI experiments with a greatly enhanced M_0. Dissolution-DNP (d-DNP) is highly efficacious; reported values for P in the liquid state range from ~ 20–40%, corresponding to at $>10^4$-fold increase in the singal-to-noise ratio compared to thermal equilibrium (c.f. Fig. 4.8 bi vs bii). This enhancement is far larger than that reported by the brute-force or parahydrogen methods, and has lead to dissolution-DNP being the "gold standard" for NMR signal enhancement.

Practically, a dissolution-DNP hyperpolariser needs several key components: a strong, low-T, high B superconducting cryostat, containing a variable temperature, variable pressure cavity into which the sample of interest can be placed. The cavity needs to either contain a microwave source, or, more likely, be resonant in the GHz region and possess a waveguide to an external, tuneable microwave source. In order to simultaneously measure polarisation, an RF resonant cavity at the frequency of interest (for a given molecular probe at B) has to be present. The frozen, polarising sample additionally has to be relatively accessible so that the media into which it is rapidly dissolved can be introduced at high temperature, under pressure, and quickly. This leads to a 'canonical' design similar to that sketched in Fig. 4.9, in which a variable temperature insert (VTI) is coupled to the helium cryostat that is required for the superconducting B field. Owing to the limited availability of high power tuneable microwave sources, there are a few regions of "acceptable" B, of which 3.35 T with W-band microwaves in the ~94 GHz range are undoubtedly the most common, in part due to the manufacturing of a commercial instrument – known as the Hypersense Hyperpolariser – by GE Healthcare and Oxford Instruments. Other reported instruments include a 9.24 T system coupled to a gyrotron [38], and commercially available systems aimed at the solid state DNP-NMR market (in which the enhancement is "used" *in situ*) manufactured by Bruker.

A relatively recent development is the creation of a "white box" DNP hyperpolariser, intended to produce sterile samples for human use, by GE Healthcare [39]. This "clinical hyperpolariser" differs from others by isolating the sample from the

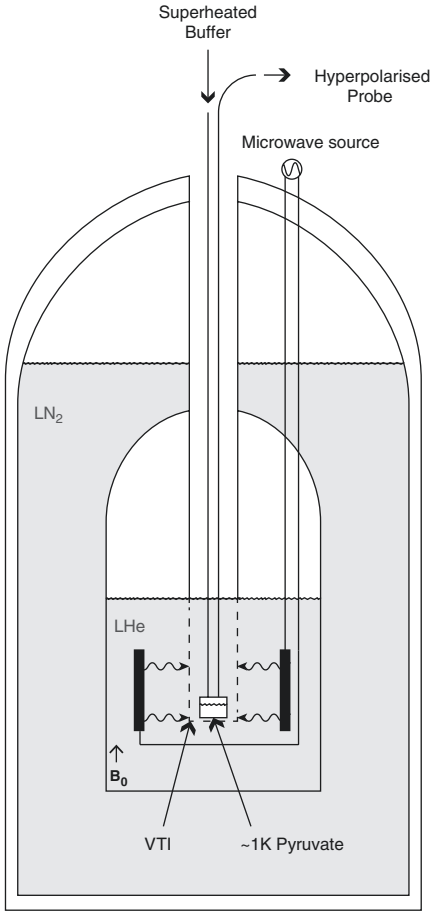

Fig. 4.9 A cartoon schematic of a dissolution-DNP polariser. A superconducting cryostat is fitted with a variable temperature insert (VTI) containing RF and microwave resonant cavities, in which sits a sample chamber that can be flooded with liquid helium under reduced pressure (typically ~ < 1 mbar) in the presence of a superconducting magnetic field. After enhancement has been generated, superheated buffer is dumped onto the solid sample and a hyperpolarised liquid with non-equilibrium M_0 is generated and expelled through a coaxial tube

helium bath through a disposable plastic fluid path, featuring closed-cycle cryogenic handling, and additionally providing up to four simultaneous 'channels' for multi-sample polarisation at the same time.

In order to effectively use dissolution DNP with a particular labelled molecule as an effective probe of *in vivo* biochemistry, a number of conditions must be met:

- The novel probe must chemically form a solution with the electronic free radical of choice that can be rapidly frozen without forming a well-defined crystal structure, i.e. as a glass. Glassing is required both to promote an efficient homogeneous and close distribution of radical and sample, ensuring an efficient interaction and transfer of polarisation between the two [40], and under circumstances to prevent lattice phonon based relaxation pathways from

reducing the nuclear T_1 dramatically under certain regions of B and T [40]. Typically, if an agent of interest does not self-glass, or is immiscible with the radical of choice, a solvent glassing agent such as DMSO or glycerol is added; or, alternatively, by ultra-rapid freezing [41]. On a related note, the probe must be soluble enough in a non-toxic dissolution media to permit rapid subsequent infusion.

- Most crucially, the nuclear T_1 for the molecule of interest has to be long enough to conceivably allow the dissolution and injection process (which takes approximately 30 s to 60 s) to complete within at least $3T_1$, ideally far less. Likewise, the biological process of interest has to occur on a timescale at least comparable to T_1, although it is worth noting that this does not have not have to be the case physiologically – hyperpolarised [1,4-^{13}C]fumarate forms an effective marker of cellular necrosis precisely *because* uptake into the cell is sufficiently slow compared to its T_1 that no subsequent malate production is observed unless the cell wall is ruptured [42]. This T_1 requirement places an ultimate limit on the timescale of all hyperpolarised experiments (include those with polarisation enhancement via a mechanism other than DNP); after ~ $5T_1$ have passed, the experiment *is* effectively complete, independent of the desires (or otherwise) of the researchers. Proponents of the technique see this as a statement of its inherent rapidity; its detractors likewise.
- Owing to the short T_1 and the fact that hyperpolarised magnetisation decays, rather than recovers, with time, it is usually desirable to limit the number of RF excitations and perform rapid imaging techniques. A long molecular T_2 is hence desirable.
- Finally, it must be the case that the environment for dissolution-DNP experiments is carefully controlled. Large, high-field NMR/MR systems have non-trivial siting requirements, and introducing another superconducting high field hyperpolariser nearby can produce regions in space between the two polarisers where $B = 0$ exactly. These field nulls are anathema to hyperpolarised experiments: taking a hyperpolarised sample through one (and out the other side to another superconducting MR system) restores the degeneracy between nuclear spin states, and instantaneously produces a sample with thermal equilibrium polarisation on the other side. Likewise, T_1 is a strong function of magnetic field; whilst, typically speaking, it decreases as B grows certain other relaxation pathways (such as by scalar coupling) can dominate at very low field. It is therefore ultimately desirable to know, and ideally control, the magnetic environment between polariser and imaging magnet. This has lead to the development of hand-held electromagnetic carriers for hyperpolarised samples between hyperpolariser and imaging system [43], as well as magnetic tunnels sheltering hyperpolarised liquids being transported pneumatically at high speed between the two systems [44].

The Molecular Menagerie of Hyperpolarised Probes

The purpose of all three of the above methods is to generate a large increase in M_0 in a labelled nucleus within a molecule of interest that ultimately is produced in the liquid state, and is suitable for rapid introduction to a living system. Given the differing mechanisms by which the techniques work, and variations to a greater or lesser extent in their widespread availability, there has been a comparatively large investigation by the community of a number of both nuclei and molecular probes. These broadly fall into two categories: metabolic probes, which are actively metabolised during the lifetime of the hyperpolarised experiment, at a rate that is usually reported to be altered in a relevant disease state; and perfusion agents, which are able to assess perfusion within the vasculature or capillary bed, either providing a quantitative measure of tissue perfusion (in ml min^{-1} g^{-1} [45]),or a semi-quantitative relative score. In comparison to relaxation agent based approaches or angiography, hyperpolarisation provides the promise of accurate vascular imaging with no signal background, a potentially linear relationship between signal intensity and M_0 of the injected agent (and hence its concentration), and no dose of ionising radiation. Likewise, metabolic imaging approaches using hyperpolarised agents are potentially revolutionary: by increasing M_0 by several orders of magnitude, they permit the *in vivo* observation of small molecules at physiological concentrations that are of key interest in disease.

Pyruvate and Metabolic Imaging Agents

[1-^{13}C]Pyruvate

Undoubtedly the 'superstar' molecule to be hyperpolarised and used as a subsequent probe of biological systems is the TCA cycle metabolite, pyruvate, labelled at the first position. Since the realisation in 2006 by Golman et al. that the dissolution DNP technique enabled the *in vivo* detection of pyruvate and its metabolic products [46], hyperpolarised [1-^{13}C]pyruvate has been shown to be of utility both in the diagnosis and management of numerous diseased states and for quantifying the fundamental biology of numerous organs. Arguably, it is for this reason that both parahydrogen and 'brute force' methods have been reported to generate hyperpolarised [1-^{13}C] pyruvate [16, 47]; though it should be mentioned that neither have, as yet, matched the enhancement factors that d-DNP provides (which is on the order of ~ 40%).

There are several reasons why pyruvate is an appealing target for hyperpolarisation techniques. Labelled in the first position, its ^{13}C T_1 is long, approximately 60 s in water; it is readily soluble, and, with an LD50 of approximately 5.6 g kg^{-1}, essentially

non toxic. However, it is the obvious biological importance of pyruvate that has lead to its use as a novel hyperpolarised contrast agent: is a small molecule that is metabolically key. Pyruvate is a highly connected node in the metabolic network, and correspondingly has multiple metabolic fates: it can be reduced in the cytosol by lactate dehydrogenase (LDH) to form lactate; irreversibly decarboxylated with coenzyme A in the pyruvate dehydrogenase complex (PDH) to produce acetyl-CoA; carboxylated by pyruvate carboxylase to form oxaloacetate; or transaminated by alanine transaminase to synthesise alanine [48, Ch. 2]. Under physiological conditions, pyruvate, whose $pK_a = 2.39$, is almost entirely dissociated into its anionic (charged) form. Accordingly, the diffusion of the molecule through lipid bilayers is not possible and it is instead actively transported by members of the monocarboxylate transporter (MCT) family of integral membrane proteins into the cell. Under physiological conditions, the majority of pyruvate used by the cell is generated endogenously from glucose by glycolysis, and from the oxidation of lactate. Under aerobic conditions, pyruvate and its flux through PDH act as the entry point for carbohydrate metabolism into the TCA cycle, which then oxidises the carbon transferred. Reflecting its role as a gateway to the TCA cycle, PDH is spatially localised to the inner mitochondrial membrane, and pyruvate is actively transported across the outer mitochondrial membrane by a family of transporters, the mitochondrial pyruvate carriers (MPCs). Carbon dioxide is cleaved from pyruvate by PDH, and is in rapid equilibrium with bicarbonate (HCO_3^-), catalysed by carbonic anhydrases in the cytosol. In the presence of fatty acid oxidation, also known as β-oxidation, acetyl-CoA is produced independently of pyruvate, and PDH flux is inhibited accordingly. The kinase pyruvate dehydrogenase kinase (PDK) also serves to inhibit PDH flux, and is itself is highly regulated. For example, high concentrations of ADP and pyruvate inhibit PDK, increasing the flux through PDH. If sufficient oxygen is not available, pyruvate can undergo reduction in the cytosol by LDH, mediated by the relative concentrations in the cytosol of NADH and NAD^+. Pyruvate Carboxylase (PC) does not ordinarily significantly contribute to pyruvate metabolism in mammals as the reaction pyruvate → oxaloacetate is energetically disfavoured, requiring ATP. The reverse reaction, oxaloacetate → pyruvate, is one of the key gluconeogenic pathways that allow the synthesis of glucose from other precursors [49–51].

The use of hyperpolarised pyruvate allows for these reactions to be measured *in vivo*, as the downstream metabolic products of pyruvate can be followed by changes in chemical shift. If labelled in the first position, hyperpolarised [1-^{13}C] pyruvate forms an effective probe of metabolism, as the visible multiple fates of pyruvate report on the rate of β-oxidation, glycolysis, and amino acid synthesis in the cell.

Likewise, if [2-^{13}C]pyruvate (or [1,2-^{13}C]pyruvate) is used, the ^{13}C label is transferred onto acetyl-CoA, and enters into the TCA cycle proper [52]; the limiting polarisation reached by d-DNP for [2-^{13}C]pyruvate is lower than that of [1-^{13}C] pyruvate, at approximately 27%. This fact, combined with the finite time taken for the passage of the ^{13}C label through the TCA cycle, means that SNR limitations form the ultimate threshold of detection around the TCA cycle for [2-^{13}C]pyruvate; typically glutamate produced from α-ketoglutarate represents the most distal

reaction that can be resolved in the healthy or ischæmic heart, occurring five enzymatic reactions downstream from the injected probe.

An illustration of the labelled products visible with hyperpolarised [1-^{13}C]pyruvate is shown in Fig. 4.10; [2-^{13}C]pyruvate is the same, but for the evolution of labelled ^{13}C-carbon dioxide and hence bicarbonate, and with further visible, localised metabolites present within the mitochondrion. In either case, decreases in glycolysis consequently serve to reduce the visible flux to lactate. An increased rate of fatty acid β-oxidation serve to increase the concentration of acetyl-CoA entering the TCA cycle, inhibiting PDH and decreasing the visible flux of [1-^{13}C]pyruvate to ^{13}C-carbon dioxide and ^{13}C-bicarbonate. These fluxes, therefore, act as the (continuous) 'logical not' of fatty acid oxidation. Arguably the simplest, and historically the first, way of quantifying these fluxes following injection of a bolus of hyperpolarised [1-^{13}C]pyruvate is to perform spectroscopic acquisitions repeatedly over time at a low flip angle, obtaining a stack of spectra acquired over ~ 3 min lifetime of the experiment, as illustrated in Fig. 4.11a. Each individual resonance in the hyperpolarised [1-^{13}C]pyruvate spectrum can then be quantified, e.g. by spectral integration or algorithms such as AMARES [54], and kinetic curves of NMR amplitude over time

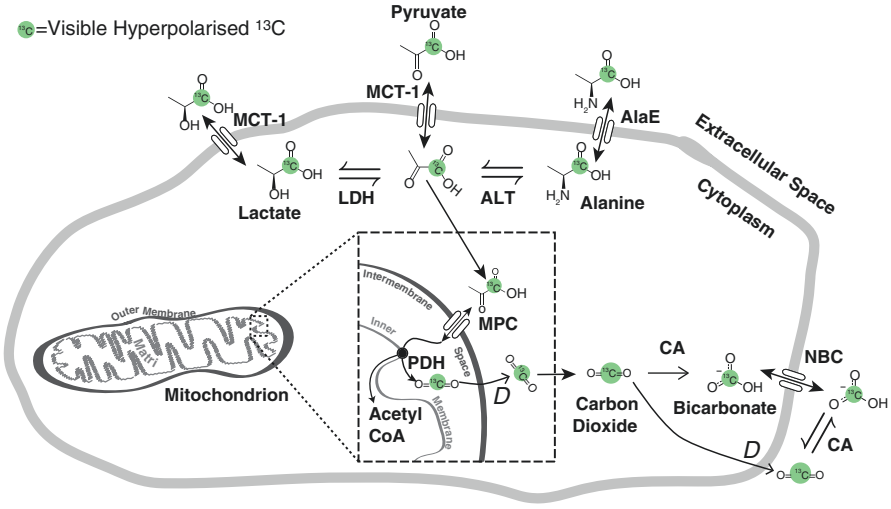

Fig. 4.10 A cartoon of the possible metabolic fates of hyperpolarised [1-^{13}C]pyruvate in the cell. Pyruvate enters the cell through the monocarboxylate transporter MCT-1 and can then either be transaminated to form alanine by ALT; removed from the cytosol by protein synthesis or by the alanine exporter AlaE; reduced by LDH to form lactate, which is then extracellularly exported by MCT-1; or transported to the intermembrane space in the mitochondrion by the mitochondrial pyruvate carrier (MPC) before being decarboxylated by PDH. The resulting labelled $^{13}CO_2$ is able to diffuse across lipid membranes before equilibrating with bicarbonate in the cytosol, catalysed by carbonic anhydrases (CA) prior to its export by the sodium bicarbonate carrier (NBC). As acid-base balance is vital to biological systems, most species also contain CAs in their circulatory systems (Figure ©2015 CC-NC-BY-SA, reprinted with permission [53])

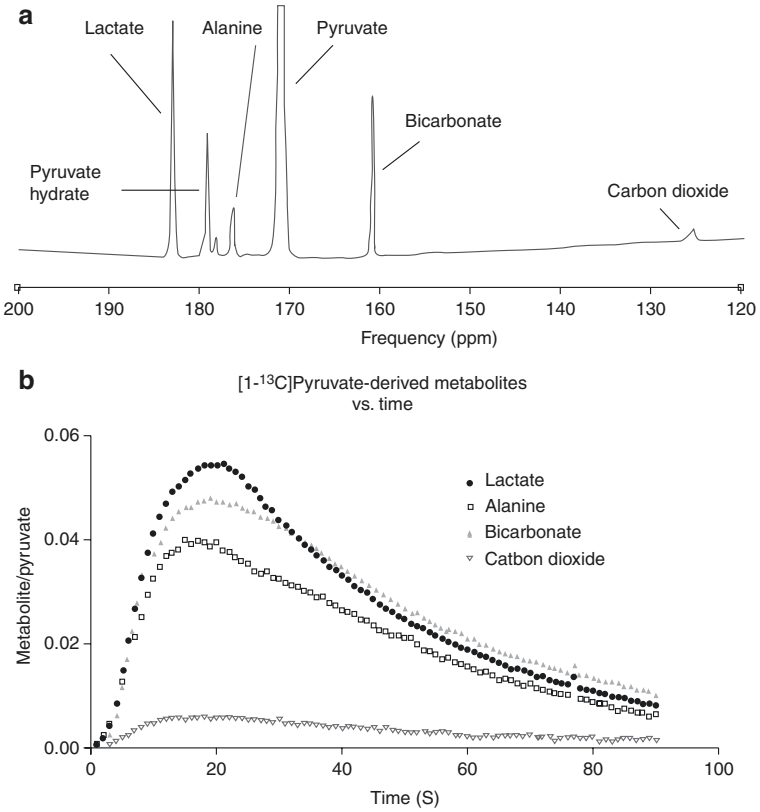

Fig. 4.11 (**a**) A representative example hyperpolarised [1-^{13}C]pyruvate spectrum, acquired during infusion of hyperpolarised [1-^{13}C]pyruvate into the perfused heart. The hyperpolarised [1-^{13}C] pyruvate signal is large, typically on the order of 10 − 100× that of the downstream visible products. The non-zero duration of the RF pulse used in observing this spectrum is responsible for the non-zero first order phase,visibleasa 'roll' in the baseline of the spectrum. (**b**) By estimating NMR peak amplitudes (here with the Amares algorithm [54] and jMRUI [55]), it is possible to obtain kinetic information about the metabolism of [1-^{13}C]pyruvate. Shown here is the metabolite-to-pyruvate ratio over time, with division by the pyruvate signal proposed as a normalisation accounting for the potentially variable initial pyruvate magnetisation and perfusion into the myocardium (Image ©2010 European Society of Cardiology, licensed CC-BY and adapted with permission [56])

obtained (Fig. 4.11b). Several models have been proposed for quantifying the resulting pseudo-pharmacokinetic dataset to obtain estimates of rate constants of interest such as $k_{\text{Pyruvate}\rightarrow\text{Lactate}}$; these range from piecewise linear integrated forms of first-order chemical kinetics [57] to simply computing the temporal integral of each metabolite, and comparing ratios. Unsurprisingly, the majority of proposed models return rate parameters that correlate highly with each other, reassuringly reflecting their common measurement of the underlying biochemical process [58, in review].

The Diseased Heart and Pyruvate Metabolism

Heart Failure

The failing heart, by definition, is unable to supply the body with sufficient blood to permit function with unaltered physiology [59]. Heart failure (HF) has several clinically distinct ætiologies that typically share either some degree of direct myocardial injury, or an increase in the expected myocardial workload. These causes can be abrupt and sudden, such as myocardial infarction or valve trauma, or gradual and progressive, such as systemic arterial pressure overloading due to hypertension or stenosis. Additionally, HF is an end-point of many diseases and disorders, ranging from the genetic to the parasitic (for example, the trypanosomiasis caused by the protozoan *Trypanosoma cruzi*, known as Chagas disease, is strongly associated with heart failure 10–30 years after infection [60, 61]). With a median survival time of 5 years, and limited options for clinical management, the prognosis for HF is poor [62]. Although traditionally HF was synonymous with a reduction in left ventricular ejection fraction, within the last two decades it has recently become increasing clear that diastolic, as well as systolic, dysfunction is readily associated with the disease. As a consequence, HF with preserved ejection fraction (HFpEF) has been identified as a distinct subpopulation of HF patients, which are demographically distinct [63]. HFpEF is associated with increased diastolic LV stiffness, and remains an area of active study [64].

It is now generally accepted that changes in myocardial metabolism are implicated in HF, although the nature of the metabolic alterations in question is contentious [65]. At the end stages of the disease, there is a profound shift towards increased glucose oxidation as opposed to fatty acid oxidation. Decreased fatty acid oxidation is present at both early and late stages of the disease, together with maladapted mitochondrial morphology, function and biogenesis, and an increase in anaplerotic reactions that channel carbon back towards the TCA cycle. These alterations are concomitant with a decrease in ATP availability in the failing heart, but the causal link between metabolic alteration and HF remains uncertain [66].

As the canonical feature of the failing heart is reduced contractile function, the traditional management of the disease consisted of pro-contractile (positively inotropic) drugs such as dobutamine that would increase the force of cardiac muscle contraction and, it was believed, increase ejection fraction. However, these drugs increase energy usage in the failing heart, which is now expected to worsen cardiac performance in the long term. They fail to have a long-term benefit in patients, but maintain a role in certain specific situations and during cardiac surgery [67]. Current chronic HF treatments focus on reducing the load on the cardiovascular system, either by surgically increasing the diameter of compromised blood vessels; by mechanically unloading the left ventricle of the heart; or by pharmacologically activating various aspects of the neurohormonal systems. Treatments such as beta-receptor blockade [68, 69], ACE inhibitors [70, 71] or angiotensin II blockers [72, 73] are energy-sparing, and may counter-intuitively improve the prognosis of HF by decreasing contractility. The efficacy of these compounds in current clinical

use motivates the development of novel pharmacoactive agents to directly target myocardial metabolism, and additionally hints at a causal link between metabolism and HF.

Fatty acid metabolism requires more oxygen per mole of ATP generated than glucose oxidation, and correspondingly results in an increase in lactate production in situations of reduced oxygen availability. As the leading causes (in the United States) of HF are believed to be vascular disease and myocardial infarction, some reduction in oxygen availability is at least transiently likely [62, 74]. Under these conditions, the continued production of lactic acid disrupts the acid-base balance of the cell and leads to tissue acidosis, which leads to a decrease in myocyte contractility [75, 76]. Accordingly, several partial inhibitors of fatty acid oxidation ("pFOX inhibitors") have been developed and show promise in ameliorating HF [77]. It is known that the agents etomoxir, oxfenicine and perhexiline are mitochondrial carnitine palmitoyl transferase I inhibitors, and therefore block mitochondrial fatty acid uptake and subsequent oxidation [78]. Unfortunately, etomoxir failed phase-II clinical trials due to excessive toxicity [79]; but clinical trials of oxfenicine [80] and perhexiline are ongoing [81, 82]. Other pFOX inhibitors have been developed, such as the piparazine derivatives trimetazidine and ranolazine, but a mechanistic understanding of their action is lacking as they were initially developed as anti-anginal agents. As others have commented [83], the successful management of HF by decreasing fatty acid utilisation is counter-intuitive, as end-stage HF is associated with a profound decrease in fatty acid oxidation.

Myocardial Ischæmia, Infarction, and Metabolic Remodelling

Ischæmia is defined as the pathological reduction of blood flow to tissue [84], and is a condition in which the metabolism of pyruvate is altered. In the heart, myocardial is chæmia commonly originates from an occlusion in the coronary arteries, and the resulting hypoxic state rapidly causes a switch towards anaerobic glycolysis to maintain ATP synthesis [85]. This is associated with a subsequent increase in the rate of glycogen breakdown and glucose uptake [86]. This increased rate of glycolysis results in the production of lactate and NADH, ultimately leading to acidosis and a decrease in myocyte contracility. In practice, patients undergoing some form of myocardial ischæmic event experience a 'wavefront' of injury, with the hypoxic region starting in the endocardium and progressing towards the epicardium (i.e. from the interior, ventricular surface of the heart out) [87, 88]. The functional response of the myocardium to ischæmia is complex, and depends on the length and severity of the ischæmic event. Prior to cell death due to prolonged ischæmia, the myocardium can be 'stunned', referring to recoverable contractile dysfunction after the return of normal blood flow; or 'hibernating', akinetic or with impaired contractile function during ischæmia [75, 89]. Both are potentially salvageable following interventional reperfusion [90]. If the ischæmic insult is sufficiently large, i.e. the degree, duration and location of occlusion is severe, the resulting acidosis is great enough to cause necrotic cell death, resulting in a

myocardial infarction (MI, commonly known as a "heart attack"). Myocardial infarction is a common cause of subsequent heart failure [91]. It is currently difficult to distinguish between viable, hibernating myocardium and tissue that is dead; accordingly, most patients believed to have acute MI are the subject of interventional revascularisation therapies that attempt to reperfuse and rescue the ischæmic myocardium. Interventional reperfusion remains the front-line treatment for acute MI [92], and it is effective: reperfusion following acute MI is associated with lower rates of early and late death following the MI, and fewer hospital readmissions for subsequent ischæmia or HF [93].

Reperfusion following ischæmia triggers an acute set of metabolic and inflammatory responses [94]. It is the set of these inflammatory responses that ordinarily lead to wound healing and scar formation following an injury elsewhere in the body. However, in the infarcted myocardium the influx of macrophages, neutrophils and lymphocytes into the tissue can be disadvantageous. Dysregulated inflammatory responses or metabolic changes that lead to further injury are termed 'reperfusion injuries', and have been shown in preclinical models of disease to worsen outcome [95, 96]. In humans, sustained inflammation following MI is strongly correlated with adverse outcome and reduced survival [97], yet attempts at improving patient outcomes through the use of anti-inflammatory drugs have not been successful [98–100]. Specifically, the use of corticosteroids or other drugs that cardiac renin-angiotensin system is associated with an increased probability of cardiac rupture [101]. and clinical reports from the mid-1980s show an increased prevalence of death by free left ventricular rupture following MI in steroid patients [102]. As a consequence, many studies with the aim of an immunomodulatory therapy for MI presented issues of impaired healing or increased risk of rupture, and therefore failed to show a benefit in addition to standard treatment [103]. Therefore, there is a need to be able to resolve this 'reperfusion conflict', and understand under which circumstances reperfusion is deleterious. The metabolic signature of inflammation – increased regional glycolysis arising from an increased density of highly glycolytic T-cells – suggests that DNP with hyperpolarised [1-^{13}C]pyruvate might provide an approach to probe the response of the heart to injury. These inflammatory changes following MI result in tissue that is metabolically distinct from the normal myocardium; the generation of an immune response necessitates considerable energy expenditure in order to support protein synthesis, and growth and proliferation in T-cells 'activated' by the nearby presence of chemical markers of injury. Such activated T-cells increase glucose metabolism and 'aerobic' glycolysis, preferentially converting pyruvate to lactate even when not limited by oxygen availability, and the molecular mechanisms behind the switch are distinct form the hypoxia-mediated mechanisms that ordinarily promote glycolysis. The reasons behind this preference for 'aerobic' glycolysis are not well understood, but are though to possibly reflect the increased conversion rates and availability of synthesis precursors in activated T-cells [104–106].

If the MI is survived, a fibrotic scar forms over a period of weeks that is believed to lessen the probability of cardiac rupture. This scar is non-contractile, and correspondingly decreases the functional performance of the organ by reducing the

ejection fraction of the relevant chamber. It is this change in functional performance that drives the development of HF from MI: the effective workload of the remaining tissue is increased following a decrease in its useful stroke volume. This period of (mal-)adaptation is known as myocardial remodelling, and occurs over a comparatively long timescale following an MI. Increasing cardiac workload is a necessary response to the inability of the damaged heart to adequately perfuse the body following MI, and is achieved by cytokine and neurohormonal signalling, resulting in increased heart rate and increased force of myocardial contraction. Such changes provide short term support by maintaining cardiac output, but ultimately can drive the descent into heart failure following MI [107].

Hyperpolarised Pyruvate and Cardiac Disease

As outlined above, metabolism is of great interest in cardiac pathology. Changes in the metabolic phenotype could act as a direct measure of the ischæmic tissue during myocardial infarction, and report on metabolic remodelling and HF over greater periods of time as the disease progresses. Such changes are of interest for basic research into the disease, as it is likely that any successful therapy for HF will have a metabolically modulating effect. As metabolic alterations in HF have been known for decades (starting with the 1939 observation of decreased creatine content in the failing heart by Herrmann and Decherd [108]), there is a considerable body of evidence showing the utility for metabolic research into the disease. Accordingly, cardiac metabolism was one of the first areas of study following the development of DNP, with Merrit et al. showing in the perfused rat heart that the production of visible bicarbonate following hyperpolarised [1-^{13}C]pyruvate injection is obtained exclusively by flux through pyruvate dehydrogenase [109]. Likewise, the *in vivo* state of PDH regulation in the rat heart was found by Schroeder et al. to be reduced by approximately 74% following an overnight fast compared to the fed state as detected through hyperpolarised [1-^{13}C]pyruvate spectroscopy. Such changes in activity are consistent with those reported in the literature obtained through traditional (i.e. invasive) biochemical means, and show that the technique could form a rapid, noninvasive probe of *in vivo* metabolic activity [110].

Concomitantly with this work, Golman et al. demonstrated a striking reduction in the visible rate of PDH flux in the post ischæmic pig myocardium by more than 90%, in which the left circumflex coronary artery was occluded by balloon catheterisation for either 15 or 45 min, and then revascularised by the deflation of the balloon (c.f. Fig. 4.12) [111]. Subsequent, independent evaluation by a radiologist who was unaware of the occlusion time showed that hyperpolarised [1-^{13}C]pyruvate images could accurately evaluate the state of the post-ischæmic myocardium with greater accuracy compared to that obtained evaluating wall motion abnormalities from CINE images alone. It was accordingly proposed that hyperpolarised [1-^{13}C]pyruvate imaging may form a more sensitive and quantitative method for detecting abnormal cardiac behaviour than standard wall motion techniques alone.

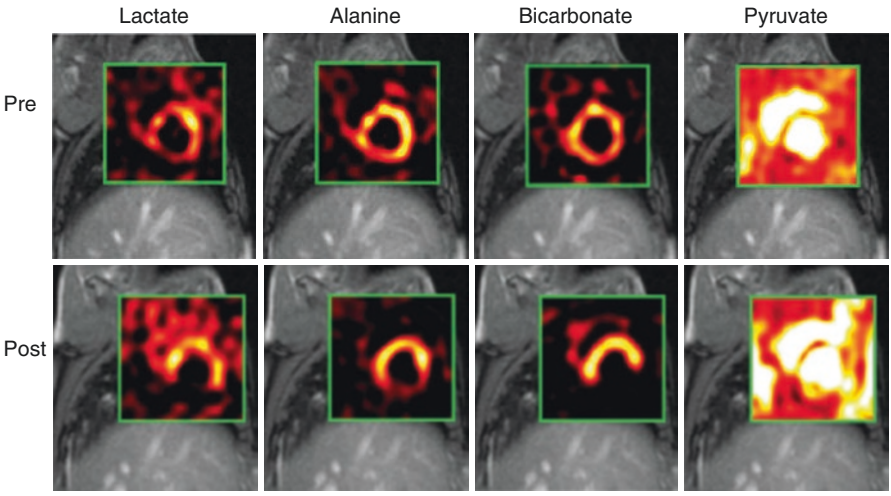

Fig. 4.12 Chemical Shift Imaging (CSI) maps returned following intravenous injection of hyperpo-larised [1-^{13}C]pyruvate from a male Swedish domestic pig before and 2 h after a 45 min period of coronary artery occlusion. Note that, common to the majority of hyperpolarised cardiac imaging experiments, the hyperpolarised agent - [1- ^{13}C]pyruvate- can be seen to be perfusing the ventricles (as it enters the blood stream), with downstream metabolic products subsequently visible in the working myocardium. Here, Golman et al. show that the rate of production of C-bicarbonate in particular is almost entirely eliminated in the insulted myocardium, leading to the appearance of a 'hole' in an otherwise nomal region of bocarbonate production that corresponds to the region of the insult (Figure ©2008 John Wiley and Sons, adapted and reproduced with permission [111])

Subsequent work in the perfused heart by Schroeder et al. [52] revealed that hyperpolarised [2-^{13}C]pyruvate could act as an effective probe of TCA cycle intermediates, and notes a substantial increase in visible lactate in the ischæmic myocardium. Moreover, following a 10 minute period of global ischæmia, it was found that the rate of label incorporation from [2-^{13}C]pyruvate into [1-^{13}C]citrate and [5-^{13}C] glutamate was immediately reduced upon reoxygenation, indicating a substantial reduction in oxidative metabolism. This fact is consistent with the reperfusion injury hypothesis. It has been hypothesised that such counter-intuitive behaviour acts in order to replete both TCA cycle intermediates and potentially cardiac glycogen, in order to 'prepare' the heart for another imminent period of ischæmia.

Additionally, hyperpolarised [1-^{13}C]pyruvate has been shown to discriminate between the acute and chronic phases following MI by metabolic phenotype, with concomitant differences in cardiac energetics (i.e. a decreased PCr/ATP ratio) as measured by ^{31}P spectroscopy and as measured by gadolinium perfusion agents. An increase in the observable lactate signal following hyperpolarised [1-^{13}C]pyruvate administration indicated increased anaerobic metabolism in the acute infarct state, which was not observed chronically [112]. Such an increase in lactate signal might reflect an underlying perfusion deficit; consequently, in the immediate post-acute

period a lack of ^{13}C-lactate signal may indicate the adequate restoration of blood flow [113, 114]. As a consequence, hyperpolarised ^{13}C MR may form a useful tool to evaluate cardiac function immediately following percutaneous coronary intervention, and provide information that is a proxy for prognosis. Unlike conventional perfusion imaging techniques, [1-^{13}C]pyruvate can distinguish between the necrotic and viable, akinetic myocardium [115, 116].

Moreover, it should be noted that hyperpolarised [1-^{13}C]pyruvate additionally provides an indirect measurement of intracellular pH, denoted pH_i. Carbonic anhydrase is a pH-sensitive enzyme, and owing to the localisation of PDH to the mitochondrion, it is believed that the detected ^{13}C-bicarbonate and $^{13}CO_2$ are produced within the cell. Therefore, the Henderson-Hasselbalch equation

$$pH = pK_a + \log_{10} \frac{\left[H^{13}CO_3^-\right]}{\left[^{13}CO_2\right]} \tag{4.10}$$

serves to permit the direct quantification of myocardial pH, initially demonstrated in the perfused heart by Schroeder et al. under both normoxic and ischæmic conditions [56, 117]. There are two main challenges to this approach: one, PDH flux has to be not otherwise inhibited and carbonic anhydrase has to be expressed in the cell of interest (which, for the heart, corresponds to performing the experiment in the fed state), and two, the expected size of the $^{13}CO_2$ peak is exceptionally small; at physiological pH, it is approximately 10% of the $H^{13}CO^-{}_3$ resonance. One approach proposed by Chen et al. to overcome the latter problem is the interleaved use of spectrally selective RF excitation to 'hit' the $^{13}CO_2$ resonance with a higher flip angle than bicarbonate, improving acquisition SNR and hence leading to the reconstruction of a pH value from the spectroscopic acquisition. As $^{13}CO_2$ is being produced throughout the duration of the experiment, and unidirectionally from flux through PDH, such approaches do not necessarily 'damage' the limited pool of initial hyperpolarised magnetisation that is available for study. As a consequence, this approach was subsequently extended by Lau, Miller and Tyler to permit the imaging of cardiac pH, by an interleaved global/spectrally selective excitation scheme and a rapid spiral readout [118]. A significant reduction in the mean myocardial pH from 7.2 ± 0.2 to 6.8 ± 0.2 was observed following a 15 min long period of high cardiac workload induced by a substantial dose of the positively inotropic agent dobutamine (Fig. 4.13), consistent with an increase in the rate of intracellular lactate production.

Hyperpolarised pyruvate has additionally been used to quantify the metabolic changes known to be occurring, but poorly understood, throughout the descent into heart failure. In comparison to PET studies with human patients using ^{11}C-glucose and ^{11}C-palmitate, hyperpolarised tracers can be administered serially without an associated radiation risk, and return usable metabolic data within seconds, rather than minutes. As a consequence, hyperpolarised MR studies have been undertaken to exactly understand the timing and consequences of shifts in metabolite substrate selection during heart failure, with the ultimate hope of exploiting knowledge of those shifts either for diagnosis or novel target selection with the disease.

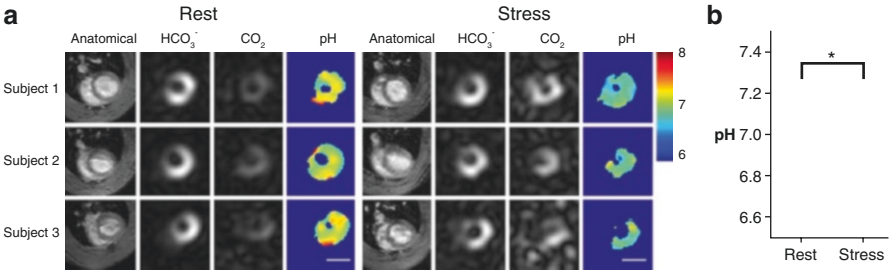

Fig. 4.13 (**a**) Anatomical, ^{13}C-bicarbonate and $^{13}CO_2$ measurements obtained from the rodent heart under rest and stress conditions, together with the corresponding pH map. (**b**) Following a period of high cardiac workload, the mean myocardial pH is significantly reduced and that the environment is therefore acidified (* denotes Student's $p < 0.05$ by an unpaired *t*-test) (Figure ©2016, licensed CC-BY and used with permission [118])

The emerging picture of the role of metabolism in heart failure and related diseases is complex. In a porcine tachycardia-induced model of dilated cardiomyopathy it was found that that the rate of label incorporation into bicarbonate was significantly reduced by 67% towards the end stages of the disease only, and was otherwise maintained [119]. Earlier in the progression of the disease, the incorporation of the ^{13}C label from [2-^{13}C]pyruvate into [5-^{13}C]glutamate was reduced, by approximately 51%, and cardiac PCr/ATP fell by approximately 26%. However, despite these early changes in cardiac energetics and ^{13}C incorporation into the Krebs cycle, pyruvate oxidation was maintained until dilated cardiomyopathy developed, associated with both a profoundly sick phenotype and a left ventricular ejection fraction of less than 30%.

In hypertension and hypertrophy, induced either via hyperthyrodism abdominal aortic banding or by use of the Spontaneously Hypertensive Rat (SHR) [120, 121], metabolic changes in hyperpolarised ^{13}C label flux are reported. Interestingly, the abdominal aortic banding model of hypertension mechanically creates a pressure overload as a model of vascular disease, and it is reported that an increase of lac-tate production, indicative of increased glycolysis, was noted throughout the disease course, with unchanged PDH flux. This stands in direct contrast to the SHR rat, wherein PDH flux is demonstrably *increased*, by approximately 85%, and the flux to ^{13}C-lactate is unchanged. Such a diversity in findings are consistent with the hypothesis that essential hypertension is a symptom with a myriad of different potential causes, with a strong metabolic component. As metabolic syndrome clinically is known be a strong, independent risk factor of developing hypertension [122], it is apparent that hyperpolarised molecular probes are well placed for further study of the field.

Clinical Translation

Dissolution-DNP with hyperpolarised [1-^{13}C]pyruvate is safe for use in humans, and represents a technique that is transitioning to the clinic. The initial approach to translation taken by Nelson, Kurhanewicz, Vigneron et al. at the University of

California in San Francisco was to render an initial prototype hyperpolariser, similar to the cartoon shown in Fig. 4.9 and featuring open-cycle cryogenics and requiring a large degree of manual interaction, suitable for human use by placing both it and its operators in a sterile clean room [123]. The sterility of the resulting generated hy-perpolarised [1-^{13}C]pyruvate would only therefore be provided by a combination of the nature of the process itself (taking the sample from 1 K to 400 K) and the use of sterile compounding reagents. Note, additionally, that the fact that the entire fluid path of the system is not necessarily guaranteed to be exposed to sterilising temperatures, and that the viability of individual pathogens after extended storage in liquid helium temperatures means that the process itself is not considered by regulatory agencies to be inherently sterilising. It is therefore the case that significant logistical and medico-legal issues had to be overcome by the relevant pharmacy team in siting an appropriate clean room adjacent to a clinical MR facility for its immediate use. Nevertheless, in 2013 Nelson et al. successfully reported an initial study using hyperpolarised [1-^{13}C]pyruvate in patients with biopsy proven unilateral prostate cancer, in which not only was the process with d-DNP and [1-^{13}C]pyruvate shown to be safe for human use, but additionally the glycolytic flux to lactate acted as a sensitive marker of disease, reflecting the fact that an increased rate of glycolysis is a hallmark of cancer [124].

In an attempt to streamline the process for future clinical practice, an alternative design of d-DNP polariser was proposed by Ardenkjær-Larsen in which the entire [1-^{13}C]pyruvate sample and fluid path is a sealed consumable, produced under sterile compounding conditions that did not necessarily need to be adjacent to the place of use (illustrated in Fig. 4.14) [39]. The high-field superconducting magnet was likewise adjusted to contain a cryocompressor and operate with entirely closed cycle cryogen handling. Other changes to the systems used for preclinical experiments centred around automated quality control measurements that would measure the pH, nuclear polarisation P_N and concentration of the dissoluted [1-^{13}C]pyruvate rapidly without breaking its sterile field. Additionally, the electronic free radical chosen for use with human intent precipitates out under an appropriate pH range such that it is removed by filtration during its passage out of the fluid path and is not injected into the human patient. Whilst no adverse toxicological effects have been reported in small animals using low concentrations of a variety of electronic free radicals commonly used with d-DNP, the removal of the compound from the delivered agent is aimed to speed regulatory approval and improve the safety profile of the agent. The proposed design is, as of 2016, installed and in use at a number of facilities world-wide but none have yet reported completed human studies demonstrating the efficacy of the technique, in part due to complex nature of the manufacture of the sterile fluid paths required for human use.

Nevertheless, the current clinical techniques used in the management of patients with MI, ischæmic diseases, or heart failure rely on indirect measures of ischæmia (such as perfusion abnormalities or changes in wall motion during stress), and it is therefore hoped that the direct visual assessment of myocardial ischæmia and viability in the form of ‘lactate and bicarbonate imaging’ will be able to aid guided interventional therapies, such as revascularisation. As revascularisation only forms

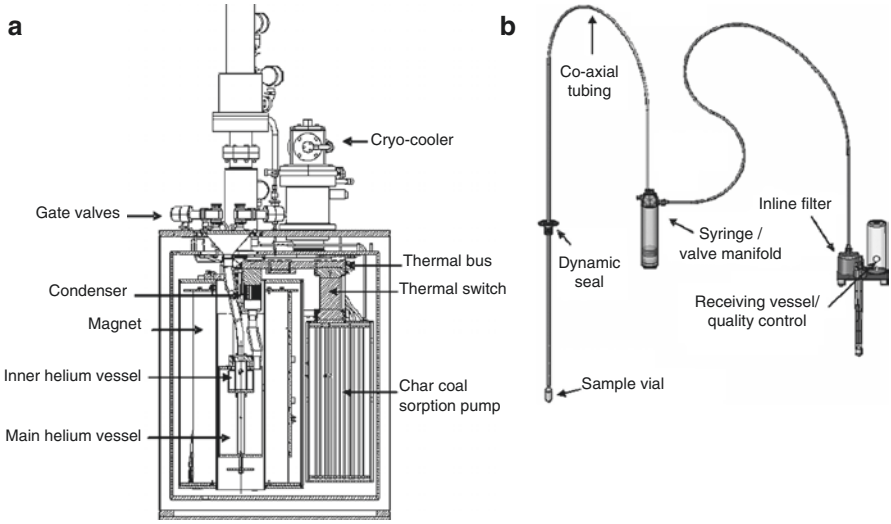

Fig. 4.14 The 'Spinlab' DNP hyperpolariser created with sterile use intent. (**a**) The superconducting cryostat itself features closed cycle cryogenics and the ability to polarise up to four samples at once within the same ~ 800 mK environment with semi-automated insertion, dissolution and removal procedures that were designed to lower the barrier of entry to the technique. (**b**) Schematic of a sterile fluid path, filled and assembled usually within an MHRA 'Grade A', ISO 5 or FDA 100 category clean room. The fluid path itself has to withstand temperatures from close to absolute zero to several 100°C, and represents a significant engineering challenge that is assembled from over 200 separate parts. It consists of a sample cup, containing [1-^{13}C]pyruvate and an electronic free radical; a high vacuum compatible 'dynamic seal' to enable the sample cup to sit in the bottom of the cryostat and the rest of the fluid path elsewhere; filters to remove the precipitated electronic free radical from solution and a final sterilisation filter; and a series of optically clear quality control cuvettes to allow the non-contact measurement of several parameters of interest, such as pH and pyruvate concentration (Figure ©2011 John Wiley & Sons, reprinted (adapted) with permission [39])

an effective therapy if targeted to the region of significant ischæmic burden, it is hoped by the community at large that hyperpolarised [1-^{13}C]pyruvate imaging will substantially improve patient outcome should it come to be used widely in the clinic [125].

Other Hyperpolarised Metabolic Probes

Whilst, as outlined above, pyruvate is a highly connected node in the metabolic network that is of great utility in probing cardiac dysfunction, it nevertheless remains only one node in a highly complex and well-connected scale-free network [126]. Accordingly, a growing number of other metabolic agents have been hyperpolarised, either via d-DNP or parahydrogen methods, and proposed as metabolically active probes.

Arguably the most straightforward path to take in developing novel ^{13}C probes with d-DNP is to attempt to hyperpolarise labelled molecules that are known to be soluble, have a T_1 long enough for *in vivo* applications, and to be rapidly metabolised on a similar timescale. As a direct consequence, several subsequent metabolites of [1-^{13}C]pyruvate and [2-^{13}C]pyruvate have been investigated. By hyperpolarising ^{13}C-bicarbonate directly, Gallagher et al. showed that its subsequent equilibration into $^{13}CO2$ by carbonic anhydrase would provide an effective *extracellular* measurement of pH, in contrast to the predominantly *intracellular* measurement obtained following administration of hyperpolarised pyruvate alone [127]. Likewise, infusion of hyperpolarised [5-^{13}C]glutamine into cultured human hepatoma cells (HepG2) revealed a detectable flux into labelled glutamate that obeyed expected chemical kinetic behaviour [128]. Such methods are of interest outside of oncological applications as amino acid metabolism is known to be profoundly altered during cardiac ischæmia, where their preferred role in catabolism and anaplerosis is believed to play a highly relevant and versatile role in maximising survival; for example, hearts without the ability to transaminate glutamate are less likely to recover from ischæmic episodes [129].

One perpetually pertinent consideration for hyperpolarised studies of metabolism is the value of ΔG for the enzymatic reactions under consideration. Lactate de-hydrogenase is known to operate near to thermodynamic equilibrium, unlike the unidirectional pyruvate dehydrogenase, and therefore the available 'pool sizes' of both labelled and unlabelled metabolites are highly relevant in order to estimate rate constants without additional cofounding factors. Hyperpolarised [1-^{13}C]lactate has been accordingly proposed as an agent that that would allow for the estimation of the pool size of pyruvate to correct for this cofound. However, the relatively small size of the endogenous pyruvate pool means that such experiments are technically difficult to perform with adequate SNR. To this end, hyperpolarised [1-^{13}C,U-^{2}H] lactate has been combined with multinuclear 2D spectroscopy to unambiguously identify the label exchange through lactate dehydrogenase *in vivo* [130–132]. Similarly, the realisation that blood phosphatases can readily remove phosphate moieties from a number of small molecules has enabled PHIP-prepared [1-^{13}C] phospholactate as another route to providing bioavailable ^{13}C-lactate by the (substantially cheaper) PHIP methods as opposed to d-DNP [133].

Starting at the other end of glycolysis, glucose has been hyperpolarised via d-DNP, and successfully used as an *in vitro* molecular probe. However, in order to increase the T_1 of the probe sufficiently to permit the observation of subsequent metabolites, it was found to be necessary to hyperpolarise deuterated, ubiquitously labelled [U-^{2}H, U-^{13}C]glucose, which possesses a T_1 of approximately 9 s at 7 T, compared to $\ll 1$ s for singly labelled glucose [134, 135]. Following subsequent injection into mouse lymphoma and lung tumours, ^{13}C-lactate was observed being spectrally produced, along with the glycolytic intermediates ^{13}C-6-phosphogluconate (6PG), di-hydroxyacetone phosphate (DHAP) and bicarbonate (c.f. Fig. 4.15). Whilst the technique has been used to study a majority of additional glycolytic and pentose phosphate pathways intermediates in yeast grown to stationary phase and EL4 tumour cells, the relatively short T_1 has precluded its reported use *in vivo*.

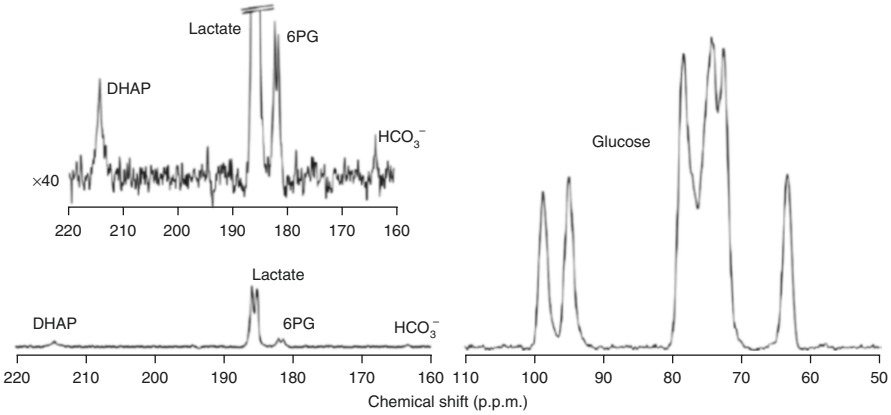

Fig. 4.15 Observed metabolic products following hyperpolarised [U- ^{2}H, U- ^{13}C]glucose infusion into tumour bearing mice, with the above spectrum being a × 40 magnified version of that displayed on the bottom. Four downstream metabolic products are observed, indicating that the labelled probe must have transversed the entirety of the glycolytic pathway in order for ^{13}C-lactate to be visible within the lifetime of the hyperpolarised experiment (54 summed spectra acquired over 6 s at a 10° flip angle). It is of note that only a select few glycolytic intermediates, 6PG and DHAP, are visible in these spectroscopic acquisitions, even though the ^{13}C label must have passed through a large number of other glycolytic intermediates (Figure ©2014 Nature Publishing Group, reproduced with permission [134])

Fatty acid oxidation has likewise been investigated by hyperpolarised MR. Ball et al. report the production and use of hyperpolarised [1-^{13}C]butyritic acid with approximately 7% polarisation and a T_1 of ~20 s [136]. Following injection into both the perfused and *in vivo* rat heart, a large number of TCA cycle intermediates (glutamate, citrate, and acetylcarnitine) were observed along with the ketone bodies acetoacetate and β-hydroxybutyrate. As is often the case for probes hyperpolarised via d-DNP, it is additionally possible to hyperpolarise [1-^{13}C]pyruvate and [1-^{13}C] butyrate simultaneously, and monitor myocardial substrate selection to a much higher degree of chemical selectivity *in vivo* [137]. As noted by Bastiaansen et al., the coinfusion of hyperpolarised metabolic fuels is a one-of-a-kind method for assessing myocardial substrate preference *in vivo*. Such metabolic versatility routinely found in the heart is consistent with the canonical description of the heart as a 'metabolic omnivore', able to consume a large number of substrates in order to maintain its continuous contractual demand for energy [129]. No difference was observed in apparent flux through to ketone bodies or TCA cycle intermediates following an overnight fast, although this is expected to not be the case in starvation. The role and regulation of butyrate metabolism in the diseased heart remains uncertain. Likewise, preliminary work by Yoshihara et al. has revealed that ^{13}C-octanoate, a medium-chain fatty acid, can be hyperpolarised via d-DNP (to $P_N \approx 11\%$ with a T_1 of ~30 s) and again could be observed undergoing β-oxidation through to [1-^{13}C] acetylcarnitine [138]. Likewise, Bastiaansen et al. report that hyperpolarised [1-^{13}C] acetate ($P \approx 13\%$ and a T_1 of ~ 15 s in blood at 9.4 T) acts as an effective *in vivo*

probe of acetyl-CoA synthetase activity as production of [1-^{13}C]acetylcarnitine can be observed *in vivo* in the rat leg [139]. Subsequently, the cardiac metabolism of [1-^{13}C]acetate and quantification of acetyl-CoA synthetase activity *in vivo* has been demonstrated in the healthy pig myocardium [140].

Arguably, one of the aims of quantifying *in vivo* fluxes of labelled molecules with hyperpolarisation techniques is the hope that the rate of these fluxes is different between disease states, leading either to an improved mechanistic understanding of that disease, and/or its direct use as a diagnostic technique. One dramatic example of a large difference in apparent rate constants between pathology and physiology is the probe [1,4-^{13}C]fumarate, which violates the conventional assumption that a probe's *in vivo* biochemistry must be sufficiently rapid compared to the T_1 of the probe. In physiology, the rate of uptake of fumarate is sufficiently slow that no ^{13}C-malate signal is observed following the injection of hyperpolarised [1,4-^{13}C]fumarate. Gallagher et al. have shown conclusively that the reason for this lack of signal is the slow transport across the plasma membrane of [1,4-^{13}C]fumarate, and not the rate of the fumarase enzyme itself. Accordingly, [1,4-^{13}C]fumarate forms a highly effective probe of cellular necrosis, in which the plasma membrane is disrupted, and 'leaked out' fumarase can produce a detectable malate signal [42]. Hyperpolarised [1,4-^{13}C]fumarate therefore can act as an effective probe of necrosis in many diseases, such as acute kidney injury, and cancer [141, 142].

Finally, one great strength of hyperpolarisation techniques is that they are not necessarily limited to probing molecules that are 'conventionally' assumed to be of importance, and, unlike PET techniques, there is no need to chemically modify the agent in question to enable its detection. As a consequence, more 'creative' probes can be devised to report upon the real-time activity of systems *in vivo*. One example is the use of hyperpolarised vitamin C, [1-^{13}C]ascorbic acid, and its oxidised form [1-^{13}C]dehydroascorbic acid to provide an accurate and quantitative measurement of the redox state of the cell *in vivo*; injection of hyperpolarised [1-^{13}C]dehydroascorbic acid lead to its rapid intracellular reduction in tumour xenografts [143]. Similarly, a choline mimetic, ^{15}N-propargylcholine, has been hyperpolarised via PHIP and field cycling methods, and its *in vitro* phosphorylation demonstrated in the MCF-7 cancer cell line [144].

In conclusion, a large number of molecular agents have been hyperpolarised and investigated to a greater or lesser degree in biological systems. Some of these, notably [2-^{13}C]pyruvate, [1-^{13}C]butyrate, and ^{13}C-acetate, have been shown to act as effective probe of central metabolism in the living heart. It is worth stressing that, in comparison to complementary metabolic imaging techniques such as PET, hyperpolarised MR chemically sensitive information rapidly, with isotopically labelled (as opposed to chemically modified) endogenous metabolites. Furthermore, whilst the ultimate limiting spatial resolution of hyperpolarised experiments is not necessarily well determined, depending upon the M_0 initially generated by a hyperpolarisation method, it is worthy of note that studies have been reported with a spatial

resolution within a factor of four of that of the theoretical limiting resolution of PET with ^{18}F-flurodeoxyglucose [145, 146]. This fundamental limitation of PET arises from the distribution of energy in the positron produced by nuclear decay, which leads to a distribution in the mean distance it subsequently travels prior to annihilation. As a consequence, sub-millimetre voxel sizes are exceptionally difficult to obtain with the technique, with the theoretical limiting FWHM of ^{18}F approximately 0.5 mm, and that of ^{82}Rb approximately 6 mm, with clinically obtainable voxel sizes on the order of $2 \times 2 \times 2$ mm^3 [147]. Clearly, hyperpolarised MR is a powerful translational tool that is of great potential in both diagnostic cardiac imaging and for quantifying the important, yet poorly understood metabolic basis of many cardiac pathologies.

Hyperpolarised Perfusion Imaging, and Hyperpolarised Probes Other than ^{13}C

It has long been realised that DNP provides a "third MR way" of imaging both the vasculature and perfusion into the tissue bed, without the potential toxicity of administering gadolinium chelates or the long scan times of endogenous proton techniques. DNP forms a favourable technique for perfusion imaging due to the relatively long signal lifetime (compared to the cardiac cycle) and low background signal of hyperpolarised agents compared to proton techniques; additionally, the linear signal response of the agent with respect to concentration also enables direct quantification and the ability to detect balanced ischæmia, where a global change in blood flow occurs in the organ of interest. These facts represent a substantial benefit compared to traditional contrast enhanced magnetic resonance angiography. Likewise, these exact same conditions of high initial signal and low background generate an exceptionally high contrast-to-noise ratio (CNR) for hyperpolarised agents, which, in bulk permit vascular angiographic applications.

Initial proof-of-concept studies demonstrating perfusion imaging with hyperpolarised compounds were performed using "metabolically inert", non-toxic ^{13}Clabelled urea [148], and subsequently both ^{13}C-urea and the non-endogenous extracellular agent known as HP001 [149] (Bis-1,1-(hydroxymethyl)-[1-^{13}C]cyclopropane-D8) have been used as probes of perfusion within the kidneys, in models of cancer, and in the hearts of large animals [150, 151]. As shown in Fig. 4.16, the high CNR of hyperpolarised agents results in the high image quality in the pig heart. Similarly, parahydrogen induced polarisation has been used to visualise the great vessels throughout the body of a rat, using a perfusion agent that, after specific hydrogenation and polarisation transfer, is a freely dissolvable straight chain carbonyl carbon compound with ^{13}C and ^{2}H labels [27]. As with d-DNP, the low background signal ensures an excellent CNR, with sub-second and sub-millimetre resolution in the rat, as illustrated in Fig. 4.17.

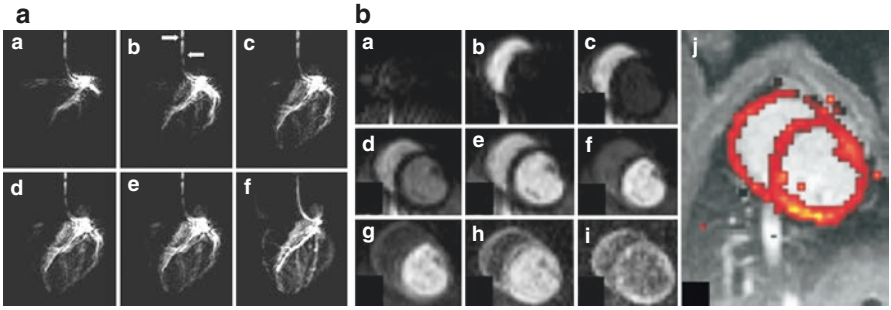

Fig. 4.16 (**a**) A series of hyperpolarised ^{13}C angiograms obtained following the direct injection of HP001 through a catheter placed in the left coronary descending artery and left circumflex artery of a pig. Time increases from a to f. Using the HP agent, it is possible to visualise the first diagonal branch and smaller septal branches of the healthy coronary arterial tree. Flow artefacts (denoted with white arrows) are visible in this SSFP acquisition due to the high flow rate inside the catheter. One image was acquired per heartbeat and the total scan time per image was 422 ms. (**b**) Following intravenous infusion of the hyperpolarised agent, myocardial perfusion can be observed and readily quantified with essentially no background, producing (via the Kety-Schmidt method) the perfusion map shown overlaid on an anatomical proton image in j (Figure ©2006 Elsevier, reprinted (adapted) from Golman and Petersson [150])

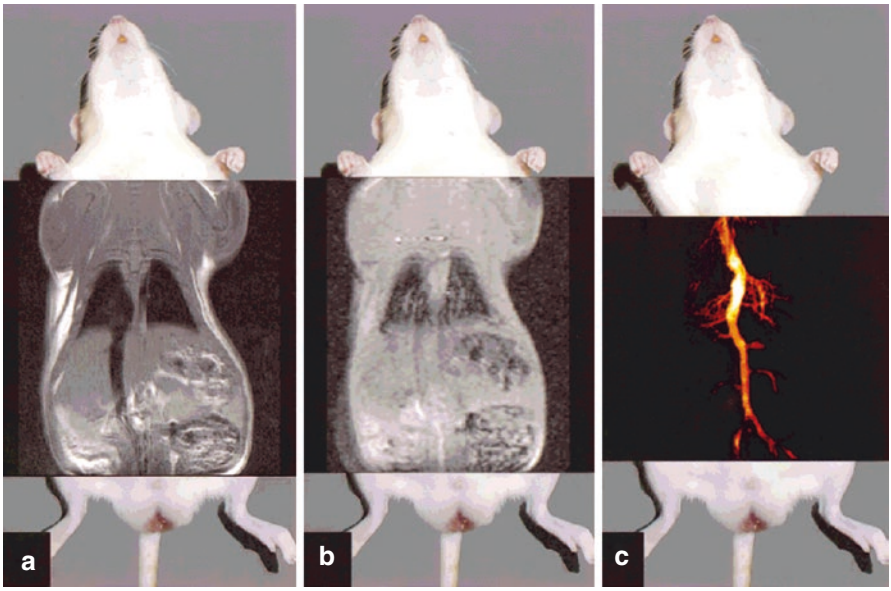

Fig. 4.17 Anatomical spin echo (**a**) and gradient echo (**b**) images superimposed over a photograph of the anaesthetised rat, together with (**c**) angiographic imaging obtained by a single-shot ^{13}C RARE sequence generated in 0.9 s following the infusion of the PHIP produced perfusion agent (Figure ©2001 John Wiley and Sons, reproduced with permission)

Hyperpolarised ^{13}C urea additionally forms a highly attractive probe of perfusion as it is possible to polarise through d-DNP a sample containing a mixture of both [1-^{13}C]pyruvate and ^{13}C-urea. Both nuclei polarise independently, and acquisition strategies have been performed to therefore estimate both cardiac perfusion and cardiac metabolic function within the same scan, with the perfusion information provided by ^{13}C urea being obtained 'for free' [116]. This flexible approach paves the way for a 'master scan' of hyperpolarised probes, in which several complementary molecules could conceivably be administered in a single bolus, further characterising the state of the working heart, and was shown to be sensitive to both changes in metabolism (provided by imaging rodents in the fasted or fed states) and perfusion (under positively inotropic cardiac stress).

Another inspired use of endogenous molecules with safety profiles well known *a priori* is the use of hyperpolarised water, $^{1}H_2O$, as a perfusion probe [152–154]. Whilst potentially sacrificing the background-free acquisition might seem like a substantial penalty to pay, it should be noted that in *in vivo* acquisitions the initial signal magnitude of the perfusion agent is approximately two orders of magnitude larger than the thermal equilibrium magnetisation. It is also the case that proton imaging is substantially less demanding of gradient hardware than ^{13}C acquisitions, and does not require a multinuclear compatible MR system. Hyperpolarised water imaging, therefore, carries the promise of higher resolution rapid imaging with a linear relationship between observed signal and agent concentration. As ever with hyperpolarised agents, however, the T_1 the probe is limiting. As the T_1 of water is on the order of 5 s at 40 °C the future utility of the technique has yet to be demonstrated, although it has been used to resolve perfusion through the vena cava over a period of approximately 20 s in the rat [155].

It should be noted that it is technically challenging to perform perfusion imaging of the rodent heart due to the high spatio-temporal resolution required to resolve the first pass of the perfusion agent through the heart and coronary vasculature. The typical thickness of the rodent myocardium is only 2 mm, and this, in conjunction with the high signal present in the lumen of the ventricles, necessitates high spatial resolution to adequately resolve perfusion agents within the tissue capillary bed. If the scan run is not of sufficiently high resolution, partial volume effects arising from the neighbouring blood pool will be significant, confounding the quantitation of my-ocardial perfusion. This has lead to MR techniques for signal segmentation, either by the use of flow suppression gradients to selectively remove signal predominantly originating in the ventricles [156], or alternatively approaches whereby information on compartmentalisation is obtained from *T2* mapping, and the use of [^{13}C, $^{15}N_2$]-urea [157]. As [^{13}C, $^{15}N_2$]-urea. is known to possess a dramatically longer T_2 than ^{13}C-urea(~ 24 s compared to ~0.09 s in water respectively), differences in effective viscosity caused by changes in biological microstructure are amplified, enabling quantitative measurements of kidney function [158]. One interesting experimental note about the use of hyperpolarised ^{13}C-ureais that at low fields an additional scalar relaxation pathway becomes prevalent, reducing T_1 dramatically in the region between the d-DNP polariser and imaging magnet. If left unchecked, this

enhanced period of decay would have a detrimental effect on the initial M_0 in the subject under study. Accordingly, a handheld 'dead man's switch' magnetic carrier has been proposed that is safe for use in the high B environment of a clinical MR scanner, but will maintain the magnetisation of the ^{13}C-urea sample [43].

In addition, parahydrogen induced polarisation probes have been directly report on microstructural properties that would not be otherwise detectable with the comparatively limited spatial resolution of non-proton MR. A ^{13}C labelled probe developed by Bhattacharya et al. that effectively binds to lipid bilayers was shown to significantly be retained in the aorta of a mouse model of atherosclerotic arterial disease, the low density lipoprotein receptor deficient mouse (LDLR mouse), compared to appropriate controls. Hyperpolarisation methods therefore have the unique luxury of being able (in theory at least) to design a specific agent for studying one particular aspect of a biochemical system, and follow its subsequent *in vivo* behaviour without an observational background [28].

One limitation to the use of hyperpolarised agents as perfusion probes is their inherent T_1, which places an upper bound on the timescale of processes that can be probed with them. Part of the motivation for developing HP001 as a perfusion agent was its engineered longer T_1, which at $T_1 \approx 96$ s in water at 3 T is substantially longer than the ^{13}C T_1 of many small molecules, including ^{13}C-urea. However, by moving away from small molecules, it is possible to produce solid-state functionalisable nanoparticle agents with substantially longer T_1 than can be obtained otherwise. At present, both silicon nanoparticles (either natural abundance or ^{29}Si enriched) and ^{13}C nanodiamonds have been proposed as probes of processes occurring over minutes to hours, as the T_1 of the probe is proportional to its diameter, and is therefore directly controllable. Accordingly, hyperpolarised nanoparticles have been used as 'perfusion' agents of the GI tract in rodents, and investigations with functionalised versions are ongoing [159–161].

Often, the goal of cardiac perfusion imaging is to provide quantitative information about oxygen availability in the tissue of interest. One alternative technique that has been proposed is the use of d-DNP hyperpolarised ^{6}Li, which possesses an advantageously long T_1 of $\sim$ 600 s in deoxygenated deuterated water, but reduces significantly in blood. Owing to the difference in magnetic susceptibility between oxygenated and deoxygenated blood, quantitative T_1 determination is therefore proposed as a probe of absolute oxygenation [162]. Perhaps somewhat surprisingly, dissolution and administration as LiCl at nM concentrations do not preclude the reception of hyperpolarised signal from the rodent brain [163].

In summary, hyperpolarised agents are well placed to provide readily quantified measures of both tissue oxygenation and vascular access *in vivo*. Despite the novelty of the technique, there is a substantial body of evidence that shows that hyperpolarised probes of perfusion are of utility in understanding the fundamental biology of interest. Given both the vital importance of perfusion and oxygenation in disease, and the excellent safety profile of many of the proposed agents (e.g. urea and water, both of which possess an LD50 on the order of g kg^{-1}), it is likely that hyperpolarised perfusion agents will soon be applied to human populations.

How Best to Eat the Cake: Pulse Sequence Strategies for Hyperpolarised Experiments

Challenges and Difficulties

Hyperpolarisation techniques represent a new paradigm for magnetic resonance experiments, and have the promise to provide vast new areas of study. However, in contrast to 'traditional' magnetic resonance experiments performed at thermal equilibrium, hyperpolarised experiments are not necessarily straightforward to perform, and are, by the nature of the technique, necessarily temporally rapid.

The greatest difference from the point of view of the experimenter (or pulse sequence programmer) is that, unlike conventional magnetic resonance techniques, the total 'amount' of signal is fixed, and determined by the concentration of the injected hyperpolarised agent, its T_1, the degree to which the hyperpolarisation technique can increase P, and the time taken to prepare the hyperpolarised agent and inject it into the subject inside the imaging magnet. The initial M_0 is fixed, therefore, at the start of each experiment, *and is independent of the field strength of the imaging magnet used*. As a consequence, the value of M_0, T_1, T_2, and T_2^* achievable for a particular combination of hyperpolarised agent and imaging field strength is paramount. Owing to the fact that $T_1 \gg T_2$ and the inevitable return to thermal equilibrium of the injected probes, it is necessarily the case that every radiofrequency (RF) excitation of the injected agent played by the experimenter effectively destroys part of M_0 in order to sample it. A single 'errant' 90° pulse is therefore sufficient to end a hyperpolarised experiment prematurely, sampling the entirety of M_0 at one point in time. Should that point be prior to the *in vivo* label exchange of interest, e.g. [1-^{13}C]pyruvate to ^{13}C-bicarbonate, then no useful metabolic information would be obtained from that experiment, representing a significant wasted expense.

Similarly, by the very nature of the technique it is necessary to prepare a labelled probe outside of the imaging magnet, and inject it (usually via central venous access) into the subject under study. As all RF coils have a finite spatial extent, and the B_1 field near the edges of the RF coil is not usually well char-acterised, performing spin echo experiments with 180° pulses represents a significant challenge unless the acquisition is started after injection of the hyperpolarised agent. For perfusion imaging, this fact represents a significant potential limitation of spin-echo based techniques [156]. By a complementary argument, the RF design of coils used for hyperpolarised experiments is of paramount importance. Owing to the depletion of the longitudinal magnetisation by each individual excitation, experiments are usually performed with low flip angles per shot (typically $\theta = 5°$ to 15°), with repeated acquisition over several minutes covering the duration of the hyperpolarised experiment. Analysis of the resulting datasets typically involves a correction term for sin θ, and therefore the flip angle delivered is of vital interest for both not unduly shortening the duration of the hyperpolarised experiment, and for its accurate quantitation. However, unlike conventional proton acquisitions, it is not feasible to obtain

reference images over the biological tissue of interest, owing to the very small endogenous ^{13}C signal. The only possible way to perform B_1 mapping schemes involves their simultaneous acquision with the hyperpolarised dataset, for example, by using a Bloch-Siegert off-resonance pulse after excitation [164]. Such schemes necessarily cannot be acquired before the hyperpolarised experiment, and may additionally fundamentally compromise it. As a result, schemes that would wish to exploit the fact that $T_2 > T_2^*$ of hyperpolarised compounds and perform spin echo experiments has to be aware that any slight deviation in delivered flip angle *anywhere* containing the hyperpolarised probe, not necessarily in the region of the coil used for reception, could have significantly deleterious effects on the experiment. Consequently, a slight majority of pulse sequences proposed for hyperpolarised experiments are of the gradient echo, rather than spin echo variety.

In a cardiac context, these sequence design challenges are magnified by the usual difficulties of cardiac imaging: the heart beats paramagnetic blood at a significant velocity continuously, and is anatomically located near a large number of air-tissue interfaces that can cause significant susceptibility artefacts. For hyperpolarised pulse sequence design, arguably the main challenge of these is ΔB_0: the naïve advantage of low-flip angle gradient echo experiments combined with the desire to limit excitation usually drives a desire to perform single-shot acquisitions, where the length of T_2^* determines the time available for the readout. Therefore, good shimming is important - and, due to the aforementioned susceptibility effects encompassing the heart, usually difficult to achieve, particularly at higher field. For single-shot approaches, cardiac flow at the start of systole is usually comparatively slow in duration to the time available for readout, and therefore provides an incentive to gat the acquisition of the image prospectively to the QRS complex of the ECG.

Pulse Sequence Strategies

As a direct consequence of the unique challenges that hyperpolarised probes pose to the experimenter, a wide variety of different pulse sequences have been proposed to effectively interrogate them. It should be stressed that the majority of sequences are highly application specific, and many described strategies reported in the literature often require specific hardware (such as computer-controllable infusion pumps or RF coils), beyond the high cost of the polariser used to generate M_0 initially.

Spectroscopic Acquisitions, Injection Protocols and Variable Flip Angle Schemes

Simple spectroscopic acquisitions arguably form the the most most straightforward approach to performing hyperpolarised experiments. “All” that is required for a successful acquisition is the preparation of the hyperpolarised probe of interest, and a low flip angle (typically θ = 10°) long readout acquisition with a short, hard

excitation pulse of adequate spectral bandwidth. Typically spectra are acquired with a TR of approximately 1 s, for a duration that is at least $\sim 5 \times T_1$. Following dissolution (if using d-DNP), the scan is started and the agent infused as a 'boxcar' bolus, i.e. at a high rate over a short period of time into the subject.

Such acquisitions are simple, comparatively robust as the only prior knowledge required is a rough estimate of the central transmitter frequency to play the hard excitation RF pulse at. Owing to the short minimum duration of a hard, non-selective low flip angle pulse, the excitation bandwidth is typically large, and there is minimal signal lost due to a long echo time. The experimenter additionally has the added benefit that the returned data will typically be of high spectral resolution, and, by summing the acquired spectra for the duration where the SNR of the acquisition supports it, can show *in vivo* metabolites produced at a slow rate or low concentration. Additionally, absolutely no information about the biochemistry of the probe has to be assumed *a priori*, meaning that simple spectroscopic acquisitions are typically among the first experiments performed during the development of a novel hyperpolarised agent. However, spatial localisation is typically limited: initial studies used a surface transmit/surface receive coil and R-wave gated spectroscopic acquisition for cardiac applications [110], which served to localise the received signal to the heart. It should be noted that surface coils used in both transmission and reception feature poor flip angle homogeneity, dropping off spatially rapidly, and therefore analysis approaches which assume a particular flip angle are likely to be at least partially compromised; using a volume transmit/surface receive coil combination offers the transmit (B_1^+) homogeneity of a volume coil together with the SNR benefit and signal localisation of a surface coil, and thus offers a substantial potential benefit, both in subsequent analysis and through the decreased likelihood of variability in subject-to-subject positioning altering the effective flip angle delivered [165, 166].

There are two additional parameters to 'play with' with hyperpolarised spectroscopic acquisitions. Firstly, the 'ideal' injection profile of the hyperpolarised agent, i.e. delivered volume as a function of time, would be that which maximises the total received signal. Owing to the fact that the paramagnetic nature of blood serves to reduce the T_1 of the majority of reported probes *in vivo* compared to in their dissolution medium. Therefore, there is an argument to be made for retaining a 'reservoir' of magnetisation outside of the subject, and infusing the agent at a controlled rate to obtain kinetic curves that maximally allow for the determination of the rate constants of interest with the least noise. Maidens and Arcak have considered this problem for the case of [1-^{13}C]pyruvate infusion, and shown with no small degree of mathematical rigour that a unique 'ideal' infusion profile can be derived given a series of appropriate constraints, although its delivery would require a computer-controlled infusion pump with millisecond temporal accuracy. Perhaps fortunately, the existence of an ideal profile can be used to show that the typical '15 s boxcar' infusion profile (whereby the total dose administered is done so at a constant rate over 15 s) obtains at least 98.7% of the global optimum [167]. It is therefore the case that the majority of reported studies do not use an injection scheme other than that of the boxcar.

Secondly, variable flip angle (VFA) schemes have the promise to likewise be ultimately more SNR efficient than constant low-flip angle schemes. Typically, a series of different angles are proposed where the flip angle increases monotonically from ~ 5° to a final 90° pulse that ends the experiment, and recovers the entirety of any remaining longitudinal magnetisation. Such approaches aim to evenly distribute the available longitudinal hyperpolarised magnetisation between successively acquired acquisitions, and therefore and to increase the temporal window of the experiment [168, 169]. Whilst such approaches can indeed bring an SNR benefit, they are highly susceptible to potentially slight errors in timing between the initiation of the VFA scheme and the arrival of the hyperpolarised agent. As myocardial perfusion is itself frequent one quantity that hyperpolarised studies aim to infer, the use of a VFA scheme should be considered carefully for any planned study.

Additionally, it is worth noting that numerous approaches have been used to localise single spectroscopic acquisitions to greater accuracy than that by provided by the use of a surface coil and a single, nonselective, excitation. Moving up in complexity, the use of slice-selective spectroscopic acquisition represents a straightforward extension to the technique. Again, pulse lengths can be kept small, and 1D-localised spectra (e.g. to the heart) are relatively routine [170]. In contrast, volume selection in 3D is more challenging due to the risk of errant high power pulses that are nominally 180° "accidentally" causing a significant reduction of signal in regions where this is not the case; Fig. 4.18 illustrates a phantom acquisition where this situation has occurred. Both modified outer volume suppression schemes and the use of adiabatic refocussing pulses have been proposed to permit 3D localised spectroscopy, although these techniques are not necessarily readily applied to regions with fast flow or during the period of the infusion of the hyperpolarised contrast agent [171, 172].

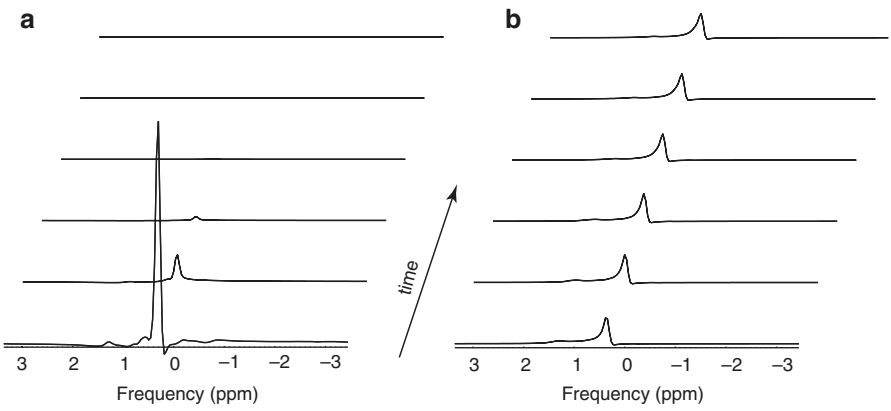

Fig. 4.18 Double spin-echo techniques with adiabatic refocussing pulses can preserve the hyperpolarised magnetisation along the z axis following a 5° excitation, and therefore perform localised spectroscopy for many subsequent acquisitions (**b**). In comparison, an errant 90° pulse effectively ends the experiment by sampling the entirety of M_0 (**a**) (Figure ©2007 Elsevier, reproduced (adapted) with permission [171])

Finally, it is worth noting that hyperpolarised perfusion agents are relatively unique in not requiring the separation of both chemical and spatial information to be of utility. As a consequence, more traditional single-shot imaging techniques, such as spiral or echo-planar acquisitions may be applied, with a low flip angle. In addition, approaches have been reported using balanced "steady-state" free procession type approaches, whereby successive flip angles are chosen to routinely keep the magnetisation vector close to M_z, and a variable flip angle scheme utilised to maximise the effective SNR. Such schemes have excellent spatio-temporal resolution (eight 8 mm slices with a 2.5×2.5 mm^2 voxel size in a 8×8 cm^2 FOV; TR per stack 2.2 s), and claim to be highly SNR efficient, although are subject to exhibiting significant partial volume artefacts [151]. An alternative approach for hyperpolarised perfusion imaging is the use of flow suppression gradients to 'toggle' dephasing of rapidly moving spins, removing signal from the lumen of the great vessels or ventricles in order to visualise the cardiac tissue bed [116, 156].

Chemical Shift Imaging

Traditionally, Chemical Shift Imaging (CSI) represents a straightforward and effective 'gold standard' tool to obtain both spatial and spectral information about the bio-distribution and biochemistry of a probe following its *in vivo* administration. However, traditional Cartesian CSI schemes are constructed by the removal of a readout gradient and its replacement with a large number of phase encoding steps in both (x, y) directions following a slab excitation. As a direct consequence, Cartesian CSI has the twin disadvantages of requiring a large number of RF excitations and a large period of time in order to obtain a fully sampled image. As a consequence, a naïve implementation of a CSI pulse sequence would weight the acquisition k space according to the order it was acquired, drastically deplete the longitudinal magnetisation, and prevent the acquisition of temporal information. Nevertheless, the canonical nature of CSI and the fact that it provides 'gold standard' spectral information, usually sampled for a significant period of time, means that it historically found use as the go-to technique for spectroscopic imaging following the injection of hyperpolarised [1-^{13}C]pyruvate into a variety of organisms under different disease conditions, including prostate cancer in man [123, 173, 174]. Typically, the only modification of the sequence required for it to return a single time-point image is the reduction of the flip angle to a few degrees.

Rapid CSI schemes use imaging gradients to encode information, and sequences such as EPSI (Echo Planar Spectroscopic Imaging) have been shown to be of utility in imaging the *in vivo* metabolism of [1-^{13}C]pyruvate following its infusion. Darpolor et al. report the successful acquisition of a 3D spectroscopic dataset with a $\sim 3.5 \times 3.5 \times 5$ mm^3 voxel size, a 500 Hz spectral bandwidth (spectral resolution 7.8 Hz, sufficient to resolve the peaks at 3 T) and a $\sim$ 35 s image TR [175, 176]. Whilst such spatial resolution is adequate for pre-clinical studies using the majority of probes investigated so far, the main disadvantage of such CSI sequences, however, is that their long acquisition time effectively preclude the resolution of tempo-

ral processes. Additionally, the introduction of any uncertainty of the injection profile of the hyperpolarised agent could have unexpected consequences in the image domain. For example, if a centric-ordered CSI acquisition was planned to acquire the origin of *k*-space in the first shot an unexpected delay in injection timing would lead to its lack of acquisition.

As a consequence, several complimentary schemes have been proposed to maintain the ability to spectrally resolve different hyperpolarised metabolites, but dramatically reduce the length of time of the CSI sequence. Whilst novel reconstruction techniques may offer the ability to directly truncate the acquisition of spectral data from the EPSI sequence [177], the most popular approaches either undersample the spatial Fourier domain, and use compressed sensing techniques to reconstruction an appropriate dataset [178–180]; or, alternatively, effectively undersample the frequency domain via one of a number of different methods. It is these latter methods that have proven more popular, and are able to further decrease the limiting spatial and temporal resolution of hyperpolarised imaging techniques.

In the context of an injected, labelled hyperpolarised probe, it is usually the case that its *in vivo* biochemistry is approximately known *a priori*: for example, the downstream metabolic products following the injection of hyperpolarised [1-^{13}C] pyruvate are well known (and are illustrated in Fig. 4.10), and hence the degree of spectral resolution actually required is essentially highly limited; it is the relative intensity of the different metabolites as a function of time that is of interest, not their spectral location. This realisation has lead to two productive areas of pulse sequence development: IDEAL CSI, in which a spatially selective excitation with a spectral bandwidth sufficient to excite each of the n expected metabolites is applied, and an 'ordinary' rapid imaging readout sequence (EPI, spiral) applied with n different echo times. Construction and subsequent deconvolution of the relevant Fourier matrix allows for the reconstruction of n individual images, corresponding to each metabolite. This approach is robust in the sense that it only requires approximately accurate information about the spectral location of each resonance, and it is fast and readily combined with existing readout techniques to produce a high-resolution final image [181]. As a consequence, IDEAL techniques have been applied *in vivo* with hyperpolarised [1-^{13}C]pyruvate, and able to resolve metabolism with a spatial resolution of 5 × 5 × 10 mm and a temporal resolution of 4 s [182]. IDEAL sequences are therefore able to dynamically resolve the metabolism of hyperpolarised [1-^{13}C] pyruvate *in vivo*, in the anaesthetised rodent heart, as illustrated in Fig. 4.19. Provided that the number of expected resonances is comparatively small, such approaches provide an effective way to undersample the spectral domain of the hyperpolarised experiment in order to improve spatio-temporal resolution, although it is reported that they are subject to ringing artefacts if there is a large difference in signal amplitude between the injected probe and its downstream metabolite [58, 183].

An alternative approach to metabolic imaging is the selective excitation of metabolites of interest, followed by the use of conventional imaging strategies. Spectral-spatial radiofrequency pulses are selective both in space and in the frequency domain, originally developed for fat-water imaging, and have found wide application in hyperpolarised studies [145, 172, 184–188]. Such pulses consist of an oscillating slice-select gradient train with a 'comb' of radiofrequency pulses played

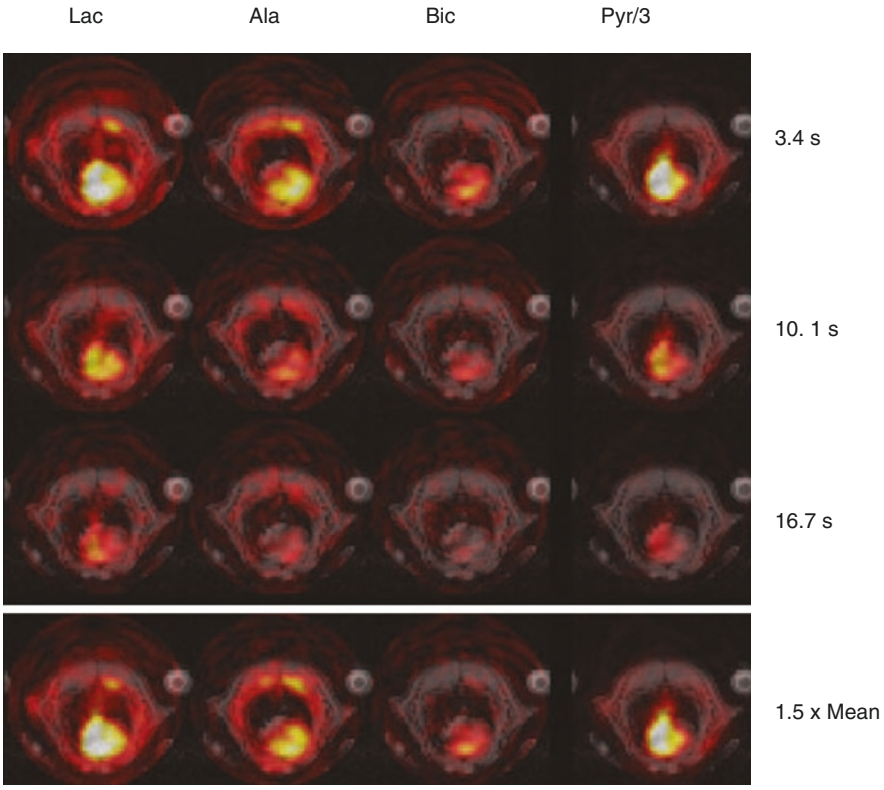

Fig. 4.19 Spectrally and spatially resolved metabolic imaging of the rat heart following the injection of hyperpolarised [1-^{13} C]pyruvate, acquired by a spiral IDEAL pulse sequence and 5 × 5 × 10 mm /4 s resolution. Individual metabolites are shown at three points in team, and also 15 × their mean signal intensity Note how pyruvate can be observed perfusing the ventricles of the heart at early times, with the concomitant production of alanine and lactate occurring at later times. Some degree of 'ringing' is present in the initial lactate, bicarbonate and alanine (Ala) images, reflecting the large magnitude of the hyperpolarised pyruvate signal compared to downstream metabolites (Figure ©2012 John Wiley & Sons, reprinted (adapted) with permission [181])

out under an overall envelop. Pulses are often developed by a combination of the analytical clarity provided by the low flip angle approximation and the use of an SLR transformation together with numerical optimisation, and are designed to excite only a molecule lying within a particular frequency band, referred to as the passband, within a given slice thickness. Owing to the finite length of the RF pulse (typically ∼ 10 ms), periodicity is apparent in the excitation pattern, leading to the concept of a 'stopband' between each excited passband of magnetisation (as illustrated in Fig. 4.20). Of particular note as a design algorithm are the open source rf tools and Spectral-Spatial-RF-Pulse-Design packages[4], which enable the ready generation of custom spectral-spatial pulses [189]. By changing the transmitter

[4] Both are downloadable from http://rsl.stanford.edu/research/software.html.

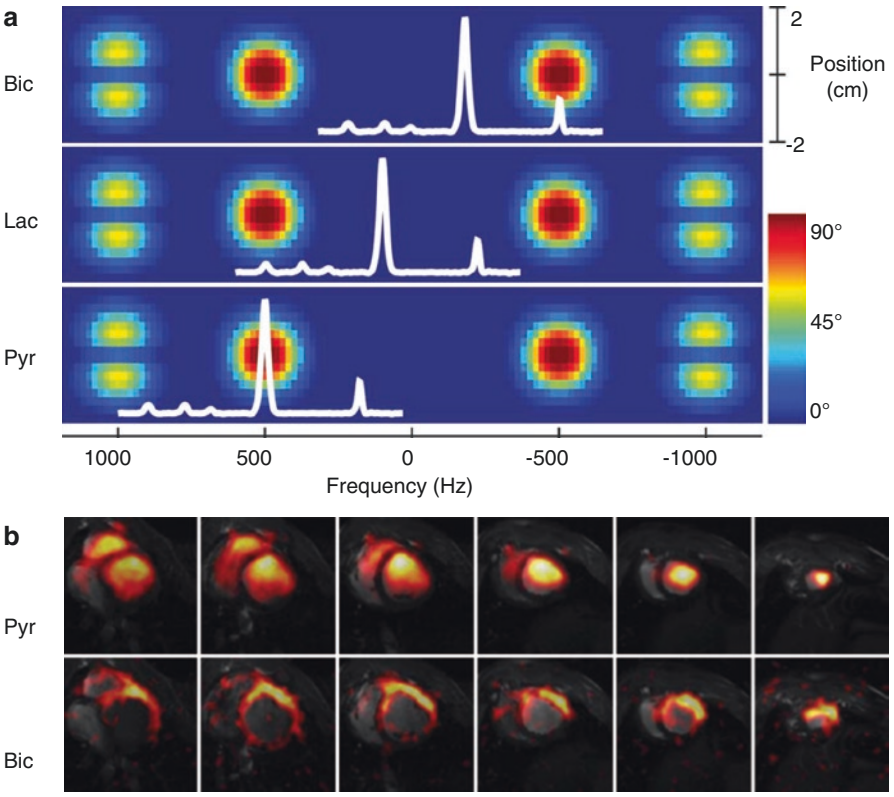

Fig. 4.20 Example $|M_{xy}|$ excitation pattern (**a**) and result (**b**) of a spectral-spatial pulse. (**a**) The net effect of a spectral-spatial pulse is the excitation of magnetisation at a particular frequency (*x-axis*) *and* region of space (*y-axis*). A nodal pattern is produced by the overall duration of the pulse, and the duration of each individual 'sub-pulse' produced. The (spectral) width of the red 'islands' of magnetisation excited by the pulse forms its passband; the width between the two its stopband. Superimposed in white is an example *in vivo* spectrum obtained following the infusion of hyperpolarised [1-^{13}C] pyruvate; by changing the transmitter frequency of the spectrometer, different resonances can be excited by the pulse. (**b**) Results obtained from the pig heart by a multi-slice spiral spectral-spatial experiment following the infusion of hyperpolarised [1-^{13}C]pyruvate. Each image is cropped to a 12 × 12 cm^2 field-of-view; in-plane resolution is 8.8 × 8.8 × 10 mm^3 with a 9 heart-beat (approximately 15 s) temporal resolution (TR = 1 RR interval)

frequency of the pulse, it is possible to therefore excite different metabolites with a different flip angle, and hence leave a larger 'reservoir' of magnetisation by hitting, e.g. [1-^{13}C]pyruvate with a lower flip angle than its downstream metabolic products. Owing to the unidirectional nature of PDH, this is particularly effective when imaging the flux from [1-^{13}C]pyruvate to ^{13}C-bicarbonate; bicarbonate is rapidly regenerated from the injected hyperpolarised [1-^{13}C]pyruvate, and can accordingly be 'hit' with a far larger flip angle than [1-^{13}C]pyruvate can. Once the pulse (with its associated gradient structure) is designed, it is relatively straightforward to incorporate any imaging readout, and iterate between multiple slices and multiple metabolites

in a given acquisition. It should be noted that centric-ordered EPI and inside-out spiral readouts are particularly well suited to spectral-spatial excitation, owing to the fact that they read 'out' into *k*-space, obtaining resolution information for as long as supported by the available T_2^*. It should be noted, however, that spectral-spatial approaches are highly reliant upon accurate *a priori* knowledge of the centre frequency of the metabolite of interest. Therefore, independent of the imaging readout used, they require excellent B_0 homogeneity; a mis-registration between the transmitter frequency and the actual frequency of the labelled hyper-polarised probe of interest would be sufficient to preclude the excitation of it, or its downstream metabolic products.

However, spectral-spatial pulses are typically designed for high-resolution imaging of a particular metabolic probe on a particular individual MR system. As the achievable slice thickness is limited by gradient duty cycle, maximum strength, and fidelity, non-linear distortions readily become apparent in the excitation profile of the spectral-spatial pulse, and as noted by Sigfridsson et al. [188], such limitations effectively place an upper limit on using the technique in a multiple-slice approach. To this end, 3D selective excitation has been proposed with phase encoding in the *z*-direction trading temporal for spatial resolution, optionally with the use of compressed sensing to reduce the effective number of (time-consuming) phase encodes required [190]. Such approaches can yield 3D spectroscopic datasets at comparatively high resolution, such as $2 \times 2 \times 4$ mm^3 with 1.8 s temporal resolution [145]. Such approaches are highly reliant upon accurate flip angle information, as the effect of the depletion of the longitudinal magnetisation throughout the phase encoding of the scan is a blurring through the plane of the image. This blurring can be minimised, and SNR improved compared to the complementary multi-slice approach, if and only if the flip angle delivered is chosen carefully [191, 192]. Such considerations effectively demand the use of a volume coil for RF excitation.

Finally, one complementary approach to the 3D-spectral spatial excitation is the use of multi-band excitation, whereby multiple resonances are excited simultaneously, but with differing flip angles [189, 193]. Standard chemical shift imaging techniques can then be used as imaging readouts, and metabolic information obtained with approximately equal SNR between the observed metabolites. Likewise, multi-band approaches can be effectively undersampled, resulting in schemes that require a short RF excitation to hit different metabolites with appropriate flip angles (as illustrated in Fig. 4.21) [188]. Such short RF pulses (and associated gradient trains) place substantially lower demands on gradient hardware than the majority of spectral-spatial pulses. A multi-echo readout can therefore reconstruct an image of each excited metabolite. This approach, however, is susceptible to frequency errors, which again would correspond to errors in the delivered flip angle, potentially 'squashing' the magnetisation in the injected probe prematurely. An alternative approach designed to be more tolerant of field inhomogeneities that might cause variation in flip angle is the use of spatiotemporal encoding (SPEN) techniques that rely upon the selective excitation of particular hyperpolarised moieties via a technically distinct class of multidimensional excitation. SPEN excitation requires a frequency-swept pulse applied in the presence of an encoding gradient, followed by its

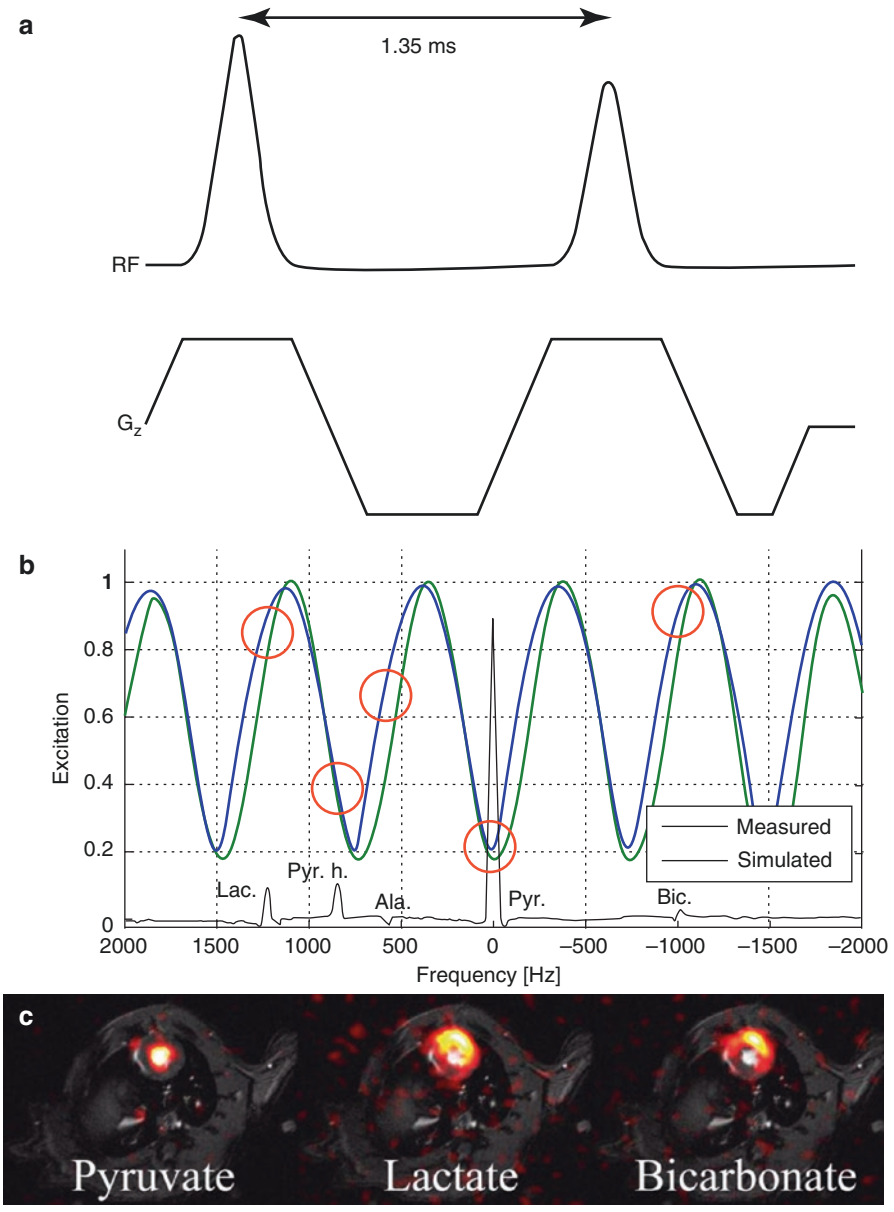

Fig. 4.21 Multiband excitation is comparatively straightforward to implement, with two RF pulses (**a**) producing a sinusoidal pattern of excitation as a function of frequency (**b**). As highlighted by *red circles*, this corresponds to an effective flip angle modulation over the [1-^{13}C]pyruvate spectrum, permitting the excitation of different metabolites with different flip angles. A multi-echo readout correspondingly allows for the reconstruction of images with approximately equivalent SNR in all three channels of interest for cardiac imaging (**c**) (Figure ©2015 John Wiley and Sons, reproduced (adapted) with permission [188])

later removal using an acquisition gradient, and are therefore not necessarily subject to the same ultimate hardware limitations in slice thickness and spectral separation as spectral-spatial excitation [194, 195]. Whilst such methods are fundamentally distinct from the majority of MR acquisitions, and may form a promising avenue for future research, their use in a cardiac imaging remains somewhat limited.

Concluding Remarks

Hyperpolarisation represents a novel method for dramatically expanding the type of biological processes that can be probed by magnetic resonance techniques. Barely more than a decade after the invention of the dissolution-DNP technique by Ardenkjaer-Larsen et al. [36], the use of DNP to generate novel probes of diseases relevant to mammalian health has been extensively shown in many different species, recently including humans [123]. Hyperpolarised [1-^{13}C]pyruvate makes for an effective and versatile probe of central metabolism, which is profoundly altered during cardiac pathology, is safe for use in humans, and is in the process of transitioning to the clinic [123, 196]. Nevertheless, the wide variety of other probes that have been investigated, including those hyperpolarised by techniques other than d-DNP, is a testament to its inherent versatility.

Technically, hyperpolarised imaging sequences are exceptionally complex, often running at or marginally beyond the hardware limitations of the machines on which they were developed. It is therefore almost impossible to recommend a stock sequence for a generalised hypothetical experiment. As ever with magnetic resonance, the large number of Fourier relationships between spatial, spectral and temporal resolution serve to make high resolution spectroscopic imaging a difficult proposition, although the use of spectral-spatial pulses to effectively downsample the spectral domain have enabled high spatio-temporal resolution imaging of the metabolism of [1-^{13}C]pyruvate. Typically, most other probes are developed and initially applied by the use of (un)-localised spectroscopy, with initial imaging applications explored by the use of a "more conventional" spectrally resolved rapid CSI technique. Such protocols are easy to devise, and have little prerequisites. Provided that the flip angle per shot is kept low ($\theta < 20°$), and both the excitation and readout bandwidth are suitable for the probe under study, such acquisitions are likely to be successful.

Whilst the financial barrier of entry to hyperpolarised MR is exceptionally high -commercial d-DNP polarisers typically are comparable in cost to high-field preclinical imaging magnets, have large running costs, and are required to be sited near a multinuclear capable MR system – the technique is able to provide truly novel information about almost the entirety of central metabolism in a necessarily limited time. It is therefore comparatively easy to incorporate hyperpolarised MR information into extant studies without significantly increasing the total scan time; given a choice of molecular probe, $5T_1$ represents an effective upper bound on the additional duration that the acquisition can take. Hyperpolarised MR, therefore, could be seen as adding significant value to any multi-parametric study of disease.

Graphical Summary: Myocyte Metabolic Imaging with Hyperpolarised MRI

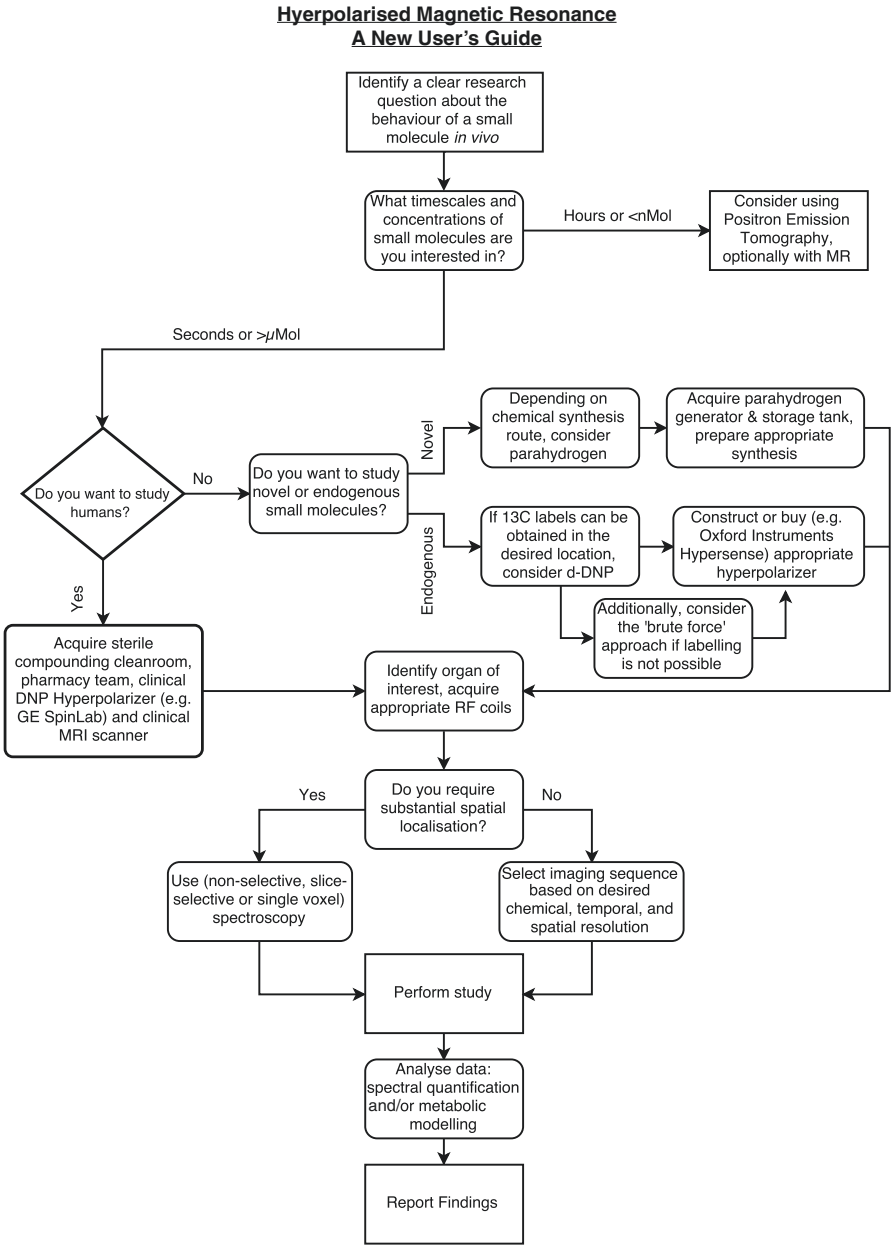

Acknowledgements JJM would like to acknowledge the kind financial support provided by an EPSRC Doctoral Prize Fellowship, ref. EP/M508111/1; the National Institute for Health Research (NIHR) Oxford Biomedical Research Centre Programme, British Heart Foundation Fellowships (FS/10/002/28078, FS/14/17/30634), British Heart Foundation Programme Grant (RG/11/9/28921), and St. Hugh's College, Oxford.

References

1. Wiesinger F, Boesiger P, Pruessmann KP. Magn Reson Med. 2004;52(2):376. doi:10.1002/mrm.20183. URL: http://doi.wiley.com/10.1002/mrm.20183.
2. Binney J, Skinner D. The physics of quantum mechanics. Oxford: Oxford University Press; 2013.
3. Slichter CP. Principles of magnetic resonance. Berlin: Springer; 1990. URL: http://www.springer.com/gb/book/9783540501572.
4. Lide DR. CRC handbook of chemistry and physics: a ready-reference book of chemical and physical data. 96th ed. Boca Raton: CRC Press;2008. URL: http://www.worldcat.org/title/crc-handbook-of-chemistry-and-physics-a-ready-reference-book-of-chemical-and-physical-datoclc/910908643.
5. Mo H, Raftery D. J Magn Reson. 2008;190(1):1. doi:10.1016/j.jmr.2007.09. 016. URL: http://www.ncbi.nlm.nih.gov/pubmed/17945521, http:/www.pubmedcentral.nih.gov/articlerender.fcgi?artid=PMC2662483.
6. Navon G, Shinar H, Eliav U, Seo Y. NMR Biomed. 2001:112–32. doi:10.1002/nbm.687. URL: http://onlinelibrary.wiley.com/doi/10.1002/nbm.687/full.
7. Szczepaniak LS, Dobbins RL, Metzger GJ, Sartoni-D'Ambrosia G, Arbique D, Vongpatanasin W, Unger R, Victor RG. Magn Reson Med. 2003;49(3):417. doi:10.1002/mrm.10372. URL: http://doi.wiley.com/10.1002/mrm.10372.
8. Ward KM, Aletras AH, Balaban RS. J Magn Reson. 2000;143(1):79. doi:10.1006/jmre.1999.1956. URL: http://linkinghub.elsevier.com/retrieve/pii/S1090780799919560, http://www.sciencedirect.com/science/article/pii/S1090780799919560.
9. Ruiz-Cabello J, Barnett BP, Bottomley PA, Bulte JWM. NMR Biomed. 2011;24(2):114. doi:10.1002/nbm.1570. URL: http://www.ncbi.nlm.nih.gov/pubmed/20842758, http://www.pubmedcentral.nih.gov/articlerender.fcgi?artid=PMC3051284.
10. Bernstein MA, King KF, Zhou XJ. Handbook of MRI pulse sequences: Elsevier; 2004. URL: http://books.google.com/books?id=d6PLHcyejEIC{\&}pgis=1.
11. Robitaille PM, Berliner LJ. Ultra high field magnetic resonance imaging. Boston: Springer; 2006.
12. Diakova G, Korb JP, Bryant RG. Magn Reson Med. 2012;68(1):272. doi 10.1002/mrm.23229. URL: http://www.ncbi.nlm.nih.gov/pubmed/22144333.
13. Bottomley PA, Foster TH, Argersinger RE, Pfeifer LM. Med Phys. 1984;11(4):425. doi:10.1118/1.595535. URL: http://scitation.aip.org/content/aapm/journal/medphys/11/4/10.1118/1.595535.
14. Gadian DG, Panesar KS, Linde AJP, Horsewill AJ, Köckenberger W, Owers-Bradley JR. Phys Chem Chem Phys. 2012;14(16):5397. doi:10.1039/C2CP23536F. URL: http://www.ncbi.nlm.nih.gov/pubmed/22407281.
15. Cho A. Science. 2009;326(5954):778. doi:10.1126/science.326 778. URL: http://www.ncbi.nlm.nih.gov/pubmed/19892947.
16. Hirsch ML, Kalechofsky N, Belzer A, Rosay M, Kempf JG. J Am Chem Soc. 2015;137(26):8428. doi:10.1021/jacs.5b01252. URL: http://pubs.acs.org/doi/abs/10.1021/jacs.5b01252.
17. Leachman JW, Jacobsen RT, Penoncello SG, Lemmon EW. J Phys Chem Ref Data. 2009;38(3):721. doi:10.1063/1.3160306. URL: http://scitation.aip.org/content/aip/journal/jpcrd/38/3/10.1063/1.3160306.
18. Farkas A. Orthohydrogen, parahydrogen and heavy hydrogen: CUP Archive; 1935. URL: https://books.google.co.uk/books?id=GzE9AAAAIAAJ.
19. Heaton CA. An introduction to industrial chemistry. Netherlands: Springer; 2012. URL: https://books.google.co.uk/books?id=yPYLBwAAQBAJ.
20. Bowers CR, Weitekamp DP. J Am Chem Soc. 1987;109(18):5541. doi:10.1021/ja00252a049. URL: http://dx.doi.org/10.1021/ja00252a049.
21. Pravica MG, Weitekamp DP, Pavrica MG, Weitekamp DP. Chem Phys Lett. 1988;145(4):255. doi:10.1016/0009-2614(88)80002-2. URL: http://linkinghub.elsevier.com/retrieve/pii/0009261488800022.

22. Adams RW, Aguilar JA, Atkinson KD, Cowley MJ, Elliott PIP, Duckett SB, Green GGR, Khazal IG, López-Serrano J, Williamson DC. Science. 2009;323(5922):1708. doi:10.1126/science.1168877.
23. Green RA, Adams RW, Duckett SB, Mewis RE, Williamson DC, Green GGR. The theory and practice of hyperpolarization in magnetic resonance using parahydrogen. Prog Nucl Magn Reson Spectrosc. 2012;67:1–48. doi:10.1016/j.pnmrs.2012.03.001.
24. Haake M, Natterer J, Bargon J. J Am Chem Soc. 1996;118(36):8688. doi:10.1021/ja960067f.
25. Chekmenev EY, Hövener J, Norton VA, Harris K, Batchelder LS, Bhattacharya P, Ross BD, Weitekamp DP. J Am Chem Soc. 2008;130(13):4212. doi:10.1021/ja7101218.
26. Zacharias NM, Chan HR, Sailasuta N, Ross BD, Bhattacharya P. J Am Chem Soc. 2012;134(2):934. doi:10.1021/ja2040865. URL: http://pubs.acs.org/doi/abs/10.1021/ja2040865.
27. Golman K, Axelsson O, Jóhannesson H, Månsson S, Olofsson C, Petersson JS. Magn Reson Med. 2001;46(1):1. doi:10.1002/mrm.1152. URL: http://doi.wiley.com/10.1002/mrm.1152.
28. Bhattacharya P, Chekmenev EY, Reynolds WF, Wagner S, Zacharias N, Chan HR, Bünger R, Ross BD. NMR Biomed. 2011;24(8):1023. doi:10.1002/nbm.1717. URL: http://doi.wiley.com/10.1002/nbm.1717.
29. Abragam A, Goldman M. Reports Prog Phys. 1978;41:395. doi:10.1088/0034-4885/41/3/002. URL: http://iopscience.iop.org/0034-4885/41/3/002.
30. Comment A, Van Den Brandt B, Uffmann K, Kurdzesau F, Jannin S, Konter JA, Hautle P, Wenckebach WT, Gruetter R, Van Der Klink JJ. Concepts Magn Reson. 2007;31B(1):255. doi:10.1002/cmr.b. URL: http://doi.wiley.com/10.1002/cmr.b.20099.
31. Borghini M. Phys Rev Lett. 1968;20(9):419. doi:10.1103/PhysRevLett.20.419. URL: http://link.aps.org/doi/10.1103/PhysRevLett.20.419.
32. Kozhushner MA, Sov J. Phys. 1969;29(1):136. URL: http://jetp.ac.ru/cgi-bin/dn/e{_}029{_}01{_}0136.pdf.
33. Saunders M. Enhancing the sensitivity of NMR by Dynamic Nuclear Polarisation. Ph.D. thesis, University of Birmingham; 2010. URL: http://etheses.bham.ac.uk/2962/1/Saunders11PhD.pdf.
34. Serra SC, Rosso A, Tedoldi F. Phys Chem Chem Phys. 2012;14(38):13299. doi:10.1039/c2cp41947e. URL: http://pubs.rsc.org/en/content/articlehtml/2012/cp/c2cp41947e.
35. Serra SC, Rosso A, Tedoldi F. Phys Chem Chem Phys. 2013;15(21):8416. doi:10.1039/c3cp44667k. URL: http://pubs.rsc.org/en/content/articlehtml/2013/cp/c3cp44667k.
36. Ardenkjaer-Larsen JH, Fridlund B, Gram A, Hansson G, Hansson L, Lerche MH,Servin R, Thaning M, Golman K. Proc Natl Acad Sci U S A. 2003;100(18):10158. doi 10.1073/pnas.1733835100. URL: http://www.pnas.org/content/100/18/10158.full.
37. Abragam A. The principles of nuclear magnetism. Oxford: Oxford University Press; 1961. URL: https://global.oup.com/academic/product/the-principles-of-nuclear-magnetism-9780198520146.
38. Jawla S, Ni QZ, Barnes A, Guss W, Daviso E, Herzfeld J, Griffin R, Temkin R. J Infrared Millimeter Terahertz Waves. 2013;34(1):42. doi:10.1007/s10762-012-9947-1. URL: http://www.ncbi.nlm.nih.gov/pubmed/23539422.
39. Ardenkjaer-Larsen JH, Leach AM, Clarke N, Urbahn J, Anderson D, Skloss TW. NMR Biomed. 2011;24(8):927. doi:10.1002/nbm.1682. URL: http://www.ncbi.nlm.nih.gov/pubmed/21416540.
40. Culvahouse JW, Unruh WP, Brice DK. Phys Rev. 1963;129(6):2430. doi:10.1103/PhysRev.129.2430. URL: http://link.aps.org/doi/10.1103/PhysRev.129.2430.
41. Lama B, Collins JHP, Downes D, Smith AN, Long JR. Expeditious dissolution dynamic nuclear polarization without glassing agents. NMR Biomed. 2016;29(3):226–31. doi:10.1002/nbm.3473. URL: http://doi.wiley.com/10.1002/nbm.3473.
42. Gallagher FA, Kettunen MI, Hu DE, Jensen PR, Zandt RI, Karlsson M, Gisselsson A, Nelson SK, Witney TH, Bohndiek SE, Hansson G, Peitersen T, Lerche MH, Brindle KM. Proc Natl Acad Sci U S A. 2009;106(47):19801. doi:10.1073/pnas.0911447106. URL: http://www.pnas.org/content/106/47/19801.short, http://www.pnas.org/cgi/content/long/106/47/19801.

43. Shang H, Skloss T, von Morze C, Carvajal L, Van Criekinge M, Milshteyn E, Larson PEZ, Hurd RE, Vigneron DB. Magn Reson Med. 2015;75(2):917–22. doi:10.1002/mrm.25657. URL: http://www.ncbi.nlm.nih.gov/pubmed/25765516.
44. Milani J, Vuichoud B, Bornet A, Miéville P, Mottier R, Jannin S, Bodenhausen G. Rev Sci Instrum. 2015;86(2) doi:10.1063/1.4908196. URL: http://scitation.aip.org/content/aip/journal/rsi/86/2/10.1063/1.4908196.
45. Vallee JP, Lazeyras F, Khan HG, Terrier F. Eur Radiol. 2000;10(8):1245. doi:10.1007/s003300000434. URL: http://www.ncbi.nlm.nih.gov/pubmed/10939483.
46. Golman K, Ardenkjaer-Larsen JH, Petersson JS, Mansson S, Leunbach I. Proc Natl Acad Sci U S A. 2003;100(18):10435. doi:10.1073/pnas.1733836100. URL: http://www.pnas.org/cgi/doi/10.1073/pnas.1733836100.
47. Reineri F, Boi T, Aime S. Nat Commun. 2015;6:5858. doi:10.1038/ncomms6858. URL: http://www.ncbi.nlm.nih.gov/pubmed/25556844.
48. Alberts B, editor. Molecular biology of the cell: reference edition. Vol 1. 5th ed. Garland Science; 2008. URL: https://www.ncbi.nlm.nih.gov/books/NBK21054/.
49. Dennis SC, Kohn MC, Anderson GJ, Garfinkel D. J Mol Cell Cardiol. 1985;17(10):987. URL: http://www.ncbi.nlm.nih.gov/pubmed/3934390.
50. Poole RC, Halestrap AP. Am J Physiol. 1993;264(4 Pt 1):C761. URL: http://www.ncbi.nlm.nih.gov/pubmed/8476015.
51. Mallet RT. Proc Soc Exp Biol Med. 2000;223(2):136. URL: http://www.ncbi.nlm.nih.gov/pubmed/10654616.
52. Schroeder MA, Atherton HJ, Ball DR, Ma C, Heather LC, Griffin JL, Clarke K, Radda GK, Tyler DJ. FASEB J. 2009;23(8):2529. doi:10.1096/fj.09-129171. URL: https://www.ncbi.nlm.nih.gov/pmc/articles/PMC2717776/?tool=pmcentrez.
53. Miller Jack J, Dynamic nuclear polarisation as a probe of metabolism in pathophysiology. Phd thesis, University of Oxford; 2015. URL: https://ora.ox.ac.uk/objects/uuid:3d6721e0-e57c-42af-91a8-4d2f6d68da5b.
54. Vanhamme L, van den Boogaart A, Van Huffel S. Magn J Reson. 1997;129(1):35. URL: http://www.ncbi.nlm.nih.gov/pubmed/9405214.
55. Stefan D, Cesare F. Meas Sci Technol. 2009;20(10). doi:10.1088/0957-0233/20/10/104035. URL: http://iopscience.iop.org/0957-0233/20/10/104035.
56. Schroeder MA, Swietach P, Atherton HJ, Gallagher FA, Lee P, Radda GK, Clarke K, Tyler DJ. Cardiovasc Res. 2010;86(1):82. doi:10.1093/cvr/cvp396. URL: http://www.ncbi.nlm.nih.gov/pubmed/20008827.
57. Zierhut ML, Yen YF, Chen AP, Bok R, Albers MJ, Zhang V, Tropp J, Park I, Vigneron DB, Kurhanewicz J, Hurd RE, Nelson SJ. J Magn Reson. 2010;202(1):85. doi:10.1016/j.jmr.2009.10.003. URL: http://dx.doi.org/10.1016/j.jmr.2009.10.003.
58. Daniels CJ, McLean MA, Schulte RF, Robb FJ, Gill AB, McGlashan N, Graves MJ, Schwaiger M, Lomas DJ, Brindle KM, Gallagher FA. NMR Biomed. 2016;29(4):387. doi:10.1002/nbm.3468. URL: http://doi.wiley.com/10.1002/nbm.3468.
59. Dorland. Dorland's illustrated medical dictionary. Elsevier Health Sciences; 2011. URL: https://books.google.com/books?id=mNACisYwbZoC{\&}pgis=1.
60. W.H. Organization. Chagas disease (American trypanosomiasis). World Health Organization; 2014. URL: http://www.who.int/mediacentre/factsheets/fs340/en/.
61. Braunwald E, Bonow RO, Mann DL, Zipes DP, Libby P. Braunwald's heart disease: a textbook of cardiovascular medicine. Philadelphia: Elsevier Health Sciences; 2011. URL: https://books.google.com/books?id=b5wADkB9oDoC{\&}pgis=1.
62. McMurray JJV, Pfeffer MA. Lancet. 2005;365(9474):1877. doi:10.1016/S0140-6736(05)66621-4. URL: http://www.sciencedirect.com/science/article/pii/S0140673605666214.
63. Quiroz R, Doros G, Shaw P, Liang CS, Gauthier DF, Sam F. Am J Cardiol. 2014;113(4):691. doi:10.1016/j.amjcard.2013.11.014. URL: http://www.ncbi.nlm.nih.gov/pubmed/24484862.
64. Borlaug BA, Paulus WJ. Eur Heart J. 2011;32(6):670. doi:10.1093/eurheartj/ehq426.
65. Neubauer S. N Engl J Med. 2007;356:1140. doi:10.1056/nejmra063052. URL: http://www.nejm.org/doi/full/10.1056/nejmra063052.

66. Doenst T, Nguyen TD, Abel ED. Circ Res. 2013;113(6):709. doi:10.1161/CIRCRESAHA.113.300376. URL: http://circres.ahajournals.org/content/113/6/709.abstract.
67. Goldhaber JI, Hamilton MA. Circulation. 2010;121(14):1655. doi:10. 1161/CIRCULATIONAHA.109.899294. URL: http://circ.ahajournals.org/content/121/14/1655.full.
68. N.Y. CIBIS Investigators and Committees. Circulation. 1994;90(4):1765. URL: http://www.ncbi.nlm.nih.gov/pubmed/7923660.
69. Packer M, Bristow MR, Cohn JN, Colucci WS, Fowler MB, Gilbert EM, Shusterman NH. N Engl J Med. 1996;334(21):1349. doi:10.1056/NEJM199605233342101. URL: http://dx.doi.org/10.1056/NEJM199605233342101.
70. T. Consensus Trial Study Group. N Engl J Med. 1987;316(23):.1429. doi:10. 1056/NEJM198706043162301. URL: http://www.ncbi.nlm.nih.gov/pubmed/2883575.
71. Pfeffer MA, Braunwald E, Moyé LA, Basta L, Brown EJ, Cuddy TE, Davis BR, Geltman EM, Goldman S, Flaker GC. N Engl J Med. 1992;327(10):669. doi:10. 1056/NEJM199209033271001. URL: http://www.ncbi.nlm.nih.gov/pubmed/1386652.
72. Cohn JN, Tognoni G. N Engl J Med. 2001;345(23):1667. doi:10.1056/NEJMoa010713. URL: http://dx.doi.org/10.1056/NEJMoa010713.
73. Pfeffer MA, Swedberg K, Granger CB, Held P, McMurray JJV, Michelson EL, Olofsson B, Ostergren J, Yusuf S, Pocock S. Lancet. 2003;362(9386):759. URL: http://www.ncbi.nlm.nih.gov/pubmed/13678868.
74. Ghoerghiade M, Bonow R. Circulation. 1998;97(3):282. doi:10.1161/01.CIR.97.3.282.
75. Schulz R, Heusch G. Heart. 2000;84(6):587. URL: https://www.ncbi.nlm.nih.gov/pmc/articles/PMC1729531/.
76. Jacobus WE, Pores IH, Lucas SK, Weisfeldt ML, Flaherty JT. J Mol Cell Cardiol. 1982;14(SUPPL. 3):13. doi:10.1016/0022-2828(82)90124-9.
77. Wolff AA, Rotmensch HH, Stanley WC, Ferrari R. Heart Fail Rev. 2002;7(k):187. URL: http://www.ncbi.nlm.nih.gov/pubmed/11988642.
78. Kennedy JA, Kiosoglous AJ, Murphy GA, Pelle MA, Horowitz JD. J Cardiovasc Pharmacol. 2000;36(6):794. URL: http://www.ncbi.nlm.nih.gov/pubmed/11117381.
79. Holubarsch CJF, Rohrbach M, Karrasch M, Boehm E, Polonski L, Ponikowski P, Rhein S. Clin Sci (Lond). 2007;113(4):205. doi:10.1042/CS20060307. URL: http://www.ncbi.nlm.nih.gov/pubmed/17319797.
80. Birmingham UH. ClinicalTrials.gov. 2011. doi:NCT00989508. URL: https://clinicaltrials.gov/ct2/show/NCT00989508.
81. Lee L, Campbell R, Scheuermann-Freestone M, Taylor R, Gunaruwan P, Williams L, Ashrafian H, Horowitz J, Fraser AG, Clarke K, Frenneaux M. Circulation. 2005;112(21):3280. doi:10.1161/CIRCULATIONAHA.105.551457. URL: http://circ.ahajournals.org/content/112/21/3280.full.
82. Singh S, Beadle R, Cameron D, Rudd A, Bruce M, Jagpal B, Schwarz K, Brindley G, Mckiddie NP, Lang C, Dawson D, Frenneaux M. Future Cardiol. 2014;10(6):693. doi:10.2217/fca.14.62. URL: http://www.futuremedicine.com/doi/abs/10.2217/fca.14.62.
83. Ashrafian H, Frenneaux MP, Opie LH. Circulation. 2007;116(4):434. doi:10.1161/CIRCULATIONAHA.107.702795. URL: http://circ.ahajournals.org/content/116/4/434.
84. Macpherson G. Black's medical dictionary. A&C Black;2002. URL: https://books.google.com/books?id=bUnCAwAAQBAJ{\&}pgis=1.
85. Cross HR, Clarke K, Opie LH, Radda GK. J Mol Cell Cardiol. 1995;27(7):1369. doi:10.1006/jmcc.1995.0130. URL: http://www.ncbi.nlm.nih.gov/pubmed/7473783.
86. Cross HR, Opie LH, Radda GK, Clarke K. Circ Res. 1996;78(3):482. URL: http://www.ncbi.nlm.nih.gov/pubmed/8593707.
87. Stanley WC, Cardiovasc J. Pharmacol Ther. 2004;9(Suppl 1):S31. URL: http://www.ncbi.nlm.nih.gov/pubmed/15378130.
88. Reimer KA, Lowe JE, Rasmussen MM, Jennings RB. Circulation. 1977;56(5):786. URL: http://www.ncbi.nlm.nih.gov/pubmed/912839.
89. Di Carli MF, Prcevski P, Singh TP, Janisse J, Ager J, Muzik O, Vander Heide R. J Nucl Med. 2000;41(7):1227. URL: http://www.ncbi.nlm.nih.gov/pubmed/10914914.

90. Conti CR. Clin Cardiol. 1991;14(9):708. doi:10.1002/clc.4960140903. URL: http://www.ncbi.nlm.nih.gov/pubmed/1742904.
91. Dargie H. Heart. 2005;91(2):ii3. doi:10.1136/hrt.2005.062018. URL: http://heart.bmj.com/content/91/suppl{_}2/ii3.abstract.
92. Montalescot G, Andersen HR, Antoniucci D, Betriu A, de Boer MJ, Grip L, Neumann FJ, Rothman MT. Heart. 2004;90(6):e37. URL: http://www.pubmedcentral.nih.gov/articlerender.fcgi?artid=1768296{\&}tool=pmcentrez{\&}rendertype=abstract.
93. Zijlstra F, Hoorntje JC, de Boer MJ, Reiffers S, Miedema K, Ottervanger JP, van't Hof AW, Suryapranata H. N Engl J Med. 1999;341(19):1413. doi:10.1056/NEJM199911043411901. URL: http://www.ncbi.nlm.nih.gov/pubmed/10547403.
94. Frangogiannis NG, Smith CW, Entman ML. Cardiovasc. Res. 2002;53(1):31. URL: http://www.ncbi.nlm.nih.gov/pubmed/11744011.
95. Dobaczewski M, Xia Y, Bujak M, Gonzalez-Quesada C, Frangogiannis NG. Am J Pathol. 2010;176(5):2177. doi:10.2353/ajpath.2010.090759. URL: http://www.pubmedcentral.nih.gov/articlerender.fcgi?artid= 2861083{\&}tool=pmcentrez{\&}rendertype=abstract.
96. Huebener P, Abou-Khamis T, Zymek P, Bujak M, Ying X, Chatila K, Haudek S, Thakker G, Frangogiannis NG. J Immunol. 2008;180(4):2625. URL: http://www.ncbi.nlm.nih.gov/pubmed/18250474.
97. de Lemos JA, Morrow DA, Blazing MA, Jarolim P, Wiviott SD, Sabatine MS, Califf RM, Braunwald E. J Am Coll Cardiol. 2007;50(22):2117. doi:10.1016/j.jacc.2007. 06.057. URL: http://www.ncbi.nlm.nih.gov/pubmed/18036447.
98. Roberts R, DeMello V, Sobel BE. Circulation. 1976;53(3 Suppl):I204. URL: http://www.ncbi.nlm.nih.gov/pubmed/1253361.
99. Faxon DP, Gibbons RJ, Chronos NAF, Gurbel PA, Sheehan F. J Am Coll Cardiol. 2002;40(7):1199. URL: http://www.ncbi.nlm.nih.gov/pubmed/12383565.
100. Armstrong PW, Granger CB, Adams PX, Hamm C, Holmes D, O'Neill WW, Todaro TG, Vahanian A, Van de Werf F. JAMA. 2007;297(1):43. doi:10.1001/jama.297.1.43. URL: http://www.ncbi.nlm.nih.gov/pubmed/17200474.
101. Ichihara S, Senbonmatsu T, Price E, Ichiki T, Gaffney FA, Inagami T. Circulation. 2002;106(17):2244. doi:10.1161/01.CIR.0000033826.52681.37. URL: http://www.ncbi.nlm.nih.gov/entrez/query.fcgi?cmd=Retrieve{\&}db=PubMed{\&}dopt=Citation{\&}list{_}uids=12390955.
102. Silverman HS, Pfeifer MP. Am J Cardiol. 1987;59(4):363. doi:10.1016/0002-9149(87)90817-4.
103. Seropian IM, Toldo S, Van Tassell BW, Abbate A. J Am Coll Cardiol. 2014;63(16):1593. doi:10.1016/j.jacc.2014.01.014. URL: http://linkinghub.elsevier.com/retrieve/pii/S0735109714003258.
104. Fox CJ, Hammerman PS, Thompson CB. Nat Rev Immunol. 2005;5(11):844. doi:10.1038/nri1710. URL: http://www.ncbi.nlm.nih.gov/pubmed/16239903.
105. Maciver NJ, Jacobs SR, Wieman HL, Wofford JA, Coloff JL, Rathmell JC, Leukoc J. Biol. 2008;84(u):949. doi:10.1189/jlb.0108024. URL: http://www.pubmedcentral.nih.gov/articlerender.fcgi?artid=2638731{\&}tool=pmcentrez{\&}rendertype=abstract.
106. Florholmen G, Aas V, Rustan AC, Lunde PK, Straumann N, Eid H, Odegaard A, Dishington H, Andersson KB, Christensen G. J Mol Cell Cardiol. 2004;37(6):1183. doi:10.1016/j.yjmcc.2004.09.008. URL: http://www.ncbi.nlm.nih.gov/pubmed/15572048.
107. Chatham JC, Young ME. Circ Res. 2012;111(6):666. doi:10.1161/CIRCRESAHA.112.277392. URL: http://circres.ahajournals.org/content/111/6/666.full.
108. Herrmann G, Decherd GM. Ann Intern Med. 1939;12(8):1233. doi:10.7326/0003-4819-12-8-1233. URL: http://annals.org/article.aspx?articleid=671709.
109. Merritt ME, Harrison C, Storey C, Jeffrey FM, Sherry AD, Malloy CR. Proc Natl Acad Sci U S A. 2007;104(50):19773. doi:10.1073/pnas.0706235104. URL: http://www.pnas.org/content/104/50/19773.short.
110. Schroeder MA, Cochlin LE, Heather LC, Clarke K, Radda GK, Tyler DJ. Proc Natl Acad Sci U S A. 2008;105:12051. doi:10.1073/pnas.0805953105. URL: http://dx.doi.org/10.1073/pnas.0805953105.

111. Golman K, Petersson JS, Magnusson P, Johansson E, Åkeson P, C-MM C, Hansson G, Mansson S. Magn Reson Med. 2008;59(5):1005. doi:10.1002/mrm.21460. URL: http://doi.wiley.com/10.1002/mrm.21460.
112. Ball DR, Cruickshank R, Carr CA, Stuckey DJ, Lee P, Clarke K, Tyler DJ. NMR Biomed. 2013;26(11):1441. doi:10.1002/nbm.2972. URL: http://www.ncbi.nlm.nih.gov/pubmed/23775685.
113. Crittenden MD. Ann Thorac Surg. 2001;72:S2220. doi 10.1016/S0003-4975(01)03296-9. URL: http://www.sciencedirect.com/science/article/pii/S0003497501032969.
114. Khabbaz KR, Zankoul F, Warner KG. Ann Thorac Surg. 2001;72(6):S2227. doi:10.1016/S0003-4975(01)03284-2. URL: http://www.sciencedirect.com/science/article/pii/S0003497501032842.
115. Schroeder MA, Clarke K, Neubauer S, Tyler DJ. Circulation. 2011;124(14):1580. doi:10.1161/CIRCULATIONAHA.111.024919. URL: http://www.ncbi.nlm.nih.gov/pubmed/21969318.
116. Lau AZ, Miller JJ, Robson MD, Tyler DJ. Magn Reson Med. 2016; doi:10.1002/mrm.26106. URL: http://www.ncbi.nlm.nih.gov/pubmed/26743440.
117. Schroeder MA, Ali MA, Hulikova A, Supuran CT, Clarke K, Vaughan-Jones RD, Tyler DJ, Swietach P. Proc Natl Acad Sci U S A. 2013;110(10):E958. doi:10.1073/pnas.1213471110. URL: http://www.pubmedcentral.nih.gov/articlerender.fcgi?artid=3593844{\&}tool=pmcentrez{\&}rendertype=abstract.
118. Lau AZ, Miller JJ, Tyler DJ. Magn Reson Med. 2016; doi:10.1002/mrm.26260. URL: http://www.ncbi.nlm.nih.gov/pubmed/27173806.
119. Schroeder MA, Lau AZ, Chen AP, Gu Y, Nagendran J, Barry J, Hu X, Dyck JRB, Tyler DJ, Clarke K, Connelly KA, Wright GA, Cunningham CH. Eur J Heart Fail. 2013;15(2):130. doi:10.1093/eurjhf/hfs192. URL: http://www.pubmedcentral.nih.gov/articlerender.fcgi?artid=3547367{\&}tool=pmcentrez{\&}rendertype=abstract.
120. Dodd MS, Ball DR, Schroeder MA, Le Page LM, Atherton HJ, Heather LC, Seymour AM, Ashrafian H, Watkins H, Clarke K, Tyler DJ. Cardiovasc Res. 2012;95(1):69. doi:10.1093/cvr/cvs164. URL: http://cardiovascres.oxfordjournals.org/content/95/1/69.short.
121. Seymour AML, Giles L, Ball V, Miller JJ, Clarke K, Carr CA, Tyler DJ, Cardiovasc Res. 2015; cvv101. doi 10.1093/cvr/cvv101. URL: http://cardiovascres.oxfordjournals.org/content/106/2/249.
122. Schillaci G, Pirro M, Vaudo G, Gemelli F, Marchesi S, Porcellati C, Mannarino E. J Am Coll Cardiol. 2004;43(10):1817. doi:10.1016/j.jacc.2003.12.049. URL: http://linkinghub.elsevier.com/retrieve/pii/S073510970400436X.
123. Nelson SJ, Kurhanewicz J, Vigneron DB, PEZ L, Harzstark AL, Ferrone M, van Criekinge M, Chang JW, Bok R, Park I, Reed G, Carvajal L, Small EJ, Munster P, Weinberg VK, Ardenkjaer-Larsen JH, Chen AP, Hurd RE, Odegardstuen LI, Robb FJ, Tropp J, Murray JA. Sci Transl Med. 2013;5(198):108. doi:10.1126/scitranslmed. 3006070. URL: http://www.ncbi.nlm.nih.gov/pubmed/23946197.
124. Hanahan D, Weinberg RA. Cell. 2011;144(5):646. doi:10.1016/j.cell.2011.02.013. URL: http://dx.doi.org/10.1016/j.cell.2011.02.013.
125. Rider OJ, Tyler DJ. J Cardiovasc Magn Reson. 2013;15(1):93. doi:10.1186/1532-429X-15-93. URL: http://jcmr-online.com/content/15/1/93.
126. Jeong H, Tombor B, Albert R, Oltvai ZN, Barabási AL. Nature. 2000;407(6804):651. doi:10.1038/35036627. http://dx.doi.org/10.1038/35036627.
127. Gallagher FA, Kettunen MI, Day SE, Hu DE, Ardenkjaer-Larsen JH, Zandt RI, Jensen PR, Karlsson M, Golman K, Lerche MH, Brindle KM. Nature. 2008;453(7197):940. doi:10.1038/nature07017. URL: http://dx.doi.org/10.1038/nature07017.
128. Gallagher FA, Kettunen MI, Day SE, Lerche M, Brindle KM. Magn Reson Med. 2008;60(2):253. doi:10.1002/mrm.21650. URL: http://doi.wiley.com/10.1002/mrm.21650.
129. Drake KJ, Sidorov VY, McGuinness OP, Wasserman DH, Wikswo JP. Exp Biol Med. 2012;237(12):1369. doi:10.1258/ebm.2012.012025. URL: http://www.ncbi.nlm.nih.gov/pubmed/23354395.

130. Kennedy BWC, Kettunen MI, Hu DE, Brindle KM. J Am Chem Soc. 2012;134(10):4969. doi:10.1021/ja300222e. URL: http://pubs.acs.org/doi/abs/10.1021/ja300222e.
131. Kettunen MI, Kennedy BWC, Hu DE, Brindle KM. Magn Reson Med. 2013;70(5):1200. doi:10.1002/mrm.24591. URL: http://www.ncbi.nlm.nih.gov/pubmed/23280500.
132. Bastiaansen JAM, Yoshihara HAI, Takado Y, Gruetter R, Comment A. Hyperpolarized 13C lactate as a substrate for in vivo metabolic studies in skeletal muscle. Metabolomics. 2014;10(5):986–94. doi:10.1007/s11306-014-0630-5. URL: http://link.springer.com/10.1007/s11306-014-0630-5.
133. Shchepin RV, Coffey AM, Waddell KW, Chekmenev EY. Anal Chem. 2014;86(12):5601. doi:10.1021/ac500952z. URL: http://pubs.acs.org/doi/abs/10.1021/ac500952z.
134. Harris T, Degani H, Frydman L. NMR Biomed. 2013;26(12):1831. doi:10.1002/nbm. 3024. URL: http://www.ncbi.nlm.nih.gov/pubmed/24115045.
135. Timm KN, Hartl J, Keller MA, Hu DE, Kettunen MI, Rodrigues TB, Ralser M, Brindle KM. Magn Reson Med. 2015;74(6):1543. doi:10.1002/mrm.25561. URL: http://www.ncbi.nlm.nih.gov/pubmed/25522215.
136. Ball DR, Rowlands B, Dodd MS, Le Page L, Ball V, Carr CA, Clarke K, Tyler DJ. Magn Reson Med. 2014;71(5):1663. doi:10.1002/mrm.24849. URL: http://dx.doi.org/10.1002/mrm.24849.
137. Bastiaansen J, Merritt M, Comment A. J Cardiovasc Magn Reson. 2015;17(1):1. doi:10.1186/1532-429x-17-s1-o15. URL: http://dx.doi.org/10.1186/1532-429X-17-S1-O15.
138. Yoshihara H, Bastiaansen JA, Karlsson M, Lerche MH, Comment A, Schwitter J. J Cardiovasc Magn Reson. 2015;17(Suppl. 1):O101. doi:10.1186/1532-429X-17-S1-O101. URL: http://jcmr-online.biomedcentral.com/articles/10.1186/1532-429X-17-S1-O101.
139. JAM B, Cheng T, Mishkovsky M, JMN D, Comment A, Gruetter R. Biochim Biophys Acta - Gen Subj. 2013;1830(8):4171. doi:10.1016/j.bbagen.2013.03. 023.
140. Flori A, Liserani M, Frijia F, Giovannetti G, Lionetti V, Casieri V, Positano V, Aquaro GD, Recchia FA, Santarelli MF, Landini L, Ardenkjaer-Larsen JH, Menichetti L. Contrast Media Mol Imaging. 2015;10(3):194. doi:10.1002/cmmi.1618. URL: http://doi.wiley.com/10.1002/cmmi.1618.
141. Clatworthy MR, Kettunen MI, Hu D-E, Mathews RJ, Witney TH, BWC K, Bohndiek SE, Gallagher FA, Jarvis LB, KGC S, Brindle KM. Proc Natl Acad Sci U S A. 2012;109(33):13374. doi:10.1073/pnas.1205539109. URL: http://www.pnas.org/content/109/33/13374.full.
142. Witney TH, Kettunen MI, De H, Gallagher FA, Bohndiek SE, Napolitano R, Brindle KM. Br J Cancer. 2010;(9):103, 1400. doi:10.1038/sj.bjc. 6605945. URL: http://www.pubmedcentral.nih.gov/articlerender.fcgi?artid=2990617{\&}tool=pmcentrez{\&}rendertype=abstract.
143. Bohndiek SE, Kettunen MI, Hu De E, BWC K, Boren J, Gallagher FA, Brindle KM. J Am Chem Soc. 2011;133(30):11795. doi:10.1021/ja2045925. URL: http://pubs.acs.org/doi/abs/10.1021/ja2045925.
144. Reineri F, Viale A, Ellena S, Alberti D, Boi T, Giovenzana GB, Gobetto R, SSD P, Aime S. J Am Chem Soc. 2012;134(27):11146. doi:10.1021/ja209884h. URL: http://pubs.acs.org/doi/abs/10.1021/ja209884h.
145. Miller JJ, Lau AZ, Teh I, Schneider JE, Kinchesh P, Smart S, Ball V, Sibson NR, Tyler DJ. Magn Reson Med. 2015;75(4):1515. doi:10.1002/mrm.25730. URL: http://doi.wiley.com/10.1002/mrm.25730.
146. Lau AZ, Chen AP, Ghugre NR, Ramanan V, Lam WW, Connelly KA, Wright GA, Cunningham CH. Magn Reson Med. 2010;64(5):1323. doi:10.1002/mrm.22525. URL: http://www.ncbi.nlm.nih.gov/pubmed/20574989.
147. Moses WW. Nucl Instrum Methods Phys Res A. 2011;648(Suppl 1):S236. doi:10.1016/j.nima.2010.11.092. URL: http://www.pubmedcentral.nih.gov/articlerender.fcgi?artid=3144741{\&}tool=pmcentrez{\&}rendertype=abstract.
148. Johansson E, Månsson S, Wirestam R, Svensson J, Petersson JS, Golman K, Ståhlberg F. Magn Reson Med. 2004;51(3):464. doi:10.1002/mrm.20013. URL: http://www.ncbi.nlm.nih.gov/pubmed/15004786, http://doi.wiley.com/10.1002/mrm.20013.

149. von Morze C, Larson PE, Hu S, Yoshihara HA, Bok RA, Goga A, Ardenkjaer-Larsen JH, Vigneron DB. Magn Reson Imaging. 2012;30(3):305. doi:10.1016/j. mri.2011.09.026. URL: http://www.sciencedirect.com/science/article/pii/S0730725X11003584.
150. Golman K, Petersson JS. Acad Radiol. 2006;13(8):932. doi:10.1016/j.acra.2006. 06.001. URL: http://www.sciencedirect.com/science/article/pii/S107663320600314X.
151. von Morze C, Larson PE, Hu S, Keshari K, Wilson DM, Ardenkjaer-Larsen JH, Goga A, Bok R, Kurhanewicz J, Vigneron DB. J Magn Reson Imaging. 2011;33(692) doi:10.1002/jmri.22484. URL: http://doi.wiley.com/10.1002/jmri.22484.
152. ER MC, Armstrong BD, Lingwood MD, Han S. Proc Natl Acad Sci U S A. 2007;104(6):1754. doi:10.1073/pnas.0610540104. URL: http://www.pnas.org/content/104/6/1754.short.
153. Lingwood MD, Siaw TA, Sailasuta N, Abulseoud OA, Chan HR, Ross BD, Bhattacharya P, Han S. Radiology. 2012;265(2):418. doi:10.1148/radiol.12111804. URL: http://radiology.rsna.org/content/265/2/418.
154. Lingwood MD, Siaw TA, Sailasuta N, Ross BD, Bhattacharya P, Han S. J Magn Reson. 2010;205(2):247. doi:10.1016/j.jmr.2010.05.008.
155. Ardenkjaer-Larsen JH, Laustsen C, Bowen S, Rizi R. Magn Reson Med. 2014;71(1):50. doi:10.1002/mrm.25033. URL: http://doi.wiley.com/10.1002/mrm.25033.
156. Lau AZ, Miller JJ, Robson MD, Tyler DJ. Magn Reson Med. 2016;75(4):1474. doi:10.1002/mrm.25713. URL: http://doi.wiley.com/10.1002/mrm.25713.
157. Reed GD, von Morze C, Bok R, Koelsch BL, Van Criekinge M, Smith KJ, Shang H, PEZ L, Kurhanewicz J, Vigneron DB. IEEE Trans Med Imaging. 2014;33(2):362. doi:10.1109/TMI.2013.2285120. URL: http://www.pubmedcentral.nih.gov/articlerender.fcgi?artid=4011557{\&}tool=pmcentrez{\&}rendertype=abstract.
158. Reed GD, von Morze C, Verkman AS, Koelsch BL, Chaumeil MM, Lustig M, Ronen SM, Sands JM, PEZ L, Wang ZJ, JHA L, Kurhanewicz J, Vigneron DB. ArXiv:physicsmed-ph. 2015;(0001):1. URL: http://arxiv.org/abs/1511.02007v1.
159. Dutta P, Martinez GV, Gillies RJ. J Phys Chem Lett. 2014;5(3):597. doi:10.1021/jz402659t. URL: http://pubs.acs.org/doi/abs/10.1021/jz402659t.
160. Aptekar J, Cassidy M, Johnson A, Barton R, Lee M, Ogier A, Vo C, Anahtar M, Ren Y, Bhatia S, Ramanathan C, Cory D, Hill A, Mair R, Rosen M, Walsworth R, Marcus C. ACS Nano. 2009;3(12):4003. doi:10.1021/nn900996p. URL: http://dx.doi.org/10.1021/nn900996p.
161. Atkins T, Cassidy M, Lee M. ACS Nano. 2013. URL: http://pubs.acs.org/doi/abs/10.1021/nn305462y.
162. Balzan R, Mishkovsky M, Simonenko Y, van Heeswijk RB, Gruetter R, Eliav U, Navon G, Comment A. Contrast Media Mol Imaging. 2016;11(1):41. doi:10.1002/cmmi.1656. URL: http://doi.wiley.com/10.1002/cmmi.1656.
163. Van Heeswijk RB, Uffmann K, Comment A, Kurdzesau F, Perazzolo C, Cudalbu C, Jannin S, Konter JA, Hautle P, Van Den Brandt B, Navon G, Van Der Klink JJ, Gruetter R. Magn Reson Med. 2009;61(6):1489. doi:10.1002/mrm.21952.
164. Lau AZ, Chen AP, Cunningham CH. Magn Reson Med. 2012;67(1):62. doi:10.1002/mrm.22977. URL: http://doi.wiley.com/10.1002/mrm.22977.
165. Giovannetti G, Hartwig V, Frijia F, Menichetti L, Positano V, Ardenkjaer-Larsen JH, Lionetti V, Aquaro GD, De Marchi D, Flori A, Landini L, Lombardi M, Santarelli MF. Appl Magn Reson. 2012;42(3):413. doi:10.1007/s00723-011-0307-4. URL: http://link.springer.com/10.1007/s00723-011-0307-4.
166. Giovannetti G, Frijia F, Menichetti L, Milanesi M, Ardenkjaer-Larsen JH, De Marchi D, Hartwig V, Positano V, Landini L, Lombardi M, Santarelli MF. Med Phys. 2010;37(10):5361. doi:10.1118/1.3491437. URL: http://scitation.aip.org/content/aapm/journal/medphys/37/10/10.1118/1.3491437.
167. Maidens J, Arcak M. 2015:6. URL: http://arxiv.org/abs/1510.00455.
168. Xing Y, Reed GD, Pauly JM, Kerr AB, PEZ L. J Magn Reson. 2013;234:75. doi:10.1016/j.jmr.2013.06.003. URL: http://www.sciencedirect.com/science/article/pii/S1090780713001419.
169. Nagashima K. J Magn Reson. 2008;190(2):183. doi:10.1016/j.jmr.2007.10.011.

170. Menichetti L, Frijia F, Flori A, Wiesinger F, Lionetti V, Giovannetti G, Aquaro GD, Recchia FA, Ardenkjaer-Larsen JH, Santarelli MF, Lombardi M. Contrast Media Mol Imaging. 2012;**7**(1):85. doi:10.1002/cmmi.480. URL: http://doi.wiley.com/10.1002/cmmi.480.
171. Cunningham CH, Chen AP, Albers MJ, Kurhanewicz J, Hurd RE, Yen YF, Pauly JM, Nelson SJ, Vigneron DB. J Magn Reson. 2007;187(2):357. doi:10.1016/j.jmr.2007. 05.014. URL: http://www.ncbi.nlm.nih.gov/pubmed/17562376.
172. Chen AP, Leung K, Lam W, Hurd RE, Vigneron DB, Cunningham CH. J Magn Reson. 2009;200(2):344. doi:10.1016/j.jmr.2009.06.021. URL: http://dx.doi.org/10.1016/j.jmr.2009.06.021.
173. Day SE, Kettunen MI, Cherukuri MK, Mitchell JB, Lizak MJ, Morris HD, Matsumoto S, Koretsky AP, Brindle KM. Magn Reson Med. 2011;65(2):557. doi:10.1002/mrm.22698. URL: http://doi.wiley.com/10.1002/mrm.22698.
174. Kohler SJ, Yen Y, Wolber J, Chen AP, Albers MJ, Bok R, Zhang V, Tropp J, Nelson S, Vigneron DB, Kurhanewicz J, Hurd RE. Magn Reson Med. 2007;58(1):65. doi:10.1002/mrm.21253. URL: http://doi.wiley.com/10.1002/mrm.21253.
175. Yen YF, Kohler SJ, Chen AP, Tropp J, Bok R, Wolber J, Albers MJ, Gram KA, Zierhut ML, Park I, Zhang V, Hu S, Nelson SJ, Vigneron DB, Kurhanewicz J, HAAM D, Hurd RE. Magn Reson Med. 2009;62(1):1. doi:10.1002/mrm.21987. URL: http://www.ncbi.nlm.nih.gov/pubmed/19319902.
176. Darpolor MM, Yen YF, Chua MS, Xing L, Clarke-Katzenberg RH, Shi W, Mayer D, Josan S, Hurd RE, Pfefferbaum A, Senadheera L, So S, Hofmann LV, Glazer GM, Spielman DM. NMR Biomed. 2011;24(5):506. doi:10.1002/nbm.1616. URL: http://doi.wiley.com/10.1002/nbm.1616.
177. ESS H, Kim S, Miller JJ, Geferath M, Morrell G, Laustsen C. Tomography. 2016;2(2):117. doi:10.18383/j.tom.2016.00154. URL: http://digitalpub.tomography.org/i/698373-vol-2-no-2-jun-2016/44.
178. Mayer D, Yen YF, Levin YS, Tropp J, Pfefferbaum A, Hurd RE, Spielman DM. J Magn Reson. 2010;204(2):340. doi:10.1016/j.jmr.2010.03.005. URL: http://www.ncbi.nlm.nih.gov/pubmed/20346717.
179. Wang JX, Merritt ME, Sherry AD, Malloy CR. Magn Reson Med. 2016. doi 10. 1002/mrm.26286. URL: http://doi.wiley.com/10.1002/mrm.26286.
180. Hu S, Lustig M, Balakrishnan A, PEZ L, Bok R, Kurhanewicz J, Nelson SJ, Goga A, Pauly JM, Vigneron DB. Magn Reson Med. 2010;63(2):312. doi:10.1002/mrm.22233. URL: http://doi.wiley.com/10.1002/mrm.22233.
181. Wiesinger F, Weidl E, Menzel MI, Janich MA, Khegai O, Glaser SJ, Haase A, Schwaiger M, Schulte RF. Magn Reson Med. 2012;68(1):8. doi:10.1002/mrm.23212. URL: http://www.ncbi.nlm.nih.gov/pubmed/22127962.
182. Khegai O, Schulte RF, Janich MA, Menzel MI, Farrell E, Otto AM, Ardenkjaer-Larsen JH, Glaser SJ, Haase A, Schwaiger M, Wiesinger F. NMR Biomed. 2014;27(10):1256. doi:10.1002/nbm.3174. URL: http://www.ncbi.nlm.nih.gov/pubmed/25156807.
183. Daniels CJ, McLean MA, McGlashan N, Graves MJ, Robb FJ, Lomas DJ, Schulte RF, Brindle KM, Gallagher FA. Proc Int Soc Magn Reson Med. 2015;23:1887. URL: http://cds.ismrm.org/protected/15MPresentations/abstracts/1887.pdf.
184. Lau AZ, Chen AP, Hurd RE, Cunningham CH. NMR Biomed. 2011;24(8):988. doi:10.1002/nbm.1743. URL: http://www.ncbi.nlm.nih.gov/pubmed/21751271.
185. Schulte RF, Sperl JI, Weidl E, Menzel MI, Janich MA, Khegai O, Durst M, Ardenkjaer-Larsen JH, Glaser SJ, Haase A, Schwaiger M, Wiesinger F. Magn Reson Med. 2012;69(5):1209. doi:10.1002/mrm.24353. URL: http://www.ncbi.nlm.nih.gov/pubmed/22648928.
186. Cunningham CH, Chen AP, Lustig M, Hargreaves BA, Lupo J, Xu D, Kurhanewicz J, Hurd RE, Pauly JM, Nelson SJ, Vigneron DB. J Magn Reson. 2008;193(1):139. doi:10.1016/j.jmr.2008.03.012. URL: http://www.pubmedcentral.nih.gov/articlerender.fcgi?artid=3051833{\&}tool=pmcentrez{\&}rendertype=abstract.

187. Bhattacharya P, Chekmenev EY, Perman WH, Harris KC, Lin AP, Norton VA, Tan CT, Ross BD, Weitekamp DP. Towards hyperpolarized 13C-succinate imaging of brain cancer. 2007;186(1):150–5 URL: http://www.sciencedirect.com/science/article/pii/S1090780707000304.
188. Sigfridsson A, Weiss K, Wissmann L, Busch J, Krajewski M, Batel M, Batsios G, Ernst M, Kozerke S. Magn Reson Med. 2014;73:1713–7. doi 10.1002/mrm.25294. URL: http://www.ncbi.nlm.nih.gov/pubmed/24845417.
189. Larson PEZ, Kerr AB, Chen AP, Lustig MS, Zierhut ML, Hu S, Cunningham CH, Pauly JM, Kurhanewicz J, Vigneron DB. J Magn Reson. 2008;194(1):121. doi 10. 1016/j.jmr.2008.06.010. URL: http://dx.doi.org/10.1016/j.jmr.2008.06.010.
190. Geraghty BJ, Lau JYC, Chen AP, Cunningham CH. Magn Reson Med. 2016. doi 10.1002/mrm.26125. URL: http://doi.wiley.com/10.1002/mrm.26125, http://www.ncbi.nlm.nih.gov/pubmed/26806525.
191. Wild JM, Woodhouse N, MNJ P, Fichele S, Said Z, Kasuboski L, van Beek EJR. Magn Reson Med. 2004;52(3):673. doi:10.1002/mrm.20164. URL: http://www.ncbi.nlm.nih.gov/pubmed/15334590.
192. Wild JM, MNJ P, Viallon M, Schreiber WG, van Beek EJR, Griffiths PD. Magn Reson Med. 2002;47(4):687. URL: http://www.ncbi.nlm.nih.gov/pubmed/11948729.
193. Von Morze C, Reed G, Shin P, PEZ L, Hu S, Bok R, Vigneron DB. J Magn Reson. 2011;211(2):109. doi:10.1016/j.jmr.2011.04.007.
194. Dumez JN, Frydman L. J Magn Reson. 2013;226:22. URL: http://www.sciencedirect.com/science/article/pii/S1090780712003321.
195. Schmidt R, Laustsen C, J-NN D, Kettunen MI, Serrao EM, Marco-Rius I, Brindle KM, Ardenkjaer-Larsen JH, Frydman L. J Magn Reson. 2014;240:8. doi:10.1016/j.jmr.2013.12.013. URL: http://www.sciencedirect.com/science/article/pii/S1090780714000044.
196. Cunningham CH, Lau JY, Chen AP, Geraghty BJ, Perks WJ, Roifman I, Wright GA, Connelly KA. Circ Res. p. CIRCRESAHA. 2016;116:309769. doi:10.1161/CIRCRESAHA.116.309769. URL: http://circres.ahajournals.org/lookup/doi/10.1161/CIRCRESAHA.116.309769.

Chapter 5
Preclinical Cardiac In Vivo Spectroscopy

Mahon L. Maguire

Abbreviations

[2,3]-DPG	Diphosphoglycerate
ADP	Adenosine diphosphate
AMP	Adenosine monophosphate
ATP	Adenosine triphosphate
BIR	B_1-insensitive rotation
CHESS	Chemical shift selective
CK	Creatine kinase
CSI	Chemical shift imaging
DANTE	Delays alternating with nutations for tailored excitation selective excitation
$Dy[PPP]_2$	Dysprosium bis-triphosphate
$Dy[TTHA]^{3-}$	Dysprosium triethylenetriamine hexaacetate
ECG	Electrocardiogram
EPSI	Echo-planar spectroscopic-imaging
FID	Free induction decay
FSW	Fourier series window
FT	Fourier transform
GAMT	Guanidoacitate *N*-methyl transferase
HPLC	High-pressure liquid chromatography
ISIS	Image selected in vivo spectroscopy
k_{fCK}	Forward reaction rate constant for creatine kinase
k_{rCK}	Reverse reaction rate constant for creatine kinase
LAD	Left anterior descending coronary artery

M.L. Maguire, PhD
BHF Experimental Magnetic Resonance Unit, Radcliffe Department of Medicine, Division of Cardiovascular Medicine, University of Oxford, Oxford, UK
e-mail: mlm23@well.ox.ac.uk

C. Constantinides (ed.), *Protocols and Methodologies in Basic Science and Clinical Cardiac MRI*, https://doi.org/10.1007/978-3-319-53001-7_5

LCx	Left circumflex artery
m-CK	Cytosolic muscle creatine kinase isoform
MR	Magnetic resonance
MRI	Magnetic resonance imaging
MRS	Magnetic resonance spectroscopy
Na_e^+	Extracellular sodium
Na_i^+	Intracellular sodium
NMR	Nuclear magnetic resonance
PCr	Phosphocreatine
P_i	Inorganic phosphate
PRESS	Point resolved spectroscopy
RAPP	Rotating frame experiment using adiabatic plane rotation pulses for phase modulation
RF	Radio frequency
SI	Spectroscopic imaging
SLAM	Spectroscopy with linear algebraic modeling
SLIM	Spectral localization by imaging
SLOOP	Spatial localization with optimum pointspread function
SNR	Signal-to-noise ratio
STEAM	Stimulated echo acquisition mode
TAC	Transverse aortic constriction
TE	Echo time
TM	Mixing time for STEAM pulse sequence
$Tm[DOTP]^{5-}$	Thulium(III)1,4,7,10 tetraazacyclododecane-N,N′,N″,N‴-tetra(methylenephosphonate)
TR	Repetition time
TSP	3-(trimethylsilyl)propionic-*2,2,3,3,*d_4 acid

Introduction

Heart disease, and specifically heart failure, result from a complex interaction of genetics, metabolism, and physical insult/ischaemia that lead to changes in myocardial metabolism, gene expression, hypertrophy, cell death, or scarring. Whilst magnetic resonance imaging (MRI) has long been the method of choice for measuring cardiac performance and remodelling, magnetic resonance spectroscopy (MRS) has yet to become established in the clinic as a routine diagnostic tool.

Metabolism is the ultimate expression of phenotype and wet lab biochemical assays have historically been used to measure metabolic processes or metabolite concentrations in ex vivo, post-mortem, tissue samples. For obvious reasons this renders longitudinal study of any individual animal impossible. It also necessitates the use of large numbers of animals in cohort studies in order to enable monitoring of disease progression over time. More recently, MRS has been employed as a key tool for probing myocardial metabolism. MRS uniquely pro-

vides a nondestructive, noninvasive, method to probe metabolism without the need for additional radioactive probes. Animal models, which mimic the characteristics of human cardiac disease have been established, enabling researchers to study the physical and metabolic changes involved at a level of detail that is typically not possible in the clinic.

The Basics of MR Spectroscopy

MRS can provide quantitative information about the population of metabolites present in a sample. Unlike MRI, which principally focusses on the proton (^{1}H) signal from water, MRS can be readily used to measure other nuclei such as ^{31}P, ^{23}Na, ^{13}C, as well as ^{1}H (Table 5.1). These nuclei, which have a noninteger value of the quantum mechanical property nuclear spin, precess about an applied magnetic field at a unique frequency known as their Larmor frequency. The spins can either align with or against the applied magnetic field, but as the two states are very close in energy, the population in the higher and lower energy states are almost identical with only a slight majority occupying the lower energy state; this difference in populations is essential for the generation of the MR signal.

Once excited by a radio frequency (RF) oscillating magnetic field, nuclei emit an RF signal at their Larmor frequency as they decay back to equilibrium. The exact frequency at which a nucleus will precess is dependent on the type of nucleus, its electronic environment and the strength of the applied magnetic field (B_0). The electronic environment of a particular nucleus is determined by the geometry and bonding of the molecule. As a result, nuclei that share identical bonding patterns within a molecule will precess at the same frequency, whilst nuclei with different bonding patterns will precess at different frequencies. The signal emitted by the sample as the nuclei decay back to equilibrium is called the free induction decay (FID). The FID can be converted from a time domain signal to a frequency domain signal using a Fourier transform (FT). The frequency domain signal is known as a spectrum, and will contain a peak corresponding to the frequency of each nucleus in the sample,

Table 5.1 Properties of commonly used MR sensitive nuclei

Nucleus	Nuclear spin	Natural abundance (%)	Normalized sensitivity cf. ^{1}H	Gyromagnetic ratio ($\gamma/2\pi$; MHz T^{-1})
^{1}H	1/2	99.98	1.000	42.576
^{7}Li	3/2	92.41	0.290	16.548
^{13}C	1/2	1.10	0.016	10.708
^{17}O	5/2	0.04	0.029	5.774
^{23}Na	3/2	100.00	0.093	11.269
^{31}P	1/2	100.00	0.067	17.252
^{59}Co	7/2	100.00	0.278	10.077
^{87}Rb	3/2	27.83	0.177	13.981

Based on Lide et al. [51]

with the peak area being proportional to the number of nuclei present in the sample at that frequency. MR signal is inherently of low amplitude due to the small difference in population of the energy states. In order to increase the signal to noise ratio (SNR) of the FID the measurement is repeated many times and the results averaged; the SNR of the signal is proportional to the square root of the number of averages. The delay between subsequent RF excitation pulses is known as the repetition time (TR). The decay of the nuclei back to equilibrium follows an exponential process known as longitudinal, or spin-lattice, relaxation with a time constant T_1. If the FIDs are acquired with a short TR, then the nuclei do not have time to fully relax and the amplitude of subsequent FIDs is reduced. In order to ensure that the sample is fully relaxed, a TR of at least $5\times T_1$ is required. The strength of the applied magnetic field will also affect the SNR of the measurement. The precessional frequency of a nucleus is proportional to the strength of the applied magnetic field; a stronger magnetic field results in a higher precessional frequency and therefore higher energy signal. Likewise, a higher field strength results in a greater energy difference between the high and low energy states and therefore greater sample polarization and consequently a larger signal to detect.

In MRI a single type of nucleus is being observed, typically the ^{1}H nucleus of water, which gives rise to a resonance. The imaging gradients used to encode position in MRI apply a linear magnetic field gradient across the sample such that each point in the sample along the gradient experiences a different magnetic field. In the case of a single type of nucleus, therefore, the frequency encodes position in space. In contrast, MRS allows us to record a metabolite spectrum from a sample, with the pattern of peaks in that spectrum being characteristic of the combination of metabolites present in the sample and the peak amplitudes being proportional to the number of molecules of each metabolite. In principle, if the volume of the sample is known, and a reference signal from a sample of known concentration and volume is present, the concentration of each metabolite in the spectrum can be calculated. If the FIDs are acquired with a short TR, then full T_1 relaxation of the nuclei does not occur and the amplitude of subsequent FIDs is reduced; this is termed T_1 saturation. When a sample contains resonances with a mixture of long and short T_1 values, using a short TR will result in saturation of the resonances with long T_1 values and little saturation of the short T_1 species. The peak amplitude of the long T_1 species will be underrepresented in the spectrum and can lead to errors in quantification. Similarily, the exponential process through which the MR signal decays in amplitude with time is called transverse, or spin-spin, relaxation and has a time constant T_2. If a resonance decays quickly (i.e. it has a short T_2), then any delay between the application of the excitation RF pulse and the start of FID acquisition will result in significant decay of the signal before any data are recorded. The amplitude of the peak in the spectrum will therefore be underestimated relative to a resonance with a long T_2; this can lead to errors in signal quantification. The signal decay during the acquisition of the FID is not only dependent on T_2 but also on B_0 inhomogeneities in the sample, with increasing inhomogeneity resulting in a more rapid signal decay; this effective signal decay that depends on the combination of B_0 and T_2 effects is termed T_2^*.

Whilst large animals can be imaged in clinical spectrometers, mice and rats have become the animal models of choice for preclinical cardiac research, and a large number of genetic and surgical models of human cardiac disease have been developed using these species (for a review, see Camacho et al. [18]). Their small size, however, means that the volume of the myocardial tissue compared to human myocardium is several orders of magnitude smaller. This means that there is a similar decrease in the amount of MR signal. High-field small animal preclinical scanners are therefore common with typical field strengths of between 7.0 and 11.7 T; this compares with typical clinical systems that have field strengths of between 1.5 and 4.0 T, with an increasing number of 7.0 T scanners being commissioned. The use of small RF coils placed close to the animal will also improve SNR, while high-performance imaging gradients reduce the time taken for spatial localization of the signal. Such refinements, however, can only partially compensate for the low signal amplitude. The fast heart rates (400–600 bpm) and breathing rates (~30–60 bpm) of mice and rats make small animal spectroscopy technically challenging, and require careful cardiac and respiratory gating to prevent image artefacts.

The Motivation Behind Cardiac Spectroscopy

MRS enables direct interrogation of the metabolism of the living heart. The heart demands a constant supply of energy to fulfil its function. Consequently many cardiac pathologies are diseases that impact myocardial energy metabolism. Using cardiac MRS, it is possible to measure metabolites such as creatine, triglycerides (lipids), lactate, phosphocreatine (PCr), adenosine triphosphate (ATP), and inorganic phosphate (P_i). Creatine and PCr serve as a shuttle carrying high-energy phosphate from the mitochondrion, where they are produced, to the myofibrils. At the myofibrils, the enzyme creatine kinase (CK) transfers the phosphate from PCr to adenosine diphosphate (ADP) to generate ATP that can be hydrolyzed during muscle contraction. PCr, ATP, and P_i can be measured using ^{31}P MRS. Total cellular creatine (free creatine + PCr) can be measured using ^{1}H MRS. From this information, it is possible to calculate myocardial pH, Mg^{2+} concentration, ADP concentration, and CK flux, as well the PCr/ATP ratio which serves as a clinical biomarker of myocardial energetic status. Lactate can be measured by ^{1}H MRS and serves as a marker of anaerobic respiration. Myocardial lipids are also known to play a role in many pathologies, and can be measured in the living heart using ^{1}H MRS. Using ^{13}C MRS, core metabolism, such as the flux through Kreb's cycle, can also be probed. The balance between intracellular and extracellular sodium concentration is driven by active transport of Na^+ across the cell membrane; through the use of chemical shift reagents, ^{23}Na MRS can monitor the concentration of intracellular and extracellular ^{23}Na and interrogate the role of the various ATP-dependent Na^+ transporters in maintaining this equilibrium. This is not an exhaustive list of what can be achieved

using MRS. The following sections of this chapter aim to give a more technical overview of what can be measured by preclinical MRS and how these measurements can be achieved.

MRS of the Perfused Heart

Historically, the majority of preclinical cardiac spectroscopy has been carried out on Langendorff perfused rat and mouse hearts. MRS studies of the perfused rat and rabbit heart were first described in the late 1970s and in the hamster and mouse heart by the late 1990s [17, 29, 30, 44, 63, 70, 83, 84]. This work typically requires the construction of a perfusion rig that can fit within the bore of a high field scanner, and is typically built within a 10 or 20 mm glass NMR tube. This system allows control of temperature, metabolite availability, and coronary perfusion. The heart and cannulated aorta can then be placed within a volume transmit/receive coil, and pulse-acquire spectra can be recorded from the entire myocardium yielding a measure of global cardiac metabolism. The pulse-acquire sequence is the simplest MR spectroscopy experiment comprising just an excitation pulse and acquisition of an FID (Fig. 5.1). It excites selected nuclei within the field of view of the RF coil and subsequently records a spectrum of the metabolites present in that volume. It is termed an unlocalized pulse sequence as it does not aim to record a spectrum from a specific volume within the field of view of the RF coil, but rather from everything that the coil can 'see'.

Similarly, T_1 or T_2 measurements can be conducted using unlocalized pulse sequences. In cases where T_2 signal decay is fast necessitating a minimal delay

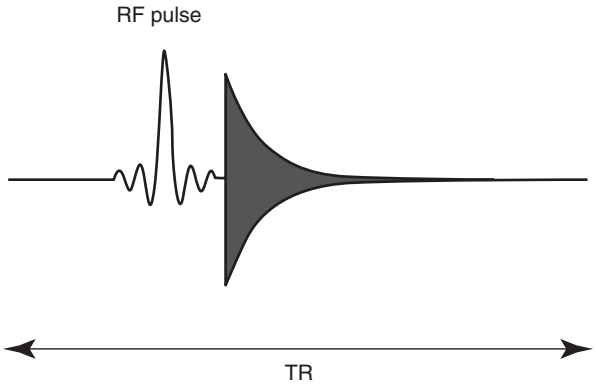

Fig. 5.1 The pulse-acquire sequence. The pulse sequence consists of an RF excitation pulse and acquisition of an FID (*dark grey*). This is an unlocalized pulse sequence. The TR for the pulse sequence is defined as the time delay between two successive RF excitation pulses, and is indicated. There is also a TR delay between the end of acquisition of the FID and the start of the next excitation pulse; this delay allows T_1 relaxation of the nuclei

between the RF pulse and the start of FID acquisition, or T_1 is long requiring a long TR to prevent excessive saturation of the signal, the ability to maximize the signal per FID by acquiring signal from the entire myocardium can be advantageous. Performing the experiment without employing phase encoding gradients for signal localization can minimize T_2 or T_2^* decay of the signal, thereby improving SNR.

The perfusion rig contains only the heart and perfusion buffer greatly simplifying the spectroscopic acquisition as there is no possibility of MR signal contamination from surrounding tissues. The balloon placed in the left ventricle to determine left ventricular pressure can be filled with a known volume of a concentration reference solution allowing metabolite signal quantification relative to the wet weight of the myocardial tissue. The heart can be paced by placing electrodes on the atrium, and the pacing signal used to trigger the MR pulse sequence such that all MR signals arise from the same phase in the cardiac cycle. Breathing motion is obviously not present meaning that respiratory motion compensation, or respiratory gating, is not required.

Ex vivo Langendorff perfusion enables a number of experiments that would be either extremely technically challenging, or impossible to conduct in the intact animal. For example, global ischaemia can be induced by restricting flow of the perfusing buffer and pharmacological compounds, many of which would otherwise prove fatal to the animal, such as a chemical shift reagent for measuring intracellular and extracellular [Na^+], can be introduced either via the perfusing buffer or via the bathing solution. However, due to the small size both of the animal hearts and the MR compatible perfusion rig, successfully performing these experiments requires a high degree of technical proficiency and experience.

^{1}H Spectroscopy of the Perfused Heart

Proton spectroscopy can be used to determine the concentration of a number of key metabolites involved in cardiac pathology. Creatine, carnitine, lactate, and lipid concentration measurements have been made using spectroscopy, with creatine and lipid levels being perhaps the most commonly studied (for an overview of early studies, see von Kienlin [86]). Due to the large concentration difference between the water and the cellular metabolites, water suppression is applied to eliminate or reduce the signal from the water such that it is of a similar order of magnitude to that of the metabolites. This ensures that the MR signal from the metabolites can be amplified without the water signal overflowing the analogue-to-digital converter in the receiver. Experiments performed in the absence of water suppression, however, can also be valuable; metabolite concentrations have often been estimated by comparison of the peak amplitude arising from the metabolite with that of the unsuppressed water resonance.

Creatine Concentration Measurement

Creatine serves as a shuttle to carry high-energy phosphate from the mitochondrion to the myofibrils where ATP can be regenerated by CK for use in muscle contraction. Creatine concentration in the myocyte is believed to play a role in cellular recovery/survival following ischaemia (for a review, see Neubauer [60]). Creatine concentration has also been measured in the perfused rat heart [72]. Hearts from wild-type Wistar rats were excised, perfused, and placed in a birdcage coil in an 11.7 T scanner. The low concentration of creatine necessitates strong suppression of the water signal. In this case, a binomial refocusing pulse was used to suppress the water signal (Fig. 5.2). An additional chemical shift selective (CHESS) water suppression module aided water suppression.

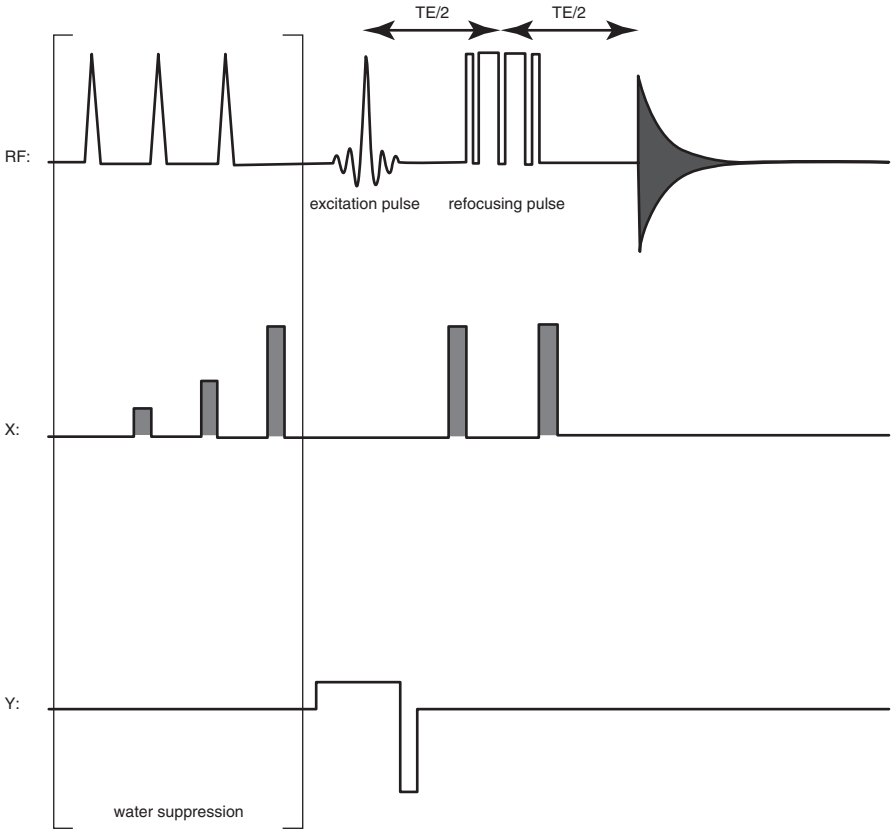

Fig. 5.2 A slice selective spin-echo spectroscopy sequence can be used to measure creatine, carnitine, and lipid concentration in the perfused rat heart. The pulse sequence consists of an optional water suppression module containing three CHESS pulses with increasing doubling gradient amplitudes (indicated by *brackets*), followed by an RF excitation pulse, binomial frequency selective refocusing pulse and acquisition of an FID (*dark grey*). The echo time (TE) is indicated, and crusher gradients are shown in *light grey*. RF indicates the RF channel. GX, and GZ are the x-, and z-gradient channels respectively (Based on Schneider et al. [72])

It was observed that the CHESS sequence was decreasing the amplitude of the creatine -CH_3 resonance; this decrease was attributed to magnetization transfer between the water and the -CH3 of creatine. Creatine concentration was calculated relative to a known concentration reference sample containing 75 mM 3-(trimethylsilyl)propionic-*2,2,3,3,d*$_4$ acid (TSP) placed in the balloon in the left ventricle cavity. All acquisitions were triggered from the pressure wave of left ventricular contraction and timed such that they coincided with mid-diastole. Inversion recovery and spin-echo measurements were made to determine the T_1 and T_2, respectively, of the creatine and TSP in order to correct for partial saturation and T_2 relaxation. A myocardial creatine concentration of 8.2 ± 2.3 mmol/kg wet weight was measured by spectroscopy compared with 14.2 ± 1.9 mmol/kg wet weight by high-pressure liquid chromatography (HPLC). This difference is attributed to a pool of creatine bound to macromolecules within the cell resulting in T_2 values too short to be observed by spin-echo [72].

Measurement of Tissue Lipid Content

Spectroscopic imaging (SI) has been used to measure myocardial lipid concentration in an ex vivo perfused model of myocardial infarction in canine hearts [80]. Alterations in myocardial lipid MR signals have been observed in a number of species following myocardial ischaemia; this is of interest considering that the majority of the heart's energy is derived from lipid metabolism. The left anterior descending coronary artery (LAD) was occluded, and 24 h later hearts were excised, perfused, and placed in an 11 cm, two turn Helmholtz coil in a 1.5 T MR scanner. Slice selective 2D spectroscopic images were acquired in short axis orientation and the acquired k-space data weighted using a sine bell, with Gaussian weighting in the readout dimension. Whilst this will degrade the spatial resolution of the images, it will significantly improve the SNR. Two chemical shift selective inversion pulses were applied 1,100 and 190 ms before the start of the SI sequence to suppress the water signal. It was observed that the lipid signal from the area at risk was significantly elevated relative to healthy control tissue, with the infarct region having an intermediate value.

^{31}P Spectroscopy of the Perfused Heart

The principal use of MRS in the perfused heart has been for the measurement of myocardial energetics. ^{31}P spectroscopy allows measurement of PCr, ATP, and P_i. Whilst in the clinic, the PCr/ATP ratio has been shown to be a good prognostic indicator of survival in cases of hypertrophic cardiomyopathy [61], and is generally accepted to be a metric of the condition of myocardial energetics, this ratio can mask changes in the absolute concentration of these metabolites. The relatively long T_1 and short T_2 decay of PCr and ATP makes ^{31}P MRS challenging as it requires a

long TR and short TE to maximize available signal. The low concentrations of ^{31}P metabolites in the cell (<20 mM, [83]) coupled with the approximately 15-fold lower MR sensitivity of ^{31}P relative to ^{1}H mean that SNR benefits significantly from the use of a small RF coil placed close to the heart. The absence of PCr, ATP, and P_i from the perfusing buffer means that what ever signal from ^{31}P metabolites is detected originates from the myocardium; there is also no requirement for solvent suppression for ^{31}P MRS.

Measurement of Myocardial pH and Mg^{2+} Concentration

The relative chemical shift difference between PCr and P_i is sensitive to pH. Consequently, measurement of a ^{31}P spectrum of the myocardium gives a direct measure of tissue pH, which can serve as a marker of ischaemia and acidosis. The intracellular pH can be calculated from a relationship derived from a titration curve. This curve can be fitted and an empirical relationship derived allowing estimation of pH in a sample. For example, Goudemant et al. defined the relationship:

$$pH = 6.73 + \log\left(\left[\delta P_i - 3.37\right]/\left[5.66 - \delta P_i\right]\right) \tag{5.1}$$

where δP_i is the chemical shift difference between PCr and P_i at 4.7 T [33]. The exact relationship between δP_i and pH may change with the magnetic field strength, however.

Similarly, the chemical shift difference between α-ATP and β-ATP resonances depends on the binding of Mg^{2+} by ATP [47, 83]. By taking into account the chemical shift of the ATP resonances, and the measured intracellular pH, it is possible to calculate the concentration of free Mg^{2+} in the cell.

Measurement of [PCr], [ATP], and PCr/ATP Ratio

The PCr/ATP ratio has been demonstrated to be reduced in an isolated perfused heart model of hypertrophy. Male Wistar rats were treated with isoproterenol for seven days prior to perfusion of the hearts and acquisition of ^{31}P spectra. It was observed that the concentration of PCr and PCr/ATP was decreased in treated versus control hearts (PCr: 11.11 ± 1.55 versus 7.61 ± 0.96 mM, PCr/ATP: 1.69 ± 0.36 versus 1.18 ± 0.21) coupled with increased oxidative stress and up-regulation of the nitric oxide pathway [24]. Similarly, Lu et al. measured PCr/ATP in male Sprague-Dawley rat hearts perfused with either normal (1.5 mM) or high (2.5 mM) [Ca^{2+}] buffer to induce high workload [52]. PCr/ATP ratio was calculated as the ratio of the peak areas of PCr and β-ATP, and was shown not to be altered by the higher cardiac workload (1.49 ± 0.16 versus 1.45 ± 0.20). In mice, a reduced PCr/ATP ratio was

observed for m-CK (cytosolic muscle creatine kinase isoform) knock-out compared to wild-type mice both at low and high work loads (1.55 ± 0.13 versus 1.65 ± 0.13, and 2.79 ± 0.07 versus 2.86 ± 0.31, [83]). Fully relaxed spectra were collected, and ATP and PCr concentrations calculated relative to a known reference standard. Recently, PCr/ATP ratios have been measured in a mouse model of Chuvash polycythemia (CP) [75]. CP is a disease in which hypoxia inducible factor (HIF) is modestly elevated; HIF appears to function as a regulator of cellular response to hypoxia and therefore HIF pathway manipulation is of therapeutic interest. It was observed that CP mice and wild-type control hearts had similar PCr/ATP ratios, but that under isoproterenol stress, CP hearts demonstrated a reduced PCr/ATP ratio.

Saturation Transfer, Creatine Kinase Flux, and Free Energy of ATP Hydrolysis

CK plays a central role in myocardial metabolism. PCr serves as an energy reserve/shuttle transferring high-energy phosphates from the mitochondrion that can then be used to regenerate ATP from ADP at the site of acto-myosin contraction (for an overview of creatine and CK in cardiac energetics, see Neubauer [60]). CK catalyzes the reaction:

$$ATP + Cr \underset{k_{r,CK}}{\overset{k_{f,CK}}{\rightleftharpoons}} ADP + PCr \tag{5.2}$$

where $k_{f,CK}$ and $k_{r,CK}$ are the forward and reverse reaction rate constants for the CK respectively. Using MRS, if the γ-ATP resonance is saturated, CK will transfer the saturated phosphorus nuclei to Cr resulting in a decrease in the amplitude of the PCr signal relative to an unsaturated control spectrum. Whilst the bandwidth of the selective saturation pulse is typically set to selective saturate only γ-ATP, the pulse can result in limited saturation of the neighbouring PCr resonance due to the bandwidth of the saturation pulse. By placing the γ-ATP saturation pulse and control saturation pulse symmetrically about PCr, such unintentional saturation of PCr becomes a systematic error in the data, and therefore does not affect the measurement of CK flux. If the T_1 of PCr in the absence of chemical exchange can be determined, then it is possible to calculate the forward rate constant for CK, typically assuming a two-state model (i.e. neglecting conversion of ATP to ADP and P_i by ATPase). Xiong et al. provide a good description of the methods and mathematics involved in calculating $k_{f,CK}$ [88]. Early applications of saturation transfer to perfused hearts were reported in the late 1970s in rabbit hearts and in rats [2, 63]. Saturation of the γ-ATP signal is typically achieved using a Delays Alternating with Nutations for Tailored Excitation selective excitation train (DANTE, [14, 58])

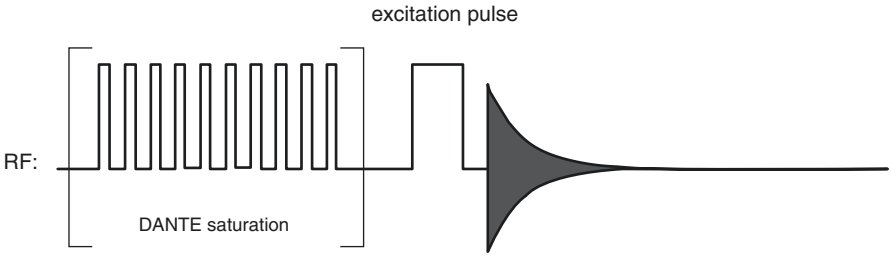

Fig. 5.3 The unlocalized saturation transfer spectroscopy sequence. The pulse sequence consists of a frequency selective DANTE saturation module (indicated by *brackets*), followed by an unlocalized RF excitation pulse and acquisition of an FID (*dark grey*). The DANTE module is used to either saturate the γ-ATP resonance at −2.5 ppm relative to PCr or for a control saturation at 2.5 ppm. RF indicates the RF channel

(Fig. 5.3). By varying the saturation time, the T_1 of PCr in the absence of chemical exchange can be measured by progressive saturation.

Proton spectroscopy and phosphorus spectroscopy provide complementary information. ^{31}P MRS can determine the concentration of PCr, and ATP in the myocardium, whilst ^{1}H MRS can determine the total creatine concentration. Taken together, the myocardial concentration of ADP can be calculated from the CK reaction equilibrium:

$$\left[ADP\right] = \left(\left[ATP\right] \times \left[Free\ Cr\right]\right) \Big/ \left(\left[PCr\right] \times \left[H^{+}\right] \times K_{eq}\right) \tag{5.3}$$

where K_{eq} is the equilibrium constant for the CK reaction (1.66×10^{9} M^{-1} [22]), [Free Cr] is the concentration of free creatine (i.e. the difference between total creatine and phosphocreatine concentrations). Consequently, it is therefore possible to determine the free energy of ATP hydrolysis in the myocardium ($\Delta G_{\sim ATP}$):

$$\Delta G_{\sim ATP} = \Delta G^{0} + RTln\left(\left[ADP\right] \times \left[P_i\right] / \left[ATP\right]\right) \tag{5.4}$$

where $\Delta G_{\sim ATP}$ is in kJ/mol, R is the universal gas constant, T is the temperature in Kelvin, and ΔG^0 is the free energy of ATP hydrolysis under standard conditions of pH, molarity, temperature, and Mg^{2+}. Measurement of $\Delta G_{\sim ATP}$ has been performed in perfused *mdx* mouse hearts [90].

^{23}Na Spectroscopy of the Perfused Heart

A sodium gradient is maintained across the membrane of the myocyte by the Na^+/K^+-ATPase. This gradient permits the electrical excitability of the myocyte, and provides the sodium motive force that drives the Na^+/H^+ and Na^+/Ca^{2+} antiporters involved in the regulation and maintenance of intracellular [Ca^{2+}] and pH. When

ATP is limiting (e.g. during ischaemia), the Na^+/K^+-ATPase can become inhibited resulting in a decrease in Na^+ efflux and an increase in intracellular [Na^+].

Chemical shift reagents such as dysprosium bis-triphosphate ($Dy[PPP]_2$), thulium(III)1,4,7,10 tetraazacyclododecane-N,N′,N″,N‴-tetra(methylenephosphonate) ($Tm[DOTP]^{5-}$), or dysprosium triethylenetriamine hexaacetate ($Dy[TTHA]^{3-}$) can cause a change in the resonance frequency of Na^+; however, these shift reagents cannot cross the cell membrane [3, 36]. If a shift reagent is administered to a perfused heart, the extracellular ^{23}Na signal will shift to a different frequency while the intracellular ^{23}Na signal will remain unchanged; the intracellular and extracellular ^{23}Na signals can therefore be distinguished by their chemical shift. The shift reagents, however, also bind Ca^{2+} resulting in a significant decrease in free Ca^{2+} and consequently have a deleterious effect on cardiac performance by preventing myocyte repolarization [74]. In vivo, these shift reagents are rapidly lethal. In the perfused heart, however, the effects of Ca^{2+} binding can be managed.

^{23}Na Imaging of Oedema

Aguor and co-workers have reported an ex vivo perfusion model of myocardial oedema [3]. MRI contrast agents can accumulate in oedematous tissue complicating or confounding diagnosis of myocardial infarction using conventional image-based methods. During oedema, it was hypothesized that extracellular Na^+ (Na_e^+) will increase but that intracellular Na^+ (Na_i^+) would remain unchanged. Perfused rat hearts were placed in a glass tube in a 20 mm diameter birdcage coil. The buffer surrounding the hearts was rapidly flushed with buffer containing Li^+ instead of Na^+ in order to eliminate ^{23}Na signal arising from the buffer bathing the heart. $Tm[DOTP]^{5-}$ (3.50 mM) was added to the perfusing buffer along with 3.42 mM Ca^{2+} to counteract the Ca^{2+} binding effect of the reagent. Short axis, acquisition-weighted 2D chemical shift images were acquired. Increasing the pressure of the perfusing buffer from 60 to 140 mmHg resulted in global myocardial oedema. An increase in Na_e^+ signal intensity was observed following an increase of the perfusion pressure from 17.4 ± 1.7 to 21.6 ± 2.2 mmHg; there was no significant change in Na_i^+.

^{23}Na Imaging of [Na_i^+] in Ischaemia

Imahashi and co-workers have reported the use of the shift reagent $Dy[TTHA]^{3-}$ to monitor Na_i^+ during ischaemia in perfused rat hearts [41]. Hearts were perfused with a solution containing 15 mM $Dy[TTHA]^{3-}$ and subjected to global ischaemia by stopping the flow of the perfusing buffer for 15 min, followed by reperfusion. Unlocalized pulse-acquire ^{23}Na spectra were acquired before, during, and after ischaemia. It was observed that Na_i^+ increased during ischaemia and decreased back to

normal levels following reperfusion. Inhibition of the Na^+/H^+ exchanger ameliorated the increase in Na_i^+ during ischaemia.

Spectroscopy of Other Nuclei in the Perfused Heart

Whilst the majority of cardiac MRS is conducted using ^{1}H, ^{31}P, or ^{23}Na nuclei, other nuclei have found uses in preclinical cardiac research. It is possible to directly measure dynamic changes in O_2 consumption due to respiration in the perfused heart. Lu and co-workers have reported a closed-loop perfusion set-up that enables efficient use of $^{17}O_2$ enriched buffer to quantify production of $H_2{}^{17}O$ production as a function of myocardial oxygen consumption rate [52]. Unlocalized pulse-acquire spectra were used to monitor $H_2{}^{17}O$ production rate before and during perfusion with high $[Ca^{2+}]$ buffer resulting in an increased cardiac workload.

Rubidium (^{87}Rb) has been used as a surrogate for measuring potassium in myocardial studies, including in studies of isolated rat and pig hearts [50]. Whilst potassium and rubidium have very different atomic weights, they have very similar hydrated ionic radii, which determines their similar biochemical behaviours (for a review, see Kupriyanov and Gruwel [49]). ^{87}Rb has spin 3/2 (Table 5.1) resulting in both a fast and slow T_2 decay. Consequently, linewidths in Rb spectroscopy are broad, and long TE can result in an underestimation of the NMR signal amplitude.

Cellular volume during hypoosmotic shock has been measured using ^{59}Co spectroscopy [5, 6]. Rat hearts were perfused with a buffer containing $K_3Co(CN)_6$, which remained in the extracellular space. With a fixed volume perfusion chamber, as the cells swell, the extracellular volume decreases reducing the amount of ^{59}Co present in the chamber thereby decreasing the amplitude of the ^{59}Co signal. Quantification of the volume of the extra- and intracellular volume is also possible [6].

The low natural abundance of ^{13}C means that natural abundance MRS is all but impossible in living tissue. By perfusing the heart with ^{13}C labelled metabolites, however, it is possible to follow the metabolic fate of the label over time. For example, O'Donnell and co-workers have monitored long-chain fatty acid metabolism in the perfused rat heart using pulse-acquire spectra [64]. By varying the labelling pattern of the long chain fatty acids supplied in the perfusing buffer, it is possible to reduce the spectral overlap of triacylglyceride resonances with those from glutamate, allowing more accurate dynamic monitoring of fatty acid oxidation.

In Vivo Cardiac Spectroscopy

Preclinical cardiac spectroscopy is challenging. The heart beats and the animal breathes potentially introducing motion artefacts into the MR data. The heart is an irregular shape (i.e. not cuboidal) meaning that the sizes of the cuboidal voxels require to be small in order to avoid partial volume contamination from surrounding tissues. The myocardium lies inside the animal behind the chest wall increasing the

distance between the RF coil and the myocardium thereby reducing sensitivity. Neighbouring tissues, especially skeletal muscle and blood, can have similar metabolite profiles that interfere with cardiac spectroscopy. Small animal spectroscopy, particularly that of rats and mice, is further confounded by the small tissue volume, and fast heart and breathing rates.

Practical Considerations for the In Vivo MRS Experiment

In vivo MRS is in many respects more challenging than ex vivo perfused heart spectroscopy. With ex vivo studies, the choice of RF coil is limited, and will typically be the smallest volume coil that will accommodate the perfusion rig. Cardiac gating is commonly controlled using pacing electrodes, and signal contamination from the buffer can be discounted. With in vivo MRS, there are a number of practical considerations that need to be taken into account when conducting an experiment. The appropriate type, size, and design of RF coil has to be selected to maximize available SNR and still be practical to use. Likewise physiological monitoring and triggering/gating needs to be considered.

Which Is the Optimal RF Coil?

The choice of RF coil for a spectroscopy experiment requires consideration. Early large animal work was typically conducted with a small transmit/receive surface coil, which was sutured directly to the myocardium [11, 38, 43, 79, 89]. This has the advantage that the small coil generates a very strong magnetic field over a small volume lying close to the coil, and is therefore extremely sensitive thereby maximizing the SNR. It also means that signal contamination from other tissues is minimal as the B_1 field does not extend much beyond the myocardium; being sutured to the myocardium also ensures that the filling factor for the coil is high (i.e. the sample occupies most of the volume covered by the B_1 of the RF coil). Unfortunately, there are a number of disadvantages with such a strategy. The B_1 field is not uniform resulting in the volume of the sample placed close to the coil receiving a high flip angle, with the volume of the sample lying further from the coil receiving a very low flip angle. By reciprocity, the coil is most sensitive to the signal originating close to the coil and is very insensitive to signals originating further from the coil. Use of adiabatic pulses can compensate for the lack of transmit uniformity, but the variation in receive sensitivity means that sample that lies at a distance greater than the radius of the coil becomes increasingly difficult to detect. Use of a small surface coil sutured to the myocardium is impractical for small animal work.

As an alternative to suturing a coil to the myocardium, larger surface coils can be placed on the chest wall and used for transmit/receive. This has the advantage that the MR protocol does not require what is generally a terminal surgical procedure to

place the RF coil. As the surface coil is relatively large, the B_1 field from the centre of the coil is more uniform, mitigating some of the issues arising from flip angle and receive profile variation. Conversely, the sensitivity of the surface coils drops as the size increases; increasing transmit power, and using adiabatic excitation pulses can compensate for the weaker, inhomogeneous B_1 field during transmission.

A compromise between the more uniform flip angle from the large surface coil and the greater sensitivity of the smaller surface coil is to use both as part of an actively decoupled system [13]. The large surface coil can be used for transmission only and is switched off resonance by a PIN diode when not being used to excite the sample. A smaller actively decoupled surface coil optimized for the geometry of the sample can then be switched on resonance and the signal detected. For optimal SNR in sample noise dominated coils, the radius of the coil should be approximately equal to the desired depth of penetration [25, 48], however adequate SNR can usually be achieved at distances approximating the diameter of the coil.

For small animal spectroscopy, where suturing a coil to the myocardium is clearly impractical, a homogeneous resonator, such as a birdcage coil, is generally preferred. It is possible to build a birdcage coil optimized for the geometry of the sample such that the animal fills the field-of-view of the coil; this optimizes the coil sensitivity as the larger the RF coil becomes, the weaker its B_1 field and hence the lower its sensitivity. The birdcage coil enables an approximately uniform B_1 field in the centre of the resonator resulting in a uniform flip angle and uniform receive profile. The downside of the birdcage coil is that whilst its B_1 field is uniform, it is relatively insensitive compared to a surface coil. This relative lack of sensitivity is not necessarily a problem as the small size of the resonator means that the field strength is often sufficient for many MRS applications.

It is also possible to use a birdcage coil as part of an actively decoupled system in conjunction with a surface coil, or coil array for signal reception. The advantages of the uniform transmit B_1 field can be combined with the sensitivity of the surface receive coils, significantly improving SNR. In cases where metabolite concentrations are low, or where the MR sensitivity of the nucleus is low, the actively decoupled volume and surface coils can be worth the added complexity.

Cardiac and Respiratory Gating

As with cardiac MRI, cardiac motion will introduce artefacts into MRS data. Unlike the clinic, preclinical MR experiments are typically conducted with the animal under general anaesthesia and breathing freely. MRS data are commonly of sufficiently low SNR necessitating acquisition of multiple averages in order to produce a spectrum with sufficient SNR to be useful. Consequently, motion artefacts will be smoothed out over time. At best, for chemical shift imaging (CSI) experiments, motion artefacts will result in a temporal average of the spatial location of the signal and will likely give an approximation of diastole. At worst, cardiac motion during localization will result in phase artefacts in the signal corrupting the FID, such that the artefacts cancel out the signal yielding unusable data. Breathing motion will also

result in data corruption, although as breathing is typically at a much lower frequency than the heart rate, the magnitude of the problem is also lower.

Typically, in vivo cardiac spectroscopy is conducted in diastole when the heart remains approximately motionless for the greatest proportion of the cardiac cycle. Triggering acquisition on the R-wave of the elecrocardiogram (ECG) results in an acquisition that occurs in end-diastole. Acquisitions can also be gated according to the respiratory signal such that data are not acquired during breathing. It is important to remember that dummy scanning during breathing events will be required in order to maintain the magnetization steady state and therefore avoid introduction of T_1 artefacts into the data.

Shimming the Sample

MR spectroscopy relies on having a uniform magnetic field across the tissue of interest. If the field is not uniform, the spectrum will record an overlapping population of resonances corresponding to the inhomogeneities in magnetic field. This results in broad and irregular line shapes making data analysis difficult and unreliable. Similarly, accurate localization requires B_0 field homogeneity to minimize distortions in slice or voxel position. Poor shimming will result in large linewidths in an MR spectrum, which can lead to overlapping resonances in the spectrum, thereby making quantification difficult. Good shimming is therefore essential. Shimming is typically performed using the ^{1}H signal from water. When broadband (i.e. for nuclei other than ^{1}H) spectroscopy is performed, the RF coil used is typically double tuned to allow ^{1}H scout images to be acquired prior to spectroscopy. This ^{1}H channel can also be used for shimming as the high SNR of the ^{1}H water signal makes shimming more reliable. Low SNR signals make estimation linewidth and signal phase prone to error.

Ideally, the volume of interest should be shimmed. Field homogeneity over the regions of the sample that are not under investigation is of secondary importance. When acquiring unlocalized spectra, the entire field of view of the coil must be shimmed. If a small surface coil is being used to localize transmit and receive, shimming based on spectral linewidth will be biased to the sensitive region of the coil (i.e. close to the coil). If a volume coil is being used, it is possible to shim the complete sample based on the spectral linewidth as there is much less spatial variation in B_1 strength.

It is possible to use a single-voxel spectroscopic sequence (e.g. point resolved spectroscopy (PRESS)) to shim based on the spectral linewidth in a defined volume of the sample. If a single-voxel metabolite spectrum is to be acquired from the septum of the heart, a large voxel encompassing the entire heart can be shimmed, and then the smaller spectroscopic voxel positioned within the shimmed region. Alternatively, an image-based shimming method can be employed. Typically, a ^{1}H image of the sample is acquired at two different echo times. The phase difference between the images is dependent on the B_0 field strength (shim) at each point in space. Thus with knowledge of the field shape of each of the shim coils, it is possible to calculate an optimal shim over a defined region of the image. This allows localized shimming over an arbitrary volume of space.

^{1}H In Vivo Cardiac Spectroscopy

Nearly all biological metabolites contain protons. ^{1}H is the most sensitive of the biologically relevant nuclei, and therefore ^{1}H MRS offers a powerful tool to investigate metabolism in the intact organism. As the metabolites in the myocardium are 10^{4}–10^{5} times lower in concentration than the ^{1}H concentration of water, water suppression is essential to in vivo ^{1}H MRS.

Small-animal cardiac ^{1}H MRS was implemented in mice and was used to measure myocardial creatine concentration in guanidoacitate *N*-methyl transferase (GAMT) deficient mice. This is a genetic model that is characterized by decreased creatine levels, and reiterates GAMT deficiency in humans [77]. A cardiac triggered, respiratory gated, PRESS sequence was used with three CHESS modules for water suppression (Fig. 5.4) [73]. For spectroscopy, a 2 μl voxel was placed in the myocardial septum. Positioning the voxel in the septum prevents myocardial signal contamination from pericardial lipids

Resonances assigned to creatine (CH_2, and CH_3), taurine, carnitine, and lipids, were quantified relative to the unsuppressed water signal. It was observed that in the GAMT knockout mice, resonances corresponding to creatine were not observable in the spectra. The same method has been applied to measure myocardial creatine

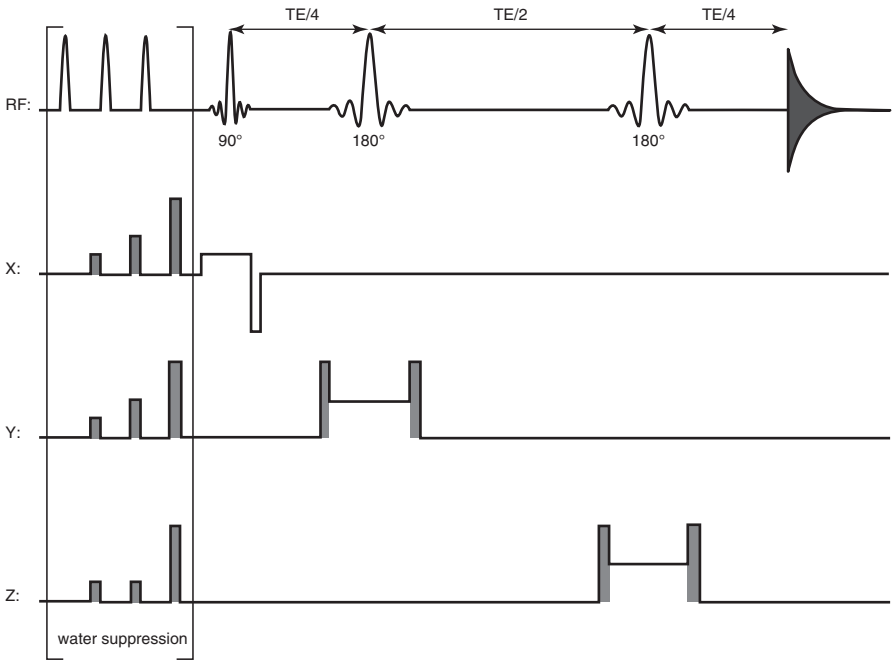

Fig. 5.4 The single-voxel PRESS sequence. The pulse sequence consists of an optional water suppression module containing three CHESS pulses with doubling gradients (indicated by *brackets*), followed by a slice selective 90° excitation pulse, two slice selective 180° refocusing pulses, and acquisition of the second half of the echo (*dark grey*). The echo time (TE) is indicated, and crusher gradients are shown in *light grey*. RF indicates the RF channel. GX, GY, and GZ are the x-, y-, and z-gradient channels respectively (Based on Schneider et al. [73])

levels in a mouse model over-expressing the creatine transporter [68], to preselect creatine transporter overexpressing mice that exhibit myocardial creatine levels 20–100% above wild-type levels prior to ex vivo perfusion studies [4]. It has been applied in mice following transverse aortic constriction (TAC) [8], to measure myocardial triglyceride levels in a long-chain acyl-CoA dehydrogenase knock-out mouse, in a mouse model of high-fat diet induced obesity [1, 9, 10], and for the measurement of the T_1 of myocardial metabolites using saturation recovery in order to allow quantification of metabolite concentration [7].

Stimulated echo acquisition mode (STEAM) spectroscopy has also been employed to measure myocardial creatine concentrations in a canine model of myocardial infarction using a 130 mm ^{1}H surface coil in a 1.5 T scanner [15] (Fig. 5.5). Unlike PRESS which uses a 90° excitation pulse and a 180° inversion pulse to generate a spin echo, STEAM uses three 90° pulses to generate a stimulated echo. STEAM places fewer demands on the MR hardware and reduces the specific absorption rate (SAR) in clinical MR systems [81]. PRESS will, however, produce approximately twice the SNR of STEAM [27] but its hardware requirements make it less practical

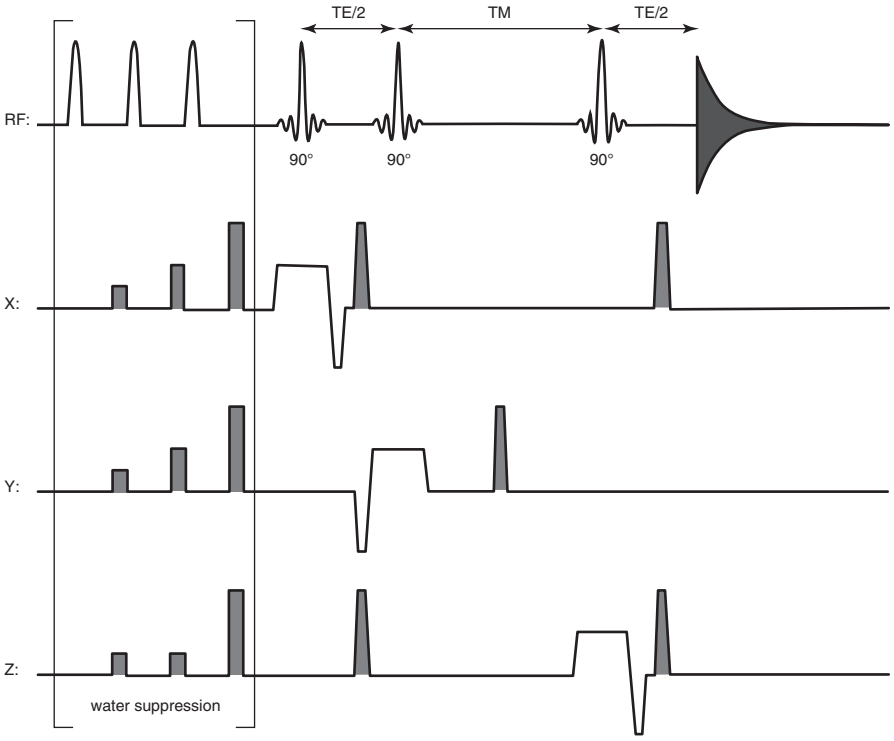

Fig. 5.5 The single voxel STEAM sequence. The pulse sequence consists of an optional water suppression module containing three CHESS pulses (indicated by *brackets*), followed by three slice-selective 90° excitation pulses, and acquisition of the second half of the stimulated echo (*dark grey*). The echo time (TE) and mixing time (TM) are indicated, and crusher gradients are indicated in *light grey*. RF indicates the RF channel. GX, GY, and GZ are the x-, y-, and z-gradient channels respectively (Based on Bottomley and Weiss [15])

to implement on a clinical system. Following scouting and shimming, voxels were defined in the infarcted anterior wall of the myocardium and in the healthy septum of the heart. Total creatine was quantified by comparison of the unsuppressed water signal and the creatine signal from the same voxel. It was observed that in the injured region the total creatine content was low (6.3 ± 3.7 μmol/g wet weight) compared to the remote healthy myocardium (24.7 ± 6.1 μmol/g wet weight).

Measuring oxygen tension in the myocardium in vivo has to be carried out indirectly owing to the spin inactive nature of the ^{16}O nucleus and the high cost of enrichment with ^{17}O. Fortunately, the oxygen transport protein myoglobin includes a ^{1}H resonance that is sensitive to the oxygen status of the protein. The intracellular oxygen tension in the myocardium was measured in vivo in a canine model of ischaemia reperfusion [19, 45]. Due to the presence of a paramagnetic centre in myoglobin, there is a large downfield shift of the $N_{\delta}H$ proton of the imidazole group of the HisF8 amino acid in the protein to ~76 to 80 ppm (compared to the chemical shift of water at 4.7 ppm). The $N_{\delta}H$ proton also has a very short T_1 and T_2, allowing a short TR but resulting in broad linewidths. However, as the linewidth is so broad, the effects of cardiac motion on the shape of the peak are minimal allowing rapid averaging without cardiac triggering. Consequently, a 28 mm surface coil was sutured to the epicardium of the left ventricle in the territory perfused by the LAD. A balloon catheter was inserted into the artery and inflated in order to induce myocardial ischaemia. By selectively exciting the resonance corresponding to the $N_{\delta}H$ proton, an unlocalized pulse-acquire spectrum of deoxy-myoglobin could be recorded (Fig. 5.1); the selective excitation of the resonance, and the large chemical shift difference between the $N_{\delta}H$ resonance and water meant that water suppression was unnecessary. It was demonstrated that there was a strong correlation between the relative blood flow to the myocardium and the change in the amplitude of the deoxy-myoglobin peak. The intracellular oxygen tension in the myocardium could also be calculated.

^{31}P In Vivo Cardiac Spectroscopy

One of the central pillars of the current understanding of cardiac disease is the fact that high-energy phosphate metabolism is perturbed in most pathologies. A decrease in the PCr/ATP ratio has been observed following myocardial infarction and dilated cardiac myopathy, and is a strong predictor of disease survival in cases of hypertrophic cardiomyopathy [12, 60, 61]. As a consequence, considerable work has been done implementing in vivo cardiac ^{31}P MRS in animal models of heart disease with most recent work focussing on small animal models.

Early ^{31}P cardiac MRS was conducted under anaethesia in open-chest swine or canine models [69, 71]. Zhang and co-workers sutured a 25 mm surface coil to the epicardium of the pig heart in an open chest model [89]. The animals had previously undergone permanent ligation of the left circumflex artery (LCx) and been allowed to recover. The animals demonstrated left ventricular remodelling or congestive heart failure. Left ventricular pressure was monitored using a catheter inserted via the apical dimple, a bipolar epicardial pacing electrode was sutured to the right atrial appendage, and the animals were ventilated. Spectra were recorded in late diastole, and data

acquisition was gated using the signal from the left ventricular pressure monitor. Respiratory gating was achieved by triggering the ventilator to the cardiac cycle during the TR delay. A variation on the image selected in vivo spectroscopy (ISIS, [65]) localization pulse sequence was used, termed rotating frame experiment using adiabatic plane rotation pulses for phase modulation-ISIS with Fourier series window (RAPP-ISIS/FSW, [37]) Fig. 5.6). RAPP-ISIS/FSW allows the selection of signal from a column of tissue normal to the plane of the surface coil. The inhomogeneous B_1 field of the surface coil is used to provide spatial localization of the signal within this column. With the surface coil sutured to the myocardium, RAPP-ISIS/FSW allowed the acquisition spectra from voxels within a 17 × 17 mm^2 column of tissue.

^{31}P spectra were collected from five voxels positioned across the myocardial wall. Cytosolic pH and [Mg^{2+}] were measured as described for ex vivo perfused hearts above. Similarly, [ADP] was estimated based on the ^{31}P metabolite measurements, the CK reaction equilibrium, and the myocardial total creatine content measured from biopsy samples. The PCr/ATP ratio in the mid-myocardium was 2.06 ± 0.16 in control animals and 1.80 ± 0.14 in infarcted animals. The open-chest pig model was later expanded to

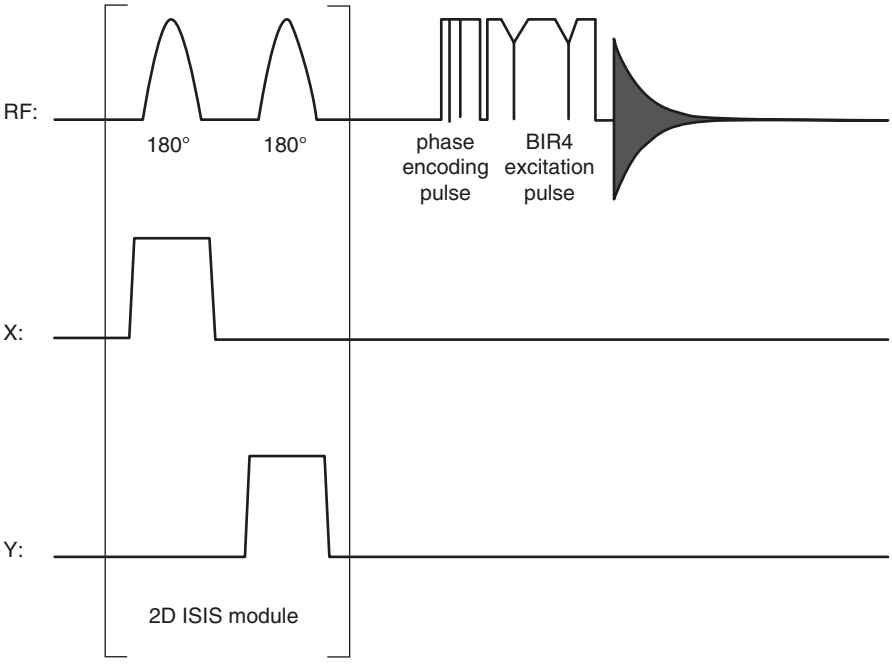

Fig. 5.6 The 1D RAPP-ISIS/FSW pulse sequence. The pulse sequence consists of a 2D ISIS module containing two adiabatic 180° slice selective pulses, which is used to localize the signal to a column of tissue normal to the plane of the surface coil (indicated by *brackets*). It is followed by a phase encoding RF pulse of increasing duration. The inhomogeneous B_1 profile of the surface coil ensures that the phase of the tissue closest to the surface coil increments faster than that of tissue further from the coil as the pulse length is increased. This enables phase encoding of position based on placement in the B_1 profile of the RF coil. An adiabatic BIR4 (B_1-insensitive rotation) excitation pulse is then used, and an FID collected (*dark grey*). RF indicates the RF channel. GX, and GY are the x-, and y-gradient channels respectively (Based on Hendrich et al. [37])

enable measurement of saturation transfer experiments to determine CK flux rates in pig hearts using an unlocalized DANTE pulse-acquire sequence [59] (Fig. 5.3).

Closed-chest ^{31}P spectroscopy of the canine heart was reported using surface coils and a 3D ISIS pulse sequence [23]. The short T_2 of the ^{31}P metabolites means that using a spin-echo experiment such as PRESS, which has an inherently long TE, results in substantial signal decay during TE and consequently very low SNR. ISIS does not rely on a spin-echo for its localization, but instead relies on signal phase cancellation from volumes outside the voxel of interest to generate a localized spectrum (Fig. 5.7). The dogs were placed under general anaesthesia, mechanically ventilated, and left ventricular pressure was monitored via a catheter

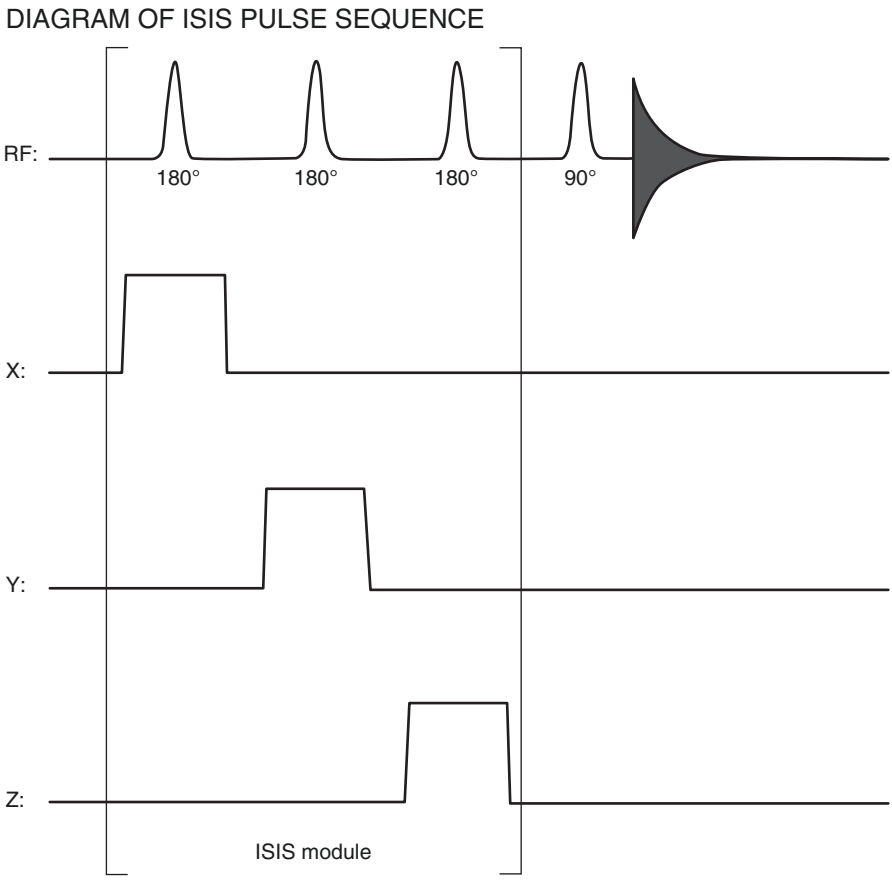

Fig. 5.7 The 3D ISIS pulse sequence. The pulse sequence consists of a 3D ISIS module containing three adiabatic 180° slice selective pulses, which is used to localize the signal to a single cuboidal volume (indicated by *brackets*). It is followed by an adiabatic 90° excitation pulse, and acquisition of an FID (*dark grey*). Adiabatic pulses are used to ensure that a known uniform flip angle is applied when using a surface coil for transmission. If the inversion pulses are spatially variant, then the signal phase cancellation from the eight step ISIS module will not be complete, and the resulting spectrum will contain artefacts. RF indicates the RF channel. GX, GY, and GZ are the x-, y-, and z-gradient channels respectively (Based on Luyten et al. [56])

inserted via the right carotid artery. Following the acquisition of ^{1}H scout and cine images, an ISIS voxel was positioned to encompass the entire left ventricle avoiding the diaphragm and chest wall, resulting in a voxel volume of 125–275 ml. To minimize the signal contamination from resonances arising from the blood, data acquisition was gated to be acquired at end-systole at the point of peak negative dP/dt_{max}. Data were acquired using a 140 mm single-turn surface coil placed on the chest wall adjacent to the heart. Adiabatic RF pulses were used to ensure flip angle accuracy despite the inhomogeneous B_1 profile of the RF coil [56]. PCr/ATP was measured and was shown to rapidly decrease with the onset of hypoxia. Mean PCr/ATP was observed to be unchanged upon angiotensin or dobutamine stress in this model, and remained close to baseline control values of ~1.5.

Similarly, Cho and co-workers implemented 3D CSI in the dog [20] (Fig. 5.8). CSI does not require a spin-echo and consequently has a short TE, which is preferable when acquiring signal from short T_2 resonances such as ATP and PCr. 3D CSI acquires a spectrum corresponding to each of a 3D array of voxels. This achieves localized spectroscopy over the entire field-of-view of the experiment. CSI therefore enables quantification of metabolite concentration variation within and between tissues. Left ventricular hypertrophy was induced by TAC. A 130×35 mm^2 quadrature driven surface coil tuned to ^{31}P was used for signal transmission and reception, while a separate ^{1}H surface coil was used for imaging and shimming. The animals were anaesthetized and ventilated, and cardiac gating was achieved by use of an

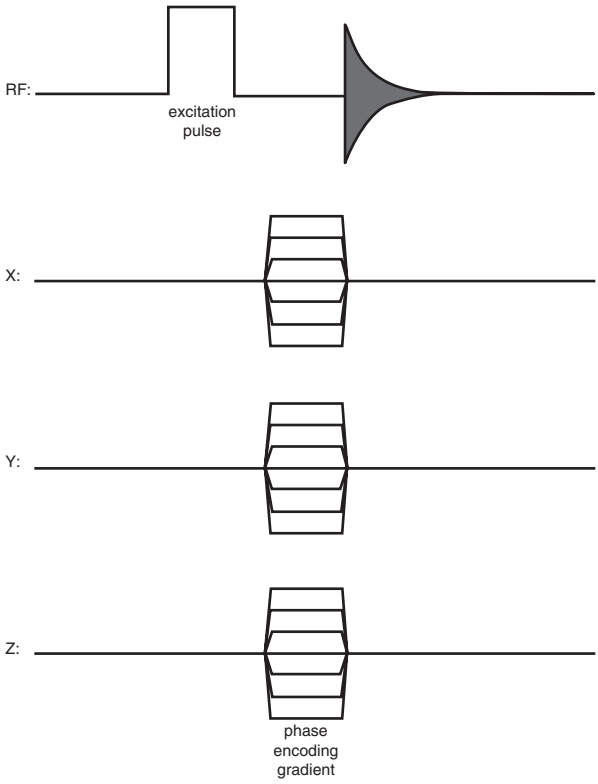

Fig. 5.8 The 3D chemical shift imaging pulse sequence. The pulse sequence consists of an unlocalized excitation pulse followed by 3D phase encoding gradients, and acquisition of an FID (*dark grey*). RF indicates the RF channel. GX, GY, and GZ are the x-, y-, and z-gradient channels respectively (Based on Cho et al. [20])

infrared sensor clipped to the ear to monitor arterial pulse. A limited subset of phase encoding steps was acquired and reconstructed using a Fourier series window approach enabling reconstruction of a spectrum from an arbitrarily positioned cylindrical voxel. Data acquisition was cardiac triggered, but was not respiratory gated as respiratory motion was determined to be minimal in the anterior LV. It was observed that subepicardial PCr/ATP was higher than subendocardial PCr/ATP, and that TAC hearts exhibited lower PCr/ATP ratios than control hearts.

One dimensional CSI has been employed to measure [PCr], [ATP], PCr/ATP, pH, and to derive [ADP] and [AMP] [15] (Fig. 5.9). 1D CSI is a relatively simple pulse sequence that relies on the limited field-of-view of the transmit/receive surface coil to provide localization parallel to the plane of the coil. The simplicity of the sequence makes it technically more straightforward to implement. Dogs were placed in a 1.5 T scanner with a 65 mm ^{31}P surface coil and a 130 mm ^{1}H surface coil placed adjacent to the heart. Scouting and shimming were carried out using the ^{1}H coil. A 1D CSI pulse sequence was used to acquire both cardiac-gated ^{1}H water spectra and ^{31}P spectra using the ^{31}P surface coil. The signal amplitude of the ^{1}H water peak was used to calculate the ^{31}P metabolite concentration. Correction for the relative sensitivity of the RF coil for ^{1}H and ^{31}P was measured using a large phantom containing a 200 mM Pi solution by acquiring a fully relaxed ^{1}H and ^{31}P CSI data set with the same spatial resolution as was used for the in vivo data acquisition; a 200 mM Pi solution was chosen so as to load the coil in a similar manner to the animal. 1D CSI provides localization in one dimension only, in this instance allow-

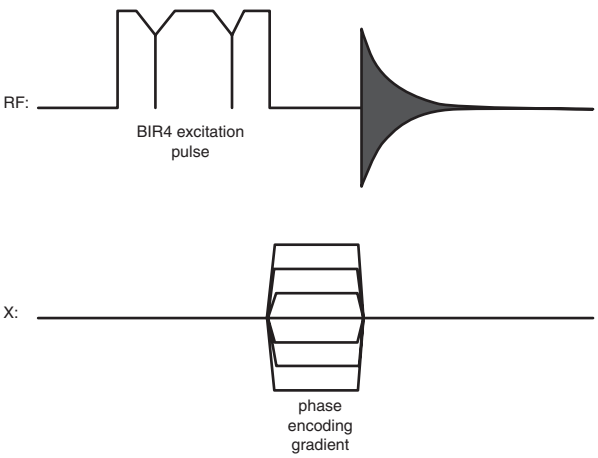

Fig. 5.9 The 1D chemical shift imaging pulse sequence. The pulse sequence consists of an unlocalized excitation pulse followed by one-dimensional phase encoding gradients, and acquisition of an FID (*dark grey*). Adiabatic excitation is used in order to deliver a known flip angle independent of the B_1 of the surface transmission coil. Phase encoding is placed normal to the plane of the coil; Fourier transformation of the phase encoding direction results in a series of planar voxels parallel to the surface coil. The small size of the surface coil restricts the effective size of the voxels parallel to the coil. RF indicates the RF channel, and GX is the x-gradient channel (Based on Bottomley and Weiss [15])

ing selection of 10 mm thick planar voxels parallel to the ^{31}P surface coil. The small size of the surface coil restricts the effective size of the voxels to the limited field-of-view of the surface coil. This means that voxels can be positioned in the anterior wall of the myocardium with minimal contamination from neighbouring skeletal muscle from the chest wall. With the addition of a frequency selective saturation pulse applied to γ-ATP (−2.5 ppm relative to PCr) and a control saturation at 2.5 ppm, 1D CSI has also been successfully expanded to enable the measurement of creatine kinase kinetics in mice [35].

Flögel, Tucci, and co-workers have reported the implementation of 2D CSI in the mouse heart using a 9.4 T scanner [26, 82] (Fig. 5.10). 2D CSI acquires spectra from a two-dimensional grid of voxels. Because it is slice selective, there are only two dimensions of phase encoding to acquire, rather than three as in 3D CSI for example. As the section of the left ventricular myocardium between the valvular plane and above the apex is approximately cylindrical, the voxels of the 2D CSI experiment can be aligned such that the through-slice direction is parallel with the

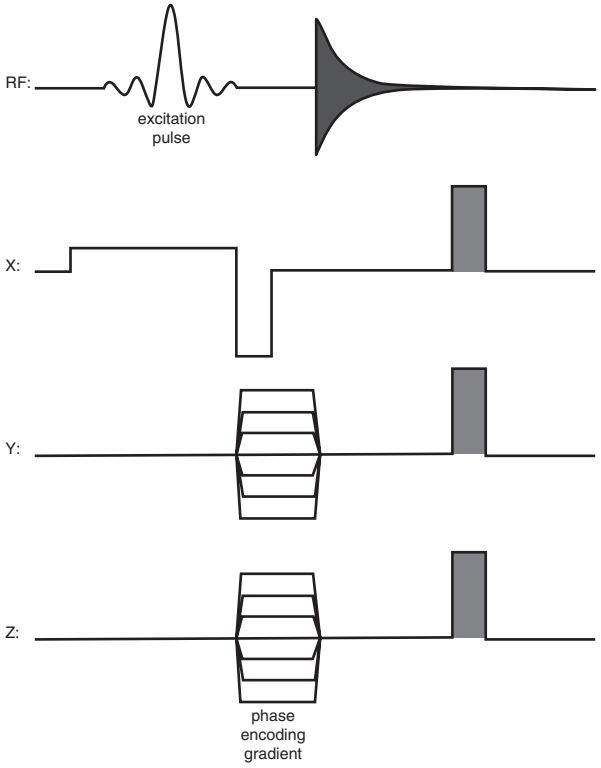

Fig. 5.10 The 2D chemical shift imaging pulse sequence. The pulse sequence consists of a slice selective excitation pulse followed by two dimensional phase encoding gradients, and acquisition of an FID (*dark grey*). Crusher gradients are shown in *light grey*. RF indicates the RF channel. GX, GY, and GZ are the x-, y-, and z-gradient channels respectively (Based on Flögel et al. [26])

long axis of the heart so that a voxel will be contained within the myocardium along the entire length of the voxel, thereby increasing the amount of myocardium in the voxel and improving SNR. In this case, using a thicker slice can therefore be advantageous. The in-plane array of voxels can then be used to more accurately describe the circular shape of the short axis of the heart. Flögel, Tucci, and co-workers placed the mice in a double tuned $^{1}H/^{31}P$ birdcage volume resonator (inner diameter 30 mm or 38 mm) allowing both ^{1}H scout imaging and shimming, and ^{31}P spectroscopy to be carried out using the same coil. Mice were anaesthetized and positioned in the animal cradle such that the heart was approximately in the isocentre of the RF coil. Flögel et al. used a shim file optimized on a homogeneous phantom in order to shim the magnet for in vivo spectroscopy, whilst Tucci et al. used fieldmap-based shimming (MAPSHIM, [46]) over the region of interest. Scaling factors to account for partial saturation effects were based on unlocalized spectra from the mouse thorax that were acquired using either the same TR and flip angle as the CSI experiment or were fully relaxed. Cardiac gating was not performed as the authors determined that the myocardial displacement due to cardiac motion was small compared to the spatial resolution of the CSI, and that diastole accounted for ~2/3 of the cardiac cycle [26]. Without cardiac gating, a uniform TR could be maintained preventing T_1 saturation artifacts from corrupting the data. Little contamination of myocardial ^{31}P spectra was observed from the diphosphoglycerate ([2, 3]-DPG) resonance from the blood except in the region of the septum, where the PCr/ATP ratio was also reduced compared to the rest of the myocardium. The same method has also been successfully applied in rats [54].

Single voxel ^{31}P spectroscopy has been implemented in a TAC model of cardiac hypertrophy in mice using 3D ISIS by Bakermans and co-workers [8] (Fig. 5.7). As with canine in vivo spectroscopy, a single ISIS voxel was placed enclosing most of the left ventricle. The voxel was placed carefully to avoid including skeletal muscle from the chest wall within the voxel. An actively decoupled, double tuned, $^{1}H/^{31}P$ birdcage volume coil was used for ^{1}H scouting and shimming and for ^{31}P excitation, and a two-turn actively decoupled 14 mm surface coil was used for ^{31}P signal reception. ^{31}P pulse calibration was performed by optimizing the flip angle based on the signal from a ~500 μl spherical phantom containing 15 M H_3PO_4 placed behind the surface coil; the phantom was removed prior to acquiring in vivo spectra. An $11 \times 11 \times 11$ mm^3 voxel was placed over the heart and shimmed manually using a cardiac-triggered, respiratory-gated, ^{1}H PRESS pulse sequence. Cardiac triggered and respiratory gated ISIS spectra were acquired. The potential for T_1 smearing from the least optimal ISIS encoding direction was minimized by placing that direction on the left-right axis avoiding signal contamination from skeletal muscle in the chest wall (dorsal-ventral axis) and liver (anterior-posterior axis) [16]. During respiratory periods, unlocalized excitation pulses were used to maintain the magnetization steady state. In order to determine correction factors for T_1 saturation of the metabolites in the spectra, fully relaxed ^{31}P spectra from a group of mice were also acquired. Blood contamination was evident in the ^{31}P spectra obtained from the voxel since a resonance corresponding to [2, 3]-DPG was present in the spectra. Ex vivo unlocalized ^{31}P spectra from 1 ml mouse blood

samples were acquired to determine the [2, 3]-DPG/ATP ratio in the blood, and consequently the amount of ATP present in the myocardial spectra that was due to the contamination from signal arising from the ventricular blood. It was determined that the proportion of the myocardial ATP signal arising from blood was ~4%, and consequently, the PCr/ATP ratio in the healthy myocardium was determined to be 1.00 ± 0.32, and 0.76 ± 0.13 for TAC hearts [8].

^{23}Na In Vivo Cardiac Spectroscopy

Homeostatic control of sodium in the myocardium is driven by active transport with ischaemia resulting in an increase in intracellular sodium. However, as intra- and extracellular ^{23}Na are co-resonant, a chemical shift reagent is required to alter the chemical shift of the extracellular signal such that the two signals do not overlap. The available chemical shift reagents, however, bind Ca^{2+} and are consequently toxic.

Balaschi demonstrated an open chest pig model of myocardial ischaemia and interrogated the metabolic profile using a combination of ^{31}P and ^{23}Na MRS [11]. The animal was anaesthetized, and a cannula inserted into the left ventricle via the left carotid artery in order to measure ventricular pressure. Cannulae were inserted into the jugular and femoral veins for drug and chemical shift reagent delivery. A shunt was inserted connecting the right carotid artery to the LAD; by occluding the right carotid artery, ischaemia could be induced in the heart. A 20 mm ^{31}P/^{23}Na surface coil was sutured to the epicardium in the territory perfused by the LAD and the animal was placed in a 4.7 T scanner. Interleaved, unlocalized, cardiac-triggered ^{23}Na and ^{31}P spectra were acquired. Assuming that the intra- and extracellular volume fractions were the same as those measured for the rabbit heart [32], and based on ex vivo biochemical measurement of blood serum samples taken from the animal, Balaschi was able to calculate the intracellular and extracellular [Na]. A solution containing 100 mM $DyTTHA^{3-}$ and 4 mM $CaCl_2$ was infused into the femoral vein at a rate sufficient to maintain ~2 ppm difference in chemical shift between Na_i^+ and Na_e^+. It was observed that the healthy myocardium had a pre-ischaemic $[Na_i^+]$ of 6.85 ± 0.96 mM. After 18 min of low flow ischaemiduring which the shunt pressure was decreased from ~76 to ~25 mmHg, $[Na_i^+]$ began to rise reaching 10.09 ± 2.75 mM after 40 min of ischaemia. In contrast, global ischaemia induced by zero-flow in ex vivo perfused rat heart experiments have reported increases in $[Na_i^+]$ of ~330% following 40 min of ischaemia [41], and ~510% following 27 min of ischaemia [42].

In mice, high resolution 3D CSI was implemented by Neuberger and coworkers [62]. Whilst imaging-based total tissue sodium measurements have been successfully performed (e.g. Constantinides et al. [21]), CSI has the potential to enable use of chemical shift reagents to quantify intra- and extracellular sodium concentrations, and to improve the SNR per unit time through use of acquisition or density weighting without sacrificing spatial resolution. It is also immune to image artefacts arising from chemical shift displacement/B_0 inhomogeneities, whilst also having a short TE that is suitable for measuring the sodium nuclues

with its extremely short T_2. Mice were anaesthetized and placed in a 17.6 T scanner. Proton scout images and shimming were carried out using a ^{1}H volume resonator. After scouting, the ^{1}H resonator was replaced with a 39 mm ^{23}Na birdcage resonator, and 1 mm isotropic 3D CSI was acquired. All acquisitions were cardiac triggered and respiratory gated. Density weighted k-space sampling was used in order to accelerate the long acquisition times required when acquiring a four-dimensional (three spatial, one spectral) data set. Density weighting allows non-uniform under-sampling of k-space points whilst maintaining the point spread function of the image so as not to degrade spatial resolution [34]. The myocardial/blood ^{23}Na ratio was measured to be 0.42 ± 0.16 and 0.46 ± 0.15 for the left and right ventricles respectively; these values compared well to the theoretical value of 0.45, and 0.46 measured from large animals [67]. The spatial resolution and SNR of the 3D CSI was high enough to distinguish the basic cardiac anatomy, although further improvements in resolution were limited by performance of the imaging gradients.

Accelerated 2D CSI has been also validated for ^{23}Na spectroscopy in the mouse heart [57]. Based on an under-sampled 2D CSI pulse sequence, high resolution chemical shift images have been acquired in healthy mice at 9.4 T using a 39 mm actively decoupled quadrature ^{23}Na volume coil for excitation and a 14 mm actively decoupled ^{23}Na surface coil for reception. Unlocalized pulse calibration was carried out using the volume coil for both transmission and reception. Cardiac triggered, respiratory gated 2D CSI data were acquired and three-fold undersampled in k-space resulting in a spatial resolution approximately two-fold higher than the 3D CSI method [62]. Data were reconstructed using a compressed sensing algorithm. Ventricular blood/myocardial ^{23}Na ratios were measured to be 0.45–0.48, which Maguire et al. calculated, assuming blood [Na] to be ~79 mM [66], gave myocardial total [Na] of 35.6–37.9 mM.

Data Processing and Analysis

MR spectroscopy provides a frequency spectrum of the population of metabolites in a given volume. Each nucleus or group of equivalent nuclei in a molecule gives rise to a peak in the spectrum generating a unique pattern of resonances. Unfortunately, the peaks from different metabolites can be close together in frequency and may overlap; this overlap is made worse when poor shimming results in broad linewidths. Consequently, identifying and quantifying the relative peak amplitudes and areas can prove to be difficult. Whilst increasing B_0 will increase the frequency dispersion of the resonances and reduce the spectral overlap, simply using a higher-field magnet to acquire a data set is not usually an option.

Spectral SNR can be improved by multiplying the FID by a filter function. Commonly, an exponential function is used resulting in a spectrum in which the SNR is improved, but in which the linewidth has been degraded by convolution of the spectrum with a Lorentzian function (the Fourier transform of an exponential

function). This line-broadening function serves to multiply the beginning of the FID (where the MR signal is of greatest amplitude) by a value of 1.0 with the end of the FID (where there is least signal and proportionally more noise) by a value approaching 0.0. Optimal improvement in SNR is achieved when the Fourier transform of the filter function has a linewidth that is equal to the linewidth in the spectrum. Multiplication of the FID by a Gaussian filter leads to a Voigt lineshape (convolution of a Lorentzian and Gaussian) in the resulting spectrum. Similarly, zerofilling the FID (adding zeros to the end of the FID to artificially increase the number of points in the FID) before the application of the Fourier transform will improve the spectral resolution of the final spectrum. Applying a line-broadening function to the FID to ensure that the FID has decayed to zero before the point at which zerofilling begins will prevent artefacts from appearing in the resulting spectrum.

Spectra are commonly analyzed as the phased, real mode component of the complex spectrum. This has the advantage that linewidths in the phased spectrum are narrower than in magnitude spectra, and the spectral noise should be Gaussian with a mean value of zero. When integrating peaks, having a baseline value of zero makes calculating peak areas simpler and more accurate. When the phase of the spectrum is not straightforward, for example where there is *J*-coupling modulation of the phase of a signal multiplet, it can be analyzed as a magnitude spectrum, however this will result in broader linewidths, and a non-zero baseline offset determined by the amplitude of the noise. The broader linewidths will lead to increased overlap of neighbouring peaks in the spectrum.

A number of approaches have been used in order to quantify cardiac MR spectra. The simplest approach is to integrate the peaks in the spectrum either by simply adding the relevant intensities in the digital spectrum, or by the application of Simpson's rule. The peak is typically integrated between the points of the spectrum where the peak returns to the spectral baseline. When the baseline of the spectrum is not flat, it can be approximated either by a polynomial or a spline, which can then be subtracted from the data. In less extreme cases, a baseline gradient can be approximated by a straight line connecting the two minima of a peak. Peak integration makes no assumptions about the shape of the line such that even poorly shimmed samples, in which the lineshape is not Lorentzian or Gausian, can be readily analyzed. However, the effects of T_2 and T_2^* decay are not taken into account leading to errors in quantification when the spectrum contains resonances with a mixture of decay rates; differential signal decay will occur during the echo time between the middle of the RF pulse and the first point of the FID resulting in an underestimation of the amplitude of signals from rapidly decaying species.

Data fitting in either the time or frequency domain is a preferred option for quantifying spectral signals. In this case, a model of the signal is built and fitted to the data in either the FID or spectrum. With typical in vivo data sets, the linewidth of the peaks in the spectrum is sufficiently broad that a model of the resonances is usually built using prior knowledge of the metabolites in the sample. Software such as jMRUI [76] includes time-domain fitting algorithms (e.g. AMARES, [85]), which are popular choices for fitting MRS data. Frequency-domain fitting can also be used and is included in software such as LC-Model (Provencher, Ontario, CA, USA) and

MestReNova (Mestrelab Research, Santiago, Spain). Custom-written fitting software is also used [53] and is commonly written in Matlab (Mathworks, Nantick, MA, USA). Data fitting can take into account the T_2 and T_2^* decay during the echo time of the experiment, and the model can be fitted to the complete FID/spectrum resulting in a more accurate estimate of peak amplitude than is possible with simple integration, particularly in cases with lower SNR.

In cases where TR<5× T_1, correction for T_1 saturation will also have to be carried out. This can either be done by measuring the T_1 of the metabolites in question (e.g. using inversion recovery, or progressive saturation approaches) and explicitly calculating the saturation of the signal, or a correction factor can be derived by acquiring a saturated (short TR) spectrum and a fully relaxed (TR>5× T_1) spectrum in a subset of samples, and comparing the difference in peak amplitudes.

Accelerated Data Acquisition Methods

In comparison to MRI, data acquisition for MRS is time-consuming. This stems from three main causes: metabolite concentrations are several orders of magnitude lower than the proton concentration of water in the tissues and often have long T_1 values; non-proton nuclei are significantly less MR sensitive than protons; and localized CSI-type experiments require collection of an extra data dimension requiring an extra phase encoding step. For ex vivo perfused heart studies, these long data acquisition times are not necessarily a problem. However, as preclinical in vivo MRS is necessarily carried out using general anaesthesia, the length of time for which the animal can safely be keep anaesthetized, and still recover afterwards, is limited. Until relatively recently, this limitation mean that the MRS acquisition time was curtailed, resulting in compromises of either SNR or spatial resolution.

Use of acquisition weighting and density weighting of k-space has been suggested as a way to accelerate CSI data acquisition by optimizing the regions of k-space that are sampled [34]. In acquisition weighting, for example, the number of averages acquired at each point in k-space can be varied using a Hanning function such that at the centre of k-space, where most SNR is derived, more averages are acquired with fewer averages being acquired at the edges of k-space. This necessarily degrades spatial resolution. However, by increasing the number of phase encoding steps (i.e. sampling further out into k-space) whilst keeping the total number of FIDs constant, this loss in spatial resolution is compensated whilst simultaneously improving SNR. The use of a Hanning weighting function means that the point-spread-function of the resulting image has significantly reduced side-lobes, thereby reducing signal contamination from neighbouring voxels. Density weighting is a similar approach in which a uniform number of averages is acquired from each sampled point in k-space, however the sampling density is high in the centre of k-space, and lower at the edges.

Optimized single-voxel spectroscopy has been attempted in clinical cardiac spectroscopy in order to define arbitrarily shaped spectroscopic voxels. Techniques such as spectral localization by imaging (SLIM), spatial localization with optimum pointspread function (SLOOP), and spectroscopy with linear algebraic modelling (SLAM) aim to use linear combinations of phase encoding steps in order to reconstruct spectroscopic signals that originate from a defined region of the sample [40, 87, 91, 92]. By defining the voxel to coincide with the annular left ventricular myocardium, it is possible to maximize the amount of myocardial tissue in the voxel improving SNR, and minimizing the amount of partial volume contamination from neighbouring tissues. These methods have not yet found much employment in preclinical spectroscopy.

The use of multiple actively-decoupled RF receiver coils, in conjunction with an actively decoupled volume coil, can also be used to accelerate spectroscopic data acquisition, analogous to their use in imaging. Multi-coil spectroscopy is being applied in clinical cardiac spectroscopy, particularly for ^{31}P spectroscopy at high B_0 [78]. Whilst multi-channel receivers are becoming more common in preclinical scanners, the use of such acceleration for preclinical cardiac spectroscopy is still in its infancy.

One of the more recent advances in MR data reconstruction is compressed sensing (also known as compressive sensing and compressive sampling) [55]. This family of methods allows under-sampling of k-space and recovery of an image without sacrificing spatial resolution. An in-depth description of compressed sensing is beyond the scope of this text, however compressed sensing reconstruction is essentially a denoising process, and relies on three components: the data must be sparse in some domain (e.g. the wavelet transform of the data would have few large coefficients, and many that are close to zero); randomly under-sampled k-space data such that the resulting image artefacts are noise-like; and a non-linear, iterative reconstruction algorithm. The ability to under-sample k-space in a CSI data set by five-fold or more and still recover the complete image is attractive and has been extensively investigated for preclinical brain spectroscopy. Accelerated echo-planar spectroscopic-imaging (EPSI), and CSI methods have been developed [28, 31, 39, 57]. The application of compressed sensing-based reconstruction to preclinical cardiac spectroscopy is still limited, but does offer the potential to accelerate data acquisition up to five-fold [57].

Conclusion

Preclinical MRS has a unique ability to probe the metabolism of living tissue without the addition of external radioactive agents. Whilst ex vivo perfusion studies have provided much insight into myocardial metabolism, the expansion of in vivo MRS has allowed the longitudinal study of myocardial disease progression in situ over time. With the increasing number of genetic models of human

cardiac disease that are being generated in mice, preclinical MRS is going to become an indispensable tool in the study of heart disease. The ability to translate preclinical MR protocols to clinical MR systems will hopefully bring some of these diagnostic measurements into the clinical world. MRS is relatively insensitive when compared to ^{1}H MRI, especially considering the increasing use of ^{1}H contrast agents in vivo. However, the increase in the use of surface coils and coil arrays for signal reception, analogous to common practice in the clinic, has enabled the acceleration of spectroscopic data acquisition. Combined with the advent of compressed sensing in the field of cardiac MRS, and the increasing use of high-field scanners, the sensitivity of in vivo spectroscopic measurements is improving rapidly. With the advent of preclinical and clinical hyperpolarized ^{13}C spectroscopy, in vivo MRS seems set to see much employment in the forseeable future.

Tabulor Summary: Preclinical In Vivo Spectroscopy

Pulse sequence	Nucleus	RF coil	Application
Pulse-acquire	^{31}P	Volume coil (e.g. birdcage, or Helmholz)	Ex vivo perfused heart, measurement of PCr, P_i, ATP, pH, [Mg^{2+}], etc.
	^{23}Na	Volume coil (e.g. birdcage, or Helmholz)	Ex vivo perfused heart, measurement of Na_i^+, Na_e^+ through use of chemical shift reagent, oedema
	^{23}Na	Surface coil sutured to the myocardium	In vivo, measurement of Na_i^+, Na_e^+ through use of chemical shift reagent
	^{1}H	Surface coil sutured to the myocardium	In vivo, measurement of deoxy-myoglobin
	^{17}O, ^{87}Rb, ^{59}Co, ^{13}C	Volume coil (e.g. birdcage, or Helmholz)	Ex vivo perfused heart
Unlocalized saturation-transfer	^{31}P	Volume coil (e.g. birdcage, or Helmholz)	Ex vivo perfused heart, measurement of CK flux
	^{31}P	Surface coil sutured to the myocardium	In vivo, measurement of CK flux
Slice-selective spin-echo	^{1}H	Volume coil (e.g. birdcage, or Helmholz)	Ex vivo perfused heart, measurement of creatine, carnitine, etc.
1D CSI	^{31}P	Surface coil	In vivo, measurement of PCr, P_i, ATP, pH, etc.
1D CSI with saturation transfer	^{31}P	Surface coil	In vivo, measurement of CK flux
2D CSI	^{1}H	Volume coil (e.g. birdcage, or Helmholz)	Ex vivo perfused heart, measurement of myocardial lipid
	^{31}P	Volume coil (e.g. birdcage, or Helmholz), actively-decoupled volume/surface coil, potentially surface coil	In vivo, measurement of PCr/ATP ratio
	^{23}Na	Actively-decoupled volume coil/surface coil	In vivo, measurement of total tissue [Na^+]
3D CSI	^{31}P	Volume coil (e.g. birdcage), or surface coil	In vivo, measurement of PCr, ATP, etc.
	^{23}Na	Volume coil (e.g. birdcage)	In vivo, measurement of total tissue [Na^+]
PRESS, STEAM	^{1}H	Volume coil (e.g. birdcage), or surface coil with use of adiabatic pulses	In vivo, measurement of creatine, carnitine, etc.
1D RAPP-ISIS/FSW	^{31}P	Surface coil sutured to the myocardium	In vivo, measurement PCr, ATP, etc.
3D ISIS	^{31}P	Volume coil (e.g. birdcage), or surface coil with use of adiabatic pulses	In vivo, measurement PCr, ATP, PCr/ATP, etc.

Summary of the pulse sequences reported in this chapter. Listed are the applications to which these sequences have been applied, along with the nuclei involved and the types of RF coils used

References

1. Abdurrachim D, Ciapaite J, Wessels B, Nabben M, Luiken JJFP, Nicolay K, Prompers JJ. Cardiac diastolic dysfunction in high-fat diet fed mice is associated with lipotoxicity without impairment of cardiac energetics in vivo. BBA Mol Cell Biol Lipids. 2014;1841(10):1525–37. doi:10.1016/j.bbalip.2014.07.016.
2. Ackerman JJH, Bore PJ, Gadian DG, Grove TH, Radda GK. Nmr-studies of metabolism in perfused organs. Philos Trans Roy Soc B. 1980;289(1037):425–36. doi:10.1098/Rstb.1980.0059.
3. Aguor ENE, van de Kolk CWA, Arslan F, Nederhoff MGJ, Doevendans PAFM, Pasterkamp G, Strijkers GJ, van Echteld CJA. Na-23 chemical shift imaging and Gd enhancement of myocardial edema. Int J Card Imaging. 2013;29(2):343–54. doi:10.1007/s10554-012-0093-6.
4. Aksentijevic D, Zervou S, Faller KME, McAndrew DJ, Schneider JE, Neubauer S, Lygate CA. Myocardial creatine levels do not influence response to acute oxidative stress in isolated perfused heart. PLoS One. 2014;9(10):e109021. doi:10.1371/Journal.Pone.0109021.
5. Askenasy N, Navon G. Continuous monitoring of intracellular volumes in isolated rat hearts during normothermic perfusion and ischemia. J Magn Reson. 1997;124(1):42–50. doi:10.1006/Jmre.1996.1026.
6. Askenasy N, Vivi A, Tassini M, Navon G, Farkas DL. NMR spectroscopic characterization of sarcolemmal permeability during myocardial ischemia and reperfusion. J Mol Cell Cardiol. 2001;33(8):1421–33. doi:10.1006/jmcc.2001.1404.
7. Bakermans AJ, Abdurrachim D, Geraedts TR, Houten SM, Nicolay K, Prompers JJ. In vivo proton T-1 relaxation times of mouse myocardial metabolites at 9.4 T. Magn Reson Med. 2015;73(6):2069–74. doi:10.1002/mrm.25340.
8. Bakermans AJ, Abdurrachim D, van Nierop BJ, Koeman A, van der Kroon I, Baartscheer A, Schumacher CA, Strijkers GJ, Houten SM, Zuurbier CJ, Nicolay K, Prompers JJ. In vivo mouse myocardial P-31 MRS using three-dimensional image-selected in vivo spectroscopy (3D ISIS): technical considerations and biochemical validations. NMR Biomed. 2015b;28(10):1218–27. doi:10.1002/nbm.3371.
9. Bakermans AJ, Dodd MS, Nicolay K, Prompers JJ, Tyler DJ, Houten SM. Myocardial energy shortage and unmet anaplerotic needs in the fasted long-chain acyl-CoA dehydrogenase knockout mouse. Cardiovasc Res. 2013;100(3):441–9. doi:10.1093/cvr/cvt212.
10. Bakermans AJ, van Weeghel M, Denis S, Nicolay K, Prompers JJ, Houten SM. Carnitine supplementation attenuates myocardial lipid accumulation in long-chain acyl-CoA dehydrogenase knockout mice. J Inherit Metab Dis. 2013;36(6):973–81. doi:10.1007/s10545-013-9604-4.
11. Balschi JA. Na-23 NMR demonstrates prolonged increase of intracellular sodium following transient regional ischemia in the in situ pig heart. Basic Res Cardiol. 1999;94(1):60–9. doi:10.1007/S003950050127.
12. Beer M, Seyfarth T, Sandstede J, Landschutz W, Lipke C, Kostler H, von Kienlin M, Harre K, Hahn D, Neubauer S (2002) Absolute concentrations of high-energy phosphate metabolites in normal, hypertrophied, and failing human myocardium measured noninvasively with P-31-SLOOP magnetic resonance spectroscopy. J Am Coll Cardiol 40 (7):1267–1274. Pii S0735-1097(02)02160-5 doi:10.1016/S0735-1097(02)02160-5.
13. Bendall MR. Portable Nmr Sample localization method using inhomogeneous Rf irradiation coils. Chem Phys Lett. 1983;99(4):310–5. doi:10.1016/0009-2614(83)87547-2.
14. Bodenhausen G, Freeman R, Morris GA. Simple pulse sequence for selective excitation in fourier-transform Nmr. J Magn Reson. 1976;23(1):171–5. doi:10.1016/0022-2364(76)90150-5.
15. Bottomley PA, Weiss RG. Noninvasive localized MR quantification of creatine kinase metabolites in normal and infarcted canine myocardium. Radiology. 2001;219(2):411–8.
16. Burger C, Buchli R, Mckinnon G, Meier D, Boesiger P. The impact of the isis experiment order on spatial contamination. Magn Reson Med. 1992;26(2):218–30. doi:10.1002/Mrm.1910260204.

17. Buser PT, Auffermann W, Wu ST, Jasmin G, Parmley WW, Wikmancoffelt J. Dobutamine potentiates amrinones beneficial-effects in moderate but not in advanced heart-failure – P-31-Mrs in isolated hamster hearts. Circ Res. 1990;66(3):747–53.
18. Camacho P, Fan HM, Liu ZM, He JQ. Small mammalian animal models of heart disease. Am J Cardiovasc Dis. 2016;6(3):70–80.
19. Chen W, Zhang JY, Eljgelshoven MHJ, Zhang Y, Zhu XH, Wang CS, Cho Y, Merkle H, Ugurbil K. Determination of deoxymyoglobin changes during graded myocardial ischemia: an in vivo H-1 NMR spectroscopy study. Magn Reson Med. 1997;38(2):193–7. doi:10.1002/Mrm.1910380206.
20. Cho YK, Merkle H, Zhang JY, Tsekos NV, Bache RJ, Ugurbil K. Noninvasive measurements of transmural myocardial metabolites using 3-D P-31 NMR spectroscopy. Am J Physiol-Heart Circ. 2001;280(1):H489–97.
21. Constantinides CD, Kraitchman DL, O'Brien KO, Boada FE, Gillen J, Bottomley PA. Noninvasive quantification of total sodium concentrations in acute reperfused myocardial infarction using Na-23 MRI. Magn Reson Med. 2001;46(6):1144–51. doi:10.1002/Mrm.1311.
22. Cross HR, Radda GK, Clarke K. The role of Na+/K+ atpase activity during low-flow ischemia in preventing myocardial injury – a P-31, Na-23 and Rb-87 Nmr spectroscopic study. Magn Reson Med. 1995;34(5):673–85. doi:10.1002/Mrm.1910340505.
23. Dell'Italia LJ, Evanochko WT, Blackwell GG, Pearce DJ, Pohost GM. Relationship between shortening load, contractility, and myocardial energetics in intact dog. Am J Phys. 1993;264(6):H2180–7.
24. Desrois M, Kober F, Lan C, Dalmasso C, Cole M, Clarke K, Cozzone PJ, Bernard M. Effect of isoproterenol on myocardial perfusion, function, energy metabolism and nitric oxide pathway in the rat heart -a longitudinal MR study. NMR Biomed. 2014;27(5):529–38. doi:10.1002/nbm.3088.
25. Edelstein WA, Foster TH, Schenck JF (1985) The relative sensitivity of surface coils to deep lying tissues. Paper presented at the Proceedings of the 4th Annual Meeting, Society of Magnetic Resonance, London.
26. Flögel U, Jacoby C, Godecke A, Schrader J. In vivo 2D mapping of impaired murine cardiac energetics in NO-induced heart failure. Magn Reson Med. 2007;57(1):50–8. doi:10.1002/mrm.21101.
27. Frahm J, Merboldt KD, Hanicke W. Localized proton spectroscopy using stimulated echoes. J Magn Reson. 1987;72(3):502–8. doi:10.1016/0022-2364(87)90154-5.
28. Furuyama JK, Wilson NE, Burns BL, Nagarajan R, Margolis DJ, Thomas MA. Application of compressed sensing to multidimensional spectroscopic imaging in human prostate. Magn Reson Med. 2012;67(6):1499–505. doi:10.1002/mrm.24265.
29. Gadian DG, Hoult DI, Radda GK, Seeley PJ, Chance B, Barlow C. Phosphorus nuclear magnetic-resonance studies on normoxic and ischemic cardiac tissue. Proc Natl Acad Sci USA. 1976;73(12):4446–8. doi:10.1073/Pnas.73.12.4446.
30. Garlick PB, Radda GK, Seeley PJ. Phosphorus Nmr-studies on perfused heart. Biochem Biophys Res Commun. 1977;74(3):1256–62. doi:10.1016/0006-291x(77)91653-9.
31. Geethanath S, Baek HM, Ganji SK, Ding Y, Maher EA, Sims RD, Choi C, Lewis MA, Kodibagkar VD. Compressive sensing could accelerate H-1 MR metabolic imaging in the clinic. Radiology. 2012;262(3):985–94. doi:10.1148/radiol.11111098.
32. Gonzalez F, Bassingthwaighte JB. Heterogeneities in regional volumes of distribution and flows in rabbit heart. Am J Phys. 1990;258(4):H1012–24.
33. Goudemant JF, Elst LV, Vanhaverbeke Y, Muller RN. P-31 Nmr kinetics study of cardiac metabolism under mild hypoxia. J Magn Reson Ser B. 1995;106(3):212–9. doi:10.1006/Jmrb.1995.1036.
34. Greiser A, von Kienlin M. Efficient k-space sampling by density-weighted phase-encoding. Magn Reson Med. 2003;50(6):1266–75. doi:10.1002/mrm.10647.
35. Gupta A, Rohlfsen C, Leppo MK, Chacko VP, Wang YB, Steenbergen C, Weiss RG. Creatine kinase-overexpression improves myocardial energetics, contractile dysfunction and survival in

murine doxorubicin cardiotoxicity. Plos One. 2013;8(10):e74675. doi:10.1371/journal.pone.0074675.
36. Gupta RK, Gupta P. Direct observation of resolved resonances from intra-cellular and extracellular Na-23 ions in Nmr-studies of intact-cells and tissues using dysprosium(Iii)tripolyphosphate as paramagnetic shift-reagent. J Magn Reson. 1982;47(2):344–50. doi:10.1016/0022-2364(82)90127-5.
37. Hendrich K, Merkle H, Weisdorf S, Vine W, Garwood M, Ugurbil K. Phase-modulated rotating-frame spectroscopic localization using an adiabatic plane-rotation pulse and a single surface coil. J Magn Reson. 1991;92(2):258–75. doi:10.1016/0022-2364(91)90269-Y.
38. Holt WW, Wendland MF, Derugin N, Finkbeiner WE, Higgins CB. Effect of repetitive brief episodes of cardiac ischemia on P-31 magnetic-resonance spectroscopy in the cat. Magn Reson Med. 1990;15(1):70–80. doi:10.1002/Mrm.1910150108.
39. Hu S, Lustig M, Balakrishnan A, Larson PEZ, Bok R, Kurhanewicz J, Nelson SJ, Goga A, Pauly JM, Vigneron DB. 3D compressed sensing for highly accelerated hyperpolarized C-13 MRSI with in vivo applications to transgenic mouse models of cancer. Magn Reson Med. 2010;63(2):312–21. doi:10.1002/mrm.22233.
40. Hu XP, Levin DN, Lauterbur PC, Spraggins T. Slim – spectral localization by imaging. Magn Reson Med. 1988;8(3):314–22. doi:10.1002/Mrm.1910080308.
41. Imahashi K, Hashimoto K, Yamaguchi H, Nishimura T, Kusuoka H. Alteration of intracellular Na+ during ischemia in diabetic rat hearts: the role of reduced activity in Na+/H+ exchange against stunning. J Mol Cell Cardiol. 1998;30(3):509–17. doi:10.1006/Jmcc.1997.0615.
42. Imahashi K, Nishimura T, Yoshioka J, Kusuoka H. Role of intracellular Na+ kinetics in preconditioned rat heart. Circ Res. 2001;88(11):1176–82. doi:10.1161/Hh1101.092139.
43. Ishikawa M, Mori T, Itoh S, Fujiki H, Koga K, Tominaga M, Yabuuchi Y. Effects of Opc-18790, a new positive inotropic agent, on energetics in the ischemic canine heart – a P-31-Mrs study. Cardiovasc Res. 1995;30(2):299–306.
44. Jacobus WE, Taylor GJ, Hollis DP, Nunnally RL. Phosphorus nuclear magnetic-resonance of perfused working rat hearts. Nature. 1977;265(5596):756–8. doi:10.1038/265756a0.
45. Jameel MN, Hu QS, Zhang JY. Myocytes oxygenation and high energy phosphate levels during hypoxia. PLoS One. 2014;9(9):101317. doi:10.1371/Journal.Pone.0101317.
46. Kanayama S, Kuhara S, Satoh K. In vivo rapid magnetic field measurement and shimming using single scan differential phase mapping. Magn Reson Med. 1996;36(4):637–42. doi:10.1002/Mrm.1910360421.
47. Kirkels JH, Vanechteld CJA, Ruigrok TJC. Intracellular magnesium during myocardial ischemia and reperfusion – possible consequences for postischemic recovery. J Mol Cell Cardiol. 1989;21(11):1209–18. doi:10.1016/0022-2828(89)90697-4.
48. Kumar A, Edelstein WA, Bottomley PA. Noise figure limits for circular loop MR coils. Magn Reson Med. 2009;61(5):1201–9. doi:10.1002/mrm.21948.
49. Kupriyanov VV, Gruwel MLH. Rubidium-87 magnetic resonance spectroscopy and imaging for analysis of mammalian K+ transport. NMR Biomed. 2005;18(2):111–24. doi:10.1002/nbm.892.
50. Kupriyanov VV, Xiang B, Sun J, Jilkina O, Dai G, Deslauriers R. Effects of ischemia on intracellular rubidium in pig and rat hearts: Rb-87 NMR imaging and spectroscopic study. Magn Reson Med. 2000;44(2):193–200.
51. Lide DR, Weast RC, Chemical Rubber Company. CRC handbook of chemistry and physics : a ready reference book of chemical and physical data. 83rd ed. Boca Raton: CRC Press; 2002.
52. Lu M, Atthe B, Mateescu GD, Flask CA, Yu X. Assessing mitochondrial respiration in isolated hearts using 17O MRS. NMR Biomed. 2012;25(6):883–9. doi:10.1002/nbm.1807.
53. Lu M, Zhu XH, Zhang Y, Chen W. Intracellular redox state revealed by in vivo P-31 MRS measurement of NAD(+) and NADH contents in brains. Magn Reson Med. 2014;71(6):1959–72. doi:10.1002/mrm.24859.
54. Luedde M, Flögel U, Knorr M, Grundt C, Hippe HJ, Brors B, Frank D, Haselmann U, Antony C, Voelkers M, Schrader J, Most P, Lemmer B, Katus HA, Frey N. Decreased contractility due

to energy deprivation in a transgenic rat model of hypertrophic cardiomyopathy. J Mol Med-JMM. 2009;87(4):411–22. doi:10.1007/s00109-008-0436-x.
55. Lustig M, Donoho D, Pauly JM. Sparse MRI: the application of compressed sensing for rapid MR imaging. Magn Reson Med. 2007;58(6):1182–95. doi:10.1002/mrm.21391.
56. Luyten PR, Groen JP, Vermeulen JWAH, Denhollander JA. Experimental approaches to image localized human P-31 Nmr-spectroscopy. Magn Reson Med. 1989;11(1):1–21. doi:10.1002/Mrm.1910110102.
57. Maguire ML, Geethanath S, Lygate CA, Kodibagkar VD, Schneider JE. Compressed sensing to accelerate magnetic resonance spectroscopic imaging: evaluation and application to Na-23-imaging of mouse hearts. J Cardiovasc Magn R. 2015;17:45. doi:Unsp 45 1186/S12968–015–0149-6 60.
58. Morris GA, Freeman R. Selective excitation in fourier-transform nuclear magnetic-resonance. J Magn Reson. 1978;29(3):433–62. doi:10.1016/0022-2364(78)90003-3.
59. Murakami Y, Zhang JY, Eijgelshoven MHJ, Chen W, Carlyle WC, Zhang Y, Gong GR, Bache RJ. Myocardial creatine kinase kinetics in hearts with postinfarction left ventricular remodeling. Am J Physiol-Heart Circ. 1999;276(3):H892–900.
60. Neubauer S. The failing heart – reply. N Engl J Med. 2007;356(24):2546–6.
61. Neubauer S, Horn M, Cramer M, Harre K, Newell JB, Peters W, Pabst T, Ertl G, Hahn D, Ingwall JS, Kochsiek K. Myocardial phosphocreatine-to-ATP ratio is a predictor of mortality in patients with dilated cardiomyopathy. Circulation. 1997;96(7):2190–6.
62. Neuberger T, Greiser A, Nahrendorf M, Jakob PM, Faber C, Webb AG. Na-23 microscopy of the mouse heart in vivo using density-weighted chemical shift imaging. Magn Reson Mater Phys. 2004;17(3–6):196–200. doi:10.1007/s10334-004-0048-6.
63. Nunnally RL, Hollis DP. Adenosine-triphosphate compartmentation in living hearts – phosphorus nuclear magnetic-resonance saturation transfer study. Biochem-US. 1979;18(16):3642–6. doi:10.1021/Bi00583a032.
64. O'Donnell JM, Fasano MJ, Lewandowski ED. Resolving confounding enrichment kinetics due to overlapping resonance signals from C-13-enriched long chain fatty acid oxidation and uptake within intact hearts. Magn Reson Med. 2015;74(2):330–5. doi:10.1002/mrm.25446.
65. Ordidge RJ, Connelly A, Lohman JAB. Image-selected in vivo spectroscopy (Isis) – a new technique for spatially selective Nmr-spectroscopy. J Magn Reson. 1986;66(2):283–94. doi:10.1016/0022-2364(86)90031-4.
66. Ouwerkerk R, Weiss RG, Bottomley PA. Measuring human cardiac tissue sodium concentrations using surface coils, adiabatic excitation, and twisted projection imaging with minimal T-2 losses. J Magn Reson Imaging. 2005;21(5):546–55. doi:10.1002/jmrt.20322.
67. Pabst T, Sandstede J, Beer M, Kenn W, Greiser A, von Kienlin M, Neubauer S, Hahn D. Optimization of ECG-triggered 3D Na-23 MRI of the human heart. Magn Reson Med. 2001;45(1):164–6. doi:10.1002/1522–2594(200101)45:1<164::Aid-Mrm1022>3.0.Co;2-S.
68. Phillips D, ten Hove M, Schneider JE, Wu CO, Sebag-Montefiore L, Aponte AM, Lygate CA, Wallis J, Clarke K, Watkins H, Balaban RS, Neubauer S. Mice over-expressing the myocardial creatine transporter develop progressive heart failure and show decreased glycolytic capacity. J Mol Cell Cardiol. 2010;48(4):582–90. doi:10.1016/j.yjmcc.2009.10.033.
69. Robitaille PM, Lew B, Merkle H, Sublett E, Lindstrom P, From AHL, Garwood M, Bache RJ, Ugurbil K. Transmural metabolite distribution in regional myocardial ischemia as studied with P-31 Nmr. Magn Reson Med. 1989;10(1):108–18. doi:10.1002/Mrm.1910100110.
70. Saupe KW, Spindler M, Tian R, Ingwall JS. Impaired cardiac energetics in mice lacking muscle-specific isoenzymes of creatine kinase. Circ Res. 1998;82(8):898–907.
71. Schaefer S, Camacho SA, Gober J, Obregon RG, Degroot MA, Botvinick EH, Massie B, Weiner MW. Response of myocardial metabolites to graded regional ischemia - P-31 Nmr-spectroscopy of porcine myocardium in vivo. Circ Res. 1989;64(5):968–76.
72. Schneider J, Fekete E, Weisser A, Neubauer S, von Kienlin M. Reduced H-1-NMR visibility of creatine in isolated rat hearts. Magn Reson Med. 2000;43(4):497–502.

73. Schneider JE, Tyler DJ, ten Hove M, Sang AE, Cassidy PJ, Fischer A, Wallis J, Sebag-Montefiore LM, Watkins H, Isbrandt D, Clarke K, Neubauer S. In vivo cardiac H-1-MRS in the mouse. Magn Reson Med. 2004;52(5):1029–35. doi:10.1002/mrm.20257.
74. Simor T, Lorand T, Szollosy A, Gaszner B, Digerness SB, Elgavish GA. Na-23 NMR shift reagents enhance cardiac staircase effect in isolated perfused rat hearts. NMR Biomed. 1999;12(5):267–74.
75. Slingo M, Cole M, Carr C, Curtis MK, Dodd M, Giles L, Heather LC, Tyler D, Clarke K, Robbins PA. The von Hippel-Lindau Chuvash mutation in mice alters cardiac substrate and high-energy phosphate metabolism. Am J Physiol-Heart Commun. 2016;311(3):H759–67. doi:10.1152/ajpheart.00912.2015.
76. Stefan D, Di Cesare F, Andrasescu A, Popa E, Lazariev A, Vescovo E, Strbak O, Williams S, Starcuk Z, Cabanas M, van Ormondt D, Graveron-Demilly D. Quantitation of magnetic resonance spectroscopy signals: the jMRUI software package. Meas Sci Technol. 2009;20(10):104035. doi:Artn 104035 1088/0957-0233/20/10/104035.
77. Stockler S, Isbrandt D, Hanefeld F, Schmidt B, vonFigura K. Guanidinoacetate methyltransferase deficiency: the first inborn error of creatine metabolism in man. Am J Hum Genet. 1996;58(5):914–22.
78. Stoll VM, Clarke WT, Levelt E, Liu A, Myerson SG, Robson MD, Neubauer S, Rodgers CT. Dilated cardiomyopathy: phosphorus 31 MR spectroscopy at 7 T. Radiology. 2016;281(2):409–17. doi:10.1148/radiol.2016152629.
79. Straeter-Knowlen IM, Butterworth EJ, Buchthal SD, den Hollander JA, Caulfield JB, Jennings RB, Evanochko WT. 'PCr overshoot': a study of the duration in canine myocardium. NMR Biomed. 2002;15(1):52–9. doi:10.1002/nbm.757.
80. StreaterKnowlen IM, Evanochko WT, denHollander JA, Wolkowicz PE, Balschi JA, Caulfield JB, Ku DD, Pohost GM. H-1 NMR spectroscopic imaging of myocardial triglycerides in excised dog hearts subjected to 24 hours of coronary occlusion. Circulation. 1996;93(7):1464–70.
81. Tal A, Gonen O. Spectroscopic localization by simultaneous acquisition of the double-spin and stimulated echoes. Magn Reson Med. 2015;73(1):31–43. doi:10.1002/mrm.25112.
82. Tucci S, Flögel U, Hermann S, Sturm M, Schafers M, Spiekerkoetter U. Development and pathomechanisms of cardiomyopathy in very long-chain acyl-CoA dehydrogenase deficient (VLCAD(−/−)) mice. BBA-Mol Basis Dis. 2014;1842(5):677–85. doi:10.1016/j.bbadis.2014.02.001.
83. van Dorsten FA, Nederhoff MGJ, Nicolay K, Van Echteld CJA. P-31 NMR studies of creatine kinase flux in M-creatine kinase-deficient mouse heart. Am J Physiol-Heart Commun. 1998;275(4):H1191–9.
84. van Dorsten FA, Reese T, Gellerich JF, van GJA E, MGJ N, Muller HJ, van Vliet G, Nicolay K. Fluxes through cytosolic and mitochondrial creatine kinase, measured by P-31 NMR. Mol Cell Biochem. 1997;174(1–2):33–42. doi:10.1023/A:1006847605088.
85. Vanhamme L, Van Huffel S, Van Hecke P, van Ormondt D. Time-domain quantification of series of biomedical magnetic resonance spectroscopy signals. J Magn Reson. 1999;140(1):120–30. doi:10.1006/Jmre.1999.1835.
86. von Kienlin M. Cardiac (1)H-MR spectroscopy. Magn Reson Mater Phys. 1998;6(2–3):107–8. doi:10.1016/S1352-8661(98)00030-1.
87. von Kienlin M. Methodological advances in cardiac (31)P-MR spectroscopy. Magn Reson Mater Phys. 2000;11(1):36–8. doi:10.1016/S1352-8661(00)00106-X.
88. Xiong QA, Du F, Zhu XH, Zhang PY, Suntharalingam P, Ippolito J, Kamdar FD, Chen W, Zhang JY. ATP production rate via creatine kinase or ATP synthase in vivo a novel superfast magnetization saturation transfer method. Circ Res. 2011;108(6):653–U265. doi:10.1161/CIRCRESAHA.110.231456.
89. Zhang JY, Wilke N, Wang Y, Zhang Y, Wang CS, Eijgelshoven MHJ, Cho YK, Murakami Y, Ugurbil K, Bache RJ, From AHL. Functional and bioenergetic consequences of postinfarction

left ventricular remodeling in a new porcine model – MRI and P-31-MRS study. Circulation. 1996;94(5):1089–100.
90. Zhang W, Ten Hove M, Schneider JE, Stuckey DJ, Sebag-Montefiore L, Bia BL, Radda GK, Davies KE, Neubauer S, Clarke K. Abnormal cardiac morphology, function and energy metabolism in the dystrophic mdx mouse: an MRI and MRS study. J Mol Cell Cardiol. 2008;45(6):754–60. doi:10.1016/j.yjmcc.2008.09.125.
91. Zhang Y, Gabr RE, Schar M, Weiss RG, Bottomley PA. Magnetic resonance Spectroscopy with Linear Algebraic Modeling (SLAM) for higher speed and sensitivity. J Magn Reson. 2012;218:66–76. doi:10.1016/j.jmr.2012.03.008.
92. Zhang Y, Gabr RE, Zhou JY, Weiss RG, Bottomley PA. Highly-accelerated quantitative 2D and 3D localized spectroscopy with linear algebraic modeling (SLAM) and sensitivity encoding. J Magn Reson. 2013;237:125–38. doi:10.1016/j.jmr.2013.09.018.

Chapter 6
Cardiac Multinuclear Imaging

Christakis Constantinides

Abbreviations

2,3-DPG	2,3 Diaphosphoglycerate
2D	Two-dimensional
3D	Three-dimensional
CK	Creatine kinase
FLASH	Fast low angle shot
FSE	Fast spin echo
GHK	Goldman-Hodgkin-Katz
GRE	Gradient echo
IDFT	Inverse discrete Fourier transform
IHD	Ischemic heart disease
MI	Myocardial infarction
MRI	Magnetic resonance imaging
NMR	Nuclear magnetic resonance
PA	Phased array
RARE	Rapid acquisition with refocussed echoes
RX	Receiver
SI	Signal intensity
SNR	Signal-to-noise ratio
SPGR	Spoiled gradient echo
SSFP	Steady state free precession
TPI	Twisted projection imaging
TX	Transmitter

C. Constantinides, PhD
BHF Experimental Magnetic Resonance Unit, Radcliffe Department of Medicine, Division of Cardiovascular Medicine, University of Oxford, Oxford, UK
e-mail: Christakis.Constantinides@cardiov.ox.ac.uk

C. Constantinides (ed.), *Protocols and Methodologies in Basic Science and Clinical Cardiac MRI*, https://doi.org/10.1007/978-3-319-53001-7_6

Introduction

Direct multinuclear imaging is a focus area in biomedicine that has attracted attention since the early days of Magnetic Resonance Imaging (MRI). It has evolved in cyclic patterns over the years, and interestingly, it has been abandoned (at each phase of its historical evolution) from widespread use.

This chapter collectively reviews the current state-of-the-art of important MR-visible nuclei other-than-protons, including ^{23}Na, ^{39}K, ^{19}F, ^{31}P, and ^{13}C, and proposes methodologies and strategies for technique implementation on a platform-independent manner. Of these, ^{31}P and ^{13}C are excluded from this review as they constitute the target/focus of two other chapters in this book.

Historically, direct, multinuclear imaging was explored early on in the history of MRI as a natural progression to significant earlier work expended on Nuclear Magnetic Resonance (NMR). ^{19}F MRI, for example, was explored early on and dates back to the time of the NMR discovery in 1942, with initial, ground-breaking work published by Gorter and Broer [30]. Resurgence in interest arose in 1977 when Holland and colleagues [35] introduced direct imaging acquisitions in the era when human MRI was under development.

While soft biological tissue contains no fluorine (with fluorinated content existing only in solid biological tissue in vivo), strategic decisions by a National Institutes of Health (NIH) task group on molecular imaging in the early 2000 led to (among others) the introduction, development, and tremendous scientific progress on the use of exogenously labelled cells using nanoparticles, efforts initially evidenced in preclinical brain/skeletal muscle applications, and more recently, in translational clinical trials [2]. In association with the introduction of stem cells (SCs) as a potential therapeutic approach for regeneration, the scientific interest on ^{19}F-MRI remains intense.

Sodium, on the other hand, had been studied extensively using NMR in solutions and blood samples early on [51, 59], but the breakthrough imaging studies were pioneered by Hilal et al. [33] in New York in the early 1980s initially for stroke, later followed by collaborative work with Cannon et al. in acute, reperfused myocardial infarction (MI) [12]. While the imaging results from such studies have been of high quality, and generated interest within the scientific community [43], multinuclear imaging efforts languished for more than 15 years, primarily due to the lack of interest from the corporate world to endorse multinuclear hardware/software technologies in conventional low-field (at the time) clinical scanners.

The resurgence in interest is primarily attributed to Robert Judd [48] who had decided in the late 1990s to develop it further and apply it to acute, reperfused MI. With R. Kim and others, Judd [28] triggered the scientific interest, and stimulated exploration of the topic area in the early/late 1990s by multiple groups

throughout the world, including Bottomley/Weiss [19], Neubauer and colleagues [57], and others, both in preclinical and clinical applications.

Since the early studies by Judd et al. [28, 48, 54], the primary focus of ^{23}Na MRI efforts was on the assessment of the cytoplasmic Na^+/K^+ ATPase in the early (acute) ischemic, and late (chronic) injury states post-infarction, with a parallel interest in ^{39}K MRI. The completed work, despite the tremendous scientific interest at the time, has progressively received lesser attention within the scientific community, particularly from widespread clinical use, as a result of the criticism it has received for its potential benefits in comparison to the existing high-resolution, high signal-to-noise ratio (SNR), contrast-enhanced ^{1}H-MRI techniques.

Phosphorus and ^{13}C complement the landscape of multinuclear imaging. They were explored early on for spectroscopic [1, 9, 13, 37, 40] and direct imaging applications [4, 42], primarily for the study of metabolism in skeletal muscle and the myocardium [46, 47]. Direct ^{13}C imaging has been recently attempted, and is under investigation at multiple centers throughout the world, in conjunction with hyperpolarized, in vivo injections [24, 41]. While ^{31}P MRI is extremely challenging in vivo (excessively long relaxation times, low in-vivo abundance, spectral multiplicity, and inherent coupling of multiplets), there is increased interest in ^{13}C studies from the metabolic standpoint that are currently in progress [23]. Both topics are treated in separate chapters in this book where the reader's attention is redirected.

Collectively, while early, documented attempts on multinuclear cardiac imaging were initiated on grounds of scientific interest, recent attempts have been driven by preclinical and clinical interest, as determined by corporate decisions for endorsement of multinuclear technologies in commercial and preclinical, low (1.5 T), and high-field (>3 T) systems. Efforts and progress in this field have been evidenced in cyclic patterns over the last 75 years, and progress has languished until technological advancements (gradients, receivers, high-field magnets) and interest to study cellular, subcellular, intracellular, and molecular processes was intensified, efforts supported by NIH strategic decisions, and with potential envisaged value in translational medicine.

While scientific interest remains, almost all multinuclear techniques (possibly with the exception of ^{19}F and ^{13}C, where efforts are still ongoing and extending in clinical applications), have not found their way into routine, clinical MRI. They do remain as research tools for basic scientists and clinical researchers.

The current phase of MRI finds cardiac multinuclear MRI at the nadir of its progress and amidst fierce competition to identify its niche role in MRI, compared to other imaging modalities, including Positron Emission Tomography (PET) and Computer Tomography (CT).

Despite the MRI's lack of inherent sensitivity, combined MRI/PET systems may provide additional benefits, efforts that are nevertheless, still in investigative phases.

NMR Physics

Multinuclear Imaging

The quantum mechanical treatment of MR is beyond the scope of this work. Instead, a macroscopic approach is endorsed to allow a simplistic reference to nuclear interactions and relaxation.

Table 6.1 summarizes the major biophysical properties of the physiologically relevant nuclei. Of importance is the distinction of nonquadrupolar and quadrupolar nuclei (e.g., for Na^+, K^+) that possess a spin quantum number of I = 3/2.

Nuclear and Quadrupolar Interactions

A spherical nuclear charge distribution is associated with nuclei with I = 1/2 (Table 6.1). In contrast, quadrupolar nuclei (I = 3/2) have an elliptic charge distribution that generates (in addition to the magnetic dipole) an electric moment that

Table 6.1 NMR characteristics of cardiac tissue for physiologically relevant (other-than-proton) nuclei

Nucleus	Sensitivity (relative to ^{1}H) (%)	Abundance (%)	Spin quantum number	Type of nuclear interactions	Relaxation values (ms)
^{13}C	1.59	1.1	I = 1/2	Nuclear magnetic	T_1 = 11.5–42.4[a]
^{19}F	83.3	100[b]	I = 1/2	Nuclear magnetic	ND[c, d]
^{23}Na	9.25	100	I = 3/2[e]	Quadrupolar	T_1 = 12–37[f] T_{2f} = 0.4–12[f] T_{2s} = 12.3–32.5[f]
^{31}P	6.63	100	I = 1/2	Nuclear magnetic	T_1 = 1,820–5,900[b, g] T_2 = 10–220[g]
^{39}K	0.051	93.1	I = 3/2[e]	Quadrupolar	T_1 = 10[h]
					T_2 = 8[h]

[a]Range applies to the field strength of 11.7 T and relates to the moieties of [1-^{13}C] pyruvate, [2-^{13}C] pyruvate [1-^{13}C] acetaldehyde, and bicarbonate [24]
[b]Fluorine does not exist in soft biological tissue but it is only found in solid forms (undetectable by conventional MRI)
[c]ND not determined
[d]Relaxation values have been reported only for exogenously administered fluorinated compounds or labels [29, 60]
[e]The nucleus exhibits bi-exponential relaxation behavior
[f]Reported values apply to field strengths in the range of 0.89–8.5 T [11, 17, 19]
[g]Range applies to field strengths of 1.5–7 T and applies to the moieties of phosphocreatine (PCr), 2,3-diphosphoglycerate (DPG), and adenosine triphosphate (ATP) [10, 25, 26, 31, 32, 44, 56]
[h]From Parish et al. [48]

ultimately causes interactions within the molecular milieau. These interactions differ along the two axes of the hydrated molecular complex (nucleus and surrounding ligands), as it translates and rotates within the molecular milieau [5].

Energy Level Diagrams

At the energy level, no NMR signal is elicited in the absence of an external magnetic field (degenerate energy levels) irrespective of the nuclear spin (Fig. 6.1). In the presence of an external magnetic field, a Boltzmann distribution of spins is established (Fig. 6.1 – top), eliciting the NMR signal. In the case of quadrupolar nuclei, four energy levels constitute their nuclear energy distribution. However, the asymmetry of nuclear charge leads to a minor modification of the four energy levels (±A) in cases where the molecular complex encounters motional restrictions due to the heterogeneity of the molecular milieau that elicit two distinct populations, namely, a fast-relaxing (accounting for 60% of the elicited signal), and a slow-relaxing component (accounting for 40% of the elicited signal).

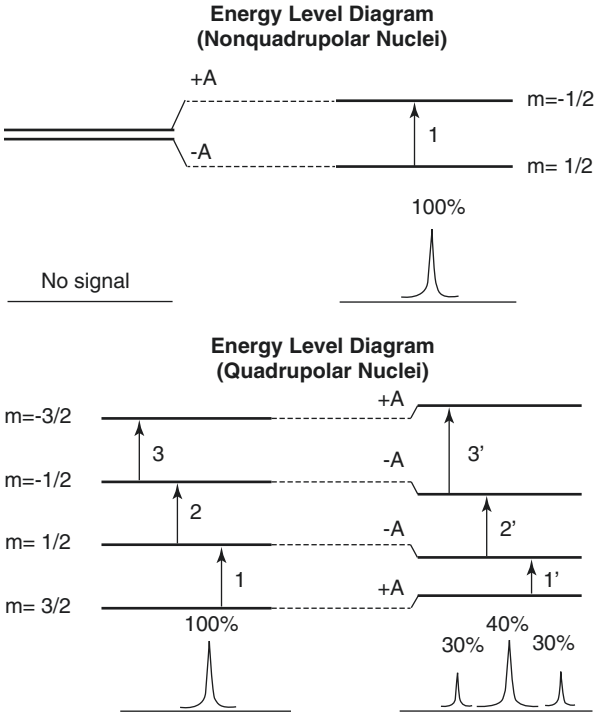

Fig. 6.1 Energy level diagrams of (*top*) nonquadrupolar and (*bottom*) quadrupolar nuclei in the (*left*) absence (lack of motional restrictions for the molecular complex) and (*right*) presence of quadrupolar interactions (*Bottom*). Bi-exponential relaxation behavior is observed in quadrupolar nuclei with fast and slow relaxing components eliciting signals at a ratio of 60:40 with regard to the total nuclear signal

Relaxation Phenomena

The fast-relaxing nuclei are associated with fast longitudinal and transverse relaxation times (T_{1f}, T_{1s}, T_{2f}, T_{2s}) [14, 22]. While it is possible to measure the transverse relaxation components in biological tissues using sequences that permit ultrashort echo time (TE) acquisitions [50, 53], T_{1f} is extremely fast and undetectable [36]. The distinction between T_{1f} and T_{1s} has thus been overseen in the literature and T_1 is commonly used to denote the relaxation of these nuclei (effectively referred to T_{1s}). As indicated in Table 6.1, for quadrupolar nuclei, T_1 ranges between 10 and 37 ms, whereas T_{2f} and T_{2s} approximately range between 0.4–12 and 8–33 ms, respectively.

The ultrashort T_{2f} imposes stringent hardware and (ultimately) pulse sequence requirements since ultrashort TE is necessary to avoid attenuation of the fast component. As discussed in the pulse sequence section that follows, pulse-acquire sequences have been favoured since they minimize TE to almost zero (with the only dependence being the transmitter (TX)/receiver (RX) blanking/unblanking delay) that spans a fraction of a ms (typically in the range of 200–400 μs with current electronics).

MR Methodologies

The different stages/phases of the evolution of multinuclear imaging did not stimulate novel hardware/instrumentation or pulse sequence methodologies/approaches, but rather capitalized on existing radiofrequency (RF) coils and pulse sequences, adapted from advancements in the field of ^{1}H MRI. Noteworthy exceptions are the developments of twisted projection imaging (TPI) developed by Fernando Boada in Keith Thulborn's group [6, 7], and the multinuclear phased array (PA) system that was developed for the clinical 1.5 T system that was implemented by P. Bottomley's group at Johns Hopkins.

Instrumentation

Primarily and foremost, dedicated, conventional, custom-made RF probes (birdcage, surface, and PA) were used for multinuclear imaging due to the lack of corporate support at the early development phase of multinuclear MRI (Fig. 6.2). Such efforts capitalized and benefitted in later years upon the availability of high field systems and their associated increased signal-to-noise (SNR) performance, increased spectral separations, facilitating implementation of selective excitation/suppression schemes (intracellular and extracellular distinction), and excitations of the multiplet ^{31}P spectral peaks.

Noteworthy was the introduction of interface electronics with the commercial 1.5 T clinical scanner, whereby, Bottomley and his group at Johns Hopkins interfaced a multinuclear PA up-converter/down-converter system that allowed concurrent multinuclear MRI on any nucleus in humans and animals [42].

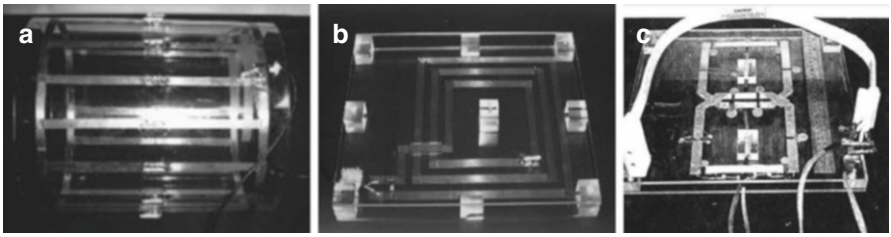

Fig. 6.2 Indicative examples of the most favoured RF coils used for multinuclear cardiac imaging in prototype forms. (**a**) Birdcage coil for animal studies, (**b**) multi-turn spiral surface coil for animal/human studies, and (**c**) the phased array system

However, the lack of clinical interest in routine, clinical, multinuclear MRI dissipated commercial interest to support these multinuclear packages. Correspondingly, corporate interest declined and availability of such packages has become optional.

Most modern systems provide nowadays the multinuclear package as an option to users that includes the necessary hardware (broadband amplifier, mixers, filters, dedicated RF probes, T/R switches) and software (pulse sequences) to allow direct multinuclear MRI. Therefore, in recent years, multinuclear MRI efforts have confined only to preclinical research studies.

Pulse Sequences

Three major sampling schemes for acquisitions have been endorsed over the years, namely, rectilinear (Spoiled Gradient Echo [SPGR]/Fast Low Angle Shot [FLASH]), radial, and TPI. Certain advantages have been documented by three-dimensional (3D) compared to two-dimensional (2D) acquisitions (using rectilinear or radial sampling schemes as a result of the ultrashort T_1 of some nuclei—e.g., Na^+ in tissue—and their increased spatial-temporal efficiency).

Over the years, only TPI has presented a major developmental effort and advancement in the acquisition strategies. It was developed by Boada et al. [6, 7] and achieved optimization of SNR, high spatial resolution (compared to conventional radial sequences associated with uneven k-space data sampling density), and spatial coverage in 3D acquisitions over multiple k-space trajectories twisted on conical surfaces of different radii (Fig. 6.3). One of the major drawbacks of the TPI is the cumbersome technical implementation and the complex reconstruction algorithm that often requires extensive programming efforts (data regridding, filtering, 3D inverse discrete Fourier transformation [IDFT], and reconstruction) (Fig. 6.4). Figure 6.3 summarizes in a schematic form the three major classes of pulse sequences used thus far. While gating options are readily available, conventionally, and in most prior applications, ungated data acquisitions have been endorsed, given the low in vivo abundance of some nuclei, and the prohibitively long relaxation times and multiplicity of the nuclear spectrum of others (^{31}P).

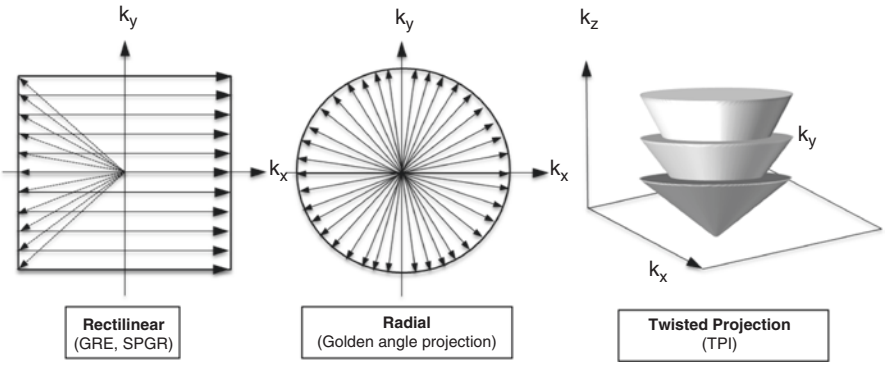

Fig. 6.3 Schematics of two- (2D) and three-dimensional (3D) k-space diagrams of extensively used pulse sequences for direct multinuclear imaging. (*Left to right*) lexicographic (*rectilinear*) k-space acquisition (Gradient Echo [*GRE*], SPGR) with complete relaxation after each excitation, radial acquisition (with projections often acquired at the Golden angle), and twisted projection imaging (*TPI*) tracing the surfaces of conical trajectories in 3D. 3D-TPI is extensively used owing to its increased time-space coverage efficiency. The listed rectilinear and radial schemes have also been extensively used in 3D acquisition modes

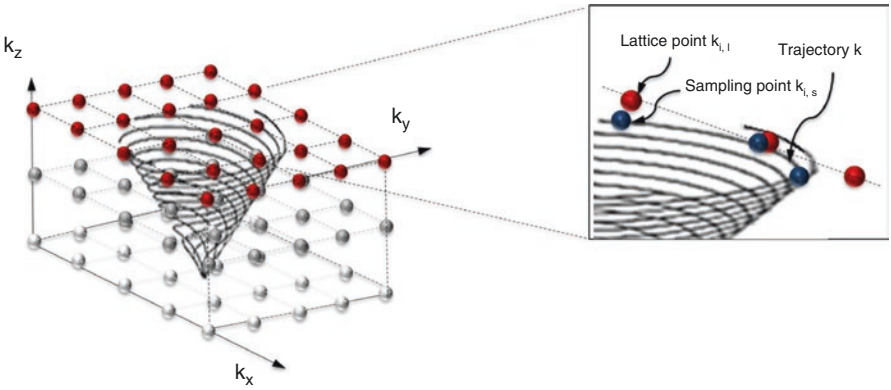

Fig. 6.4 (*Left*) Three-dimensional twisted trajectories and overlayed 3D lattice over which reconstruction is performed. (*Right-insert*) Sampled points on the conical trajectory are interpolated using a weighing function to their nearest lattice counterpart, filtered, and reconstructed using the inverse 3D discrete Fourier transform (3D-IDFT)

Gated and Ungated Acquisitions

Ungated acquisitions benefit imaging of nuclei with short relaxation values in relation to image SNR. Nevertheless, there may exist deleterious effects due to the cardiac and respiratory motions. While the effects of motion on the accurate quantification of metabolite concentrations have only been partially addressed, prior studies by Constantinides et al. [17] on ^{23}Na MRI have shown absence of

Table 6.2 Conventional pulse sequences used for cardiac MRI for nuclei-other-than ^{1}H

Nucleus	Pulse sequence	Cardiac imaging
^{19}F	GRE/ SPGR/ SSFP/FSE (RARE)	Lack of endogenous fluorinated compounds in soft biological tissue; long relaxation times (TRs) for exogenously administered compounds. Fast imaging is preferred in conjunction with averaging. Steady state free precession (SSFP) and radial sequences are optimal in signal-to-noise ratio (SNR) performance
^{23}Na	GRE/ SPGR/TPI	Short relaxation times allow use of minimum TR and fast imaging. Typically, ungated, 2D and 3D acquisitions have been preferred for their time-space efficiency. Twisted projection imaging (TPI) is optimal in SNR and resolution
^{31}P	GRE/SPGR	Limited imaging work has been reported due to long relaxation values and multiplicity of the phosphorus spectrum. Recent attempts have focussed on spectroscopic chemical shift imaging
^{13}C	Spiral/EPI	Extremely long relaxation values (T_1 values of the order of 20–30 s). Tremendous interest for in-vivo human applications-requires pre-polarized samples with short-lived lifetimes. The primary scientific interest is on the study of metabolic pathways
^{39}K	GRE/ SPGR/TPI	Short relaxation times allow use of minimum TR and fast imaging. Typically, ungated, 2D and 3D acquisitions have been preferred for their time-space efficiency. TPI is optimal in SNR and resolution

EPI echo planar imaging, *GRE* gradient echo, *FSE* fast spin echo, *RARE* rapid acquisition with refocussed echoes, *SPGR* spoiled-gradient echo, *SSFP* steady state at fee precession, *TPI* twisted projection imaging

quantitative effects in ungated, direct sodium imaging in vivo, most likely due to the spatio-temporal averaging. Added benefits have also been attributed to steady state free precession (SSFP) in the case of direct ^{19}F-MRI (Table 6.2).

Image Processing

Custom-made software have been implemented for radial/TPI reconstruction [6, 7]. Conventional sum-of-squares reconstruction has been employed for SPGR/SSFP and FSE/RARE reconstruction. Additional processing is only required for image-based quantification, however, most centers have addressed this through in-house implementations, and thus through the use of available image processing scanner software.

Image-Based Quantification

One of the most attractive features of direct multinuclear imaging has been the ability to quantify absolute in vivo concentration units (or ^{19}F atoms/cell in the case of exogenously administered ^{19}F labels) directly from reconstructed images. To achieve this, external reference phantoms of known concentrations are often placed

within the field-of-view (Fig. 6.4), thereby providing the ability to generate a signal intensity (SI) – concentration calibration curve, against which the unknown biological signal intensity is extrapolated for estimation of its concentration.

The mathematical formulation of the region-of-interest (ROI)-based quantification is in accordance to

$$[X]_{tissue} = [X]_{ref} \cdot \frac{SI_{tissue}\left(B_{1,tissue,corrected}\right)}{SI_{ref}\left(B_{1,ref,corrected}\right)} \cdot \frac{C_{tissue}}{C_{ref}} \tag{6.1}$$

where $[X]_{tissue}$, $[X]_{ref}$ are the corresponding concentrations of tissue and the reference standard of the nucleus X (or the estimated calibration curve of the standard), often expressed in mM; SI_{tissue} and SI_{ref}, are the corresponding ROI-based mean signal intensities of tissue and reference (corrected for B_1 non-uniformity), and C_{tissue}, C_{ref}, are the corresponding compound correction factors that account for the choices of the pulse sequence, TR, TE, and T_1 and T_2. They are ultimately dependent on the closed-form expressions of SI for the chosen pulse sequence at steady state. For example, in the case of the conventional SPGR sequence:

$$C = \left[\frac{\left(1 - e^{-TR/T_1}\right).\sin a}{\left(1 - e^{-TR/T_1}.\cos a\right)}\right]^{-1} \tag{6.2}$$

where α is the flip angle. Given that aqueous solutions are often used as reference standards, biological tissue and reference T_1 and T_2 values often differ. Table 6.3 lists indicative types of reference phantoms, typical concentrations, and relevant relaxation times for various field strength ranges, as published in the literature. Typical T_1/T_2 values for cardiac ^{23}Na multinuclear studies are summarized by Constantinides et al. [16, 17] and Bottomley [11], while corresponding summaries for fluorinated NPs are found in Srinivas et al. [60] and Fox et al. [29]. ^{31}P values have been published by numerous groups [25, 26, 31, 32, 44, 56], while limited reference studies exist in the case of ^{39}K [28].

Table 6.3 Typical reference phantoms, concentrations, and relaxation values, used for cardiac, image-based quantification of physiologically relevant nuclei other than ^{1}H

Reference phantoms	Typical concentrations (mM)	Relaxation values (ms)	Field strength (T)
NaF/TFA	0.5–100	T_1 = 1,000–2,700[a]	1.5–9.4
		T_2 = 1,000–2,700[a]	
NaCl, saline	5–100	T_1 = 53–71[b], T_{2s} = 54–60[b]	0.89–8.5
K_2PO_3, H_2PO_4, P_i (doped with $NiCl_2$)	0.0006–15	T_1 = 2,300, T_2 = 70[c]	1.5–4.1[c]
KCl	1–100	ND	–

[a]Constantinides et al. [20]
[b]Constantinides et al. [17], Constantinides [19]
[c]El-Sharkawy et al. [25–27]

Importantly, in this process, it is necessary to obtain estimates for B_1-dependent effects in the cases of surface coil transmission/reception (surface coils, PAs), in view of the inhomogeneous excitation/reception coil responses and the spatially distinct locations of the references and tissue of interest within the field-of-view. Difference schemes have been endorsed over the years and include: (a) direct sample B_1-calibration corrections [3, 8], and (b) direct sample-reference B_1-calibration correction schemes [3–18].

Preclinical and Clinical Cardiac Applications: Pathophysiological Relevance

While tremendous interest existed (and still exists) in direct ^{31}P cardiac imaging [15], the technical limitations involved have not allowed further exploitation. The current interest in ^{13}C, and the metabolic pathways linking cellular status, mitochondria, and the intermediate creatine-kinase (CK) flux (pyruvate-lactate conversion kinetics) have extended to a limited number of clinical studies that are currently under way.

On the forefront of ^{19}F, cardiac efforts are ongoing. Whether the interest will persist and whether it will extend to studies with clinical applications, it will be primarily dependent on the fate and success of stem cells, immune cells, and the use of molecular probes for tracking, regenerative, or anti-tumor therapeutic imaging strategies [2].

Corresponding, the only major attempt of multinuclear imaging has been thus far the targeted assessment of the Na^+-K^+ ATPase on the cytoplasmic surface, and the quantification of the intracellular and extracellular Na^+/K^+ concentrations following ischemic injury and MI (Figs. 6.6 and 6.7).

Figure 6.5 depicts in a simplified form, the ionic gradient alterations of the Na^+/K^+ concentrations in ischemic heart disease (IHD). Under normoxic conditions,

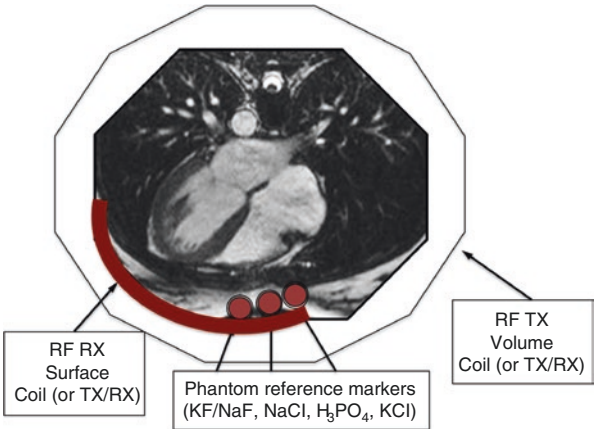

Fig. 6.5 Schematic of radiofrequency (RF) coil and reference phantom positioning scheme for cardiac multinuclear imaging and quantification. More elaborate adiabatic excitation schemes are often employed for ensuring homogenous B_1 response in tissue and reference regions

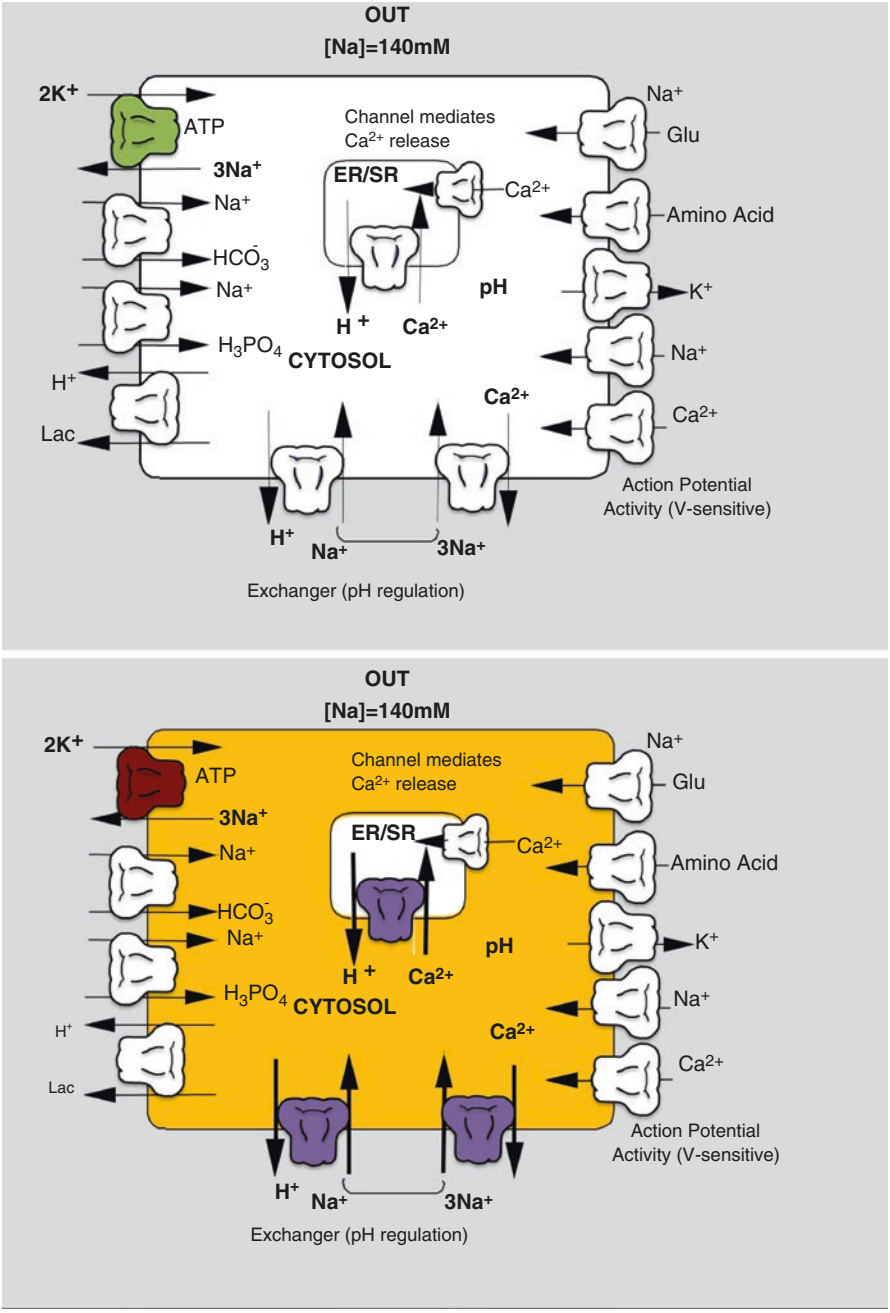

Fig. 6.6 Schematics of cellular states at (*top*) normoxic and (*bottom*) ischemic/infarcted states in the acute phase. Indicative carriers and ion-transporters and some cytoplasmic compartments are shown only. Multi-fold intracellular elevations are documented following ischemia (*highlighted in yellow*) as a result of compromised Na^+-K^+-ATPase function

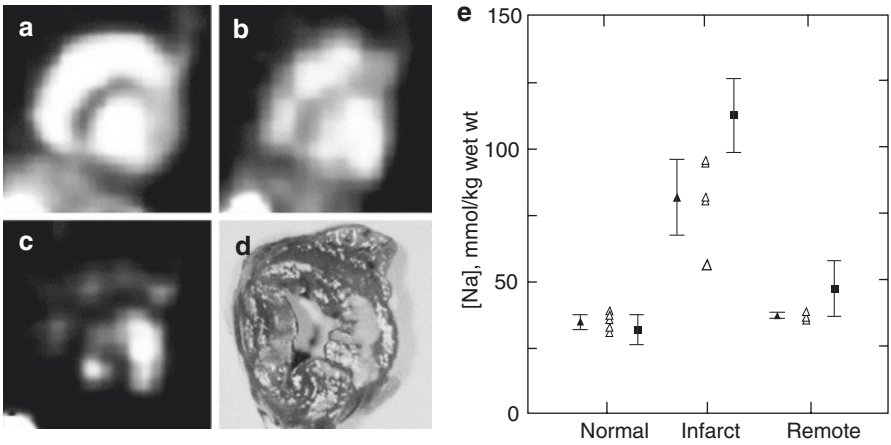

Fig. 6.7 Examples of preclinical cardiac multinuclear imaging. (**a**) ^{23}Na of the infarcted canine heart, and (**b**, **c**) following increasing doses of superparamagnetic iron oxide (MION) administered in the vascular space, thereby leading to the delineation of the infarct area. (**d**) Histologically matched TTC stained image of the same heart. (**e**) Quantification of ^{23}Na concentrations in the normal, infarcted, and contralateral canine heart using ^{23}Na MRI (*triangles*) and atomic absorption spectrophotometry (*AAS*) (*squares*) (Reproduced from Constantinides et al. [17, 21], with permission)

sodium is in rapid exchange between the vascular (~80 mM), extracellular (~140 mM), and intracellular (~10–15 mM) spaces. Correspondingly, normal functioning of the Na^+-K^+ ATPase maintains the intracellular potassium concentration at 140 mM, and the extracellular concentration at ~10 mM. Under homeostatic conditions, intracellular and extracellular ionic fluxes (primarily and foremost through the respective voltage-gated channels) maintain the gradients, yet allow action potential propagation, and electrical excitability in accordance to the Goldman-Hodgkin-Katz (GHK) equation.

In ischemia, flow/perfusion is reduced, and the diminished/depleted intracellular energy stores cause sodium accumulation and potassium depletion. Corresponding concentration changes can be formulated in accordance to:

$$Na_{total} = \frac{1}{s}\left(\left[Na\right]_{in} V_{in} + \left(1 - V_{in}\right)\left[Na\right]_{extra}\right) \tag{6.3}$$

where s is the cardiac tissue specific gravity equal to 1.03 kg/L, $[Na]_{in}$, $[Na]_{extra}$ are the respective sodium concentrations in the intracellular and extracellular spaces, and V_{in}, V_{extra} are the corresponding volumes of the two spaces (typically set to V_{in} = 75% and V_{extra} = 25% for myocardium), where $V_{in} + V_{extra} = 1$. Assuming that the primary components of the extracellular space are the interstitial and vascular components (in rapid equilibrium), and assuming that the relaxation times of the three domains differ, Eq. 6.3 can be rewritten as:

$$SI_{Na_{total}} = [Na]_{in} . V_{in} . f(TR, TE, T_1, T_2)_{in} + [Na]_{out} . (1 - V_{in} - V_{vascular}) . f(TR, TE, T_1, T_2)_{extra} + [Na]_{vascular} . V_{vascular} . f(TR, TE, T_1, T_2)_{vascular} \quad (6.4)$$

where f() are the functions defining the dependencies of the imaging parameters and relaxation parameters, and are dependent on the chosen pulse sequences (as indicated in section "Image Processing").

If ischemia persists, intracellular and subcellular changes ensue and significantly disrupt the sodium/potassium gradients. In brief, metabolic reserves deplete, diminishing ATP levels, causing the functional activity of the cytoplasmic Na^+/K^+ pump to slow down. The pump progressively becomes unable to sustain the transfer of Na^+ and K^+ against the established concentration gradients, leading to significant accumulation of sodium (and depletion of K^+) intracellularly. Prior quantitative reports argue for multi-fold elevations of intracellular sodium [52]. The pre-apoptotic (yet still viable) cell triggers mechanisms to compensate for these changes. The intracellular acidification (breakdown of enzymes, other key regulatory proteins) stimulates the activation of the H^+/Na^+ exchanger, which in its effort to extrude the excess H^+ (to restore pH) allows the influx of additional Na^+. Compensatory mechanisms still in effect subsequently stimulate the Na^+/Ca^{2+} exchanger, which, given the ionic disruptions, operates in reverse. In its effort to pump Na^+ outside the cell, the protein allows the influx of Ca^{2+}. Eventually, this leads to a calcium overload. In addition to this, other ultrastructural changes (e.g., the release of free radicals and reactive oxygen species) initiate a cascade of reactions that ultimately cause cell lysis, gradient dissipations, and cellular death. Specifically, the activation of proteases, lipases, and phospholipases, is triggered, inhibiting oxidative phosphorylation and pump activity. In association with the cessation of anaerobic glycolysis, this sequence of events ultimately leads to rigor contracture. Catabolite accumulation, enzyme denaturation, impaired mitochondrial function, and membrane damage follow. Correspondingly, the leaky cytoplasmic membrane causes a dissipation of the transmembrane ion gradients and unavoidably leads to cell death. Almost one billion cells die following an incident of acute MI in the human, an event that invariably causes increases in the extracellular volume (and corresponding decreases in the intracellular volume).

From the MRI perspective, the sodium accumulation following ischemic injury is reflected in the voxel signal elevations as the end product of initial (acute MI) intracellular/extracellular changes, and corresponding volume and relaxation changes. As shown by Judd/Kim and colleagues [38, 39], the chronic phase (post-remodelling) is associated with significant fibrosis, and leads to significant, steady-state signal elevations due to the high Na^+ collagen content of fibrotic tissue [34, 55]. Thus, the acute (and chronic) signal elevations can be understood through a simplistic formulation of the sodium signal and its changes following volume, relaxation, and concentration changes (Eq. 6.4).

Preclinical studies in canine were followed by clinical studies in humans [11, 45, 49, 57, 58], however, the high-resolution/high quality imaging benefits of the late

gadolinium enhanced (LGE) ^{1}H MRI towards the assessment of the functional extent of ischemic injury under rest/stress conditions outperformed ^{23}Na MRI. Correspondingly, ^{23}Na MRI failed to convince the clinical community for the benefits and the necessity to incorporate it in routine clinical practice (despite the comparable image/diagnostic quality against the long-standing clinical gold-standard, MI diagnostic screening approaches, using ^{99}Tc SPECT imaging).

The Future of Multinuclear Imaging

While the importance of cardiac multinuclear imaging has been proven (manifested through its long-existence), expended efforts over the last 40 years have not been successful in identifying a prominent role in clinical practice. Correspondingly, multinuclear imaging still remains a niche area in cardiovascular MRI, and developed techniques constitute (and will continue to do so) valuable clinical/research tools. Exceptions to this include ^{19}F-MRI and ^{13}C-MRI, techniques that have shown potential for translational value, primarily in cancer and ischemic heart disease (IHD). Thus, despite the existence of techniques with increased sensitivity and specificity, the potential translational role of MRI must not be undermined or undervalued.

Tabular Summary: Cardiac Multinuclear Imaging

For direct and practical implementation of multinuclear cardiac MRI, the following summarized protocols are included herein that address both preclinical and clinical scenaria listing indicative pulse sequence and parameter values.

Summary of cardiac multinuclear MRI protocols for preclinical and clinical applications

Cardiac multinuclear imaging protocol			
Setup and preparation			
Mouse	Technical details	Human	Technical details
Induce (2–5% ISO)	ISO or ketamine/xylazine	Position volunteer/patient on the imaging table	Breath-hold imaging
Position in cradle/coil	Custom-made cradles easily manufactured using rapid prototyping (for example: http://www.civm.duhs.duke.edu/SharedData/DataSupplements.htm)	Place the RF coil, respiratory bellows and/or pulse-oximeter device	Real-time recording of ECG, respiratory, and blood oxygenation
Maintain (1–2% ISO)	Calibrated vaporiser and flowmeters are required. Additional calibrations are required for anesthetic dose delivery at the nose cone	Landmark position of anatomical region of interest	
Place reference phantoms	Plastic cylindrical or Eppendorf tubes containing standard solutions with different concentrations (see Table 6.3)	Place reference markers	Plastic cylindrical or other tubes (typically incorporated in the coil's frame) containing different concentrations of standard solutions (see Table 6.3) for generation of SI-concentration calibration curve
Scout imaging			
Run localizer scout (ensure proper placement – reposition body/coil if necessary)	Simple or three-plane	Run localizer scout (ensure proper placement – reposition body/coil if necessary)	Standard fast-gated sequence acquisition
Shimming and power calibration			

Cardiac multinuclear imaging protocol			
Setup and preparation			
Mouse	Technical details	Human	Technical details
Perform non-localized (or localized) shimming over volume of interest (or voxel of interest if possible) at the ^{1}H resonance	Use either available, commercial automated shimming or custom-developed phase map correction schemes	Alternatively, run in pre-scan mode and use image projection profiles to optimize power and conduct power calibration	
Setup power calibration for optimal 90°/180° excitations at nucleus of interest (either use spin echo imaging at various flip angles or non-localized spectroscopy or other image-based approaches)		Run in spectroscopy mode – un-localized or localized. Use peak amplitudes and linewidths for assessment. Setup power calibration for optimal 90°/180° excitations at nucleus of interest (either use spin echo imaging at various flip angles or non-localized spectroscopy or other image-based approaches)	
Run direct phantom and/or animal B_1 correction	Use progressively increased RF power with object in place to implement prior published correction scheme or base correction on surface markers and post-processing of acquired data		
^{1}H cardiac imaging			
Perform ^{1}H pseudo long, pseudo short, and short/long axis imaging with full LV coverage	Gated	Gated, breath-hold (often segmented k-space acquisitions)	
	Prescribe oblique slice through mid-septum and RV	Multi-slice, multi-phase coverage are often acquired	
	Use reconstructed image to define long-axis (apex-mitral valve orientation)		
	Obtain second long-axis scan (orthogonal orientation to the first scan)		
	Use long-axis to prescribe short and/or CINE		

Cardiac multinuclear imaging protocol			
Setup and preparation			
Mouse	Technical details	Human	Technical details
^{1}H/multinuclear MRI			
Clone RX used for short/long axis acquisition and switch TX frequencies to the nucleus of interest	Depending on the research system, different hardware/software settings must be set	Clone RX used for short/long axis acquisition and switch TX frequencies to the nucleus of interest	
Acquire ^{1}H-matched multinuclear images (ungated or gated)	Cross-correlative studies	Acquire multinuclear images (ungated or gated)	
	May need to be corrected for possible off-resonance transmitter settings		
Absolute quantification			
Repeat at fully relaxed conditions for image-based quantification. If this is prohibitively long, acquire images at short TR in conjunction with quantification of T_1 and T_2	Custom-written software or free-source programs (ImageJ/MATLAB) may be used for ROI-based analyses		
	Fast (short TR) scans require corrections subject to T_1, T_2, and chosen imaging parameters		

Acknowledgements The project leading to this article has received funding from the European Union's Horizon 2020 research and innovation programme under the Marie Sklodowska-Curie grant agreement No. 652986.

References

1. Ackerman JJ, Grove TH, Wong GG, Gadian DG, Radda GK. Mapping of metabolites in whole animals by ^{31}P NMR using surface coils. Nature. 1980;283(5743):167–70.
2. Ahrens ET, Helfer BM, O'Hanlon CF, Schirda C. Clinical cell therapy imaging using a perfluorocarbon tracer and fluorine-19 MRI. Magn Reson Med. 2014;72(6):1696–701. doi:10.1002/mrm.25454.
3. Barker GJ, Simmons A, Arridge SR, Tofts PS. A simple method for investigating the effects of non-uniformity of radiofrequency transmission and radiofrequency reception in MRI. Br J Radiol. 1998;71(841):59–67.
4. Bendel P, Lai CM, Lauterbur PC. ^{31}P spectroscopic zeugmatography of phosphorus metabolites. Magn Reson Med. 1980;38:343–56.
5. Berendsen HJ, Edzes HT. The observation and general interpretation of sodium magnetic resonance in biological material. Ann N Y Acad Sci. 1973;204:459–85.
6. Boada FE, Christensen JD, Huang-Hellinger FR, Reese TG, Thurborn KR. Quantitative in vivo tissue sodium concentration maps: the effects of biexponential relaxation. Magn Reson Med. 1994;32:219–23.
7. Boada FE, Gillen JS, Shen GX, Chang SY, Thulborn KR. Fast three dimensional sodium imaging. Magn Reson Med. 1997;37:706–15.
8. Boada FE, Gillen JS, Noll DC, Shen GX, Thulborn KR. Data acquisition and postprocessing strategies for fast quantitative sodium imaging. Int J Imaging Syst Technol. 1997;8:544–50.
9. Bottomley PA. Noninvasive study of high-energy phosphate metabolism in human heart by depth-resolved ^{31}P NMR spectroscopy. Science. 1985;229(4715):769–72.
10. Bottomley PA. NMR spectroscopy of the human heart. In: Harris RK, Wasylishen RE, editors. Encyclopedia of magnetic resonance. Chichester: Wiley; 2009. doi:10.1002/9780470034590.emrstm0345.pub2.
11. Bottomley PA. Sodium MRI in human heart: a review. NMR Biomed. 2015;29(2):187–96.
12. Cannon PJ, Maudsley AA, Hilal SK, Simon HE, Cassidy F. Sodium nuclear magnetic resonance imaging of myocardial tissue of dogs after coronary artery occlusion and reperfusion. J Am Coll Cardiol. 1986;7(3):573–9.
13. Canby RC, Evanochko WT, Barrett LV, Kirklin JK, McGiffin DC, Sakai TT, Brown ME, Foster RE, Reeves RC, Pohost GM. Monitoring the bioenergetics of cardiac allograft rejection using in vivo P-31 nuclear magnetic resonance spectroscopy. J Am Coll Cardiol. 1987;9(5):1067–74.
14. Chang DC, Woessner DE. Spin-Echo of ^{23}Na relaxation in skeletal muscle. Evidence for sodium ion binding inside a biological cell. J Magn Reson. 1978;30:185–91.
15. Clarke WT, Robson MD, Rodgers CT. Bloch-Siegert B_1^+-mapping for human cardiac ^{31}P-MRS at 7 Tesla. Magn Reson Med. 2015; doi:10.1002/mrm.2600.
16. Constantinides CD, Gillen JS, Boada FE, Pomper MG, Bottomley PA. Human skeletal muscle: sodium MR imaging and quantification-potential applications in exercise and disease. Radiology. 2000;216:559–68.
17. Constantinides CD, Kraitchman DL, O'Brien KO, Boada FE, Gillen J, Bottomley PA. Noninvasive quantification of total sodium concentrations in acute reperfused myocardial infarction using ^{23}Na MRI. Magn Reson Med. 2001;46:1144–51.
18. Constantinides CD, Weiss RG, Lee R, Bolar D, Bottomley PA. Restoration of low resolution metabolic images with a priori anatomic information: ^{23}Na MRI in myocardial infarction. Magn Reson Imaging. 2000;18:461–71.
19. Constantinides CD. Sodium MRI Techniques and applications to acute reperfused myocardial infarction. Doctorate thesis. Johns Hopkins University, 2000.
20. Constantinides C, McNeill E, Benson M, Sainz-Urruela R, Padilla S, Malandraki-Miller S, Maguire ML, Swider E, Ghaffari S, Carr CA, Srinivas M, Schneider JE. Improvements in the cellular uptake of perfluorocarbon nanoparticles and ^{19}F MRS/MRI detectability using the transfection agent FuGENE. ISMRM workshop on molecular & cellular MRI: Focus on Integration: Amsterdam, June 2016.

21. Constantinides, et al. Superparamagnetic iron oxide MION as a contrast agent for sodium MRI in myocardial infarction. Magn Reson Med. 2001;46:1164–8.
22. Cope FW. Nuclear magnetic resonance evidence for complexing of sodium ions in muscle. Biochemistry. 1965;54:225–7.
23. Cunningham CH, Lau JYC, Chen AP, Geraghty BJ, Perks WJ, Roifman I, Wright GA, Connelly KA. Hyperpolarized ^{13}C metabolic MRI of the human heart: initial experience. Circ Res 2016. pii: CIRCRESAHA.116.309769. [Epub ahead of print].
24. Dzien P, Tee SS, Kettunen MI, Lyons SK, Larkin TJ, Timm KN, Hu DE, Wright A, Rodrigues TB, Serrao EM, Marco-Rius I, Mannion E, D'Santos P, Kennedy BW, Brindle KM. ^{13}C magnetic resonance spectroscopy measurements with hyperpolarized [1-^{13}C] pyruvate can be used to detect the expression of transgenic pyruvate decarboxylase activity in vivo. Magn Reson Med. 2015; doi:10.1002/mrm.25879.
25. El-Sharkawy AM, Schar M, Ouwerkerk R, Weiss RG, Bottomley PA. Quantitative cardiac P-31 spectroscopy at 3 Tesla using adiabatic pulses. Magn Reson Med. 2009;61:785–95.
26. El-Sharkawy AM, Michael S, Ouwerkerk R, Weiss R, Bottomley PA. ^{31}P cardiac spectroscopy at 3 T: T_1 quantification. J Cardiovasc Magn Reson. 2008;10(Suppl 1):A48.
27. El-Sharkawy AM, Gabr RE, Schär M, Weiss RG, Bottomley PA. Quantification of human high-energy phosphate metabolite concentrations at 3 T with partial volume and sensitivity corrections. NMR Biomed. 2013;26(11):1363–71.
28. Fieno DS, Kim R, Rehwald WG, Judd RM. Physiological basis for potassium (^{39}K) magnetic resonance imaging of the heart. Circ Res. 1999;84:913–20.
29. Fox MS, Gaudet JM, Foster PJ. Fluorine-19 MRI contrast agents for cell tracking and lung imaging. Magn Reson Insights. 2015;8(S1):53–67.
30. Gorter CJ, Broer LJF. Negative result of an attempt to observe nuclear magnetic resonance in solids. Physica. 1942;9(6):591–6.
31. Hetherington HP, Luney DJE, Vaughan JT, Pan JW, Ponder SL, Tschendel O, Twieg DB, Pohost GM. 3D ^{31}P spectroscopic imaging of the human heart at 4.1 T. Magn Reson Med. 1995;33:427–31.
32. Hetherington HP, Spencer DD, Vaughan JT, Pan JW. Quantitative 31P spectroscopic imaging of human brain at 4 Tesla: assessment of gray and white matter differences of phosphocreatine and ATP. Magn Reson Med. 2001;45(1):46–52.
33. Hilal SK, Maudsley AA, Simon HE, Perman WH, Bonn J, Mawad ME, Silver AJ, Ganti SR, Sane P, Chien IC. In vivo NMR imaging of tissue sodium in the intact cat before and after acute cerebral stroke. Am J Neuroradiol. 1983;4:245–9.
34. Hillenbrand HB, Becker LC, Kharrazian R, Hu K, Rochitte CE, Kim JE, Chen EL, Ertl G, Hruban RH, Lima JAC. ^{23}Na MRI combined with contrast-enhanced ^{1}H MRI provides in vivo characterization of infarct healing. Magn Reson Med. 2005;53:843–50.
35. Holland GN, Bottomley PA, Hinshaw WA. ^{19}F Magnetic resonance imaging. J Magn Reson. 1977;28:133–6.
36. Hubbard PS. Nonexponential nuclear magnetic relaxation by quadrupolar interactions. J Chem Phys. 1970;53(3):985–7.
37. Kemp GJ, Sanderson AL, Thompson CH, Radda GK. Regulation of oxidative and glycogenolytic ATP synthesis in exercising rat skeletal muscle studied by ^{31}P magnetic resonance spectroscopy. NMR Biomed. 1996;9(6):261–70.
38. Kim HW, Farzaneh-Far A, Kim RJ. Cardiovascular magnetic resonance in patients with myocardial infarction: current and emerging applications. J Am Coll Cardiol. 2010;55:1–16.
39. Kim RJ, Hillenbrand HB, Judd RM. Evaluation of myocardial viability by MRI. Herz. 2000;25:417–30.
40. Muller N, Lauterbur PC, Goldenson J. Nuclear magnetic resonance spectra of phosphorus compounds. J Am Chem Soc. 1956;78(15):3557–61.
41. Lau AZ, Chen AP, Ghugre NR, Ramanan V, Lam WW, Connelly KA, Wright GA, Cunningham CH. Rapid multislice imaging of hyperpolarized ^{13}C pyruvate and bicarbonate in the heart. Magn Reson Med. 2010;64:1323–31.

42. Lee RF, Giaquinto R, Constantinides C, Souza S, Weiss RG, Bottomley PA. A broadband phased-array system for direct phosphorus and sodium metabolic MRI on a clinical scanner. Magn Reson Med. 2000;43:209–77.
43. Maudsley AA, Hilal SK. Biological aspects of sodium-23 imaging. Br Med Bull. 1984;40(2): 165–6.
44. Menon RS, Hendrich K, Hu X, Ugurbil K. ^{31}P NMR spectroscopy of the human heart at 4 T: detection of substantially uncontaminated cardiac spectra and differentiation of supepicardium and subendocardium. Magn Reson Med. 1992;26:368–76.
45. Ouwerkerk R, Weiss RG, Bottomley PA. Measuing human cardiac tissue sodium concentrations using surface coils, adiabatic excitation, and twisted projection imaging with minimal T_2 losses. J Magn Reson Imaging. 2005;21:546–55.
46. Parasoglou P, Zia D, Chang G, Regatte RR. 3D-Mapping of phosphocreatine concentration in the human calf muscle at 7T: comparison to 3T. Magn Reson Med. 2013;70(6):1619–25.
47. Parasoglou P, Ding X, Chang G, Regatte RR. Three-dimensional saturation transfer ^{31}P-MRI in muscles of the lower leg at 3.0 T. Sci Rep. 2014;4:5219. doi:10.1038/srep05219.
48. Parish TB, Fieno DS, Fitzgerald SW, Judd RM. Theoretical basis for sodium and potassium MRI of the human heart at 1.5 T. Magn Reson Med. 1997;38:653–61.
49. Pabst T, Sandstede J, Beer M, Kenn W, Neubauer S, Hahn D. Sodium T_2* relaxation times in human heart muscle. J Magn Reson Imaging. 2002;15:215–8.
50. Perman WH, Thomasson DM, Bernstein MA, Turski PA. Multiple short-echo (2.5 ms) quantitation of in vivo sodium T_2 relaxation. Magn Reson Med. 1989;9:153–60.
51. Pettegrew JW, Wossner DE, Minshew NJ, Glonek T. Sodium-23 NMR analysis of human whole blood, erythrocytes, and plasma. J Magn Reson. 1984;57:185–96.
52. Pike MN, Kitakaze M, Marban M. ^{23}Na NMR measurements of intracellular sodium in intact perfused ferret hearts during ischemia and reperfusion. Am J Physiol. 1990;259:H1767–73.
53. Ra JB, Hilal SK, Cho ZH. A method for in vivo MR imaging of the short T_2 component of sodium-23. Magn Reson Med. 1986;3:296–302.
54. Rehwald W, Fieno DS, Chen EL, Kim RJ, Judd RM. Myocardial magnetic resonance imaging contrast agent concentrations after reversible and irreversible ischemic injury. Circulation. 2002;105:224–9.
55. Rochitte CE, Kim RJ, Hillenbrand HB, Chen EL, Lima JAC. Microvascular integrity and the time course of myocardial sodium accumulation after acute infarction. Circ Res. 2000;87: 648–55.
56. Rodgers CT, Clarke WT, Snyder C, Vaughan T, Neubauer S, Robson MD. Human cardiac 31P Magnetic Resonance Spectroscopy at 7 Tesla. Magn Reson Med. 2014;72:304–15.
57. Sandstede JJW, Pabst T, Beer M, Lipke C, Baurle K, Butter F, Harre K, Kenn W, Voelker W, Neubauer S, Hahn D. Assessment of myocardial infarction in humans with ^{23}Na MR imaging: comparison with cine MR imaging and delayed contrast enhancement. Radiology. 2001;221:222–8.
58. Sandstede HHW, Hillenbrand H, Beer M, Pabst T, Butter F, Machann W, Bauer W, Hahn D, Neubauer S. Time course of ^{23}Na signal intensity after myocardial infarction in humans. Magn Reson Med. 2004;52:545–51.
59. Shinar H, Navon G. Sodium-23 NMR relaxation times in body fluids. Magn Reson Med. 1986;3:927–34.
60. Srinivas M, Boehm-Sturm P, Figdor CG, de Vries IJ, Hoehn M. Labeling cells for in vivo tracking using 19F MRI. Biomaterials. 2012;33:8830–40.

Chapter 7
Cardiac Magnetic Resonance Elastography

Arunark Kolipaka

Abbreviations

DI	Direct inversion
DTI	Diffusion tensor imaging
ECV	Extra-cellular volume
ED	End-diastole
ES	End-systole
FDA	Food and Drug Administration
GRE	Gradient-recalled echo
HCM	Hypertrophic cardiomyopathy
HF	Heart failure
HFpEF	Heart failure with preserved ejection fraction
HFrEF	Heart failure with reduced ejection fraction
LFE	Local frequency estimation
LV	Left ventricular
MEG	Motion encoding gradient
MI	Myocardial infarction
MRE	Magnetic resonance elastography
MRI	Magnetic resonance imaging
PG	Phase gradient
P-V	Pressure-volume
TE	Echo time
TR	Repetition time
UE	Ultrasound elastography

A. Kolipaka, PhD, FAHA
Department of Radiology, The Ohio State University, Columbus, OH 43210, USA
e-mail: arunark.kolipaka@osumc.edu

C. Constantinides (ed.), *Protocols and Methodologies in Basic Science and Clinical Cardiac MRI*, https://doi.org/10.1007/978-3-319-53001-7_7

Introduction

Myocardial stiffness is a major determinant of cardiac function, with large changes in stiffness associated with heart failure (HF) [1]. Stiffness is thought to be a major determinant of the ventricular filling function, which directly affects the systolic contraction force through the Frank-Starling mechanism. It is known that myocardial stiffness is increased in many diseases, including ischemia [2], diastolic dysfunction and/or heart failure with preserved ejection fraction (HFpEF) [1], hypertension [3], and hypertrophic cardiomyopathy (HCM) [4].

It is now recognized that over one-third of patients with HF symptoms appear to have a normal ejection fraction (>50%) but impaired ventricular filling (i.e., HFpEF), as opposed to those who present primarily with impaired contractile performance (i.e., heart failure with reduced ejection fraction, HFrEF). Patients with HFpEF typically have clinical conditions causing afterload elevating (e.g., systemic arterial hypertension, aortic stenosis) and characteristically present evidence/findings of normal left ventricular (LV) volumes, increased LV mass, diastolic dysfunction, elevated filling pressures and/or elevated blood natriuretic peptide measurements. Patients with HFrEF present the signs and symptoms of classical HF due to reduced systolic performance [5]. Both forms of HF have a poor 5-year mortality of ~50% [6].

In the range of presented HF phenotypes/clinical findings it is difficult to characterize patients effectively, to determine if the differences in filling and ejection are due to increased myocardial stiffness, impaired relaxation, impaired contractility, or some combination of these [7]. However, many studies have shown that patients with HFpEF and HFrEF demonstrate increased myocardial stiffness [8, 9].

Invasive Myocardial Stiffness Estimation

Pressure-Volume (P-V) derived stiffness dates back to the late nineteenth century when Otto Frank [10] related ventricular pressure and volume to myocardial mechanics and function in isolated hearts. Mechanical testing of skeletal muscle was introduced in the nineteenth century [11], and applied to the myocardium in the form of isolated papillary muscle [12] and myocardial strips [13]. Technological breakthroughs in the 1950s and 1960s led to increased interest in both the P-V stiffness and mechanical testing, which in turn led to numerous studies in the 1970s and 1980s that form the basis of our current understanding of cardiac mechanics and physiology. From these studies we know that increased stiffness impairs diastolic filling [8], and that regions of myocardial infarction are initially soft and gradually become stiffer [9]. However, P-V methods are invasive, and assess the LV chamber rather than the true intrinsic properties of the myocardium. Similarly, current technology of mechanical testing utilizes myocardial strips to estimate passive stiffness in a uniaxial [14] or biaxial [15] directions and do not account for the dynamic behavior for the heart.

Noninvasive Myocardial Stiffness Estimation

A major problem is that there is currently no noninvasive way to measure LV stiffness in vivo. Methods currently used to infer stiffness include inflow and tissue velocity indices, such as Doppler E and A inflow parameters, and E′ and A′ tissue velocity parameters [16], strain and strain-rate imaging, such as circumferential strain or torsion [17], or structural imaging, including eccentric and concentric remodeling indices. As we already know, the slope of stress vs. strain curve provides modulus (referred to as stiffness). The current methods provide strain measurement and the stress information can be obtained from the invasive pressure measurements. Therefore, only the strain measurements cannot quantify stiffness, and the characterization of disease processes and the quantification of the effects of treatment are currently problematic.

Ultrasound elastography (UE) has two main forms, neither of which has found application in the heart. The first form is often called "static" UE, in which a superficial tissue is compressed and the deformation of the tissue is used to estimate stiffness. Static UE has found application in superficial structures, such as the thyroid [18] and breast [19], but cannot be practically performed in deep intrathoracic organs (e.g. heart). The other form of UE is often called "dynamic" or "transient" UE, in which a shear wave is externally applied by a device fixed within the ultrasound transducer. The wave speed of this externally applied shear wave is tracked, and then converted to a stiffness measurement. Dynamic UE has found application in the liver [20], spleen [21], and other abdominal organs. However, to date, cardiac UE has been technically difficult and the only in vivo cardiac application has been in open-chested animals [22].

Magnetic Resonance Elastography (MRE)

MRE is a noninvasive phase-contrast MR imaging technique used to estimate the stiffness of soft tissues. MRE involves three steps, as shown in Fig. 7.1. First, noninvasive sinusoidal vibrations are induced in the region-of-interest (i.e., in a phantom with stiff and soft inclusions). Second, these vibrations are synchronized with the motion encoding gradients (MEG) in a phase-contrast MRI sequence (Fig. 7.2) to encode the displacement field (i.e., a wave image with the red to blue color band indicating the wavelength) in the phase of an MR image. Third, these displacement fields are processed using a mathematical algorithm known as *inversion* [23] to obtain a spatial stiffness map called elastogram, showing soft and stiff inclusions.

Stiffer objects have longer wavelength (red to blue band) with higher wave speeds compared to softer objects. Shear stiffness in a tissue of interest can be estimated by estimating the wave speed of the propagating wave using Eq. 7.1. The wave speed is related to wavelength of the propagating wave using Eq. 7.2.

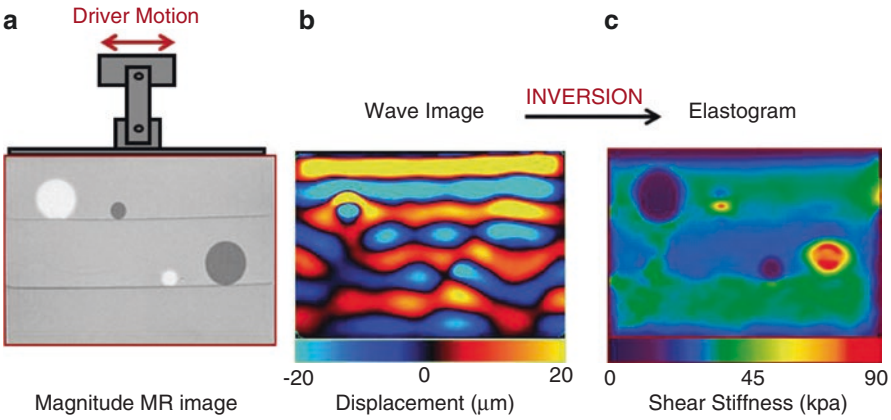

Fig. 7.1 Principle of magnetic resonance elastography (MRE). (**a**) Mechanical vibrations are induced in a phantom with four inclusions. (**b**) These vibrations are captured in the phase of an MR image, with *red* to *blue* region representing the wavelength of the propagating wave. (**c**) The wave images are processed to obtain a stiffness map known as elastogram to report soft and stiff inclusions

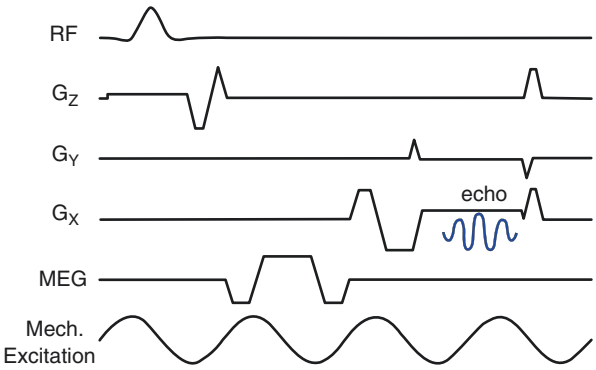

Fig. 7.2 Magnetic resonance elastography (MRE) pulse sequence. A gradient-recalled echo (GRE) MRE pulse sequence with motion-encoding gradient (MEG) gradients shown separately, which can be applied on any axis (i.e. X, Y, Z) to encode the displacement field in respective spatial directions. These MEG gradients are synchronized with the external mechanical excitation

$$\mu = \rho c^2 \tag{7.1}$$

$$c = f\lambda \tag{7.2}$$

where, μ is the shear stiffness, ρ is the density of the material, c is the wave speed, f is the frequency of excitation, and λ is the wavelength.

MRE Drivers

There are numerous methods used to induce vibrations for MRE applications and these vibrations are typically in the range of 20–1000 Hz [24]. The electromagnetic actuator is one of the oldest methods based on the principle of the Lorentzian force, where a voice coil is placed in the magnetic field (i.e., the MRI scanner), and the alternating currents in the coil generate required vibrations (Fig. 7.3a). This device is simple and flexible, but generates less power. It also causes image artifacts because of interference with the main magnetic field, and may not be suitable for in vivo applications [25]. Piezoelectric drivers (Fig. 7.3b) have been designed for use in MRE, but are very fragile and low-power and generate a low-displacement field, which may not be suitable for in vivo applications targeting deeper tissues of interest [25]. Finally, an acoustic driver system (Fig. 7.3c) designed in early 2000 involved an active driver (i.e., an acoustic speaker) and a passive driver. The active driver is placed outside the scan room and the passive driver is in contact with the subject's region-of-interest to induce the vibrations.

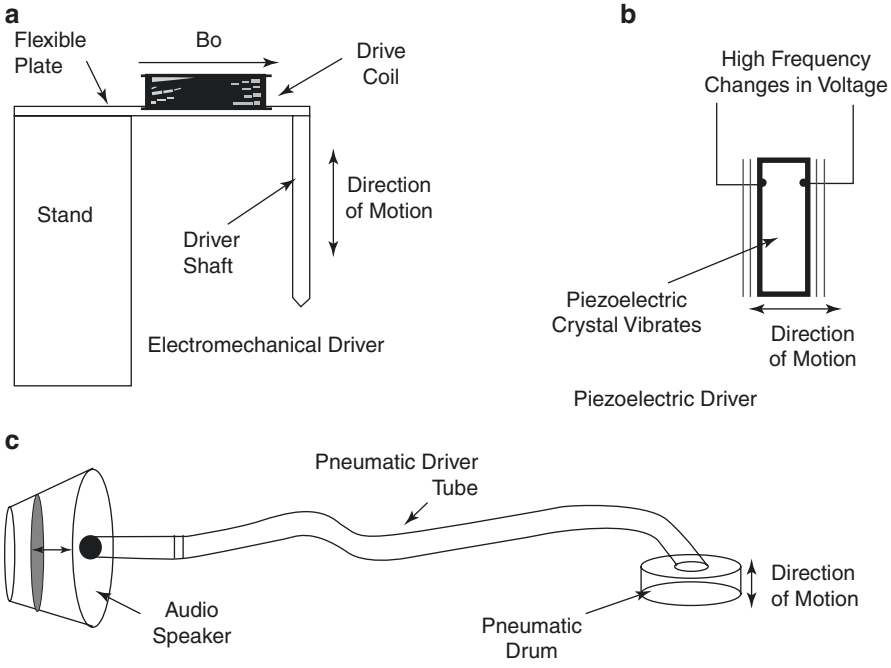

Fig. 7.3 Magnetic resonance elastography (MRE) driver systems. (**a**) Electromechanical driver placed in the scanner with Bo indicating magnetic field direction and vibration direction. (**b**) Piezoelectric driver showing vibration direction. (**c**) Pneumatic driver system with a speaker (active driver) connected to a drum (passive driver) via a plastic tube showing vibration direction

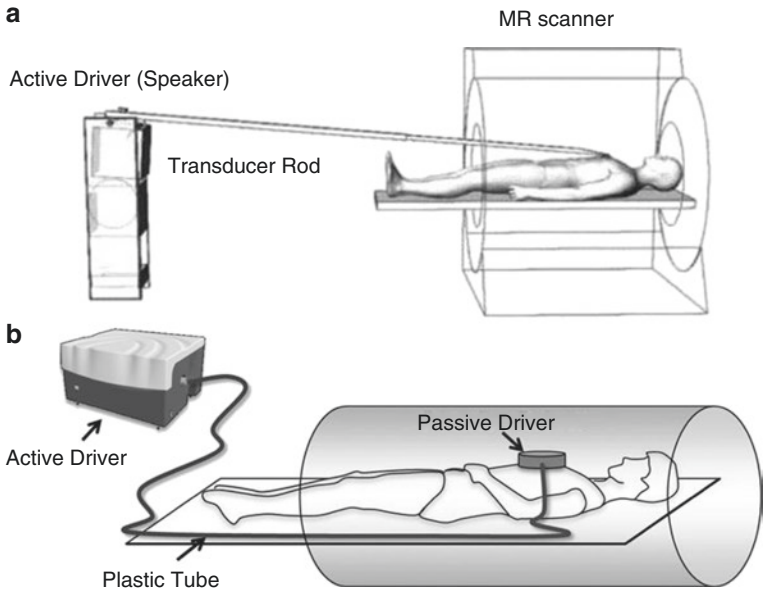

Fig. 7.4 In vivo magnetic resonance elastography (MRE) driver systems. (**a**) Schematic of pneumatic driver system with active driver (speaker) connected to a passive driver (plate) via a transducer rod. (**b**) Active driver (speaker) connected to a passive driver (drum) via a plastic tube

There are a couple of ways of connecting the active and passive drivers. In one of the methods, the active driver is connected to the passive driver (a plate) via a long transducer rod, as shown in Fig. 7.4a [26]. In another method, the active driver and the passive driver (i.e., the plastic drum with a thin diaphragm) are connected via a plastic tube as shown in Fig. 7.4b [27]. The latter is currently commercially available through Resoundant Inc. (Rochester, MN). This driver is approved by the United States Food and Drug Administration (FDA) and is clinically used for liver MRE in staging fibrosis.

Cardiac MRE Driver System

The pneumatic driver system is suitable to generate the required displacement field in the heart. This driver system was tested in the in vivo porcine model using four different configurations, as shown in Fig. 7.5 [28]. In this study [28] a single, large passive driver, (Fig. 7.5a) was compared against two small passive drivers (Fig. 7.5b), an open-chest invasive suture setup (Fig. 7.5c), and an open-chest small passive driver, in direct contact with the heart. It was shown that the large passive driver had generated mean displacement amplitudes similar to that of the direct contact driver setup. Therefore, the large passive driver with the pneumatic system was used to

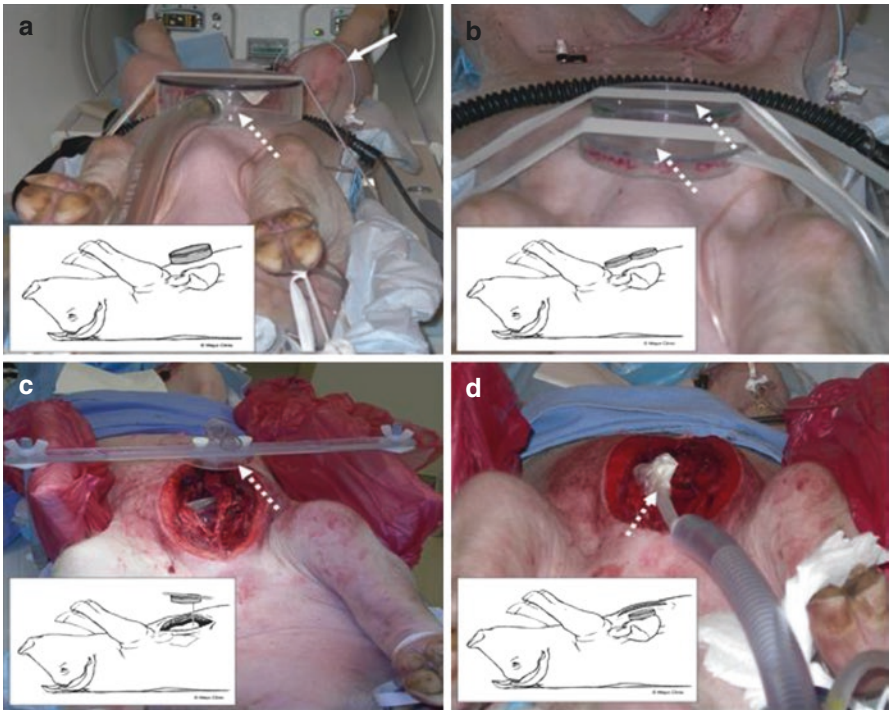

Fig. 7.5 Pneumatic driver system. (**a**) Large passive driver on the chest wall. (**b**) Two small passive drivers on the chest wall. (**c**) Open-chest suture setup. (**d**) Open-chest small passive driver directly placed on the heart

generate the required displacement field at 80 Hz in volunteers in vivo, as shown in Fig. 7.4b [27]. Similarly, a pneumatic driver system with a long transducer rod with a plate on the chest wall was used to generate the required displacement field at 24.3 Hz in the heart [26] in volunteers in vivo (Fig. 7.4a).

Cardiac MRE Pulse Sequence

As explained earlier, MRE is a phase-contrast technique in which MEG is synchronized with the external motion. Figure 7.2 shows a gradient-recalled echo (GRE) MRE sequence with MEG gradients that can be applied along any spatial direction. It is important to understand that imaging the heart using a MRE sequence is challenging when compared to imaging other static organs. Cardiac MRE sequences must acquire multiple offsets of external motion, multiple encoding directions of the wave displacement field, over multiple phases of the cardiac cycle, in a breathhold or separate breathholds for each motion encoding direction. Furthermore, multiple slices should also be acquired to cover the entire left ventricle. A retrospectively

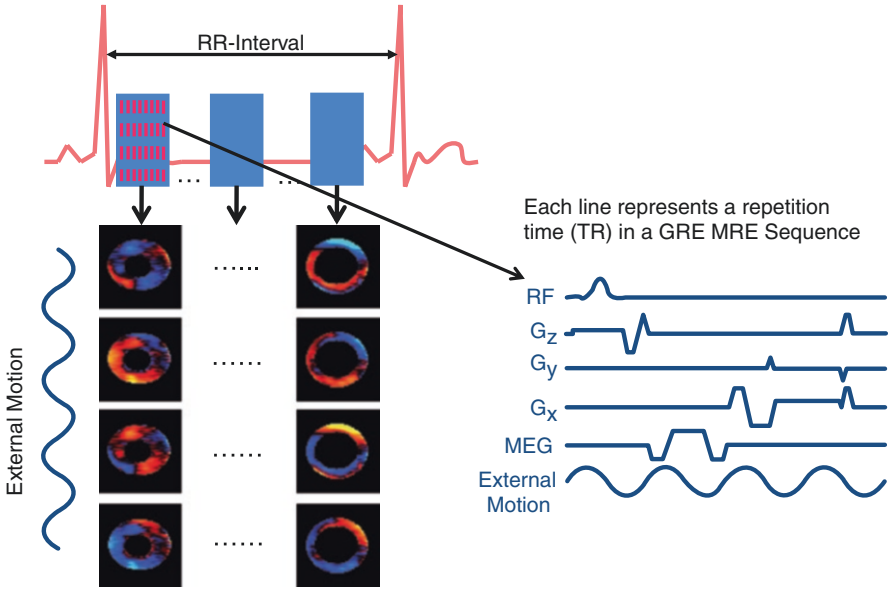

Fig. 7.6 Cine cardiac magnetic resonance elastography (MRE) sequence. In a R-R interval eight positive motion encoding and eight negative motion encodings are shared to reconstruct a cardiac phase. Each line with in a segment represents one repetition time (TR) in a gradient-recalled echo (GRE) MRE sequence. At each phase of a cardiac cycle, the external motion is tracked at four time points to encode the propagating wave in the heart. 16 R-R intervals are needed to reconstruct wave data with all cardiac phases in one encoding direction in a single slice

ECG-gated cine GRE MRE sequence shown in Fig. 7.6 was developed and validated in a phantom [29]. This sequence is based on the segmented acquisition, where eight segments with positive and negative MEG's were applied to reconstruct one cardiac phase. For a heart rate of 60 bpm with an acceleration factor of 2, a 16 s breathhold is required to encode the motion in one direction for one slice and obtaining multiple cardiac phases across a cardiac cycle. Similarly, another GRE-based MRE sequence was also in use. However, it has higher temporal resolution and a longer acquisition time [30].

Furthermore, a spin-echo echo planar imaging sequence [31] was also developed for use in cardiac MRE, which is a single-shot sequence but acquires only one phase of the cardiac cycle in a longer breathhold. The sequence parameters for all the above acquisition strategies are shown in Table 7.1.

Cardiac MRE Inversion

The conversion of wave displacement fields into stiffness maps is known as *inversion*. There were many methods to achieve this, such as local frequency estimation (LFE), phase gradient (PG), and direct inversion (DI), developed to

Table 7.1 Different pulse sequences for cardiac Magnetic Resonance Elastography (MRE) application with details of sequence parameters used

Parameters	GRE MRE 1	GRE MRE 2	SE-EPI MRE
Echo Time (TE)	~8.9–9.3 ms	3.29 ms	55–72 ms
Repetition Time (TR)	12.5 ms	5.18 ms	R-R interval
Excitation frequency	80 Hz	24.13 Hz	140 Hz
Motion Encoding Gradient (MEG) frequency	160 Hz	500 Hz	140 Hz
Acceleration factor	2	2	2
Acquisition matrix	256×64	128×96	64×64
#Segments	8 (+ and –ve MEG)	1	Single shot
MRE phase offset	4	4	4
#Cardiac phases	8	360 (multiple R-R intervals)	1
Acquisition time	~16 s	3–4 min	~25 s

convert displacement fields into stiffness maps [23]. All these inversions assume that the waves are propagating in an infinite, uniform, homogenous medium and are solved based on the Helmholtz wave equation denoted by Eq. 7.3. These assumptions are completely violated in the heart owing to its complex anisotropic structure related to its fibrous and layered architecture. Initially, a thin spherical shell inversion [32] was developed by assuming that the heart is a sphere, as shown in Eq. 7.4. However, this inversion also considers that the waves are propagating in an isotropic, homogenous, spherical shell. An example of displacement fields and the corresponding stiffness maps in a spherical shell phantom validating spherical shell inversion using finite element simulation and MRE experiment performed in a silicone rubber spherical phantom is shown in Fig. 7.7. This inversion requires higher order derivatives (i.e. 3rd and 4th order as indicated in Eq. 7.4), which is more sensitive to the noise present in the data. Therefore, this inversion is not widely used. Inversions, such as LFE [27] and DI [31], are extensively used with the application of curl processing to avoid geometric and boundary effects to a certain extent, by simultaneously removing longitudinal waves that could potentially bias the stiffness estimates. LFE is based on the principle of estimating local spatial frequency from the first harmonic displacement field by applying lognormal filters and solving for shear stiffness using Eq. 7.5. Whereas, DI is directly solved by using Eq. 7.3 for obtaining shear stiffness estimates. All of the above inversions can provide spatial stiffness maps across the cardiac cycle to report the "effective" stiffness estimates.

$$\mu \nabla^2 U = -\rho \omega^2 U \tag{7.3}$$

where U is the first harmonic displacement field, and ω is the rotational frequency (2πf).

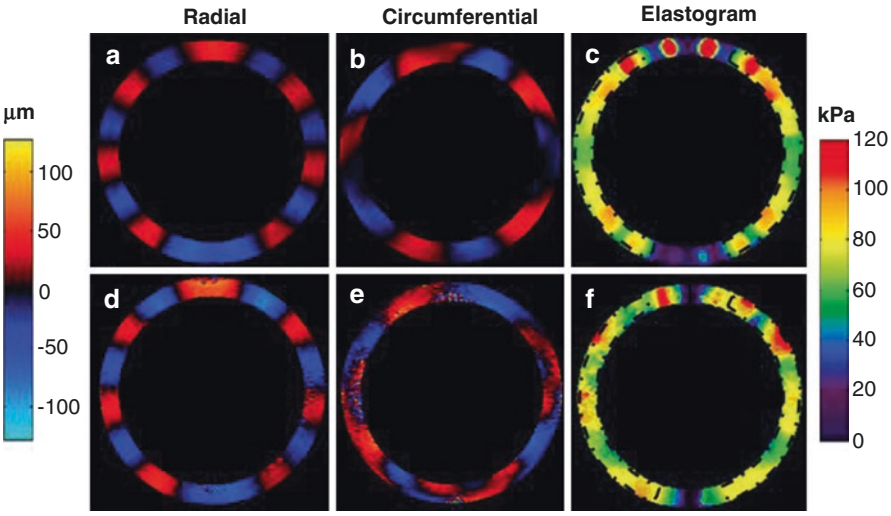

Fig. 7.7 Thin spherical shell inversion. (**a**–**c**) Radial and circumferential component of displacement field in a finite element simulation and the corresponding stiffness map. (**d**–**f**) Similarly, magnetic resonance elastography (MRE) experiment performed in a silicone rubber spherical phantom with displacement fields and the corresponding stiffness map

$$\begin{aligned}
&\beta^2\frac{\partial^3 u}{\partial\theta^3}+2\beta^2\cot\theta\frac{\partial^2 u}{\partial\theta^2}-\left[\left(1+v\right)\left(1+\beta^2\right)+\beta^2\cot^2\theta\right]\frac{\partial u}{\partial\theta}\\
&\quad+\cot\theta\left(2-v+\cot^2\theta\right)\beta^2-\left(1+v\right)u-\beta^2\frac{\partial^4 w}{\partial\theta^4}\\
&\quad-2\beta^2\cot\theta\frac{\partial^3 w}{\partial\theta^3}+\beta^2\left(1+v+\cot^2\theta\right)\frac{\partial^2 w}{\partial\theta^2}\\
&\quad-\beta^2\cot\theta\left(2-v+\cot^2\theta\right)\frac{\partial w}{\partial\theta}-2\left(1+v\right)w-\frac{a^2\ddot{w}}{c_p^2}\\
&\quad=-p_a\frac{\left(1-v^2\right)a^2}{Eh}
\end{aligned}\tag{7.4}$$

where, a is the shell inner radius, u is the circumferential component of displacement, w is the radial component of displacement, c_p is the flexural plate speed ($c_p^2 = E/(1-\nu^2)\rho$), E is the Young's modulus, ρ is the density (assumed to be 1 g/cm^3), ν is the Poisson's ratio (assumed to be 0.5), β is the $h^2/12a^2$, h is the thickness of the shell, p_a is the applied load and shear stiffness, $\mu = E/[2(1+\nu)]$.

$$\mu = \rho\left(\frac{f_{\text{mechanical}}}{f_{\text{spatial}}}\right)^2 \tag{7.5}$$

where, $f_{\text{mechanical}}$ is the excitation frequency, f_{spatial} is the spatial frequency determined from first harmonic displacement field.

Additionally, an alternative strategy based on the first harmonic amplitude of the displacement field is used to determine the stiffness of the heart muscle [26, 30]. This methodology is based on the principle that tissue with a higher stiffness generates lower amplitudes compared to the tissue with lower stiffness for a given force of excitation. However, this methodology requires that the coupling of the driver to the chest wall and relative position of the heart with respect to the driver be consistent for comparison between subjects. To minimize this bias for comparison between subjects at different phases of the cardiac cycle, the amplitude of the displacement field obtained in the heart was normalized with respect to the amplitudes generated in the chest wall (as the chest wall is considered to be static) within the same subject.

In addition to the above inversions, recent developments have enabled waveguide MRE to estimate the anisotropic stiffness of the heart. Waveguide MRE [33] involves performing diffusion tensor imaging (DTI) to obtain fiber direction along with MRE to encode the displacement field at the same resolution as that of DTI. The displacement fields along and across the fibers are resolved to separate the longitudinal and transverse components and solved using Eq. 7.3 along different directions to obtain the anisotropic stiffness of the LV myocardium.

Cardiac MRE Applications

Over the years, various studies were performed to determine the feasibility as well as validating cardiac MRE techniques in phantoms, animal models, as well as in patients. The initial study was conducted in a heart simulating spherical shell phantom [34] demonstrated that cardiac MRE can be performed in a dynamic object showing a high correlation between stiffness and pressure, which was also validated against an established P-V model of estimating shear stiffness, as shown in Fig. 7.8.

After phantom studies, in vivo studies were performed in the porcine animal models [28, 35–37] demonstrating a good linear correlation ($R^2 = 0.84$) between invasive LV catheter pressure measurements against MRE-derived stiffness measurements, and led to a good comparison between P-V loops and stiffness-volume loops, as shown in Fig. 7.9 [28]. From earlier studies [34, 35], it is known that stiffness and pressure are linearly correlated and would expect to have a good comparison between P-V loops and stiffness-volume loops. Therefore, these studies have provided initial feasibility and validation of the in vivo cardiac MRE technique, which can potentially replace invasive P-V loops.

An additional study in a porcine animal model had demonstrated the use of MRE to measure myocardial contractility [36]. In this study, an ionotropic agent, such as epinephrine was used to increase the myocardial contractility, which increased LV stiffness. Figure 7.10 shows that baseline myocardial stiffness during end-systole (ES) was lower than that injected after the fifth infusion of epinephrine, indicating an increase in myocardial contractility.

Furthermore, in another porcine animal study, Dextran-40 was infused to cause volume overload, which the increased end-diastolic (ED) pressure, causing an increase in ED stiffness, as shown in Fig. 7.11 [37].

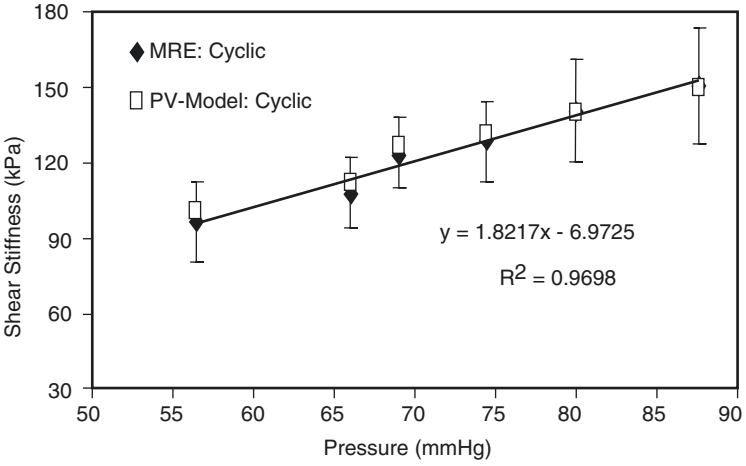

Fig. 7.8 Magnetic resonance elastography (MRE) in an heart simulation phantom. Good correlation between shear stiffness and pressure was obtained using MRE in a heart simulating spherical phantom, which was validated using pressure-volume (P-V) model of estimating the shear stiffness

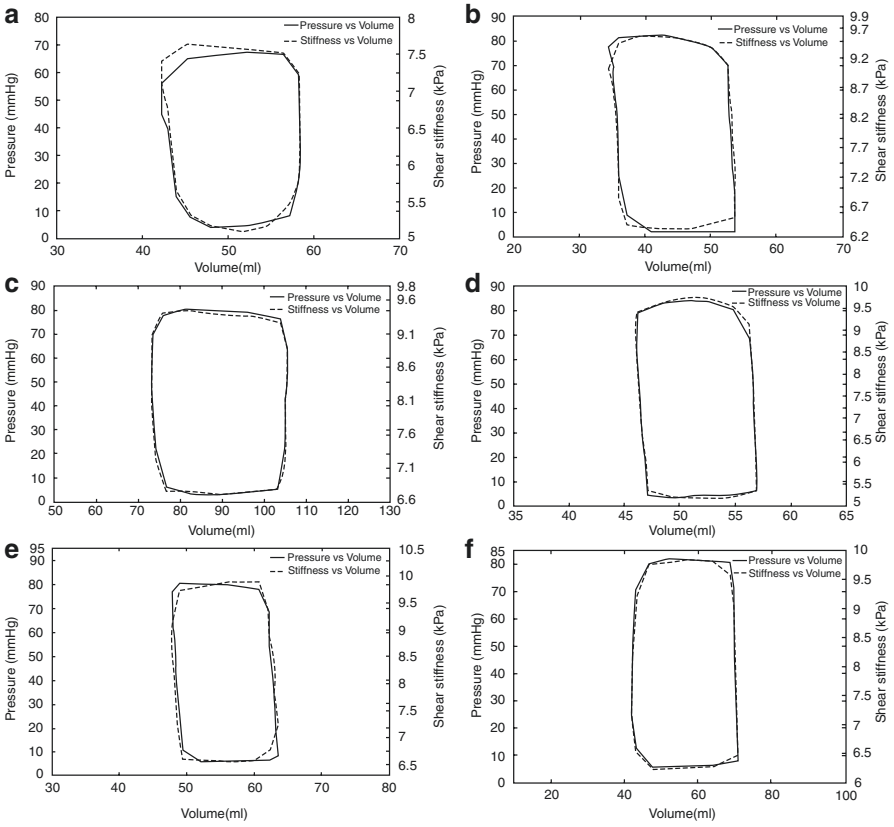

Fig. 7.9 Pressure-volume (P-V) loops vs. stiffness-volume loops. (**a**–**f**) Plots of P-V loops and stiffness-volume loops in six porcine animals showing good comparison

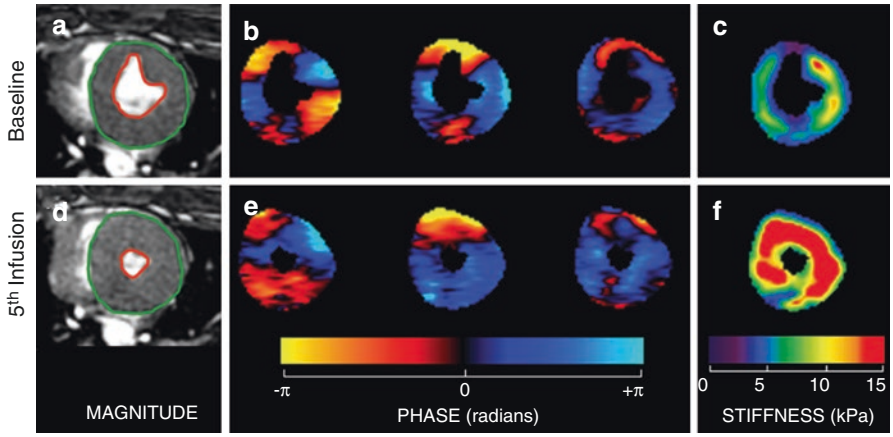

Fig. 7.10 Myocardial contractility. (**a**, **d**) Magnitude image with *red* and *green* contours delineating left ventricular myocardium, (**b**, **e**) snapshot of wave images along x, y, and z directions and (**c**, **f**) corresponding stiffness maps at baseline and after fifth injection of epinephrine during end-systolic phase

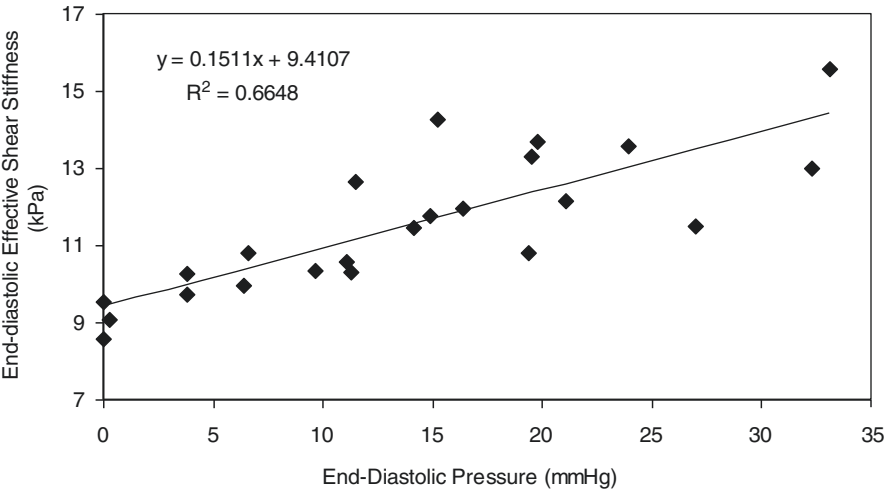

Fig. 7.11 End-diastolic (ED) stiffness vs pressure. Plots of ED stiffness versus pressure showing good correlation with $R^2 = 0.66$

Recently, cardiac MRE was performed in a myocardial infarct (MI) porcine animal model and the MRE-derived stiffness was measured at baseline, day 10, and day 21, post-infarct [38]. At the end of imaging on day 21, the animals were euthanized, and strips of both remote and infarct myocardium underwent uniaxial biomechanical testing to obtain the stiffness of two regions. During imaging at baseline, day 10 and day 21, delayed enhancement imaging, T1 mapping, extra cellular matrix (ECV) content, and tagging were also performed to obtain circumferential strain. Delayed enhancement imaging enabled identification of the infarct and remote zones of the myocardium, and regions-of-interest were drawn to obtain

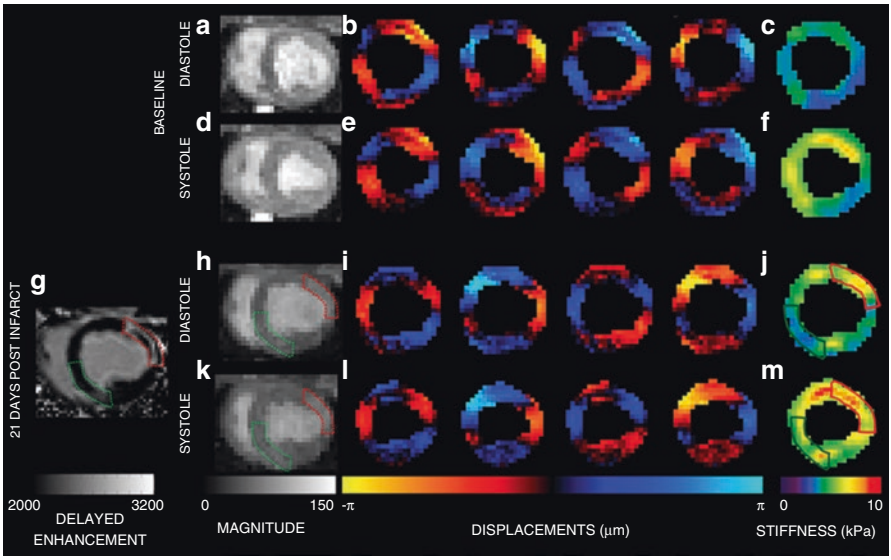

Fig. 7.12 Myocardial infarction (MI) model. (**a**, **d**, **h**, **k**) Magnitude images, (**b**, **e**, **i**, **l**) snapshot of wave images and (**c**, **f**, **j**, **m**) corresponding stiffness maps at baseline and after 21 days post MI with *red* contour identifying the infarct region and *green* contour the remote normal myocardium within the same animal. (**g**) Delayed enhancement image with infarct zone (*red* contour) and remote normal myocardium (*green* contour)

MRE-derived stiffness, T1 values, ECV, and circumferential strain measurements. Figure 7.12 shows the delayed enhancement image, magnitude images, wave images, and the corresponding stiffness maps, at baseline and day 21 showing that the infarct region has a higher stiffness compared to the remote region.

Figure 7.13 shows that there is a good correlation between MRE-derived stiffness and: (1) mechanical testing, (2) T1 values, (3) ECV, and (4) circumferential strain. Additionally, the MRE-derived stiffness significantly increased from baseline to day 10 to day 21 in the infarct zone during systole and diastole. This study confirms that cardiac MRE can potentially quantify MI based on stiffness estimates non-invasively.

Cardiac MRE was also performed in an established animal model of HFpEF, where stiffness is known to increase [39]. Renal wrapping surgery was performed in a porcine model creating hypertension and hypertrophy eventually leading to HFpEF. LV catheterization and cardiac MRE were performed to measure invasive LV pressure and LV stiffness at baseline, and at the end of months 1 and 2 post-surgery. An example of ED and ES magnitudes, wave images, and the corresponding stiffness maps, at baseline, month 1, and month 2, are shown in Fig. 7.14. This study confirmed that the LV stiffness increased from baseline to month 1 to month 2 (Fig. 7.15), and demonstrating linear positive correlation between pressure, LV thickness, and stiffness, as shown in Fig. 7.15. Therefore, this study had demonstrated that cardiac MRE can be a potential tool to diagnose HFpEF.

In-vivo human cardiac MRE studies were performed in normal volunteers as well as in patients. In order to determine normal range and reproducibility of LV stiffness values, cardiac MRE was performed in 29 volunteers [27]. The volunteers were laid

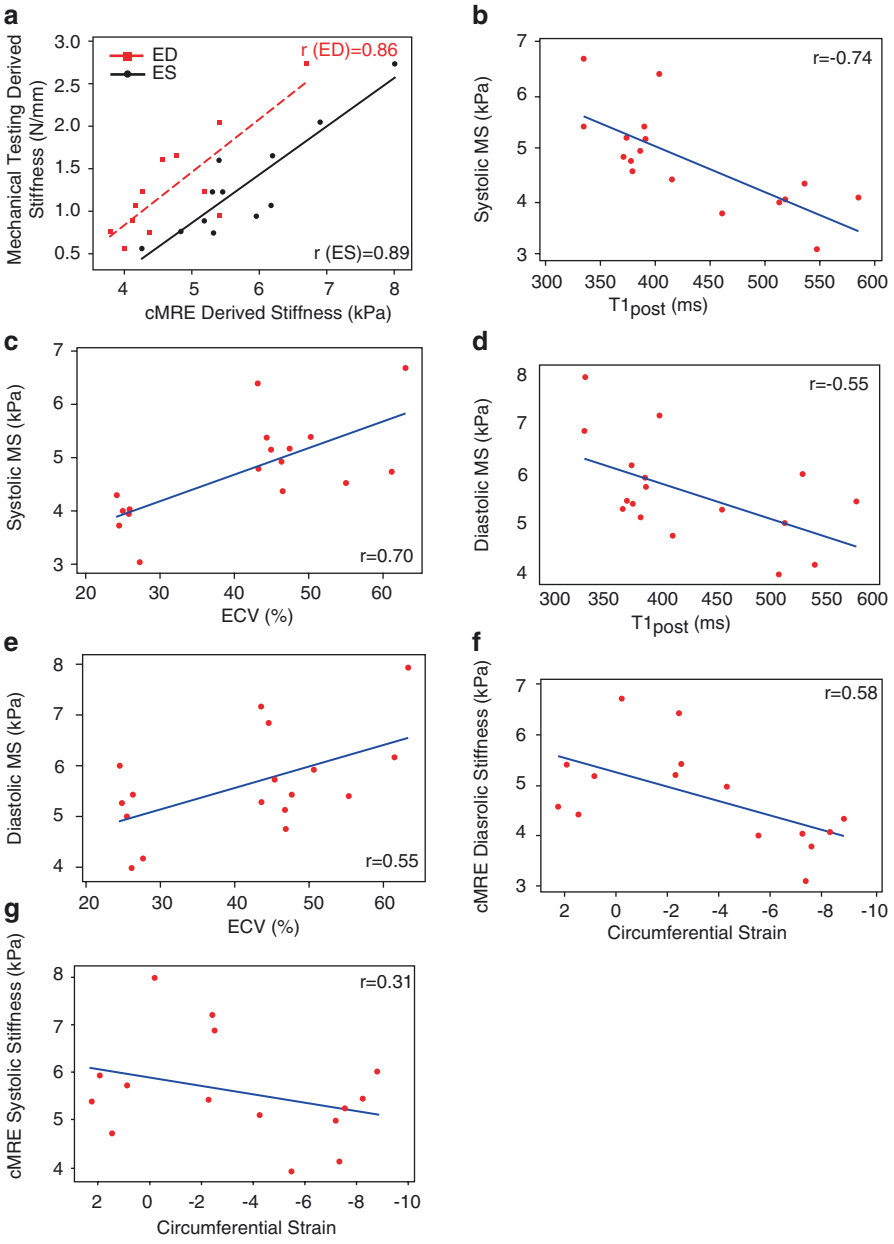

Fig. 7.13 Myocardial infarction stiffness. (**a**) Plot of mechanical testing derived-stiffness vs magnetic resonance elastography (MRE)-derived stiffness; (**b**, **d**) MRE-derived stiffness vs T1post gadolinium in infarct zone during systole and diastole; (**c**, **e**) MRE-derived stiffness vs extra cellular volume (ECV) fraction in infarct zone during systole and diastole; (**f**, **g**) MRE-derived stiffness vs circumferential strain in infarct zone during systole and diastole

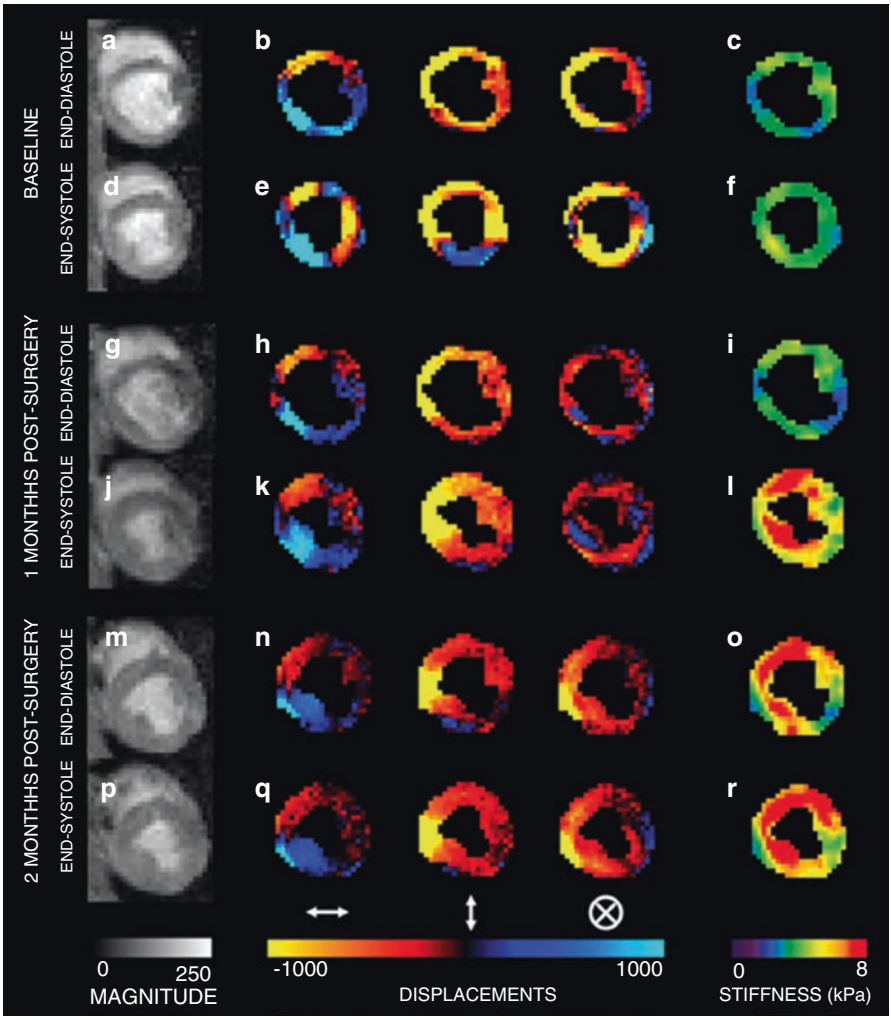

Fig. 7.14 Heart failure with preserved ejection fraction (HFpEF) model. (**a**–**f**) Magnitude images, snapshot of wave images in x, y, z directions and corresponding stiffness map at baseline during end-systole and end-diastole; (**g**–**l**) at month 1 and (**m**–**r**) at month 2 demonstrating increase in stiffness from baseline to month 2

supine with head first in a 1.5T scanner, as shown in Fig. 7.4b. For the reproducibility study, the volunteers were asked to leave the scan room after the first scan, and were repositioned to perform a repeat scan. A retrospectively, cardiac-gated, cine MRE sequence (Fig. 7.6) was used to obtain the displacement data, which was inverted using 3D LFE with curl processing to obtain the stiffness maps. Figure 7.16 shows that MRE-derived LV stiffness measurements are reproducible with a concordance correlation of 0.93 ($p < 0.0001$) and an example of wave images, and the corresponding stiffness maps in a volunteer at ED and ES are respectively shown in Fig. 7.16b, c. MRE-derived LV stiffness was significantly higher at ES compared to ED (Fig. 7.16d) and also varies cyclically across the cardiac cycle (Fig. 7.16e).

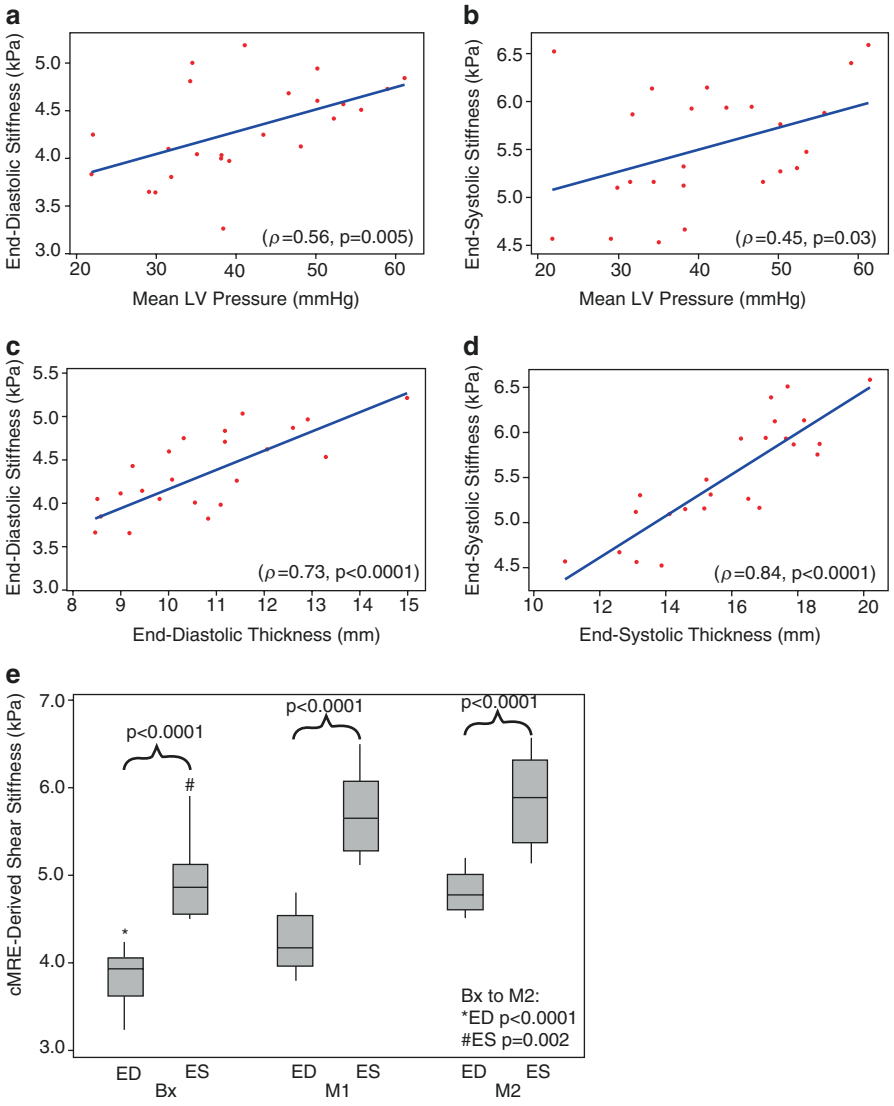

Fig. 7.15 Heart failure with preserved ejection fraction (HFpEF) stiffness. (**a**, **b**) Plot of magnetic resonance elastography (MRE)-derived stiffness vs mean left ventricular (LV) pressure both during end-diastole (ED) and end-systole (ES), respectively. (**c**, **d**) Plot of MRE-derived stiffness vs LV thickness both during ED and ES, respectively. (**e**) *Box* plot showing significant increase in stiffness from baseline to month 2 for both ES and ED

Similarly, cardiac MRE was performed in hypertrophic cardiomyopathy patients showed higher LV stiffness compared to normals. An example in one of the patients with magnitude, wave images, and the stiffness map, is shown in Fig. 7.17.

Cardiac MRE performed in a heart transplant patient to estimate LV stiffness at 8, 9, and 13 weeks post-transplant, compared well with the rejection grade based on biopsy (Fig. 7.18). Furthermore, cardiac MRE studies were performed in diastolic

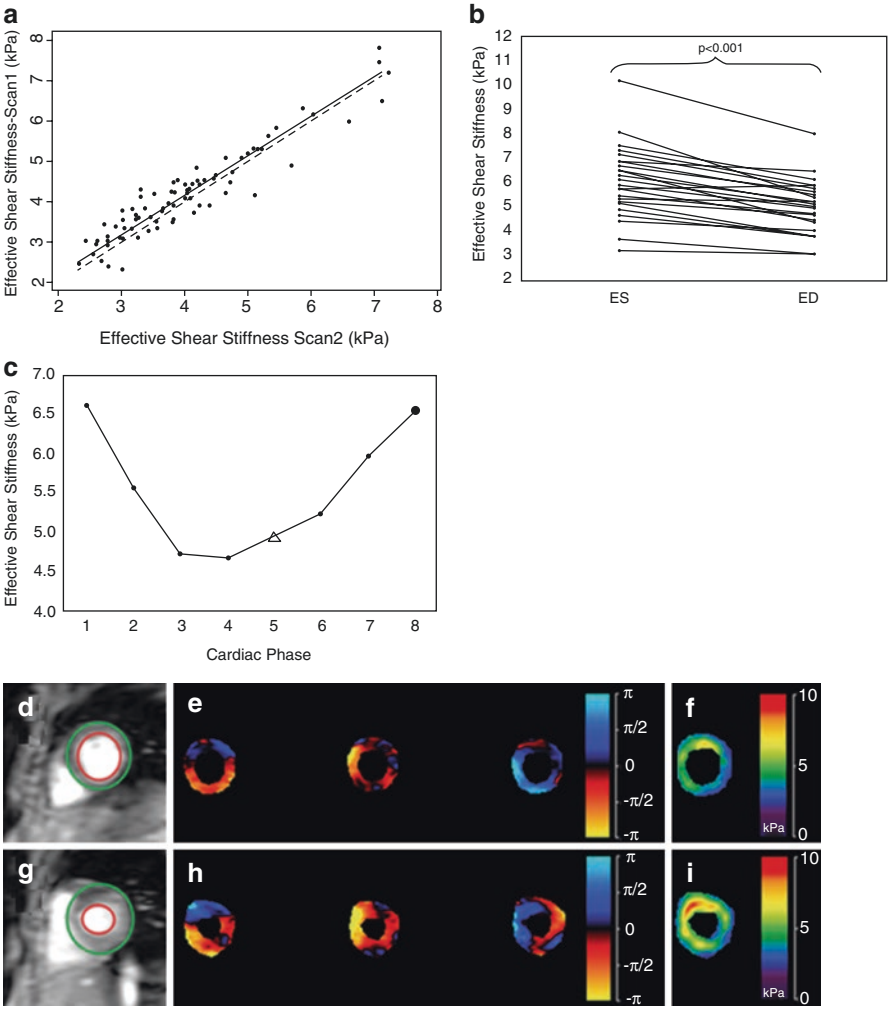

Fig. 7.16 Cardiac magnetic resonance elastography (MRE)-derived left ventricular (LV) stiffness in human subjects. (**a**) Shows reproducibility of cardiac MRE-derived isotropic LV stiffness with concordance correlation of 0.93 performed on same volunteers with time interval of 48 h apart. (**b**) Shows myocardial stiffness at end-systole (ES) is significantly higher than that at end-diastole (ED). (**c**) An example showing cyclic variation of stiffness in one of the subjects across cardiac cycle. (**d**, **g**) Shows an example in a subject with magnitude data at ED and ES with corresponding snapshots of wave data (**e**, **h**) in all three encoding directions and the stiffness maps (**f**, **i**)

dysfunction patients [40–42] demonstrating that shear wave amplitudes were significantly lower compared to normals, indicating that diastolic dysfunction patients had increased myocardial stiffness.

All the above studies have demonstrated the use of MRE for diagnosing different cardiac diseases. However, further advances have to be achieved in order to establish cardiac MRE as a clinical tool. Currently, cardiac MRE acquires only 2D data with each encoding direction requiring a separate breathhold. Therefore, highly accelerated imaging using compressed sensing reconstruction approaches should be developed

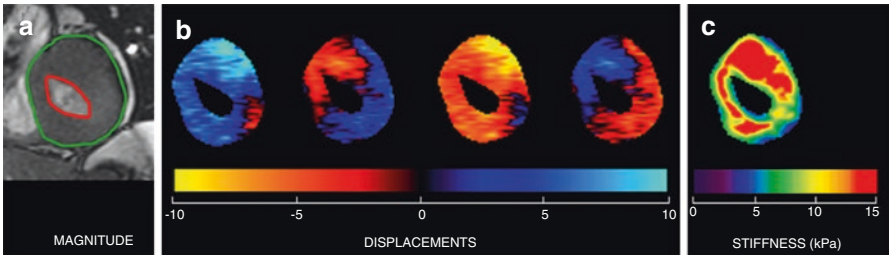

Fig. 7.17 Cardiac magnetic resonance elastography (MRE) in Hypertrophic Cardiomyopathy. (**a**) Magnitude image of the myocardium in end-systole with epicardial (*green*) and endocardial (*red*) contours delineating left ventricle. (**b**) Four phases of the through-plane component of the propagating waves and (**c**) Weighted stiffness map from three encoding directions with a mean stiffness of 12 ± 6.8 kPa

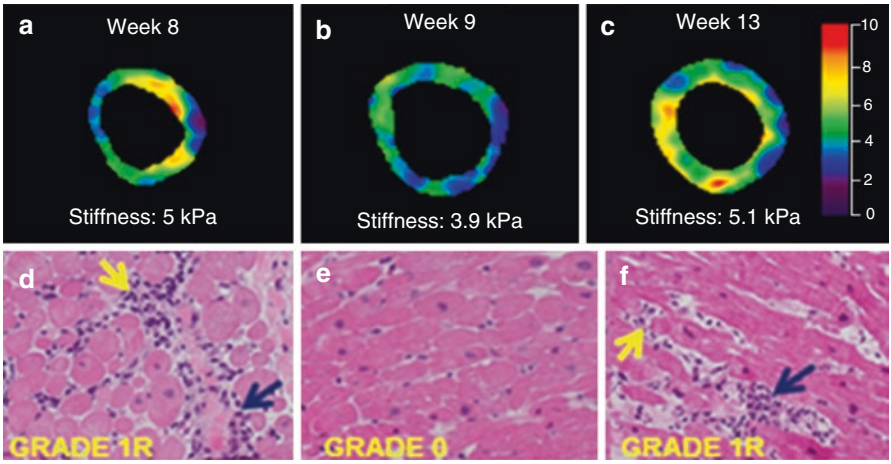

Fig. 7.18 In vivo cardiac magnetic resonance elastography (MRE) in heart transplant patient comparison to histopathology. (**a**–**c**) Mean end-diastolic cardiac MRE-derived myocardial stiffness compared to (**d**–**f**) biopsy in a heart transplant patient post 8, 9 and 13 weeks demonstrating that cardiac MRE can map the dynamic changes similar to biopsy

to acquire full 3D data in a breathhold. In addition, a free-breathing approach, which will enable to acquire full 3D data along all three-encoding directions, will be advantageous in patients who cannot withstand long breathholds. Additionally, an anisotropic inversion is required to estimate the stiffness tensor/matrix of the myocardium [33, 43]. Furthermore, more studies are warranted in large cohorts of patients with different disease states to enable cardiac MRE as a robust clinical tool.

In conclusion, this chapter has provided an overview of MRE listing/indicating the requirement of drivers, pulse sequences, and inversions for cardiac application. Additionally, details of performing in vivo studies in animals, humans, and patients, have been presented with validation of the MRE-derived stiffness results against the current gold-standards. Furthermore, cardiac MRE studies were performed in different cardiac diseases, such as HFpEF, HFrEF (i.e., MI), HCM, and heart transplant, to demonstrate that MRE-derived stiffness can be a potential tool to diagnose these diseases.

Graphical Summary: Cardiac Magnetic Resonance Elastography

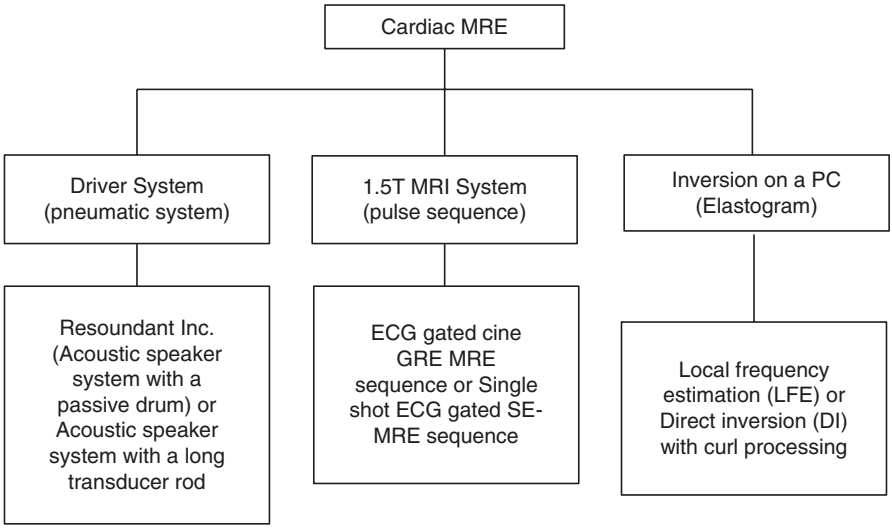

This flow chart describes the hardware and software requirements to perform cardiac MRE. Additional details regarding the driver system, pulse sequences used and inversions applied to obtain stiffness maps are provided in the respective sections of this chapter.

References

1. Zile MR, Baicu CF, Gaasch WH. Diastolic heart failure – abnormalities in active relaxation and passive stiffness of the left ventricle. N Engl J Med. 2004;350(19):1953–9.
2. Pislaru C, Bruce CJ, Anagnostopoulos PC, Allen JL, Seward JB, Pellikka PA, Ritman EL, Greenleaf JF. Ultrasound strain imaging of altered myocardial stiffness: stunned versus infarcted reperfused myocardium. Circulation. 2004;109(23):2905–10.
3. Cingolani HE, Rebolledo OR, Portiansky EL, Perez NG, Camilion de Hurtado MC. Regression of hypertensive myocardial fibrosis by Na(+)/H(+) exchange inhibition. Hypertension. 2003;41(2):373–7.
4. Hoskins AC, Jacques A, Bardswell SC, McKenna W, Tsang V, Dos Remedios CG, Ehler E, Adams K, Jalilzadeh S, Avkiran M, et al. Normal passive viscoelasticity but abnormal myofibrillar force generation in human hypertrophic cardiomyopathy. J Mol Cell Cardiol. 2010;49(5):737–45.
5. Al-Mohammad A, Mant J, Laramee P, Swain S. Diagnosis and management of adults with chronic heart failure: summary of updated NICE guidance. BMJ. 2010;341:c4130.
6. Lam CS, Lyass A, Kraigher-Krainer E, Massaro JM, Lee DS, Ho JE, Levy D, Redfield MM, Pieske BM, Benjamin EJ, et al. Cardiac dysfunction and noncardiac dysfunction as precursors of heart failure with reduced and preserved ejection fraction in the community. Circulation. 2011;124(1):24–30.
7. De Keulenaer GW, Brutsaert DL. The heart failure spectrum: time for a phenotype-oriented approach. Circulation. 2009;119(24):3044–6.
8. Zile MR, Baicu CF, Ikonomidis JS, Stroud RE, Nietert PJ, Bradshaw AD, Slater R, Palmer BM, Van Buren P, Meyer M, et al. Myocardial stiffness in patients with heart failure and a preserved ejection fraction contributions of collagen and titin. Circulation. 2015;131(14):1247–59.
9. Holmes JW, Borg TK, Covell JW. Structure and mechanics of healing myocardial infarcts. Annu Rev Biomed Eng. 2005;7:223–53.
10. Frank O. Zur Dynamik des Herzmuskels. Z Biol. 1895;32:370–437.
11. Blix M. Die Lange und die Spannung des Muskels. Skand Arch Physiol. 1892;3:295–318.
12. Abbott BC, Mommaerts WF. A study of inotropic mechanisms in the papillary muscle preparation. J Gen Physiol. 1959;42(3):533–51.
13. Abbott BC, Lowy J. Stress relaxation in muscle. Proc R Soc Lond B Biol Sci. 1956; 146(923):281–8.
14. Connelly CM, Vogel WM, Wiegner AW, Osmers EL, Bing OH, Kloner RA, Dunn-Lanchantin DM, Franzblau C, Apstein CS. Effects of reperfusion after coronary artery occlusion on post-infarction scar tissue. Circ Res. 1985;57(4):562–77.
15. Gupta KB, Ratcliffe MB, Fallert MA, Edmunds Jr LH, Bogen DK. Changes in passive mechanical stiffness of myocardial tissue with aneurysm formation. Circulation. 1994;89(5):2315–26.
16. Paulus WJ, van Ballegoij JJ. Treatment of heart failure with normal ejection fraction: an inconvenient truth! J Am Coll Cardiol. 2010;55(6):526–37.
17. Perk G, Kronzon I. Non-Doppler two dimensional strain imaging for evaluation of coronary artery disease. Echocardiography. 2009;26(3):299–306.
18. Hong Y, Liu X, Li Z, Zhang X, Chen M, Luo Z. Real-time ultrasound elastography in the differential diagnosis of benign and malignant thyroid nodules. J Ultrasound Med. 2009;28(7):861–7.
19. Zhu QL, Jiang YX, Liu JB, Liu H, Sun Q, Dai Q, Chen X. Real-time ultrasound elastography: its potential role in the assessment of breast lesions. Ultrasound Med Biol. 2008;34(8):1232–8.
20. Piscaglia F, Salvatore V, Di Donato R, D'Onofrio M, Gualandi S, Gallotti A, Peri E, Borghi A, Conti F, Fattovich G, et al. Accuracy of virtual touch Acoustic Radiation Force Impulse (ARFI) imaging for the diagnosis of cirrhosis during liver ultrasonography. Ultraschall Med. 2011;32(2):167–75.
21. Stefanescu H, Grigorescu M, Lupsor M, Procopet B, Maniu A, Badea R. Spleen stiffness measurement using Fibroscan for the noninvasive assessment of esophageal varices in liver cirrhosis patients. J Gastroenterol Hepatol. 2011;26(1):164–70.

22. Pislaru C, Urban MW, Nenadic I, Greenleaf JF. Shearwave dispersion ultrasound vibrometry applied to in vivo myocardium. Conf Proc IEEE Eng Med Biol Soc. 2009;2009:2891–4.
23. Manduca A, Oliphant TE, Dresner MA, Mahowald JL, Kruse SA, Amromin E, Felmlee JP, Greenleaf JF, Ehman RL. Magnetic resonance elastography: non-invasive mapping of tissue elasticity. Med Image Anal. 2001;5(4):237–54.
24. Tse ZTH, Janssen H, Hamed A, Ristic M, Young I, Lamperth M. Magnetic resonance elastography hardware design: a survey. Proc Inst Mech Eng Part H J Eng Med. 2009;223(H4): 497–514.
25. Litwiller DV, Mariappan YK, Ehman RL. Magnetic resonance elastography. Curr Med Imaging Rev. 2012;8(1):46–55.
26. Elgeti T, Rump J, Hamhaber U, Papazoglou S, Hamm B, Braun J, Sack I. Cardiac magnetic resonance elastography. Initial results. Investig Radiol. 2008;43(11):762–72.
27. Wassenaar PA, Eleswarpu CN, Schroeder SA, Mo X, Raterman BD, White RD, Kolipaka A. Measuring age-dependent myocardial stiffness across the cardiac cycle using MR elastography: a reproducibility study. Magn Reson Med. 2016;75(4):1586–93.
28. Kolipaka A, Araoz PA, McGee KP, Manduca A, Ehman RL. Magnetic resonance elastography as a method for the assessment of effective myocardial stiffness throughout the cardiac cycle. Magn Reson Med. 2010;64(3):862–70.
29. Kolipaka A, McGee KP, Araoz PA, Glaser KJ, Manduca A, Ehman RL. Evaluation of a rapid, multiphase MRE sequence in a heart-simulating phantom. Magn Reson Med. 2009;62(3):691–8.
30. Sack I, Rump J, Elgeti T, Samani A, Braun J. MR elastography of the human heart: noninvasive assessment of myocardial elasticity changes by shear wave amplitude variations. Magn Magn Reson Med. 2009;61(3):668–77.
31. Arani A, Glaser KL, Arunachalam SP, Rossman PJ, Lake DS, Trzasko JD, Manduca A, McGee KP, Ehman RL, Araoz PA. In vivo, high-frequency three-dimensional cardiac MR elastography: feasibility in normal volunteers. Magn Reson Med. 2017;77(1):351–60.
32. Kolipaka A, McGee KP, Manduca A, Romano AJ, Glaser KJ, Araoz PA, Ehman RL. Magnetic resonance elastography: inversions in bounded media. Magn Reson Med. 2009;62(6): 1533–42.
33. Romano A, Mazumdar R, Choi S, Clymer B, White RD, Kolipaka A. Waveguide magnetic resonance elastography of the heart. Proceedings in ISMRM. Salt Lake City. 2013.
34. Kolipaka A, McGee KP, Araoz PA, Glaser KJ, Manduca A, Romano AJ, Ehman RL. MR elastography as a method for the assessment of myocardial stiffness: comparison with an established pressure-volume model in a left ventricular model of the heart. Magn Reson Med. 2009;62(1):135–40.
35. Elgeti T, Laule M, Kaufels N, Schnorr J, Hamm B, Samani A, Braun J, Sack I. Cardiac MR elastography: comparison with left ventricular pressure measurement. J Cardiovasc Magn Reson. 2009;11:44.
36. Kolipaka A, Aggarwal SR, McGee KP, Anavekar N, Manduca A, Ehman RL, Araoz PA. Magnetic resonance elastography as a method to estimate myocardial contractility. J Magn Reson Imaging. 2012;36(1):120–7.
37. Kolipaka A, McGee KP, Manduca A, Anavekar N, Ehman RL, Araoz PA. In vivo assessment of MR elastography-derived effective end-diastolic myocardial stiffness under different loading conditions. J Magn Reson Imaging. 2011;33(5):1224–8.
38. Mazumder R, Schroeder S, Mo X, Litsky AS, Clymer BD, White RD, Kolipaka A. In vivo magnetic resonance elastography to estimate left ventricular stiffness in a myocardial infarction induced porcine model. J Magn Reson Imaging. 2016. Epub ahead of print.
39. Mazumder R, Schroeder S, Mo X, Clymer BD, White RD, Kolipaka A. In vivo quantification of myocardial stiffness in hypertensive porcine hearts using MR elastography. J Magn Reson Imaging. 2017;45(3):813–20.
40. Elgeti T, Beling M, Hamm B, Braun J, Sack I. Cardiac magnetic resonance elastography: toward the diagnosis of abnormal myocardial relaxation. Investig Radiol. 2010;45(12): 782–7.

41. Elgeti T, Knebel F, Hattasch R, Hamm B, Braun J, Sack I. Shear-wave amplitudes measured with cardiac MR elastography for diagnosis of diastolic dysfunction. Radiology. 2014;271(3):681–7.
42. Elgeti T, Steffen IG, Knebel F, Hattasch R, Hamm B, Braun J, Sack I. Time-resolved analysis of left ventricular shear wave amplitudes in cardiac elastography for the diagnosis of diastolic dysfunction. Investig Radiol. 2016;51(1):1–6.
43. Mazumder A, Clymer BD, White RD, Romano A, Kolipaka A. In-vivo waveguide cardiac magnetic resonance elastography. J Cardiovasc Magn Reson. 2015;17(Suppl 1):35.

Chapter 8
Atherosclerotic Plaque Imaging

Begoña Lavin Plaza, Pierre Gebhardt, Alkystis Phinikaridou, and René M. Botnar

Abbreviations

18F–FDG	[18F] fluorodeoxyglucose
18F–FDM	[18F] fluorodeoxymannose
18F-NaF	18F-sodium-fluoride
64Cu-TNP	64Cu-labeled triple reporter nanoparticle
89Zr-DNP	89Zr labelled dextran nanoparticles
α-act	Alpha – actin
a.u.	Arbitrary units
ACS	Acute coronary syndrome
AM	Acute marginal branch
Ao	Aorta
ApoE	Apolipoprotein E
Arg	Arginine
Asp	Aspartic

B. Lavin Plaza, PhD (✉) • A. Phinikaridou
Division of Imaging Sciences and Biomedical Engineering, King's College London, St. Thomas' Hospital, 4th Floor, Lambeth Wing, London SE1 7EH, UK
e-mail: begona.lavin_plaza@kcl.ac.uk

P. Gebhardt
Division of Imaging Sciences and Biomedical Engineering, King's College London, St. Thomas' Hospital, 4th Floor, Lambeth Wing, London SE1 7EH, UK

Department of Physics of Molecular Imaging, Institute of Experimental Molecular Imaging, RWTH Aachen University, Aachen, Germany

R.M. Botnar
Division of Imaging Sciences and Biomedical Engineering, King's College London, St. Thomas' Hospital, 4th Floor, Lambeth Wing, London SE1 7EH, UK

The British Heart Foundation Centre of Excellence, Cardiovascular Division, King's College London, London, UK

C. Constantinides (ed.), *Protocols and Methodologies in Basic Science and Clinical Cardiac MRI*, https://doi.org/10.1007/978-3-319-53001-7_8

Au	Gold
AV	Atrioventricular node branch
B0	Static magnetic field
B1	Oscillating magnetic field
CAD	Coronary artery disease
CD206	Mannose receptor
CE-CMR	Contrast-enhanced cardiac magnetic resonance
CE-MRA	Contrast-enhanced magnetic resonance angiography
CMRA	Cardiac magnetic resonance angiography
CMRI	Cardiac magnetic resonance imaging
CNR	Contrast-to-noise ratio
CT	Computer tomography
CTA	Computer tomography angiography
Cu	Copper
CVD	Cardiovascular diseases
DCE-MRI	Dynamic contrast-enhanced – magnetic resonance imaging
DE-MRI	Delayed-enhanced magnetic resonance imaging
DI	First-order diagonal branch vessel
DTPA	Diethylenetriaminepentaacetic acid
EC	Endothelial cell
ECM	Extracellular matrix
ESMA	Elastin-specific gadolinium-based contrast agent
F	Fluor
FD-OCT	Frequency domain – optical coherence tomography
FFR	Fractional flow reverse
GAPDH	Glyceraldehyde 3-phosphate dehydrogenase
Gd	Gadolinium
Gly	Glycine
HDL	High density lipoprotein
HFD	High fat diet
ICAM-1	Intercellular cell adhesion molecule 1
IEL	Internal elastic lamina
IVUS	Intravascular ultrasonography
IVUS-VH	Intravascular ultrasonography – virtual histology
LAD	Left anterior descending artery
LCX	Left circumflex artery
LDL	Low density lipoprotein
LDLR	Low density lipoprotein receptor
LGE	Late gadolinium-enhancement
LM	Left main coronary artery
LOX-1	Lysyl oxidase 1
LV	Left ventricle
M1	Classically-activated or pro-inflammatory macrophages
M2	Alternatively- activated or resolving macrophages

MDCT	Cardiac magnetic computed tomography
MI	Myocardial infarction
MMPs	Matrix metalloproteinases
MPO	Myeloperoxidase
MR	Magnetic resonance
MRA	Magnetic resonance angiography
MRI	Magnetic resonance imaging
MTC	Magnetization transfer contrast
Mxy	Transverse magnetization
Mz	Longitudinal magnetization
Mz0	Equilibrium magnetization
Na	Sodium
NIFS	Near infrared fluorescence spectroscopy
NMR	Nuclear magnetic resonance
OCT	Optical coherence tomography
oxLDL	Oxidized low density lipoprotein
PBR	Benzodiazepine receptor
PC	Phase contrast
PCI	Percutaneous coronary intervention
PECAM-1	Platelet endothelial cell adhesion molecule 1
PET	Positron emission tomography
PET-CT	Positron emission tomography – computer tomography
PET-MRI	Positron emission tomography – magnetic resonance imaging
QCA	Quantitative coronary angiography
RCA	Right coronary artery
RF	Radio frequency
RGD	Arginine – glycine – aspartic
RV	Right ventricle
SD	Standard deviation
SGM	Susceptibility gradient mapping
SNR	Signal-to-noise ratio
SPIR	Spectral presaturation with inversion recovery
SR-AI	Scavenger receptor type A member I
SSFP	Steady state free precession
STIR	Short tau inversion recovery
SUV	Standard uptake value
TEM	Transmission electron microscopy
TOF	Time-of-flight
TV	Total variation
V	Vacuole
VCAM-1	Vascular cell adhesion molecule 1
VSMCs	Vascular smooth muscle cells
Zr	Zirconium

Introduction

Cardiovascular diseases (CVD) are among the leading cause of death in western societies, accounting for 17.3 million deaths per year, a number that is expected to grow to more than 23.6 million by 2030 [1]. In the US, 85.6 millions of people are living with some form of CVD or the after effects of stroke, causing direct and indirect costs to the country of $320.1 billions per year. To improve the cardiovascular health of Americans by 20% and reduce the CVD-related deaths and stroke by 20%, by the year 2020 the American Heart Association (AHA) has developed the program "Life's Simple 7". This program consists of the following seven key health factors and behaviors that includes no smoking, physical activity, healthy diet, body weight, and control of cholesterol, blood pressure and blood sugar, to achieve considerable reduction in heart disease by 2020 [2]. Similarly, CVD is the leading cause of death in Europe, and it is still responsible for over four million deaths per year, close to half of all deaths in Europe.

Coronary artery disease (CAD) and myocardial infarction (MI) account for more than 50% of CVD deaths in Europe and are the result of atherosclerosis and plaque rupture with subsequent thrombosis. However, myocardial infarction and associated sudden cardiac death remains an unpredictable event and is usually the first clinical manifestation of underlying atherosclerosis. The widely used traditional cardiovascular risk factors remain imprecise in estimating the risk of MI. In addition, current imaging technologies used to diagnose heart disease also fail in assessing patients risk of having a cardiac event and thus fail to personalize treatment guidance and to improve patient outcome.

Significant technical advances have been made in both invasive and noninvasive imaging modalities. Invasive modalities are based on surgery and catheterization using dedicated catheters (depending on the artery of interest) and administration non-specific or target specific contrast media that help in the visualization of the vessel lumen and wall. In the last decade, great advances in catheter and probe design have allowed the acquisition of multiple functional and structural parameters, providing relevant information beyond the classical assessment of luminal stenosis. For example, the use of fractional flow reserve (FFR) at the time of coronary angiography allows measurement of blood flow and pressure [3]; intravascular ultrasonography (IVUS) allows imaging of some plaque characteristics [4]; and more recently, the use of optical coherence tomography (OCT) has allowed detailed imaging of the plaque surface that provides additional structural information on plaque stability [5]. The latest developments include the use of molecular probes and near infrared fluorescence spectroscopy (NIFS) to detect intraplaque lipid or inflammatory cells to better identify plaques that are more likely to rupture and have greater thrombogenic potential [6]. However, these imaging methodologies cannot be used as screening tests due to their invasiveness [7–9]. Therefore, new noninvasive approaches to detect potentially unstable plaque are urgently needed and have been undergoing significant development and improvement. Nowadays, it is feasible to obtain detailed coronary plaque assessment with multi detector computed tomography (MDCT) providing information on plaque burden, positive vs. negative remodeling, calcification and lipid content (CT attenuation) [10]. However, this

technique requires the use of ionizing radiation and thus is not ideal for screening or follow up examination. Cardiac magnetic resonance imaging (CMRI) has become a routine clinical tool to assess cardiac function, structure and tissue characterization with additional potential for coronary lumen and plaque imaging. The advantages of MRI compared to CT are the higher soft-tissue contrast, higher sensitivity for contrast agent detection and MRI is not affected by calcium blooming nor does it require the use of ionizing radiation or iodinated contrast agents. In addition, the use of target specific MR contrast agents can provide information about plaque biology including endothelial dysfunction, inflammation, vascular remodeling and hemorrhage. The potential of targeted contrast-enhanced cardiac MR (CE-CMR) for biological characterization of coronary thrombus and plaque has been demonstrated in small and large animal models and in humans [11–15]. These advances make MRI an attractive screening method that could allow early disease detection, evaluation of disease progression and treatment interventions. Finally, the development of hybrid systems (PET-CT, PET-MRI) can help to overcome limitations such as sensitivity or resolution that occur when the techniques are used individually, obtaining significantly higher information in a single scan. In this book chapter, we will describe the current and emerging methodologies, highlighting the potential of MRI as a promising tool to image atherosclerosis.

Pathophysiology of Atherosclerosis

Atherosclerosis is a chronic, progressive, inflammatory disease that affects medium and large size arteries usually from the middle age onwards. Atherosclerosis remains asymptomatic until the late stage of disease when plaques enlarge and reduce blood supply or suddenly rupture or erode causing thrombotic occlusion and ultimately acute ischemic events [14–16]. Atherosclerosis is initiated in areas with multidirectional shear stress and disturbed blood flow (e.g. arterial branches), which can damage the endothelium and give rise to the influx of blood proteins such as low density lipoproteins (LDL) [17]. Endothelial dysfunction is characterized by several structural and molecular alterations, including increased width of the tight junctions [18, 19] and the activation of cell adhesion molecules, such as intercellular and vascular cell adhesion molecule-1 (ICAM-1 and VCAM-1) and E- and P-selectins [14], that collectively increase vascular permeability. In addition, hypercholesterolemia leads to the accumulation of low-density lipoproteins (LDL) in the vessel wall where they undergo oxidation [20] contributing to the dysfunctional stage of the endothelium. Deposits of oxidized LDL (oxLDL) are abundant in early atherosclerotic lesions and are known as fatty streaks [21]. The combination of endothelial damage and lipid oxidation results in a complex signaling cascade that leads to the recruitment of monocytes and the deposition of extracellular matrix (ECM) proteins in the inner layer of the vessel wall [14, 22]. These initial lesions often do not progress to advanced lesions and in some cases they even regress. However, the continuous recruitment of immune cells, mainly monocytes, that will differentiate into tissue resident macrophages [23] and the inefficient elimination of LDL produces an inflammatory

imbalance that promotes atherosclerosis progression. Macrophages uptake oxLDL using the scavenger receptors and as a result of continued intra-cellular LDL accumulation in macrophages, they transform into foam cells, which constitute a major component of the plaque [14, 24]. Subsequent steps include proliferation and activation of vascular smooth muscle cells (VSMCs) that produce extracellular matrix (ECM) components (e.g. elastin, collagen) and accumulation of apoptotic foam cells that collectively form the necrotic core in advanced stages [25]. Inflammatory cytokines, matrix metalloproteinases (MMPs) and other tissue factors, generally produced by macrophages, play a potential role in fibrous cap destabilization and plaque rupture or superficial erosion. Clinically, atherosclerotic lesions can be divided into low-risk (stable plaques) and high-risk (vulnerable/unstable plaques). Stable plaques are usually fibrotic, with a thick fibrous cap and low count of inflammatory cells [26, 27]. Conversely, vulnerable plaques are characterized by large plaque burden, necrotic core, extensive inflammation, thin fibrous cap, neovascularization, intraplaque hemorrhage, (micro)calcifications and positive/ expansive remodeling. At advanced stages, the enlargement of the plaque results in intraplaque hypoxia that triggers additional inflammatory cell infiltration and promotes formation of leaky neovessels (neoangiogenesis) that provide the growing plaque with nutrients. These neovessels have been shown to be associated with unstable plaques [28–30] (Fig. 8.1).

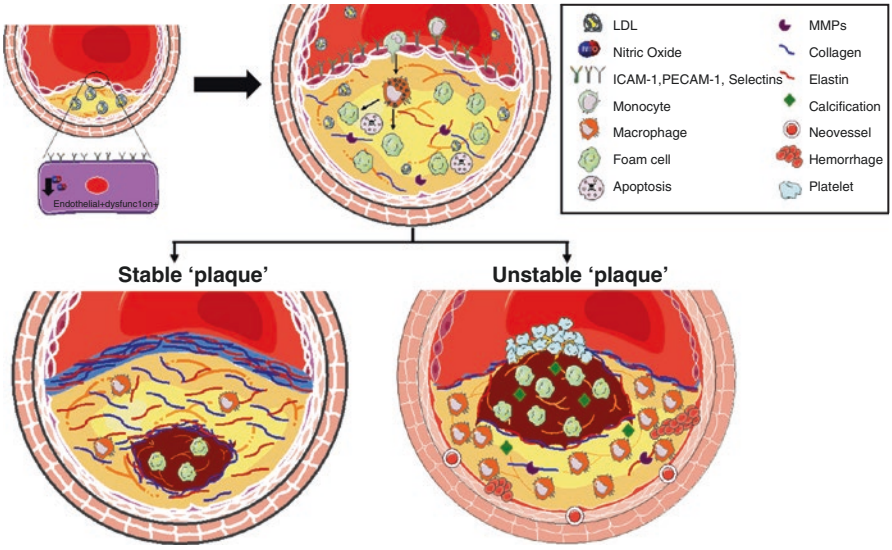

Fig. 8.1 Pathogenesis of atherosclerotic plaque development. Endothelial dysfunction initiates inflammatory processes and leads to the migration of immune cells and LDL into the vessel wall where monocytes differentiate into macrophages which transform themselves, with increasing intake of lipids and cholesterol, into foam cells. Subsequently, atherosclerotic plaques develop, which are characterized by activation of platelets and smooth muscle cells, followed by deposition of extracellular connective matrix components and endothelial proliferation and necrotic core formation. *LDL* lipoproteins, *NO* nitric oxide, *MMPs* metalloproteinases

Current Invasive Imaging Modalities

Angiography

Coronary angiography is considered the gold standard for diagnosing coronary heart disease. Since Claude Bernard made the first cardiac catheterization in a horse in 1844, followed by the first catheterization in a living person performed by Werner Forssmann in 1929, the advances in the field have been enormous [31]. Nowadays, angiography is used not only as a diagnostic tool but also for guiding percutaneous coronary interventions (PCI). This technique involves injection of an iodine contrast agent though a catheter placed in the coronary ostium to opacify the lumen, providing real-time fluoroscopic assessment of the coronary luminal anatomy and the detection of any existing stenosis. However, atherosclerotic plaques cannot be imaged directly and may be much larger than suspected from luminal angiogram evaluations. Initially, and in response to plaque accumulation, arteries enlarge (positive remodeling) in order to maintain an adequate lumen area. Stenoses smaller than 40% seem to remain independent of the lumen area and therefore not detectable by angiography [7]. Another limitation of this technique is the poor correlation between visual assessment of luminal stenosis and functional severity [32]. Although this correlation can be slightly improved by using quantitative coronary angiography, these limitations have increased the use of other invasive methods to evaluate the functional significance of coronary stenosis. Over the past decade, the use of fractional flow reserve, or FFR, has significantly increased in coronary catheterization. This technique is a guide wire-based procedure that can accurately measure blood flow and pressure at the time of angiography in a specific segment of the coronary artery. The measurement involves determining the ratio between the maximum achievable blood flow in a diseased coronary artery and the theoretical maximum flow in a normal coronary artery. An FFR of 1.0 is widely accepted as normal, whereas FFR values lower than 0.75–0.80 are generally considered to be associated with myocardial ischemia [3]. The use of FFR is an excellent tool for physicians to decide if medical therapy is sufficient in cases where the blood flow is not severely affected or, if the blockage or lesion is severe enough to intervene and revascularize the affected vessel [32].

Intravascular Ultrasonography (IVUS)

Intravascular ultrasound (IVUS) or intravascular echocardiography is a combination of echocardiography and cardiac catheterization. IVUS uses a catheter incorporating a miniaturized transducer to record high ultrasound frequencies (between 20 and 50 MHz), to generate grey-scale images of the arterial wall. The main value of this technique compared to angiography is that it allows not only measurement of the lumen, but also the assessment of plaque characteristics. IVUS provides, to

some extent, plaque-compositional information. For example, lipid-laden lesions appear hypoechoic, fibromuscular lesions generate low-intensity echoes, and fibrous or calcified tissues are relatively echogenic [4]. Recently, the feasibility of IVUS in providing accurate information about plaque burden as a powerful predictor of disease progression and possible clinical outcome has also been demonstrated [33]. However, accurate assessment of specific plaque components and subtypes is limited by the limited axial resolution (∼100 μm). Despite the independent value of IVUS, this technique should be considered supplementary to angiography, and not as a comprehensive alternative. In clinical practice, however, IVUS is time-consuming and therefore its use is limited. Additionally, the current physical size of the ultrasound catheters impedes the imaging of severe stenosis.

Virtual histology IVUS (VH-IVUS) uses spectral analysis of the backscattered ultrasound signal and color-coding schemes to classify plaque into four categories: fibrous (green), calcium (white), necrotic core (red) and fibrofatty (green/yellow). This technique has been validated using in vitro and ex vivo human and animal models with good accuracy [34]. However, recent in vivo studies have highlighted that the sensitivity and specificity of IVUS-VH in detecting different tissue types is not as high as shown by previous studies. One possible explanation is that early or not complex lesions could not be accurately characterized because of the limited resolution of IVUS [35].

Optical Coherence Tomography (OCT)

Optical coherence tomography (OCT) has been traditionally used in ophthalmic applications. Early applications in 1993 included imaging of the retina [36], while new approaches focus on the evaluation of other tissue types that require high resolution, including the imaging of atherosclerotic lesions in the vasculature. This invasive technique uses light with a long wavelength (in the near-infrared spectrum) emitted by a fiber-optic wire introduced via a catheter into the vessel of interest. The light waves that are backscattered from the tissue, interfere with the reference beam, and this interference pattern is used to obtain images with excellent axial resolution (10–15 μm) in vivo [37]. One of the drawbacks of this technique is the interference of blood with infrared light propagation, causing artifacts and therefore reducing the quality of the images. To avoid this problem, the blood has to be displaced from the imaging area. The first approaches involved very complex techniques with simultaneous occlusion of the luminal area with an inflated balloon and flushing of the artery with saline. Recently, non-occlusive methodologies employing only small flushes of saline or contrast media allow high quality vessel wall visualization [5]. The main advantage of OCT is not only the possibility to detect atherosclerotic plaques but also the ability to measure the thickness of the fibrous cap, providing important information about plaque vulnerability. Additionally, other surface features such as, plaque erosion, plaque rupture or thrombus can be detected, that are key components in the evaluation of disease stage and progression [38]. However,

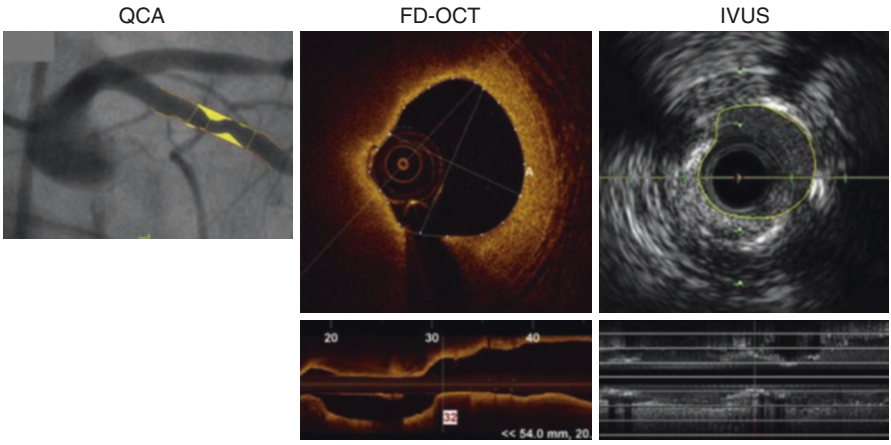

Fig. 8.2 Representative images of proximal circumflex artery stenosis using the current invasive imaging modalities. In Vivo Measurements of Lumen Dimensions by quantitative coronary angiography (*QCA*), frequency domain optical coherence tomography (*FD-OCT*), and intravascular ultrasound (*IVUS*) [39]

one of the main limitations of OCT is the limited tissue penetration (between 1.5 and 3 mm). Although it is possible to detect structures such as necrotic core or calcification, some internal vessel structures such as the lipid core or extracellular matrix deposition cannot be accurately visualized in cases of advanced atherosclerotic plaques. During clinical procedures, OCT is usually performed in conjunction with angiography to obtain more detailed images of the underlying atherosclerotic plaque, and also to detect possible complications after stent implantation. Overall, this technique offers important information to physicians and aids personalized treatment guidance in patients (Fig. 8.2).

Current Non-invasive Imaging Technologies

Computed Tomography (CT)

Computed tomography angiography (CTA) has emerged as an alternative non-invasive imaging modality for detection and grading of coronary stenosis [40] but also for plaque assessment and characterization [41, 42]. While detection of vessel wall narrowing does not necessarily allow the differentiation between stable and unstable plaque, calcium detection and quantification (calcium score) is considered as a clinically established technique and is used to determine global atherosclerotic burden and to predict future coronary events [43–46]. Calcification often occurs in the presence of apoptosis of smooth muscle cells and macrophages with matrix vesicles accompanied by expression of osteogenic markers within the vessel wall [47, 48] as a means to stabilize plaque. Initially, the size of calcifications arising

from smooth muscle cell apoptosis is typically ≥0.5 μm and <15 μm in diameter. Early calcifications are called microcalcifications or spotty calcifications [48–50] and have been associated with plaque instability. As the disease progresses, calcifications increase with macrophage infiltration into the lipid pool where they undergo apoptosis and release additional matrix vesicles. [47, 48]. These macrocalcifications are larger in size (>100 μm) [48, 50] and have been associated with plaque stabilization. The detailed mechanisms of atherosclerotic calcification are not entirely understood and is the subject of ongoing research [51, 52]. Current clinical CT imaging allows visualization of macrocalcification with diameters around 200–500 μm [50]. However, microcalcifications are below the current resolution of CTA systems. Additionally, it has been demonstrated that thin-cap fibroatheroma could be visualized as a ring-like enhancement using coronary CTA [53]. The lack of resolution of clinical CT scanners does not allow precise measurement of the fibrous cap thickness [54], particularly in the case of rupture-prone plaque (≤65 μm) [55].

CTA is excellent for providing high-resolution anatomical information, while it has limited use for measuring biological processes, which can be better visualized and quantified with molecular MRI or positron emission tomography (PET). Combining CT with PET allows to spatially localize (anatomical images) with the metabolic or molecular information provided by PET (Fig. 8.3).

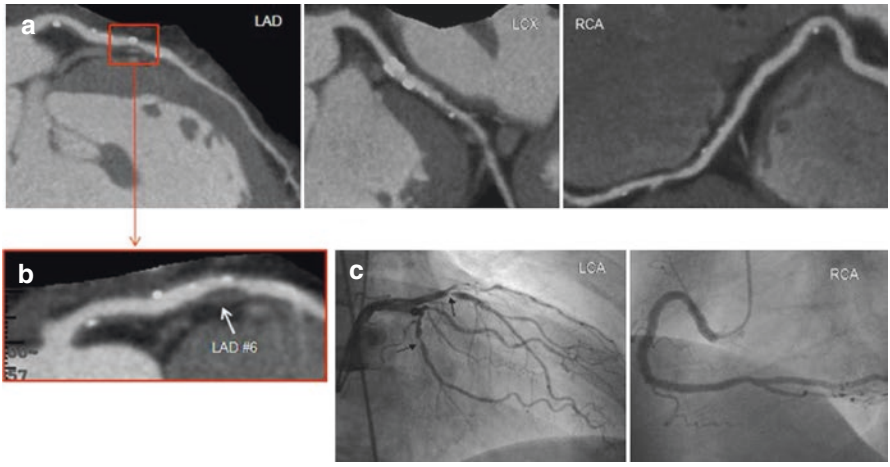

Fig. 8.3 Example of a patient with acute coronary syndrome 6 months after CT angiography. (**a**) Curved multiplanar reformation images of left anterior descending artery (*LAD*), left circumflex artery (*LCX*), and right coronary artery (*RCA*). (**b**) Positive remodeling, low-attenuation plaque, and spotty calcification were detected in LAD #6 on coronary computed tomography (*CT*) angiography. (**c**) Acute coronary syndrome (*ACS*) occurred 6 months after CT angiography. LAD #6 was determined as the culprit lesion based on invasive coronary angiogram findings. Please note the location of the lesion proximal to the first septal branch, both in CT angiography before the event and coronary angiogram after the event when the patient was brought to the catheterization laboratory for percutaneous coronary intervention. *LCA* left coronary artery [10]

Emerging Non-invasive Technologies

Magnetic Resonance Imaging (MRI)

Many scientists have contributed to the development of MRI. One of the fundamental discoveries in physics made in 1882 by Nikola Tesla was the discovery of the rotating magnetic field. After this initial discovery, more than 50 years lapsed until Professor Isidor I. Rabi observed the quantum phenomenon dubbed nuclear magnetic resonance (NMR). He described how the atomic nuclei show their presence by absorbing or emitting radiofrequency waves when exposed to a sufficiently strong magnetic field. Following these two crucial achievements, the door was pushed wide open and led to several ground breaking discoveries and inventions including the magnetic resonance phenomenon (1946, F. Bloch and E. Purcell), first one-dimensional MR image (1950s, H. Carr) and the construction of the first MRI scanner (1977, R. Damadian, M. Goldmith and P. Minkoff). The first scan was performed in 1977 in a healthy volunteer and 1 year later, the first clinical scan was performed in a patient with cancer. Following that, functional MRI of the brain was introduced in 1993 and in the mid-late 1990s cardiac MRI, fetal MRI and functional MRI have been further developed and become routine in many imaging centers.

MRI is based on the nuclear magnetic properties of atoms (mainly hydrogen) and involves the interplay of three components to generate tomographic images: the main magnetic field of the MR scanner (static magnetic field, B_0) which generates a net magnetization along the scanner axis, the gradient fields which are used for spatial localization, and the oscillating magnetic field, B_1, of the radio frequency (RF) pulses. In the classical physics view, the RF pulses tip the longitudinal magnetization (M_z) of the water protons away from the main axis (z-direction) in to the transverse plane (x, y-direction) to generate transverse magnetization (M_{xy}) which oscillates with the Larmor frequency and resulting in a MR signal that can be detected with a receiver coil. Signal detection can also be understood in the macroscopic view; after the RF pulses are turned off, the net magnetization of the protons (M_z) returns to the equilibrium magnetization (M_{z0}) by emitting radio waves when transitioning between spin up and spin down energy states. These radio waves can be detected with dedicated RF receiver coils. This process is known as relaxation and can be separated in two independent parts, T1 relaxation or T1 recovery due to spin lattice interaction and the loss of phase coherence in the transverse magnetization (T2 relaxation or T2 decay) by spin-spin interaction. The rate of T1/T2 allows the differentiation and characterization of different tissues and pathologies within the body. In addition, the use of contrast agents that alter T1/T2 relaxation improves the detection and characterization of some pathologies. Although both T1 and T2 are affected by the introduction of exogenous contrast agents, some contrast agents primarily shorten T1 and structures appear brighter on T1-weighted images. Other contrast agents aim to shorten T2, generating images where the structures appear dark on the T2-weighted images. The most

commonly used T1 shortening contrast agents gadolinium (Gd^{3+}) chelates that alter the T1 of surrounding protons as a result of its strong paramagnetic properties. In the case of T2-shortening agents, the most commonly used substances are iron oxide particles, that shorten the T2 relaxation times of the nearby hydrogen atoms thereby reducing the signal intensity. The use of contrast agents to image biological processes related to atherosclerosis are detailed in the section about contrast agents.

Magnetic Resonance Angiography (MRA)

Various MRI sequences have been developed for visualization of the coronary, cerebral and peripheral arteries, and are clinically established for extracardiac vessels. MRA methods can be divided in two categories, depending on whether they produce bright or dark signal of the blood.

Bright Blood MRA Methods

Generally, bright-blood sequences are based on gradient echo sequences. To increase the signal intensity, these sequences need to be planned perpendicularly to the flow and with thin slices. Longer TRs and shorter TEs will also help to maximize the inflow related enhancement. There are three main clinical techniques used to perform MRA: time-of-flight (TOF) and phase-contrast (PC) that do not require the use of exogenous contrast agents and contrast-enhanced (CE-MRA) imaging. In addition, blood contrast enhancing prepulses such as T2prep or magnetization transfer contrast (MTC) and/or blood contrast enhancing imaging sequences such as steady state free precession (SSFP) can be used for non-contrast enhanced angiography. MRA using TOF is the oldest and most popular method of non-contrast MRA. This sequence is based on the exposure of protons to repetitive excitation pulses in rapid succession that saturate stationary tissues. Moving tissues, such as the blood, that enters the imaging slice has the full magnetization, and thus generates high signal leading to the creation of a background signal suppressed angiogram. MRA using phase-contrast (PC) has the advantage that, in addition to the angiogram, it produces velocity maps that allow for flow quantification. This method is based on the phase effects that stationary and moving spins undergo when subjected to a pair of bipolar gradients. In the presence of bipolar gradients, spins in stationary tissues gain no net phase shift, while moving tissues acquire a net phase shift that is proportional to their velocity. This phase difference can be used to generate image contrast between

blood and soft tissues. Contrast-enhanced MRA (CE-MRA) is similar to contrast enhanced CT angiography, but uses gadolinium probes instead of iodine compounds. After the intravenous injection of the gadolinium probe, the T1 of blood is significantly shortened, generating high signal intensity on T1 weighted MR images. CE-MRA has several advantages compared to TOF or PC. This method is faster, can be acquired in any orientation and produces images that are flow-independent. Therefore, the overestimation of stenoses is significantly reduced compared to non-contrast methods. However, the principal limitation of this method is the contra-indication to the use of gadolinium probes in patients with severe renal failure or allergies. In the particular case of coronary arteries, T2 prepared SSFP sequences are being preferred to generate non-contrast coronary angiograms. This sequence takes advantage of the long T2 of arterial blood leading to high blood signal while signal from myocardium is suppressed due to its short T2. In addition, it is important to take into account that the coronary arteries are embedded in epicardial fat, and therefore an effective fat suppression method is required to avoid unwanted signal arising from fat that can compromise vessel delineation and thus can lead to a decrease in the diagnostic value of MRI. Several fat suppression techniques have been proposed, and the spectral presaturation with inversion recovery (SPIR) technique is currently the most widely used method for coronary arteries. This method is based on the relaxation time (T1) and chemical shift differences between fat and water. The frequency-selective RF pulse saturates the magnetization of fat while maintaining the magnetization of water. Data acquisition begins immediately after the fat saturation pulse. This allows acquisition of images that have higher SNR compared to short tau inversion recovery (STIR) prepulse that only takes advantages of the T1 differences between water and fat. More recent methods using water-fat separation such as Dixon provided improved CMRA image quality at 3 T compared to the SPIR technique without the need of a contrast agent. This method may provide additional diagnostic information due to pericardial fat signal visualization without increasing the overall scan time [56] (Fig. 8.4).

Dark Blood MRA Methods

Generally, black-blood sequences are based on spin echo sequences, that rely on flow–related signal loss and minimize flow-related enhancement. These techniques are suitable to detect vessel wall pathologies like atherosclerosis, vascular occlusion or thrombosed portions of aneurysms. The advantage of these techniques is the improved signal quality in cases of turbulent flow that causes signal loss when using the bright blood methods. Furthermore, spin echo based sequences are also less susceptible to image artifacts from metallic implants such as sternal wires (Fig. 8.5).

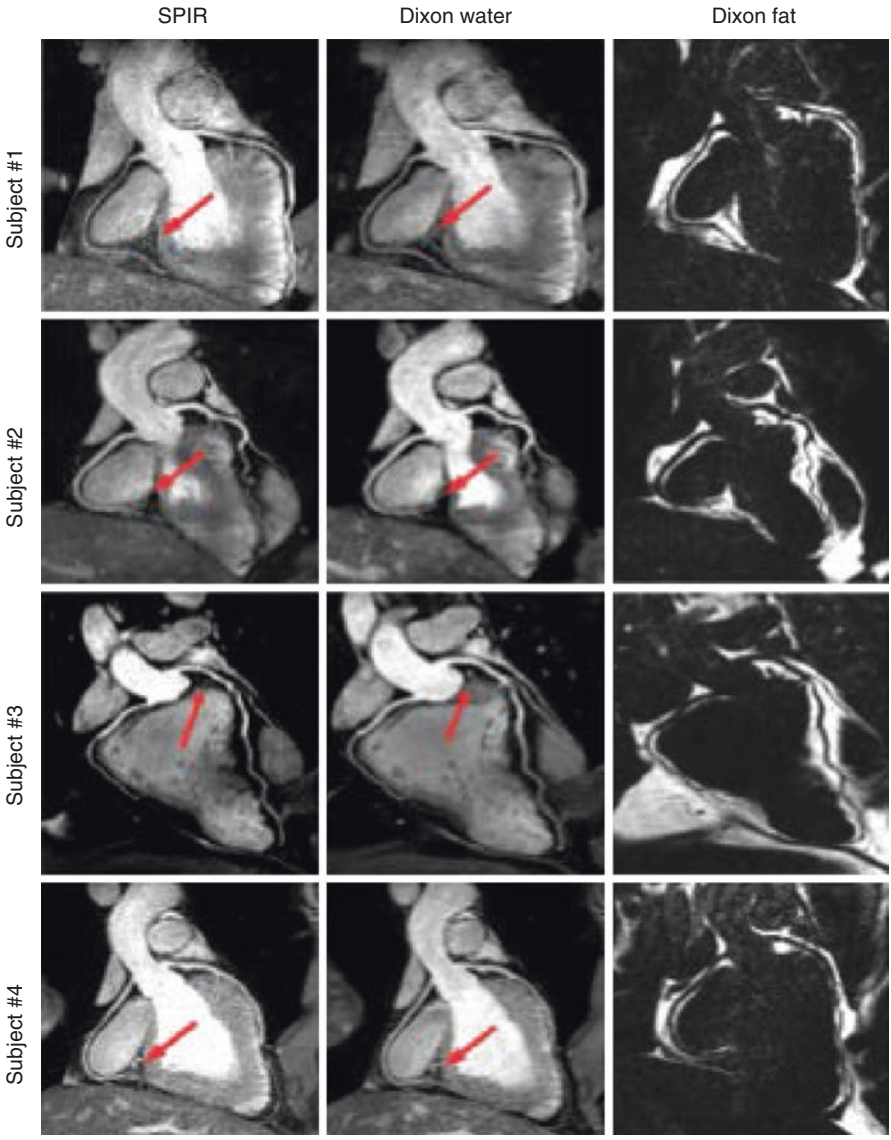

Fig. 8.4 Reformatted whole heart CMRA using SPIR (*first column*) fat suppression and Dixon water (*second column*), fat (*third column*) separation in four representative volunteers. *Arrows* point to locations in the images where fat suppression was improved with the Dixon compared to the SPIR fat suppression method. Reformatted images demonstrate that fat suppression is good with both techniques at 3 T without the use of a contrast agent. In addition, the Dixon technique provides a fat image which can be used for diagnostic purposes or to improve vessel tracking as distal segments are often displayed better in the fat images [56]

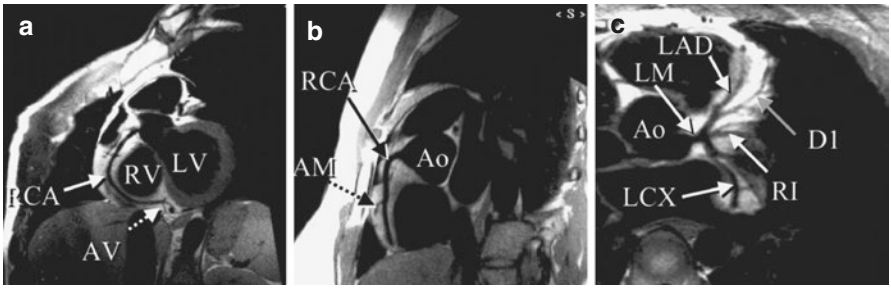

Fig. 8.5 High-spatial-resolution free-breathing black-blood coronary MR angiograms acquired in three healthy adult subjects depict (**a**, **b**) the right coronary artery system and (**c**) the left coronary artery system. All images were acquired in a double-oblique orientation along the major axes of the coronary arteries. *AM* acute marginal branch, *Ao* ascending aorta, *AV* atrioventricular node branch, *DI* first-order diagonal branch vessel, *LAD* left anterior descending, *LCX* left circumflex, *LM* left main coronary arteries, *LV* left ventricle, *RI* ramus intermedius, *RV* right ventricle [57]

Cardiovascular Imaging-Challenges and Solutions

Imaging of the coronary arteries remains one of the most technically challenging areas in MRI. Coronary vessels have a relatively small diameter of 3–4 mm, tortuous geometry, move throughout the cardiac and respiratory cycle and are embedded in epicardial fat requiring high spatial resolution, whole heart coverage and fat suppression, thus leading to long scan times that preclude beathholding. To address these challenges coronary arteries are usually acquired with motion corrected high spatial resolution, fat suppressed T2 prepared 3D steady state free precession (SSFP) sequences during free-breathing. To suppress cardiac motion, data are only acquired during mid-diastolic or end-systolic rest periods. To suppress respiratory motion, navigators have been employed, which measure the position of the diaphragm allowing data reconstruction only when the diaphragm is in a predefined position, typically end-expiration. However, current motion correction methods discard large amounts of data acquired and prolong scan time. Thus, current research focuses on novel motion correction techniques that use all acquired data for reconstruction (100% scan efficiency) either by applying 3D affine or non-rigid motion correction or by resolving the cardiac and/or respiratory motion states using total variation (TV) compressed sensing reconstruction [58, 59].

MR Contrast Agents

Endothelial Dysfunction

Extensive research has shown that local hemodynamic factors such as increased shear stress and disturbed blood flow cause structural and functional changes of the vascular endothelium, condition known as endothelial dysfunction, that it is the

initiating step of atherosclerosis [60]. Dysfunctional endothelium is characterized by impaired vasodilation, in response to endothelium-dependent stressors, and increased permeability, that allows the extravasation of blood components such as LDL and inflammatory cells into the vessel wall [14]. Activated endothelial cells upregulate the expression of surface specific adhesion molecules including VCAM-1, ICAM-1 and E- and P-selectins that facilitate the uptake of immune cells into the vessel wall [14]. Recent non-invasive studies using MRI have shown that endothelial function is closely related to local atherosclerotic burden in patients with coronary artery disease [26, 27]. Gadofosveset trisodium is a gadolinium based contrast agent that reversibly binds to blood albumin and is used for MR angiography in clinics [61, 62]. Preclinical studies in atherosclerotic murine models have shown the feasibility of gadofosveset to image vascular permeability [63] and effectiveness of therapeutic interventions [64]. The uptake of albumin binding contrast agents has been correlated with increased neovessel formation in atherosclerotic rabbits [65, 66]. Gadofosveset has also been used to image the healing response following vessel wall injury in a murine [67] and swine models [68]. A small clinical translational study has shown higher uptake of gadofosveset in symptomatic patients with carotid artery disease [69], suggesting that could be used to identify plaque instability.

Endothelial adhesion molecules are highly expressed in the early stages of atherosclerosis and therefore different approaches have been developed to specifically image those molecules. In vivo imaging of atherosclerotic plaque has been successfully performed in ApoE$^{-/-}$ mice using VCAM-1-specific nanoparticles [70–72]. ICAM-1 targeted microbubbles and liposomal Gd-based MRI agents have been successfully employed to visualize activated endothelium in vitro [73, 74], although in vivo validation still needs to be performed (Fig. 8.6).

Lipids

Uptake of lipids into the vessel wall is one of the processes present throughout the development of atherosclerosis [14, 75]. Since oxidized LDL (oxLDL) is crucial for promoting vessel wall inflammation and endothelial dysfunction, the detection of oxLDL represents an interesting imaging target. Gadofluorine M is a gadolinium-based contrast agent that has been successfully used to image increased neovascularization in advanced lipid-rich atherosclerotic lesions in rabbits [76]. Moreover, the incorporation of an ApoE-derived lipopeptide (P2fA2) into the lipid layer of HDL nanoparticles (rHDL-P2A2) has been developed as a platform for molecular MRI of macrophages in atherosclerotic plaques in vivo [77]. Finally, Gd-based specific probes targeting the oxidized low-density lipoprotein receptor (LDLR) LOX-1 have been developed, showing a significant Gd enhancement in atherosclerotic plaques in LDLR$^{(-/-)}$ mice [78].

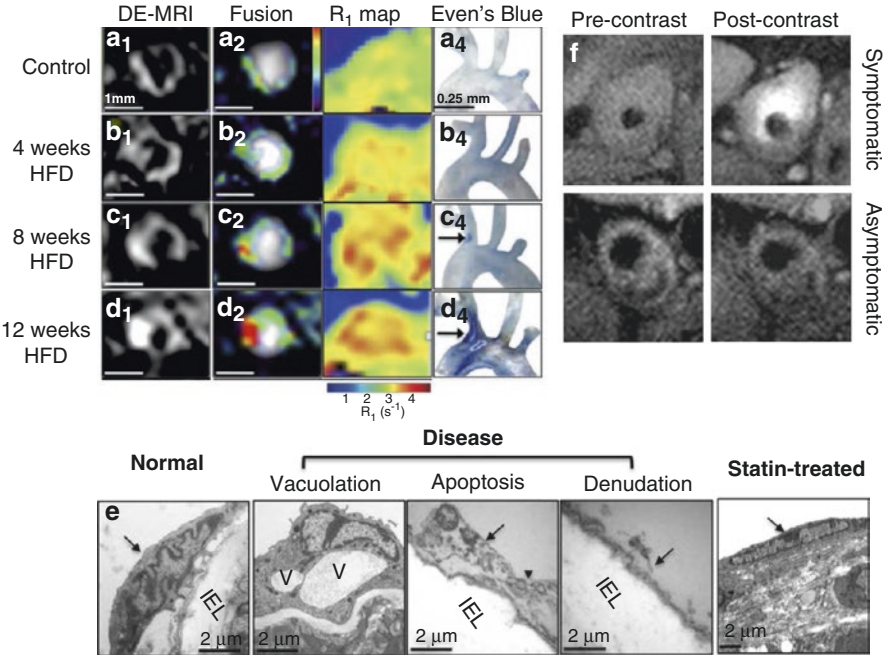

Fig. 8.6 Uptake of an albumin binding MR contrast agent correlates with endothelial permeability and plaque progression. Late gadolinium enhancement (*LGE*) MRI and T_1 mapping of endothelial permeability throughout the course of plaque development in high fat diet (*HFD*) fed apoE$^{-/-}$ mice using an albumin binding contrast agent, gadofosveset, (**a_1–d_1**) and (**a_3–d_3**). Evan's *Blue* dye staining of the artic arch and brachiocephalic artery shows good agreement (**a_4–d_4**). TEM of endothelial cell (*EC*) morphology (**e**) showed gradual disease development starting with vacuolation and almost complete EC denudation after 12 weeks of HFD and normalization in mice treated with statins (Adapted from Phinikaridou et al. [63]). Clinical data (**f**) demonstrate increased gadofosveset uptake in patients with symptomatic carotid artery disease, which correlated with increased neovessel density and macrophage count (Adapted from Lobbes et al. [69])

Angiogenesis

At advanced stages of atherosclerosis, the enlargement of the plaque results in areas of local hypoxia that trigger specific signaling cascades leading to formation of leaky neovessels (neoangiogenesis) [79]. This process, as alluded to above, has been associated with unstable plaque [80], and therefore imaging of this neovessels could represent a novel imaging biomarker for plaque stratification. As the new vessels are characterized by higher vascular permeability, they allow higher extravasation of contrast agents, e.g., gadofosveset, leading to higher contrast agent accumulation in the neovessel-rich areas of the lesion [69, 81, 82].

Alternatively, several studies using clinically approved gadolinium based contrast agents (e.g. Gd-DTPA) were performed in patients with carotid atherosclerosis angiogenesis and demonstrated increased contrast uptake [83–86]. However, these studies did not allow any quantification of the extent of the neovascularization or its characteristics. To overcome this problem, dynamic contrast enhanced T1-weighted MR imaging (DCE-MRI) has been investigated. However, for accurate assessment of neovascularization the lesion thickness needed to be greater than 2 mm due to the close proximity of the enhancing vessel lumen, which would make vessel wall segmentation challenging [87]. In addition, short-term reproducibility of black-blood DCE-MRI has been successfully implemented in atherosclerotic rabbits to evaluate its potential as a reliable readout of plaque progression and/or regression upon therapeutic intervention [87]. Several studies have shown a good correlation between the parameters derived from this technique (such as K^{trans}) and plaque neovascularization in both patients and animal models [88–91].

More specific targets have been developed to image immature neovessels. In contrast to mature vessels, the endothelial cells of immature neovessels are activated and express the surface marker $\alpha_v\beta_3$ in significant amounts [92, 93]. In order to develop targeted nanoparticles to $\alpha_v\beta_3$, the RGD (Arg-Gly-Asp) peptide sequence was employed. This sequence is the ligand to the attachment site of a large number of proteins involved in different processes including the extracellular matrix, blood and cell aggregation. It has been demonstrated that $\alpha_v\beta_3$ targeted paramagnetic nanoparticles allow the non-invasive assessment of early stages of atherosclerosis in hyperlipidemic rabbits [94] and aortic angiogenesis in rats [95].

Inflammation

All stages of atherosclerosis are characterized by a recruitment of immune cells, mainly monocytes, that differentiate into mature macrophages engulfing large amounts of lipids becoming foam cells [14]. In response to the local stimuli, macrophages can differentiate in two subtypes known as M1, classically-activated or pro-inflammatory macrophages and M2, alternatively-activated or resolving macrophages through a phenomenon known as macrophage polarization [75]. Different stages of atherosclerosis have been associated with different macrophage subtypes [75] making the development of functionalized nanoparticles to distinguish between macrophage subtypes one of major remaining challenges and its translation and validation in humans. Several approaches have been proposed to image macrophages. One of the approaches is known as passive targeting and is usually based on the use of iron oxide particles with different coatings that will be uptaken by monocytes due to their phagocytic properties. This approach has been successfully implemented in animal models [96–102] and humans [103–107]. However, the use of iron oxide particles produces a negative signal, which can be more difficult to detect, although several strategies have been proposed to overcome this limitation [102, 108]. Fluorine-containing nanoparticles that are uptaken by

phagocytes (macrophages and neutrophils) are another example of passive targeting. Due to the absence of fluorine in the body, the measurement of fluorine uptake allows local detection and quantification of the inflammatory response to an injury over time and have been successfully used to evaluate cardiac and cerebral ischemia in vivo [109]. An alternative to non-specific nanoparticles are receptor-specific probes. Activated macrophages and foam cells overexpress scavenger receptors on their surfaces, but not by other cells [110]. The scavenger receptor CD206, also known as mannose receptor, has been successfully imaged in atherosclerotic plaques of ApoE$^{-/-}$ mice by using targeted gadolinium immunomicelles [110]. The use of specifically scavenger receptor type A member I (SR-AI) targeted USPIOs has been validated in animal models of atherosclerosis and produces higher accumulation compared to non-targeted USPIOs. Moreover, functionalized LDL [111] and HDL-like [112–114] nanoparticles have been developed and validated for imaging of macrophages in mouse models of atherosclerosis (Fig. 8.7).

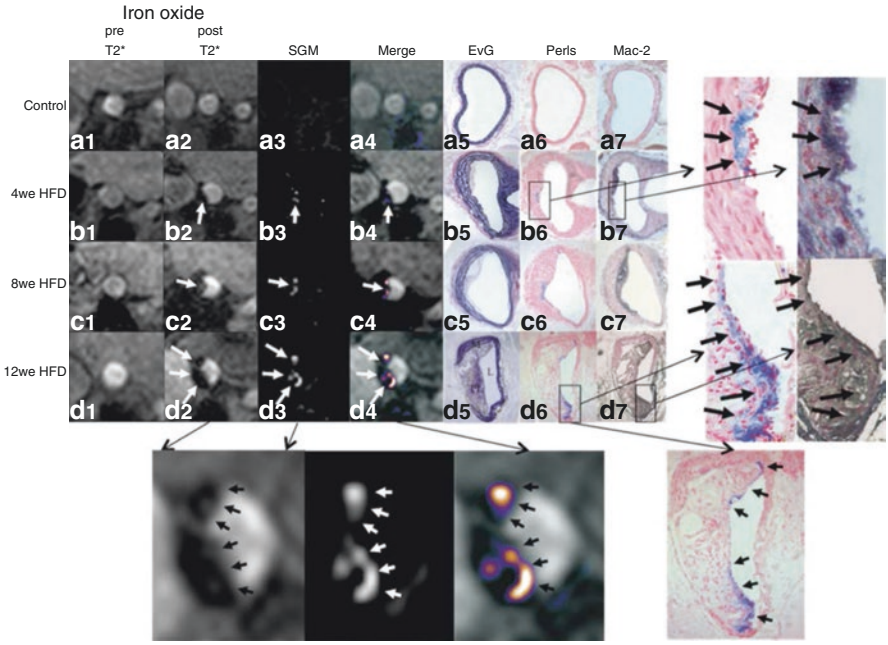

Fig. 8.7 In vivo imaging of macrophages in the brachiocephalic artery of apoE/mice on HFD. Bright-blood imaging was performed such that a 2D slice was obtained perpendicular through the brachiocephalic artery ($\mathbf{a}_{1-2}$, $\mathbf{b}_{1-2}$, $\mathbf{c}_{1-2}$, and $\mathbf{d}_{1-2}$). SGM-positive contrast images were derived and merged with the bright-blood images ($\mathbf{a}_{3-4}$, $\mathbf{b}_{3-4}$, $\mathbf{c}_{3-4}$, and $\mathbf{d}_{3-4}$). Representative images after the injection of the iron oxide agent from control as well as mice on the HFD for 4, 8, and 12 weeks and corresponding elastica–van Giesson stain, Perls stain, and immunohistochemical analysis for Mac-2 (macrophage marker). Contiguous histological sections were taken in a similar orientation as the in vivo MRI of the brachiocephalic artery. Perls staining was used to demonstrate colocalization of iron-positive areas ($\mathbf{a}_6$, $\mathbf{b}_6$, $\mathbf{c}_6$, and $\mathbf{d}_6$) with Mac-2-positive ($\mathbf{a}_7$, $\mathbf{b}_7$, $\mathbf{c}_7$, and $\mathbf{d}_7$) (*M* indicates media, *Pl* plaque, and *L* lumen). *HFD* high fat diet (Adapted from Makowski et al. [102])

Apoptosis

Hypoxic conditions develop in advanced stages of atherosclerosis and can also lead to cellular apoptosis within the plaque. Apoptosis is programmed cell death where the cell shrinks and condenses, but most importantly, the cell surface is altered, displaying properties that cause the dying cell to be rapidly phagocytized, either by neighboring cells or by macrophages. These alterations in the cell surface can be used as possible targets for the non-invasive detection of apoptotic cells. Apoptosis has been described as another marker of plaque instability [115].

One of the cell surface markers expressed during apoptosis is Annexin-5 [116], which has been successfully targeted in atherosclerotic ApoE$^{-/-}$ mice by using annexin A5-functionalized micellar nanoparticles [117]. Caspases are a family of protease enzymes that are implicated in the removal of unwanted or damaged cells in a controlled manner to avoid damage of surrounding cells and the activation of the immune system. First approaches to image these proteases have been performed by using caspase-3/7-activatable Gd-based probe (C-SNAM) in experimental murine tumors [13]. However, the use of caspase-targeted contrast agents has not yet been validated in atherosclerosis.

Extracellular Plaque Components and Proteolytic Enzymes

Extracellular matrix (ECM) is an interesting molecular target for the assessment of atherosclerosis. The ECM is a non-cellular intricate network of macromolecules such as proteins and polysaccharides that confers a scaffold to stabilize the physical structure of tissues. In atherosclerotic plaques, the ECM is highly abundant and undergoes extensive remodeling, thus representing an excellent target for magnetic resonance imaging. The cells producing and secreting ECM in the atherosclerotic plaques are predominantly macrophages and VSMCs. Among the many structural proteins that form the ECM, collagen and elastin are the main components and undergo degradation and production in atherosclerosis [118]. To detect the alteration of the ECM under pathological conditions, a small molecular weight elastin-specific gadolinium-based contrast agent (ESMA) has been developed. The ability of ESMA to detect plaque burden and ECM remodeling has been demonstrated at different stages of atherosclerosis in a murine model and in a porcine model of coronary injury [119–121] (Figs. 8.8 and 8.9).

In addition to quantifying plaque burden, ESMA also allowed in vivo classification of vascular remodeling into negative, intermediate, or positive, which aided the detection of “high risk/vulnerable” plaque in a rabbit model of experimentally induced thrombosis [122] (Fig. 8.10).

Similarly, to prospective clinical studies in humans with coronary artery disease using X-RAY and CT angiography [10, 123, 124], the rabbit study showed that

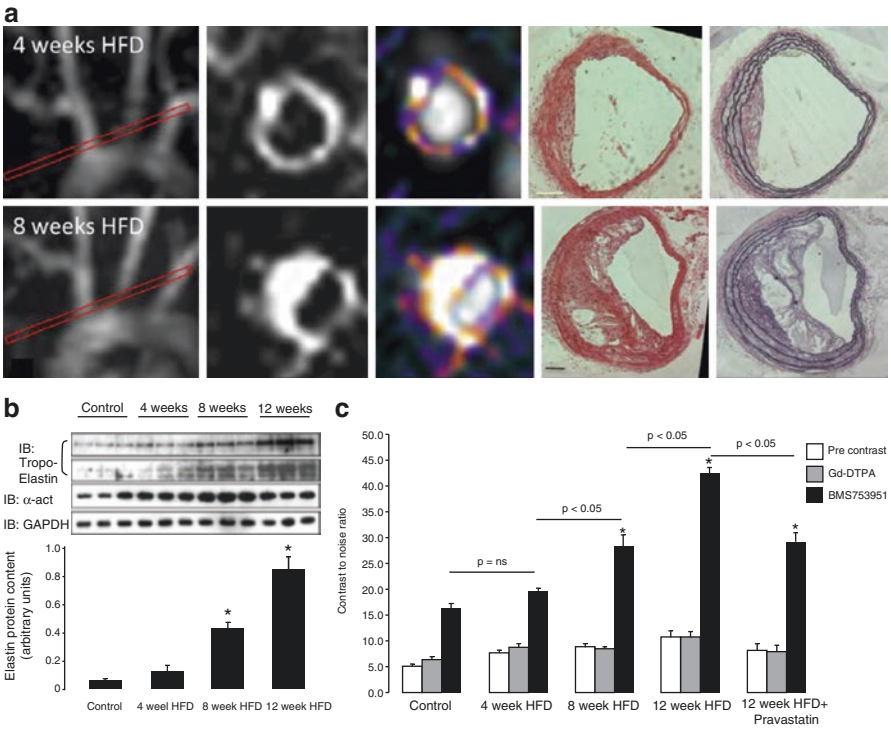

Fig. 8.8 MRI of extracellular matrix remodeling in an apoE$^{-/-}$ mouse model of accelerated atherosclerosis at 4 and 8 weeks after commencement of HFD using an elastin specific MR contrast agent (**a**), ESMA (Lantheus Medical Systems, North Billerica, MA, USA). (**b**, **c**) Contrast-to-noise values after ESMA injection increased with the duration of the HFD, which was paralleled by an increase in tropoelastin by western blotting (Adapted from Makowski et al. [121])

positive remodeling measured after administration of ESMA was associated with plaque instability.

Another approach to image the ECM consists in developing specific contrast agents to detect collagen. The contrast agent EP-3533 contains a collagen-specific peptide as the targeting vector and has been successfully used to evaluate fibrosis in a murine model myocardial infarction [125, 126]. However, the use of this contrast agent has not been validated in atherosclerosis, yet. Additionally, the use of paramagnetic/fluorescent micellar nanoparticles functionalized with collagen-binding proteins was successfully used to investigate the role of collagen remodeling in a murine model of atherosclerosis [127].

Matrix metalloproteinases (MMPs), also called matrixins, are proteinases that participate in the degradation of the macromolecules that form the ECM. Under physiological conditions, their activation, activity and inhibition are precisely regulated. Unregulated expression and activity of the MMPs may result in diseases

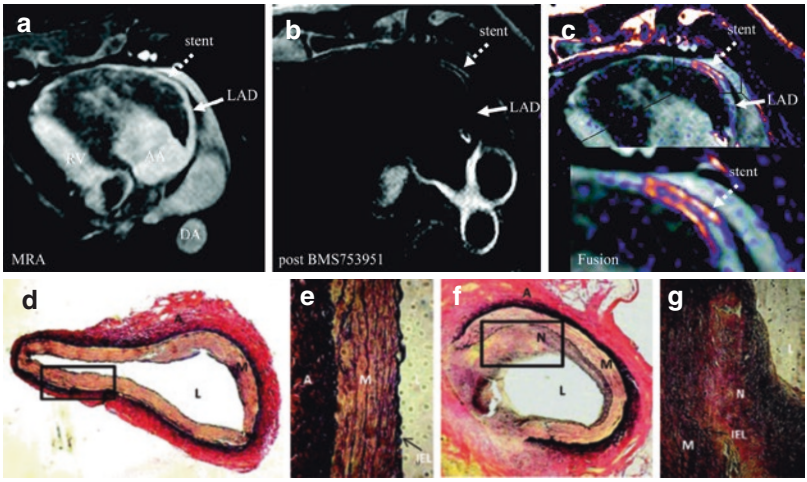

Fig. 8.9 Elastin imaging of coronary remodelling. Comparison of coronary MRA (**a**) delayed-enhancement MRI (**b**) and positron-emission CT–like fusion of (**a**–**c**) of stented and control coronary vessel segments and corresponding histology (**d**, **e**). Strong enhancement can be observed at the stent location (*dotted white arrow*), whereas little to no enhancement is visible in the normal noninjured left anterior descending artery segment (**b**, **c**). Elastic von Gieson stain of noninjured coronary vessel segment (**d**) shows intact internal elastic lamina (*IEL*) and circular arranged elastin fibers (*black*) in the media. Elastic von Gieson of stented vessel segment (**e**) demonstrates disruption of IEL and neointima formation with diffuse elastin deposition (*black dots*). Elastic van Gieson of stented vessel segment (**f** and **g**) demonstrates disruption of IEL and neointima formation with diffuse elastin deposition (*black dots*). (**e**) and (**g**), Magnifications of (**d**) and (**f**) (Adapted from von Bary et al. [119])

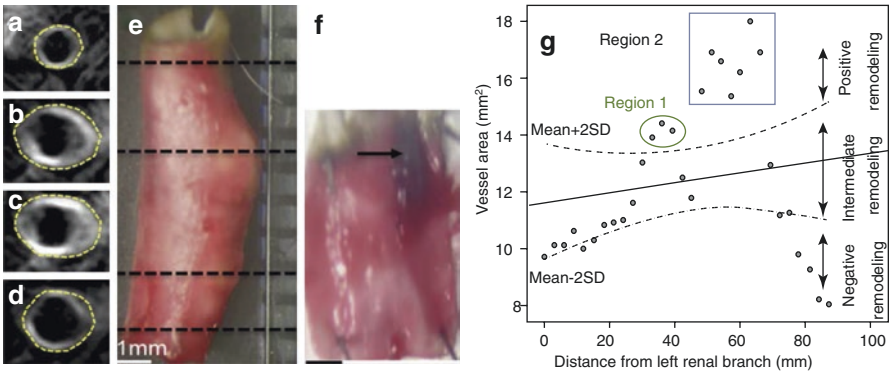

Fig. 8.10 Positive vascular remodeling in disrupted plaques. (**a–d**) DE MR images obtained after administration of elastin-specific contrast agent show positive remodeling, as defined by enlargement of vessel area (*yellow contours*). (**e**) Corresponding *en face* photograph verifies presence of positive vascular remodeling. (**f**) *En face* photograph of longitudinally open vessel shows thrombus (*arrow*) attached to vessel wall at proximal end of positive remodeling. (**g**) Scatterplot shows change in vessel area measured on consecutive slices along aorta, starting from left renal branch (0 mm) to iliac bifurcation (86 mm). Two regions of the vessel wall underwent positive remodeling, with vessel areas falling above the mean + 2 SD margin. Both plaques disrupted after triggering. Four of seven sections covering the vulnerable region 2 are illustrated in (**a–d**) (Adapted from Phinikaridou et al. [122])

such as arthritis, cancer, atherosclerosis, aneurysms and fibrosis [128]. During atherosclerosis, MMPs are mainly secreted by activated macrophages and are linked to plaque instability [129]. Therefore, MMP targeted contrast agents may provide valuable diagnostic information on plaque stability and composition. Noninvasive imaging of MMPs has been successfully performed using a gadolinium chelate targeted to a MMP inhibitor (P947) in murine and rabbit experimental models [130, 131]. Moreover, the enzyme myeloperoxidase (MPO) has been used as an emerging biomarker of plaque instability and future acute events [132]. The feasibility of a specific gadolinium-based probe that targets MPO-Gd to image atherosclerosis in hyperlipidemic rabbits has also been demonstrated [133]. In addition, MPO-Gd enhancement was shown to colocalize with plaque areas rich in infiltrated macrophages [133].

Fibrin and Thrombus Formation

Fibrin is highly abundant after plaque rupture and is one of the main proteins of acute and subacute thrombus [134]. In addition, fibrin deposition within the matrix of plaques plays an important role in atherosclerosis progression and enters the growing plaque mainly due to leaky neovessels, [135–139]. Several studies have shown the feasibility of gadolinium-based nanoparticles and small molecular weight fibrin-binding contrast agent to image thrombosis in both, animal models and humans [119, 136, 137, 140–142]. A small translational clinical study has also been successfully performed to evaluate aortic and carotid thrombosis in vivo by using EP-2104R [140] (Fig. 8.11).

Spectral CT

The scintillation detectors of a conventional CT system measure signals which are proportional to the integral of the energy spectrum and thus do not allow extracting information about the composition of the irradiated material or tissue. By using energy resolved x-ray detectors, spectral CT (also referred to as multicolour CT) different types of materials can be distinguished by exploiting the characteristic energy-dependent attenuation of x-rays [143]. This novel technology was used to detect gold high-density lipoprotein nanoparticles (Au-HDL) localized in macrophages within aortic atherosclerotic plaques in ApoE$^{-/-}$ mice [144]. Additionally, spectral CT allowed the differentiation between iodine-based contrast probes and calcium phosphate initially in phantoms and later in vessels and bones [145]. Finally, human high-risk carotid plaque tissue characterization with spectral CT was compared with corresponding histological findings and yielded successful differentiation between lipids, calcium and iron deposits with high spatial resolution [146].

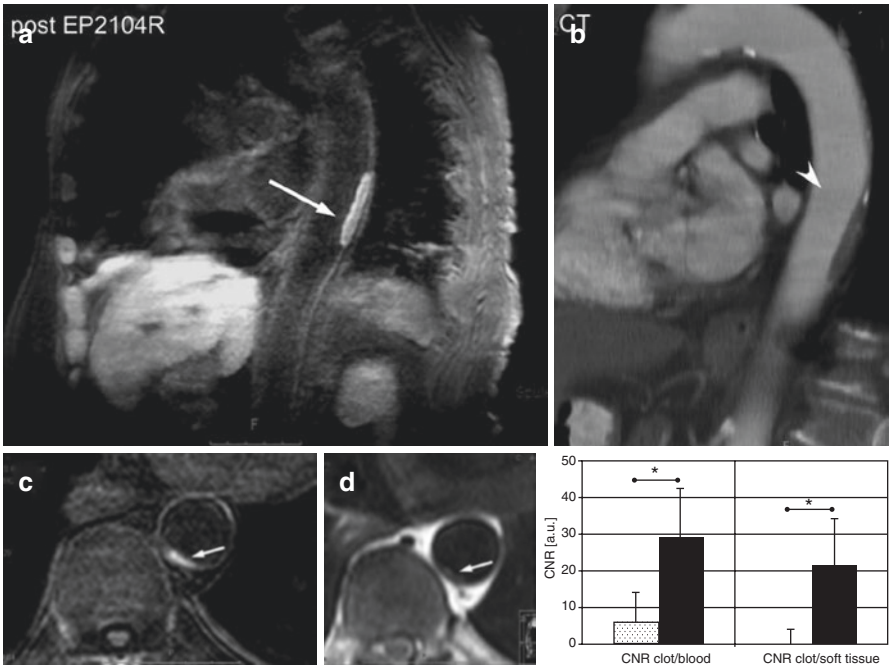

Fig. 8.11 Phase II clinical trial validating clinical feasibility of fibrin specific MR contrast agent. Human thrombus imaging using EP-2104R, a fibrin binding contrast agent, in a patient with aortic thrombus. A mural aortic thrombus is well delineated on in-plane post EP-2104R black blood MR images (**a**) while differentiation between thrombus and vessel wall is poor on multi slice CT images (**b**). Excellent aortic thrombus visualization on cross-sectional delayed enhancement images post EP-2104R (**c**) while differentiation between thrombus and vessel wall is poor on pre contrast black blood turbo spin echo (**d**) MR images (Adapted from Spuentrup et al. [140])

Hybrid Imaging Technologies

PET/CT and PET/MRI

Positron Emission Tomography (PET) is a nuclear medicine imaging modality that allows the observation of biomedical processes at a cellular and/or molecular level with very high sensitivity (picomolar range). PET visualizes the distribution of a radionuclide-labeled biomarker (also referred to as radio-tracer) that either targets a protein of interest or a metabolic process. In addition to the high sensitivity, PET can be used to quantify tracer distribution which is crucial for the assessment of treatment response. Since the late 1990s, PET has been combined with CT to improve the clinical workflow and diagnostic accuracy by obtaining complementary information with high-resolution anatomical imaging provided by CT [147, 148]. In addition to the established clinical workflow, multi-modality imaging techniques such as PET/CT are increasingly used for biomarker and drug development (e.g. pharmacokinetic studies), and to study molecular and biochemical processes (Fig. 8.12).

Compared to CT, MRI offers high soft-tissue contrast, no ionizing radiation and, in addition to high-resolution anatomical images, it can provide tissue perfusion, diffusion, T1, T2 and spectroscopic data, which add complementary functional information to the PET examination. Furthermore, unlike CT, MRI can be simulta-

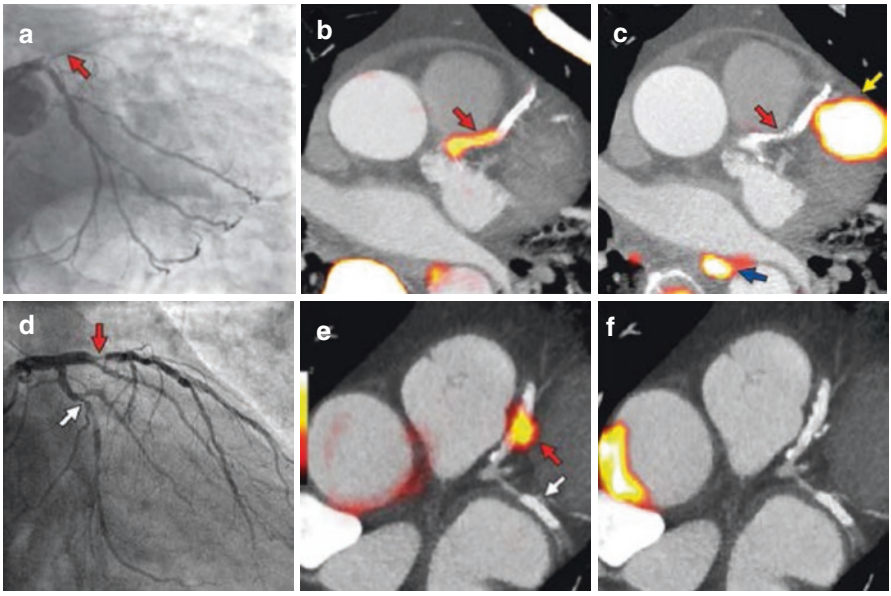

Fig. 8.12 Focal ^{18}F-fluoride and ^{18}F-fluorodeoxyglucose uptake in patients with myocardial infarction and stable angina. Patient with acute ST-segment elevation myocardial infarction with (**a**) proximal occlusion (*red arrow*) of the left anterior descending artery on invasive coronary angiography and (**b**) intense focal ^{18}F-fluoride uptake (*yellow-red*) at the site of the culprit plaque (*red arrow*) on the combined positron emission and computed tomogram (*PET-CT*). Corresponding ^{18}F-fluorodeoxyglucose PET-CT image (**c**) showing no uptake at the site of the culprit plaque. Note the significant myocardial uptake overlapping with the coronary artery (*yellow arrow*) and uptake within the oesophagus (*blue arrow*). Patient with anterior non-ST-segment elevation myocardial infarction with (**d**) culprit (*red arrow*; left anterior descending artery) and bystander non-culprit (*white arrow*; circumflex artery) lesions on invasive coronary angiography that were both stented during the index admission. Only the culprit lesion had increased ^{18}F-NaF uptake on PET-CT. (**e**) after percutaneous coronary intervention. Corresponding ^{18}F-fluorodeoxyglucose PET-CT showing no uptake either at the culprit or the bystander stented lesion. (**f**) Note intense uptake within the ascending aorta. In a patient with stable angina with previous coronary artery bypass grafting, invasive coronary angiography (**g**) showed non-obstructive disease in the right coronary artery. Corresponding PET-CT scan (**h**) showed a region of increased ^{18}F-NaF activity (positive lesion, *red line*) in the mid-right coronary artery and a region without increased uptake in the proximal vessel (negative lesion, *yellow line*). Radiofrequency intravascular ultrasound shows that the ^{18}F-NaF negative plaque (**i**) is principally composed of fibrous and fibrofatty tissue (*green*) with confluent calcium (*white with acoustic shadow*) but little evidence of necrosis. On the contrary, the ^{18}F-NaF positive plaque (**j**) shows high-risk features such as a large necrotic core (*red*) and microcalcification (*white*)

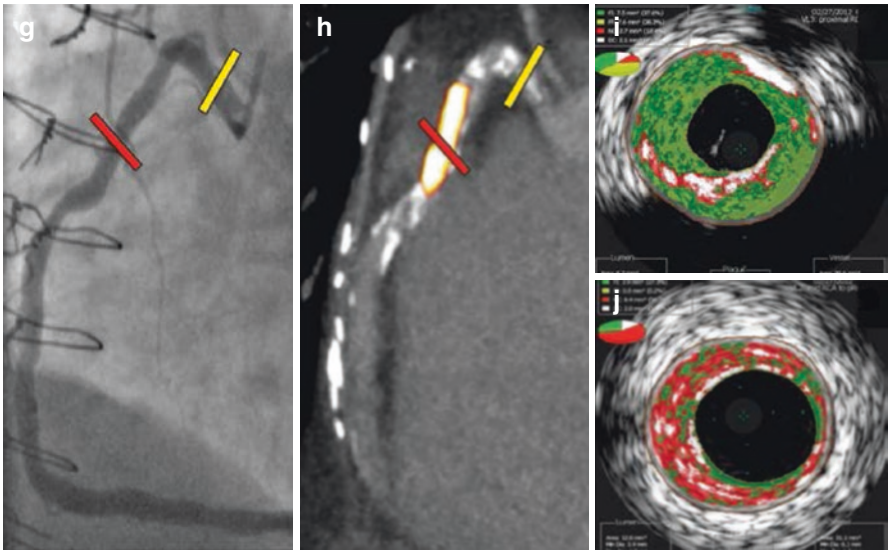

Fig. 8.12 (continued)

neously operated with PET allowing temporal and spatial correlation of images acquired with both modalities. This approach is particularly applicable for cardiovascular imaging, as cardiac and respiratory motion, causing artifacts in both PET and MRI images, can be reduced by applying MRI-based motion correction methods. Multimodal molecular imaging of atherosclerosis using PET/CT and more recently PET/MRI has been a field of ongoing research since the beginning of the new millennium. Examples of these approaches are discussed below.

Inflammation Assessment Using Other Modalities

Among all clinical PET tracers, [^{18}F]fluorodeoxyglucose (^{18}F-FDG) has been the most extensively used. It is a glucose analogue predominantly applied for cancer diagnosis and treatment monitoring [149, 150]. ^{18}F-FDG has also been evaluated in the area of cardiovascular diseases (CVD) as a tracer for atherosclerotic plaque imaging. Cells with high metabolic activity such as macrophages have increased FDG uptake and could be visualized using ^{18}F-FDG PET in atherosclerotic lesions [151–153]. Ex vivo studies using excised human plaques revealed an increase of macrophage infiltration during all stages of atherosclerosis [154]. Growing plaques lead to intraplaque hypoxia which, in turn, promotes glucose uptake by macrophages and thus yields an increased PET signal [153, 154]. However, increased glucolytic activity was also detected in vascular smooth muscle cells (VSMCs) and endothelial cells [155]. Different mechanisms for stimulation of macrophages, VSMCs, and

endothelial cells may contribute importantly to increased glucose uptake and, hence, to ^{18}F-FDG signal in atherosclerotic plaques. When cultivated in vitro, macrophages or foam cells, which are abundant constituents of inflamed atheromata, do not seem to increase glucose uptake in response to inflammatory stimulation, although VSMCs and endothelial cells do so [155]. In vitro studies have even suggested that pro-inflammatory macrophages (M1) preferentially accumulate ^{18}F-FDG, compared to reparative macrophages (M2), suggesting that ^{18}F-FDG PET could be a useful method for imaging M1 macrophages [156]. Conversely, another study showed that only resting macrophages, but not M1 or M2 polarized macrophages, showed increased glucose uptake, suggesting that glucose metabolism is regulated independently of the polarization state and macrophage polarization may not be detectable by ^{18}F-FDG PET [157]. Further studies are required to clarify the importance of glucose uptake by macrophages and other cell types within the plaque.

A recently-proposed tracer, ^{18}F-labeled mannose (2-deoxy-2-[^{18}F]fluoro-d-mannose, [^{18}F-]FDM), was designed to have higher specificity than ^{18}F-FDG to macrophage subtypes. ^{18}F-FDM is a glucose isomer that, in addition to macrophage glucose uptake, targets mannose receptors that are only expressed by M2 but not M1 macrophages [158]. In vitro macrophage studies revealed higher ^{18}F-FDM uptake compared to ^{18}F-FDG in M2 macrophages. However, clinical studies are now warranted to demonstrate the association of higher ^{18}F-FDM PET signal with in-vivo macrophage biology and plaque instability.

Several clinical studies showed that ^{18}F-FDG can be used to visualize carotid and aortic plaque inflammation with PET [13, 159–161]. ^{18}F-FDG-based coronary artery imaging, however has been less successful due to the enhancement of the myocardium itself. The high background signal obscures ^{18}F-FDG-uptake originating from coronary atherosclerotic lesions and hampers the identification of coronary lesions [13, 51, 162]. Targeting macrophages for imaging purposes, while avoiding a low contrast-to-noise (CNR) due to PET signal uptake by the myocardium, motivated the development of novel biomarkers. ^{68}Ga-DOTATATE, a clinically approved tracer, was used as an alternative to ^{18}F-FDG to detect macrophage burden in coronary arteries [162]. This tracer binds to somatostatin receptors type 2 that are expressed on macrophages but not in the myocardium and thus is advantageous for coronary artery imaging compared to ^{18}F-FDG. In this study, CT was used to localize calcium deposits in plaques, which also showed significantly increased ^{68}Ga-DOTATATE uptake, thereby suggesting that this tracer may be a potential alternative to FDG for imaging of coronary atherosclerosis [162].

Another way of imaging macrophages takes advantage of their phagocytic properties using radio-labeled nanomaterials. Iron-oxide nanoparticles, which are know to be taken up by macrophages were linked to a near-infrared fluorochrome (Vivotag-680) and labelled with the radio-isotope ^{64}Cu, (^{64}Cu-TNP) and tested in vivo [163]. ^{64}Cu-TNP was shown to target macrophages in atherosclerotic ApoE$^{-/-}$ mice and could be imaged with PET, MRI and fluorescence imaging. Additionally, a polymeric nanoparticle modified with desferoxamine to allow for conjugation with the near-infrared fluorochrome Vivotag-680 and radio-labeling with ^{89}Zr (^{89}Zr-DNP) was developed and used for imaging inflammation in ApoE$^{-/-}$ mice by

PET/MRI [164]. Ex vivo flow cytometry analysis showed 77% of the tracer co-localized with monocytes and macrophages whereas the remaining 23% was detected in neutrophils and lymphocytes [164].

Following macrophage polarization, these cells express high levels of benzodiazepine receptors (PBR), which could be an interesting target for direct visualization of inflammation [165]. A radiolabelled compound (^{11}C-PK11195) that selectively binds to PBR was developed and assessed in patients with carotid atherosclerotic plaques [166]. Imaging of intraplaque inflammation in vivo with ^{11}C-PK11195 PET/CTA was feasible and could distinguish between symptomatic and asymptomatic plaques. Patients with a recent ischemic event had ipsilateral plaques with lower CT attenuation and increased ^{11}C-PK11195 uptake.

Calcification

Imaging plaque calcification is important, as the location, structure and size of the calcium deposits within the atheroma indicates lesion severity (stable or vulnerable). Compared to macrocalcifications, which primarily develop in stable plaque and are detectable by CT, microcalcifications within the thin fibrous cap can cause mechanical stress that may promote microfractures and plaque rupture [48, 167, 168]. ^{18}F-sodium-fluoride (^{18}F-NaF) is a clinically approved and established PET tracer used for bone imaging [169] which binds to calcified areas as a result of a chemical reaction with hydroxyapatite [170]. ^{18}F-NaF does not penetrate into inner layers of macrocalcifications, but only binds to the outer layers. Since microcalcifications have a small volume and large surface area, ^{18}F-NaF uptake is higher in microcalcifications compared to macrocalcifications [50]. The binding properties of ^{18}F-NaF have been evaluated to better image vascular spotty calcifications in the aorta, carotid and coronary arteries of patients compared clinical CT [13, 171, 172]. A small study including patients with aortic stenosis revealed that valvular ^{18}F-NaF uptake allows identification of active tissue calcification that could be used to predict disease progression [159]. Confirmed by histological analysis, the information provided by ^{18}F-NaF-PET was considered to be complementary to CT calcium scoring which quantifies macroscopic calcification with no indication on active or inactive calcification [159]. In a prospective study including patients with symptomatic carotid artery disease, ^{18}F-NaF was localized in all ruptured carotid plaques and was linked to histological findings of active calcification, inflammation, apoptosis and necrosis, that are indicators of rupture-prone plaques [13]. A clinical study including 119 subjects showed that coronary plaque uptake of ^{18}F-NaF identified patients with a high Framingham Risk Score [172]. Moreover, patients with recent myocardial infarction showed a higher ^{18}F-NaF uptake in ruptured plaques compared to non-ruptured plaques [13]. In the same study, coronary artery plaques of patients with stable angina had microcalcifications identified by higher ^{18}F-NaF-PET uptake that co-localized with necrotic cores and positive remodeling detected by IVUS, all of which are imaging characteristics of high-risk plaques.

The promising results of aortic, carotid and coronary plaque imaging with PET demonstrate that PET may provide in-vivo plaque characterization. Larger prospective clinical trials are now needed to investigate if PET can identify patients with higher cardiovascular risk and ultimately improve guidance of medical treatment. Currently, two clinical trials are ongoing. A multi-center observational study *(ClinicalTrials.gov. Prediction of Recurrent Events With 18F-Fluoride (PREFFIR) https://clinicaltrials.gov/ct2/show/NCT02278211 (2015))* aims to evaluate the predictive value of ^{18}F-NaF in patients with CAD with respect to future cardiovascular events. The second clinical trial *(ClinicalTrials.gov. DIAMOND – Dual Antiplatelet Therapy to Reduce Myocardial Injury (DIAMOND) https://clinicaltrials.gov/ct2/show/NCT02110303 (2015))* aims to study the effect of an antiplatelet drug (Ticagrelor) on plaque stability using ^{18}F-NaF-PET.

Gating and Motion Correction

Coronary plaque images obtained with PET/CT could be improved by respiratory- and electrocardiography-gated PET data prior to the PET/CT image registration step [173–175]. Clinical electrocardiography-gated PET/CT imaging of coronary arteries was performed with ^{18}F-NaF to compare the image quality of PET images reconstructed from different numbers of bins per cardiac cycle [176]. Subsequently, a local, nonlinear motion correction method guided by the coronary arteries extracted from the CTA images was applied to register the gated PET data. This led to increased global PET image SNR and target-to-background ratio [176]. Fully simultaneous PET/MRI systems now offer MRI-based motion-corrected PET data and motion-corrected high-resolution MR coronary angiograms with a high accuracy of co-registration. On-going research focuses on MR-based PET motion correction [177–181] and novel promising MR motion-correction correction techniques [182–185] could be used to improve the diagnostic accuracy for CAD assessment by PET/MRI. In addition, the use of novel MR contrast agents together with PET tracers could provide complementary information for advanced plaque characterization and ultimately allow more accurate assessment of plaque stability/instability. Studies comparing PET/CT with PET/MR for atherosclerosis assessment are underway. First publications comparing carotid plaque imaging using ^{18}F-FDG with PET/CT and PET/MRI yielded good correlation of PET signal quantification in terms of standard uptake value (SUV) between both imaging modalities [160, 161]. However, the SUVs determined with PET/MRI were underestimated compared to those calculated from PET/CT which was attributed to the PET attenuation correction method used by the PET/MRI system that ignored bone material [161].

PET/MRI is also a promising candidate for monitoring atherosclerotic disease progression and regression following medical treatment or intervention. However, further clinical studies are required demonstrate the utility of PET/MRI for the assessment of atherosclerosis and its added clinical value for diagnosis and therapy monitoring in addition to PET/CT (Fig. 8.13).

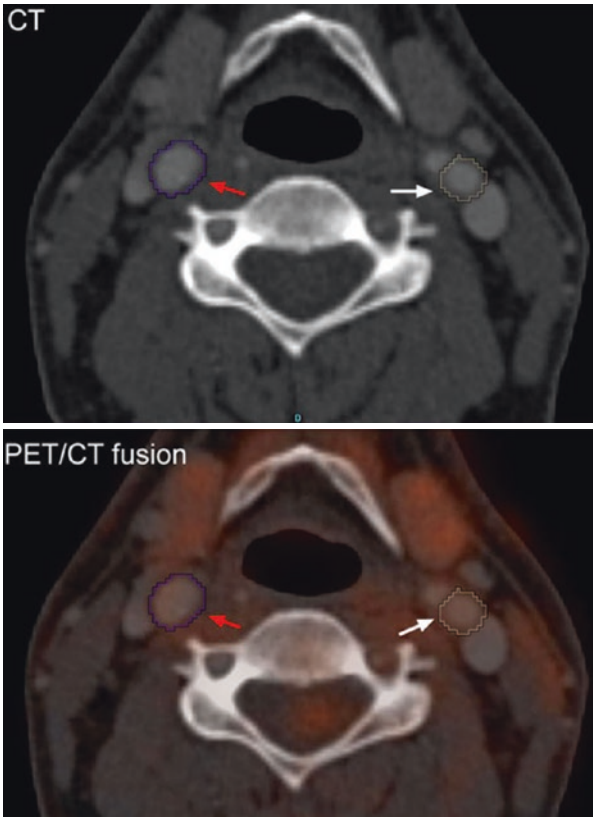

Fig. 8.13 CT and fused FDG-PET/CT. Example of transverse CT and fused FDG-PET/CT. The right common carotid artery is marked by a *red arrow* on the left internal carotid artery is marked by a *white arrow*. A ROI including both the vessel wall and lumen is drawn

Conclusions

Advances in imaging technology and contrast agent design have enabled non-invasive plaque visualization and characterization in large vessels but also in the coronary arteries. Ongoing technical research aims at further improving image quality, ease of use and reducing scan time while contrast agent research aims at increasing the specificity and sensitivity of imaging agents while maintaining fast clearance and good safety profiles. With the advent of multi modal imaging such as PET/MRI comprehensive coronary plaque imaging is in our reach and continued research will tell us if non-invasive coronary plaque imaging will become reality or remain a dream.

Graphical Summary: Atherosclerotic Plaque Imaging

Modality	Endothelial dysfunction	Lipids	Angiogenesis	Inflammation	Apoptosis	ECM and proteolytic enzymes	Fibrin and Thrombus formation	Calcification
MRI	• Gadofosveset	• Gadofluorine M • rHDL-P2A2 • LOX1-Liposomes	• $\alpha_v\beta_3$	• CD206-immunomicelles		• ESMA • CP-3533 • P947 • MPO	• EP-2104R	
	• VCAM-1 specific nanoparticles			• Iron particles • SR-A1 USPIOs • HDL-like nanoparticles	• Annexin-5-funcionalized micellar nanoparticles			
				• ^{19}F-containing particles				
PET				• [^{18}F]-FDG • [^{18}F]-FDM • [^{69}Ga]-DOTATATE • [^{64}Cu]-TNP • [^{89}Zr]-DPN • [^{11}C]-PK11195				• [^{18}F]-NaF

Gadolinium-based contrast agents

Iron oxide-based contrast agents

Fluorine-based contrast agents

Radioactive-based contrast agents

Acknowledgments The authors acknowledge financial support from: (1) the British Heart Foundation (RG/12/1/29262), (2) the Centre of Excellence in Medical Engineering funded by the Wellcome Trust and EPSRC (WT 088641/Z/09/Z), (3) the British Heart Foundation Centre of Excellence and (4) the Department of Health via the National Institute for Health Research (NIHR) comprehensive Biomedical Research Centre award to Guy's & St Thomas' NHS Foundation Trust in partnership with King's College London and King's College Hospital NHS Foundation Trust. The views expressed are those of the authors and not necessarily those of the NHS, the NIHR or the Department of Health.

References

1. Writing Group, M, et al. Heart disease and stroke statistics-2016 update: a report from the American Heart Association. Circulation. 2016;133(4):e38–60.
2. Sacco RL. The new American Heart Association 2020 goal: achieving ideal cardiovascular health. J Cardiovasc Med (Hagerstown). 2011;12(4):255–7.
3. Pijls NH, et al. Measurement of fractional flow reserve to assess the functional severity of coronary-artery stenoses. N Engl J Med. 1996;334(26):1703–8.
4. Nissen SE, Yock P. Intravascular ultrasound: novel pathophysiological insights and current clinical applications. Circulation. 2001;103(4):604–16.
5. Asrar Ul Haq M, et al. The invasive assessment of coronary atherosclerosis and stents using optical coherence tomography: a clinical update. Heart Asia. 2013;5(1):154–61.
6. Vinegoni C, et al. Indocyanine green enables near-infrared fluorescence imaging of lipid-rich, inflamed atherosclerotic plaques. Sci Transl Med. 2011;3(84):84ra45.
7. Glagov S, et al. Compensatory enlargement of human atherosclerotic coronary arteries. N Engl J Med. 1987;316(22):1371–5.
8. Ali ZA, et al. Increased thin-cap neoatheroma and periprocedural myocardial infarction in drug-eluting stent restenosis: multimodality intravascular imaging of drug-eluting and bare-metal stents. Circ Cardiovasc Interv. 2013;6(5):507–17.
9. Madder RD, Wohns DH, Muller JE. Detection by intracoronary near-infrared spectroscopy of lipid core plaque at culprit sites in survivors of cardiac arrest. J Invasive Cardiol. 2014;26(2):78–9.
10. Motoyama S, et al. Computed tomographic angiography characteristics of atherosclerotic plaques subsequently resulting in acute coronary syndrome. J Am Coll Cardiol. 2009;54(1):49–57.
11. de Boer SP, et al. Determinants of high cardiovascular risk in relation to plaque-composition of a non-culprit coronary segment visualized by near-infrared spectroscopy in patients undergoing percutaneous coronary intervention. Eur Heart J. 2014;35(5):282–9.
12. Wykrzykowska J, et al. Imaging of inflamed and vulnerable plaque in coronary arteries with 18F-FDG PET/CT in patients with suppression of myocardial uptake using a low-carbohydrate, high-fat preparation. J Nucl Med. 2009;50(4):563–8.
13. Joshi NV, et al. 18F-fluoride positron emission tomography for identification of ruptured and high-risk coronary atherosclerotic plaques: a prospective clinical trial. Lancet. 2014;383(9918):705–13.
14. Libby P, Ridker PM, Hansson GK. Progress and challenges in translating the biology of atherosclerosis. Nature. 2011;473(7347):317–25.
15. Miao C, et al. Positive remodeling of the coronary arteries detected by magnetic resonance imaging in an asymptomatic population: MESA (Multi-Ethnic Study of Atherosclerosis). J Am Coll Cardiol. 2009;53(18):1708–15.
16. Gerretsen SC, et al. Visualization of coronary wall atherosclerosis in asymptomatic subjects and patients with coronary artery disease using magnetic resonance imaging. PLoS One. 2010;5(9):e12998.
17. Chiu JJ, Chien S. Effects of disturbed flow on vascular endothelium: pathophysiological basis and clinical perspectives. Physiol Rev. 2011;91(1):327–87.
18. Schar M, et al. The impact of spatial resolution and respiratory motion on MR imaging of atherosclerotic plaque. J Magn Reson Imaging. 2003;17(5):538–44.
19. Kim WY, et al. Subclinical coronary and aortic atherosclerosis detected by magnetic resonance imaging in type 1 diabetes with and without diabetic nephropathy. Circulation. 2007;115(2):228–35.
20. Skalen K, et al. Subendothelial retention of atherogenic lipoproteins in early atherosclerosis. Nature. 2002;417(6890):750–4.
21. Bentzon JF, et al. Mechanisms of plaque formation and rupture. Circ Res. 2014;114(12):1852–66.

22. Noguchi T, et al. High-intensity signals in carotid plaques on T1-weighted magnetic resonance imaging predict coronary events in patients with coronary artery disease. J Am Coll Cardiol. 2011;58(4):416–22.
23. Tanaka A, et al. Hyperintense plaque with noncontrast T1-weighted magnetic resonance coronary plaque imaging leading to acute coronary syndrome. Circulation. 2009;120(23):2400–1.
24. Jansen CH, et al. Detection of intracoronary thrombus by magnetic resonance imaging in patients with acute myocardial infarction. Circulation. 2011;124(4):416–24.
25. Ehara S, et al. Hyperintense plaque identified by magnetic resonance imaging relates to intracoronary thrombus as detected by optical coherence tomography in patients with angina pectoris. Eur Heart J Cardiovasc Imaging. 2012;13(5):394–9.
26. Hays AG, et al. Noninvasive visualization of coronary artery endothelial function in healthy subjects and in patients with coronary artery disease. J Am Coll Cardiol. 2010;56(20):1657–65.
27. Hays AG, et al. Regional coronary endothelial function is closely related to local early coronary atherosclerosis in patients with mild coronary artery disease: pilot study. Circ Cardiovasc Imaging. 2012;5(3):341–8.
28. Libby P. Mechanisms of acute coronary syndromes and their implications for therapy. N Engl J Med. 2013;368(21):2004–13.
29. Brown AJ, et al. Role of biomechanical forces in the natural history of coronary atherosclerosis. Nat Rev Cardiol. 2016;13(4):210–20.
30. Stary HC, et al. A definition of initial, fatty streak, and intermediate lesions of atherosclerosis. A report from the Committee on Vascular Lesions of the Council on Arteriosclerosis, American Heart Association. Circulation. 1994;89(5):2462–78.
31. Nossaman BD, et al. History of right heart catheterization: 100 years of experimentation and methodology development. Cardiol Rev. 2010;18(2):94–101.
32. Tonino PA, et al. Fractional flow reserve versus angiography for guiding percutaneous coronary intervention. N Engl J Med. 2009;360(3):213–24.
33. Nicholls SJ, et al. Intravascular ultrasound-derived measures of coronary atherosclerotic plaque burden and clinical outcome. J Am Coll Cardiol. 2010;55(21):2399–407.
34. Nair A, et al. Coronary plaque classification with intravascular ultrasound radiofrequency data analysis. Circulation. 2002;106(17):2200–6.
35. Granada JF, et al. In vivo plaque characterization using intravascular ultrasound-virtual histology in a porcine model of complex coronary lesions. Arterioscler Thromb Vasc Biol. 2007;27(2):387–93.
36. Swanson EA, et al. In vivo retinal imaging by optical coherence tomography. Opt Lett. 1993;18(21):1864–6.
37. Roleder T, et al. The basics of intravascular optical coherence tomography. Postepy Kardiol Interwencyjnej. 2015;11(2):74–83.
38. Kubo T, et al. Assessment of coronary atherosclerosis using optical coherence tomography. J Atheroscler Thromb. 2014;21(9):895–903.
39. Kubo T, et al. OCT compared with IVUS in a coronary lesion assessment: the OPUS-CLASS study. JACC Cardiovasc Imaging. 2013;6(10):1095–104.
40. Sanz J, Fayad ZA. Imaging of atherosclerotic cardiovascular disease. Nature. 2008;451(7181):953–7.
41. Leber AW, et al. Accuracy of 64-slice computed tomography to classify and quantify plaque volumes in the proximal coronary system: a comparative study using intravascular ultrasound. J Am Coll Cardiol. 2006;47(3):672–7.
42. Ovrehus KA, et al. Reproducibility of semi-automatic coronary plaque quantification in coronary CT angiography with sub-mSv radiation dose. J Cardiovasc Comput Tomogr. 2016;10(2):114–20.
43. Tavakoli S, Vashist A, Sadeghi MM. Molecular imaging of plaque vulnerability. J Nucl Cardiol. 2014;21(6):1112–28; quiz 1129.
44. Polonsky TS, et al. Coronary artery calcium score and risk classification for coronary heart disease prediction. JAMA. 2010;303(16):1610–6.
45. Agatston AS, et al. Quantification of coronary artery calcium using ultrafast computed tomography. J Am Coll Cardiol. 1990;15(4):827–32.

46. Pletcher MJ, et al. Using the coronary artery calcium score to predict coronary heart disease events: a systematic review and meta-analysis. Arch Intern Med. 2004;164(12): 1285–92.
47. New SE, et al. Macrophage-derived matrix vesicles: an alternative novel mechanism for microcalcification in atherosclerotic plaques. Circ Res. 2013;113(1):72–7.
48. Otsuka F, et al. Has our understanding of calcification in human coronary atherosclerosis progressed? Arterioscler Thromb Vasc Biol. 2014;34(4):724–36.
49. Kelly-Arnold A, et al. Revised microcalcification hypothesis for fibrous cap rupture in human coronary arteries. Proc Natl Acad Sci U S A. 2013;110(26):10741–6.
50. Irkle A, et al. Identifying active vascular microcalcification by (18)F-sodium fluoride positron emission tomography. Nat Commun. 2015;6:7495.
51. Rogers IS, et al. Feasibility of FDG imaging of the coronary arteries: comparison between acute coronary syndrome and stable angina. JACC Cardiovasc Imaging. 2010;3(4): 388–97.
52. Aikawa E, et al. Osteogenesis associates with inflammation in early-stage atherosclerosis evaluated by molecular imaging in vivo. Circulation. 2007;116(24):2841–50.
53. Maurovich-Horvat P, et al. The napkin-ring sign indicates advanced atherosclerotic lesions in coronary CT angiography. JACC Cardiovasc Imaging. 2012;5(12):1243–52.
54. Kashiwagi M, et al. Feasibility of noninvasive assessment of thin-cap fibroatheroma by multidetector computed tomography. JACC Cardiovasc Imaging. 2009;2(12):1412–9.
55. Virmani R, et al. Pathology of the thin-cap fibroatheroma: a type of vulnerable plaque. J Interv Cardiol. 2003;16(3):267–72.
56. Nezafat M, et al. Coronary MR angiography at 3 T: fat suppression versus water-fat separation. MAGMA. 2016;29:733–8.
57. Stuber M, et al. Free-breathing black-blood coronary MR angiography: initial results. Radiology. 2001;219(1):278–83.
58. Dweck MR, et al. MR imaging of coronary arteries and plaques. JACC Cardiovasc Imaging. 2016;9(3):306–16.
59. Piccini D, et al. Four-dimensional respiratory motion-resolved whole heart coronary MR angiography. Magn Reson Med. 2016.
60. Cines DB, et al. Endothelial cells in physiology and in the pathophysiology of vascular disorders. Blood. 1998;91(10):3527–61.
61. Caravan P, et al. The interaction of MS-325 with human serum albumin and its effect on proton relaxation rates. J Am Chem Soc. 2002;124(12):3152–62.
62. Caravan P, et al. Gadolinium(III) Chelates as MRI contrast agents: structure, dynamics, and applications. Chem Rev. 1999;99(9):2293–352.
63. Phinikaridou A, et al. Noninvasive magnetic resonance imaging evaluation of endothelial permeability in murine atherosclerosis using an albumin-binding contrast agent. Circulation. 2012;126(6):707–19.
64. Phinikaridou A, et al. Noninvasive MRI monitoring of the effect of interventions on endothelial permeability in murine atherosclerosis using an albumin-binding contrast agent. J Am Heart Assoc. 2013;2(5):e000402.
65. Lobbes MB, et al. Atherosclerosis: contrast-enhanced MR imaging of vessel wall in rabbit model – comparison of gadofosveset and gadopentetate dimeglumine. Radiology. 2009;250(3): 682–91.
66. Cornily JC, et al. Evaluation of neovessels in atherosclerotic plaques of rabbits using an albumin-binding intravascular contrast agent and MRI. J Magn Reson Imaging. 2008;27(6): 1406–11.
67. Lavin B, et al. Monitoring vascular permeability and remodeling after endothelial injury in a murine model using a magnetic resonance albumin-binding contrast agent. Circ Cardiovasc Imaging. 2015:8(4).
68. Pedersen SF, et al. CMR assessment of endothelial damage and angiogenesis in porcine coronary arteries using gadofosveset. J Cardiovasc Magn Reson. 2011;13:10.
69. Lobbes MB, et al. Gadofosveset-enhanced magnetic resonance imaging of human carotid atherosclerotic plaques: a proof-of-concept study. Investig Radiol. 2010;45(5):275–81.

70. McAteer MA, et al. Magnetic resonance imaging of endothelial adhesion molecules in mouse atherosclerosis using dual-targeted microparticles of iron oxide. Arterioscler Thromb Vasc Biol. 2008;28(1):77–83.
71. Nahrendorf M, et al. Noninvasive vascular cell adhesion molecule-1 imaging identifies inflammatory activation of cells in atherosclerosis. Circulation. 2006;114(14):1504–11.
72. Michalska M, et al. Visualization of vascular inflammation in the atherosclerotic mouse by ultrasmall superparamagnetic iron oxide vascular cell adhesion molecule-1-specific nanoparticles. Arterioscler Thromb Vasc Biol. 2012;32(10):2350–7.
73. Villanueva FS, et al. Microbubbles targeted to intercellular adhesion molecule-1 bind to activated coronary artery endothelial cells. Circulation. 1998;98(1):1–5.
74. Paulis LE, et al. Targeting of ICAM-1 on vascular endothelium under static and shear stress conditions using a liposomal Gd-based MRI contrast agent. J Nanomater. 2012;10:25.
75. Pello OM, et al. A glimpse on the phenomenon of macrophage polarization during atherosclerosis. Immunobiology. 2011;216(11):1172–6.
76. Sirol M, et al. Lipid-rich atherosclerotic plaques detected by gadofluorine-enhanced in vivo magnetic resonance imaging. Circulation. 2004;109(23):2890–6.
77. Chen W, et al. Incorporation of an apoE-derived lipopeptide in high-density lipoprotein MRI contrast agents for enhanced imaging of macrophages in atherosclerosis. Contrast Media Mol Imaging. 2008;3(6):233–42.
78. Li D, et al. Molecular imaging of atherosclerotic plaques targeted to oxidized LDL receptor LOX-1 by SPECT/CT and magnetic resonance. Circ Cardiovasc Imaging. 2010;3(4):464–72.
79. Sluimer JC, et al. Thin-walled microvessels in human coronary atherosclerotic plaques show incomplete endothelial junctions relevance of compromised structural integrity for intraplaque microvascular leakage. J Am Coll Cardiol. 2009;53(17):1517–27.
80. Kolodgie FD, et al. Elimination of neoangiogenesis for plaque stabilization: is there a role for local drug therapy? J Am Coll Cardiol. 2007;49(21):2093–101.
81. Russell DA, Abbott CR, Gough MJ. Vascular endothelial growth factor is associated with histological instability of carotid plaques. Br J Surg. 2008;95(5):576–81.
82. Virmani R, et al. Atherosclerotic plaque progression and vulnerability to rupture: angiogenesis as a source of intraplaque hemorrhage. Arterioscler Thromb Vasc Biol. 2005;25(10):2054–61.
83. Wasserman BA, et al. Carotid artery atherosclerosis: in vivo morphologic characterization with gadolinium-enhanced double-oblique MR imaging initial results. Radiology. 2002;223(2):566–73.
84. Wasserman BA, et al. Wash-in kinetics for gadolinium-enhanced magnetic resonance imaging of carotid atheroma. J Magn Reson Imaging. 2005;21(1):91–5.
85. Yuan C, et al. Contrast-enhanced high resolution MRI for atherosclerotic carotid artery tissue characterization. J Magn Reson Imaging. 2002;15(1):62–7.
86. Cai J, et al. In vivo quantitative measurement of intact fibrous cap and lipid-rich necrotic core size in atherosclerotic carotid plaque: comparison of high-resolution, contrast-enhanced magnetic resonance imaging and histology. Circulation. 2005;112(22):3437–44.
87. Calcagno C, et al. Reproducibility of black blood dynamic contrast-enhanced magnetic resonance imaging in aortic plaques of atherosclerotic rabbits. J Magn Reson Imaging. 2010;32(1):191–8.
88. Kerwin W, et al. Quantitative magnetic resonance imaging analysis of neovasculature volume in carotid atherosclerotic plaque. Circulation. 2003;107(6):851–6.
89. Kerwin WS, et al. Inflammation in carotid atherosclerotic plaque: a dynamic contrast-enhanced MR imaging study. Radiology. 2006;241(2):459–68.
90. Kerwin WS, et al. MR imaging of adventitial vasa vasorum in carotid atherosclerosis. Magn Reson Med. 2008;59(3):507–14.
91. Calcagno C, et al. Detection of neovessels in atherosclerotic plaques of rabbits using dynamic contrast enhanced MRI and 18F-FDG PET. Arterioscler Thromb Vasc Biol. 2008;28(7):1311–7.
92. Manduteanu I, Simionescu M. Inflammation in atherosclerosis: a cause or a result of vascular disorders? J Cell Mol Med. 2012;16(9):1978–90.

93. Purushothaman KR, et al. Atherosclerosis neovascularization and imaging. Curr Mol Med. 2006;6(5):549–56.
94. Winter PM, et al. Molecular imaging of angiogenesis in early-stage atherosclerosis with alpha(v)beta3-integrin-targeted nanoparticles. Circulation. 2003;108(18):2270–4.
95. Cai K, et al. MR molecular imaging of aortic angiogenesis. JACC Cardiovasc Imaging. 2010;3(8):824–32.
96. Ruehm SG, et al. Magnetic resonance imaging of atherosclerotic plaque with ultrasmall superparamagnetic particles of iron oxide in hyperlipidemic rabbits. Circulation. 2001;103(3):415–22.
97. Durand E, et al. Magnetic resonance imaging of ruptured plaques in the rabbit with ultrasmall superparamagnetic particles of iron oxide. J Vasc Res. 2007;44(2):119–28.
98. Morishige K, et al. High-resolution magnetic resonance imaging enhanced with superparamagnetic nanoparticles measures macrophage burden in atherosclerosis. Circulation. 2010;122(17):1707–15.
99. Schmitz SA, et al. Superparamagnetic iron oxide-enhanced MRI of atherosclerotic plaques in Watanabe hereditable hyperlipidemic rabbits. Investig Radiol. 2000;35(8):460–71.
100. Sigovan M, et al. Rapid-clearance iron nanoparticles for inflammation imaging of atherosclerotic plaque: initial experience in animal model. Radiology. 2009;252(2):401–9.
101. Smith BR, et al. Localization to atherosclerotic plaque and biodistribution of biochemically derivatized superparamagnetic iron oxide nanoparticles (SPIONs) contrast particles for magnetic resonance imaging (MRI). Biomed Microdevices. 2007;9(5):719–27.
102. Makowski MR, et al. Noninvasive assessment of atherosclerotic plaque progression in ApoE−/− mice using susceptibility gradient mapping. Circ Cardiovasc Imaging. 2011;4(3):295–303.
103. Kooi ME, et al. Accumulation of ultrasmall superparamagnetic particles of iron oxide in human atherosclerotic plaques can be detected by in vivo magnetic resonance imaging. Circulation. 2003;107(19):2453–8.
104. Tang TY, et al. Temporal dependence of in vivo USPIO-enhanced MRI signal changes in human carotid atheromatous plaques. Neuroradiology. 2009;51(7):457–65.
105. Tang TY, et al. The ATHEROMA (Atorvastatin Therapy: Effects on Reduction of Macrophage Activity) Study. Evaluation using ultrasmall superparamagnetic iron oxide-enhanced magnetic resonance imaging in carotid disease. J Am Coll Cardiol. 2009;53(22):2039–50.
106. Tang TY, et al. Correlation of carotid atheromatous plaque inflammation with biomechanical stress: utility of USPIO enhanced MR imaging and finite element analysis. Atherosclerosis. 2008;196(2):879–87.
107. Trivedi RA, et al. Identifying inflamed carotid plaques using in vivo USPIO-enhanced MR imaging to label plaque macrophages. Arterioscler Thromb Vasc Biol. 2006;26(7):1601–6.
108. Korosoglou G, et al. Noninvasive detection of macrophage-rich atherosclerotic plaque in hyperlipidemic rabbits using "positive contrast" magnetic resonance imaging. J Am Coll Cardiol. 2008;52(6):483–91.
109. Flogel U, et al. In vivo monitoring of inflammation after cardiac and cerebral ischemia by fluorine magnetic resonance imaging. Circulation. 2008;118(2):140–8.
110. Amirbekian V, et al. Detecting and assessing macrophages in vivo to evaluate atherosclerosis noninvasively using molecular MRI. Proc Natl Acad Sci U S A. 2007;104(3):961–6.
111. Yamakoshi Y, et al. LDL-based nanoparticles for contrast enhanced MRI of atheroplaques in mouse models. Chem Commun (Camb). 2011;47(31):8835–7.
112. Frias JC, et al. Recombinant HDL-like nanoparticles: a specific contrast agent for MRI of atherosclerotic plaques. J Am Chem Soc. 2004;126(50):16316–7.
113. Frias JC, et al. Properties of a versatile nanoparticle platform contrast agent to image and characterize atherosclerotic plaques by magnetic resonance imaging. Nano Lett. 2006;6(10):2220–4.
114. Cormode DP, et al. Comparison of synthetic high density lipoprotein (HDL) contrast agents for MR imaging of atherosclerosis. Bioconjug Chem. 2009;20(5):937–43.

115. Jaffer FA, et al. Cellular imaging of inflammation in atherosclerosis using magnetofluorescent nanomaterials. Mol Imaging. 2006;5(2):85–92.
116. Tait JF. Imaging of apoptosis. J Nucl Med. 2008;49(10):1573–6.
117. van Tilborg GA, et al. Annexin A5-functionalized bimodal nanoparticles for MRI and fluorescence imaging of atherosclerotic plaques. Bioconjug Chem. 2010;21(10):1794–803.
118. Katsuda S, Kaji T. Atherosclerosis and extracellular matrix. J Atheroscler Thromb. 2003;10(5):267–74.
119. von Bary C, et al. MRI of coronary wall remodeling in a swine model of coronary injury using an elastin-binding contrast agent. Circ Cardiovasc Imaging. 2011;4(2):147–55.
120. Makowski MR, et al. Three-dimensional imaging of the aortic vessel wall using an elastin-specific magnetic resonance contrast agent. Investig Radiol. 2012;47(7):438–44.
121. Makowski MR, et al. Assessment of atherosclerotic plaque burden with an elastin-specific magnetic resonance contrast agent. Nat Med. 2011;17(3):383–8.
122. Phinikaridou A, et al. Vascular remodeling and plaque vulnerability in a rabbit model of atherosclerosis: comparison of delayed-enhancement MR imaging with an elastin-specific contrast agent and unenhanced black-blood MR imaging. Radiology. 2014;271(2):390–9.
123. Motoyama S, et al. Multislice computed tomographic characteristics of coronary lesions in acute coronary syndromes. J Am Coll Cardiol. 2007;50(4):319–26.
124. Stone GW, et al. A prospective natural-history study of coronary atherosclerosis. N Engl J Med. 2011;364(3):226–35.
125. Caravan P, et al. Collagen-targeted MRI contrast agent for molecular imaging of fibrosis. Angew Chem Int Ed Eng. 2007;46(43):8171–3.
126. Helm PA, et al. Postinfarction myocardial scarring in mice: molecular MR imaging with use of a collagen-targeting contrast agent. Radiology. 2008;247(3):788–96.
127. Chen W, et al. Collagen-specific peptide conjugated HDL nanoparticles as MRI contrast agent to evaluate compositional changes in atherosclerotic plaque regression. JACC Cardiovasc Imaging. 2013;6(3):373–84.
128. Visse R, Nagase H. Matrix metalloproteinases and tissue inhibitors of metalloproteinases: structure, function, and biochemistry. Circ Res. 2003;92(8):827–39.
129. Newby AC. Metalloproteinases and vulnerable atherosclerotic plaques. Trends Cardiovasc Med. 2007;17(8):253–8.
130. Lancelot E, et al. Evaluation of matrix metalloproteinases in atherosclerosis using a novel noninvasive imaging approach. Arterioscler Thromb Vasc Biol. 2008;28(3):425–32.
131. Hyafil F, et al. Monitoring of arterial wall remodelling in atherosclerotic rabbits with a magnetic resonance imaging contrast agent binding to matrix metalloproteinases. Eur Heart J. 2011;32(12):1561–71.
132. Nicholls SJ, Hazen SL. Myeloperoxidase and cardiovascular disease. Arterioscler Thromb Vasc Biol. 2005;25(6):1102–11.
133. Ronald JA, et al. Enzyme-sensitive magnetic resonance imaging targeting myeloperoxidase identifies active inflammation in experimental rabbit atherosclerotic plaques. Circulation. 2009;120(7):592–9.
134. Tavora F, et al. Immunolocalisation of fibrin in coronary atherosclerosis: implications for necrotic core development. Pathology. 2010;42(1):15–22.
135. Flacke S, et al. Novel MRI contrast agent for molecular imaging of fibrin: implications for detecting vulnerable plaques. Circulation. 2001;104(11):1280–5.
136. Botnar RM, et al. In vivo magnetic resonance imaging of coronary thrombosis using a fibrin-binding molecular magnetic resonance contrast agent. Circulation. 2004;110(11):1463–6.
137. Botnar RM, et al. In vivo molecular imaging of acute and subacute thrombosis using a fibrin-binding magnetic resonance imaging contrast agent. Circulation. 2004;109(16):2023–9.
138. Spuentrup E, et al. Molecular magnetic resonance imaging of coronary thrombosis and pulmonary emboli with a novel fibrin-targeted contrast agent. Circulation. 2005;111(11):1377–82.
139. Falk E, Shah PK, Fuster V. Coronary plaque disruption. Circulation. 1995;92(3):657–71.

140. Spuentrup E, et al. MR imaging of thrombi using EP-2104R, a fibrin-specific contrast agent: initial results in patients. Eur Radiol. 2008;18(9):1995–2005.
141. Vymazal J, et al. Thrombus imaging with fibrin-specific gadolinium-based MR contrast agent EP-2104R: results of a phase II clinical study of feasibility. Investig Radiol. 2009;44(11):697–704.
142. Andia ME, et al. Fibrin-targeted magnetic resonance imaging allows in vivo quantification of thrombus fibrin content and identifies thrombi amenable for thrombolysis. Arterioscler Thromb Vasc Biol. 2014;34(6):1193–8.
143. Roessl E, Proksa R. K-edge imaging in x-ray computed tomography using multi-bin photon counting detectors. Phys Med Biol. 2007;52(15):4679–96.
144. Cormode DP, et al. Atherosclerotic plaque composition: analysis with multicolor CT and targeted gold nanoparticles. Radiology. 2010;256(3):774–82.
145. Pan D, et al. Multicolor computed tomographic molecular imaging with noncrystalline high-metal-density nanobeacons. Contrast Media Mol Imaging. 2014;9(1):13–25.
146. Zainon R, et al. Spectral CT of carotid atherosclerotic plaque: comparison with histology. Eur Radiol. 2012;22(12):2581–8.
147. Townsend DW. Combined positron emission tomography-computed tomography: the historical perspective. Semin Ultrasound CT MR. 2008;29(4):232–5.
148. Beyer T, et al. A combined PET/CT scanner for clinical oncology. J Nucl Med. 2000;41(8):1369–79.
149. Sean LK, et al. Clinical applications of positron emission tomography (PET) imaging in medicine: oncology. Brain Dis Cardiol Curr Radiopharm. 2009;2(4):224–53.
150. Bailey DL, et al. Positron emission tomography: basic sciences. London: Springer; 2005. p. 1–3.
151. Rudd JH, et al. Imaging atherosclerotic plaque inflammation with [18F]-fluorodeoxyglucose positron emission tomography. Circulation. 2002;105(23):2708–11.
152. Rominger A, et al. 18F-FDG PET/CT identifies patients at risk for future vascular events in an otherwise asymptomatic cohort with neoplastic disease. J Nucl Med. 2009;50(10):1611–20.
153. Rudd JH, et al. Imaging atherosclerotic plaque inflammation by fluorodeoxyglucose with positron emission tomography: ready for prime time? J Am Coll Cardiol. 2010;55(23):2527–35.
154. Stoger JL, et al. Distribution of macrophage polarization markers in human atherosclerosis. Atherosclerosis. 2012;225(2):461–8.
155. Folco EJ, et al. Hypoxia but not inflammation augments glucose uptake in human macrophages: implications for imaging atherosclerosis with 18fluorine-labeled 2-deoxy-D-glucose positron emission tomography. J Am Coll Cardiol. 2011;58(6):603–14.
156. Satomi T, et al. Comparison of contrast agents for atherosclerosis imaging using cultured macrophages: FDG versus ultrasmall superparamagnetic iron oxide. J Nucl Med. 2013;54(6):999–1004.
157. Tavakoli S, et al. Bioenergetic profiles diverge during macrophage polarization: implications for the interpretation of 18F-FDG PET imaging of atherosclerosis. J Nucl Med. 2013;54(9):1661–7.
158. Tahara N, et al. 2-deoxy-2-[18F]fluoro-D-mannose positron emission tomography imaging in atherosclerosis. Nat Med. 2014;20(2):215–9.
159. Dweck MR, et al. 18F-sodium fluoride uptake is a marker of active calcification and disease progression in patients with aortic stenosis. Circ Cardiovasc Imaging. 2014;7(2):371–8.
160. Ripa RS, et al. Feasibility of simultaneous PET/MR of the carotid artery: first clinical experience and comparison to PET/CT. Am J Nucl Med Mol Imaging. 2013;3(4):361–71.
161. Li X, et al. Quantitative assessment of atherosclerotic plaques on (18)F-FDG PET/MRI: comparison with a PET/CT hybrid system. Eur J Nucl Med Mol Imaging. 2016;43(8):1503–12.
162. Rominger A, et al. In vivo imaging of macrophage activity in the coronary arteries using 68Ga-DOTATATE PET/CT: correlation with coronary calcium burden and risk factors. J Nucl Med. 2010;51(2):193–7.

163. Nahrendorf M, et al. Nanoparticle PET-CT imaging of macrophages in inflammatory atherosclerosis. Circulation. 2008;117(3):379–87.
164. Majmudar MD, et al. Polymeric nanoparticle PET/MR imaging allows macrophage detection in atherosclerotic plaques. Circ Res. 2013;112(5):755–61.
165. Fujimura Y, et al. Increased peripheral benzodiazepine receptors in arterial plaque of patients with atherosclerosis: an autoradiographic study with [(3)H]PK 11195. Atherosclerosis. 2008;201(1):108–11.
166. Gaemperli O, et al. Imaging intraplaque inflammation in carotid atherosclerosis with 11C-PK11195 positron emission tomography/computed tomography. Eur Heart J. 2012;33(15):1902–10.
167. Vengrenyuk Y, et al. A hypothesis for vulnerable plaque rupture due to stress-induced debonding around cellular microcalcifications in thin fibrous caps. Proc Natl Acad Sci U S A. 2006;103(40):14678–83.
168. Derlin T, et al. In vivo imaging of mineral deposition in carotid plaque using 18F-sodium fluoride PET/CT: correlation with atherogenic risk factors. J Nucl Med. 2011;52(3):362–8.
169. Czernin J, Satyamurthy N, Schiepers C. Molecular mechanisms of bone 18F-NaF deposition. J Nucl Med. 2010;51(12):1826–9.
170. Blau M, Ganatra R, Bender MA. 18 F-fluoride for bone imaging. Semin Nucl Med. 1972;2(1):31–7.
171. Derlin T, et al. Feasibility of 18F-sodium fluoride PET/CT for imaging of atherosclerotic plaque. J Nucl Med. 2010;51(6):862–5.
172. Dweck MR, et al. Coronary arterial 18F-sodium fluoride uptake: a novel marker of plaque biology. J Am Coll Cardiol. 2012;59(17):1539–48.
173. Martinez-Moller A, et al. Dual cardiac-respiratory gated PET: implementation and results from a feasibility study. Eur J Nucl Med Mol Imaging. 2007;34(9):1447–54.
174. Livieratos L, et al. Respiratory gating of cardiac PET data in list-mode acquisition. Eur J Nucl Med Mol Imaging. 2006;33(5):584–8.
175. Livieratos L, et al. Rigid-body transformation of list-mode projection data for respiratory motion correction in cardiac PET. Phys Med Biol. 2005;50(14):3313–22.
176. Rubeaux M, et al. Motion correction of 18F-NaF PET for imaging coronary atherosclerotic plaques. J Nucl Med. 2016;57(1):54–9.
177. Catana C. Motion correction options in PET/MRI. Semin Nucl Med. 2015;45(3):212–23.
178. Polycarpou I, et al. Impact of respiratory motion correction and spatial resolution on lesion detection in PET: a simulation study based on real MR dynamic data. Phys Med Biol. 2014;59(3):697–713.
179. Furst S, et al. Motion correction strategies for integrated PET/MR. J Nucl Med. 2015;56(2):261–9.
180. Baumgartner CF, et al. High-resolution dynamic MR imaging of the thorax for respiratory motion correction of PET using groupwise manifold alignment. Med Image Anal. 2014;18(7):939–52.
181. Kolbitsch C, et al. A 3D MR-acquisition scheme for nonrigid bulk motion correction in simultaneous PET-MR. Med Phys. 2014;41(8):082304.
182. Henningsson M, et al. Whole-heart coronary MR angiography with 2D self-navigated image reconstruction. Magn Reson Med. 2012;67(2):437–45.
183. Andia ME, et al. Flow-independent 3D whole-heart vessel wall imaging using an interleaved T2-preparation acquisition. Magn Reson Med. 2013;69(1):150–7.
184. Prieto C, et al. Highly efficient respiratory motion compensated free-breathing coronary MRA using golden-step Cartesian acquisition. J Magn Reson Imaging. 2015;41(3):738–46.
185. Cruz G, et al. Highly efficient nonrigid motion-corrected 3D whole-heart coronary vessel wall imaging. Magn Reson Med. 2016.

Chapter 9
Compressed Sensing and Beyond

Tobias Wech and Jürgen Ernst Schneider

Abbreviations

ASL	Arterial spin labelling
BLOSM	Block low-rank sparsity with motion-guidance
CS	Compressed sensing
CSI	Chemical shift imaging
FISTA	Fast iterative shrinkage/thresholding algorithm
MPR	Myocardial perfusion reserve
MRS	Magnetic resonance spectroscopy
PI	Parallel imaging
POCS	Projection onto convex sets
RF	Radio frequency
TPSF	Transform point spread function
TV	Total variation
TWIST	Two step iterative shrinkage/thresholding algorithm

T. Wech (✉)
Department of Diagnostic and Interventional Radiology, University of Würzburg, Würzburg, Germany
e-mail: Wech_T@ukw.de

J.E. Schneider
British Heart Foundation Magnetic Resonance Imaging Unit (BMRU), Division of Cardiovascular Medicine, Wellcome Trust of Human Genetics of Oxford, Oxford, UK
e-mail: Wech_T@ukw.de

C. Constantinides (ed.), *Protocols and Methodologies in Basic Science and Clinical Cardiac MRI*, https://doi.org/10.1007/978-3-319-53001-7_9

Introduction

Magnetic Resonance Imaging (MRI) and Spectroscopy (MRS) have become well-established tools in pre-clinical research to comprehensively phenotype small animal models of human diseases. The need for high spatial and – in the case of cardiac applications – temporal resolution, combined with signal-to-noise ratio (SNR) places high demands on hardware and software implementations. However, the lack of dedicated acceleration techniques limits the application of these versatile techniques, as many investigations are accompanied by rather long acquisition times. This frequently prevents multi-parametric imaging in individual animals, which may in turn, increase the number of animals needed to conduct a comprehensive study.

Therefore, acceleration of the acquisition process itself in both clinical and pre-clinical setting is presently an active research topic. Information theory has been successfully applied to allow for full reconstructions from accelerated data acquisitions violating the Nyquist criterion. The most popular technique in this field is known as Parallel Imaging [PI, [1, 2]], where only the signals of every *R*th *k*-space line (*R*: undersampling factor) are acquired simultaneously with several small radio frequency (RF) coils featuring localized sensitivity (e.g. coil-array). The knowledge of these sensitivity profiles of the individual receiver coils is exploited in post-processing as additional encoding information, allowing the reconstruction of the undersampled datasets. The introduction of PI has resulted in a paradigm shift in clinical cardiac MRI as it shortened the acquisition time for many cardiac sequences to fit within a breath-hold of the patient. Despite these advantages of PI, one major limitation is the image noise enhancement. If the coil geometry is not optimal, a spatially dependent deterioration of the SNR in addition to the inevitable loss due to shortened scan-times will occur. Furthermore, while RF coil arrays (typically up to 32 elements or more) are readily available on clinical MR-systems, pre-clinical (cardiac) MR frequently uses only single transmit-receive coils.

An alternative method, which also enables the reconstruction of undersampled datasets, is known as *Compressed Sensing (CS)* [3] or *Compressive Sampling* [4]. In contrast to PI, however, it does not require a special RF coil setup, and can in principle be applied on any MR system. The basic principle of this technique is to provide additional information on the object to be imaged into a non-linear reconstruction of the undersampled data acquisition. Specifically, the prior knowledge about the compressibility of the majority of medical images in some transform domain is frequently exploited.

The mathematical concept of CS has been introduced in 2006 by Donoho [3] and Candès et al. [4]. One year later, Lustig et al. [5] and Block et al. [6] reported the first application of this very general theory to MRI. Since then, a significant number of studies reported on CS accelerated methods covering almost all special fields of MR. Owing to a frequent high redundancy of the image series in the temporal domain, dynamic acquisitions (including most of those of the heart) in particular have proven to be well suited for this new method. Following the acceleration of cardiac functional imaging in patients [7–9], applications were also developed for

first pass perfusion measurements [10], late gadolinium enhancement [11, 12], or velocity mapping [13]. In almost all of these techniques, CS has been used in combination with PI acceleration to obtain maximum speed-up.

As more and more clinical applications of CS emerged, the new technique also gained interest in the pre-clinical MR community. A number of publications on CS in cardiac MRI reported on accelerating the assessment of left ventricular (LV) functional parameters using cine MRI [14–17]. Li et al. [18] and Chen et al. [19] described CS-based methods for efficient parameter mapping (i.e. T_1, T_2) in mice. Naresh et al. [20] reported on a motion-compensated CS algorithm, which enabled dual-contrast first-pass perfusion MRI in free-breathing mice. Gadolinium-based pre-clinical molecular imaging was accelerated and evaluated by Prieto et al. [21], while Christodoulou et al. [22] proposed a low rank model in conjunction with highly undersampled non-Cartesian trajectories to accelerate various investigations of the heart in rats and mice. Finally, CS was also used to successfully accelerate the spectroscopic imaging of the mouse heart [23].

Imaging Physics Fundamentals

CS represents a general theory for signal processing and is not limited to the particular application in MR. However, since the MR experiment meets the fundamental requirements of CS, the application of CS gained significant interest in clinical and basic science MR imaging over the last decade. The following short summary of the CS theory is adapted to an application in MRI, i.e., the signals to be reconstructed are represent by image space information, which are sampled in the Fourier conjugate of the image space, namely the *k*-space.

According to the classical signal theory, *k*-space has to be sampled at a frequency of at least the Nyquist limit to allow for reconstruction of the image space free of aliasing artefacts. Consequently, a fixed amount of data has to be acquired, to image an object at a given field of view (FOV) and spatial resolution. The Nyquist limit has to be considered a fixed limit, if solely the information gathered through data acquisition is used for image reconstruction.

Conversely, CS describes a theory, which enables full signal reconstructions by exploiting both the sampled data and some "prior knowledge" about the object to be imaged, thereby allowing for a violation of the Nyquist limit and, ultimately, an acceleration of the acquisition process. The prior knowledge is thereby typically given by the sparsity or compressibility of the image in any known transform domain. For example, the image compression technique JPEG-2000 is often considered as a precursor of CS, as it exploits the usually existing sparsity or compressibility of natural digital images in the wavelet domain for efficient data storage [24]. For example, the image data transformed into the wavelet domain contain only few coefficients that are significantly larger than zero and can therefore be efficiently stored in a compressed fashion. Unlike JPEG, where images are fully sampled and subsequently compressed, CS aims to reconstruct an already compressed, and thus accelerated, measurement.

Let ρ be an image (column) vector ρ of length n with elements $\rho_j (j = 1, \ldots, n)$, and Ψ an orthonormal basis represented by an $n \times n$ matrix with column vectors $\Psi_i (i = 1, \ldots, n)$. The transform of ρ into the basis Ψ can then be formulated as

$$\rho = \sum_{i=1}^{n} s_i \Psi_i \quad \text{or} \quad \rho = \Psi s, \tag{9.1}$$

where ρ is fully described by the n coefficients s_i. ρ is S-sparse with respect to Ψ, if only S entries of s_i are different from zero [25, 26]. A somewhat weaker characteristic (which however still can be used to estimate the preconditions of a CS-reconstruction) is the compressibility of a signal: If the coefficients s_i are sorted according to their absolute value, ρ is compressible in Ψ with rate ω and constant C, if the k-largest coefficient $s_i^{(k)}$ fulfills [27]

$$\left| s_i^{(k)} \right| \leq C \cdot k^{-\omega}. \tag{9.2}$$

A large k means high compressibility, and therefore high potential for CS acceleration. A noisy signal can still be highly compressible, but by definition it cannot be sparse (see Fig. 9.1).

If the signal has already a sparse or compressible representation in the image space, such as in angiography for example, Ψ can be set to the unity matrix **1.** It will be shown later, however, that various typical MR acquisitions allow for a transformation of the data into a domain where the coefficients are compressible.

The second essential requirement for the application of CS is a linear measurement for data acquisition. This means, that discrete coefficients (pixels) are not measured directly in image space, but linear combinations of these. One reason why MRI is most appropriate for CS application is that Fourier sampling represents exactly such a linear measurement. Since only a reduced dataset is acquired when applying CS, it is essential that maximum information is contained in the limited number of sampling points. A metric that classifies such an acquisition is the coherence $\gamma(M, \Psi)$ between the orthonormal measuring domain M and the domain Ψ where the signal/image has a sparse or compressible representation [26, 27]. Let M again be an $n \times n$ matrix with column vectors $M_k (k = 1, \ldots n)$ and $\langle \cdot, \cdot \rangle$ the inner product of two vectors, then

$$\gamma\left(\mathrm{M}, \Psi\right) = \sqrt{n} \cdot \max_{1 \leq k, i \leq n} \left| \langle \boldsymbol{M}_k, \boldsymbol{\psi}_i \rangle \right|, \tag{9.3}$$

describes the highest correlation of two elements of M and Ψ. Values range from $\left[1, \sqrt{n}\right]$, while a low γ is beneficial for a successful application of CS. The smaller the coherence γ, the higher the spread of the sparse image in the measurement domain M, which leads to a high probability that even an undersampled acquisition contains sufficient information for a full reconstruction. The Fourier transform pair in classical MRI consisting of k- and image-space fortunately exhibits $\gamma = 1$.

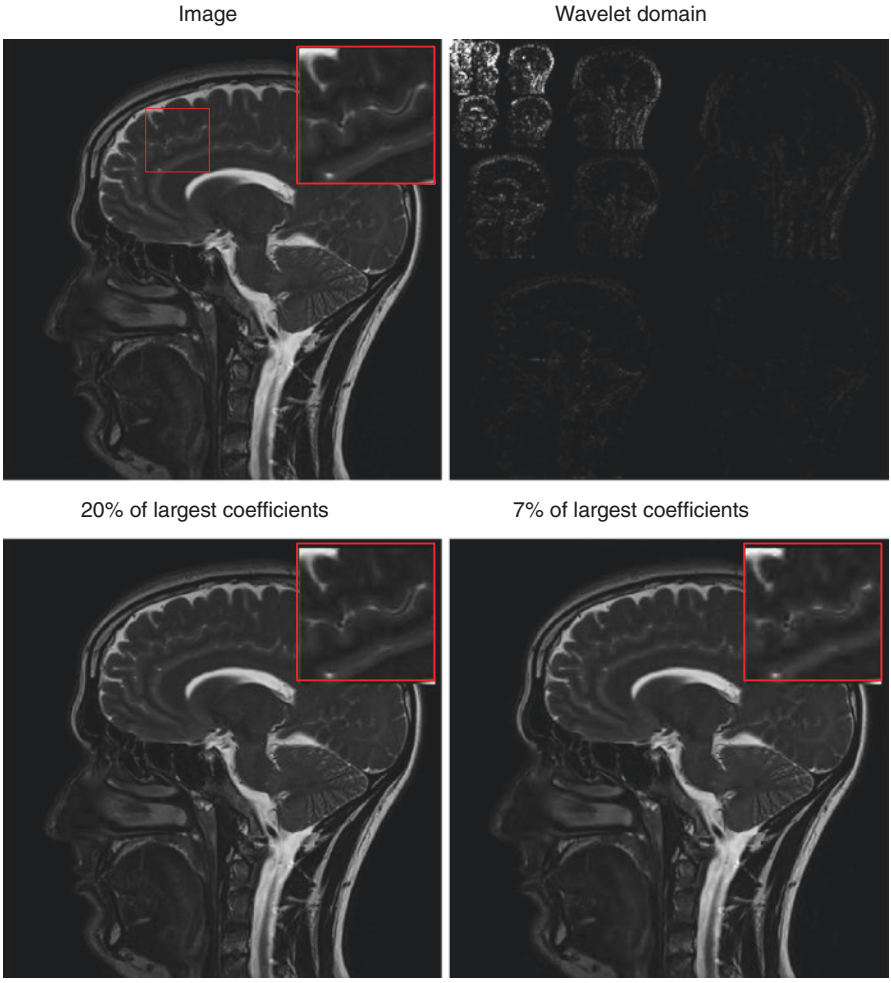

Fig. 9.1 MR image of a human head (*top left*) and its representation in the Wavelet domain (Daubechies-Wavelets, *top right*). The bottom images were created by keeping only 20 and 7% of the largest Wavelet-coefficients, setting all other coefficients to zero and transforming back into image space. While the image on the left still features an image quality comparable to the image using all coefficients, the image on the right already lacks some finer structures of the brain (see zoomed region)

The measurement process can be written

$$y = P^T \rho, \tag{9.4}$$

where the discrete partial Fourier operator P^T represents a $n \times m$ matrix ($m < n$) and determines an undersampled k-space dataset y of length m with elements y_l ($l = 1, \ldots, m$). Equation 9.4 represents an underdetermined system of equations,

such that ρ cannot uniquely be determined from y. In its most straightforward version, CS thus introduces an additional constraint to jointly exploit the measurement and the sparsity model in an optimisation-based reconstruction [27]

$$\min_{\hat{\rho}} \left\| \Psi^T \hat{\rho} \right\|_0 \; subject\; to \; y = P^T \hat{\rho}. \tag{9.5}$$

$\|v\|_0$, the so called l_0 norm of a vector v, directly measures the sparsity $S = \|v\|_0 = \#[t : v_t \neq 0]$ as the number of elements v_t in v that are unequal zero, such that $\min_{\hat{\rho}} \left\| \Psi^T \hat{\rho} \right\|_0$ enforces the sparsity of $\Psi^T \hat{\rho}$. The constraint on the right hand side of (9.5) guarantees that $\hat{\rho}$ is in accordance with the measurement.

This approach, however, has two significant disadvantages. Firstly, algorithms used to solve the problem in (9.5) can be associated with extremely long convergence times. Secondly, the l_0 norm is not meaningful for noisy data.

A better choice for enforcing sparsity is the l_1 norm $\|v\|_1 = \sum_{t=1}^{n} |v_t|$. The convex optimisation [3, 4]

$$\min_{\hat{\rho}} \left\| \Psi^T \hat{\rho} \right\|_1 \; \text{subject}\; to \; y = P^T \hat{\rho} \tag{9.6}$$

has a smaller complexity and can therefore be solved more efficiently. In particular, it can be shown that an S-sparse image vector of length n can be reconstructed out of m randomly chosen k-space measurements with a probability close to 1 if

$$m > S \cdot \log n. \tag{9.7}$$

Finally, the data consistency term is also usually relaxed to allow a tolerance of ε for the noisy acquisition [5, 26, 27]:

$$\min_{\hat{\rho}} \left\| \Psi^T \hat{\rho} \right\|_0 \; \text{subject}\; to \quad \left\| y - P^T \hat{\rho} \right\|_2 < \varepsilon. \tag{9.8}$$

The constrained problem in (9.8) is often transformed into an unconstrained Langrangian form to solve it through the use of non-linear optimisation algorithms [5, 27]:

$$\min_{\hat{\rho}} \left\| \Psi^T \hat{\rho} \right\|_1 + \lambda \left\| y - P^T \hat{\rho} \right\|_2^2. \tag{9.9}$$

The regularization parameter λ hereby specifies the trade-off between the sparsity enforcement and data consistency. Expression (9.9) represents probably the most common formulation of a CS reconstruction. However, any complex sparsity model is conceivable, such that (9.9) often has multiple l_1 penalty terms enforcing sparsity in multiple domains. While this promises an even further reduction of the necessary measurements, multiple regularization parameters – highly impacting the result of the reconstruction – also have to be tuned.

A very intuitive algorithm used to solve the optimisation problem is the *iterative soft thresholding* approach [28], which alternates between a thresholding step in the sparse domain to minimize the l1 term and a data consistency operation. This proximal gradient method can be classified as a so-called projection onto convex sets (POCS, [29]. Figure 9.2 illustrates an undersampled acquisition of a head, which is reconstructed by a POCS algorithm exploiting sparsity in the wavelet domain. The iterative process is initialized with the undersampled k-space measurement, while the non-acquired coefficients are highlighted in red (Fig. 9.2a). The first step involves the transform of the signal into the sparse domain Ψ , which in this case is an inverse Fourier transform of the undersampled data (with zero entries, where data have not been acquired) into image space (Fig. 9.2b) followed by the application of a wavelet transform (Fig. 9.2c). As the sampling positions in k-space were chosen randomly, undersampling artefacts appear incoherently or "noise-like" in the wavelet domain. A threshold τ is then applied, setting coefficients with absolute values smaller than τ to zero and reducing the absolute values of the remaining ones by τ (Fig. 9.2d). The resulting signal is then transformed back to k-space and used to fill the red gaps (Fig. 9.2e). This signal is finally used to start the next iteration. The process is repeated until incoherent artefacts are removed and the sparse coefficients remain (convergence – Fig. 9.2f).

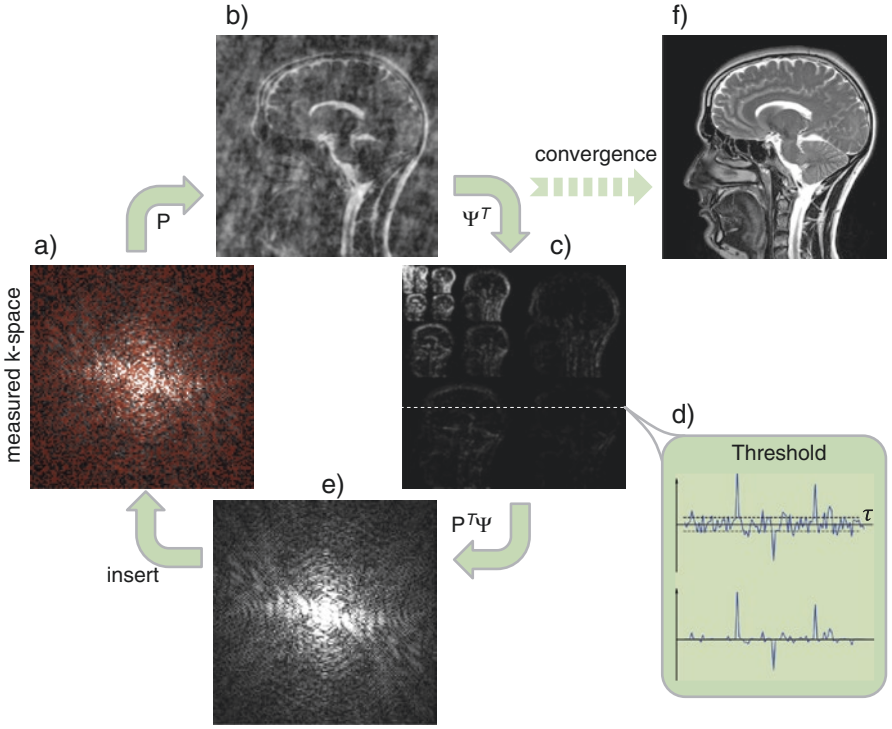

Fig. 9.2 Schematic illustration of a POCS algorithm

An entire collection of solvers has been developed since the theory was introduced, and some popular ones will be presented in section Algorithms.

In summary, the application of CS (in MRI) has three main criteria:

- The image has to be sparse in any known transform domain Ψ
- The sampling pattern of the accelerated acquisition in k-space has to induce incoherent aliasing artefacts in Ψ
- The image has to be reconstructed using a non-linear optimisation algorithm, capable of exploiting both the undersampled measurement and the sparsity model

Methodology

Hardware

Pre-clinical MR-systems typically comprise ultra-high field magnets with magnetic field strengths ≥7 Tesla. The higher magnetic field strengths benefits SNR, which is essential to spatially and temporally resolve the small, fast beating rodent heart (e.g., the murine heart is approximately 1/2000th the size of the human heart, but beats ~10× faster at around 600 beats per minute). A substantial SNR gain is achieved by the use of dedicated RF coils, which, ideally, are optimised in geometry and magnetic properties for cardiac application in mice and rats. Notably, unlike PI, CS does not rely on multiple receiver coils, but can be applied to single RF coil acquisitions. Strong, fast switching gradient systems, allow for short echo and repetition times, which in turn minimize the influence of cardiac and respiratory motion on the MR signal.

Pulse Sequences

The use of ultra-high magnetic field strengths makes the application of steady-state free-precession sequences, which are well established on clinical 1.5 Tesla and 3 Tesla MR systems and highly successful for cardiac diagnostics, very challenging. Thus, most MR sequences on pre-clinical MR systems are based on fast (low-angle), Cartesian gradient echo sequences [30, 31]. Non-Cartesian (i.e., radial and spiral) imaging sequences for cardiac MRI have also been reported [32], but are presently less common.

Sampling Patterns

It was stated in section "Imaging Physics Fundamentals" that the sampled coefficients μ_i in M have to be chosen randomly, i.e., the positions where data are acquired in the undersampled k-space are not deterministic. To heuristically estimate the quality of a sampling pattern for an efficient CS acquisition, Lustig et al. [5] introduced the *transform point spread function* (*TPSF*), which represents the transform

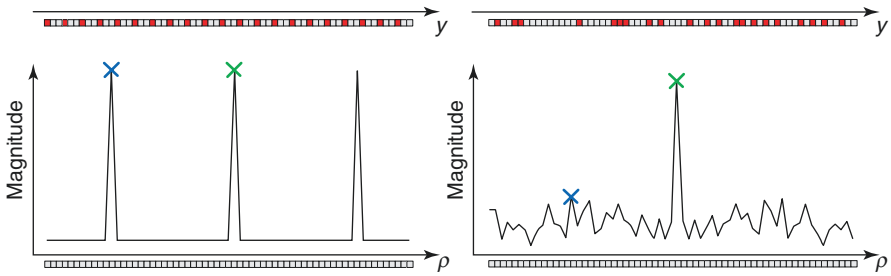

Fig. 9.3 Exemplary transform point spread function (*TPSF*) for regular undersampling (*left*) and a random pattern (*right*). Both k-spaces are undersampled with a factor of $R = 3$. Ψ is set to 1, such that y and ρ are Fourier pairs. The pattern on the *left*, which is perfectly suited for an application of parallel imaging features a TPSF with a sidelobe-to-peak of 1 and is therefore not practicable for an acceleration using compressed sensing. The TPSF on the right has a far lower sidelobe-to-peak ratio of ~0.3, which means undersampling artifacts spread the image space ρ incoherently. This pattern is thus appropriate for an acquisition and subsequent reconstruction using compressed sensing. While this example illustrates the TPSF for a 1D k-space, the TPSF (and ist sidelobe-to-peak ratio) can be determined for higher-dimensional acquisitions accordingly

of the sampling matrix (matrix with value 1, where data were acquired and zero elsewhere) into the sparse domain Ψ. If Ψ, for example, represents the spatial wavelet domain, the sampling pattern is first transformed into image space by applying a discrete inverse Fourier transform, followed by the application of a discrete wavelet transform. The ratio between the second largest absolute entry of the TPSF and the largest one can be used as a measure of the incoherency of the undersampling artefacts. The smaller the sidelobe-to-peak-ratio, the more homogeneous is the artefacts' spread in the sparse domain, which is beneficial for an effective reconstruction using CS (see Fig. 9.3).

In a real MR measurement, a completely randomly chosen set of data points is not practicable. The imaging process for the majority of MR imaging examples comprises a fast encoding (i.e., frequency encoding) and a slow encoding direction (i.e., phase encoding). For a conventional 2D acquisition, consisting of repeated readouts (i.e., frequency encodings) under varying phase encoding steps (e.g., any Cartesian spin echo or gradient echo-based sequence), it is meaningful to only undersample the phase encoding direction, as undersampling the frequency encoding direction does not speed up the acquisition process. It has been shown, that a random choice of phase encoding steps with a higher probability of sampling towards the centre of k-space is superior to a completely random choice of the coefficients [5]. Efficient alternative approaches are (2D) non-Cartesian sequences, i.e. radial projection imaging. It has been previously shown that a radial sampling pattern is appropriate for the application of CS [6], as it undersamples both directions of a 2D k-space, and therefore spreads undersampling artefacts across the entire sparse domain. Furthermore, it inherently incorporates the already mentioned higher sampling rate in the centre of k-space. Following these considerations, the most efficient 2D sampling strategy for CS-accelerated MRI is probably the spiral trajectory. However, it is also technically challenging to apply these waveforms free from deviations, which significantly deteriorate the image quality [33, 34].

An increased freedom for the choice of the sampling patterns is given for 3D acquisitions. In a "Cartesian-like" trajectory, both phase encoding directions can be sampled in arbitrary manner. Most popular approaches are again based on a random sampling with variable density, or the so-called *Poisson-disc* sampling. The latter one guarantees a good trade-off between incoherent aliasing artefacts and small sampling gaps in k-space [35].

Image Processing

Sparsifying Transforms

A wide range of different strategies to efficiently sparsify cardiac MR acquisitions has been proposed. Many of them combine several models, which are jointly enforced within the reconstruction algorithm. As cardiac MRI typically acquires a series of images, which vary only in a small part of the encoded field-of-view (e.g., cardiac motion in cine MRI, breath-hold), the redundancy in the temporal domain of such measurements can be exploited (see Fig. 9.4). A very simple and intuitive strategy is to determine a (spatially) fully sampled temporally averaged image from the series, which can be subtracted from each individual frame, thereby erasing all static parts in the image [14]. The k-space sampling pattern has thus to be varied from frame to frame to cover all frequencies through time. A similar transform is to apply a discrete gradient operator along the temporal (and/or in the spatial) domain of a dynamic image series, also known as total variation [TV, [7, 11, 36–38]].

A further popular approach is the application of a 1D Fourier-transform along the temporal domain of an image series as for example in [10, 39]. This is particularly effective if the Fourier spectrum of the temporal dynamics exhibits only few modes, which are significantly different from zero.

In [9], Otazo et al. describe an alternative method to separate static background from the sparse dynamics in a series of (cardiac) images. As the matrices spanning all dimensions of such a measurement, they are usually low-rank, which means that the so-called nuclear norm of these (or trace norm, i.e., the sum of the singular values of the matrix) can be minimized in a constrained reconstruction. A penalty term is used to enforce the sparsity of the residual between the image series and the low-rank approximation, which is mainly representing motion or signal enhancement due to a contrast agent.

Finally, in many papers [e.g., in [39–41]] the wavelet-sparsification in the image and/or temporal domain is used in addition to previously named transforms to push the gain in image speed even higher.

Algorithms

Each CS reconstruction has to employ a solver for the optimisation problem modelling the acquisition [e.g., Expr. (9.9)]. Fortunately, many authors of CS related papers (e.g., Michael Lustig, PhD or Ricardo Otazo, PhD) have made the source

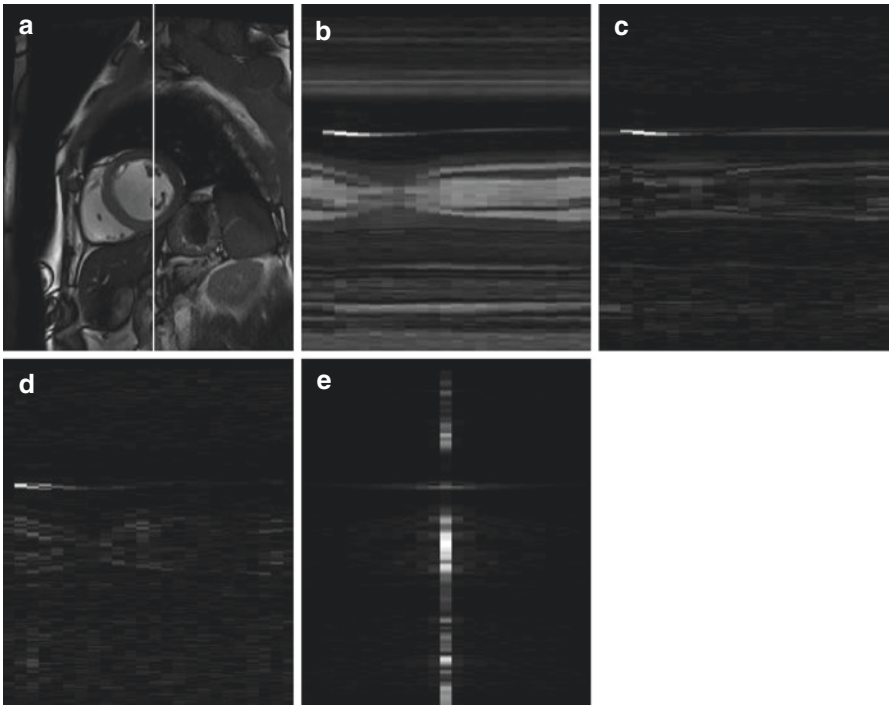

Fig. 9.4 (**a**) Shows one frame of a cardiac cine acquisition in SAX. (**b**) Shows the temporal course for the white line drawn in (**a**). In (**c**) the image series was sparsified by subtracting a temporal average image from each individual frame, while (**d**) shows the result if a temporal total variation (*TV*) operator is applied. In figure (**e**) a Fourier transform was performed along the temporal domain

code of their algorithms publically available (see for example https://people.eecs.berkeley.edu/~mlustig/Software.html or http://cai2r.net/resources/software). This makes access into this field of research easier and avoids the necessity to implement own methods afresh.

Consequently, a substantial part of the so far developed CS accelerated MR techniques employ the l1-penalized non-linear conjugate gradient and backtracking line-search method (or adjusted versions of it) presented in Lustig's seminal paper [5]. It already contains TV and Wavelet sparsification, and thus represents a perfect starting point to develop own methods.

In section "Imaging Physics Fundamentals", straightforward iterative soft thresholding was already presented as an example for a POCS-type CS algorithm. This method is intuitive and easy to implement, and it also provides an uncomplicated access to CS based acceleration. While iterative soft-thresholding is capable of handling also large-scale datasets, it is not very effective with respect to the rates of convergence. Faster POCS-type techniques, are for example, the two-step iterative shrinkage/thresholding algorithm [TwIST, [42]] or the fast iterative shrinkage thresholding algorithm [FISTA, [43]].

Alternatively, greedy algorithms like orthogonal matching pursuit (OMP, [44]) are frequently employed (e.g. in [45, 46]) due to their speed and robustness against noise.

Besides the solvers listed above, an entire range of different optimisation methods for CS has been introduced. Indeed, advancing existing and developing novel and optimised algorithms to solve the minimization problems [Expr. (9.6, 9.8, and 9.9), or equivalent] has become a field in its own right in mathematical research. It is therefore well beyond the scope of this chapter to provide a general classification and comparison of algorithms in terms of performance, robustness to noise, convergence or speed. Please refer to [27, 47–49] or the CS resources webpage of Rice University, Houston, TX (http://dsp.rice.edu/cs) for further reading.

Combination with Parallel Imaging

It is of interest to point out that CS can be combined with PI techniques to achieve higher acceleration factors compared to either method alone. The most straightforward approach represents a modular combination, where the PI reconstruction precedes the CS reconstruction. This has, for example, allowed for real-time imaging of the mouse heart, where undersampling factors >30 achieved a temporal resolution of <12 ms [17]. Conversely, PI and CS reconstruction can be integrated into one joint optimisation framework [35, 50]. In pre-clinical cardiac MRI, Buonincontri et al. employed this to perform functional assessment of the mouse heart within 1 min [16].

Cardiac Applications

CS has facilitated the acceleration of various applications of cardiac MR in small animals, the most prominent of which are given below.

Left Ventricular Function

As mentioned before, multi-frame (cine) MR imaging is particularly suitable for the application of CS due to the high redundancy in the temporal domain. Wech et al. were first to report on the application CS for accelerating LV functional assessment in mice [14]. In this study, the phase encoding direction for each frame of a Cartesian cine sequence was randomly undersampled, using a Gaussian weighting function, followed by the application of the sparsity-promoting difference operator. Fully sampled data sets were subsequently obtained using a modified version of an algorithm by Ma et al. [51].This early work demonstrated that acceleration factors of three were possible without comprising the accuracy of the quantified ventricular volumes and mass. Motaal et al. used CS-accelerated cine-MRI to improve on the temporal resolution at which the cardiac cycle was sampled and to maintain physiologically acceptable scan times [15]. In this case, the stochastic nature of the retrospectively gated cine sequence produced a randomly undersampled *k-t* space and facilitated CS reconstruction using a TV approach. Acceleration factors of 2–3 resulted in scan times of <3 min per slice. Montesinos et al. extended the Split Bregman technique [52] to

retrospectively gate cine-MRI in rat hearts [53]. This approach achieved undersampling factors of up to 15, albeit at a limited temporal resolution (i.e., only 8–16 frames were reconstructed, corresponding to a temporal resolution of ~10–20 ms).

Relaxometry

CS has also been used to accelerate T_1-relaxation time measurements, which are very time-consuming due to the long waiting times for the magnetization to return into equilibrium. In this context, CS was combined with dynamic contrast- (i.e., Manganese (Mn^{2+})) enhanced MRI (DCE-MRI). Manganese Enhanced MRI (‘*MEMRI’*) allows for the investigation of the myocardial viability and perfusion by probing potentially altered (Ca^{2+}) homeostasis. It has been shown in myocardium that the relaxation rate ($R_1 = 1/T_1$) correlated linearly with the Mn^{2+} concentration [54]. Li et al. used a saturation recovery Look-Locker sequence to map T1 in the myocardium during the infusion of $MnCl_2$ [55]. The sparsity of the signals in the T_1 recovery direction was exploited to remove the aliasing artefacts associated with undersampling, and a model-based CS method allowed for reconstructing the fully sampled images [18]. In order to evaluate the reconstruction accuracy for various experimental conditions (such as T_1 or SNR dependence, etc.), simulations were performed and validation in phantom studies was carried out. The optimised, two-fold accelerated method was then applied in vivo to longitudinally monitor the change in myocardial T_1 following the administration of $MnCl_2$-with a temporal resolution of <80 s. More recently, the same group used CS to accelerate cardiac T2-measurements in mice. Two different CS reconstructions were compared. Chen found, unlike in the human settings, the non-linear conjugated gradient method to be superior to dictionary-based approach with orthogonal matching pursuit algorithm [19]. Single-slice T_2-maps of the mouse heart could be acquired within 1 min, which allowed for investigation of myocardial T_2-changes during $MnCl_2$ infusion.

Perfusion

Arterial Spin Labelling (ASL) based methods were applied first to assess myocardial blood flow in mouse hearts [56, 57]. First-pass perfusion techniques, which are clinically well established, are technically much more challenging in mice due to the miniature size of the heart and the high heart rates. Early first-pass perfusion studies used a segmented gradient echo sequence, acquired over three heart beats. Conversely, CS can help in this context to reduce the acquisition time for each frame to fit within the diastolic phase of the murine cardiac cycle (~45 ms) as demonstrated by Naresh et al. [20]. Two slices per RR-interval were acquired with undersampling factors 6 and 4 to estimate the arterial input and the tissue function respectively. The motion-compensated compressed-sensing technique Block LOw-rank Sparsity with Motion-guidance [BLOSM, [58]], which is based on the concept of spatiotemporal low rank sparsity, was used to reconstruct the images. BLOSM

divides the image into regions (i.e., blocks), which are motion-tracked within an iterative algorithm, and to which regional low-rank sparsity is applied. The short scan protocol allowed for first-pass imaging at either rest or stress with a vaso dilating reagent, and enabled the assessment of myocardial perfusion reserve (MPR).

MR Spectroscopic Imaging (MRSI)

Spectroscopic or chemical shift imaging (CSI) requires an additional dimension to obtain metabolic information. In a conventional CSI, the frequency information of the metabolites is acquired in the fastest encoding direction of the experiment (i.e., in each acquisition), while the experiment has to be repeated with different phase-encoding gradient values/directions to provide the spatial information. Thus, a three-dimensional CSI experiment requires $N_x \times N_y \times N_z$ acquisitions, with N_i being the number of phase encoding steps in x, y and z, respectively. Even low acceleration factors can therefore result in significant time saving. A significantly reduced sensitivity of a CSI compared to an imaging experiment as a result of several orders of magnitudes lower metabolite concentrations (typically in the millimolar range compared to ~70 M for water protons used for imaging) and intrinsically low MR sensitivity of non-proton nuclei, typically precludes the application of PI techniques. CS may represent a way forward due to the added benefit of denoising [5]. The first applications of CS in metabolic imaging have been reported in oncology, where it was used to provide resolution enhancement of hyperpolarized 13C-MRSI experiments in prostate [59] and liver cancer [60]. In this context, CS allowed improvement of the spatial resolution of the short-lived hyperpolarized ^{13}C-nuclei. Maguire et al. reported a CS-accelerated ^{23}Na-MRSI in mouse hearts in vivo [23]. This study demonstrated that high-resolution, threefold accelerated ^{23}Na-MRSI of the murine myocardium could be obtained within a scan time of approximately 23 min. Importantly, this proof-of-concept work is not limited to organ and/or nucleus, and may therefore open new avenues for (pre-) clinical metabolic studies.

Discussion and Future Directions

Limitations

Even though CS is very promising for a more effective application of MRI and MRS in humans and animal models alike, it is still an active field of research. Being model-based, CS-exploiting methods are of a distinct different nature compared to conventional imaging techniques, and consequently, it is relevant to thoroughly evaluate their performance prior to routine application.

Conventional MRI represents in good approximation a linear and stationary or shift-invariant system, which can be comprehensively described using a single point spread function (PSF), or, equivalently, a modulation transfer function (MTF). These

allow for determining significant metrics like, for example, the spatial resolution of an experiment. The application of CS, however, establishes MRI/MRS as a non-linear and non-stationary system, where the determination of a universal PSF/MTF is no longer possible. The image itself highly impacts on the reconstruction performance, which is in radical contrast to the large majority of MR imaging techniques applied so far.

The inevitable qualification of newly developed methods incorporating CS, thus also has to consider the object to be imaged, and cannot be generalized to the imaging system alone [61]. In practice, it is consequently not sufficient to evaluate the spatial/temporal resolution, the SNR, or similar measures just once, e.g. in a phantom study, but individually for each organ (brain, heart, etc.) and even for different views of an organ (e.g., short-axis, long-axis). It can, however, be reasonably assumed that at least these image quality parameters do not drastically vary between several comparable experiments in different animals/patients.

In addition, the performance of CS is highly dependent on the choice of the enforced (sparsity) model. If the data do not completely fit the model, artefacts will remain in the reconstructed image. This especially accounts also for the trajectories assumed for the k-space-acquisition in case of non-Cartesian techniques: small deviations in the k-space coordinates lead to significant blurring or streaking in image space [62]. As data fidelity is enforced iteratively in CS, exact knowledge of the actual k-space trajectory is therefore mandatory to achieve virtually artefact-free, images reconstructions [33, 34, 63].

While multiple sparsity models within an optimisation might potentially increase the achievable acceleration, they also come with additional regularization parameters, which have to be tuned towards a meaningful weight for each individual term/model. Empirically, the adjustment of these regularization parameters has significant impact on the final reconstruction result and has thus to be chosen to optimize the image quality parameters named above. Notably, with any additional regularization parameter, this optimisation significantly grows in complexity.

Future Directions

The term CS is typically used for undersampled measurements reconstructed by exploiting the sparsity of the signal in some known transform domain. The entire field of model-based imaging might be superordinate to CS, however, the majority of "non-CS" techniques enforcing some model in the reconstruction process could be reformulated to fit into the scheme employing a sparsity term [e.g., [64]]. With the introduction of MR-fingerprinting [65], the idea of model-based imaging was generalized such that even the acquisition does no longer follow traditional k-space-sampling. Furthermore, acquisition parameters (flip-angle, TR, TE etc.) are varied in a pseudo-random fashion for every other readout, and the obtained signal evolution is fitted to an over-complete dictionary of evolutions determined by Bloch simulations. This allows the determination of quantitative maps for multiple parameters (T1, T2, diffusion, etc.) by means of an extremely short acquisition, and has the potential to lead this modality to a new era.

Graphical Summary: Compressed Sensing and Beyond

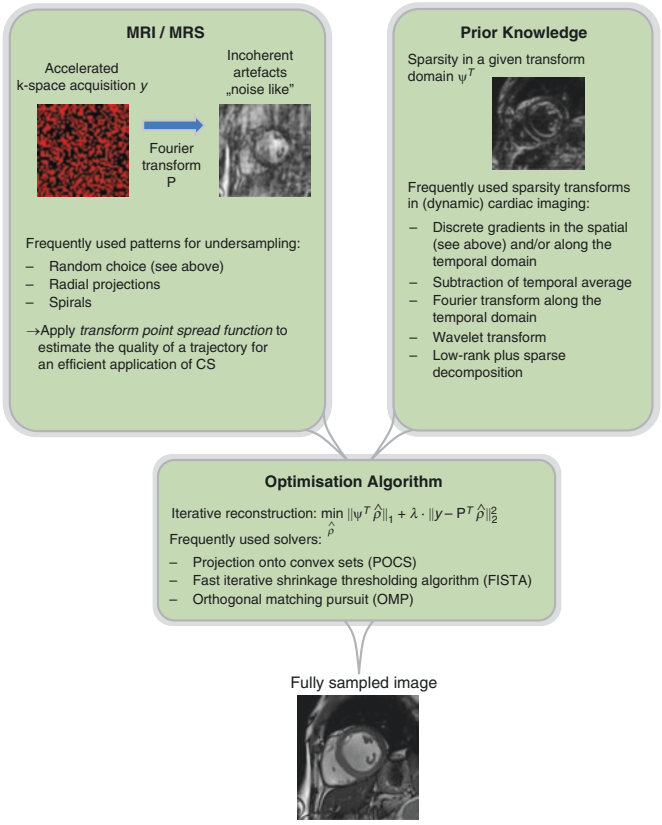

Acknowledgements TW acknowledges funding from the Deutsche Forschungsgemeinschaft (DFG, KO 2938/4-1) and from Siemens Healthcare GmbH. JES is a Senior British Heart Foundation (BHF) Basic Science Research Fellow (FS/11/50/29038), and acknowledges funding from the BHF, the Oxford Centre of Research Excellence, and the Oxbridge Centre of Regenerative Medicine.

References

1. Griswold MA, Jakob PM, Heidemann RM, Nittka M, Jellus V, Wang J, Kiefer B, Haase A. Generalized autocalibrating partially parallel acquisitions (GRAPPA). Magn Reson Med. 2002;47(6):1202–10.
2. Pruessmann KP, Weiger M, Scheidegger MB, Boesiger P. SENSE: sensitivity encoding for fast MRI. Magn Reson Med. 1999;42(5):952–62.
3. Donoho DL. Compressed sensing. IEEE Trans Inf Theory. 2006;52(4):1289–306.
4. Candes EJ, Romberg J, Tao T. Robust uncertainty principles: exact signal reconstruction from highly incomplete frequency information. IEEE Trans Inf Theory. 2006;52(2):489–509.
5. Lustig M, Donoho D, Pauly JM. Sparse MRI: the application of compressed sensing for rapid MR imaging. Magn Reson Med. 2007;58(6):1182–95.
6. Block KT, Uecker M, Frahm J. Undersampled radial MRI with multiple coils. Iterative image reconstruction using a total variation constraint. Magn Reson Med. 2007;57(6):1086–98.
7. Feng L, Srichai MB, Lim RP, Harrison A, King W, Adluru G, Dibella EV, Sodickson DK, Otazo R, Kim D. Highly accelerated real-time cardiac cine MRI using k-t SPARSE-SENSE. Magn Reson Med. 2012;70(1):64–74.
8. Wech T, Gutberlet M, Greiser A, Stab D, Ritter CO, Beer M, Hahn D, Kostler H. High-resolution functional cardiac MR imaging using density-weighted real-time acquisition and a combination of compressed sensing and parallel imaging for image reconstruction. RöFo. 2010;182(8):676–81.
9. Otazo R, Candes E, Sodickson DK. Low-rank plus sparse matrix decomposition for accelerated dynamic MRI with separation of background and dynamic components. Magn Reson Med. 2015;73(3):1125–36.
10. Otazo R, Kim D, Axel L, Sodickson DK. Combination of compressed sensing and parallel imaging for highly accelerated first-pass cardiac perfusion MRI. Magn Reson Med. 2010;64(3):767–76.
11. Adluru G, Chen L, Kim SE, Burgon N, Kholmovski EG, Marrouche NF, Dibella EV. Three-dimensional late gadolinium enhancement imaging of the left atrium with a hybrid radial acquisition and compressed sensing. J Magn Reson Imaging. 2011;34(6):1465–71.
12. Akcakaya M, Rayatzadeh H, Basha TA, Hong SN, Chan RH, Kissinger KV, Hauser TH, Josephson ME, Manning WJ, Nezafat R. Accelerated late gadolinium enhancement cardiac MR imaging with isotropic spatial resolution using compressed sensing: initial experience. Radiology. 2012;264(3):691–9.
13. Hilbert F, Wech T, Hahn D, Kostler H. Accelerated radial Fourier-velocity encoding using compressed sensing. Z Med Phys. 2014;24(3):190–200.
14. Wech T, Lemke A, Medway D, Stork LA, Lygate CA, Neubauer S, Kostler H, Schneider JE. Accelerating cine-MR imaging in mouse hearts using compressed sensing. J Magn Reson Imaging. 2011;34(5):1072–9.
15. Motaal AG, Coolen BF, Abdurrachim D, Castro RM, Prompers JJ, Florack LM, Nicolay K, Strijkers GJ. Accelerated high-frame-rate mouse heart cine-MRI using compressed sensing reconstruction. NMR Biomed. 2013;26(4):451–7.
16. Buonincontri G, Methner C, Krieg T, Carpenter TA, Sawiak SJ. Functional assessment of the mouse heart by MRI with a 1-min acquisition. NMR Biomed. 2014;27(6):733–7.
17. Wech T, Seiberlich N, Schindele A, Grau V, Diffley L, Gyngell ML, Borzì A, Köstler H, Schneider JE. Development of real-time magnetic resonance imaging of mouse hearts at 9.4 Tesla–simulations and first application. IEEE Trans Med Imaging. 2016;35(3):912–20. doi:10.1109/TMI.2015.2501832.
18. Li W, Griswold M, Yu X. Fast cardiac T1 mapping in mice using a model-based compressed sensing method. Magn Reson Med. 2012;68(4):1127–34.
19. Chen Y, Li W, Jiang K, Wang CY, Yu X. Rapid T2 mapping of mouse heart using the carr-purcell-meiboom-gill sequence and compressed sensing reconstruction. J Magn Reson Imaging. 2016;44(2):375–82. doi:10.1002/jmri.25175.

20. Naresh NK, Chen X, Roy RJ, Antkowiak PF, Annex BH, Epstein FH. Accelerated dual-contrast first-pass perfusion MRI of the mouse heart: development and application to diet-induced obese mice. Magn Reson Med. 2015;73(3):1237–45.
21. Prieto C, Andia ME, von Bary C, Onthank DC, Schaeffter T, Botnar RM. Accelerating three-dimensional molecular cardiovascular MR imaging using compressed sensing. J Magn Reson Imaging. 2012;36(6):1362–71.
22. Christodoulou AG, Hitchens TK, Wu YL, Ho C, Liang ZP. Improved subspace estimation for low-rank model-based accelerated cardiac imaging. IEEE Trans Biomed Eng. 2014;61(9):2451–7.
23. Maguire ML, Geethanath S, Lygate CA, Kodibagkar VD, Schneider JE. Compressed sensing to accelerate magnetic resonance spectroscopic imaging: evaluation and application to 23Na-imaging of mouse hearts. J Cardiovasc Magn Reson. 2015;17:45.
24. Taubman DS, Marcellin MW. JPEG2000: image compression fundamentals, standards, and practice. Boston: Kluwer Academic Publishers; 2002.
25. Baraniuk RG. Compressive sensing. IEEE Signal Process Mag. 2007;24(4):118.
26. Candes EJ, Wakin MB. An introduction to compressive sampling. IEEE Signal Process Mag. 2008;25(2):21–30.
27. Eldar YC, Kutyniok G. Compressed sensing: theory and applications. Cambridge, MA: Cambridge University Press; 2012.
28. Daubechies I, Defrise M, De Mol C. An iterative thresholding algorithm for linear inverse problems with a sparsity constraint. Commun Pure Appl Math. 2004;57(11):1413–57.
29. Lustig M, Alley M, Vasanawala S, Donoho DL, Pauly JM. L1 SPIRiT: autocalibrating parallel imaging compressed sensing. In: Proceedings of the 17th annual meeting of ISMRM, Honolulu, 2009. p. 379.
30. Ruff J, Wiesmann F, Hiller KH, Voll S, von Kienlin M, Bauer WR, Rommel E, Neubauer S, Haase A. Magnetic resonance microimaging for noninvasive quantification of myocardial function and mass in the mouse. Magn Reson Med. 1998;40(1):43–8.
31. Schneider JE, Cassidy PJ, Lygate C, Tyler DJ, Wiesmann F, Grieve SM, Hulbert K, Clarke K, Neubauer S. Fast, high-resolution in vivo cine magnetic resonance imaging in normal and failing mouse hearts on a vertical 11.7 T system. J Magn Reson Imaging. 2003;18(6):691–701.
32. Hiba B, Richard N, Thibault H, Janier M. Cardiac and respiratory self-gated cine MRI in the mouse: comparison between radial and rectilinear techniques at 7 T. Magn Reson Med. 2007;58(4):745–53.
33. Campbell-Washburn AE, Xue H, Lederman RJ, Faranesh AZ, Hansen MS. Real-time distortion correction of spiral and echo planar images using the gradient system impulse response function. Magn Reson Med. 2016;75(6):2278–85.
34. Vannesjo SJ, Graedel NN, Kasper L, Gross S, Busch J, Haeberlin M, Barmet C, Pruessmann KP. Image reconstruction using a gradient impulse response model for trajectory prediction. Magn Reson Med. 2016;76(1):45–58.
35. Lustig M, Pauly JM. SPIRiT: iterative self-consistent parallel imaging reconstruction from arbitrary k-space. Magn Reson Med. 2010;64(2):457–71.
36. Caballero J, Price AN, Rueckert D, Hajnal JV. Dictionary learning and time sparsity for dynamic MR data reconstruction. IEEE Trans Med Imaging. 2014;33(4):979–94.
37. Chen C, Li Y, Axel L, Huang J. Real time dynamic MRI by exploiting spatial and temporal sparsity. Magn Reson Imaging. 2016;34(4):473–82.
38. Wang H, Bangerter NK, Park DJ, Adluru G, Kholmovski EG, Xu J, DiBella E. Comparison of centric and reverse-centric trajectories for highly accelerated three-dimensional saturation recovery cardiac perfusion imaging. Magn Reson Med. 2015;74(4):1070–6.
39. Lustig M, Santos JM, Donoho D, Pauly J. k-t SPARSE: high frame rate dynamic MRI exploiting spatio temporal sparsity. In: Proceedings of the 14th annual meeting of ISMRM, Seattle, 2006. p. 2420.
40. Akcakaya M, Basha TA, Goddu B, Goepfert LA, Kissinger KV, Tarokh V, Manning WJ, Nezafat R. Low-dimensional-structure self-learning and thresholding: regularization beyond compressed sensing for MRI reconstruction. Magn Reson Med. 2011;66(3):756–67.

41. Qu X, Guo D, Ning B, Hou Y, Lin Y, Cai S, Chen Z. Undersampled MRI reconstruction with patch-based directional wavelets. Magn Reson Imaging. 2012;30(7):964–77.
42. Bioucas-Dias JM, Figueiredo MAT. A new TwIST: two-step iterative shrinkage/thresholding algorithms for image restoration. IEEE Trans Image Process. 2007;16(12):2992–3004.
43. Beck A, Teboulle M. A fast iterative shrinkage-thresholding algorithm for linear inverse problems. Siam J Imaging Sci. 2009;2(1):183–202.
44. Tropp JA, Gilbert AC. Signal recovery from random measurements via orthogonal matching pursuit. IEEE Trans Inf Theory. 2007;53(12):4655–66.
45. Gamper U, Boesiger P, Kozerke S. Compressed sensing in dynamic MRI. Magn Reson Med. 2008;59(2):365–73.
46. Usman M, Prieto C, Odille F, Atkinson D, Schaeffter T, Batchelor PG. A computationally efficient OMP-based compressed sensing reconstruction for dynamic MRI. Phys Med Biol. 2011;56(7):N99–114.
47. Theodoridis S, Kopsinis Y, Slavakis K. Sparsity- aware learning and compressed sensing: an overview. In: Theodoridis S, Chellappa R, editors. Library in signal processing, Vol 1. Academic Press, Elsevier; 2013.
48. Pope G. Compressive sensing – a summary of reconstruction algorithms. Zürich: Eidgenössische Technische Hochschule; 2009.
49. Qaisar S, Bilal RM, Iqbal W, Naureen M, Lee S. Compressive sensing: from theory to applications, a survey. J Commun Netw-S Kor. 2013;15(5):443–56.
50. Weller DS, Polimeni JR, Grady L, Wald LL, Adalsteinsson E, Goyal VK. Combined compressed sensing and parallel mri compared for uniform and random cartesian undersampling of K-space. Acoustics, Speech and Signal Processing (ICASSP), 2011 IEEE International Conference on 2011, p. 553–6.
51. Ma S, Yin W, Zhang Y, Chakraborty A. An efficient algorithm for compressed mr imaging using total variation and wavelets. IEEE Conference on Computer Vision and Pattern Recognition (CVPR) 2008.
52. Goldstein T, Osher S. The split Bregman method for L1- regularized problems. Siam J Imaging Sci. 2009;2(2):323–43.
53. Montesinos P, Abascal JF, Cusso L, Vaquero JJ, Desco M. Application of the compressed sensing technique to self-gated cardiac cine sequences in small animals. Magn Reson Med. 2013;72(2):369–80.
54. Waghorn B, Edwards T, Yang Y, Chuang KH, Yanasak N, Hu TC. Monitoring dynamic alterations in calcium homeostasis by T (1)-weighted and T (1)-mapping cardiac manganese-enhanced MRI in a murine myocardial infarction model. NMR Biomed. 2008;21(10):1102–11.
55. Li W, Griswold M, Yu X. Rapid T1 mapping of mouse myocardium with saturation recovery Look-Locker method. Magn Reson Med. 2010;64(5):1296–303.
56. Kober F, Iltis I, Cozzone PJ, Bernard M. Myocardial blood flow mapping in mice using high-resolution spin labeling magnetic resonance imaging: influence of ketamine/xylazine and isoflurane anesthesia. Magn Reson Med. 2005;53(3):601–6.
57. Streif JU, Nahrendorf M, Hiller KH, Waller C, Wiesmann F, Rommel E, Haase A, Bauer WR. In vivo assessment of absolute perfusion and intracapillary blood volume in the murine myocardium by spin labeling magnetic resonance imaging. Magn Reson Med. 2005;53(3):584–92.
58. Chen X, Salerno M, Yang Y, Epstein FH. Motion-compensated compressed sensing for dynamic contrast-enhanced MRI using regional spatiotemporal sparsity and region tracking: block low-rank sparsity with motion-guidance (BLOSM). Magn Reson Med. 2014;72(4):1028–38.
59. Hu S, Lustig M, Chen AP, Crane J, Kerr A, Kelley DA, Hurd R, Kurhanewicz J, Nelson SJ, Pauly JM, Vigneron DB. Compressed sensing for resolution enhancement of hyperpolarized 13C flyback 3D-MRSI. J Magn Reson. 2008;192(2):258–64.
60. Larson PE, Hu S, Lustig M, Kerr AB, Nelson SJ, Kurhanewicz J, Pauly JM, Vigneron DB. Fast dynamic 3D MR spectroscopic imaging with compressed sensing and multiband excitation pulses for hyperpolarized 13C studies. Magn Reson Med. 2011;65(3):610–9.

61. Wech T, Stab D, Budich JC, Fischer A, Tran-Gia J, Hahn D, Kostler H. Resolution evaluation of MR images reconstructed by iterative thresholding algorithms for compressed sensing. Med Phys. 2012;39(7):4328–38.
62. Peters DC, Derbyshire JA, McVeigh ER. Centering the projection reconstruction trajectory: reducing gradient delay errors. Magn Reson Med. 2003;50(1):1–6.
63. Vannesjo SJ, Haeberlin M, Kasper L, Pavan M, Wilm BJ, Barmet C, Pruessmann KP. Gradient system characterization by impulse response measurements with a dynamic field camera. Magn Reson Med. 2013;69(2):583–93.
64. Tran-Gia J, Stab D, Wech T, Hahn D, Kostler H. Model-based acceleration of parameter mapping (MAP) for saturation prepared radially acquired data. Magn Reson Med. 2013;70(6):1524–34.
65. Ma D, Gulani V, Seiberlich N, Liu K, Sunshine JL, Duerk JL, Griswold MA. Magnetic resonance fingerprinting. Nature. 2013;495(7440):187–92.

Part II
Clinical Cardiac Imaging

Chapter 10
MR Flow and Quantification

Christopher Francois

Abbreviations

ϕ	Phase difference, phase shift
ΔP	Pressure difference
2D	Two-dimensional
3D	Three-dimensional
4D	Four-dimensional, used in reference to three-dimensional, three-directional velocity, sensitive phase contrast magnetic resonance imaging
bSSFP	Balanced steady state free precession
CHD	Congenital heart disease
CMR	Cardiovascular magnetic resonance
m_0	First measurement of flow acquisition
m_1	Second measurement of flow acquisition
MRI	Magnetic resonance imaging
PC	Phase contrast
Q_P	Pulmonary flow
Q_S	Systemic flow
SNR	Signal to noise ratio
TR	Repetition time
V1	Velocity proximal to stenosis
V2	Velocity distal to stenosis
VENC	Velocity encoding
VNR	Velocity to noise ratio

C. Francois, MD, PhD
Department of Radiology, University of Winsonsin Madison, Madison, WI, USA
e-mail: CFrancois@uwhealth.org

C. Constantinides (ed.), *Protocols and Methodologies in Basic Science and Clinical Cardiac MRI*, https://doi.org/10.1007/978-3-319-53001-7_10

Introduction

Blood flow visualization and quantification are essential components of cardiovascular magnetic resonance (CMR) imaging studies. Applications for CMR flow include the assessment of flow velocities and volumes to quantify the severity of valvular regurgitation and stenosis, measurement of pulmonary (Q_P) to systemic (Q_S) circulation shunt ratios, and estimation of pressure gradients. After briefly reviewing the basic imaging physics and fundamentals that are specific to CMR flow imaging, this chapter will review the practical methodology for performing and analyzing CMR flow data. Common cardiac applications and future directions for CMR flow imaging will also be presented.

Imaging Physics: Fundamentals

An understanding of the fundamental imaging physics of imaging flow and motion with CMR is essential. Imaging flow with MRI was first described by P.R. Moran in 1982 [1]. The basic techniques used today for imaging blood flow are very similar to those used over 30 years ago with several improvements by Moran [2] and others [3–9] to improve the accuracy and robustness of the techniques.

In a constant magnetic field, all protons spin with the same phase (Fig. 10.1a). When a gradient is applied to the magnetic field (Fig. 10.1b), however, the position of the protons affects their precession, resulting in spins precessing with different phases, depending upon their location within the magnetic field gradient. When protons move through a magnetic field gradient, they acquire a phase shift relative to the protons in adjacent stationary tissues. The difference in phases between moving and adjacent stationary protons (Phase Contrast, PC) is proportional to the velocity of the moving protons.

To measure blood flow with one-directional flow-sensitive PC CMR, two measurements are acquired for each voxel (Fig. 10.2). The two images are subtracted, to account for the unknown phase of stationary background tissues. The first measurement (m_o) is a flow-compensated acquisition that serves as a reference for the second measurement (m_1) which is motion sensitive, or velocity encoded. Subtraction of the two measurements (m_0–m_1) provides the final PC CMR image. The timing of the two measurements, m_0 and m_1, with respect to the cardiac cycle is synchronized through the electrocardiographic signal.

Bipolar gradients, with a net zero area, provide the flow-encoding in one-directional flow sensitive PC CMR. As a result, moving protons have a residual phase relative to stationary tissues. The residual relative phase in moving protons, which is proportional to their velocity, is then used to quantify velocity. Flow compensation techniques are used to obtain an image with completely refocused spinning protons with the same phase in both stationary and moving tissues.

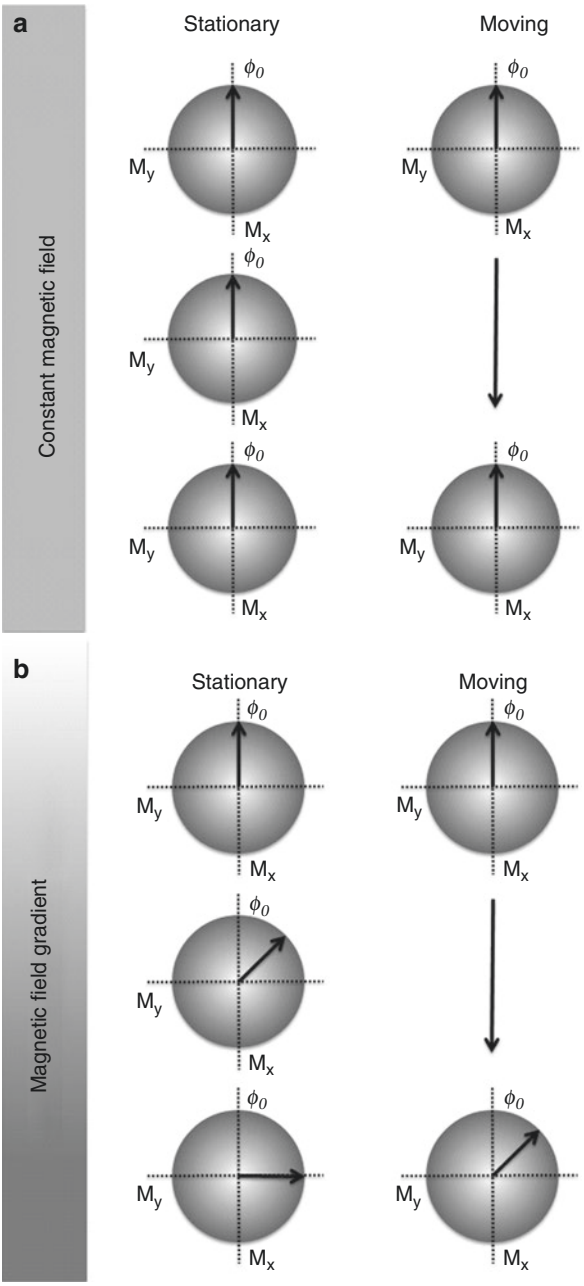

Fig. 10.1 (**a**) Static and moving tissues all have the same phase, Φ, when in constant magnetic field. (**b**) In a magnetic field gradient, static and moving tissues have different phases, Φ, depending upon their location in the field gradient. The difference in phase between the moving spin and the adjacent stationary spin is proportional to the velocity that the spin is moving. *Arrows* indicate the phase, Φ, of the spin vector with respect to the XY-plane

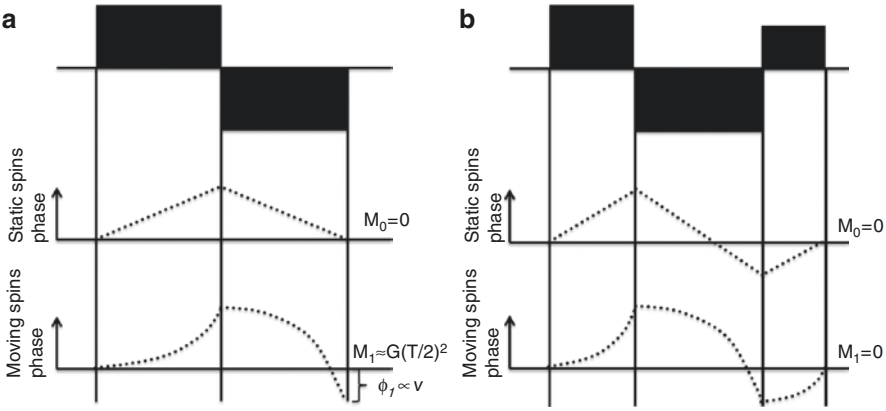

Fig. 10.2 (**a**) Bipolar gradient without flow compensation. The residual phase accumulated after the bipolar gradient by the moving spins is used to calculate the phase difference (Φ). Φ is proportional to the velocity of the moving spins. (**b**) Bipolar gradient with flow compensation. When flow compensation is used, static and moving spins have zero residual phase difference at the end of the bipolar gradient

The measured phase difference (ϕ) is proportional to the velocity of the spins moving through the imaging plane through the following equation:

$$\phi = 2\pi\gamma \mathrm{G}\Delta\delta v \tag{10.1}$$

where γ is the gyromagnetic ratio; G, Δ, and δ are related to the gradient amplitudes and times; and ν is the velocity of the moving spins. The phase shifts (ϕ) are measured in degrees, and range from −180 to +180°. The sign of the phase shift corresponds to the direction of flow relative to the slice, either forward (+) or backward (−). Stationary tissues have phase shifts of 0°, or zero velocity. The maximum velocity that can be resolved without aliasing is determined by the velocity encoding sensitivity (VENC). When velocities are faster than the VENC selected, aliasing occurs because the phase shifts are more than ±180°. At the same time, it is critical to not set the VENC to high values because the velocity-to-noise-ratio (VNR) performance, or dynamic range, is inversely related to the VENC selected. Specifically, the ratio of velocity within the image to the VENC selected determines the VNR through the following equation [10]:

$$\mathrm{VNR} = \left(\pi / 2\right) \times \left(\mathrm{v} / \mathrm{VENC}\right) \times \mathrm{SNR} \tag{10.2}$$

where SNR is the signal to noise rate and ν is the velocity.

In areas with widely variable velocities, variable velocity-encoding [11] or dual velocity-encoding [12] strategies have been used to improve the VNR in areas with slower flow and avoid aliasing in the areas with faster flow velocities. As seen in

Eq. 10.2, the VNR is proportional to the SNR of the acquisition. Therefore, other methods of improving VNR include increasing the field strength from 1.5 to 3.0 T [13] or by performing the acquisition after gadolinium-based contrast agent administration [14].

Methodology

Pulse Sequences and Post-processing

Although one-directional flow-sensitive PC CMR is typically conducted with the direction of flow sensitivity through the plane, flow-encoding can be done in any of the three orthogonal gradient directions (Fig. 10.3). Flow quantification is performed from images with flow-encoding in the slice direction. Flow-encoding in the frequency or phase directions can be used to assess flow features within the plane of the image, such as in patients with intracardiac shunts or valvular heart disease.

Synchronizing image acquisition to the phases of the cardiac cycle is necessary to visualize and quantify changes in flow throughout the heartbeat. This can be done

Fig. 10.3 (**a**) 2D PC CMR with through-plane flow-encoding. In this flow image acquired perpendicular to the ascending aorta (*arrow*), the signal intensity in the ascending and descending aorta is proportional to the flow through the imaging plane. Because the directions of flow in the ascending and descending aorta are opposite to each other, the signal intensities are also opposite (*black* in the ascending aorta, *arrow*, and *white* in the descending aorta, *asterisk*). (**b**) 2D PC CMR with in-plane flow-encoding. In this patient with hypertrophic cardiomyopathy and systolic anterior motion of the anterior mitral valve leaflet, flow-encoding is in the anterior-posterior direction such that the mitral regurgitation jet is directed toward the posterior wall of the left atrium (*arrowheads*) and the signal intensity in the left ventricular outflow tract (*white arrow*) during systole is proportional to the velocity of flow leaving the left ventricle

with either prospective or retrospective gating [15] in which PC CMR imaging is performed over multiple heartbeats. For a given acquisition, a fraction of the lines of k-space for each of the desired number of time-frames is acquired during each heartbeat. The number of heartbeats required to complete a series of time-resolved PC CMR data depends upon the matrix size chosen. Specifically, the number of k-space lines acquired for each image and the number of lines required to fill k-space will affect the length of the acquisition. The main advantage of retrospective cardiac gating is that data is acquired from throughout the cardiac cycle [15]. This is more important when diastolic flow contributes more substantially to the overall flow through the region of interest. However, retrospective gating usually takes longer scan times than prospective cardiac gating.

PC CMR images are typically reconstructed with two sets of co-registered time-resolved images. Standard gradient echo magnitude anatomical images are used to assess the anatomy while the accompanying phase images provide the velocity information. The phase images are most often generated with a grayscale display, corresponding to the range of velocities from −VENC to +VENC. For each flow CMR image from the time-resolved series, the instantaneous flow through the area of interest at that phase of the cardiac cycle is determined from the vectorial sum of the velocities in each voxel multiplied by the area of each voxel in the area of inter-

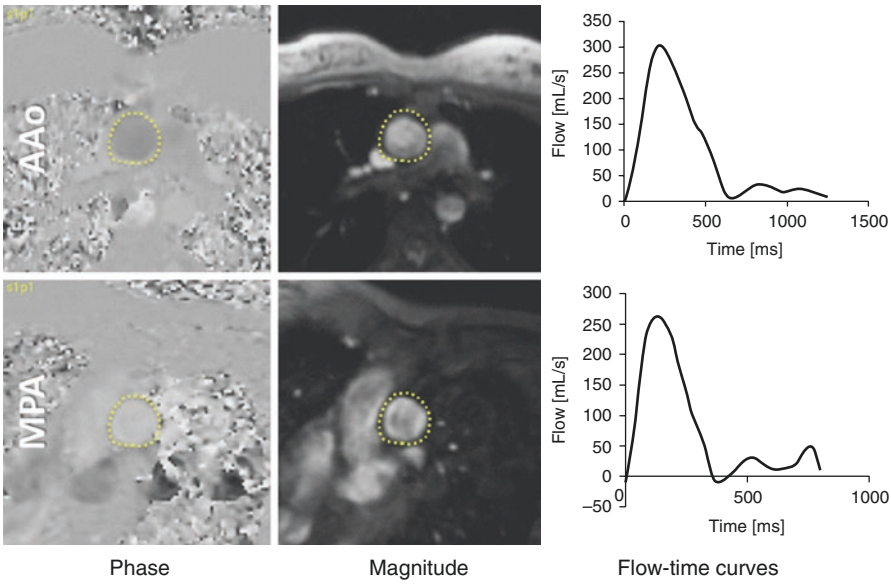

Fig. 10.4 2D, one-directional velocity encoded MRI through the ascending aorta (*AAo*, *top row*) and main pulmonary artery (*MPA*, *bottom row*). The greyscale values on the phase images (*left column*) are proportional to the velocity of blood flow. The magnitude images, middle column, assist with anatomical localization. Flow-time curves (*right column*) are obtained from integration of flow velocities within a region of interest (*dotted curves*) placed over the AAo and MPA

est. The flow throughout the cardiac cycle is then calculated by summing the flows from each of the phases of the cardiac cycle (Fig. 10.4).

As with Doppler ultrasound, errors in velocity measurements are minimized by ensuring that the orientation of the slice is perpendicular to the flow direction. Placing the area of interest in the center of the field of view, as close to the isocenter of the scanner's magnet, ensures maximum homogeneity in the magnetic field and helps minimize background errors. Experiments in phantoms, pre-clinical models and human subjects have shown that flow quantification with 2D PC CMR is both accurate and reproducible [8, 9, 13, 16, 17]. In human subjects, validation of 2D PC CMR measurements can be conducted by comparing the net flow volumes through the aorta and pulmonary artery to the stroke volume from the left ventricle and right ventricle, respectively. Specifically, in patients without valvular regurgitation or shunts, the net flow volumes through the aorta and pulmonary arteries should be the same as the stroke volumes of the left ventricle and right ventricle, respectively (Fig. 10.4). Furthermore, the flow through the aorta and pulmonary artery should be very similar. Clinical studies have revealed that errors in flow measurements are approximately 3–5% and intra- and inter-observer variability of approximately 2–3% [16].

Sources of error in 2D PC CMR images include user-related errors, from incorrect VENC selection (Fig. 10.5) and inappropriate orientation of the slice perpendicular to the direction of flow, and errors related to the MR hardware and sequence [16, 18, 19]. Although a complete discussion of the causes and corrections of the multiple sources of error in flow CMR, a few of the more common types of error will be presented because of their importance when considering potential sources for variability in CMR flow measurements. Imperfections in the MR scanner lead-

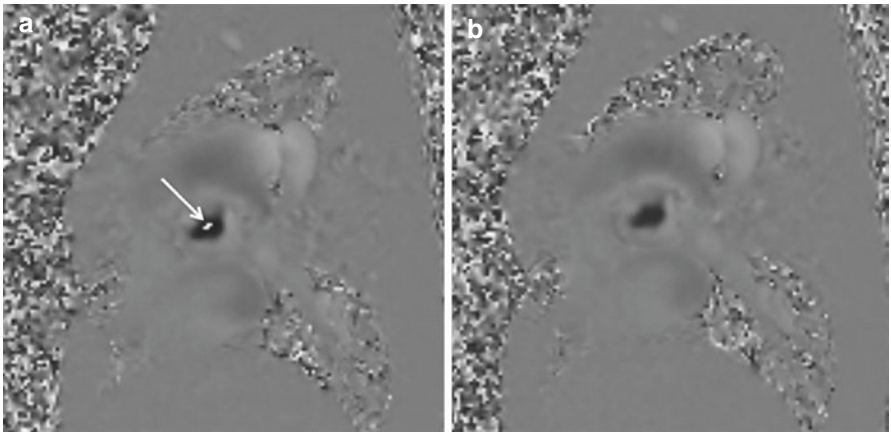

Fig. 10.5 Aliasing is present in the flow image in (**a**) because the velocity encoding chosen (250 cm/s) was lower than the peak velocity in the center of the bicuspid aortic valve (*arrow*). Increasing the velocity encoding to 300 cm/s resolves this issue and aliasing is no longer present in the image in (**b**)

ing to concomitant gradients [20], eddy currents [21] and magnetic field non-linearity contribute to hardware-related errors. Optimizing the sequence parameters and acquisition can correct some of these errors [18, 22]. Additional methods of correcting these 'background errors' include subtracting the measured flow in stationary tissue in proximity to the area of interest from the measured flow through the vessel of interest (Fig. 10.6). A more robust, but time-consuming approach is to repeat the PC CMR scan with the exact same scan parameters with a stationary

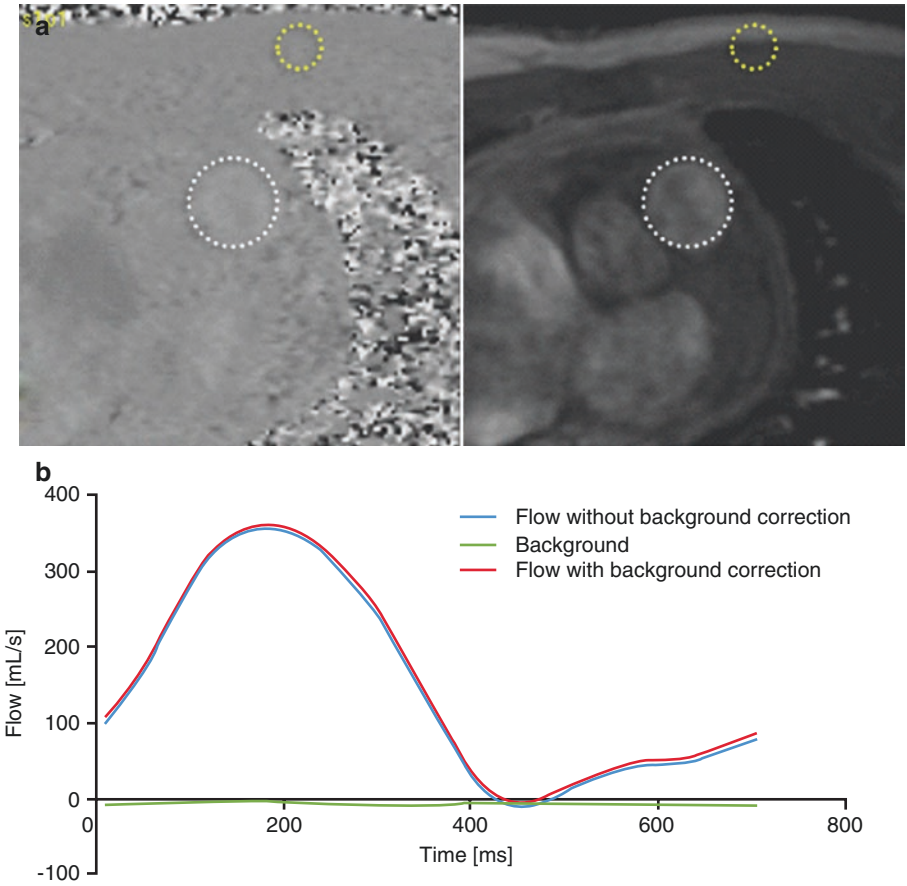

Fig. 10.6 Background correction is often necessary to improve the accuracy of flow measurements. (**a**) A region of interest in stationary soft tissues (*yellow dotted circles*) and then subtracted from the flow through the vessel of interest (*white dotted circles*). (**b**) Although the flow measured in the background is small at each phase in the cardiac cycle as in this case, the background should have zero phase/velocity and it is important to take these errors into account to improve the accuracy of flow MRI measurements

phantom once the patient has completed the exam and has gotten off of the scanner [23, 24].

Cardiac Applications

Clinical applications for PC CMR include (a) measurement of peak velocities and flow volumes in patients with known or suspected valvular heart disease [15, 25], (b) quantification of flow volumes through the thoracic vessels in patients with known or suspected congenital heart disease [26–28], or (c) estimate pressure drops in areas of stenosis [29–31]. Examples of each of these applications will be described in further detail.

Valvular Heart Disease

In patients with valvular heart disease, flow CMR can be used to grade the severity of the stenosis by measuring the peak velocity distal to the stenosis [17] or grade the severity of regurgitation by quantifying the amount of backward flow through an insufficient valve [32, 33]. To minimize errors in velocity and flow measurements, it is critical that the through-plane flow MRI acquisitions be performed orthogonal to the direction of blood flow. For the aorta, the PC CMR acquisition is set up using three-chamber and left ventricular outflow tract views (Fig. 10.7). For the pulmonary artery, the PC CMR acquisition is set up using two orthogonal right ventricular

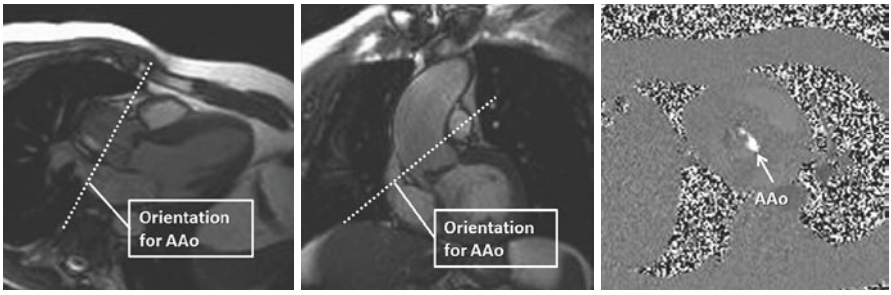

Fig. 10.7 Setting up the ascending aorta (*AAo*) flow CMR acquisition. Three-chamber (*left*) and left ventricular outflow tract (*middle*) images are used to prescribe the orientation of the 2D PC CMR acquisition (*dashed lines*) through the ascending aorta (*right*)

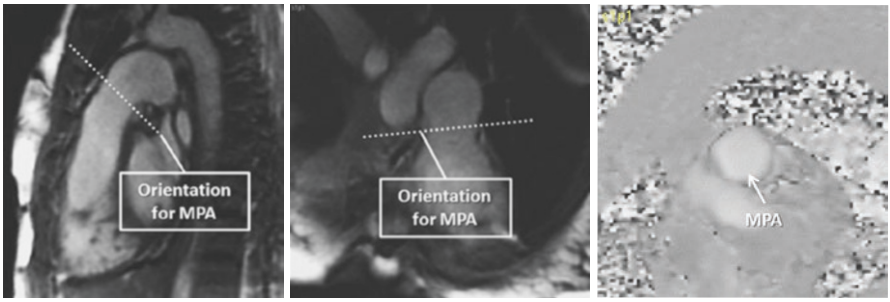

Fig. 10.8 Setting up the main pulmonary artery flow CMR acquisition. Flow through the main pulmonary artery (*MPA*) is set up from a sagittal oblique view (*left*) and an axial oblique view (*middle*) through the right ventricular outflow tract and proximal MPA

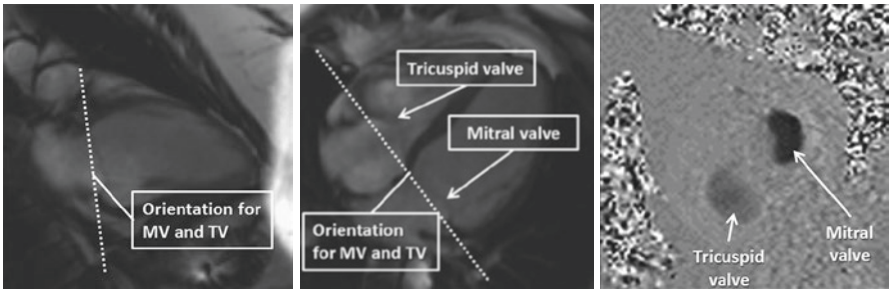

Fig. 10.9 Setting up the mitral valve and tricuspid valve flow CMR acquisition. Flow through the mitral and tricuspid valve planes (*right*) is set up from two chamber (*left*) and four chamber (*middle*) views

outflow tract views (Fig. 10.8). For the mitral and tricuspid valves, the PC CMR acquisition is set up using two long-axis views (Fig. 10.9).

To accurately measure the peak velocities, it can be helpful to first acquire long-axis in-plane PC CMR images through the stenotic valve to identify the location of the peak velocity. A through-plane acquisition is then used to quantify the peak velocity and measure the flow. For example, in patients with aortic stenosis, the in-plane PC CMR acquisition could be performed in either the 3-chamber or left ventricular outflow tract orientation. Alternatively, the corresponding balanced steady-state free precession (bSSFP) images can be used to identify the location of greatest spin dephasing, which would typically correspond to the location of highest velocity. The through-plane PC CMR imaging plane is then perpendicular to the direction of flow through the aortic root, at the level of the maximum flow velocity.

To minimize errors in peak velocity measurement, the orientation of the 2D PC CMR acquisition should be perpendicular to the direction of flow. Determining the severity of aortic and pulmonic valve stenosis includes the peak systolic velocity [34]. For aortic valve stenosis, the following criteria, based on the ACC/AHA 2006 guidelines, are used:

Peak systolic velocity (m/s)	Aortic valve stenosis severity
≤3.0	Mild
3.0–4.0	Moderate
≥4.0	Severe

Similarly, pulmonic valve stenosis is severe when the peak velocity is ≥4.0 m/s [34].

The volume of flow through the valves can be measured from 2D PC CMR images by integrating the area under the flow-time curve. Q_P and Q_S are determined by measuring the flow through the main pulmonary artery and aorta, respectively. In the absence of valvular regurgitation, the Q_P and Q_S values should be within 5% of each other and should be very close to the cardiac output determined using volumetric methods. When Q_P and Q_S are not equal to the volumetric measurements obtained from cine bSSFP images, then valvular regurgitation should be suspected if not already detected on other CMR imaging. Aortic [32] and pulmonary [33] valve regurgitation are fairly straight forward to assess with flow MRI. From the flow-time curve, antegrade and retrograde flows are calculated separately. The severity of the valvular insufficiency can then be expressed by either the volume of regurgitation per heartbeat or as a percentage of the total forward flow. For aortic valve regurgitation (Fig. 10.10a, b), the following criteria, based on the ACC/AHA 2006 guidelines, can be used [34]:

Regurgitant volume (mL/heartbeat)	Regurgitant fraction (%)	Aortic regurgitation severity
≤30	≤30	Mild
30–56	30–59	Moderate
≥60	≥60	Severe

For pulmonary regurgitation (Fig. 10.10c, d), a regurgitant fraction ≥40% has traditionally been considered severe [35]. More recently, Wald, et al. found that the pulmonary regurgitant volume indexed to body surface area was able to more reliably differentiate repaired tetralogy of Fallot patients with moderate and severe right ventricular dilation from pulmonary regurgitation [33].

The atrioventricular (tricuspid and mitral) valves typically move more than 10 mm from the base to the apex of the heart between end-diastole and end-systole. As a result, tricuspid and mitral valve regurgitation is less straight forward to quantify. Rather than measuring the regurgitant volume and fraction direction from 2D PC CMR images through the atrioventricular valves, the severity of tricuspid and

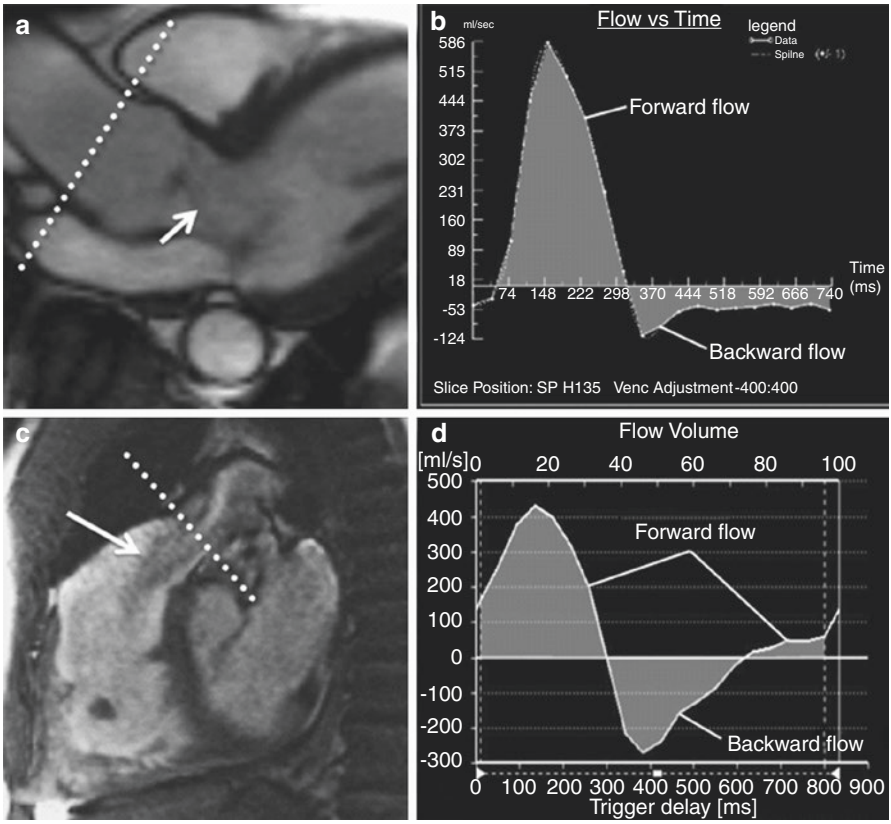

Fig. 10.10 Quantification of aortic (**a**, **b**) and pulmonary (**c**, **d**) valve regurgitation. 2D PC CMR is performed in an orientation (*dotted lines*) that is perpendicular to the proximal ascending aorta (**a**) and main pulmonary artery (**c**). From the flow-time curves (**b**, **d**), the regurgitant fraction is calculated from the ratio of the backward flow to the forward flow

mitral valve regurgitation is determined by comparing Q_P and Q_S to the RV and LV stroke volumes (SV), respectively, determined from cine bSSFP images.

Tricuspid valve regurgitation fraction = (RVSV - Q_P)/RVSV

Mitral valve regurgitation fraction = (LVSV - Q_S)/LVSV

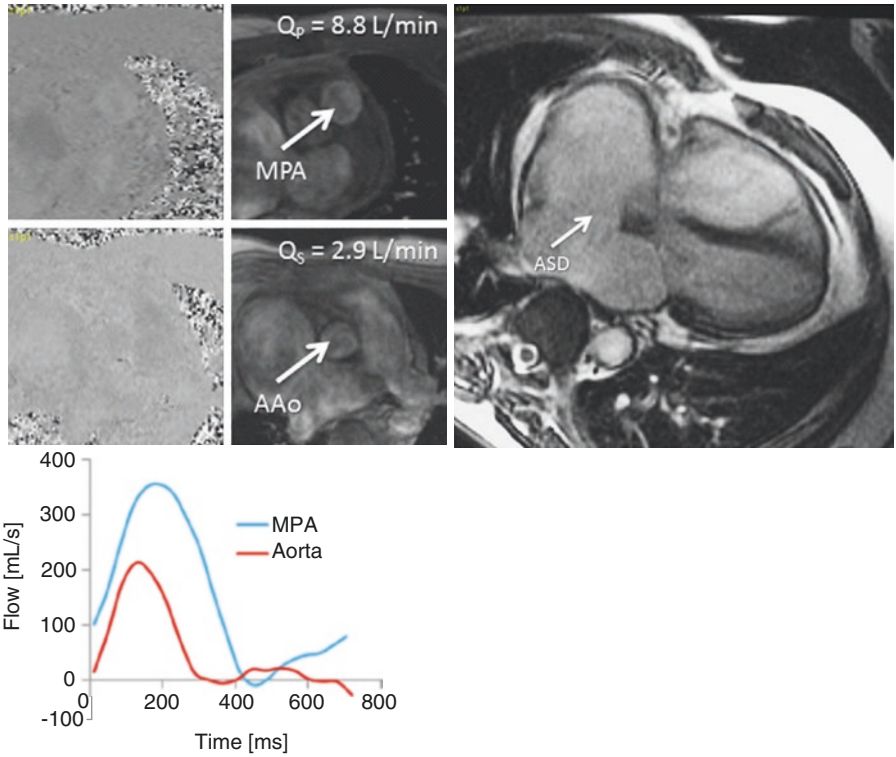

Fig. 10.11 Calculation of QP/QS in a patient with secundum atrial septal defect (*ASD*). The ratio of the flow through the pulmonary circulation (main pulmonary artery, *MPA*, *QP*) to systemic circulation (ascending aorta, *AAo*, *QS*) corresponds to the shunt fraction. In this patient the QP/QS is 8.8/2.9 = 3.03

Congenital Heart Disease

Flow MRI is an essential part of any CMR study performed to evaluate patients with known or suspected congenital heart disease (CHD). Specifically, flow MRI is used to identify signs of intra- or extra-cardiac shunting [36]. The Q_P/Q_S ratio should be within the range of 1.0–1.1 in patients without a shunt. The assessment of Q_P/Q_S in complex congenital heart disease is particularly important because of the difficulty in accurately quantifying Q_P using echocardiography. In adults with atrial septal defects, a Q_P/Q_S greater than 1.5 (Fig. 10.11) is an indication for closure [37]. In adults with ventricular septal defects, a Q_P/Q_S greater than 2.0 is an indication for closure [38]. In-plane flow CMR can be used to subjectively determine the direction of flow through shunts.

Pressure Gradients

The peak velocity distal to a focal stenosis is associated with the pressure difference (ΔP) across the stenosis. The equation commonly used to estimate ΔP is the simpli-

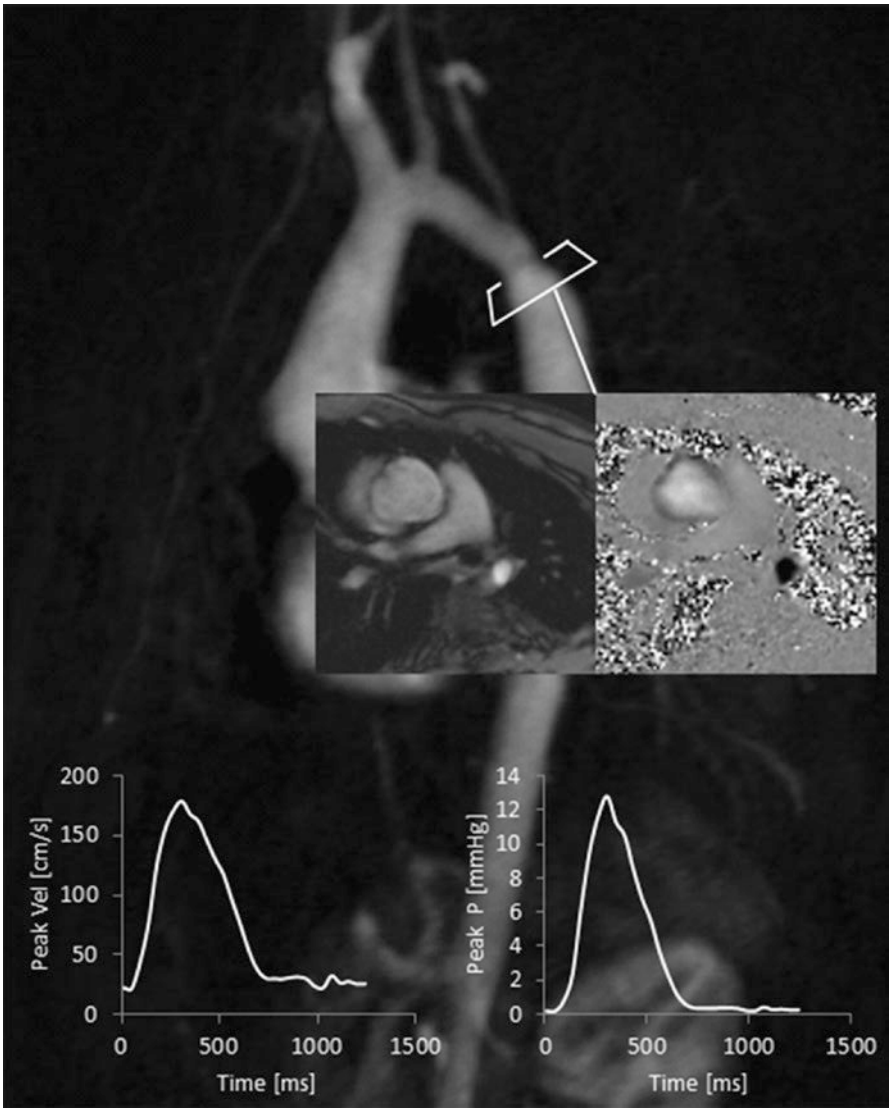

Fig. 10.12 Measurement of peak velocity and estimation of pressure gradient in patient with repaired coarctation. The 2D PC CMR images are obtained just distal to the coarctation, as indicated by in the inset. The peak velocities (*bottom left curve*) can be used to estimate the pressure difference (*bottom right curve*) using the modified Bernoulli equation.

fied Bernoulli equation [29, 39]:

$$\Delta P \approx 4\left(V2 - V1\right)^2 \tag{10.3}$$

where V1 and V2 are the peak velocities proximal and distal to the stenosis, respectively. In general, V1 is much smaller than V2, in which case Eq. 10.3 can be simplified even further:

$$\Delta P \approx 4V^2 \tag{10.4}$$

where V is the peak velocity distal to the stenosis. In CMR, this approach to estimating the pressure gradient can be used to assess the pulmonary artery stenosis or aortic coarctation severity (Fig. 10.12). Several important assumptions are made with the simplified Bernoulli equation (Eq. 10.4) that affect its accuracy. These include the assumptions that (A) blood is nonviscous and incompressible and (B) flow is steady. In patients with milder stenoses, when the velocity distal to the stenosis is not much greater than the velocity proximal to the stenosis, including the peak velocity proximal to the stenosis in the calculation (Eq. 10.3) can improve the accuracy of the estimation.

Discussion and Future Directions

Flow MRI is an integral part of many clinical CMR studies, particularly in patients with valvular and congenital heart disease. 2D PC CMR techniques are well established, having been developed over 30 years ago, but continue to evolve in an effort to improve their accuracy and simplify their acquisition. Given the susceptibility of the flow MRI sequences to user, hardware and sequence related errors, it is critical that CMR practitioners be aware of methods to minimize or mitigate their effects.

Recent developments in flow MRI have focused on extending standard 2D PC CMR techniques to 3D volumetric, three-directional flow sensitive (often referred as '4D flow MRI') PC CMR techniques [40–42] because of their ability to simplify the acquisition of flow data and provide further insights into our understanding of normal and pathological blood flow. As described in the section on 2D PC CMR, flow encoding can be prescribed in any orthogonal direction and the sequence can be set up to be sensitive to flow in one direction or in all three orthogonal directions. Three-directional velocity encoding, when the flow MRI sequence is set up to detect flow in all three orthogonal directions, can be applied to a 2D planar acquisition or extended to a 3D volumetric acquisition.

In patients with complex congenital heart disease, 4D flow MRI can simplify the acquisition when flow measurements are made through numerous vessels and valves of interest. It is not unusual in complex CHD to perform ten or more 2D PC CMR acquisitions, which need to be prescribed a priori by the monitoring physician at the

scanner while the patient is still on the scanner. With 4D flow MRI, one acquisition covering the entire heart is performed and the analysis is performed a posteriori after the conclusion of the study. 4D flow MRI can qualitatively and quantitatively evaluate flow characteristics volumetrically, opening new opportunities to quantify additional hemodynamic parameters non-invasively.

As described in the "Imaging Physics-Fundamentals" section, one-directional velocity-encoding acquisitions require one reference scan (m_0) and one flow-sensitive scan (m_1). In 4D PC CMR imaging, additional flow-sensitive scans are acquired, for each orthogonal direction. In the case of a four-point referenced, 4D flow MRI acquisition, the reference acquisition (m_0) is followed by three flow-sensitive acquisitions (m_{1X}, m_{1Y}, m_{1Z}). As a result, four repetition times (TR's) are required for each line of k-space, rather than two TR's for a single-direction flow MRI sequence. Multiple image acquisition acceleration strategies have been implemented to reduce the scan time for 4D flow MRI to a clinically acceptable amount of time of approximately10–15 min, or less with newer acceleration techniques.

In addition to further shortening the scan times necessary for acquiring the 4D flow MRI data, much effort is currently being placed in developing the necessary software for post-processing these very large datasets. A variety of commercial and investigational software are available for visualization and quantitative analysis. For qualitative assessment of the multiple directional flow features, color-coded streamlines, particle traces, and velocity vectors are used to visualize the direction and complexity of flow through the heart [40, 42–44].

The indications for 4D flow MRI clinically are still being established. Relatively small, single-center studies have confirmed its utility in (A) basic flow quantification [45] , including measuring Q_P/Q_S [46], (B) detection of abnormal flow patterns in CHD [47, 48] and thoracic aortic aneurysms [49–53] , and (C) calculation of advanced hemodynamic parameters [40–42], such as wall shear stress [45, 54, 55], pulse wave velocity [56, 57], kinetic energy [58] and relative pressure. Alterations in intra- and extra-cardiac flow patterns in a wide range of cardiac and vascular diseases are readily identified with 4D flow MRI.

Tabular Summary: MR Flow and Quantification

Parameter	Recommendation(s)	Comments
Field strength	1.5 T or 3.0 T	
In-plane resolution (mm)	1.0–2.0	Optimized to size of patient
		At least 1/10th of the vessel diameter
Slice thickness (mm)	5–8	Optimized to size of patient
Reconstructed phases per cardiac cycle	25–30	
Velocity encoding (cm/s)	200	Artery (increase as necessary to avoid aliasing)
	100	Vein
	150	Atrioventricular valve inflow
Velocity encoding direction	Through-plane	For velocity and flow quantification
		Orthogonal to direction of flow with vessel of interest in center of field of view and iso-center of the magnet
	In-plane	For detection of flow direction
Cardiac gating	Retrospective	Prospective acceptable if retrospective gating is not available
Respiratory motion compensation	Breath-hold	Appropriate for systemic arteries that are not affected by respiration
	Free-breathing, multiple averages	Appropriate for systemic veins and pulmonary arteries that are affected by respiration due to changes in intrathoracic pressures

Recommended parameters for blood velocity and flow quantification with magnetic resonance imaging, adapted from the Society for Cardiovascular Magnetic Resonance guidelines [59, 60]

References

1. Moran PR. A flow velocity zeugmatographic interlace for NMR imaging in humans. Magn Reson Imaging. 1982;1:197–203.
2. Moran PR, Moran RA, Karstaedt N. Verification and evaluation of internal flow and motion. True magnetic resonance imaging by the phase gradient modulation method. Radiology. 1985;154:433–41.
3. Bryant DJ, Payne JA, Firmin DN, Longmore DB. Measurement of flow with NMR imaging using a gradient pulse and phase difference technique. J Comput Assist Tomogr. 1984;8:588–93.
4. Nayler GL, Firmin DN, Longmore DB. Blood flow imaging by cine magnetic resonance. J Comput Assist Tomogr. 1986;10:715–22.
5. Dumoulin CL, Souza SP, Darrow RD, Pelc NJ, Adams WJ, Ash SA. Simultaneous acquisition of phase-contrast angiograms and stationary-tissue images with Hadamard encoding of flow-induced phase shifts. J Magn Reson Imaging. 1991;1:399–404.
6. Pelc NJ, Bernstein MA, Shimakawa A, Glover GH. Encoding strategies for three-direction phase-contrast MR imaging of flow. J Magn Reson Imaging. 1991;1:405–13.
7. Bernstein MA, Shimakawa A, Pelc NJ. Minimizing TE in moment-nulled or flow-encoded two- and three-dimensional gradient-echo imaging. J Magn Reson Imaging. 1992;2:583–8.
8. Pelc LR, Pelc NJ, Rayhill SC, Castro LJ, Glover GH, Herfkens RJ, Miller DC, Jeffrey RB. Arterial and venous blood flow: noninvasive quantitation with MR imaging. Radiology. 1992;185:809–12.
9. Evans AJ, Iwai F, Grist TA, Sostman HD, Hedlund LW, Spritzer CE, Negro-Vilar R, Beam CA, Pelc NJ. Magnetic resonance imaging of blood flow with a phase subtraction technique. In vitro and in vivo validation. Investig Radiol. 1993;28:109–15.
10. Conturo TE, Smith GD. Signal-to-noise in phase angle reconstruction: dynamic range extension using phase reference offsets. Magn Reson Med. 1990;15:420–37.
11. Buonocore MH. Blood flow measurement using variable velocity encoding in the RR interval. Magn Reson Med. 1993;29:790–5.
12. Nett EJ, Johnson KM, Frydrychowicz A, Del Rio AM, Schrauben E, Francois CJ, Wieben O. Four-dimensional phase contrast MRI with accelerated dual velocity encoding. J Magn Reson Imaging. 2012;35:1462–71.
13. Lotz J, Doker R, Noeske R, Schuttert M, Felix R, Galanski M, Gutberlet M, Meyer GP. In vitro validation of phase-contrast flow measurements at 3 T in comparison to 1.5 T: precision, accuracy, and signal-to-noise ratios. J Magn Reson Imaging. 2005;21:604–10.
14. Bock J, Frydrychowicz A, Stalder AF, Bley TA, Burkhardt H, Hennig J, Markl M. 4D phase contrast MRI at 3 T: effect of standard and blood-pool contrast agents on SNR, PC-MRA, and blood flow visualization. Magn Reson Med. 2010;63:330–8.
15. Sondergaard L, Stahlberg F, Thomsen C, Spraggins TA, Gymoese E, Malmgren L, Muller E, Henriksen O. Comparison between retrospective gating and ECG triggering in magnetic resonance velocity mapping. Magn Reson Imaging. 1993;11:533–7.
16. Lotz J, Meier C, Leppert A, Galanski M. Cardiovascular flow measurement with phase-contrast MR imaging: basic facts and implementation. Radiographics. 2002;22:651–71.
17. Kilner PJ, Manzara CC, Mohiaddin RH, Pennell DJ, Sutton MG, Firmin DN, Underwood SR, Longmore DB. Magnetic resonance jet velocity mapping in mitral and aortic valve stenosis. Circulation. 1993;87:1239–48.
18. Rolf MP, Hofman MB, Gatehouse PD, Markenroth-Bloch K, Heymans MW, Ebbers T, Graves MJ, Totman JJ, Werner B, van Rossum AC, Kilner PJ, Heethaar RM. Sequence optimization to reduce velocity offsets in cardiovascular magnetic resonance volume flow quantification – a multi-vendor study. J Cardiovasc Magn Reson. 2011;13:18.
19. Gatehouse PD, Rolf MP, Graves MJ, Hofman MB, Totman J, Werner B, Quest RA, Liu Y, von Spiczak J, Dieringer M, Firmin DN, van Rossum A, Lombardi M, Schwitter J, Schulz-Menger J,

Kilner PJ. Flow measurement by cardiovascular magnetic resonance: a multi-centre multi-vendor study of background phase offset errors that can compromise the accuracy of derived regurgitant or shunt flow measurements. J Cardiovasc Magn Reson. 2010;12:5.
20. Bernstein MA, Zhou XJ, Polzin JA, King KF, Ganin A, Pelc NJ, Glover GH. Concomitant gradient terms in phase contrast MR: analysis and correction. Magn Reson Med. 1998;39:300–8.
21. Ahn CB, Cho ZH. Analysis of eddy currents in nuclear magnetic resonance imaging. Magn Reson Med. 1991;17:149–63.
22. Morgan VL, Price RR, Lorenz CH. Application of linear optimization techniques to MRI phase contrast blood flow measurements. Magn Reson Imaging. 1996;14:1043–51.
23. Chernobelsky A, Shubayev O, Comeau CR, Wolff SD. Baseline correction of phase contrast images improves quantification of blood flow in the great vessels. J Cardiovasc Magn Reson. 2007;9:681–5.
24. Miller TA, Landes AB, Moran AM. Improved accuracy in flow mapping of congenital heart disease using stationary phantom technique. J Cardiovasc Magn Reson. 2009;11:52.
25. Sondergaard L, Hildebrandt P, Lindvig K, Thomsen C, Stahlberg F, Kassis E, Henriksen O. Valve area and cardiac output in aortic stenosis: quantification by magnetic resonance velocity mapping. Am Heart J. 1993;126:1156–64.
26. Hundley WG, Li HF, Lange RA, Pfeifer DP, Meshack BM, Willard JE, Landau C, Willett D, Hillis LD, Peshock RM. Assessment of left-to-right intracardiac shunting by velocity-encoded, phase-difference magnetic resonance imaging. A comparison with oximetric and indicator dilution techniques. Circulation. 1995;91:2955–60.
27. Arheden H, Holmqvist C, Thilen U, Hanseus K, Bjorkhem G, Pahlm O, Laurin S, Stahlberg F. Left-to-right cardiac shunts: comparison of measurements obtained with MR velocity mapping and with radionuclide angiography. Radiology. 1999;211:453–8.
28. Beerbaum P, Korperich H, Barth P, Esdorn H, Gieseke J, Meyer H. Noninvasive quantification of left-to-right shunt in pediatric patients: phase-contrast cine magnetic resonance imaging compared with invasive oximetry. Circulation. 2001;103:2476–82.
29. Oshinski JN, Parks WJ, Markou CP, Bergman HL, Larson BE, Ku DN, Mukundan Jr S, Pettigrew RI. Improved measurement of pressure gradients in aortic coarctation by magnetic resonance imaging. J Am Coll Cardiol. 1996;28:1818–26.
30. Kilner PJ, Firmin DN, Rees RS, Martinez J, Pennell DJ, Mohiaddin RH, Underwood SR, Longmore DB. Valve and great vessel stenosis: assessment with MR jet velocity mapping. Radiology. 1991;178:229–35.
31. Mohiaddin RH, Kilner PJ, Rees S, Longmore DB. Magnetic resonance volume flow and jet velocity mapping in aortic coarctation. J Am Coll Cardiol. 1993;22:1515–21.
32. Sondergaard L, Lindvig K, Hildebrandt P, Thomsen C, Stahlberg F, Joen T, Henriksen O. Quantification of aortic regurgitation by magnetic resonance velocity mapping. Am Heart J. 1993;125:1081–90.
33. Wald RM, Redington AN, Pereira A, Provost YL, Paul NS, Oechslin EN, Silversides CK. Refining the assessment of pulmonary regurgitation in adults after tetralogy of Fallot repair: should we be measuring regurgitant fraction or regurgitant volume? Eur Heart J. 2009;30:356–61.
34. Bonow RO, Carabello BA, Chatterjee K, de Leon Jr AC, Faxon DP, Freed MD, Gaasch WH, Lytle BW, Nishimura RA, O'Gara PT, O'Rourke RA, Otto CM, Shah PM, Shanewise JS. 2008 focused update incorporated into the ACC/AHA 2006 guidelines for the management of patients with valvular heart disease: a report of the American College of Cardiology/American Heart Association Task Force on practice guidelines (writing committee to revise the 1998 guidelines for the management of patients with valvular heart disease): endorsed by the Society of Cardiovascular Anesthesiologists, Society for Cardiovascular Angiography and Interventions, and Society of Thoracic Surgeons. Circulation. 2008;118:e523–661.

35. Rebergen SA, Chin JG, Ottenkamp J, van der Wall EE, de Roos A. Pulmonary regurgitation in the late postoperative follow-up of tetralogy of Fallot. Volumetric quantitation by nuclear magnetic resonance velocity mapping. Circulation. 1993;88:2257–66.
36. Devos DG, Kilner PJ. Calculations of cardiovascular shunts and regurgitation using magnetic resonance ventricular volume and aortic and pulmonary flow measurements. Eur Radiol. 2010;20:410–21.
37. Webb G, Gatzoulis MA. Atrial septal defects in the adult: recent progress and overview. Circulation. 2006;114:1645–53.
38. Warnes CA, Williams RG, Bashore TM, Child JS, Connolly HM, Dearani JA, Del Nido P, Fasules JW, Graham Jr TP, Hijazi ZM, Hunt SA, King ME, Landzberg MJ, Miner PD, Radford MJ, Walsh EP, Webb GD. ACC/AHA 2008 guidelines for the management of adults with congenital heart disease: executive summary: a report of the American College of Cardiology/American Heart Association Task Force on practice guidelines (writing committee to develop guidelines for the management of adults with congenital heart disease). Circulation. 2008;118:2395–451.
39. Sondergaard L, Stahlberg F, Thomsen C, Stensgaard A, Lindvig K, Henriksen O. Accuracy and precision of MR velocity mapping in measurement of stenotic cross-sectional area, flow rate, and pressure gradient. J Magn Reson Imaging. 1993;3:433–7.
40. Markl M, Frydrychowicz A, Kozerke S, Hope M, Wieben O. 4D flow MRI. J Magn Reson Imaging. 2012;36:1015–36.
41. Frydrychowicz A, Francois CJ, Turski PA. Four-dimensional phase contrast magnetic resonance angiography: potential clinical applications. Eur J Radiol. 2011;80:24–35.
42. Hope MD, Sedlic T, Dyverfeldt P. Cardiothoracic magnetic resonance flow imaging. J Thorac Imaging. 2013;28:217.
43. Napel S, Lee DH, Frayne R, Rutt BK. Visualizing three-dimensional flow with simulated streamlines and three-dimensional phase-contrast MR imaging. J Magn Reson Imaging. 1992;2:143–53.
44. Buonocore MH. Visualizing blood flow patterns using streamlines, arrows, and particle paths. Magn Reson Med. 1998;40:210–26.
45. Stalder AF, Russe MF, Frydrychowicz A, Bock J, Hennig J, Markl M. Quantitative 2D and 3D phase contrast MRI: optimized analysis of blood flow and vessel wall parameters. Magn Reson Med. 2008;60:1218–31.
46. Hsiao A, Lustig M, Alley MT, Murphy M, Chan FP, Herfkens RJ, Vasanawala SS. Rapid pediatric cardiac assessment of flow and ventricular volume with compressed sensing parallel imaging volumetric cine phase-contrast MRI. AJR Am J Roentgenol. 2012;198:W250–9.
47. Kilner PJ, Yang GZ, Wilkes AJ, Mohiaddin RH, Firmin DN, Yacoub MH. Asymmetric redirection of flow through the heart. Nature. 2000;404:759–61.
48. Bachler P, Valverde I, Pinochet N, Nordmeyer S, Kuehne T, Crelier G, Tejos C, Irarrazaval P, Beerbaum P, Uribe S. Caval blood flow distribution in patients with Fontan circulation: quantification by using particle traces from 4D flow MR imaging. Radiology. 2013;267:67–75.
49. Markl M, Draney MT, Hope MD, Levin JM, Chan FP, Alley MT, Pelc NJ, Herfkens RJ. Time-resolved 3-dimensional velocity mapping in the thoracic aorta: visualization of 3-directional blood flow patterns in healthy volunteers and patients. J Comput Assist Tomogr. 2004;28:459–68.
50. Hope TA, Markl M, Wigstrom L, Alley MT, Miller DC, Herfkens RJ. Comparison of flow patterns in ascending aortic aneurysms and volunteers using four-dimensional magnetic resonance velocity mapping. J Magn Reson Imaging. 2007;26:1471–9.
51. Bogren HG, Buonocore MH. 4D magnetic resonance velocity mapping of blood flow patterns in the aorta in young vs. elderly normal subjects. J Magn Reson Imaging. 1999;10:861–9.
52. Bogren HG, Buonocore MH. Complex flow patterns in the great vessels: a review. Int J Card Imaging. 1999;15:105–13.
53. Buonocore MH, Bogren HG. Analysis of flow patterns using MRI. Int J Card Imaging. 1999;15:99–103.

54. Frydrychowicz A, Stalder AF, Russe MF, Bock J, Bauer S, Harloff A, Berger A, Langer M, Hennig J, Markl M. Three-dimensional analysis of segmental wall shear stress in the aorta by flow-sensitive four-dimensional-MRI. J Magn Reson Imaging. 2009;30:77–84.
55. Bieging ET, Frydrychowicz A, Wentland A, Landgraf BR, Johnson KM, Wieben O, Francois CJ. In vivo three-dimensional MR wall shear stress estimation in ascending aortic dilatation. J Magn Reson Imaging. 2011;33:589–97.
56. Markl M, Wallis W, Strecker C, Gladstone BP, Vach W, Harloff A. Analysis of pulse wave velocity in the thoracic aorta by flow-sensitive four-dimensional MRI: reproducibility and correlation with characteristics in patients with aortic atherosclerosis. J Magn Reson Imaging. 2012;35:1162–8.
57. Wentland AL, Wieben O, Francois CJ, Boncyk C, Munoz Del Rio A, Johnson KM, Grist TM, Frydrychowicz A. Aortic pulse wave velocity measurements with undersampled 4D flow-sensitive MRI: comparison with 2D and algorithm determination. J Magn Reson Imaging. 2013;37:853–9.
58. Carlsson M, Heiberg E, Toger J, Arheden H. Quantification of left and right ventricular kinetic energy using four-dimensional intracardiac magnetic resonance imaging flow measurements. Am J Physiol Heart Circ Physiol. 2012;302:H893–900.
59. Fratz S, Chung T, Greil GF, Samyn MM, Taylor AM, Valsangiacomo Buechel ER, Yoo SJ, Powell AJ. Guidelines and protocols for cardiovascular magnetic resonance in children and adults with congenital heart disease: SCMR expert consensus group on congenital heart disease. J Cardiovasc Magn Reson. 2013;15:51.
60. Kramer CM, Barkhausen J, Flamm SD, Kim RJ, Nagel E, Society for Cardiovascular Magnetic Resonance Board of Trustees Task Force on Standardized P. Standardized cardiovascular magnetic resonance (CMR) protocols 2013 update. J Cardiovasc Magn Reson. 2013;15:91.

Chapter 11
Myocardial Viability in Ischaemic Heart Disease

Mohammad Alkhalil and Erica Dall'Armellina

Abbreviations

AV	Atrioventricular
bSSFP	Balanced steady state free precession
CAD	Coronary artery disease
CMR	Cardiovascular magnetic resonance
CNR	Contrast to noise ratio
DTI	Diffusion tensor imaging
ECV	Extra cellular volume
EDV	End diastolic volume
EDWT	End-diastolic wall thickness
EF	Ejection fraction
eGFR	Estimated glomerular filtration rate
ESV	End systolic volume
FWHM	Full width half maximum
HLA	Horizontal long axis
IR-FGE	Inversion recovery segmented, fast (or turbo) gradient echo sequence
LAD	Left anterior descending artery
LCx	Left circumflex artery
LDDs CMR	Low dose dobutamine stress cardiac magnetic resonance
LDDs	Low does dobutamine stress
LDDSE	Low dose dobutamine stress echocardiography

M. Alkhalil, MD
RDM Cardiovascular Medicine University of Oxford, John Radcliffe Hospital, Oxford, UK
e-mail: mohammad.alkhalil@cardiov.ox.ac.uk

E. D'Armellina (✉)
Leeds Institute of Cardiovascular and Metabolic Medicine, Division of Biomedical Imaging, University of Leeds, LIGHT Building, Clarendon Way, Leeds LS2 9JT, UK
e-mail: E.DallArmellina@leeds.ac.uk

C. Constantinides (ed.), *Protocols and Methodologies in Basic Science and Clinical Cardiac MRI*, https://doi.org/10.1007/978-3-319-53001-7_11

LGE	Late gadolinium enhancement
LV	Left ventricle
LVOT	Left ventricular outflow tract
MACE	Major adverse cardiovascular events
MVO	Microvascular obstruction
PET	Positron emission tomography
PPCI	Primary percutaneous coronary intervention
PSIR	Phase-sensitive inversion recovery
RCA	Right coronary artery
RF	Radiofrequency
ROI	Region of interest
SA	Short-axis
SCMR	Society for Cardiovascular Magnetic Resonance
SI	Signal intensity
SPECT	Single photon emission computer tomography
STEMI	ST elevation myocardial infarction
T1,	Longitudinal relaxation time
T2 W	T2 weighted
TI	Time to inversion
VLA	Vertical long axis

Introduction

Coronary artery disease (CAD) is the leading cause of mortality and congestive cardiac failure worldwide [1, 2]. Despite the reduction in mortality rates following advances in primary prevention and secondary care over the last three decades [1–3], ischemic left ventricular remodelling and congestive cardiac failure continue to represent a significant economic burden for health care systems [1, 4–6]. Revascularization strategies aiming to treat ischemic injury and improve myocardial viability have been shown to improve patients' prognosis [7]. International guidelines recommend non-invasive assessment of myocardial viability to address invasive treatment, such as coronary percutaneous intervention, or coronary artery bypass [8].

Different non-invasive imaging modalities are available to assess myocardial viability [9–13]. This chapter will focus specifically on cardiac magnetic resonance (CMR). Alternatives include single photon emission computer tomography (SPECT), positron emission tomography (PET), and low-dose dobutamine echocardiography. Each of these techniques depicts viable myocardium by assessing, either the membrane integrity of the myocytes (SPECT) [14], or their metabolism (i.e., the glucose uptake by PET) [15], or the contractility of myocardial fibers (low

dose dobutamine echocardiography) [9, 12] Each of the above ischemic changes occur at different levels and at different stages in the ischemic cascade, and hence the resulting sensitivity in assessing viability varies among techniques. The extent of the lack of contractile reserve assessed by dobutamine stress echocardiography may not be in agreement with the SPECT findings of preserved myocyte cellular integrity. PET has 87% negative predictive value for recovery after revascularisation compared to 83% for DSE and 79% for SPECT [16].

Cardiac magnetic resonance (CMR) is considered as the gold standard for viability assessment since it can overcome the challenges and limitations of the other available non-invasive imaging techniques [17, 18]. It provides an accurate and comprehensive assessment of myocardial viability, and is the gold standard stratification imaging technique to identify CAD patients who are candidates for revascularisation [19].The advantage of using CMR over other techniques is its capability in depicting changes in regional function as well as myocardial perfusion and tissue composition/myocyte loss in one exam and with major spatial resolution [19, 20].

Definition of Myocardial Viability

Death of myocytes following an ischemic insult results in the loss of myocardial viability and LV dysfunction/remodelling [21–23]. By saving the myocardium from the ischemic insult, targeted revascularization therapies confer risk reduction on long-term mortality [24–26]. Recognising the myocardium at risk of severe ischemic injury but not yet dead (i.e. salvageable myocardium), has become of crucial clinical importance to determine the efficacy of infarct size reduction therapies and potentially address therapy [10, 24, 27, 28].

In clinical practice, the standard diagnostic tools available to establish ischemic injury/myocardial infarction at presentation, include ECG, blood enzymes, echocardiography and coronary angiography These provide us with biomarkers with different levels of accuracy and precision (Fig. 11.1) [29]. In most cases, an accurate assessment of viability and stratification of patients requires comprehensive investigations and cannot rely on a single test.

The reduction in myocardial perfusion results in the unfolding of the ischemic cascade from the initial loss of contractile function only, to the changes in metabolic functions, loss of membrane integrity, and cellular death.

Ultimately, the existence of viability should be reflected by the presence of reversible function after restoring perfusion. Despite the fact that contractile impairment being one of the first and easier to assess biomarkers by echocardiography, it can only provide us with partial information. Frequent are the cases of dysfunctional but still viable myocardium, referred to as stunned or hibernating myocardium [31–33]. Stunned myocardium has been defined as myocardium with reversible

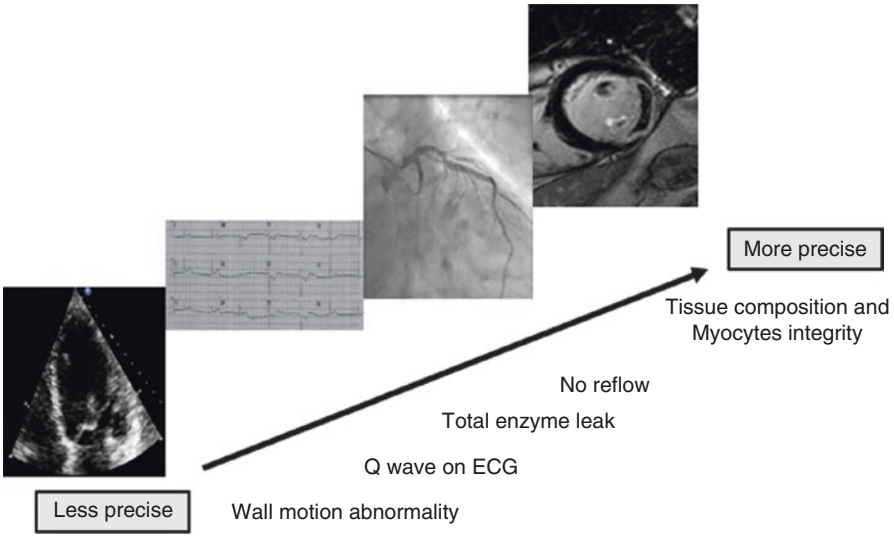

Fig. 11.1 Clinical biomarkers to diagnose ischemic injury at presentation. Following an ischemic insult, Severe 'changes to myocytes' occur. Standard clinical tools provide us with few markers of varying accuracy and precision, such as wall motion by echocardiography, developing Q wave or ST/T wave changes on ECG, patency of epicardial coronary vessel and microcirculation on coronary angiogram, and finally tissue changes detected on CMR [30]

contractile dysfunction in the presence of normal resting myocardial blood flow. Hibernation follows persistent and chronic reduction of perfusion with concomitant dysfunctional myocardium. In such a scenario, revascularization of the epicardial vessels would restore flow and LV function.

ECG and enzymes (such as Troponin) can also partly contribute to patient stratification in that they allow: (a) diagnosis of patients with ST elevation MI in need for urgent treatment and (b) assessment of the severity of damage to myocytes death resulting in the leak of the Troponin into the bloodstream.

Coronary angiography determines the patency of the coronary vessel and allows to indirectly deriving measurements of the patency/function of the microvasculature using pressure wires; however, coronary angiography is much less informative on the status of the myocardial blood perfusion in relation to the tissue composition including presence of oedema, microvascular obstruction or intra myocardial haemorrhage which are accurately detected and quantified using CMR (Fig. 11.1).

CMR is an advanced technique, which offers a comprehensive assessment, and leads to an accurate definition of reversibly versus irreversibly injured myocardium in acute settings or optimal quantification of scarred tissue on chronic stable ischemic coronary artery disease. The assessment of myocardial viability using CMR is mainly achieved through late gadolinium enhancement (LGE) only, or in combination with low-dose dobutamine stress for assessment of contractile reserve. This

chapter will focus mainly on these two CMR techniques with some inherent considerations on other biomarkers, such as wall thickness.

Imaging Physics: Fundamentals and Contrast Agents' Effect

Late Gadolinium Enhancement Techniques

Historically, T2 weighted spin-echo was used in an attempt to identify acute myocardial infarction, more than three decades ago [34–38]. The increase in tissue oedema and water content associated with acute ischemic injury leads to increase in the T2 relaxation time and changes in T2 weighted signal intensity enabling operators to localise and identify infarcted regions [36–38]. However, this change in signal can be subtle and difficult to assess using non-contrast techniques and in subacute or chronic settings.

Late gadolinium enhancement (LGE) techniques allowed overcoming the limitations of non-contrast techniques and achieving better delineation of viable versus non-viable myocardium [39]. LGE is the most commonly used and validated CMR imaging technique to assess myocardial viability, and it is performed using T1 weighted inversion recovery sequences following administration of gadolinium-chelated contrast agents. Gadolinium–chelate contrast agents are intravascular agents that accumulate within infarcted regions within 10–20 min post contrast administration, and do not enter the myocytes with intact membranes. As described below in more detail, these agents have paramagnetic properties, and as such, they modify tissue properties that directly affect T1 and T2 signal intensities on CMR. As a consequence, contrast agents yield a bright signal in the infarcted areas where they accumulate compared to normal myocardium. LGE images are acquired several minutes after injection of gadolinium to give the contrast time to achieve an equilibrium state between normal and infarcted myocardium. A commonly used LGE sequence is the inversion recovery segmented, fast (or turbo) gradient echo sequence (IR-FGE) [40, 41]. Imaging data are acquired during a short 150–200 ms interval at mid-diastole to avoid cardiac motion. The data acquisition is preceded by a non-selective 180° inversion recovery excitation which will invert the magnetization on the z axis for all tissues within the imaged section. The so-called magnetization preparation will allow the reacquisition of a T1 weighted image, and also nulling any other T1 signal from other areas of myocardium, increasing the contrast within the image [39, 42]. By carefully choosing the time delay after inversion, optimal contrast between tissues and data acquisition of the tissues with longer T1 can be achieved when "normal myocardium" T1 relaxation is closer to zero. This time specific is referred to as time to inversion (TI) (Fig. 11.2) [42]. The cardiac triggering parameters are set to acquire image data at every second heartbeat to allow sufficient signal recovery over 2-RR intervals.

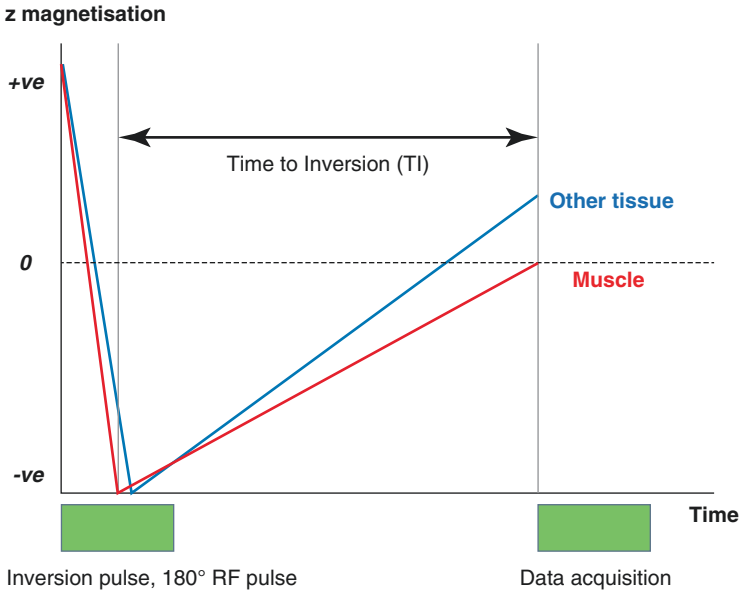

Fig. 11.2 Time to inversion (TI). Following a 180° radiofrequency pulse (inversion pulse), the total z magnetisation from all tissues is inverted, and subsequently starts to recover. Data acquisition will be obtained after a period of time that allows only cardiac muscle's z-magnetisation to reach zero (nulling the signal from the normal myocardium), while other tissues have different recovery rate (shown here to possess faster recovery rate than normal cardiac muscle)

The optimal TI is dependent on numerous factors, including the patient's hemodynamic response, contrast dose, acquisition time, and also operator expertise [40, 42]. Therefore the TI scout is often used to establish the ideal timing to null the myocardium. Subsequently, this time will be incrementally changed during successive image acquisitions. The TI scout could be repeated in order to identify the best TI to null the myocardium. Any small deviations from the optimal TI will potentially result in changes of the signal intensity and reduction in image contrast (myocardium appears grey) [40]. Kellman et al. [40] proposed to use phase-sensitive inversion recovery (PSIR) to restore magnetisation polarity in inversion recovery sequence [43]. This approach alleviated the problem of accurately establishing optimal TI and permitted a longer time range to highlight contrast among different tissue's components.

The third clinically-used sequence used for viability assessment is the free breathing single shot technique [44]. This technique allows multi-slice imaging with a single breath-hold with a degree of accuracy comparable to standard inversion recovery gradient echo sequence [41, 45]. However, the use of the inversion pulse and parameters for prepared T1-weighted as opposed to T2-weighted image (short TR and TE with flip angle of 60°) may potentially and incorrectly classify the oedematous area as infarction. Therefore, it can be argued that using a balance steady state free precession (bSSFP) sequence, the infarct size in acute and sub-

acute settings could be overestimated. Overall, this technique is clinically helpful in cases of reduced compliance, difficulties in breatholding, and arrhythmias.

Low-Dose Dobutamine Imaging

SSFP sequences have successfully been used in dobutamine stress CMR, especially in patients with regional wall motion abnormalities [46]. In the setting of impaired cardiac function, slow-flow artefacts adjacent to the hypokinetic segments may influence the accuracy of image interpretation [46]. This will be ameliorated by employing the SSFP technique since it delineates endocardial borders better and provides high-blood signals and higher contrast to noise ratio (CNR) between the ventricular lumen and myocardium [46, 47]. Other techniques, like real time imaging, have been attempted [48]. Although real time imaging technique overcomes issues with breath-holding and cardiac arrhythmia, its lower spatial and temporal resolution is considered a major drawback [46].

Contrast Agents, MR Physics and Mechanisms of Contrast Enhancement

Contrast agents, such as gadolinium, have been recognised as agents that significantly improve the delineation of infarcted areas [49]. CMR contrast agents work by altering the physical properties of the imaged tissues with subsequent effects on image contrast [42, 50]. This involves mainly shortening the longitudinal relaxation time (T1) of water protons within the same compartment as the contrast agent (Fig. 11.3).

The ability of contrast agents to cause shortening of T1 is referred to as relaxivity, and is related to the concentration of the contrast agent [42]. However, relaxivity does not only cause T1 but also T2 shortening.[42]. Whilst the shortening of T1 produces bright and increased signal within the acquired image, reducing T2 yields the opposite image contrast. Therefore, most sequences are set up to ensure that the image intensity is a strong function of T1 weighted images and the dose of contrast agents is calculated and administered to enhance the delineation between infarcted and normal myocardium. The ability of contrast agents to reduce T1 is secondary to the paramagnetic features within these agents. By definition, paramagnetism occurs when electrons of a metal ion become magnetised for a short period over a short spatial range when exposed to a magnetic field [42, 51, 52]. This will enable energy transfer from precessed hydrogen nuclei of water protons to the unpaired electrons on the outer orbit of the gadolinium ion for example [42, 52]. Since the latter has seven unpaired electrons gadolinium is considered to be of the strongest paramagnetic ions [42]. It is worth noting that the naturally existing gadolinium ion is a toxic element and not safe for use in humans, thus, it has to be chelated to a ligand or a larger molecule to be safe for use in imaging.

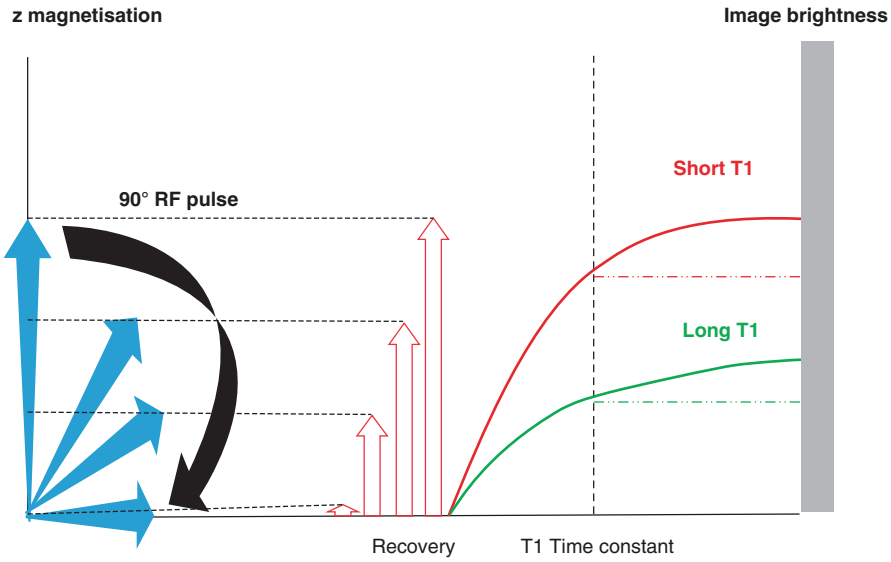

Fig. 11.3 Shortening of longitudinal relaxation time using contrast agents. Following a radiofrequency pulse, the magnetization of protons start tips by 90° leaving virtually no magnetization component on the z-axis. As time elapses, protons magnetization starts to recover creating a larger component of z magnetisation (*green curve* on the *right*). The existence of contrast agent leads to a faster energy transfer between protons and the surrounding tissue and, thus, to a faster recovery. This is demonstrated as the red curve passes with shorter T1 time, and subsequently brighter image intensity

There is a close spatial relationship between gadolinium enhancement and myocardial infarction [27]. This is explained by the difference in kinetics between normal and infarcted myocardium and, secondly, by the change in volume of distribution in acute and chronic myocardial infarction [17, 37, 53–55]. For gadolinium to reach both normal and infarcted myocardium, it requires a patent epicardial artery and microvascular network. The delay in the wash-in and wash-out of gadolinium and the difference in the rate of reaching normal and infarcted myocardium contribute to variations in contrast enhancement after myocardial infarction [17, 37, 53, 56]. In addition, gadolinium is an extracellular agent which has a small volume of distribution (intracellular space occupies nearly two thirds of the normal myocardial volume) [57]. In acute myocardial infarction with subsequent cellular membrane rupture, the distribution volume of gadolinium is increased [54]. On the other hand, viable myocytes with intact cellular membrane will continue to occupy the larger space within the myocardium, leaving gadolinium within the extracellular compartment, including interstitial space. Likewise, in chronic myocardial infarction, the form of scar of collagen fibers occupies larger space than the dense living myocytes [55]. This leads to an enlarged extracellular space as a potential mechanism of gadolinium enhancement [55]. Therefore, gadolinium enhancement has close spatial distribution with both chronic and acute myocardial infarction [58].

Methodology

Late Gadolinium Enhancement

The established method to assess viability requires administration of a contrast agent, such as gadolinium, via a peripheral intravenous line. Prior to imaging, patients are screened to ensure there is no previous allergic reaction to contrast agents. In addition, a renal function status check is mandatory as nephrogenic systemic fibrosis has been associated with impaired renal function and a value of eGFR <30 mL/min [59–61]. Other side effects, such as nausea, should be mentioned before scanning. The contrast media, and the saline used for flushing, should be checked for type, amount, batch number, and expiry date.

The LGE scanning protocol includes the acquisition of long-axis images [such as horizontal (HLA), vertical (VLA) and left ventricular outflow tract (LVOT) long-axis] matching the cine acquisitions and short-axis slices covering the LV (Fig. 11.4).

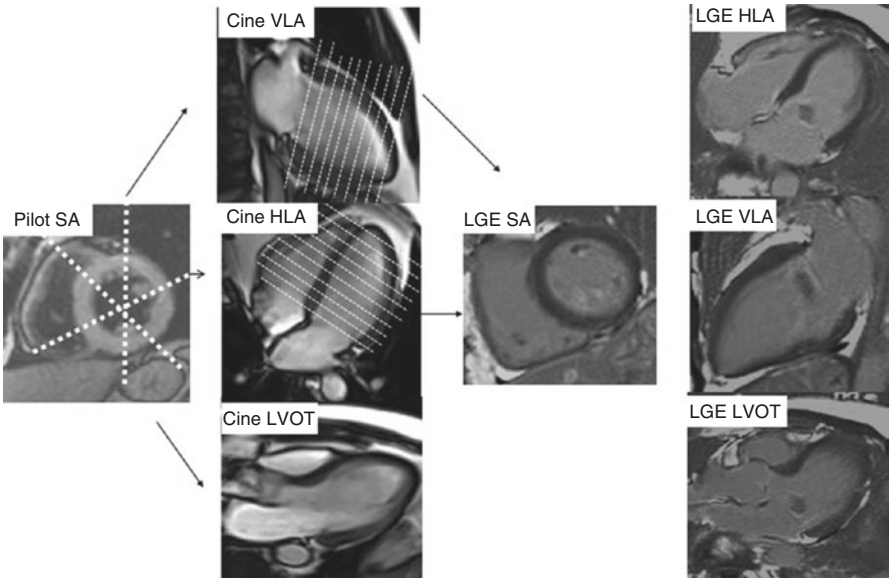

Fig. 11.4 Scanning protocol for LGE acquisition. LGE images are usually acquired at the end of the scan post-administration of gadolinium. Therefore, usually both long and shot-axis images will match the earlier functional acquisitions. In the figure, functional long axis slices are planned on a short-axis pilot image at roughly equiangular sections to derive the horizontal long axis (*HLA*), vertical long axis (*VLA*), and the left ventricular outflow tract (*LVOT*) long axis. Short-axis acquisitions will be acquired perpendicularly to the long-axis in planes parallel to the AV groove. Equidistant short-axis will be acquired to cover the full left ventricle. (*SA* short-axis, *VLA* vertical long-axis, *HLA* horizontal long-axis, *LVOT* left ventricle outflow tract, *LGE* late gadolinium enhancement, *AV* atrioventricular)

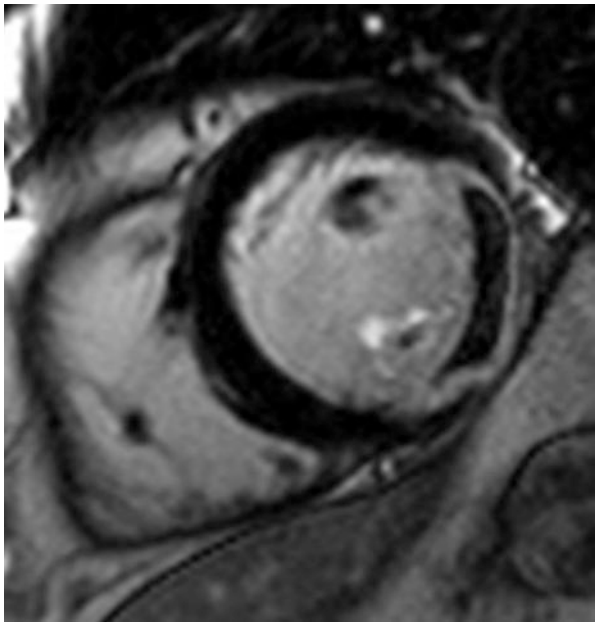

Fig. 11.5 Microvascular obstruction (MVO). MVO as assessed by LGE appears as a dark core in the infarcted myocardium. This figure shows a lateral scar with a large microvascular obstruction (MVO) on patient with lateral ST elevation myocardial infarction and occluded dominant left circumflex coronary artery. Despite successful revascularisation and opening of the occluded vessel, large MVO on the lateral wall is shown on CMR 5 days post procedure

Following intravenous administration of a gadolinium bolus of 0.1–0.2 mmol/kg, delayed-enhanced images are usually acquired with a delay of 10–15 min. Such a delay has been shown to be crucial to obtain reproducible and accurate measurements of infarct size and for avoiding overestimation [62, 63] The size of enhancement is stable if the acquisition is performed in a time frame not earlier than 15 min and up to 30 min [64, 65].

In addition, CMR allows the detection of microvascular obstruction (MVO). Few standard techniques are available to assess MVO: first pass perfusion, early gadolinium acquired after 2–5 min of gadolinium injection or using LGE where it would appear as a hypo-intense area within the enhanced myocardium [66] (Fig. 11.5). LGE technique to detect MVO is probably the most commonly used for clinical purposes. Novel quantitative mapping techniques have recently been validated: these might provide more insight into the mechanistic and pathophysiology of MVO (see further discussion in the paragraphs below).

Low-Dose Dobutamine

Low-dose dobutamine stress CMR requires additional steps to ensure patients' safety. Dobutamine is a synthetic catecholamine that is modified from isoproterenol [67]. It is primarily ß1 agonist and to a lesser extent α1 and β2 agonist [67]. At low doses (<10 mcg/kg/min) it enhances myocardial contractility, and as such, is used for viability assessment [46]. Besides standard MRI screening

questions, contraindications to dobutamine should be established. These contraindications include, severe hypertension (systolic and diastolic blood pressure of more than 220 and 120, respectively), severe cardiac arrhythmias, unstable angina, congestive cardiac failure, severe aortic stenosis, hypertrophic cardiomyopathy, or previous sensitivity to the administered drug [46]. The initial steps include baseline long-axis acquisitions of HLA, VLA, and LVOT, in addition to the short axis slices of left ventricle. Dobutamine will be initially administered at 5 mcg/kg/min and increased up to 10 mcg/kg/min before the acquisition of MRI images. CMR operators can sometimes repeat the image acquisition if patients develop tachycardia after 5 min, but not longer than 10 min, after starting the dobutamine infusion [68]. Potential side effects which require abandonment the procedure are intractable symptoms, cardiac arrhythmia, severe hypertension (>220/120) or drop in blood pressure of more than 40 mmHg during dobutamine infusion.

Image Interpretation and Post Acquisition Processing

Image interpretation and post processing have been defined in standardized protocols by the Society for Cardiovascular Magnetic Resonance (SCMR) Board of Trustees Task Force [69].

Late Gadolinium Enhancement

CMR allows for accurate tissue characterization on both short and longitudinal planes of the left ventricle. Visual assessment is usually informative for clinical diagnosis, and it is based on identification of an area of high signal intensity (bright hyper-enhanced regions) compared to the dark normal myocardium. A typical CAD LGE pattern features sub endocardial enhancement in a coronary territory. The 17-segment model as recommended by The American Heart Association, aids the definition of the location and extent of the scarred myocardium [70], as shown in Fig. 11.6. The segmental hyper enhancement is graded according to the transmurality of high signal intensity across the thickness of the myocardial wall [24]. In the case of acute/subacute myocardial scarring, microvascular obstruction appear to have a dark core within the hyper-enhanced area and should be included as part of the scarred myocardium.

When using quantitative assessment, a signal intensity-based method is used. The signal intensity of a region-of-interest positioned in the remote myocardium is used as reference for normal signal intensity. The area of hyper-enhancement will result using threshold methods of five to six standard deviation (SD) above the intensity of the remote myocardium, or by using the full width half maximum (FWHM) method (Fig. 11.7) [71–73].

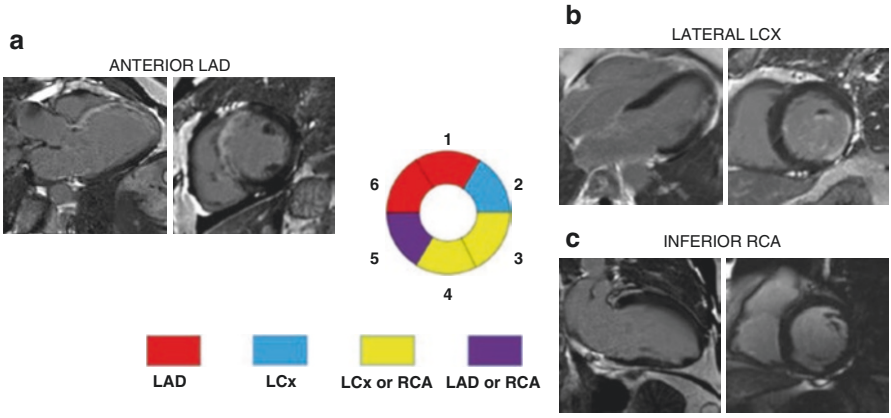

Fig. 11.6 LGE distribution in acute myocardial infarction. Gadolinium hyper-enhancement in short- and long-axis views in three different coronary artery territories after successful percutaneous intervention in patients who presented with ST elevation myocardial infarction. (**a**) Represented long- and short-axis view of a patient presented with anterior ST elevation myocardial infarction where left anterior descending (*LAD*) artery was successfully treated. (**b**) Demonstrated gadolinium enhancement in the left circumflex (*LCx*) artery in a patient that presented with lateral ST elevation myocardial infarction. (**c**) Belonged to a patient with inferior ST elevation and occluded right coronary artery (*RCA*) which was successfully re-opened

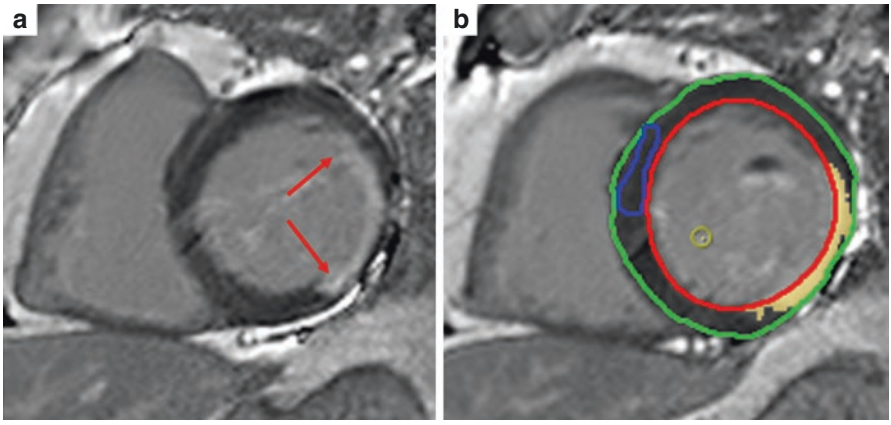

Fig. 11.7 LGE post processing. In (**a**), a short-axis LGE image of a patient with chronic scarred myocardium in the lateral wall (*red arrow*). (**b**) Demonstrates signal intensity- based image analysis. After delineation of the epicardial (*green* contour) and endocardial (*red* contour) borders to define myocardial mass, and a region-of-interest (ROI) showing in *blue* in the remote myocardium as the reference of the normal signal intensity, the myocardium with a SI >5SD of the reference normal SI ROI will automatically highlight, as shown in (**b**). The derived scar percentage of the myocardial mass in this short axis slice is 18%

Low Dose Dobutamine

Similar to the 17-segment model by the American Heart Association is employed to analyse the acquired data by comparing images at rest and with low-dose dobutamine side-by-side. The segment is defined as viable if the wall thickness on the short-axis is >2 mm or if this thickness cut-off was achieved using dobutamine infusion [13, 74].

Below is a table summarising the methodology, hardware and sequences to assess viability in clinical settings.

Clinical Applications

CMR is considered the gold standard for viability assessment [17, 18]. Establishing viability is essential for establishing prognosis and guiding revascularisation in both acute and chronic settings [8].

Late Gadolinium Enhancement (LGE)

The volume of LGE has been shown to correlate with acute necrotic myocardium and with chronic established scar [27, 56]. In animal models, the LGE planimetric extent has been shown to strongly correlate with the extent of necrotic tissue on histological samples both in acute and chronic myocardial infarction, regardless of whether perfusion is restored [27].

Such results were validated and translated in clinical applications by Kim et al. [24] who was the first to demonstrate that LGE has the ability to detect viable segments in patients with left ventricular dysfunction [24]. He firstly demonstrated that the absence of enhancement, and enhancement in excess of 75% of the transmural of myocardial segments were the best predictors of functional recovery. Secondly, LGE was shown to have greater accuracy in segments with the greatest dysfunction, as opposed to known reduced accuracy of contractile reserve in the presence of severe LV dysfunction in dobutamine echocardiography.

Romero et al. [16] in a meta-analysis of 24 prospective trials and 698 patients compared the diagnostic accuracy of three different CMR methods [end-diastolic wall thickness, low-dose dobutamine stress, and late gadolinium enhancement (LGE)] for myocardial viability assessment in patients with coronary artery disease and chronic LV dysfunction. When comparing LGE to other CMR techniques to detect viability, it was shown that the former has superior sensitivity with higher negative predictive values [16]. In the ischemic cascade, scar formation is the last

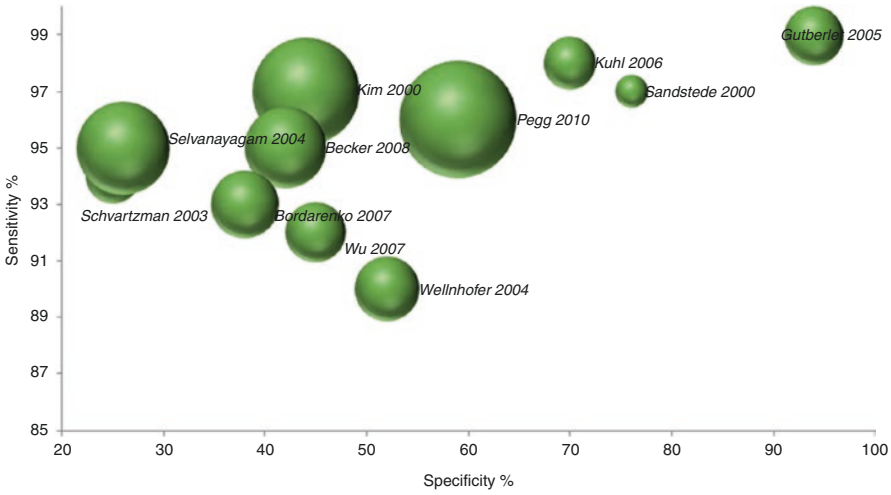

Fig. 11.8 LGE specificity and sensitivity across reported studies. Along the Y-axis, most of the studies have reported sensitivity of more than 89%, while specificity on the X-axis has varied significantly across studies from less than 30% to more than 90%. The size of the sphere within the diagram is proportional to the total sample size included in that study

manifestation and, therefore, hyper enhancement would have the highest sensitivity to predict the absence of recovery. The sensitivity of LGE in predicting viability, defined as improvement in wall motion or thickness, has been consistent across studies over the last decade (Fig. 11.8). This has constantly been reported to be more than 90%. On the other hand, specificity was not consistent and previous studies have reported a wide range of LGE specificity between 20% to nearly 100%. It is worth noting that the degree of left ventricular dysfunction and, subsequently, the regional wall motion abnormalities may play a role in the variability of LGE specificity. Gutberlet et al. [75] reported the highest specificity of nearly 96%. In this study, the average left ventricular function before surgery was 28%, compared to the study performed by Selvanayagam et al. where mean ejection fraction was 62% [76]. This was reflected by the highest specificity of 96% in comparison to 26%. Other factors, like the prevalence of myocardial infarction, methods of revascularisation, incomplete revascularisation, and microvascular disease have some potential influence on LGE specificity in predicting functional recovery. Overall, LGE is less specific but very sensitive in predicting functional recovery post-revascularisation.

In addition, the timing of LGE-CMR post revascularisation may potentially contribute to this level of discrepancy in LGE specificity to detect viability. Selvanayagam et al. [76] have demonstrated better improvement of dysfunctional segments compared to Kim et al. [24] as their follow up CMR was performed 180 days after revascularisation compared to the mean of 70 days in the latter study. They argued that their time frame was closer to "true" time of functional recovery and, therefore, the number of improved segments was higher (64% versus 59%). Similarly, the

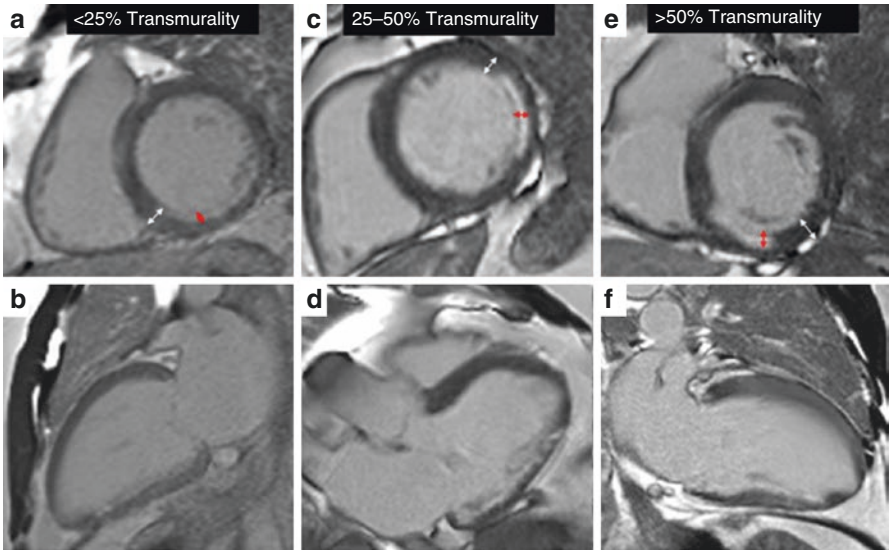

Fig. 11.9 Sub-endocardial myocardial infarction. Sub-endocardial infarction in different coronary territories (**a**, **b**) Represent an inferior myocardial infarction with less than 25% of full wall thickness. (**c**, **d**) Show larger infarct spanning nearly 50% of the wall thickness following LCx occlusion. Panel (**e**, **f**) show CMR performed after dominant RCA occlusion and successful intervention. LGE is just over 50% of the wall thickness

influence of timing of cardiac imaging post-revascularisation was demonstrated when the studies performed by Kuhl et al. [19] and Wu et al. [77] are compared. In the former study, CMR was performed after 6 months of revascularisation with specificity to detect viability using LGE of more than 70%, while the latter study showed only less than 45% specificity when imaging was done 2–3 weeks after revascularisation.

Thanks to the major spatial resolution, CMR allows for detection of small sub-endocardial infarcts (Fig. 11.9). Compared to other imaging techniques for assessment of viability, such as SPECT, CMR has superior sensitivity with higher negative predictive values [16]. CMR and SPECT are similarly accurate in detecting transmural infarction (defined as more than 75% of wall thickness). However, histological studies have shown that CMR detects up to 92% of subendocardial scarring (<50%) versus 38% by SPECT [78]. When translating this into clinical applications, evidence reports a missed diagnosis by SPECT in 13% of patients with identifiable sub-endocardial infarcts on CMR [78]. This is an important finding since even small areas of infarcts carry significant prognostic features. Unrecognised small infarcts on ECG (the infarct size was only 8% of the left ventricular mass) predicts subsequent mortality with 11-fold increase in all-cause mortality and 17-fold in cardiovascular mortality [79].

In conclusion, in daily clinical practice, the absence of or mild (<25%) LGE with normal wall motion or segmental dysfunction correlates with the likelihood of

recovery of contractile function, in contrast to >75% LGE in a segment with wall motion abnormality, indicating limited recovery in non-viable myocardium. Using such LGE transmurality cutoff has good specificity and a positive predictive value [16]. Intermediate values of LGE transmurality (between 25% and 75%) currently represent a grey clinical area. The likelihood of long-term functional improvement for segments with scarring of 50% the wall thickness is less predictable. In this context, the combination of low-dose dobutamine to assess contractile reserve, and LGE to determine the presence of scar, may offer the optimal combination of imaging parameters for establishing viability.

Low-Dose Dobutamine Stress (LDDs)

Historically, low-dose dobutamine stress echocardiography (LDDSE) has been one of the earliest methods used to identify viability and detect the hibernating myocardium [80, 81]. LDDSE was validated against other non-invasive techniques [82, 83] and it is now well-established. Low dose dobutamine stress CMR is performed in accordance to the LDDSE protocols and its high accuracy has been repeatedly demonstrated, in particularly when compared to LDDSE [16, 23, 84]. The high spatial resolution and superior image quality of CMR enables us to detect subtle contractile response to dobutamine with superior specificity and positive predictive value compared to DSE (68% vs 91% and 66% vs 93% respectively) [9, 16, 84, 85], with greatest advantage in those patients with poor acoustic windows [84]. Moreover, the superior diagnostic accuracy of LDDs CMR is independent of the different anatomical location of the infarct compared to LDDSE [86].

In a recent meta-analysis comparing different CMR techniques [end-diastolic wall thickness (EDWT), low-dose dobutamine (LDD), and LGE], LDDs CMR was shown to have an overall accuracy of 84% in predicting functional recovery post-revascularisation with the highest specificity (91%) and positive predictive value (93%) [16]. However, its sensitivity (81%) and negative predictive value (75%) are inferior to LGE [16]. The superior specificity of LDDs CMR can be explained by the multiple criteria needed to fulfil the definition of viability using this technique: (a) a significant amount of myocytes able to contract, resulting in a change in thickness, (b) a sufficient perfusion reserve in response to the inotropes to match the contractile reserve.

An important limitation to the use of LDDs CMR is the reduced sensitivity when assessing much thinned wall segments [23]. Such segments are mostly seen in severe LV dysfunction, and are the ones which do benefit most from revascularisation.

In cases of hibernating myocardium, using both low- and high-dose dobutamine stress imaging, a biphasic response occurs: the myocardium shows an improvement in contractility on low-dose dobutamine segments followed by deterioration on high

dose dobutamine (up to 40 μg/kg/min) [87]. This biphasic phenomenon is considered the best predictor of functional recovery post-revascularisation [88, 89]. However, high dose dobutamine may pose risks on patients, and it is, thus, not extensively used clinically [21, 23].

Combining two CMR techniques in detecting viability is an attractive option. While LGE is better in detecting non-viable segment (better sensitivity), LDDs is superior in detecting segments which are viable (superior specificity). In practice, LGE is easier to perform with lower risk, and may be sufficient without exposing patients to stress test. Studies have suggested that LDDs CMR may have a role where LGE is not sufficient, in particularly, where hyper enhancement is within intermediate range (50–75%) [90, 91].

Myocardial Wall Thickness

Myocardial wall thinning has always been considered as a feature of previous myocardial infarction [12]. This was established in early histological studies where areas of myocardial necrosis had thinned myocardium with a greater extent of muscle loss exceeding that of viable myocardium [92, 93]. The 2012 third universal definition of myocardial infarction reported by the joint European Society of Cardiology, American College of Cardiology, American Heart Association and World Heart Federation task force, stated that prior myocardial infarction could be confirmed if there is an imaging evidence of thinned myocardium which fails to contract in the absence of a non-ischemic cause [94]. Therefore, it is argued that viability testing in these regions is not needed as they represent scar with no likelihood of functional recovery. A cut-off value of end-diastolic wall thickness (EDWT) <5.5 mm [74] has been established as the threshold for non–viable irreversibly injured myocardium [16]. Such cut-off was shown to have sensitivity and specificity values of 96% and 38%, respectively, in predicting low likelihood of contractile recovery post-revascularisation [11, 12].

However, few reports have indicated that even when EDWT <5 mm, viable myocardium may still exist and that wall thinning does not preclude potential functional recovery, as long as there is no or minimal gadolinium enhancement (<25%) [23, 95].

A recent study carried out with 1,055 consecutive patients with coronary artery disease undergoing coronary revascularization, demonstrated that in patients with late gadolinium enhancement less than 50% of the wall thickness, the EDWT of thinned segments increased from 4.4 to 7.5 mm, with a mean increase of 2.3 mm in absolute systolic wall thickness ($P < 0.001$) following revascularization [96]. Importantly, this improvement was not replicated in patients with extensive gadolinium enhancement. Thinned and dysfunctional segments should not always be considered permanently damaged, although there is less than 20% chance of contractile recovery after revascularisation.

Myocardial Viability in Acute Myocardial Infarction

In the past decade, the potential clinical applications of CMR in the acute setting have emerged. LGE acquired in the first days following ischemic injury was shown to allow assessment of necrotic myocardium, and most importantly to predict long term functional recovery [97–99] Similar to findings in stable coronary artery disease [24], the likelihood of functional recovery was shown to be dependent on the transmural extent of gadolinium enhancement [97, 99]. As shown in a recent meta-analysis on 634 patients, using a cut-off for transmural hyperenhancement of 50% of the wall thickness, the presence of stunned myocardium (i.e., viable myocardium in the context of acute myocardial infarction) can be accurately diagnosed with a negative predictive value of 72% and a positive predictive value of 83% [100]. In a trend similar to chronic infarction, increasing the cut-off of gadolinium enhancement led to higher sensitivity but lower specificity, and vice versa [100].

The additional clinical utility of acute LGE imaging became fully exploited, thanks to the optimization of CMR techniques to differentiate ischemic from necrotic tissue [101]. T2-weighted imaging is a validated technique used to assess myocardial oedema in acutely ischemic reversibly injured myocardium [102]. AS such T2W oedema imaging differentiates acute from chronic myocardial infarction. Thanks to the combination of T2W and LGE acquisitions, salvage myocardium can be derived by subtracting the area of necrotic myocardium by LGE from the much larger area of ischemic oedema (Fig. 11.10) [103].

The area of salvaged myocardium represents myocardium at risk of irreversible injury if not appropriately treated. It conveys valuable information to assess

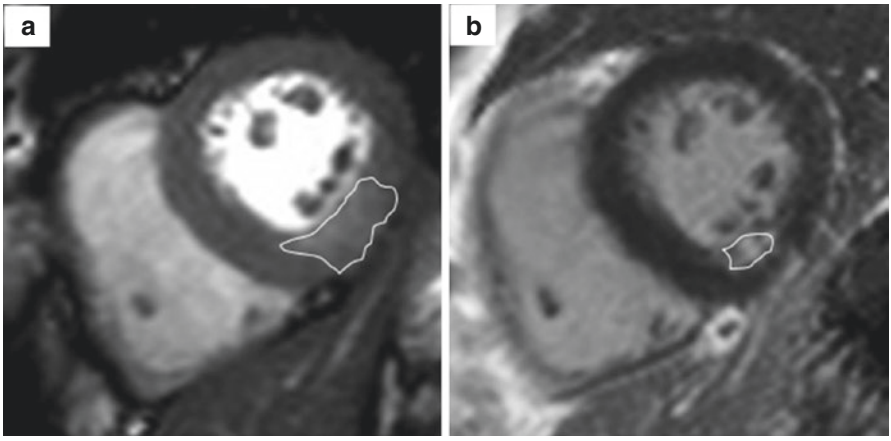

Fig. 11.10 Myocardial salvage. (**a**) Demonstrates oedematous ischaemic area following an inferior ST elevation myocardial infarction. It shows as a high signal intensity on T2-weighted images. However, scarred myocardium is only demonstrated on (**b**). The difference between both areas is the salvaged myocardium and represents the effect of emergency percutaneous intervention

the efficacy of cardioprotective strategies [103, 104]. Furthermore, salvaged myocardium has been identified as a useful prognostic marker of clinical outcomes [105, 106].

In addition, CMR provides a unique opportunity to study the status of microvascular network after acute myocardial infarction. No reflow or microvascular obstruction (MVO) is considered a complication of reperfusion therapy to the occluded coronary artery [107]. CMR allows quantification of MVO alongside the infarct size by LGE [107]. Alternative techniques, such as early gadolinium enhancement, or first pass perfusion can also be used to depict MVO [108]. The presence of MVO correlates with the size of infarction and cardiovascular outcomes [109]. In a recent meta-analysis, MVO was found to be a strong predictor of major adverse cardiovascular events and to correlate with a lower ejection fraction, a larger infarct size, and an increased likelihood to develop left ventricle remodelling [110].

Given that the acute ischemic myocardial injury is a dynamic and complex process, the applications of acute LGE imaging can present challenges compared to the applications in stable coronary artery disease. There are different considerations to be made in this regard: (a) the temporal course of the imaging features reflective of the underlying histopathology are not fully clear as yet, and (b) in order to produce reliable and reproducible results, it is crucial to address methodological factors when performing LGE techniques and when analysing LGE images, in addition, (c) we are living in a scientifically rapidly evolving time when boundaries are pushed and acute CMR imaging is conducted at very early stages after ischemic injury revealing imaging biomarker previously unknown.

Late gadolinium enhancement assessment can change over time: evidence shows that the volume of LGE decreases significantly in the first week post MI [111, 112], and subsequently stabilises at 3 months (Fig. 11.11) [113].

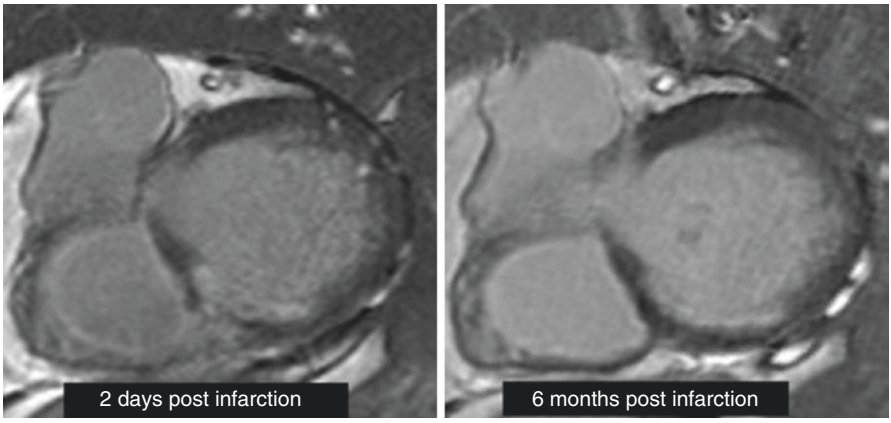

Fig. 11.11 LGE size reduction over time. Reduction in late gadolinium enhancement between 1 week post infarction and 6 months. The size and the thickness of the LGE has gradually decreased over the time interval

The translational aspects of such findings are important as the assessment of transmurality as early as 24 h might not reflect the long term functional recovery, as previously demonstrated in stable CAD.

CMR assessment of acute myocardial necrosis requires rigorous acquisition of late gadolinium enhancement with an adequate time delay to allow for appropriate nulling of the myocardium. Whilst this is the case also in stable coronary artery disease, it is even more crucial in acute MI where a short time delay, and consequent early acquisition might result in the overestimation of the infarct size [64]. This is due to the wash out effect of the gadolinium in oedematous myocardium with increased extracellular volume [114]. Stringent criteria are also needed when interpreting acute LGE images. Thresholds as high as 5 SD above the signal intensity of the remote myocardium will allow for a correct assessment of the extent of the necrotic core of the injured myocardium and avoid inclusion of oedematous areas.

Finally, it is important to recognise that since acute CMR imaging is becoming more extensively used, and the timeframe for performing the scans post-acute MI is changing from the standard 24–72 h to a window of up to 8 h [115]. Such early scans reveal new imaging features most likely reflective of the underlying dynamic histopathological changes [116].

Effect on Global LV Function and Patients' Outcome

Saving the myocardium from irreversible injury in an effort to minimize long-term remodeling is a key aim of current treatment strategies in STEMI [117]. LV remodelling is defined as the increase of more than 20% of left ventricular end diastolic volume from 6 months after the index scan [118].

Despite several data published on the predictive value of the final infarct size rather than transmurality and microvascular obstruction or salvaged myocardium, compared to EF, establishing which predictor carries the most prognostic weight for clinical outcomes is challenging and yet unclear.

Importantly the prognostic value of irreversible left ventricular systolic dysfunction assessed by EF, ESV, EDV has long been recognized [119]. The importance of negative remodeling and reduction in EF, increases in LV volumes, and infarct size, have been confirmed in over 2,300 survivors of STEMI receiving reperfusion therapy [120].

More recently published evidence using CMR as the gold standard non-invasive imaging technique, have demonstrated that larger infarcts are consistently associated with adverse remodeling, larger ventricular volumes, reduced EF, and increased MVO, that occurs in approximately 50% of patients treated by PPCI [121–123].

Several studies have shown the superiority of scar quantification in predicting MACE beyond left ventricular volumes and EF [110, 124–126]. In particular, infarct size assessed by CMR in STEMI survivors has been shown to be the only independent predictor of MACE at 2 years [124, 125]. Kwong et al. [124] performed a

multi-variable analysis on 195 patients with history of myocardial infarction and established that the presence of scar is the strongest predictor of cardiovascular events. Furthermore, the presence of MVO on CMR is also a recognized predictor of the intermediate incidence of MACE up to 1 year. The incidence of MACE in those with no MVO vs. MVO was 6.1% vs. 43.7% respectively [126]. The results reported by meta-analysis studies are still contradictive and indicate that further studies are needed to establish whether infarct size or MVO have major prognostic value [127, 128].

Distinguishing viable from non-viable segments is important, but the application of this separation to predict patients' outcome is of more significance [91]. Viability has been studied to predict patients' outcomes in the past. In two meta-analyses, the strong association between myocardial viability and survival after revascularisation was confirmed, while lack of viability had similar outcomes irrespective of treatment (medical versus revascularisation) [7, 31]. Gerber et al. [129] evaluated the prognostic value of using LGE as a viability assessment for patients undergoing revascularisation. Authors reported that 3-year survival was significantly worsened in non-revascularised patients with viable myocardium than with non-viable myocardium (48% versus 77% survival, P = 0.02). Viable myocardium was defined according to Bax et al. and patient was considered to have viable myocardium if there are more than four dysfunctional segments with LGE of less than 50% the wall thickness [130]. Therefore, viability assessment appears to add significant prognostic value not only to the dysfunctional segments but could also be extended to the overall myocardium, and further to predict patients' outcomes. It is currently been implemented in the European Society of Cardiology guidelines to assess patients prior revascularisation [8].

Future Directions

While gadolinium enhancement has been established as the gold standard of viability assessment, this technique has limitations in assessing patients with renal impairment. In addition, choosing the inversion time for optimal nulling of the myocardium is operator dependent which sometimes poses more difficulties when someone tries to establish the best time delay to null the myocardium. Novel CMR developments are on-going and efforts are being directed towards alternative and more precise techniques, potentially providing novel imaging biomarkers for patient stratification. In the next discussion, we will focus on promising techniques which are more likely to be implemented in clinical practice in the near future. However, the reader should know that techniques such as CMR fingerprinting [131], CMR spectroscopy for assessment of cellular metabolism [132], or CMR hyperpolarization [133] are on the horizon and, exhibiting great potential.

Quantitative pre-contrast myocardial mapping techniques (T1, T2 and T2*) (Fig. 11.12) are very promising tools and are currently under validation for clinical use.

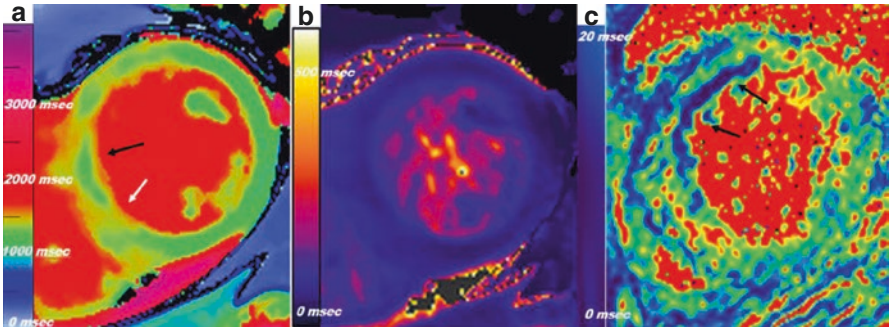

Fig. 11.12 Quantitative mapping techniques. (**a**) Shows a short-axis T1 mapping obtained in a patient with anterior ST elevation myocardial infarction. The area of oedema will show high values (appearing *red* on the map) at the level of the septum (indicated by the *white arrow*) but reduced values in the central core (appearing *green*, and corresponding to "normal" T1 s- indicated by the *black arrow*) in keeping with T1 core. (**b**) Represents the same slice but using T2 mapping technique. (**c**) Is the T2* map and the blue area (indicated by the *black arrow*) represent very low T2* (<20 ms) suggesting intra myocardial haemorrhage

Mapping techniques allow quantification of the tissue composition on a voxel-by-voxel basis and provide a more precise, robust, and reproducible quantification compared to standard signal intensity based methods used in clinical practice [134–136].

T1 mapping depicts the relaxation time of the proton spin-lattice (T1) of the pixels within imaged tissue; [134, 137, 138] different tissues display typical T1 values which will alter in relation to pathological process, such as myocardial infarction, resulting in an increase in water content or collagen [135, 139]. In acute oedematous infarcted myocardium, the increase in water content correlates with the increase in the absolute values of T1 mapping [137, 140]and the severity of injury [141]. Non-contrast T1 mapping also depicts areas of microvascular obstruction [142] and has been demonstrated to be an important prognostic value for future cardiovascular events. Interestingly, by depicting the severity of injury and enabling the identification of small changes in tissue composition [118], T1 mapping sheds light onto scientific questions, which could not be answered by signal intensity based techniques. Specifically, recently published data showed an increase in T1 values in the remote myocardium as reflective of a possible underlying systemic inflammatory process in addition to the mechanical accumulation of oedema in the injured myocardium [143].

In chronic stable artery disease, pre-contrast T1 mapping could have a potential clinical use in depicting chronically scarred myocardium [144] and in potentially assessing ischemic myocardium by depicting high T1 values resulting from increased blood volume under adenosine stress conditions [140]. T1 mapping could represent an optimal non–contrast alternative to LGE to establish myocardial viability.

By acquiring T1 mapping pre- and post-administration of contrast, the extracellular volume (ECV) can be quantified by calculating the volume of distribution of gadolinium [145]. This would represent a completely novel way to investigate

changes happening in the myocardium post-MI which were not previously available. The clinical meaning and prognostic value of ECV as an imaging biomarker is yet to be fully defined although initial evidence is promising [146, 147].

T2 mapping is also used to assess myocardial oedema (Fig. 11.12b). It has been found to be more robust and reliable when compared to T2-weighted imaging [136, 148]. Compared to T1 mapping techniques, T2 has limitations in that the range of T2 values is not as broad as for T1. Hence, the accuracy of T2 mapping could be inferior in case of mild degree of injury. By using T2 mapping techniques to assess the changes happening in the myocardium early after an acute ischaemic event, recent studies have published unique and controversial evidence suggesting the existence of different types of insult of the myocardium (an early one related to reperfusion injury followed by systemic inflammatory one) [115, 116]. Such results would be revolutionary, and if proven true, would nicely complement the previous molecular and genetic studies proving the existence of a systemic inflammatory reaction [149, 150].

Out of all the quantitative techniques, T2* is probably the most established one [145]. T2* is the measure of transverse relaxation mainly due to the inhomogeneity of the magnetic field, thus, T2* is always less than T2 relaxation time [145]. The deposition of myocardial iron is the main mechanism behind the shortening of T2* relaxation time and subsequently, myocardial haemorrhage in the context of acute MI is potentially identified using this technique [145]. In patients with acute MI, T2* values would display as reduced in the core of the MI compared to the values in the remote myocardium (Fig. 11.12c) [151].

The second technique, which may represent an alternative to LGE is diffusion tensor imaging (DTI) [152, 153]. DTI is a technique, which allows the assessment of the orientation of myocardial fibers and architecture using water motion directions within the fibers at a cellular level [154, 155]. Myocardial infarction and subsequent disrupted fibers cause deviations in DTI parameters (such as the helical angle, fractional anisotropy, and apparent diffusion coefficient), and thereby, identifying and localising infarcted and potentially non-viable region [156]. This technique is promising and currently is being studied and compared with established contrast enhancement techniques.

Finally, molecular imaging is another encouraging technique in CMR. It relies on identifying imaging probes to target a specific molecular process [157]. CMR standard techniques allow for functional assessment, myocardial perfusion quantification, and tissue characterization, but there are no techniques to image cells or enzymes within the cells, or pathological processes, such as myocardial apoptosis, or angiogenesis. Promising molecular imaging agents have been investigated, including annexin-based nanoparticles to assess cell apoptosis [158], fluorescent superparamagnetic iron oxide nanoparticles to track monocytes and macrophage infiltration [159, 160], paramagnetic nanoparticles targeting endothelium to quantify angiogenesis [161], or fibrin target CMR probes to assess fibrotic processes [162]. Overall, molecular imaging provides new opportunities for precise diagnosis and offers a tool for disease monitoring and future prognosis. However further clinical validation is needed (Table 11.1).

Tabular Summary: Myocardial Viability in Ischaemic Heart Disease

Techniques and sequence	Imaging biomarker and pathophysiology	Acquisition workflow	CMR post processing
Rest cine imaging *Sequence*: bSSFP mostly used, although other sequences are available for functional imaging) [163–165]	Regional wall motion abnormalities (RWMA) End-diastolic myocardial wall thickness (non-viable if <5-5.5 mm) Systolic myocardial thickening	Long axis (vertical, horizontal and left ventricular outflow views) Multislice short axis to cover the LV (slice thickness 6–10 mm, gap 0–4 mm, spatial resolution 1–2×1–2 mm); The short axis can be acquired after administration of gadolinium before LGE acquisition	*Qualitative assessment* Visual definition of myocardial contractility as: normokinetic, hypokinetic, akinetic, diskinetic Visual definition of distribution of RWMA per coronary territories *Quantitative assessment* Segmental myocardial thickening obtained drawing endocardial and epicardial contours at end-systole and end-diastole in each data set/slice of the LV
Low dose dobutamine stress. Rest and stress cine imaging *Sequence:* bSSFP mostly used but other sequences are also available [46]	Change in regional wall motion abnormalities (RWMA) from rest to stress Myocardial wall thickening in response to inotropes infusion (viable >2 mm)	Initial baseline acquisition of long-axis in addition to at least three slices (base, mid ventricle and apex) short-axis slices of the left ventricle. It is recommended to obtain full length short-axis slices of left ventricle to calculate left ventricle volume [46] Slice thickness 8 mm, with in-plane spatial resolution of 1–2×1–2 mm [46] Inotropes infusion up to 10 mcg/kg/min and re-acquisition of long- and short-axis slices under stress conditions	*Qualitative assessment of the change in contractility* Side-by-side comparison of myocardial contractility at rest and stress An improvement in contractility will indicate viable myocardium: akinetic/hypokinetic→normokinet [46, 68] A lack of improvement in contractility will indicate non-viable myocardium akinetic→akinetic

Late gadolinium enhancement (LGE)	Contrast enhanced myocardium due to increase in volume of distribution of gadolinium secondary to ruptured myocytes LGE transmurality Microvascular obstruction (MVO)	Administration of gadolinium contrast bolus Waiting time delay of 10–15 min Acquisition of long axis and short axis covering the LV and matching functional imaging Slice thickness is similar to cine imaging with in-plane resolution of 1.4–1.8 mm [166] 3 T vs 1.5 T The inversion time to null the myocardium will be longer due to prolongation of T1 relaxation time at 3 T Imaging artefact will be more frequent at 3 T	*Qualitative assessment*: LGE localization and extent per coronary territory (17AHA segment model) [70] Transmurality (1–25%, 26–50%, 51–75%, 76–100%) [16, 24] Presence of MVO *Quantitative assessment* LV% damaged fraction obtained by: Drawing endocardial and epicardial contour for each slice for quantification of myocardial mass Delineating a region of interest (ROI) in remote myocardium as the reference for normal signal intensity Establishing a threshold of signal intensity above the reference ROI (i.e. 5 standard deviations) [71–73] Or using the full width half maximum (FWHM) [71–73] MVO quantification is defined as the region within hyper enhancement area where signal intensity is at least -2SD from ROI. The latter should be placed within hyper enhancement area

(continued)

Table 11.1 (continued)

Techniques and sequence	Imaging biomarker and pathophysiology	Acquisition workflow	CMR post processing
Sequences: Inversion recovery gradient echo sequence (IR-GRE)		Requires accurate time delay to "null" myocardium so optimal contrast is achieved	
Phase sensitive inversion recovery (PSIR)		Less dependent on operator experience in choosing Time to Inversion (TI)	
Free breathing single shot technique		More prone to artefacts in particularly when using 3 T but very useful when scanning patients with difficulties in breath holding or arrhythmia	

Methodology, hardware and sequences for viability assessment

References

1. Piepoli MF, Hoes AW, Agewall S, Albus C, Brotons C, Catapano AL, Cooney MT, Corra U, Cosyns B, Deaton C, Graham I, Hall MS, Hobbs FD, Lochen ML, Lollgen H, Marques-Vidal P, Perk J, Prescott E, Redon J, Richter DJ, Sattar N, Smulders Y, Tiberi M, van der Worp HB, van Dis I, Verschuren WM, Authors/Task Force M. 2016 European guidelines on cardiovascular disease prevention in clinical practice: the Sixth Joint Task Force of the European Society of Cardiology and other societies on cardiovascular disease prevention in clinical practice (constituted by representatives of 10 societies and by invited experts): developed with the special contribution of the European Association for Cardiovascular Prevention & Rehabilitation (EACPR). Eur Heart J. 2016; doi:10.1093/eurheartj/ehw106.
2. Wilmot KA, O'Flaherty M, Capewell S, Ford ES, Vaccarino V. Coronary heart disease mortality declines in the United States from 1979 through 2011: evidence for stagnation in young adults, especially women. Circulation. 2015;132(11):997–1002. doi:10.1161/CIRCULATIONAHA.115.015293.
3. Jousilahti P, Laatikainen T, Peltonen M, Borodulin K, Mannisto S, Jula A, Salomaa V, Harald K, Puska P, Vartiainen E. Primary prevention and risk factor reduction in coronary heart disease mortality among working aged men and women in eastern Finland over 40 years: population based observational study. BMJ. 2016;352:i721. doi:10.1136/bmj.i721.
4. Braunwald E. Research advances in heart failure: a compendium. Circ Res. 2013;113(6):633–45. doi:10.1161/CIRCRESAHA.113.302254.
5. Bleumink GS, Knetsch AM, Sturkenboom MC, Straus SM, Hofman A, Deckers JW, Witteman JC, Stricker BH. Quantifying the heart failure epidemic: prevalence, incidence rate, lifetime risk and prognosis of heart failure The Rotterdam Study. Eur Heart J. 2004;25(18):1614–9. doi:10.1016/j.ehj.2004.06.038.
6. Braunwald E. Heart failure. JACC Heart Fail. 2013;1(1):1–20. doi:10.1016/j.jchf.2012.10.002.
7. Allman KC, Shaw LJ, Hachamovitch R, Udelson JE. Myocardial viability testing and impact of revascularization on prognosis in patients with coronary artery disease and left ventricular dysfunction: a meta-analysis. J Am Coll Cardiol. 2002;39(7):1151–8.
8. Authors/Task Force m, Windecker S, Kolh P, Alfonso F, Collet JP, Cremer J, Falk V, Filippatos G, Hamm C, Head SJ, Juni P, Kappetein AP, Kastrati A, Knuuti J, Landmesser U, Laufer G, Neumann FJ, Richter DJ, Schauerte P, Sousa Uva M, Stefanini GG, Taggart DP, Torracca L, Valgimigli M, Wijns W, Witkowski A. 2014 ESC/EACTS guidelines on myocardial revascularization: the Task Force on Myocardial Revascularization of the European Society of Cardiology (ESC) and the European Association for Cardio-Thoracic Surgery (EACTS) developed with the special contribution of the European Association of Percutaneous Cardiovascular Interventions (EAPCI). Eur Heart J. 2014;35(37):2541–619. doi:10.1093/eurheartj/ehu278.
9. La Canna G, Alfieri O, Giubbini R, Gargano M, Ferrari R, Visioli O. Echocardiography during infusion of dobutamine for identification of reversibly dysfunction in patients with chronic coronary artery disease. J Am Coll Cardiol. 1994;23(3):617–26.
10. Perrone-Filardi P, Pace L, Prastaro M, Squame F, Betocchi S, Soricelli A, Piscione F, Indolfi C, Crisci T, Salvatore M, Chiariello M. Assessment of myocardial viability in patients with chronic coronary artery disease. Rest-4-hour-24-hour 201Tl tomography versus dobutamine echocardiography. Circulation. 1996;94(11):2712–9.
11. Schinkel AF, Bax JJ, Boersma E, Elhendy A, Vourvouri EC, Roelandt JR, Poldermans D. Assessment of residual myocardial viability in regions with chronic electrocardiographic Q-wave infarction. Am Heart J. 2002;144(5):865–9.
12. Cwajg JM, Cwajg E, Nagueh SF, He ZX, Qureshi U, Olmos LI, Quinones MA, Verani MS, Winters WL, Zoghbi WA. End-diastolic wall thickness as a predictor of recovery of function in myocardial hibernation: relation to rest-redistribution T1-201 tomography and dobutamine stress echocardiography. J Am Coll Cardiol. 2000;35(5):1152–61.

13. Schmidt M, Voth E, Schneider CA, Theissen P, Wagner R, Baer FM, Schicha H. F-18-FDG uptake is a reliable predictory of functional recovery of akinetic but viable infarct regions as defined by magnetic resonance imaging before and after revascularization. Magn Reson Imaging. 2004;22(2):229–36. doi:10.1016/j.mri.2003.07.006.
14. Underwood SR, Bax JJ, vom Dahl J, Henein MY, Knuuti J, van Rossum AC, Schwarz ER, Vanoverschelde JL, van der Wall EE, Wijns W, Study Group of the European Society of C. Imaging techniques for the assessment of myocardial hibernation. Report of a study group of the European Society of Cardiology. Eur Heart J. 2004;25(10):815–36. doi:10.1016/j.ehj.2004.03.012.
15. Chareonthaitawee P, Schaefers K, Baker CS, Turkheimer F, Stegger L, Banner NR, Yacoub M, Bonser RS, Iozzo P, Camici PG, Rimoldi O. Assessment of infarct size by positron emission tomography and [18F]2-fluoro-2-deoxy-D-glucose: a new absolute threshold technique. Eur J Nucl Med Mol Imaging. 2002;29(2):203–15.
16. Romero J, Xue X, Gonzalez W, Garcia MJ. CMR imaging assessing viability in patients with chronic ventricular dysfunction due to coronary artery disease: a meta-analysis of prospective trials. JACC Cardiovasc Imaging. 2012;5(5):494–508. doi:10.1016/j.jcmg.2012.02.009.
17. Kellman P, Arai AE. Cardiac imaging techniques for physicians: late enhancement. J Magn Reson Imaging. 2012;36(3):529–42. doi:10.1002/jmri.23605.
18. Fieno DS, Kim RJ, Chen EL, Lomasney JW, Klocke FJ, Judd RM. Contrast-enhanced magnetic resonance imaging of myocardium at risk: distinction between reversible and irreversible injury throughout infarct healing. J Am Coll Cardiol. 2000;36(6):1985–91.
19. Kuhl HP, Lipke CS, Krombach GA, Katoh M, Battenberg TF, Nowak B, Heussen N, Buecker A, Schaefer WM. Assessment of reversible myocardial dysfunction in chronic ischaemic heart disease: comparison of contrast-enhanced cardiovascular magnetic resonance and a combined positron emission tomography-single photon emission computed tomography imaging protocol. Eur Heart J. 2006;27(7):846–53. doi:10.1093/eurheartj/ehi747.
20. Shan K, Constantine G, Sivananthan M, Flamm SD. Role of cardiac magnetic resonance imaging in the assessment of myocardial viability. Circulation. 2004;109(11):1328–34. doi:10.1161/01.CIR.0000120294.67948.E3.
21. Bondarenko O, Beek AM, McCann GP, van Rossum AC. Revascularization in patients with chronic ischaemic myocardial dysfunction: insights from cardiovascular magnetic resonance imaging. Eur Heart J Cardiovasc Imaging. 2012;13(12):985–90. doi:10.1093/ehjci/jes194.
22. Schwitter J, Arai AE. Assessment of cardiac ischaemia and viability: role of cardiovascular magnetic resonance. Eur Heart J. 2011;32(7):799–809. doi:10.1093/eurheartj/ehq481.
23. Beek AM, van Rossum AC. Use of cardiovascular magnetic resonance imaging in the assessment of left ventricular function, scar and viability in patients with ischaemic cardiomyopathy and chronic myocardial infarction. Heart. 2010;96(18):1494–501. doi:10.1136/hrt.2009.181123.
24. Kim RJ, Wu E, Rafael A, Chen EL, Parker MA, Simonetti O, Klocke FJ, Bonow RO, Judd RM. The use of contrast-enhanced magnetic resonance imaging to identify reversible myocardial dysfunction. N Engl J Med. 2000;343(20):1445–53. doi:10.1056/NEJM200011163432003.
25. Velazquez EJ, Lee KL, Deja MA, Jain A, Sopko G, Marchenko A, Ali IS, Pohost G, Gradinac S, Abraham WT, Yii M, Prabhakaran D, Szwed H, Ferrazzi P, Petrie MC, O'Connor CM, Panchavinnin P, She L, Bonow RO, Rankin GR, Jones RH, Rouleau JL, Investigators S. Coronary-artery bypass surgery in patients with left ventricular dysfunction. N Engl J Med. 2011;364(17):1607–16. doi:10.1056/NEJMoa1100356.
26. Velazquez EJ, Lee KL, Jones RH, Al-Khalidi HR, Hill JA, Panza JA, Michler RE, Bonow RO, Doenst T, Petrie MC, Oh JK, She L, Moore VL, Desvigne-Nickens P, Sopko G, Rouleau JL, Investigators S. Coronary-artery bypass surgery in patients with ischemic cardiomyopathy. N Engl J Med. 2016;374(16):1511–20. doi:10.1056/NEJMoa1602001.

27. Kim RJ, Fieno DS, Parrish TB, Harris K, Chen EL, Simonetti O, Bundy J, Finn JP, Klocke FJ, Judd RM. Relationship of MRI delayed contrast enhancement to irreversible injury, infarct age, and contractile function. Circulation. 1999;100(19):1992–2002.
28. Yokota C, Nonogi H, Miyazaki S, Goto Y, Maeno M, Daikoku S, Itoh A, Haze K, Yamada N. Gadolinium-enhanced magnetic resonance imaging in acute myocardial infarction. Am J Cardiol. 1995;75(8):577–81.
29. Mahrholdt H, Klem I, Sechtem U. Cardiovascular MRI for detection of myocardial viability and ischaemia. Heart. 2007;93(1):122–9. doi:10.1136/hrt.2005.071290.
30. Kaul S. Assessing the myocardium after attempted reperfusion: should we bother? Circulation. 1998;98(7):625–7.
31. Camici PG, Prasad SK, Rimoldi OE. Stunning, hibernation, and assessment of myocardial viability. Circulation. 2008;117(1):103–14. doi:10.1161/CIRCULATIONAHA.107.702993.
32. Becker LC, Levine JH, DiPaula AF, Guarnieri T, Aversano T. Reversal of dysfunction in postischemic stunned myocardium by epinephrine and postextrasystolic potentiation. J Am Coll Cardiol. 1986;7(3):580–9.
33. Kitakaze M, Marban E. Cellular mechanism of the modulation of contractile function by coronary perfusion pressure in ferret hearts. J Physiol. 1989;414:455–72.
34. Filipchuk NG, Peshock RM, Malloy CR, Corbett JR, Rehr RB, Buja LM, Jansen DE, Redish GR, Gabliani GI, Parkey RW, et al. Detection and localization of recent myocardial infarction by magnetic resonance imaging. Am J Cardiol. 1986;58(3):214–9.
35. McNamara MT, Higgins CB, Schechtmann N, Botvinick E, Lipton MJ, Chatterjee K, Amparo EG. Detection and characterization of acute myocardial infarction in man with use of gated magnetic resonance. Circulation. 1985;71(4):717–24.
36. Pflugfelder PW, Wisenberg G, Prato FS, Carroll SE, Turner KL. Early detection of canine myocardial infarction by magnetic resonance imaging in vivo. Circulation. 1985;71(3):587–94.
37. Mahrholdt H, Wagner A, Judd RM, Sechtem U. Assessment of myocardial viability by cardiovascular magnetic resonance imaging. Eur Heart J. 2002;23(8):602–19. doi:10.1053/euhj.2001.3038.
38. Inoue S, Murakami Y, Ochiai K, Kitamura J, Ishibashi Y, Kawamitsu H, Sugimura K, Shimada T. The contributory role of interstitial water in Gd-DTPA-enhanced MRI in myocardial infarction. J Magn Reson Imaging: JMRI. 1999;9(2):215–9.
39. Wu E, Judd RM, Vargas JD, Klocke FJ, Bonow RO, Kim RJ. Visualisation of presence, location, and transmural extent of healed Q-wave and non-Q-wave myocardial infarction. Lancet. 2001;357(9249):21–8. doi:10.1016/S0140-6736(00)03567-4.
40. Kellman P, Arai AE, McVeigh ER, Aletras AH. Phase-sensitive inversion recovery for detecting myocardial infarction using gadolinium-delayed hyperenhancement. Magn Reson Med. 2002;47(2):372–83.
41. Huber A, Bauner K, Wintersperger BJ, Reeder SB, Stadie F, Mueller E, Schmidt M, Winnik E, Reiser MF, Schoenberg SO. Phase-sensitive inversion recovery (PSIR) single-shot TrueFISP for assessment of myocardial infarction at 3 tesla. Investig Radiol. 2006;41(2):148–53.
42. Biglands JD, Radjenovic A, Ridgway JP. Cardiovascular magnetic resonance physics for clinicians: part II. J Cardiovas Magn Reson: Off J Soc Cardiovasc Magn Reson. 2012;14:66. doi:10.1186/1532-429X-14-66.
43. Gowland P, Leach M. A simple method for the restoration of signal polarity in multiimage inversion recovery sequences for measuring T1. Magn Reson Med. 1991;18:224–31.
44. Scheffler K, Hennig J. T(1) quantification with inversion recovery TrueFISP. Magn Reson Med. 2001;45(4):720–3.
45. Huber A, Schoenberg SO, Spannagl B, Rieber J, Erhard I, Klauss V, Reiser MF. Single-shot inversion recovery TrueFISP for assessment of myocardial infarction. AJR Am J Roentgenol. 2006;186(3):627–33. doi:10.2214/AJR.04.0746.

46. Charoenpanichkit C, Hundley WG. The 20 year evolution of dobutamine stress cardiovascular magnetic resonance. J Cardiovasc Magn Reson: Off J Soc Cardiovasc Magn Reson. 2010;12:59. doi:10.1186/1532-429X-12-59.
47. Thiele H, Nagel E, Paetsch I, Schnackenburg B, Bornstedt A, Kouwenhoven M, Wahl A, Schuler G, Fleck E. Functional cardiac MR imaging with steady-state free precession (SSFP) significantly improves endocardial border delineation without contrast agents. J Magn Reson Imag: JMRI. 2001;14(4):362–7.
48. Schalla S, Klein C, Paetsch I, Lehmkuhl H, Bornstedt A, Schnackenburg B, Fleck E, Nagel E. Real-time MR image acquisition during high-dose dobutamine hydrochloride stress for detecting left ventricular wall-motion abnormalities in patients with coronary arterial disease. Radiology. 2002;224(3):845–51. doi:10.1148/radiol.2243010945.
49. van Dijkman PR, van der Wall EE, de Roos A, Doornbos J, van der Laarse A, Matheijssen NA, van Rossum AC, van Voorthuisen AE, Bruschke AV. Gadolinium-enhanced magnetic resonance imaging in acute myocardial infarction. Eur J Radiol. 1990;11(1):1–9.
50. Wesbey GE, Higgins CB, McNamara MT, Engelstad BL, Lipton MJ, Sievers R, Ehman RL, Lovin J, Brasch RC. Effect of gadolinium-DTPA on the magnetic relaxation times of normal and infarcted myocardium. Radiology. 1984;153(1):165–9. doi:10.1148/radiology.153.1.6473778.
51. Schaefer M. Properties of paramagnetic metals in MRI. Metal-Based Drugs. 1997;4(3):159–71. doi:10.1155/MBD.1997.159.
52. Lee DH. Mechanisms of contrast enhancement in magnetic resonance imaging. Can Assoc Rad J = J Assoc Can Radiol. 1991;42(1):6–12.
53. Arheden H, Saeed M, Higgins CB, Gao DW, Bremerich J, Wyttenbach R, Dae MW, Wendland MF. Measurement of the distribution volume of gadopentetate dimeglumine at echo-planar MR imaging to quantify myocardial infarction: comparison with 99mTc-DTPA autoradiography in rats. Radiology. 1999;211(3):698–708. doi:10.1148/radiology.211.3.r99jn41698.
54. Klein C, Schmal TR, Nekolla SG, Schnackenburg B, Fleck E, Nagel E. Mechanism of late gadolinium enhancement in patients with acute myocardial infarction. J Cardiovasc Magn Reson: Off J Soc Cardiovasc Magn Reson. 2007;9(4):653–8. doi:10.1080/10976640601105614.
55. Mallory FB, Parker F. Fixing and staining methods for lead and copper in tissues. Am J Pathol. 1939;15(5):517–22.. 515
56. Kim RJ, Chen EL, Lima JA, Judd RM. Myocardial Gd-DTPA kinetics determine MRI contrast enhancement and reflect the extent and severity of myocardial injury after acute reperfused infarction. Circulation. 1996;94(12):3318–26.
57. Polimeni PI. Extracellular space and ionic distribution in rat ventricle. Am J Phys. 1974;227(3):676–83.
58. Rehwald WG, Fieno DS, Chen EL, Kim RJ, Judd RM. Myocardial magnetic resonance imaging contrast agent concentrations after reversible and irreversible ischemic injury. Circulation. 2002;105(2):224–9.
59. Grobner T. Gadolinium – a specific trigger for the development of nephrogenic fibrosing dermopathy and nephrogenic systemic fibrosis? Nephrol Dial Transplant: Off Publ Eur Dial Transplant Assoc Eur Ren Assoc. 2006;21(4):1104–8. doi:10.1093/ndt/gfk062.
60. Marckmann P, Skov L, Rossen K, Dupont A, Damholt MB, Heaf JG, Thomsen HS. Nephrogenic systemic fibrosis: suspected causative role of gadodiamide used for contrast-enhanced magnetic resonance imaging. J Am Soc Nephrol: JASN. 2006;17(9):2359–62. doi:10.1681/ASN.2006060601.
61. Kanal E, Barkovich AJ, Bell C, Borgstede JP, Bradley Jr WG, Froelich JW, Gilk T, Gimbel JR, Gosbee J, Kuhni-Kaminski E, Lester Jr JW, Nyenhuis J, Parag Y, Schaefer DJ, Sebek-Scoumis EA, Weinreb J, Zaremba LA, Wilcox P, Lucey L, Sass N, Safety ACRBRPoM. ACR guidance document for safe MR practices: 2007. AJR Am J Roentgenol. 2007;188(6):1447–74. doi:10.2214/AJR.06.1616.
62. Fedele F, Montesano T, Ferro-Luzzi M, Di Cesare E, Di Renzi P, Scopinaro F, Agati L, Penco M, Serri F, Vitarelli A, et al. Identification of viable myocardium in patients with chronic

coronary artery disease and left ventricular dysfunction: role of magnetic resonance imaging. Am Heart J. 1994;128(3):484–9.
63. Ramani K, Judd RM, Holly TA, Parrish TB, Rigolin VH, Parker MA, Callahan C, Fitzgerald SW, Bonow RO, Klocke FJ. Contrast magnetic resonance imaging in the assessment of myocardial viability in patients with stable coronary artery disease and left ventricular dysfunction. Circulation. 1998;98(24):2687–94.
64. Matsumoto H, Matsuda T, Miyamoto K, Shimada T, Ushimaru S, Mikuri M, Yamazaki T. Temporal change of enhancement after gadolinium injection on contrast-enhanced CMR in reperfused acute myocardial infarction. J Cardiol. 2015;65(1):76–81. doi:10.1016/j.jjcc.2014.04.005.
65. de Roos A, van Rossum AC, van der Wall E, Postema S, Doornbos J, Matheijssen N, van Dijkman PR, Visser FC, van Voorthuisen AE. Reperfused and nonreperfused myocardial infarction: diagnostic potential of Gd-DTPA – enhanced MR imaging. Radiology. 1989;172(3):717–20. doi:10.1148/radiology.172.3.2772179.
66. Mayr A, Klug G, Schocke M, Trieb T, Mair J, Pedarnig K, Pachinger O, Jaschke W, Metzler B. Late microvascular obstruction after acute myocardial infarction: relation with cardiac and inflammatory markers. Int J Cardiol. 2012;157(3):391–6. doi:10.1016/j.ijcard.2010.12.090.
67. Tuttle RR, Mills J. Dobutamine: development of a new catecholamine to selectively increase cardiac contractility. Circ Res. 1975;36(1):185–96.
68. Sandstede JJ, Bertsch G, Beer M, Kenn W, Werner E, Pabst T, Lipke C, Kretschmer S, Neubauer S, Hahn D. Detection of myocardial viability by low-dose dobutamine Cine MR imaging. Magn Reson Imaging. 1999;17(10):1437–43.
69. Schulz-Menger J, Bluemke DA, Bremerich J, Flamm SD, Fogel MA, Friedrich MG, Kim RJ, von Knobelsdorff-Brenkenhoff F, Kramer CM, Pennell DJ, Plein S, Nagel E. Standardized image interpretation and post processing in cardiovascular magnetic resonance: Society for Cardiovascular Magnetic Resonance (SCMR) board of trustees task force on standardized post processing. J Cardiovasc Magn Reson. 2013;15:35. doi:10.1186/1532-429X-15-35.
70. Cerqueira MD, Weissman NJ, Dilsizian V, Jacobs AK, Kaul S, Laskey WK, Pennell DJ, Rumberger JA, Ryan T, Verani MS, American Heart Association Writing Group on Myocardial S, Registration for Cardiac I. Standardized myocardial segmentation and nomenclature for tomographic imaging of the heart. A statement for healthcare professionals from the Cardiac Imaging Committee of the Council on Clinical Cardiology of the American Heart Association. Circulation. 2002;105(4):539–42.
71. Bondarenko O, Beek AM, Hofman MB, Kuhl HP, Twisk JW, van Dockum WG, Visser CA, van Rossum AC. Standardizing the definition of hyperenhancement in the quantitative assessment of infarct size and myocardial viability using delayed contrast-enhanced CMR. J Cardiovasc Magn Reson. 2005;7(2):481–5.
72. Flett AS, Hasleton J, Cook C, Hausenloy D, Quarta G, Ariti C, Muthurangu V, Moon JC. Evaluation of techniques for the quantification of myocardial scar of differing etiology using cardiac magnetic resonance. JACC Cardiovasc Imaging. 2011;4(2):150–6. doi:10.1016/j.jcmg.2010.11.015.
73. Beek AM, Bondarenko O, Afsharzada F, van Rossum AC. Quantification of late gadolinium enhanced CMR in viability assessment in chronic ischemic heart disease: a comparison to functional outcome. J Cardiovasc Magn Reson: Off J Soc Cardiovasc Magn Reson. 2009;11:6. doi:10.1186/1532-429X-11-6.
74. Baer FM, Theissen P, Schneider CA, Voth E, Sechtem U, Schicha H, Erdmann E. Dobutamine magnetic resonance imaging predicts contractile recovery of chronically dysfunctional myocardium after successful revascularization. J Am Coll Cardiol. 1998;31(5):1040–8.
75. Gutberlet M, Frohlich M, Mehl S, Amthauer H, Hausmann H, Meyer R, Siniawski H, Ruf J, Plotkin M, Denecke T, Schnackenburg B, Hetzer R, Felix R. Myocardial viability assessment in patients with highly impaired left ventricular function: comparison of delayed enhancement, dobutamine stress MRI, end-diastolic wall thickness, and TI201-SPECT with functional

recovery after revascularization. Eur Radiol. 2005;15(5):872–80. doi:10.1007/s00330-005-2653-9.
76. Selvanayagam JB, Kardos A, Francis JM, Wiesmann F, Petersen SE, Taggart DP, Neubauer S. Value of delayed-enhancement cardiovascular magnetic resonance imaging in predicting myocardial viability after surgical revascularization. Circulation. 2004;110(12):1535–41. doi:10.1161/01.CIR.0000142045.22628.74.
77. Wu YW, Tadamura E, Yamamuro M, Kanao S, Marui A, Tanabara K, Komeda M, Togashi K. Comparison of contrast-enhanced MRI with (18)F-FDG PET/201Tl SPECT in dysfunctional myocardium: relation to early functional outcome after surgical revascularization in chronic ischemic heart disease. J Nucl Med: Off Publ Soc Nucl Med. 2007;48(7):1096–103. doi:10.2967/jnumed.106.038596.
78. Wagner A, Mahrholdt H, Holly TA, Elliott MD, Regenfus M, Parker M, Klocke FJ, Bonow RO, Kim RJ, Judd RM. Contrast-enhanced MRI and routine single photon emission computed tomography (SPECT) perfusion imaging for detection of subendocardial myocardial infarcts: an imaging study. Lancet. 2003;361(9355):374–9. doi:10.1016/S0140-6736(03)12389-6.
79. Kim HW, Klem I, Shah DJ, Wu E, Meyers SN, Parker MA, Crowley AL, Bonow RO, Judd RM, Kim RJ. Unrecognized non-Q-wave myocardial infarction: prevalence and prognostic significance in patients with suspected coronary disease. PLoS Med. 2009;6(4):e1000057. doi:10.1371/journal.pmed.1000057.
80. Cigarroa CG, deFilippi CR, Brickner ME, Alvarez LG, Wait MA, Grayburn PA. Dobutamine stress echocardiography identifies hibernating myocardium and predicts recovery of left ventricular function after coronary revascularization. Circulation. 1993;88(2):430–6.
81. Barilla F, Gheorghiade M, Alam M, Khaja F, Goldstein S. Low-dose dobutamine in patients with acute myocardial infarction identifies viable but not contractile myocardium and predicts the magnitude of improvement in wall motion abnormalities in response to coronary revascularization. Am Heart J. 1991;122(6):1522–31.
82. Smart SC, Sawada S, Ryan T, Segar D, Atherton L, Berkovitz K, Bourdillon PD, Feigenbaum H. Low-dose dobutamine echocardiography detects reversible dysfunction after thrombolytic therapy of acute myocardial infarction. Circulation. 1993;88(2):405–15.
83. Pierard LA, De Landsheere CM, Berthe C, Rigo P, Kulbertus HE. Identification of viable myocardium by echocardiography during dobutamine infusion in patients with myocardial infarction after thrombolytic therapy: comparison with positron emission tomography. J Am Coll Cardiol. 1990;15(5):1021–31.
84. Baer FM, Theissen P, Crnac J, Schmidt M, Deutsch HJ, Sechtem U, Schicha H, Erdmann E. Head to head comparison of dobutamine-transoesophageal echocardiography and dobutamine-magnetic resonance imaging for the prediction of left ventricular functional recovery in patients with chronic coronary artery disease. Eur Heart J. 2000;21(12):981–91.
85. Zaglavara T, Pillay T, Karvounis H, Haaverstad R, Parharidis G, Louridas G, Kenny A. Detection of myocardial viability by dobutamine stress echocardiography: incremental value of diastolic wall thickness measurement. Heart. 2005;91(5):613–7. doi:10.1136/hrt.2003.028316.
86. Giovagnoni A, Ligabue G, Rossi R, Muia N, Modena MG, Romagnoli R. Cine magnetic resonance with dobutamine following a myocardial infarct. La Radiol Med. 1999;98(6):482–9.
87. Kramer CM, Barkhausen J, Flamm SD, Kim RJ, Nagel E, Society for Cardiovascular Magnetic Resonance Board of Trustees Task Force on Standardized P. Standardized cardiovascular magnetic resonance imaging (CMR) protocols, society for cardiovascular magnetic resonance: board of trustees task force on standardized protocols. J Cardiovascular Magn Reson: Off J Soc Cardiovasc Magn Reson. 2008;10:35. doi:10.1186/1532-429X-10-35.
88. Afridi I, Kleiman NS, Raizner AE, Zoghbi WA. Dobutamine echocardiography in myocardial hibernation. Optimal dose and accuracy in predicting recovery of ventricular function after coronary angioplasty. Circulation. 1995;91(3):663–70.

89. Bax JJ, Poldermans D, Elhendy A, Boersma E, Rahimtoola SH. Sensitivity, specificity, and predictive accuracies of various noninvasive techniques for detecting hibernating myocardium. Curr Probl Cardiol. 2001;26(2):147–86.
90. Kaandorp TA, Bax JJ, Schuijf JD, Viergever EP, van Der Wall EE, de Roos A, Lamb HJ. Head-to-head comparison between contrast-enhanced magnetic resonance imaging and dobutamine magnetic resonance imaging in men with ischemic cardiomyopathy. Am J Cardiol. 2004;93(12):1461–4. doi:10.1016/j.amjcard.2004.03.003.
91. Nagel E, Schuster A. Myocardial viability: dead or alive is not the question! JACC Cardiovasc Imaging. 2012;5(5):509–12. doi:10.1016/j.jcmg.2012.03.005.
92. Pagano D, Camici PG. Relation of contractile reserve of hibernating myocardium to myocardial structure in humans. Circulation. 2000;102(25):E189–90.
93. Roberts CS, Maclean D, Maroko P, Kloner RA. Early and late remodeling of the left ventricle after acute myocardial infarction. Am J Cardiol. 1984;54(3):407–10.
94. Thygesen K, Alpert JS, Jaffe AS, Simoons ML, Chaitman BR, White HD, Writing Group on the Joint ESCAAHAWHFTFftUDoMI, Thygesen K, Alpert JS, White HD, Jaffe AS, Katus HA, Apple FS, Lindahl B, Morrow DA, Chaitman BA, Clemmensen PM, Johanson P, Hod H, Underwood R, Bax JJ, Bonow RO, Pinto F, Gibbons RJ, Fox KA, Atar D, Newby LK, Galvani M, Hamm CW, Uretsky BF, Steg PG, Wijns W, Bassand JP, Menasche P, Ravkilde J, Ohman EM, Antman EM, Wallentin LC, Armstrong PW, Simoons ML, Januzzi JL, Nieminen MS, Gheorghiade M, Filippatos G, Luepker RV, Fortmann SP, Rosamond WD, Levy D, Wood D, Smith SC, Hu D, Lopez-Sendon JL, Robertson RM, Weaver D, Tendera M, Bove AA, Parkhomenko AN, Vasilieva EJ, Mendis S, Guidelines ESCCfP. Third universal definition of myocardial infarction. Eur Heart J. 2012;33(20):2551–67. doi:10.1093/eurheartj/ehs184.
95. Kim RJ, Shah DJ. Fundamental concepts in myocardial viability assessment revisited: when knowing how much is “alive” is not enough. Heart. 2004;90(2):137–40.
96. Shah DJ, Kim HW, James O, Parker M, Wu E, Bonow RO, Judd RM, Kim RJ. Prevalence of regional myocardial thinning and relationship with myocardial scarring in patients with coronary artery disease. JAMA. 2013;309(9):909–18. doi:10.1001/jama.2013.1381.
97. Choi KM, Kim RJ, Gubernikoff G, Vargas JD, Parker M, Judd RM. Transmural extent of acute myocardial infarction predicts long-term improvement in contractile function. Circulation. 2001;104(10):1101–7.
98. Gerber BL, Garot J, Bluemke DA, Wu KC, Lima JA. Accuracy of contrast-enhanced magnetic resonance imaging in predicting improvement of regional myocardial function in patients after acute myocardial infarction. Circulation. 2002;106(9):1083–9.
99. Beek AM, Kuhl HP, Bondarenko O, Twisk JW, Hofman MB, van Dockum WG, Visser CA, van Rossum AC. Delayed contrast-enhanced magnetic resonance imaging for the prediction of regional functional improvement after acute myocardial infarction. J Am Coll Cardiol. 2003;42(5):895–901.
100. Romero J, Kahan J, Kelesidis I, Makani H, Wever-Pinzon O, Medina H, Garcia MJ. CMR imaging for the evaluation of myocardial stunning after acute myocardial infarction: a meta-analysis of prospective trials. Eur Heart J Cardiovasc Imaging. 2013;14(11):1080–91. doi:10.1093/ehjci/jet040.
101. Abdel-Aty H, Zagrosek A, Schulz-Menger J, Taylor AJ, Messroghli D, Kumar A, Gross M, Dietz R, Friedrich MG. Delayed enhancement and T2-weighted cardiovascular magnetic resonance imaging differentiate acute from chronic myocardial infarction. Circulation. 2004;109(20):2411–6. doi:10.1161/01.CIR.0000127428.10985.C6.
102. Friedrich MG, Abdel-Aty H, Taylor A, Schulz-Menger J, Messroghli D, Dietz R. The salvaged area at risk in reperfused acute myocardial infarction as visualized by cardiovascular magnetic resonance. J Am Coll Cardiol. 2008;51(16):1581–7. doi:10.1016/j.jacc.2008.01.019.
103. Pennell D. Myocardial salvage: retrospection, resolution, and radio waves. Circulation. 2006;113(15):1821–3. doi:10.1161/CIRCULATIONAHA.105.618942.
104. Larose E, Tizon-Marcos H, RodÈs-Cabau J, Rinfret S, DÈry J-P, Nguyen CM, Gleeton O, Boudreault J-R, Roy L, NoÎl B, Proulx G, Rouleau J, Barbeau G, LarochelliËre RD, Bertrand

OF. Improving myocardial salvage in late presentation acute ST-elevation myocardial infarction with proximal embolic protection. Catheter Cardiovasc Interv. 2010;76(4):461–70.
105. Botker HE, Kaltoft AK, Pedersen SF, Kim WY. Measuring myocardial salvage. Cardiovasc Res. 2012;94(2):266–75. doi:10.1093/cvr/cvs081.
106. Eitel I, Desch S, Fuernau G, Hildebrand L, Gutberlet M, Schuler G, Thiele H. Prognostic significance and determinants of myocardial salvage assessed by cardiovascular magnetic resonance in acute reperfused myocardial infarction. J Am Coll Cardiol. 2010;55(22):2470–9.
107. Wu KC. CMR of microvascular obstruction and hemorrhage in myocardial infarction. J Cardiovasc Magn Reson: Off J Soc Cardiovasc Magn Reson. 2012;14:68. doi:10.1186/1532-429X-14-68.
108. Bekkers SC, Backes WH, Kim RJ, Snoep G, Gorgels AP, Passos VL, Waltenberger J, Crijns HJ, Schalla S. Detection and characteristics of microvascular obstruction in reperfused acute myocardial infarction using an optimized protocol for contrast-enhanced cardiovascular magnetic resonance imaging. Eur Radiol. 2009;19(12):2904–12. doi:10.1007/s00330-009-1489-0.
109. Wu KC, Zerhouni EA, Judd RM, Lugo-Olivieri CH, Barouch LA, Schulman SP, Blumenthal RS, Lima JA. Prognostic significance of microvascular obstruction by magnetic resonance imaging in patients with acute myocardial infarction. Circulation. 1998;97(8):765–72.
110. Hamirani YS, Wong A, Kramer CM, Salerno M. Effect of microvascular obstruction and intramyocardial hemorrhage by CMR on LV remodeling and outcomes after myocardial infarction: a systematic review and meta-analysis. JACC Cardiovasc Imaging. 2014;7(9):940–52. doi:10.1016/j.jcmg.2014.06.012.
111. Dall'Armellina E, Karia N, Lindsay AC, Karamitsos TD, Ferreira V, Robson MD, Kellman P, Francis JM, Forfar C, Prendergast BD, Banning AP, Channon KM, Kharbanda RK, Neubauer S, Choudhury RP. Dynamic changes of edema and late gadolinium enhancement after acute myocardial infarction and their relationship to functional recovery and salvage index. Circ Cardiovasc Imaging. 2011;4(3):228–36. doi:10.1161/CIRCIMAGING.111.963421.
112. Engblom H, Hedstrom E, Heiberg E, Wagner GS, Pahlm O, Arheden H. Rapid initial reduction of hyperenhanced myocardium after reperfused first myocardial infarction suggests recovery of the peri-infarction zone: one-year follow-up by MRI. Circ Cardiovasc Imaging. 2009;2(1):47–55. doi:10.1161/CIRCIMAGING.108.802199.
113. Mather AN, Fairbairn TA, Artis NJ, Greenwood JP, Plein S. Timing of cardiovascular MR imaging after acute myocardial infarction: effect on estimates of infarct characteristics and prediction of late ventricular remodeling. Radiology. 2011;261(1):116–26. doi:10.1148/radiol.11110228.
114. Hammer-Hansen S, Bandettini WP, Hsu LY, Leung SW, Shanbhag S, Mancini C, Greve AM, Kober L, Thune JJ, Kellman P, Arai AE. Mechanisms for overestimating acute myocardial infarct size with gadolinium-enhanced cardiovascular magnetic resonance imaging in humans: a quantitative and kinetic study dagger. Eur Heart J Cardiovasc Imaging. 2016;17(1):76–84. doi:10.1093/ehjci/jev123.
115. Carrick D, Haig C, Ahmed N, Rauhalammi S, Clerfond G, Carberry J, Mordi I, McEntegart M, Petrie MC, Eteiba H, Hood S, Watkins S, Lindsay MM, Mahrous A, Welsh P, Sattar N, Ford I, Oldroyd KG, Radjenovic A, Berry C. Temporal evolution of myocardial hemorrhage and edema in patients after acute ST-segment elevation myocardial infarction: pathophysiological insights and clinical implications. J Am Heart Assoc. 2016;5(2) doi:10.1161/JAHA.115.002834.
116. Fernandez-Jimenez R, Sanchez-Gonzalez J, Aguero J, Garcia-Prieto J, Lopez-Martin GJ, Garcia-Ruiz JM, Molina-Iracheta A, Rossello X, Fernandez-Friera L, Pizarro G, Garcia-Alvarez A, Dall'Armellina E, Macaya C, Choudhury RP, Fuster V, Ibanez B. Myocardial edema after ischemia/reperfusion is not stable and follows a bimodal pattern: imaging and histological tissue characterization. J Am Coll Cardiol. 2015;65(4):315–23. doi:10.1016/j.jacc.2014.11.004.

117. Risk stratification and survival after myocardial infarction. N Engl J Med. 1983;309(6):331–336. doi:10.1056/NEJM198308113090602.
118. Carrick D, Haig C, Rauhalammi S, Ahmed N, Mordi I, McEntegart M, Petrie MC, Eteiba H, Hood S, Watkins S, Lindsay M, Mahrous A, Ford I, Tzemos N, Sattar N, Welsh P, Radjenovic A, Oldroyd KG, Berry C. Prognostic significance of infarct core pathology revealed by quantitative non-contrast in comparison with contrast cardiac magnetic resonance imaging in reperfused ST-elevation myocardial infarction survivors. Eur Heart J. 2016;37(13):1044–59. doi:10.1093/eurheartj/ehv372.
119. White HD, Norris RM, Brown MA, Brandt PW, Whitlock RM, Wild CJ. Left ventricular end-systolic volume as the major determinant of survival after recovery from myocardial infarction. Circulation. 1987;76(1):44–51.
120. Burns RJ, Gibbons RJ, Yi Q, Roberts RS, Miller TD, Schaer GL, Anderson JL, Yusuf S. The relationships of left ventricular ejection fraction, end-systolic volume index and infarct size to six-month mortality after hospital discharge following myocardial infarction treated by thrombolysis. J Am Coll Cardiol. 2002;39:30–6.
121. Hombach V, Grebe O, Merkle N, Waldenmaier S, Hoher M, Kochs M, Wohrle J, Kestler HA. Sequelae of acute myocardial infarction regarding cardiac structure and function and their prognostic significance as assessed by magnetic resonance imaging. Eur Heart J. 2005;26(6):549–57. doi:10.1093/eurheartj/ehi147.
122. Lund GK, Stork A, Muellerleile K, Barmeyer AA, Bansmann MP, Knefel M, Schlichting U, Muller M, Verde PE, Adam G, Meinertz T, Saeed M. Prediction of left ventricular remodeling and analysis of infarct resorption in patients with reperfused myocardial infarcts by using contrast-enhanced MR imaging1. Radiology. 2007;245(1):95–102. doi:10.1148/radiol.2451061219.
123. Nijveldt R, Beek AM, Hirsch A, Stoel MG, Hofman MB, Umans VA, Algra PR, Twisk JW, van Rossum AC. Functional recovery after acute myocardial infarction: comparison between angiography, electrocardiography, and cardiovascular magnetic resonance measures of microvascular injury. J Am Coll Cardiol. 2008;52(3):181–9. doi:10.1016/j.jacc.2008.04.006.
124. Kwong RY, Chan AK, Brown KA, Chan CW, Reynolds HG, Tsang S, Davis RB. Impact of unrecognized myocardial scar detected by cardiac magnetic resonance imaging on event-free survival in patients presenting with signs or symptoms of coronary artery disease. Circulation. 2006;113(23):2733–43. doi:10.1161/CIRCULATIONAHA.105.570648.
125. Roes SD, Kelle S, Kaandorp TA, Kokocinski T, Poldermans D, Lamb HJ, Boersma E, van der Wall EE, Fleck E, de Roos A, Nagel E, Bax JJ. Comparison of myocardial infarct size assessed with contrast-enhanced magnetic resonance imaging and left ventricular function and volumes to predict mortality in patients with healed myocardial infarction. Am J Cardiol. 2007;100(6):930–6. doi:10.1016/j.amjcard.2007.04.029.
126. de Waha S, Desch S, Eitel I, Fuernau G, Zachrau J, Leuschner A, Gutberlet M, Schuler G, Thiele H. Impact of early vs. late microvascular obstruction assessed by magnetic resonance imaging on long-term outcome after ST-elevation myocardial infarction: a comparison with traditional prognostic markers. Eur Heart J. 2010;31(21):2660–8. doi:10.1093/eurheartj/ehq247.
127. van Kranenburg M, Magro M, Thiele H, de Waha S, Eitel I, Cochet A, Cottin Y, Atar D, Buser P, Wu E, Lee D, Bodi V, Klug G, Metzler B, Delewi R, Bernhardt P, Rottbauer W, Boersma E, Zijlstra F, van Geuns RJ. Prognostic value of microvascular obstruction and infarct size, as measured by CMR in STEMI patients. JACC Cardiovasc Imaging. 2014;7(9):930–9. doi:10.1016/j.jcmg.2014.05.010.
128. El Aidi H, Adams A, Moons KG, Den Ruijter HM, Mali WP, Doevendans PA, Nagel E, Schalla S, Bots ML, Leiner T. Cardiac magnetic resonance imaging findings and the risk of cardiovascular events in patients with recent myocardial infarction or suspected or known coronary artery disease: a systematic review of prognostic studies. J Am Coll Cardiol. 2014;63(11):1031–45. doi:10.1016/j.jacc.2013.11.048.
129. Gerber BL, Rousseau MF, Ahn SA, le Polain de Waroux JB, Pouleur AC, Phlips T, Vancraeynest D, Pasquet A, Vanoverschelde JL. Prognostic value of myocardial viability by delayed-enhanced magnetic resonance in patients with coronary artery disease and low

ejection fraction: impact of revascularization therapy. J Am Coll Cardiol. 2012;59(9):825–35. doi:10.1016/j.jacc.2011.09.073.
130. Bax JJ, Poldermans D, Elhendy A, Cornel JH, Boersma E, Rambaldi R, Roelandt JR, Fioretti PM. Improvement of left ventricular ejection fraction, heart failure symptoms and prognosis after revascularization in patients with chronic coronary artery disease and viable myocardium detected by dobutamine stress echocardiography. J Am Coll Cardiol. 1999;34(1):163–9.
131. Ma D, Gulani V, Seiberlich N, Liu K, Sunshine JL, Duerk JL, Griswold MA. Magnetic resonance fingerprinting. Nature. 2013;495(7440):187–92. doi:10.1038/nature11971.
132. Hudsmith LE, Neubauer S. Magnetic resonance spectroscopy in myocardial disease. JACC Cardiovasc Imaging. 2009;2(1):87–96. doi:10.1016/j.jcmg.2008.08.005.
133. Rider OJ, Tyler DJ. Clinical Implications of cardiac hyperpolarized magnetic resonance Imaging. J Cardiovasc Magn Reson. 2013;15(1):93. doi:10.1186/1532-429X-15-93.
134. Piechnik SK, Ferreira VM, Dall'Armellina E, Cochlin LE, Greiser A, Neubauer S, Robson MD. Shortened Modified Look-Locker Inversion recovery (ShMOLLI) for clinical myocardial T1-mapping at 1.5 and 3 T within a 9 heartbeat breathhold. J Cardiovasc Magn Reson: Off J Soc Cardiovasc Magn Reson. 2010;12:69. doi:10.1186/1532-429X-12-69.
135. Messroghli DR, Walters K, Plein S, Sparrow P, Friedrich MG, Ridgway JP, Sivananthan MU. Myocardial T1 mapping: application to patients with acute and chronic myocardial infarction. Magn Reson Med. 2007;58(1):34–40. doi:10.1002/mrm.21272.
136. Giri S, Chung YC, Merchant A, Mihai G, Rajagopalan S, Raman SV, Simonetti OP. T2 quantification for improved detection of myocardial edema. J Cardiovasc Magn Reson: Off J Soc Cardiovasc Magn Reson. 2009;11:56. doi:10.1186/1532-429X-11-56.
137. Piechnik SK, Ferreira VM, Lewandowski AJ, Ntusi NA, Banerjee R, Holloway C, Hofman MB, Sado DM, Maestrini V, White SK, Lazdam M, Karamitsos T, Moon JC, Neubauer S, Leeson P, Robson MD. Normal variation of magnetic resonance T1 relaxation times in the human population at 1.5 T using ShMOLLI. J Cardiovasc Magn Reson: Off J Soc Cardiovasc Magn Reson. 2013;15:13. doi:10.1186/1532-429X-15-13.
138. Bottomley PA, Foster TH, Argersinger RE, Pfeifer LM. A review of normal tissue hydrogen NMR relaxation times and relaxation mechanisms from 1–100 MHz: dependence on tissue type, NMR frequency, temperature, species, excision, and age. Med Phys. 1984;11(4):425–48. doi:10.1118/1.595535.
139. Messroghli DR, Niendorf T, Schulz-Menger J, Dietz R, Friedrich MG. T1 mapping in patients with acute myocardial infarction. J Cardiovasc Magn Reson: Off J Soc Cardiovasc Magn Reson. 2003;5(2):353–9.
140. Liu A, Wijesurendra RS, Francis JM, Robson MD, Neubauer S, Piechnik SK, Ferreira VM. Adenosine stress and rest T1 mapping can differentiate between ischemic, infarcted, remote, and normal myocardium without the need for gadolinium contrast agents. JACC Cardiovasc Imaging. 2016;9(1):27–36. doi:10.1016/j.jcmg.2015.08.018.
141. Dall'armellina E, Piechnik SK, Ferreira VM, Le Si Q, Robson MD, Francis JM, Cuculi F, Kharbanda RK, Banning AP, Choudhury RP, Karamitsos TD, Neubauer S. Cardiovascular magnetic resonance by non contrast T1 mapping allows assessment of severity of injury in acute myocardial infarction. J Cardiovasc Magn Reson: Off J Soc Cardiovasc Magn Reson. 2012;14(1):15. doi:10.1186/1532-429X-14-15.
142. Dall'armellina E, Ferreira VM, Kharbanda RK, Prendergast B, Piechnik SK, Robson MD, Jones M, Francis JM, Choudhury RP, Neubauer S. Diagnostic value of pre-contrast t1 mapping in acute and chronic myocardial infarction. JACC Cardiovasc Imaging. 2013;6(6):739–42. doi:10.1016/j.jcmg.2012.11.020.
143. Carrick D, Haig C, Rauhalammi S, Ahmed N, Mordi I, McEntegart M, Petrie MC, Eteiba H, Lindsay M, Watkins S, Hood S, Davie A, Mahrous A, Sattar N, Welsh P, Tzemos N, Radjenovic A, Ford I, Oldroyd KG, Berry C. Pathophysiology of LV remodeling in survivors of STEMI: inflammation, remote myocardium, and prognosis. JACC Cardiovasc Imaging. 2015;8(7):779–89. doi:10.1016/j.jcmg.2015.03.007.

144. Kali A, Choi EY, Sharif B, Kim YJ, Bi X, Spottiswoode B, Cokic I, Yang HJ, Tighiouart M, Conte AH, Li D, Berman DS, Choi BW, Chang HJ, Dharmakumar R. Native T1 Mapping by 3-T CMR imaging for characterization of chronic myocardial infarctions. JACC Cardiovasc Imaging. 2015;8(9):1019–30. doi:10.1016/j.jcmg.2015.04.018.
145. Salerno M, Kramer CM. Advances in parametric mapping with CMR imaging. JACC Cardiovasc Imaging. 2013;6(7):806–22. doi:10.1016/j.jcmg.2013.05.005.
146. Wong TC, Piehler KM, Kang IA, Kadakkal A, Kellman P, Schwartzman DS, Mulukutla SR, Simon MA, Shroff SG, Kuller LH, Schelbert EB. Myocardial extracellular volume fraction quantified by cardiovascular magnetic resonance is increased in diabetes and associated with mortality and incident heart failure admission. Eur Heart J. 2014;35(10):657–64. doi:10.1093/eurheartj/eht193.
147. Wong TC, Piehler K, Meier CG, Testa SM, Klock AM, Aneizi AA, Shakesprere J, Kellman P, Shroff SG, Schwartzman DS, Mulukutla SR, Simon MA, Schelbert EB. Association between extracellular matrix expansion quantified by cardiovascular magnetic resonance and short-term mortality. Circulation. 2012;126(10):1206–16. doi:10.1161/CIRCULATIONAHA.111.089409.
148. Verhaert D, Thavendiranathan P, Giri S, Mihai G, Rajagopalan S, Simonetti OP, Raman SV. Direct T2 quantification of myocardial edema in acute ischemic injury. JACC Cardiovasc Imag. 2011;4(3):269–78. doi:10.1016/j.jcmg.2010.09.023.
149. Ruparelia N, Godec J, Lee R, Chai JT, Dall'Armellina E, McAndrew D, Digby JE, Forfar JC, Prendergast BD, Kharbanda RK, Banning AP, Neubauer S, Lygate CA, Channon KM, Haining NW, Choudhury RP. Acute myocardial infarction activates distinct inflammation and proliferation pathways in circulating monocytes, prior to recruitment, and identified through conserved transcriptional responses in mice and humans. Eur Heart J. 2015;36(29):1923–34. doi:10.1093/eurheartj/ehv195.
150. Lee WW, Marinelli B, van der Laan AM, Sena BF, Gorbatov R, Leuschner F, Dutta P, Iwamoto Y, Ueno T, Begieneman MP, Niessen HW, Piek JJ, Vinegoni C, Pittet MJ, Swirski FK, Tawakol A, Di Carli M, Weissleder R, Nahrendorf M. PET/MRI of inflammation in myocardial infarction. J Am Coll Cardiol. 2012;59(2):153–63. doi:10.1016/j.jacc.2011.08.066.
151. Zia MI, Ghugre NR, Connelly KA, Strauss BH, Sparkes JD, Dick AJ, Wright GA. Characterizing myocardial edema and hemorrhage using quantitative T2 and T2* mapping at multiple time intervals post ST-segment elevation myocardial infarction. Circ Cardiovasc Imaging. 2012;5(5):566–72. doi:10.1161/CIRCIMAGING.112.973222.
152. Sosnovik DE, Wang R, Dai G, Reese TG, Wedeen VJ. Diffusion MR tractography of the heart. J Cardiovasc Magn Reson: Off J Soc Cardiovasc Magn Reson. 2009;11:47. doi:10.1186/1532-429X-11-47.
153. Mekkaoui C, Huang S, Chen HH, Dai G, Reese TG, Kostis WJ, Thiagalingam A, Maurovich-Horvat P, Ruskin JN, Hoffmann U, Jackowski MP, Sosnovik DE. Fiber architecture in remodeled myocardium revealed with a quantitative diffusion CMR tractography framework and histological validation. J Cardiovasc Magn Reson: Off J Soc Cardiovasc Magn Reson. 2012;14:70. doi:10.1186/1532-429X-14-70.
154. Tseng WY, Dou J, Reese TG, Wedeen VJ. Imaging myocardial fiber disarray and intramural strain hypokinesis in hypertrophic cardiomyopathy with MRI. J Magn Reson Imaging: JMRI. 2006;23(1):1–8. doi:10.1002/jmri.20473.
155. Gamper U, Boesiger P, Kozerke S. Diffusion imaging of the in vivo heart using spin echoes – considerations on bulk motion sensitivity. Magn Reson Med. 2007;57(2):331–7. doi:10.1002/mrm.21127.
156. Wu MT, Tseng WY, Su MY, Liu CP, Chiou KR, Wedeen VJ, Reese TG, Yang CF. Diffusion tensor magnetic resonance imaging mapping the fiber architecture remodeling in human myocardium after infarction: correlation with viability and wall motion. Circulation. 2006;114(10):1036–45. doi:10.1161/CIRCULATIONAHA.105.545863.
157. Lindner JR, Sinusas A. Molecular imaging in cardiovascular disease: which methods, which diseases? J Nucl Cardiol: Off Publ Am Soc Nucl Cardiol. 2013;20(6):990–1001. doi:10.1007/s12350-013-9785-0.

158. Chen HH, Josephson L, Sosnovik DE. Imaging of apoptosis in the heart with nanoparticle technology. Wiley Interdiscip Rev Nanomedicine Nanobiotechnol. 2011;3(1):86–99. doi:10.1002/wnan.115.
159. Yilmaz A, Dengler MA, van der Kuip H, Yildiz H, Rosch S, Klumpp S, Klingel K, Kandolf R, Helluy X, Hiller KH, Jakob PM, Sechtem U. Imaging of myocardial infarction using ultrasmall superparamagnetic iron oxide nanoparticles: a human study using a multi-parametric cardiovascular magnetic resonance imaging approach. Eur Heart J. 2013;34(6):462–75. doi:10.1093/eurheartj/ehs366.
160. Naresh NK, Xu Y, Klibanov AL, Vandsburger MH, Meyer CH, Leor J, Kramer CM, French BA, Epstein FH. Monocyte and/or macrophage infiltration of heart after myocardial infarction: MR imaging by using T1-shortening liposomes. Radiology. 2012;264(2):428–35. doi:10.1148/radiol.12111863.
161. Winter PM, Neubauer AM, Caruthers SD, Harris TD, Robertson JD, Williams TA, Schmieder AH, Hu G, Allen JS, Lacy EK, Zhang H, Wickline SA, Lanza GM. Endothelial alpha(v)beta3 integrin-targeted fumagillin nanoparticles inhibit angiogenesis in atherosclerosis. Arterioscler Thromb Vasc Biol. 2006;26(9):2103–9. doi:10.1161/01.ATV.0000235724.11299.76.
162. Andia ME, Saha P, Jenkins J, Modarai B, Wiethoff AJ, Phinikaridou A, Grover SP, Patel AS, Schaeffter T, Smith A, Botnar RM. Fibrin-targeted magnetic resonance imaging allows in vivo quantification of thrombus fibrin content and identifies thrombi amenable for thrombolysis. Arterioscler Thromb Vasc Biol. 2014;34(6):1193–8. doi:10.1161/ATVBAHA.113.302931.
163. Amano Y, Suzuki Y, van Cauteren M. Evaluation of global cardiac functional parameters using single-breath-hold three-dimensional cine steady-state free precession MR imaging with two types of speed-up techniques: comparison with two-dimensional cine imaging. Comput Med Imaging Graph: Off J Comp Med Imaging Soc. 2008;32(1):61–6. doi:10.1016/j.compmedimag.2007.09.003.
164. Mascarenhas NB, Muthupillai R, Cheong B, Pereyra M, Flamm SD. Fast 3D cine steady-state free precession imaging with sensitivity encoding for assessment of left ventricular function in a single breath-hold. AJR Am J Roentgenol. 2006;187(5):1235–9. doi:10.2214/AJR.06.0169.
165. Uribe S, Tangchaoren T, Parish V, Wolf I, Razavi R, Greil G, Schaeffter T. Volumetric cardiac quantification by using 3D dual-phase whole-heart MR imaging. Radiology. 2008;248(2):606–14. doi:10.1148/radiol.2482071568.
166. Kramer CM, Barkhausen J, Flamm SD, Kim RJ, Nagel E, Society for Cardiovascular Magnetic Resonance Board of Trustees Task Force on Standardized P. Standardized cardiovascular magnetic resonance (CMR) protocols 2013 update. J Cardiovasc Magn Reson: Off J Soc Cardiovasc Magn Reson. 2013;15:91. doi:10.1186/1532-429X-15-91.

Chapter 12
Pediatric and Congenital Heart Disease

Vivek Muthurangu

Abbreviations

3D	Three-dimensional
3D	Two-dimensional
bSSFP	Balanced steady state free precession
CEMRA	Contrast enhanced MR angiography
CHD	Congenital heart disease
CMR	Cardiovascular magnetic resonance
GRE	Gradient echo
PCMR	Phase contrast magnetic resonance
Qp:Qs	Pulmonary to systemic blood flow ratio
RV	Right ventricle
TE	Echo time
TR	Repetition time
VENC	Maximum encoded velocity

Introduction

Cardiovascular magnetic resonance (CMR) in congenital heart disease (CHD) and paediatric heart disease is similar to CMR in adult acquired heart disease. However, the clinical questions in CHD are different and consequently, there is a different emphasis in terms of the sequences used and processing performed. In the following

V. Muthurangu
Institute of Cardiovascular Science, University College London, London, UK

Department of Cardiology, Great Ormond Street Hospital, London, UK
e-mail: v.muthurangu@ucl.ac.uk

C. Constantinides (ed.), *Protocols and Methodologies in Basic Science and Clinical Cardiac MRI*, https://doi.org/10.1007/978-3-319-53001-7_12

section, the main sequences used in congenital and pediatric heart disease will be reviewed and optimizations for the paediatric population discussed.

Balanced Steady State Free Precession (SSFP)

Imaging Physics and Fundamentals

Balanced steady state free precession (bSSFP) is a gradient echo sequence that primarily relies on steady state magnetisation for signal production. In bSSFP sequences, the steady state signal is optimised using both an alternating excitation pulse train and balancing all the gradients [1]. Balancing of the gradients is achieved by (i) the addition of a second negative lobe in the readout direction (ii) a second phase encode gradient in the opposite direction after the readout (rewinder gradient) and (iii) full balancing of the slice select gradient. By balancing the gradients, the magnetization has increased coherency prior to the next excitation. This coherent magnetisation is flipped alternatively by +α° and -α°, and this leads to the magnetisation reaching a steady state. Since balancing of the gradients takes approximately the same time to apply as the encoding gradients, repetition time (TR) equals 2 times the echo time (TE) in bSSFP sequences.

Unlike spoiled gradient sequences, the steady state signal in bSSFP sequences is dependant on the square root of the T2/T1 ratio and the proton density [1]. Consequently, the blood signal is much higher than the myocardial signal (blood: T1 = 1,200 ms, T2 = 200 ms, myocardium: T1 = 867 ms, T2 = 57 ms at 1.5 T) [2]. The bSSFP signal is also dependent on the optimum flip angle, which is different in different tissues. The optimum flip angle for blood is 45° while for myocardium it is approximately 30°. Thus, when performing b-SSFP imaging with a flip angle of 45° the blood signal is approximately two times greater than the myocardial signal. These facts make bSSFP technique well suited for cardiac applications and two of the techniques widely used in congenital heart disease are described below.

Two-Dimensional SSFP Cine Imaging

Two-dimensional (2D) SSFP cine imaging is used extensively in the evaluation of CHD. Specifically, it is used to dynamically assess anatomy (i.e. left ventricular outflow tract obstruction), valvular dysfunction (i.e. pulmonary regurgitation), and ventricular function. Unlike spoiled gradient-echo cine sequences, bSSFP sequences are partially flow compensated and the blood pool signal is mostly homogenous throughout the cardiac cycle [1]. This provides better delineation of the cardiac structures across the entire cardiac cycle, which is useful when

dynamically assessing anatomy. It should also be noted that high velocity jets cause signal loss and this can be used to qualitatively assess stenosed valves or obstructed conduits.

Multi-slice 2D SSFP cine imaging is also useful in congenital imaging since it is the reference standard method of assessing ventricular volumes. This is because, unlike echocardiography, CMR evaluation of ventricular volumes does not rely on geometrical models. The robust assessment of ventricular volumes is particularly important in congenital heart disease for two reasons. Firstly, the right ventricle (RV) is usually of more interest than the left ventricle (i.e. in repaired tetralogy of Fallot or post atrial switch) and the RV is difficult to fully visualize using echocardiography. Secondly, ventricular anatomy may be very abnormal in CHD, which renders geometrical models or assessment from limited 2D views inaccurate. One issue with conventional 2D SSFP cine sequences is that they require breath holds. This may not be tolerated in children, particularly those with significant cardiac disease. Consequently, general anaesthesia is often used in children less than 8 years of age to guarantee apnoea during CMR scanning.

Methodology and optimization for the paediatric population: Adult bSSFP cine protocols will often result in sub-optimal images when used in the paediatric population. This is because several optimizations are required to successfully image children. One of the most obvious differences between children and adults are the smaller cardiac structures. Conventionally, one would increase spatial resolution to compensate for smaller structures. However, there are problems with this approach when performing 2D SSFP cine imaging in children. Firstly, increasing spatial resolution results in a longer TR, which increases dark band artefacts. Dark-band artefacts are caused by dephasing due to magnetic field inhomogeneities. Increasing TR results in greater phase accrual and this increases dark-band artefacts. This is particularly problematic in the presence of turbulent flow and it is empirically better in these cases if the TR does not exceed 3.5 ms. Secondly, increasing spatial resolution results in a reduction in signal to noise ratio. This can adversely affect image quality and may make it difficult to evaluate fine cardiac structures. Finally, increasing spatial resolution will also increase scan time and thus, prolong breath holds. This might be difficult in small children and increases the likelihood of motion artefacts due to residual respiratory motion. Thus, increasing spatial resolution can actually lead to poorer image quality (Fig. 12.1) and this should be considered when optimizing cine imaging for small children.

Another significant difference between children and adults that must be considered when optimizing scan parameters is higher heart rate. This is particularly important when deciding on the temporal resolution of dynamic cine imaging. Most cine sequences are now retrospectively cardiac gated and images can be reconstructed with an arbitrary number of phases in the cardiac cycle. However, the arbitrary phases produced in retrospective gating are the result of interpolation. Thus, the true temporal resolution is still related to the number of lines per segment. An estimate of the true temporal resolution can be found by multiplying the TR by the

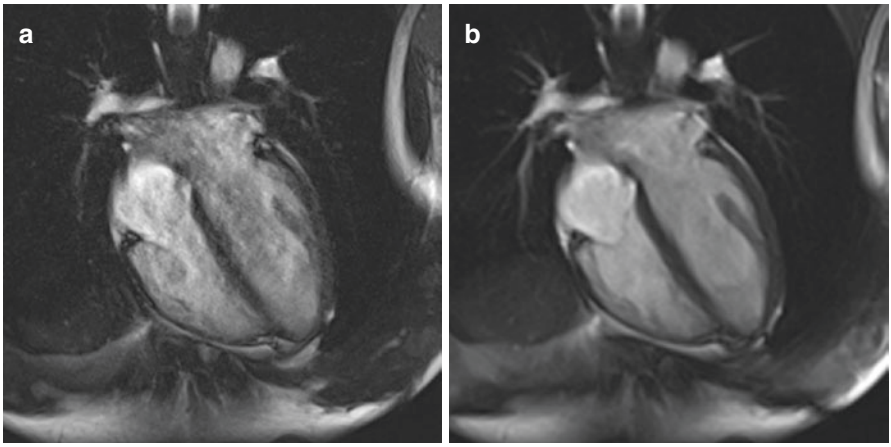

Fig. 12.1 4-chamber SSFP cine (**a**) high resolution with increased artefacts due to higher SNR and dark bands (**b**) normal resolution with better image quality

Table 12.1 Representative parameters for 2D SSFP cine imaging in different age groups

Parameter	Adult	Child	Infant
FOV (mm)	350	300	250
TR/TE (ms)	3.0/1.5	3.2/1.6	3.2/1.6
Number of phase encode steps	256	208–224	192–208
Slice thickness (mm)	8–10	6–8	5–6
Spatial resolution (mm)	1.4	1.3–1.4	1.2–1.3
Parallel imaging acceleration factor	2	2	1–2
Temporal resolution (ms)	40	30	20

number of lines per segment (not exact because of retrospective gating). There has been considerable amount of work into the determination of number of cardiac phases required for accurate delineation of cardiac motion and most studies suggest that approximately 20 true phases per cardiac cycle are necessary [3]. Suggested parameters for imaging in different age groups are shown in Table 12.1.

3D SSFP Whole Heart Imaging

Three-dimensional (3D) SSFP whole heart techniques have enabled improved visualisation of cardiac anatomy without contrast or the requirement for expert planning [4]. In congenital heart disease, this is particularly desirable as anatomy is often complex and image planning during acquisition can be difficult and time consuming. Most whole heart techniques are single-phase acquisitions triggered in a period of relative cardiac quiescence. This reduces cardiac motion artefacts and enables robust assessment of intra-cardiac anatomy. Unfortunately, cardiac gated 3D

acquisitions are time consuming and whole heart acquisitions cannot be conventionally acquired in a single breath hold. Consequently, most whole heart acquisitions are acquired using respiratory navigators during free breathing. Respiratory navigators are simple MR measurements of diaphragmatic position that can be used to restrict data acquisition to a certain position in the respiratory cycle. A navigator usually consists of a 2D RF pulse that excites a cylinder of tissue (a so-called pencil beam excitation) and a single readout along the length of the cylinder. The navigator is usually placed on the dome of the right hemi-diaphragm and the inverse Fourier transform of the readout allows identification of the position of the diaphragm in real-time [5]. This navigator signal can then used to limit data acquisition to specific diaphragmatic positions (2–4 mm excursion). This removes respiratory motion artifact but does result in scan times of up to 10–15 min.

In order to improve contrast, several magnetization preparation schemes are also utilized in 3D whole heart imaging. The first is T2 preparation, which significantly improves myocardial blood pool contrast. This is important in 3D SSFP techniques, as contrast is lower than in 2D SSFP techniques due to saturation affects. The second is fat saturation usually accomplished using a spectral inversion recovery pulse. This reduces pericardial fat signal and is particularly important when imaging the coronary arteries. The resultant images have high myocardial /blood pool contrast and sharp edges (Fig. 12.2), allowing volume and surface rendering based on simple thresholding techniques. In addition, reconstructed voxel size is usually almost isotropic allowing accurate multi-planar reformatting [4].

Methodology and optimization for the paediatric population: Whole heart imaging often produces poor quality images when performed without optimization. This is partly due to issues related to bSSFP readout, as discussed in the section of 2D bSSFP cine imaging. However, there are also issues specific to whole heart imaging that should be considered [6]. The first is the need to acquire data in a period of rela-

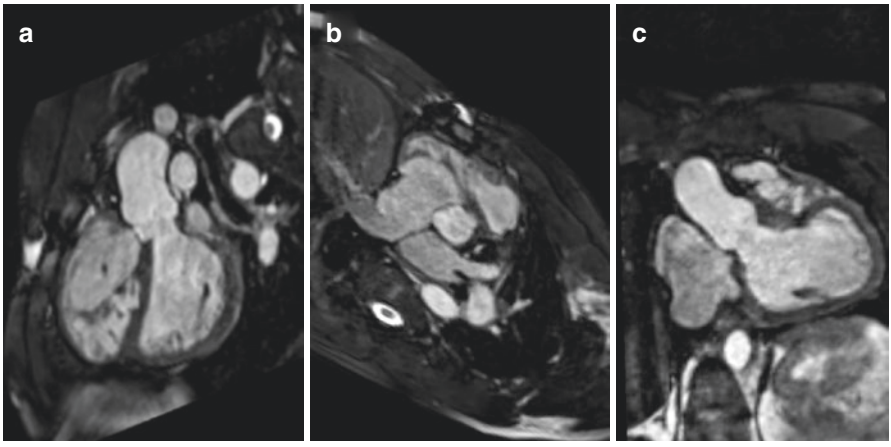

Fig. 12.2 Multi-planar reformat of a 3D SSFP whole heart of a child with repaired tetralogy of Fallot showing excellent myocardial blood pool contrast: (**a**) sagittal oblique reformat, (**b**) transverse oblique reformat, (**c**) coronal oblique reformat

Table 12.2 Representative parameters for 3D whole heart SSFP imaging in different age groups

Parameter	Adult	Child	Infant
FOV (mm)	400	330	300
TR/TE (ms)	3.0/1.5	3.2/1.6	3.2/1.6
Number of phase encode steps	256–272	256	256
Slice thickness (mm)	1.5–1.6	1.3	1.2
Spatial resolution (mm)	1.5–1.6	1.3	1.2
Parallel imaging acceleration factor	2–3	2	1–2
Acquisition window (ms)	80–100	60–80	50–60

tive cardiac quiescence. In adults, this period is usually diastasis and acquiring data towards the end of the cardiac cycle is often sufficient to ensure sharp delineation of intra-cardiac structures. This is not the case in children, as the position and length of the period cardiac quiescence is often variable often being in end systole [7]. Thus in the pediatric population, the position and length of cardiac quiescence often requires patient specific identification. This can be accomplished by evaluating the motion during the cardiac cycle using a suitable cine (i.e. using the four chamber view). From the cine images the exact location (systole or diastole) and length of cardiac quiescence can be evaluated and the whole heart sequence optimized accordingly. A further useful optimization in children is to perform 3D bSSFP imaging just after gadolinium contrast administration. Even though whole heart bSSFP sequences are theoretically 'non-contrast', they do benefit from the presence of Gadolinium due to its T1 shortening effect. It must be remembered that 3D whole heart imaging in neonates is still difficult and likely produces poorer quality imaging, due to very high heart rates, a lower signal to noise ratio and increased flow related artefacts. Suggested parameters for imaging in different age groups are shown in Table 12.2.

Spoiled Gradient Echo Imaging

Imaging Physics and Fundamentals

Gradient echo (GRE) sequences are commonly used to dynamically image the heart. The fundamental difference between GRE and spin echo sequences is the lack of a refocusing pulse, and the use of a partial flip angle (less than 90°). Although faster than spin echo sequences, dephasing due to external field inhomogeneities is still present resulting in reduced signal.

In GRE sequences, tissue contrast is heavily influenced by TR and flip angle. Short TR's and high flip angles increase T1 weighting because they allow less magnetization to recover. As TR's are often kept short for cardiac applications, cardiac GRE sequences are consequently heavily T1 weighted. GRE sequences also exhibit inflow related signal enhancement. In GRE imaging, the longitudinal magnetisation does not fully recover before the next RF pulse. This results in less magnetization being available for excitation during the next RF excitation (the basis of T1 weighting). However,

if unexcited protons move into the imaging slice (i.e. due to blood moving in the through plane direction), the total magnetisation available to be flipped into the transverse plane is increased. Thus, structures that contain blood moving in the through-plane direction appear brighter than surrounding stationary tissue.

One important issue with gradient echo imaging is the presence of coherent transverse magnetization at the end of each TR. Unfortunately, coherent transverse magnetization combines with the flipped magnetization from the next pulse in an unpredictable way and this cause artifacts. Consequently, at the end of each TR the transverse magnetization is usually spoiled using either RF or gradient spoiling. This type of sequence is called a spoiled gradient echo sequence and is the most commonly used simple GRE sequence. Spoiled GRE sequences were initially the mainstay of dynamic cardiac MR. However due to poor myocardial blood pool contrast, they have been replaced by balanced SSFP imaging. Nevertheless, these sequences are still used in specific situations as described below.

Velocity Encoded Phase Contrast MR

Evaluation of blood flow and velocity is vital in the imaging follow-up of patients with congenital heart disease. Quantification of pulmonary to systemic blood flow ratio (Qp:Qs), valvular regurgitation fraction and vascular stenosis, are used to assess disease progression, as well as timing and suitability for surgery. Velocity encoded phase contrast magnetic resonance (PCMR) enables non-invasive quantification of blood flow in major vessels and is heavily used in congenital heart disease CMR. A PCMR sequence is basically a spoiled gradient echo sequence combined with an additional velocity-encoding gradient. Velocity encoding can be better understood by considering the simplified model of a vessel surrounded by static tissue (Fig. 12.3).

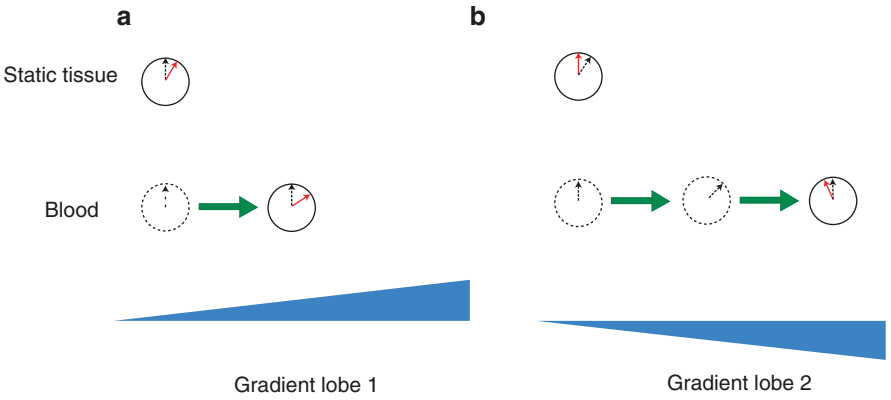

Fig. 12.3 The phase contrast experiment. (**a**) When a gradient is applied in the direction of flow the static tissue dephases, however moving spins dephase more because they are moving into a stronger magnetic field. (**b**) When the negative gradient is applied the static spins rephrase, however as the moving spins are moving into an even higher magnetic field they are *left* with residual phase at the end of the experiment

After RF excitation all magnetization is in phase. If a gradient is then applied in the z-direction, the static tissue will accrue phase depending on their spatial position. However, as the blood is moving through the gradient field, it will accrue more, or less phase, depending on its direction and velocity. If the gradient is then reversed, the phase in the static tissue will return to zero, but the phase in the moving blood will not go back to zero and this 'excess' is dependent on velocity. The described bipolar velocity-encoding gradient is the basic building block of PCMR, but phase shifts can also be caused by other factors (inhomogeneities, tissue interfaces, etc.). Therefore, a repeat measurement is also acquired without the velocity-encoding gradient (or alternatively by using two opposite gradients). When these two measurements are subtracted any phase secondary to other factors is eliminated. The end-result is a phase map from which accurate velocity and flow can be calculated as follows. First, the individual pixel velocities and volume flows (velocity multiplied by pixel area) in each phase of the cardiac cycle are evaluated. The flow through a vessel can then be calculated as the sum of the pixel volume flows in a region of interest drawn around the vessel. Subsequent integration over time provides evaluation of stroke volume and cardiac output. Cardiac output and the pulmonary to systemic flow ratio (Qp:Qs) measured using this technique have been shown to be accurate when compared to invasive oximetry [8, 9]. Furthermore, PCMR has been validated in numerous phantom experiments [9, 10]. Thus, PCMR is now considered the non-invasive reference standard method for assessing volume flow (including shunts and valvar regurgitation). It should be noted that PCMR also allows estimation of pressure gradients across stenosis. However, PCMR techniques tend to underestimate the peak velocity due to intravoxel averaging and this should be remembered if comparisons are being made with Doppler echocardiographic measures [11].

Methodology and optimization for the paediatric population: Accurate and reproducible measurement of flow relies on optimization for the paediatric population. The most important consideration is spatial resolution due to the smaller vessel size in children. Studies have been performed to investigate the relationship between spatial resolution and accurate assessment of volume flow [12]. Based on these studies, it is now generally accepted that at least 16 pixels should be present in the vessel of interest [13] to ensure accuracy. Since this may limit the ability to use conventional breath hold imaging, it is recommended that free breathing PCMR is used in paediatric patients. To reduce any breathing artefact, it is also advised that data is acquired with two to three signals averages. Recently, newer accelerated PCMR sequences have been used to acquire high-resolution data in a breath hold, but these are not widely available for routine clinical use [14]. Temporal resolution is also important in maintaining accuracy. This is particularly true for vessels that undergo significant in-plane translation during the cardiac cycle, since a low temporal resolution will result in vessel blurring and ghosting. Studies have shown that approximately 20–30 phases in the cardiac cycle are sufficient for accurate flow measurement [12]. Similar to bSSFP cine imaging, most PCMR sequences are now retrospectively cardiac gated and temporal resolution is controlled in a similar manner as described above. Another important aspect specific to PCMR is setting the

strength of the velocity-encoding gradient. This is achieved by setting the maximum encoded velocity (VENC), with any velocities above the VENC aliasing. For optimum velocity to noise ratio, the VENC should be set just above (~120%) the maximum expected velocity in the vessel of interest. The peak velocity can be measured using a velocity scout (a low-resolution PCMR sequence), which allows very accurate setting of VENC. However, this is a time consuming approach and in clinical practice the maximum expected velocity is simply estimated. When estimating the peak velocity, it should be remembered that shunts and valvar regurgitation result in increased peak velocity, even in the absence of any stenosis. Conversely, if the vessel is dilated (i.e. Marfan's syndrome or pulmonary hypertension) the peak velocity will be reduced even with normal flow. Therefore, it is vital when setting VENC that the physiology of the specific lesion is also taken into consideration.

Gadolinium Contrast-Enhanced MR Angiography

Gadolinium contrast enhanced MR angiography (CEMRA) is often used to assess vascular anatomy in CHD [15]. It relies on the T1 shortening effect of dilute gadolinium combined with fast 3D spoiled GRE imaging. Currently, all Gadolinium chelate contrast agents used in the paediatric population are extracellular fluid agents. This means that they rapidly leave the blood pool, equilibrating within the extracellular fluid. Consequently, imaging of the vasculature is best performed in the first or second pass of contrast, which translates into imaging in the first minute after contrast administration. To accomplish this, MRA sequences must be acquired quickly and this precludes the use of cardiac gating. The consequence of imaging without cardiac gating is that images acquired using CEMRA represent an temporal average across the cardiac cycle. This explains the poor delineation of intra-cardiac structures using this technique. This issue is less important when assessing vascular anatomy and vascular CEMRA has been shown to compare well with x-ray angiography and surgical findings both in infants and children [12].

Methodology and optimization for the paediatric population: There are several optimizations that should be considered when performing CEMRA in children. Conventional CEMRA consists of early and late-phase angiograms, each acquired in a 10 and 20 s breath hold. Usually, there is a short gap (10 s) between these acquisitions, which allows the patient to take a few breaths.

If this were done in infants, the rapid passage of contrast would result in significant wash out in the late phase. Thus, both phases are usually acquired without a gap, which results in a long breath hold. Most infants could not perform this voluntarily and CEMRA is one of main reasons for general anaesthesia in this age group. Exact triggering of CEMRA is vital to ensure optimum contrast in the anatomy of interest. This is usually achieved using some form of bolus tracking. Bolus tracking sequences utilize a single coronal thick slice that covers the heart and great vessels and allows visualization of the passage of contrast in almost real-time. The acquisition of CEMRA is triggered when the contrast has reached the anatomy of interest. Since most MRA sequences are centrically encoded (the centre of k-space is

Table 12.3 Representative parameters for CE-MRA spoiled GRE imaging in different age groups

Parameter	Adult	Child	Infant
FOV (mm)	400	350	250
TR/TE (ms)	2.0/0.8	2.0/0.8	3.0/1.0
Number of Phase Encode Steps	272	224–256	192–256
Slice thickness (mm)	1.5	1.3–1.6	1.0–1.3
Spatial resolution (mm)	1.5	1.3–1.6	1.0–1.3
Parallel Imaging acceleration factor	2–4	2–4	1–4

acquired first) it is important not to trigger too early, as this will result in poor contrast in the anatomy of interest. Another issue when performing CEMRA in children is the spatial resolution. Unfortunately, the affect of increasing spatial resolution is to lower the signal to noise ratio and increase scan times. Therefore, it is recommended not to scan with spatial resolutions of less than 1 mm. Suggested parameters for imaging in different age groups are shown in Table 12.3.

Anesthesia, Sedation and Respiratory Compensation

Compensation for respiratory motion is vital in CMR and can often be challenging in children. The conventional CMR sequences described above combine data acquired in timescales ranging from a few seconds to a few minutes. At these timescales, respiration motion becomes important and if not controlled leads to significant motion-related artefacts. The usual method of compensating for respiratory motion in adults is to perform a breath hold. In this group of patients, breath holding is robust and produces excellent image quality. However, breath holding is more difficult in children. For example, below the age of eight the majority of children will not be able to fully comply with breath hold instructions. Even above the age of eight, some children find it difficult to maintain long breath-holds. In these patients, images are often affected by residual motion that occurs towards the end of the acquisition. When performing breath hold imaging in these patients, it is vital that scan times are kept to a length that is appropriate for the child. This may mean compromising spatial or temporal resolution in an attempt to acquire images without respiratory artefacts. In children who cannot perform breath holds there are three possible solutions. Firstly, one can perform CMR under general anaesthesia and neuromuscular blockade. The benefit of this approach is that there is complete abolishment of respiratory motion during imaging. This can be particularly useful when performing long scans such CEMRA or cine imaging without parallel imaging (done in order to increase SNR). However, general anaesthesia is associated with some risk [16], and is unpleasant for the patient, and costly for the institution. An

alternative approach is to perform CMR under simple sedation [17]. This is much easier to perform and is associated with no greater risks than general anaesthesia in congenital heart disease [17]. However, a sedated child can no longer comply with breath-hold instructions and in sedated children multiple signal averages are often used to reduce respiratory motion artefacts. Although signal averaging is routinely used in PCMR, it is less useful in bSSFP cine imaging due to blurring of edges and residual artefacts. In infants under 1 year another option is feed and wrap CMR [18]. In this technique, the infant is starved for up to 4 h prior to imaging then fed and swaddled with the aim that the child will fall asleep. This technique has the advantage of not exposing the patient to anaesthesia or sedation and is therefore, low risk. However, this approach is less robust than general anaesthesia [18].

Final Tips and Tricks

Using CMR in the paediatric population is often challenging. However, it can be successful if time is spent thinking about the optimization of sequences. Of course any modification to improve imaging in a child will also have a negative effect (i.e. increasing spatial resolution reduces signal to noise ratio). These effects should be considered and particular consideration should be given to the clinical question being asked and the specific patients being imaged. Fundamentally, optimization is only useful if it increases the overall likelihood of obtaining the necessary clinical information. Nevertheless, if done correctly adapting CMR for the pediatric population can be rewarding.

Summary

Cardiovascular MR is becoming increasingly important in the evaluation of pediatric and congenital heart disease. Pediatric CMR is possible on all modern 1.5 T scanners. Imaging children at 3 T is more difficult, but still possible using the modern generation of 3 T scanners with fast gradients. Processing software must include the ability to perform ventricular volumetric and flow analysis. Specific protocols are disease specific but most will include assessment of biventricular volumes, measurement of flow in the aorta and pulmonary arteries and contrast or non-contrast three-dimensional anatomical evaluation. Full description of protocols for different diseases can be found in “Guidelines and protocols for cardiovascular magnetic resonance in children and adults with congenital heart disease: SCMR expert consensus group on congenital heart disease”.

Tabular Summary: Pediatric and Congenital Heart Disease

Sequence	Use
2D bSSFP cine	Assessment of ventricular volumes and anatomy
3D bSSFP whole heart imaging	Assessment of vascular and intracardiac anatomy
PCMR	Assessment of great vessel flow, shunts and valvular reguritation
CEMRA	Assessment of vascular anatomy

References

1. Scheffler K, Lehnhardt S. Principles and applications of balanced SSFP techniques. Eur Radiol. 2003;13(11):2409–18.
2. Schar M, Kozerke S, Fischer SE, Boesiger P. Cardiac SSFP imaging at 3 Tesla. Magn Reson Med. 2004;51(4):799–806.
3. Guidelines on patient dose to promote the optimisation of protection for diagnostic medical exposures, vol 10. National Radiation Protection Board; 1999.
4. Sorensen TS, Korperich H, Greil GF, Eichhorn J, Barth P, Meyer H, Pedersen EM, Beerbaum P. Operator-independent isotropic three-dimensional magnetic resonance imaging for morphology in congenital heart disease: a validation study. Circulation. 2004;110(2):163–9.
5. McLeish K, Hill DL, Atkinson D, Blackall JM, Razavi R. A study of the motion and deformation of the heart due to respiration. IEEE Trans Med Imaging. 2002;21(9):1142–50.
6. Fenchel M, Greil GF, Martirosian P, Kramer U, Schick F, Claussen CD, Sieverding L, Miller S. Three-dimensional morphological magnetic resonance imaging in infants and children with congenital heart disease. Pediatr Radiol. 2006;36(12):1265–72.
7. Hussain T, Lossnitzer D, Bellsham-Revell H, Valverde I, Beerbaum P, Razavi R, Bell AJ, Schaeffter T, Botnar RM, Uribe SA, Greil GF. Three-dimensional dual-phase whole-heart MR imaging: clinical implications for congenital heart disease. Radiology. 2012;263(2):547–54.
8. Beerbaum P, Korperich H, Barth P, Esdorn H, Gieseke J, Meyer H. Noninvasive quantification of left-to-right shunt in pediatric patients: phase-contrast cine magnetic resonance imaging compared with invasive oximetry. Circulation. 2001;103(20):2476–82.
9. Muthurangu V, Taylor A, Andriantsimiavona R, Hegde S, Miquel ME, Tulloh R, Baker E, Hill DL, Razavi RS. Novel method of quantifying pulmonary vascular resistance by use of simultaneous invasive pressure monitoring and phase-contrast magnetic resonance flow. Circulation. 2004;110(7):826–34.
10. Hundley WG, Li HF, Hillis LD, Meshack BM, Lange RA, Willard JE, Landau C, Peshock RM. Quantitation of cardiac output with velocity-encoded, phase-difference magnetic resonance imaging. Am J Cardiol. 1995;75(17):1250–5.
11. Steeden JA, Jones A, Pandya B, Atkinson D, Taylor AM, Muthurangu V. High-resolution slice-selective Fourier velocity encoding in congenital heart disease using spiral SENSE with velocity unwrap. Magn Reson Med. 2012;67(6):1538–46.
12. Lotz J, Meier C, Leppert A, Galanski M. Cardiovascular flow measurement with phase-contrast MR imaging: basic facts and implementation. Radiographics. 2002;22(3):651–71.
13. Tang C, Blatter DD, Parker DL. Accuracy of phase-contrast flow measurements in the presence of partial-volume effects. J Magn Reson Imaging. 1993;3(2):377–85.
14. Steeden JA, Atkinson D, Hansen MS, Taylor AM, Muthurangu V. Rapid flow assessment of congenital heart disease with high-spatiotemporal-resolution gated spiral phase-contrast MR imaging. Radiology. 2011;260(1):79–87.
15. Valsangiacomo Buchel ER, DiBernardo S, Bauersfeld U, Berger F. Contrast-enhanced magnetic resonance angiography of the great arteries in patients with congenital heart disease: an accurate tool for planning catheter-guided interventions. Int J Cardiovasc Imaging. 2005;21(2–3):313–22.
16. Stockton E, Hughes M, Broadhead M, Taylor A, McEwan A. A prospective audit of safety issues associated with general anesthesia for pediatric cardiac magnetic resonance imaging. Paediatr Anaesth. 2012;22(11):1087–93.
17. Fogel MA, Weinberg PM, Parave E, Harris C, Montenegro L, Harris MA, Concepcion M. Deep sedation for cardiac magnetic resonance imaging: a comparison with cardiac anesthesia. J Pediatr. 2008;152(4):534–9.. 9 e1
18. Windram J, Grosse-Wortmann L, Shariat M, Greer ML, Crawford MW, Yoo SJ. Cardiovascular MRI without sedation or general anesthesia using a feed-and-sleep technique in neonates and infants. Pediatr Radiol. 2012;42(2):183–7.

Chapter 13
Cardiac MR Angiography

Claudia Prieto, Marcus R. Makowski, W. Yong Kim, Warren J. Manning, and René M. Botnar

Abbreviations

Ao	Aorta
CAD	Coronary artery disease
CT	Computed tomography
EEG	Electrocardiogram
FH	Foot-head
GRAPPA	Generalized autocalibrating partially parallel acquisitions
iNAV	Image navigator
LAD	Left anterior descending coronary artery
LCX	Left circumflex coronary artery
LDL	Low-density lipoproteins

C. Prieto (✉)
King's College London, Imaging Sciences Division, St Thomas' Hospital, 4th Floor, Lambeth Wing, London SE1 7EH, UK

Division of Imaging Sciences and Biomedical Engineering, King's College London, London, UK
e-mail: claudia.prieto@kcl.ac.uk

M.R. Makowski
Department of Radiology, Charité-University Medicine, Berlin, Germany

W.Y. Kim
Department of Cardiology, Aarhus University Hospital, Aarhus, Denmark

W.J. Manning
Division of Cardiology, Beth Israel Deaconess Medical Center, Boston, MA, USA

R.M. Botnar
Division of Imaging Sciences and Biomedical Engineering, King's College London, London, UK

The British Heart Foundation Centre of Excellence, Cardiovascular Division, King's College London, London, UK

C. Constantinides (ed.), *Protocols and Methodologies in Basic Science and Clinical Cardiac MRI*, https://doi.org/10.1007/978-3-319-53001-7_13

LGE	Late gadolinium enhancement
MRA	Magnetic resonance angiography
MRI	Magnetic resonance imaging
PET	Positron emission tomography
RCA	Right coronary artery
RF	Radiofrequency
SENSE	Sensitivity encoding
SNR	Signal-to-noise-ratio
SSFP	Balanced steady-state-free-precession
SSFP	Steady-state-free-precession

Introduction

Despite ongoing advances in prevention, early diagnosis and treatment, coronary artery disease (CAD) remains the leading single cause of death in the Western world and developing countries [2]. CAD is the result of narrowing of the coronary lumen due to the progressive accumulation of low-density lipoproteins (LDL) in the coronary artery wall and the subsequent formation of coronary atherosclerotic plaque. This progressive lumen narrowing produces an imbalance in the demand and supply of oxygen-rich blood flow to the myocardial territory supplied by the respective coronary artery, triggering a pathophysiological response known as the ischemic cascade [3]. Progressive coronary lumen narrowing leads to exertional angina and subsequent rest angina and myocardial infarction [4]. Catheter-based, invasive, ionizing radiation based x-ray coronary angiography is the current gold standard for the diagnosis of significant (>50% diameter stenosis) CAD. However in current practice a large minority of patients (more than 40%) referred for this invasive procedure are found not to need an intervention, yet are exposed to its expense and potential morbidity [5, 6]. Furthermore, it is increasingly understood that coronary atherosclerosis is not necessarily stenotic due to outward remodelling of the vessel wall. The ideal CAD diagnostic test should therefore be non-invasive, have minimal risks, no exposure to ionizing radiation, and should allow identification of location and severity of lumen stenosis as well as an assessment of plaque characterization to enable early and comprehensive detection and management of coronary atherosclerosis.

Magnetic Resonance Imaging (MRI) is a very promising non-invasive tool for comprehensive early risk assessment, guidance of therapy and evaluation of treatment response in CAD. MRI is considered a gold standard for the assessment of cardiac anatomy, biventricular systolic function (CINE-MRI), myocardial viability (late gadolinium enhancement, LGE-MRI) and myocardial perfusion (MR-Perfusion) [7–10] due to its excellent soft tissue contrast, high spatial resolution and lack of ionizing radiation according to the Society for Magnetic Resonance (SCMR) expert consensus statement [11]. Clinical research studies also have demonstrated its use-

fulness for quantitative myocardial tissue characterization (T1 and T2 relaxation time mapping) and its ability to differentiate between healthy and diseased tissue [12, 13]. However, MRI assessment of coronary lumen integrity and plaque burden/activity remains challenging. Nevertheless, MRI has shown great research potential for coronary lumen [14, 15], plaque (with and without contrast agents) [16–18] and thrombus/haemorrhage [19, 20] visualization. The combination of these techniques could add invaluable prognostic information for patients at risk or with known CAD. Thus technical developments are currently being investigated to allow MRI to achieve similar diagnostic lumen accuracy as the current clinical gold standard as well as plaque characterization. The main technical challenges include suboptimal spatial resolution (due to required long acquisition times), and coronary motion suppression with unpredictable scan times (depending largely on the breathing pattern of the subject). This chapter reviews the technical challenges and general imaging strategies for coronary MRI and provides an overview of its current clinical applications.

Technical Challenges for Coronary MRI

The two major challenges in coronary MRI are (1) image quality degradation due to pronounced cardiac and respiratory motion during the acquisition, and (2) long scan times required for high spatial resolution coronary MRI due to the small calibre of the coronary arteries (2–4 mm) and their tortuous course.

Motion Compensation

Since MRI acquisition is slow compared to physiological coronary motion, the extensive cardiac- and respiratory- induced motion of the heart during the acquisition period can degrade image quality by introducing ghosting and/or blurring artefacts. The following sections describe some of the technical solutions proposed to minimize or compensate for physiological motion during coronary MR acquisition.

Cardiac-Induced Motion

High spatial resolution three-dimensional (3D) coronary MRI requires an acquisition time that exceeds by far the duration of the typical cardiac cycle. Therefore data have to be acquired over multiple cardiac cycles, under the assumption that cardiac motion is the same (or nearly the same) between heartbeats. External electrocardiogram (ECG) devices are usually employed to synchronize the acquisition with the cardiac cycle. Vector ECG approaches [21] are preferred since the ECG signal in the

main magnetic field is distorted by both the magnetohydrodynamic effect and by the rapidly switching gradient waveforms.

To minimize motion within the cardiac cycle, the acquisition is targeted to periods with minimal cardiac motion [22]. Resting periods occur during end-systole (~50 ms) and mid-diastole (~100 ms). The mid-diastolic rest period is usually preferred due to the higher blood flow and longer acquisition window. End-systolic rest period is used in subjects with high heart rates (thus shortened mid-diastolic rest periods) or in cases of highly variable heart rates. The optimal trigger delay (time lapsed from the R-wave of the ECG to the beginning of data acquisition) and the length of the acquisition window are subject dependent. It is advised therefore that the optimal trigger delay and length of resting period are identified for each subject from a high-temporal resolution CINE scan, orthogonal to the long axis of the coronary artery, performed shortly before the coronary MRI acquisition with respiratory suppression similar to that of the subsequent coronary acquisition. Importantly the rest period for the right coronary artery (RCA) is typically shorter compared to the left coronary system. Thus the length of the acquisition window of a whole-heart scan should be based on the RCA diastasis period. Furthermore correction for heart rate variability using an adaptive real-time arrhythmia rejection algorithm is recommended to further improve image quality by rejecting irregular heartbeats [23].

Respiratory-Induced Motion

Normal breathing leads to a shift and deformation of the heart, primarily in the foot-head (FH) direction [24] but also leads to additional 3D affine and non-linear motion components that differ strongly between different subjects [25–28].

A simple approach to minimize respiratory-induced motion artefacts is to perform the acquisition during one or multiple breathholds (~15–20 s). However, this approach is incompatible with clinically preferred high-resolution 3D targeted or 3D whole-heart coronary MRI due to the long scan time required to satisfy signal-to-noise and spatial resolution requirements. Similar to cardiac motion minimization, respiratory motion monitoring (or surrogates) can be used in free breathing 3D coronary MRI to combine data from multiple breathing cycles acquired at a similar respiratory position. Surrogates are used to relate the chest wall or diaphragmatic motion directly to the respiratory motion of the heart. Systems to monitor the motion of the chest wall include external devices such as pneumatic respiratory bellows [29, 30], while techniques to monitor the hemi-diaphragm position include the commonly used one-dimensional (1D) navigator echoes [31].

A navigator echo acquires signal from a long narrow volume oriented along the FH direction to monitor the position of the lung-liver (right hemi-diaphragm) interface. This 1D navigator signal can be achieved using two dimensional (2D)-selective RF pulses (pencil-beam navigator) [32, 33] or using a spin echo technique with obliquely aligned excitation and refocusing planes, so that signal is only acquired from the intersection of the two planes [31, 34]. In both methods a single line of k-space is sampled so that Fourier reconstruction yields a projection of the volume

onto the FH direction. Therefore, the repetitive acquisition of navigator echoes provides continuous monitoring of the diaphragmatic FH translation as shown in Fig. 13.1. The respiratory signal provided by the navigator echoes is used to gate the acquisition. Using gating, data are accepted/acquired only when the respiratory signal is within a predefined acceptance window of the breathing cycle (typically end-expiration) with all other data being rejected (Fig. 13.1). Rejected data have to be reacquired in the subsequent cardiac cycles. This approach has shown to considerably reduce motion artifacts when small gating windows are employed (3–5 mm), however progressively smaller gating windows lead to more prolonged scan times since a smaller fraction of the acquired data are then accepted for reconstruction (referred to as scan efficiency). For example a high-resolution 3D scan with a nominal scan time of 5–6 min may take 10–20 min for a typical scan efficiency of ~25–50%. Moreover, in subjects with highly irregular breathing patterns drift in respiratory motion can lead to scan abortions due to zero gating efficiency.

1D navigators can be also used to correct for residual motion within the gating window, an approach usually referred as gate and track. This method assumes that the heart motion is dominated by translation in the FH direction, and that this displacement is proportional to that of the diaphragm [24]. The measured displacement at the diaphragm can be used to correct for motion within the acceptance window by prospectively adapting the position of the imaging slice to the measured respiratory position (slice tracking) or by retrospectively applying a linear phase to the k-space data. The proportional scaling factor between the diaphragmatic and cardiac displacements is known as the tracking factor. Commonly a fixed scaling factor of 0.6, as suggested by Wang et al. [24], is used for slice tracking, however, additional methods have been proposed to derive subject-specific correction factors [35, 36]. This correction method is however limited because it does not measure directly the motion of the heart, and does not account for non-linearities including hysteresis

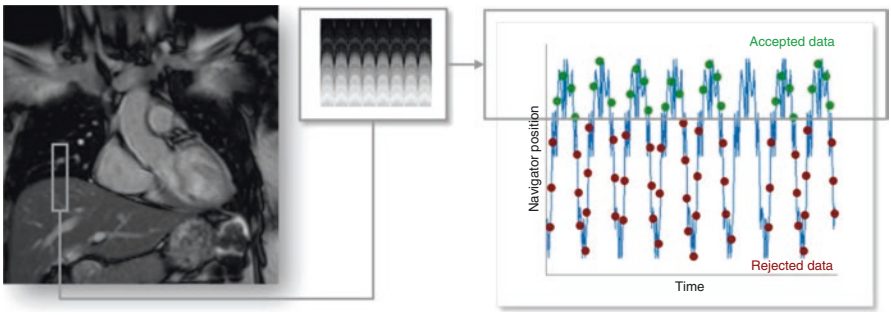

Fig. 13.1 Coronal identification of a 2D selective "pencil-beam" navigator at the dome of the right hemi-diaphragm. The diaphragmatic navigator captures the displacement of the lung (superior) and liver (inferior) interface along the foot-head direction over time, from which a 1D respiratory signal can be derived. In respiratory gating, data are accepted only if the lung-liver interface (navigator position) is within the acceptance of the gating window (typically 3–5 mm). Data acquired outside the gating window are rejected and need to be reacquired during subsequent heartbeats

effects between inspiration and expiration [27]. Furthermore, neither more complex multidimensional rotational, affine or non-linear motion components are included.

Self-navigation methods have been proposed to derive the respiratory-induced motion of the heart from the acquired data itself without the need of either a 1D navigator echo or a heart-diaphragm tracking factor. Respiratory-induced displacements of the heart can be directly estimated from the repetitive acquisition of the central k-space point [37] or the central k-space line [38–41], corresponding to zero-dimensional or one-dimensional projections of the field of view. Similar to the 1D navigator echo approaches self-navigation methods typically perform motion correction only in the FH translational motion direction. Another drawback of the 1D self-navigation approach is the inclusion of static structures, such as the chest wall, which can degrade motion estimation and correction.

To overcome these problems and account for more complex motion, several 2D and 3D image-based navigator (iNAV) approaches have recently been proposed for coronary MRI [42–49]. In these approaches a low-resolution 2D or 3D image is acquired in every heartbeat before (or after) the coronary MRI data. The main advantage of this approach is that the moving heart can be spatially isolated from surrounding static tissues and the respiratory-induced cardiac motion can be directly estimated via (rigid or affine) image-registration of iNAVs at different respiratory positions.

Self-navigation and image-based navigator methods can be used to gate the acquisition and correct for motion within a small gating window as described for 1D navigator echoes. Furthermore, since these methods directly track heart motion/position, a much larger gating window can be used, or it can be removed entirely, thereby increasing the scan efficiency to or close to 100%. These promising approaches may lead to shorter and predictable scan times, as described in the next section.

Acquisition Speed

The major coronary arteries, consisting of RCA and the left main (LM) coronary artery which branches into the left anterior descending (LAD) artery and the left circumflex (LCX) artery, have a proximal normal diameter of 3–5 mm and 1–2 mm in more distal segments. Therefore an isotropic high spatial resolution, ideally below 1 mm, is needed to correctly visualize and characterize the coronary lumen. This results in long MRI acquisition times.

Several approaches have been proposed to accelerate data acquisition including fast trajectories, undersampling reconstruction techniques and motion correction approaches with 100% scan efficiency. Advantages of fast trajectories, including spiral and radial acquisitions, are more efficient filling of k-space, incoherence undersampling and decreased sensitivity to motion [50–54]. At present

these technical approaches have not yet become established standards for coronary MRI due to their off-resonance sensitivity (spiral) or signal-to-noise ratio penalty (radial). However 3D radial acquisitions combined with self-gating signals have recently been demonstrated to achieve 100% scan efficiency with promising initial results [55–57]. Moreover 3D radial acquisitions have been used to reconstruct coronary MR images at multiple cardiac phases (four-dimensional, 4D, reconstruction), enabling simultaneous left ventricular functional assessment and whole-heart coronary artery visualization from a single free-running scan [58, 59]. Example results of 4D radial coronary MR angiography are shown in Fig. 13.2.

Parallel imaging reconstruction techniques such as SENSE or GRAPPA [60–63] with acceleration factors of 1.5–2 times have become the standard to reduce the acquisition time in coronary MR acquisitions while maintaining image quality. Further acceleration may be achieved with compressed sensing techniques [64, 65] although its efficacy in clinical practice has yet to be established.

Self-navigation and image-based navigator methods have been proposed to accelerate the scan to achieve ~100% scan efficiency. This is accomplished by acquiring data during free breathing with no, or minimal rejection, and correcting for respiratory motion. Most of these approaches correct respiratory motion in a beat-to-beat fashion, however they are typically limited to 1D, 2D or 3D translational motion only. To account for more complex affine and non-linear motion,

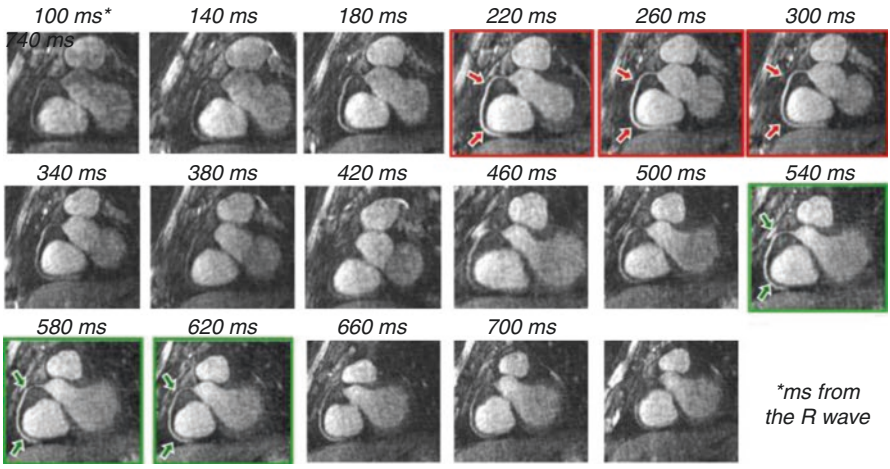

Fig. 13.2 Reformatted whole-heart coronary MR angiography with data acquired throughout the entire cardiac cycle (100–740 ms after the R-wave) using a 4D acquisition. Whole-heart 3D volumes are reconstructed every 40 ms with a 140 ms reconstruction window width. The right coronary artery is well visible during both the systolic (red frames, 220–300 ms) and the diastolic rest periods (green frames, 540–620 ms) (Reproduced from Coppo et al. Mag Reson Med 2015; 74: 1306–16 with permission)

'respiratory binning' techniques have been proposed recently [55, 56, 66–70]. With these approaches, a 1D respiratory signal is used to divide the coronary MRI data into several states of the breathing cycle or respiratory "bins". Images reconstructed at each respiratory bin are then registered to estimate the motion and correction for coronary motion is performed in a bin-to-bin fashion. Motion correction can be performed directly in k-space (for rigid and affine motion), incorporated into the reconstruction process (for general non-linear motion) or can be achieved by averaging images from different motion states after warping them to a common reference position (to reduce computational costs). A schematic of a ~100% scan efficiency motion correction framework is shown in Fig. 13.3. Example results of a combined iNAV-based beat-to-beat 2D translational and respiratory bin-to-bin 3D non-linear motion correction approach are shown in Fig. 13.4 for coronary MR angiography. These methods show promising results in healthy subjects and have the potential to be combined with undersampled reconstruction techniques to further accelerate the acquisition. An alternative approach to nonlinear motion correction has also been introduced in the form of localized autofocusing techniques [42, 46, 71]. These novel technical developments are currently mainly in the proof-of-concept state and clinical validation is awaited to establish their clinical efficacy.

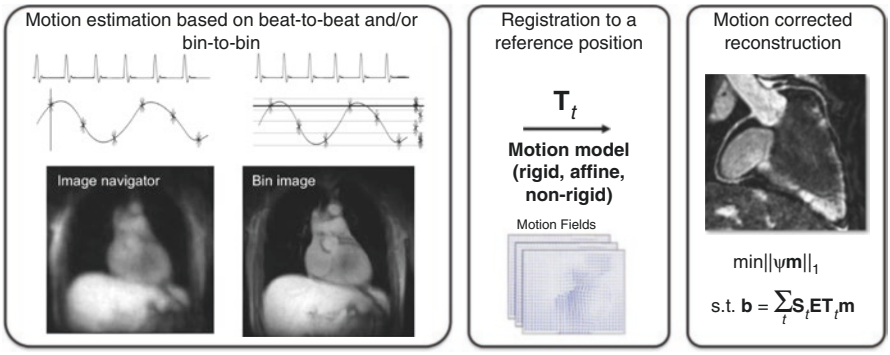

Fig. 13.3 Schematic of ~100% scan efficiency motion correction framework based on image-registration. Data are acquired under free breathing with no, or minimal rejection. Motion during the acquisition can be corrected in a beat-to-beat and/or a respiratory bin-to-bin fashion. Self-navigation signals or image navigators can be used to estimate motion in a beat-to-beat fashion, but they are usually limited to translation or rigid motion estimation only. Respiratory binning techniques have been proposed to account for more complex affine or non-linear motion by dividing the MR data into several states of the breathing cycle or "bins" with high spatial resolution but low temporal resolution. Image navigators and/or bin images are then registered to a reference position to estimate the motion fields. Respiratory motion correction can be performed directly in k-space (for rigid and affine motion), can be achieved by averaging images from different motion states after warping them to a common reference position (to reduce computational costs) or can be incorporated directly in the reconstruction process (for general non-linear motion). The example shows the formulation for a motion corrected compressed sensing reconstruction for general non-linear motion correction (b: acquired motion corrupted data, m: motion corrected reconstructed image, T_t non-linear motion fields for motion state t, E encoding matrix, S_t sampling pattern for motion state t, ψ sparsity domain)

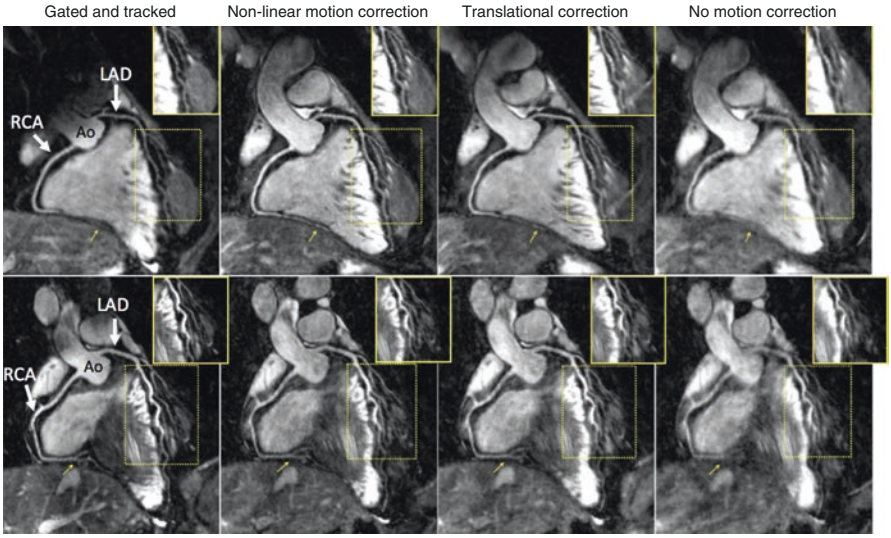

Fig. 13.4 Non-rigid motion correction coronary MR angiography with nearly 100% scan efficiency. This approach is based on beat-to-beat translation correction followed by bin-to-bin non-linear motion correction. Reformatted images are shown for conventional navigator gated and tracked acquisition, non-rigid motion correction, translation correction only and no motion correction for two different subjects. Blurring present in the no motion correction images is reduced with translation correction and sharpness further increased with the non-linear motion correction approach (*boxes*). The distal part of both the *right* (RCA) and the *left* (LAD) coronaries is particularly affected by motion (*arrows*). The non-linear motion correction approach has similar image quality to the conventional navigator gated and tracked acquisition however the latter require significantly longer scan times. *RCA* right coronary artery, *LAD* left anterior descending coronary artery, *Ao* aorta

Imaging Techniques for Coronary MRI

A generic coronary MRI sequence is shown in Fig. 13.5 and comprises: (a) ECG triggering to minimize cardiac motion artefacts by synchronizing data acquisition with the electrocardiogram; (b) respiratory navigation for compensation of the respiratory motion (with or without gating) during the acquisition, (c) magnetization preparation, such as T2 preparation and fat suppression, to enhance image contrast and (d) the imaging sequence.

Coronary Artery Imaging

The first approaches for coronary MR angiography (MRA) by Edelman et al. [72] and Manning et al. [73] used 2D gradient-echo techniques and acquired each slice in a single breath-hold of ~16 s. With the introduction of respiratory navigator

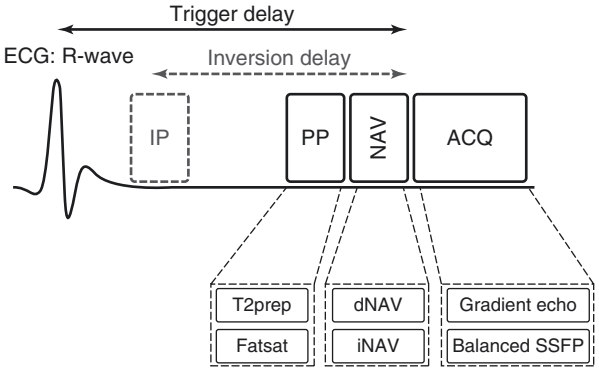

Fig. 13.5 Schematic of generic coronary MRI pulse sequence. ECG triggering is used to minimize cardiac motion by synchronizing the data acquisition (*ACQ*) with the heart motion. Data are acquired following a time delay (trigger delay) from the R-wave, typically at the mid-diastolic rest period. Respiratory motion compensation can be performed using respiratory navigation (*NAV*) techniques such as 1D diaphragmatic navigators (*dNAV*) or image navigators (*iNAV*). Preparation pulses (*PP*), such as T2 preparation (*T2prep*) and fat suppression (Fatsat), can be used to improve visualization of the lumen of the coronary arteries in bright blood imaging. In the case of coronary vessel wall imaging black-blood contrast can be achieved for example with an inversion preparation pulse (*IP*), where an inversion delay is used to null signal from the blood and fat suppression is used to null the fat signal

techniques 3D free-breathing acquisitions became feasible and are preferred in clinical routine. 3D approaches result in significantly improved signal to noise ratio (SNR) and enable higher spatial resolution, however the contrast between blood and myocardium is reduced due to less in-flow effects. Therefore, contrast enhancing spin preparation approaches in combination with balanced steady-state-free-precession (bSSFP) techniques have been developed to improve visualization of the coronary arteries [74, 75]. bSSFP techniques are currently preferred on 1.5 T systems due to the intrinsic higher SNR and better blood-myocardium contrast [74, 76, 77]. With bSSFP techniques improved contrast and visualization is achieved using short repetitions times and large flip angles. This limits the application of bSSFP sequences at 3 T and at higher fields systems where T1-weighted gradient echo techniques are preferred due to higher magnetic field inhomogeneities and increased radiofrequency (RF) energy deposition, [78–80]. Reformatted whole heart coronary MR angiography images acquired at 1.5 T and 3 T are shown in Fig. 13.6.

Further improvement of the contrast between blood and myocardium can be achieved by the application of various magnetization preparation pulses such as T2 preparation and fat suppression [81, 82]. T2 preparation pulses improve the contrast between the coronary lumen and the underlying myocardium, since blood and myocardium have similar T1 but different T2 values. Fat suppression is required to allow visualization of the coronaries, as they are embedded in epicardial fat. Cardiac fat may also provide important diagnostic information and thus water/fat coronary MRI has also been proposed [79, 83–85].

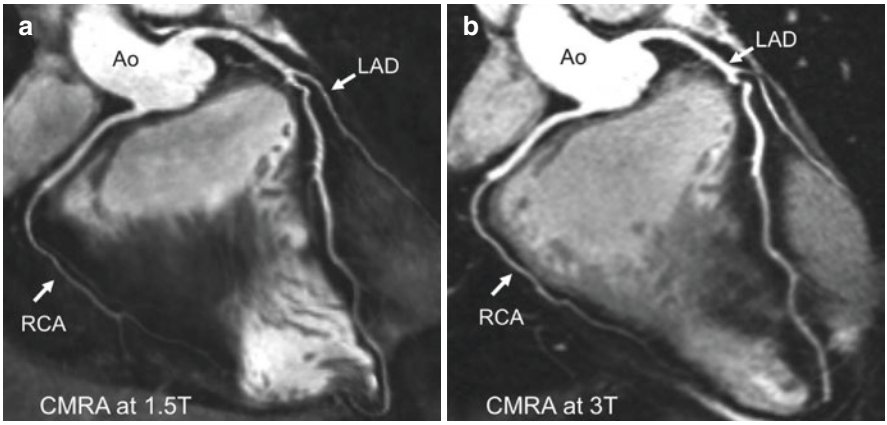

Fig. 13.6 Reformatted whole heart coronary MR angiography (CMRA) at (**a**) 1.5 T (balanced SSFP, resolution 1 × 1× 2 mm) and (**b**) 3 T (T1-weighted gradient echo, resolution 1.2 mm isotropic) using T2 preparation pulse. *RCA* right coronary artery, *LAD* left anterior descending coronary artery, *Ao* aorta

Gadolinium based MRI contrast agents can also be used to enhance the contrast between blood and myocardium. These include extracellular, blood-pool and weak albumin-binding contrast agents [86–92]. Each of these contrast agents has slightly different characteristics and the appropriate one should be chosen depending on the clinical information requested. For example weak albumin-binding contrast agents appear most promising for combined coronary artery and infarct imaging due to their prolonged retention time in the blood and their higher relaxivities [93]. With the use of these gadolinium based agents, consideration of nephrogenic systemic fibrosis in patients with co-existent renal dysfunction needs to be considered [94].

Coronary Artery Wall Imaging

As with coronary lumen MRI, the first in vivo MRI demonstrating the coronary vessel wall were obtained using 2D fat saturated fast spin echo techniques [95, 96]. A double inversion recovery preparation pulse was applied to obtain black-blood images and improved contrast between the blood and the vessel wall [97]. Further developments of the technique include the combination of the double inversion recovery preparation with fast gradient echo readout techniques [98] and with spiral [99] and radial [100] acquisition trajectories. Examples of in-plane and cross-sectional coronary vessel wall images with double inversion recovery preparation and radial and spiral acquisitions are shown in Figs. 13.7 and 13.8 respectively. Clinical studies demonstrated outward positive remodelling with lumen preservation in patients with established CAD and increased vessel wall thickness in patients with type I diabetes and renal dysfunction [17, 101].

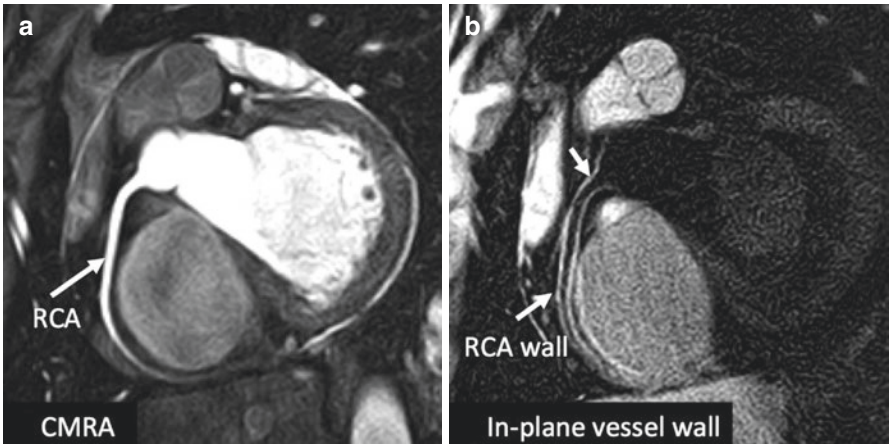

Fig. 13.7 (**a**) Coronary MRA, (**b**) 3D in-plane coronary vessel wall imaging. The acquisition was performed using a local inversion preparation pulse and a 3D stack-of-stars (radial) scan with an in-plane spatial resolution of 0.9 × 0.9 mm and a slice thickness of 2.4 mm. *RCA* right coronary artery

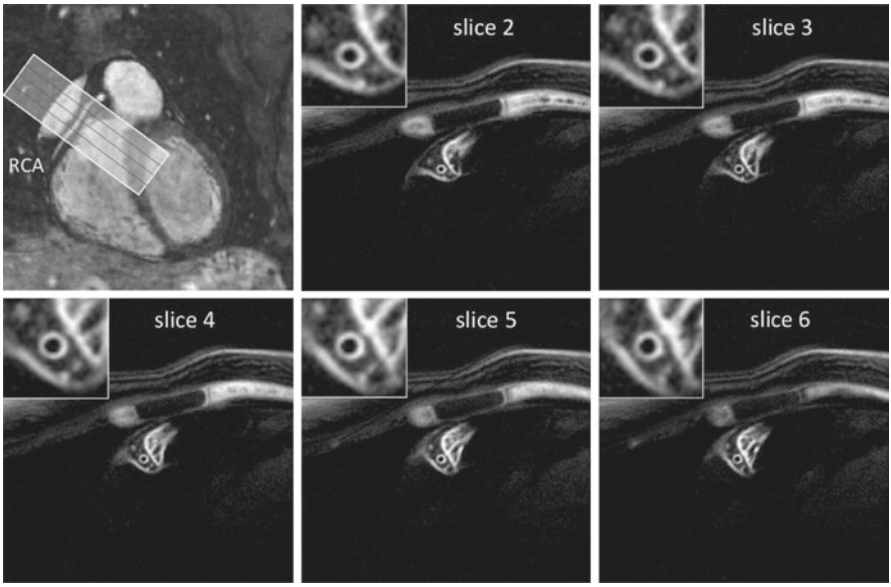

Fig. 13.8 3D cross-sectional coronary vessel wall imaging. Acquisition was performed at 3 T using a local inversion preparation pulse and a 3D stack-of-spirals scan with in-plane spatial resolution of 0.6× 0.6 mm and a slice thickness of 3 mm. To acquire cross-sectional slices of the vessel wall, the 3D imaging volume (six slices) was positioned perpendicular to a relatively linear portion of the proximal/mid right coronary artery (RCA) (Adapted from Peel et al. J Magn Reson Imaging 2012; 35: 969–75 with permission)

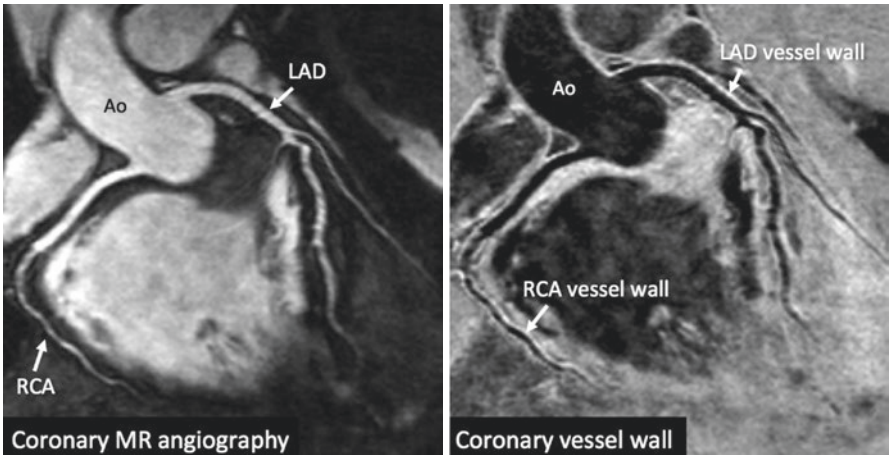

Fig. 13.9 Reformatted whole-heart coronary imaging using interleaved T2 preparation acquisition at 1.5 T. Interleaved acquisition and subtraction of bSSFP data with and without a T2 preparation pulse allows for nulling of signal from arterial blood (coronary lumen) while maintaining the signal of myocardium and the coronary vessel wall. This acquisition provides simultaneous coronary lumen MRI and coronary vessel wall imaging. *RCA* right coronary artery, *LAD* left anterior descending coronary artery, *Ao* aorta

One limitation of black-blood approaches for coronary vessel wall is that these techniques rely on blood flow, which may be insufficient in patients with very low coronary flow or heavily calcified coronary plaque. Furthermore these acquisitions are limited in coverage to 2D acquisitions or targeted 3D scans, and because the coronary arteries have a tortuous course, complicated scan planning is required.

A 3D flow independent approach for vessel wall imaging was proposed based on an interleaved acquisition and subtraction of bSSFP data with and without a T2 preparation pulse [102]. This allows for efficient nulling of arterial blood signal while maintaining myocardial and vessel wall signal. While this approach provides simultaneously coronary lumen and vessel wall images, the required subtraction is particularly sensitive to respiratory motion corruption. An example of reformatted whole-heart coronary imaging (combined coronary MR lumen and coronary vessel wall) using interleaved T2 preparation acquisition is shown in Fig. 13.9. Further recent improvements include the combination of this technique with an image-navigator based non-rigid motion correction approach [68].

Planning of Coronary MRI examination

Two different approaches are currently used for coronary MR examinations: 3D targeted imaging and 3D whole-heart imaging (Fig. 13.10).

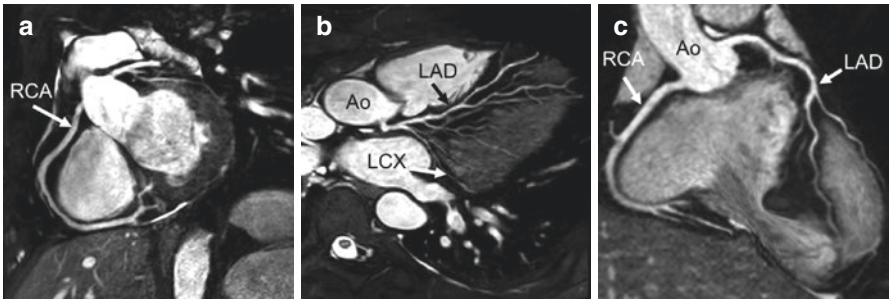

Fig. 13.10 Visualization of the right and left coronary arteries by the 3D targeted (**a**. **b**) and 3D whole heart scan (**c**). *RCA* right coronary artery, *LAD* left anterior descending coronary artery, *LCX* left coronary circumflex, *Ao* aorta

In the targeted approach, the left and right coronary systems are acquired subsequently in two individually planned volumes. The location of the central slice is defined by manual identification of three-points located along the major coronary arteries. Non-isotropic spatial resolutions in the order of 0.5 × 0.5× 2–5 mm are usually employed.

In the whole-heart approach, axial or coronal volumes are commonly used. The volume should preferably be with isotropic spatial resolution to enable reformatting along the entire course of the coronary arteries. Isotropic resolutions in the order of 1.15 – 1.3 mm^3 are usually achievable in whole-heart approaches. These approaches require longer acquisition times than targeted imaging but significantly facilitate planning and enable isotropic resolution.

Clinical Applications

Coronary MR Angiography

The primary current clinical application of coronary MRA is the assessment of the coronary artery anomalies (class I indication) and the evaluation of aortocoronary bypass grafts (class II indication) [103]. Using bSSFP or free-breathing navigator-gated fast gradient echo imaging techniques, the primary coronary arteries can be reliably visualized up to the medial/distal segments. Different studies have shown that the proximal part of the coronary arteries can be reliably visualized using coronary MRA, this includes the entire left main, and the proximal 50 mm of the LAD, 80 mm of the RCA and 40 mm of the LCX [73, 81,

104–109]. For this distance, there is a high agreement between coronary MRI lumen and x-ray angiography regarding the vessel lumen diameters [110]. Even though substantial technical advancements have been achieved in recent years, including the development and optimization of coronary MRA techniques at high field strength – up to 9.4 T – the spatial resolution of coronary MRA remains limited compared to invasive angiography and computed tomography (CT) angiography. The assessment of the small coronary branches is therefore limited with coronary MRI. The proximal and mid part of the main coronary arteries can however reliably be evaluated. This includes a normal coronary lumen as well as a stenotic coronary artery, which can be identified as a signal voids in the otherwise bright vascular lumen. This signal void can be explained by the overall small diameter of the stenotic lumen and the turbulence of the blood flow (non-contrast methods) in the area of the stenosis, which leads to an increase in turbulence and therefore a signal void. Different studies have shown that the effects can lead to a relevant overestimation of the degree of stenosis compared to x-ray angiography [111]. The diagnostic accuracy of coronary MRA was evaluated in a multicenter study and a high sensitivity (92%) for the detection of coronary artery disease could be demonstrated. However, only a moderate specificity [59] was achieved using quantitative x-ray angiography as the gold standard. Nevertheless, a high sensitivity and negative predictive value (100%) could be observed for the exclusion of three vessel disease and left main CAD. Smaller single center studies have confirmed these results [81, 112–120]. In this context, a subsequent multicenter study demonstrated that native whole-heart coronary MRA enabled the detection of coronary artery disease with a sensitivity of 88% and a specificity of 72% [14] (Fig. 13.11). A negative predictive value of 88% for the exclusion of CAD was achieved [14], which is comparable to what was achieved in a coronary CT multicenter study [6].

A combined protocol has been proposed which combines coronary MRI with myocardial late gadolinium enhancement to exclude ischemia in patients with dilated cardiomyopathy [103]. This study demonstrates that coronary MRA should not be used as a standalone technique. It should be integrated into an extensive clinical cardiac MRI protocol which includes the assessment of cardiac function, myocardial perfusion and myocardial viability.

Besides the assessment of CAD, coronary MRA enables the visualization of coronary aneurysms with a high sensitivity and specificity. This is due to the fact that coronary aneurysms have a larger luminal diameter and are in most cases located in the proximal part of the coronary arteries. This technique is especially useful in children and younger patients with e.g. Kawasaki disease [103, 121, 122] (Fig. 13.12) for whom avoiding ionizing radiation approaches (e.g., CT and x-ray angiography) is very important.

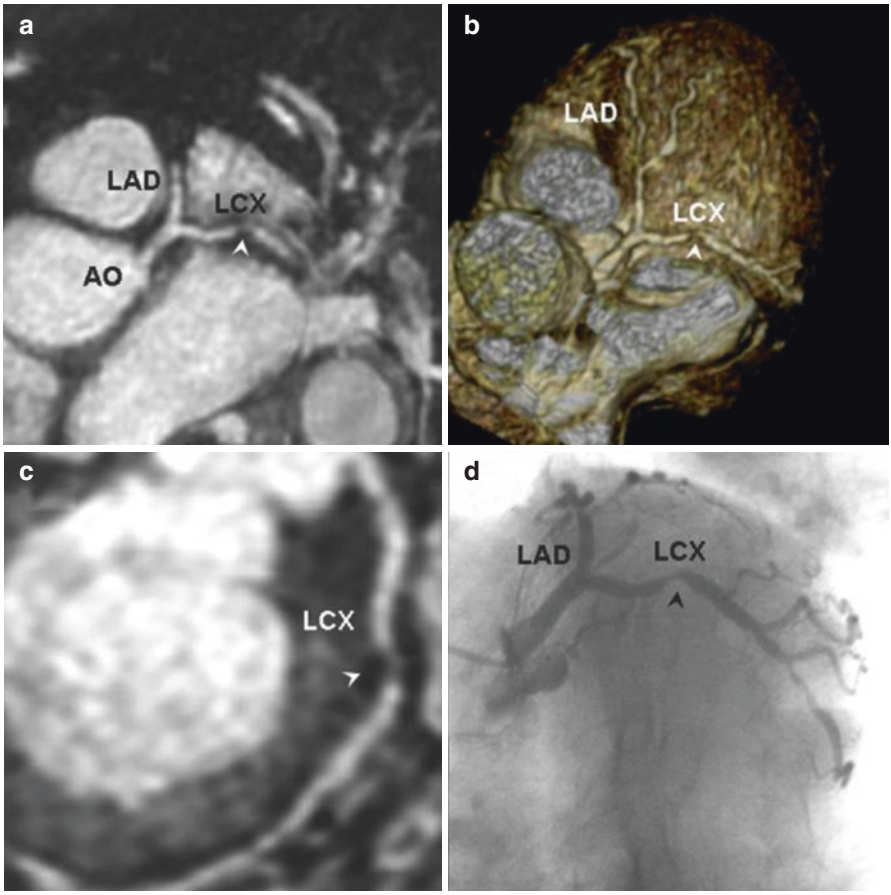

Fig. 13.11 Non-contrast enhanced 1.5 T whole-heart coronary MRA in a 66-year-old woman. Significant coronary artery stenosis in the LCX (*white arrowhead*) is observed in the sliding thin-slab maximum intensity projection image (**a**), the volume-rendered image (**b**), and the curved planar reconstruction image (**c**), with good correlation with x-ray coronary angiography (*black arrowhead*) (**d**). *LAD* left anterior descending coronary artery, *LCX* left coronary circumflex, *Ao* aorta (Reproduced from Kato et al. [14] with permission)

Besides the coronary arteries, coronary MRA techniques also enable the visualization of coronary bypass grafts. As coronary bypass grafts usually have a larger diameter and a relative linear course their MR-based visualization is relatively straightforward both with spin echo and gradient-echo techniques [123–126]. To enhance the intraluminal signal, the positive effect of the additional application of gadolinium contrast agents has been demonstrated in different studies [127–129]. In the context of coronary bypass grafts it has to be mentioned that coronary MRI is limited by metal clips which cause strong susceptibility artifacts in both black blood and bright blood methods.

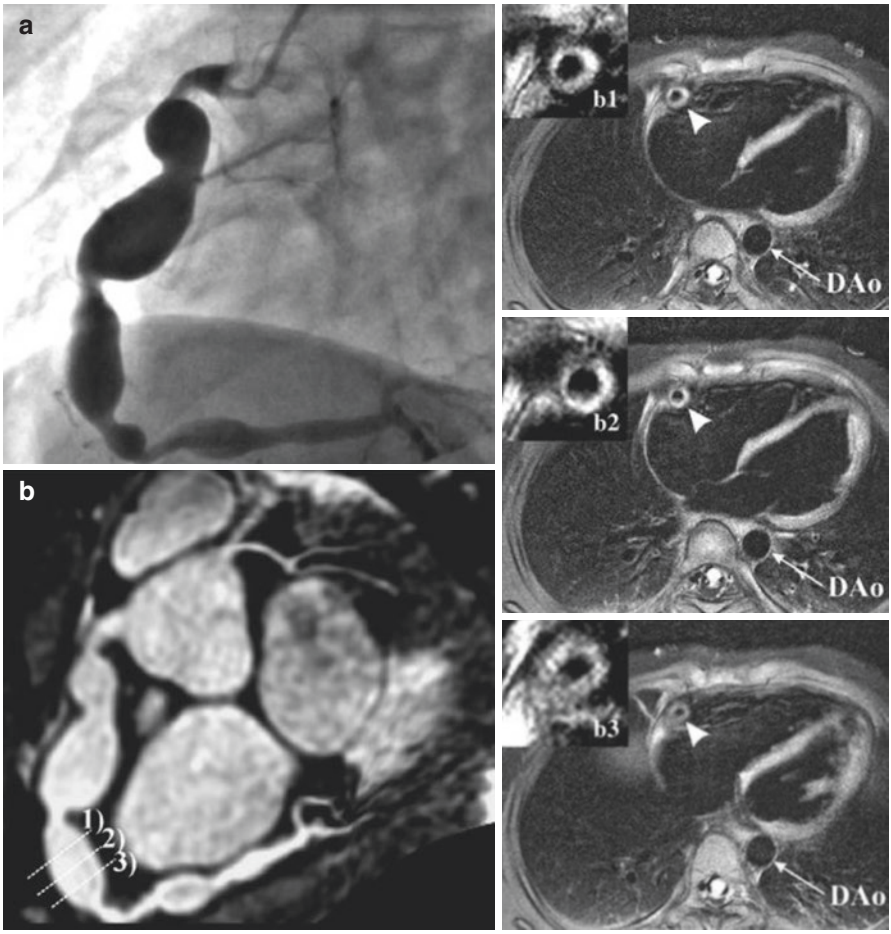

Fig. 13.12 Good agreement between the x-ray angiogram (**a**) and the corresponding coronary MRA image (**b**) for detection of a right coronary artery aneurysm in a 7.8-year-old boy with Kawasaki disease. MR images were acquired with a whole-heart, 3D SSFP technique without the use of contrast agents. Sequential cross-sectional views of the aneurysm demonstrate a thickened vessel wall (*arrowheads*) at three different locations (*b1*, *b2* and *b3*). Vessel wall images were acquired with a 2D double inversion recovery black-blood segmented turbo spin echo technique. In contrast to the right coronary artery aneurysm (*b1*, *b2* and *b3*), the wall of the aorta (DAo) is normal (Reproduced from Greil et al. [122] with permission)

Coronary MR Vessel Wall Imaging

Non-contrast Enhanced Coronary MRI for the Detection of Atherosclerosis, Vascular Remodeling and Plaque Burden

In clinical practice, the detection and assessment of the severity of coronary atherosclerosis is based on x-ray angiography and/or intravascular ultrasound (IVUS) and

optical coherence tomography (OCT). With x-ray the degree of luminal stenosis or negative vascular remodeling can reliably be assessed. However, coronary atherosclerosis not only results in a narrowing of the coronary lumen but also in an enlargement of the outer vessel wall, or positive vascular remodeling. Coronary remodeling during the development of coronary atherosclerosis is thus not observed by x-ray coronary angiography [130, 131]. In contrast to x-ray angiography, IVUS and OCT provide high-resolution images of coronary plaque but they are invasive and thus not suitable for screening or follow-up. In this context, it was shown by invasive studies with IVUS and postmortem studies that a large proportion of myocardial infarcts are triggered by atherosclerotic plaques with less than 50% reduction in luminal area [132]. The overall volume of atherosclerotic plaques, including positive and negative vascular remodeling, is represented by the plaque burden. Positive vascular remodeling and plaque burden were shown to be stronger predictors for major cardiovascular events, compared to the luminal stenosis or negative remodeling [133]. Additionally, it has been shown that lipid-lowering therapies using statins result in a reduction of the local progression of coronary atherosclerosis quantified by the plaque burden [134]. Non-contrast enhanced MRI allows the detection and quantification of positive coronary remodeling and the overall plaque burden [96, 135]. In this context, various studies have shown that non-contrast enhanced MRI can achieve comparable results to invasive techniques, such as intravascular ultrasound [136, 137]. A major advantage of non-contrast enhanced coronary MRI is that it is a noninvasive and radiation free technique which does not rely on the use of contrast agents. This is especially important for the assessment of the coronary arteries in children and young patients.

One of the initial non-contrast enhanced coronary MRI vessel wall studies demonstrated positive remodeling in patients with subclinical coronary atherosclerosis [101]. In a subsequent large multi ethnic study (MESA), investigating an asymptomatic study population, an increase in positive vascular remodeling was measured in a relevant number of participants which had no prior history of CAD [138, 139]. In a comparable study an increase in positive vascular remodeling in asymptomatic patients was observed [140]. These studies demonstrate that non-contrast enhanced coronary vessel wall MRI has the potential to be used as a screening tool in asymptomatic subjects for the quantification of positive vascular remodeling and plaque burden. The value of non-contrast enhanced coronary vessel wall MRI was also shown in patients with diabetes type I. In this patient collective significantly lower plaque burden was measured in patients without nephropathy compared to patients with nephropathy [17] (Fig. 13.13). Regarding the assessment of response to therapy, patients were imaged prior to and 6 months following the initiation of an antiatherosclerotic therapy. A significant decrease in plaque burden and positive vascular remodeling could be measured [141]. A high reproducibility between imaging studies has also been demonstrated [142, 143]. A limitation of non-contrast enhanced coronary vessel wall MRI, especially compared to CT, is the long scan time. Additionally, the technical performance of coronary vessel wall MRI is more challenging.

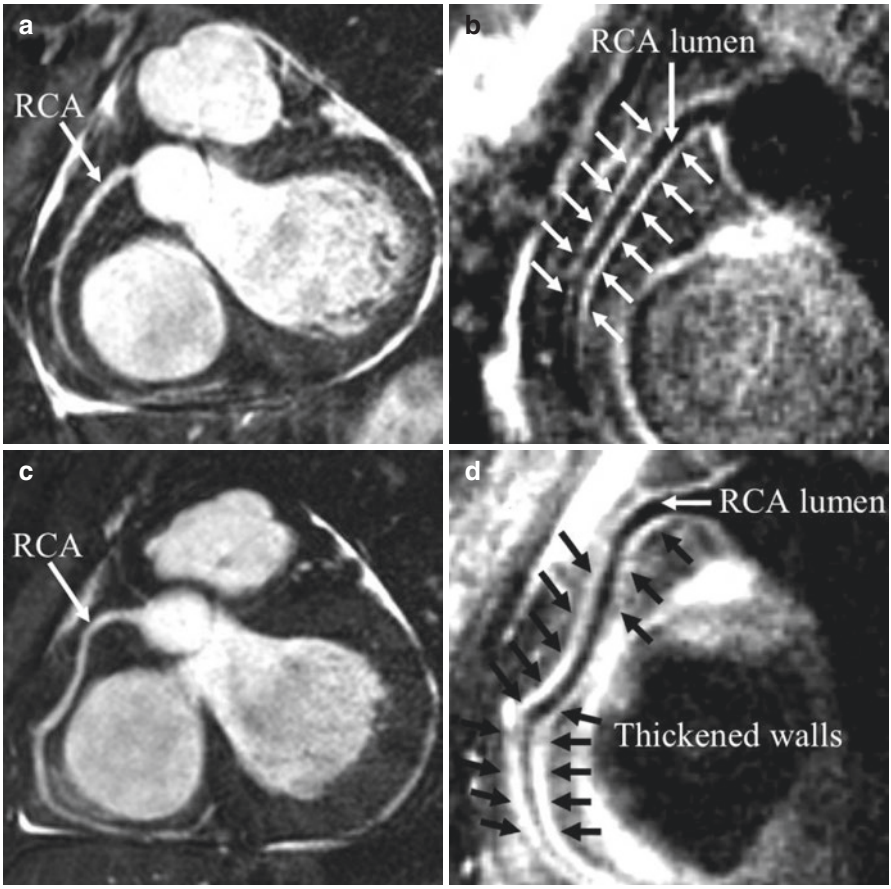

Fig. 13.13 3D reformatted coronary MRA of the proximal right coronary artery (*RCA*) in two subjects without coronary luminal stenosis: a 58-year-old man with long-standing type 1 diabetes and normoalbuminuria (**a**) and a 44-year-old man with long-standing type 1 diabetes and diabetic nephropathy (**c**). The corresponding 3D black-blood coronary vessel wall MRI shows no evidence of atherosclerotic plaque (**b**) average and maximum vessel wall thickness, 1.1 and 1.3 mm, respectively) and an increased atherosclerotic plaque burden (**d**) average and maximum vessel wall thickness, 2.3 and 3.0 mm, respectively). The anterior and posterior RCA walls are indicated by *arrows* (Reproduced from Kim WY et al. Circulation 2007; 115: 228–235 with permission)

Non-contrast Enhanced Coronary MRI for the Evaluation of Endothelial Function

Non-contrast enhanced MRI enables the acquisition of functional parameters, in addition to morphological changes. One of these parameters is coronary endothelial function. It represents a clinically important parameter as an abnormal coronary artery response or evidence of endothelial dysfunction is an independent predictor

for adverse cardiovascular events [144]. In a clinical setting, endothelial function is currently assessed by invasive x-ray angiography in combination with Doppler flow measurements. These measurements are associated with an increased radiation exposure as measurements have to be performed prior to and following the administration of pharmacological vasodilation. Different studies have shown that non-contrast enhanced MRI could represent an alternative approach to invasive techniques as it enables the assessment and quantification of coronary vasodilation following pharmacological stimuli [145, 146]. In a recent study the potential of non-contrast enhanced coronary artery MRI was tested for the quantification of the coronary response to the so-called "isometric handgrip exercise". In this study it was shown that pathological coronary artery vasodilation can be assessed by MRI and that it was associated with an increase in local plaque burden. In contrast, pathological coronary artery vascular flow was associated with systemic atherosclerosis [147]. A further parameter which can be assessed by MRI is coronary distensibility (CD), defined as:

$$CD = \frac{\text{ESLA} - \text{EDLA}}{PP \times \text{EDLA}}$$

where ESLA is the end-systolic lumen-area, EDLA is the end-diastolic lumen-area and PP is the pulse-pressure. Coronary distensibility can be quantified by non-enhanced coronary MRI and differences between patients with CAD and healthy subjects can be measured [148].

Non-contrast Enhanced MRI for the Detection of Coronary Thrombi

Intracoronary thrombi can be visualized with MRI by taking advantage of the T1 shortening effect that methemoglobin exerts on neighboring protons. Local accumulation of methemoglobin leads to a shortening of the T1 relaxation time, comparable to that of a gadolinium-based MR contrast agent, and therefore leads to a bright signal on T1-weighted images. This effect was first recognized and investigated in patients with carotid thrombi following acute ischemic stroke [149]. However, compared to the carotid arteries, imaging of the coronaries is more challenging, due to the extensive coronary motion and advanced motion compensation sequences have to be used. High signal intensity coronary atherosclerotic plaques on non-contrast enhanced T1 weighted coronary MRI scans have been investigated using CT, angiographic coronary flow and IVUS [150]. T1 hyperintense coronary atherosclerotic plaques were associated with transient reduced coronary flow on angiography, lower Hounsfield units and focal calcifications on CT, and increased remodeling on intravascular ultrasound. The direct detection of coronary artery

thrombi was investigated in patients with acute coronary syndromes [19, 20] as shown in Fig. 13.14. Intracoronary thrombi could be detected with a high sensitivity and specificity. In a different study in patients with angina pectoris these findings were confirmed by optical coherence tomography, which was used as reference standard [151].

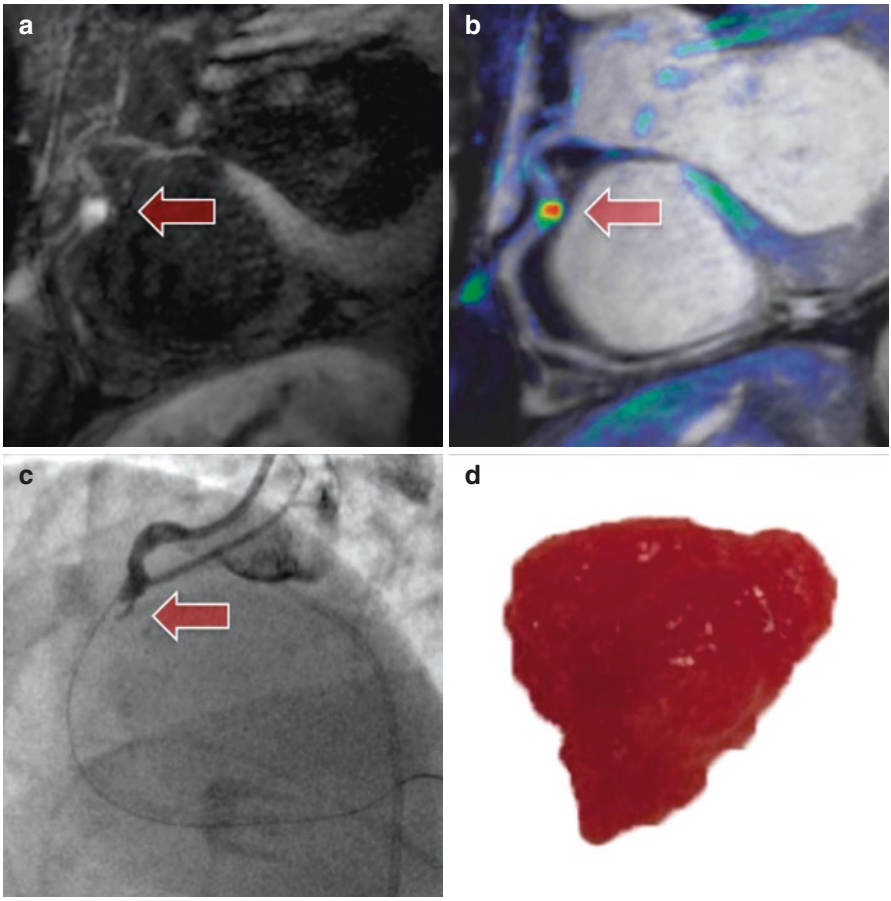

Fig. 13.14 T1 weighted non-contrast enhanced MRI for direct intracoronary thrombus visualization. (**a**) T1 weighted coronary non-contrast enhanced MRI of the right coronary artery (RCA) in a patient with inferior myocardial infarction after failed thrombolysis. T1-weighted non-contrast enhanced MRI shows a bright focal spot (*arrow*) within the mid RCA indicating thrombus formation. (**b**) Image fusion confirms the intracoronary location. (**c**) x-ray angiography demonstrating a complete RCA occlusion. (**d**) Example of removed thrombotic material following thrombosuction

Non-contrast Enhanced MRI for Edema in the Coronary Vessel Wall

Different studies investigated the use of T2-weighted non-contrast enhanced MRI for the detection of coronary vessel wall edema (Fig. 13.15). In the presence of both acute vascular injury and acute coronary syndrome, the presence of coronary edema was successfully visualized by non-contrast enhanced MRI [152, 153].

Contrast Enhanced Coronary MRI for the Characterization of Atherosclerosis

FDA and European Union approved extracellular gadolinium based contrast agents enable an alternative approach for the detection and characterization of coronary artery wall plaque. The primary reason for the accumulation of these contrast agents in atherosclerotic plaques is the fast extravasation from the lumen into the

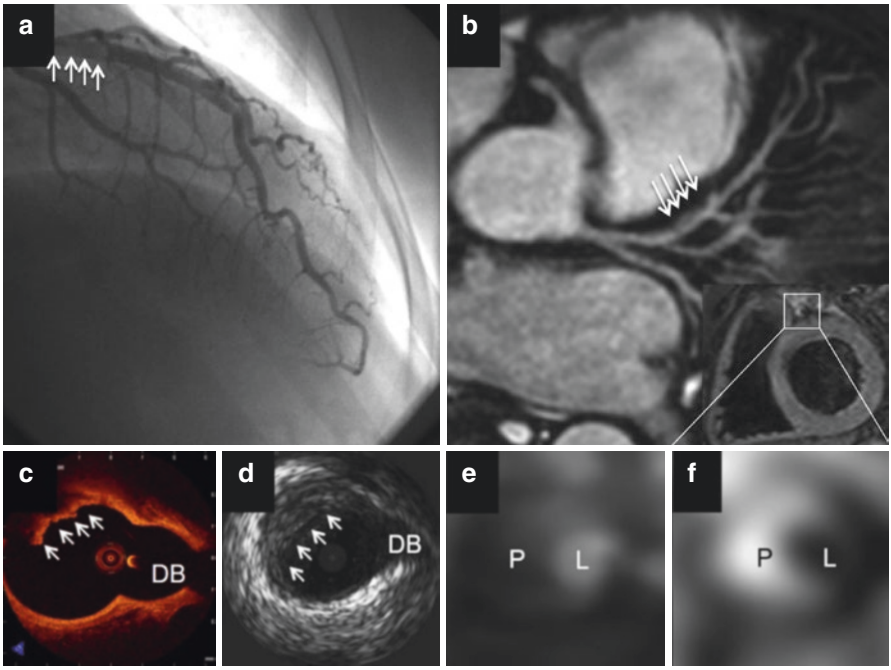

Fig. 13.15 Non-contrast-enhanced MRI for the visualization of coronary plaque edema. (**a**) x-ray angiography shows an intraluminal filling defect in the proximal left anterior descending (LAD) coronary artery (*arrows*). (**b**) Coronary MR angiography shows a large non-stenotic plaque (*arrows*). (**c**) Optical coherence tomography demonstrates a high-attenuation plaque with residual luminal thrombosis (*arrows*) opposite to the first diagonal branch (*DB*), indicating a ruptured thin-cap fibroatheroma. (**d**) Intravascular ultrasound demonstrates an eccentric plaque in the proximal LAD. (**e**) Computed tomography coronary angiography shows a large remodeled plaque (P), indicating a thin-cap fibroatheroma. The coronary lumen (*L*) is depicted with a bright signal. (**f**) T2-weighted STIR with black blood spin echo coronary MR shows hyperintense signal (edema) in the eccentric plaque (*P*), indicating inflammation or angiogenesis. The coronary lumen (*L*) appears black as the result of suppression of signal from the coronary blood pool

extracellular space of the atherosclerotic vessel wall following intravenous administration. Increased accumulation was observed in areas with increased neovascularization and an increase in extracellular volume. One of the earliest studies demonstrated that contrast enhancement in the coronary artery wall correlates with the degree of atherosclerosis. In this study quantitative x-ray angiography and CT were used as reference standard [18]. In a different study of patients with giant cell arteritis or Takayasu's arteritis, an increased uptake of the contrast agent was observed in the coronary artery wall. The accumulation of the contrast agent was suggested to be associated with coronary edema and acute inflammation [154]. A further study investigated the uptake of nonspecific gadolinium based contrast agent in coronary plaque in patients following acute myocardial infarction (Fig. 13.16).

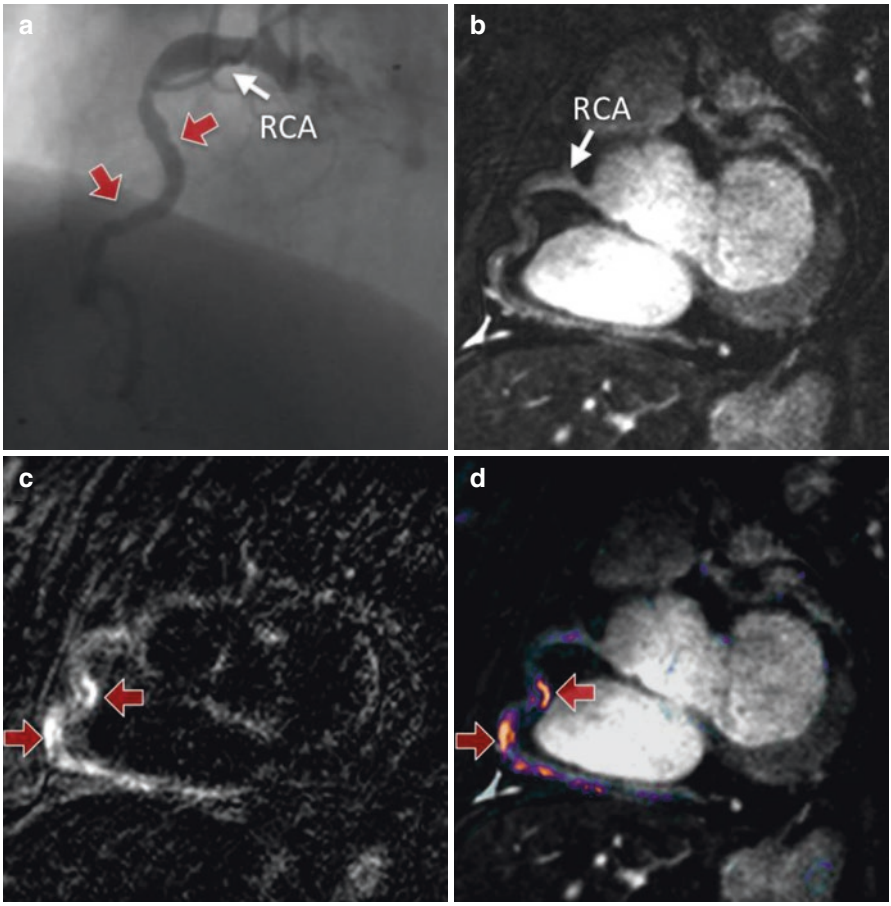

Fig. 13.16 Contrast enhanced vessel wall MRI [16]. (**a**) x-ray angiography of a patient with unstable angina and significant rise in C-reactive protein showing luminal irregularities (*red arrows*) of the mid right coronary artery (RCA). (**b**) Multiplanar reformatted coronary MRA of the RCA and (**c**) corresponding late gadolinium enhancement demonstrating increased contrast uptake (*red arrows*) of the coronary artery vessel wall, indicative of an increased atherosclerotic plaque burden and possible inflammation. (**d**) Fusion of coronary MRA and late gadolinium enhancement vessel wall image. Areas of increased vessel wall uptake appear *light orange* (*red arrows*)

Three to 6 days post myocardial infarction contrast enhancement was significantly increased and decreased after 3 months on follow-up scans [16]. It was hypothesized that the decrease in contrast agent was associated with a reduction in coronary vessel wall inflammation. Taken together these studies demonstrate that contrast agent uptake in the coronary artery wall could be associated with both, a change in atherosclerotic plaque composition (e.g. fibrous vs. atheromatous) and inflammatory processes [155–157]. The potential of contrast enhanced MRI was also demonstrated at 3 T. The higher field strength allowed an increase in spatial resolution as well as contrast-to-noise ratio [158].

Future Perspectives

Since the first demonstration of MR coronary angiography in the early 1990s [72] and coronary plaque imaging in 2000 [92] there have continued to be ongoing advances in image acquisition, motion correction, and undersampled reconstruction as well as in contrast agent development. New self-navigated and image-navigator based motion correction techniques have allowed increasing the scan efficacy to nearly 100% and significantly improved the ease of use and robustness of coronary MRA. Many of these techniques are not yet available in the commercial software packages of the major MR vendors but initial studies holds promise of a comprehensive coronary examination in the foreseeable future. Recently introduced free running self-navigated coronary MRA even promises to remove the necessity to synchronize the scan with the ECG or to correct for respiratory motion. Thus, data can be sorted in cardiac and respiratory motion phases and subsequently reconstructed using undersampled reconstruction techniques such as compressed sensing, thereby providing both cardiac function and cardiac and respiratory motion resolved coronary artery images. In addition, assessment of coronary intraplaque haemorrhage and thrombus has been shown to be a very promising imaging biomarker to predict future coronary events and may provide new invaluable information in addition to current cardiac MR exams that currently consist of cardiac function, stress perfusion, late gadolinium enhancement and T1 mapping. Progress in contrast agent research and the advent of multi modality imaging, namely the development of clinical PET-MR systems has opened the door to combine myocardial function, structure and tissue characterization provided by MRI with molecular and metabolic information of the myocardium and, potentially even coronary plaque, thereby allowing for a comprehensive examination of the cardiovascular system. In conclusion, the future of cardiac magnetic resonance imaging is bright and may benefit from continued efforts to make novel acquisition and reconstruction methods available for wider clinical use to make an impact on daily patient management.

Coronary MR Protocol Summary

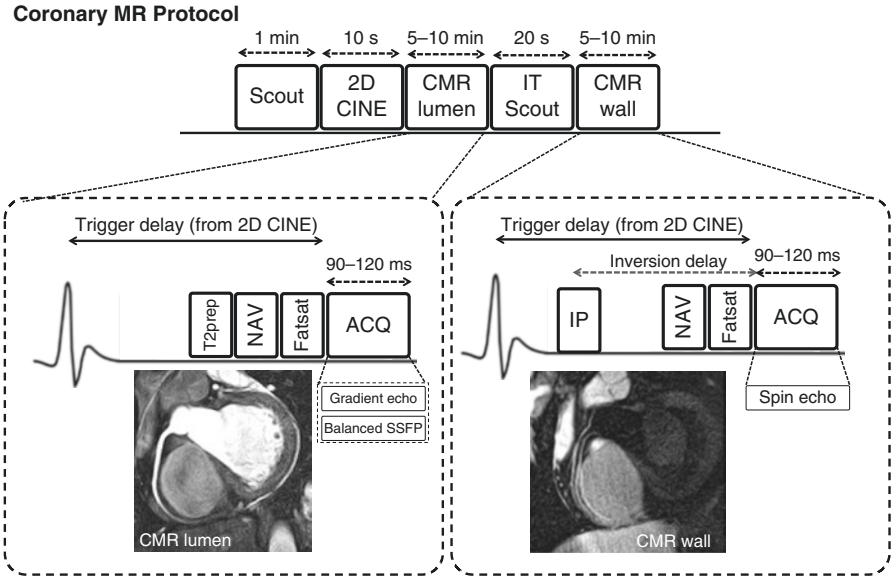

Schematic of generic coronary MRI acquisition protocol. An anatomic survey is acquired to plan 3D targeted or 3D whole heart acquisitions (Scout). A high-temporal resolution 2D CINE scan is performed shortly before the coronary MRI acquisition to determine mid-diastolic (or systolic) rest period, defining trigger delay and acquisition window (typically 90–120 ms in mid-diastole) for coronary MR lumen (CMR lumen) and coronary MR wall (CMR wall) imaging. Respiratory motion compensation can be performed using respiratory navigation (NAV) techniques such as 1D diaphragmatic navigators, self-navigators or image navigators. T2 preparation (T2prep) and fat suppression (Fatsat) are used to improve visualization of the lumen of the coronary arteries in bright blood imaging. In the case of coronary vessel wall imaging black-blood contrast can be achieved for example with an inversion preparation pulse (IP), where an inversion delay is used to null signal from the blood and fat suppression (Fatsat) is used to null the epicardial fat signal. The inversion delay is determined from a scout scan (IT Scout) performed before the coronary vessel wall acquisition. Coronary lumen imaging is typically acquired with gradient echo sequences at 3 T and with balanced SSFP sequences at 1.5 T. Coronary wall imaging is typically acquired with spin echo sequences.

References

1. Karamitsos TD, Francis JM, Myerson S, Selvanayagam JB, Neubauer S. The role of cardiovascular magnetic resonance imaging in heart failure. J Am Coll Cardiol. 2009;54(15):1407–24.
2. Go AS, Mozaffarian D, Roger VL, Benjamin EJ, Berry JD, Blaha MJ, et al. Heart disease and stroke statistics – 2014 update: a report from the American Heart Association. Circulation. 2014;129(3):e28–e292.
3. Nesto RW, Kowalchuk GJ. The ischemic cascade: temporal sequence of hemodynamic, electrocardiographic and symptomatic expressions of ischemia. Am J Cardiol. 1987;59(7):23C–30C.
4. Mehta D, Curwin J, Gomes JA, Fuster V. Sudden death in coronary artery disease: acute ischemia versus myocardial substrate. Circulation. 1997;96(9):3215–23.
5. Chow BJ, Abraham A, Wells GA, Chen L, Ruddy TD, Yam Y, et al. Diagnostic accuracy and impact of computed tomographic coronary angiography on utilization of invasive coronary angiography. Circ Cardiovasc Imag. 2009;2(1):16–23.
6. Miller JM, Rochitte CE, Dewey M, Arbab-Zadeh A, Niinuma H, Gottlieb I, et al. Diagnostic performance of coronary angiography by 64-row CT. N Engl J Med. 2008;359(22):2324–36.
7. Bandettini WP, Arai AE. Advances in clinical applications of cardiovascular magnetic resonance imaging. Heart. 2008;94(11):1485–95.
8. Gore TB, Rollings RC, Gore 3rd AW. The many facets of cardiovascular magnetic resonance imaging: review of background, clinical utility, and increasing use in the community hospital. South Med J. 2009;102(7):719–24.
9. Lockie T, Nagel E, Redwood S, Plein S. Use of cardiovascular magnetic resonance imaging in acute coronary syndromes. Circulation. 2009;119(12):1671–81.
10. Greenwood JP, Maredia N, Younger JF, Brown JM, Nixon J, Everett CC, et al. Cardiovascular magnetic resonance and single-photon emission computed tomography for diagnosis of coronary heart disease (CE-MARC): a prospective trial. Lancet. 2012;379(9814):453–60.
11. Fratz S, Chung T, Greil GF, Samyn MM, Taylor AM, Valsangiacomo Buechel ER, et al. Guidelines and protocols for cardiovascular magnetic resonance in children and adults with congenital heart disease: SCMR expert consensus group on congenital heart disease. J Cardiovasc Magn Reson. 2013;15:51.
12. Ferreira VM, Piechnik SK, Robson MD, Neubauer S, Karamitsos TD. Myocardial tissue characterization by magnetic resonance imaging: novel applications of T1 and T2 mapping. J Thorac Imaging. 2014;29(3):147–54.
13. Salerno M, Kramer CM. Advances in parametric mapping with CMR imaging. JACC Cardiovasc Imaging. 2013;6(7):806–22.
14. Kato S, Kitagawa K, Ishida N, Ishida M, Nagata M, Ichikawa Y, et al. Assessment of coronary artery disease using magnetic resonance coronary angiography: a national multicenter trial. J Am Coll Cardiol. 2010;56(12):983–91.
15. Yoon YE, Kitagawa K, Kato S, Ishida M, Nakajima H, Kurita T, et al. Prognostic value of coronary magnetic resonance angiography for prediction of cardiac events in patients with suspected coronary artery disease. J Am Coll Cardiol. 2012;60(22):2316–22.
16. Ibrahim T, Makowski MR, Jankauskas A, Maintz D, Karch M, Schachoff S, et al. Serial contrast-enhanced cardiac magnetic resonance imaging demonstrates regression of hyperenhancement within the coronary artery wall in patients after acute myocardial infarction. JACC Cardiovascular imaging. 2009;2(5):580–8.
17. Kim WY, Astrup AS, Stuber M, Tarnow L, Falk E, Botnar RM, et al. Subclinical coronary and aortic atherosclerosis detected by magnetic resonance imaging in type 1 diabetes with and without diabetic nephropathy. Circulation. 2007;115(2):228–35.
18. Yeon SB, Sabir A, Clouse M, Martinezclark PO, Peters DC, Hauser TH, et al. Delayed-enhancement cardiovascular magnetic resonance coronary artery wall imaging: comparison

with multislice computed tomography and quantitative coronary angiography. J Am Coll Cardiol. 2007;50(5):441–7.
19. Jansen CH, Perera D, Makowski MR, Wiethoff AJ, Phinikaridou A, Razavi RM, et al. Detection of intracoronary thrombus by magnetic resonance imaging in patients with acute myocardial infarction. Circulation. 2011;124(4):416–24.
20. Noguchi T, Kawasaki T, Tanaka A, Yasuda S, Goto Y, Ishihara M, et al. High-intensity signals in coronary plaques on noncontrast T1-weighted magnetic resonance imaging as a novel determinant of coronary events. J Am Coll Cardiol. 2014;63(10):989–99.
21. Fischer SE, Wickline SA, Lorenz CH. Novel real-time R-wave detection algorithm based on the vectorcardiogram for accurate gated magnetic resonance acquisitions. Magn Reson Med. 1999;42(2):361–70.
22. Kim WY, Stuber M, Kissinger KV, Andersen NT, Manning WJ, Botnar RM. Impact of bulk cardiac motion on right coronary MR angiography and vessel wall imaging. J Magn Reson Imag: JMRI. 2001;14(4):383–90.
23. Leiner T, Katsimaglis G, Yeh EN, Kissinger KV, van Yperen G, Eggers H, et al. Correction for heart rate variability improves coronary magnetic resonance angiography. J Magn Reson Imaging. 2005;22(4):577–82.
24. Wang Y, Riederer SJ, Ehman RL. Respiratory motion of the heart: kinematics and the implications for the spatial resolution in coronary imaging. Magn Reson Med. 1995;33(5):713–9.
25. Danias PG, Stuber M, Botnar RM, Kissinger KV, Edelman RR, Manning WJ. Relationship between motion of coronary arteries and diaphragm during free breathing: lessons from real-time MR imaging. AJR Am J Roentgenol. 1999;172(4):1061–5.
26. McLeish K, Hill DL, Atkinson D, Blackall JM, Razavi R. A study of the motion and deformation of the heart due to respiration. IEEE Trans Med Imaging. 2002;21(9):1142–50.
27. Nehrke K, Bornert P, Manke D, Bock JC. Free-breathing cardiac MR imaging: study of implications of respiratory motion – initial results. Radiology. 2001;220(3):810–5.
28. Shechter G, Ozturk C, Resar JR, McVeigh ER. Respiratory motion of the heart from free breathing coronary angiograms. IEEE Trans Med Imaging. 2004;23(8):1046–56.
29. McConnell MV, Khasgiwala VC, Savord BJ, Chen MH, Chuang ML, Edelman RR, et al. Comparison of respiratory suppression methods and navigator locations for MR coronary angiography. AJR Am J Roentgenol. 1997;168(5):1369–75.
30. Santelli C, Nezafat R, Goddu B, Manning WJ, Smink J, Kozerke S, et al. Respiratory bellows revisited for motion compensation: preliminary experience for cardiovascular MR. Magn Reson Med. 2011;65(4):1097–102.
31. Ehman RL, Felmlee JP. Adaptive technique for high-definition MR imaging of moving structures. Radiology. 1989;173(1):255–63.
32. Danias PG, McConnell MV, Khasgiwala VC, Chuang ML, Edelman RR, Manning WJ. Prospective navigator correction of image position for coronary MR angiography. Radiology. 1997;203(3):733–6.
33. Nehrke K, Bornert P, Groen J, Smink J, Bock JC. On the performance and accuracy of 2D navigator pulses. Magn Reson Imaging. 1999;17(8):1173–81.
34. Firmin D, Keegan J. Navigator echoes in cardiac magnetic resonance. J Cardiovasc Magn Reson. 2001;3(3):183–93.
35. Moghari MH, Hu P, Kissinger KV, Goddu B, Goepfert L, Ngo L, et al. Subject-specific estimation of respiratory navigator tracking factor for free-breathing cardiovascular MR. Magn Reson Med. 2012;67(6):1665–72.
36. Taylor AM, Keegan J, Jhooti P, Firmin DN, Pennell DJ. Calculation of a subject-specific adaptive motion-correction factor for improved real-time navigator echo-gated magnetic resonance coronary angiography. J Cardiovasc Magn Reson: Off J Soc Cardiovasc Magn Reson. 1999;1(2):131–8.
37. Buehrer M, Curcic J, Boesiger P, Kozerke S. Prospective self-gating for simultaneous compensation of cardiac and respiratory motion. Magn Reson Med. 2008;60(3):683–90.

38. Kim WS, Mun CW, Kim DJ, Cho ZH. Extraction of cardiac and respiratory motion cycles by use of projection data and its applications to NMR imaging. Magn Reson Med. 1990;13(1):25–37.
39. Lai P, Bi X, Jerecic R, Li D. A respiratory self-gating technique with 3D-translation compensation for free-breathing whole-heart coronary MRA. Magn Reson Med. 2009;62(3):731–8.
40. Piccini D, Littmann A, Nielles-Vallespin S, Zenge MO. Respiratory self-navigation for whole-heart bright-blood coronary MRI: methods for robust isolation and automatic segmentation of the blood pool. Magn Reson Med. 2012;68(2):571–9.
41. Stehning C, Bornert P, Nehrke K, Eggers H, Stuber M. Free-breathing whole-heart coronary MRA with 3D radial SSFP and self-navigated image reconstruction. Magn Reson Med. 2005;54(2):476–80.
42. Addy NO, Ingle RR, Luo J, Baron CA, Yang PC, Hu BS, et al. 3D image-based navigators for coronary MR angiography. Magn Reson Med. 2016. doi:10.1002/mrm.26269. [Epub ahead of print].
43. Henningsson M, Koken P, Stehning C, Razavi R, Prieto C, Botnar RM. Whole-heart coronary MR angiography with 2D self-navigated image reconstruction. Magn Reson Med. 2012;67(2):437–45.
44. Henningsson M, Smink J, Razavi R, Botnar RM. Prospective respiratory motion correction for coronary MR angiography using a 2D image navigator. Magn Reson Med. 2013;69(2):486–94.
45. Kawaji K, Spincemaille P, Nguyen TD, Thimmappa N, Cooper MA, Prince MR, et al. Direct coronary motion extraction from a 2D fat image navigator for prospectively gated coronary MR angiography. Magn Reson Med. 2014;71(2):599–607.
46. Luo J, Addy NO, Ingle RR, Baron CA, Cheng JY, Hu BS, et al. Nonrigid motion correction with 3D image-based navigators for coronary MR angiography. Magn Reson Med. 2016. doi:10.1002/mrm.26273. [Epub ahead of print].
47. Moghari MH, Annese D, Geva T, Powell AJ. Three-dimensional heart locator and compressed sensing for whole-heart MR angiography. Magn Reson Med. 2016;75(5):2086–93.
48. Moghari MH, Roujol S, Henningsson M, Kissinger KV, Annese D, Nezafat R, et al. Three-dimensional heart locator for whole-heart coronary magnetic resonance angiography. Magn Reson Med. 2014;71(6):2118–26.
49. Wu HH, Gurney PT, Hu BS, Nishimura DG, McConnell MV. Free-breathing multiphase whole-heart coronary MR angiography using image-based navigators and three-dimensional cones imaging. Magn Reson Med. 2013;69(4):1083–93.
50. Bornert P, Aldefeld B, Nehrke K. Improved 3D spiral imaging for coronary MR angiography. Magn Reson Med. 2001;45(1):172–5.
51. Bornert P, Stuber M, Botnar RM, Kissinger KV, Koken P, Spuentrup E, et al. Direct comparison of 3D spiral vs. Cartesian gradient-echo coronary magnetic resonance angiography. Magn Reson Med. 2001;46(4):789–94.
52. Jahnke C, Paetsch I, Schnackenburg B, Gebker R, Kohler U, Bornstedt A, et al. Comparison of radial and Cartesian imaging techniques for MR coronary angiography. J Cardiovasc Magn Reson: Off J Soc Cardiovasc Magn Reson. 2004;6(4):865–75.
53. Priest AN, Bansmann PM, Mullerleile K, Adam G. Coronary vessel-wall and lumen imaging using radial k-space acquisition with MRI at 3 Tesla. Eur Radiol. 2007;17(2):339–46.
54. Spuentrup E, Katoh M, Buecker A, Manning WJ, Schaeffter T, Nguyen TH, et al. Free-breathing 3D steady-state free precession coronary MR angiography with radial k-space sampling: comparison with cartesian k-space sampling and cartesian gradient-echo coronary MR angiography – pilot study. Radiology. 2004;231(2):581–6.
55. Bhat H, Ge L, Nielles-Vallespin S, Zuehlsdorff S, Li D. 3D radial sampling and 3D affine transform-based respiratory motion correction technique for free-breathing whole-heart coronary MRA with 100% imaging efficiency. Magn Reson Med. 2011;65(5):1269–77.
56. Pang J, Sharif B, Arsanjani R, Bi X, Fan Z, Yang Q, et al. Accelerated whole-heart coronary MRA using motion-corrected sensitivity encoding with three-dimensional projection reconstruction. Magn Reson Med. 2015;73(1):284–91.
57. Piccini D, Monney P, Sierro C, Coppo S, Bonanno G, van Heeswijk RB, et al. Respiratory self-navigated postcontrast whole-heart coronary MR angiography: initial experience in patients. Radiology. 2014;270(2):378–86.

58. Coppo S, Piccini D, Bonanno G, Chaptinel J, Vincenti G, Feliciano H, et al. Free-running 4D whole-heart self-navigated golden angle MRI: initial results. Magn Reson Med. 2015;74(5):1306–16.
59. Pang J, Sharif B, Fan Z, Bi X, Arsanjani R, Berman DS, et al. ECG and navigator-free four-dimensional whole-heart coronary MRA for simultaneous visualization of cardiac anatomy and function. Magn Reson Med. 2014;72(5):1208–17.
60. Griswold MA, Jakob PM, Heidemann RM, Nittka M, Jellus V, Wang J, et al. Generalized auto-calibrating partially parallel acquisitions (GRAPPA). Magn Reson Med. 2002;47(6):1202–10.
61. Pruessmann KP, Weiger M, Scheidegger MB, Boesiger P. SENSE: sensitivity encoding for fast MRI. Magn Reson Med. 1999;42(5):952–62.
62. Niendorf T, Hardy CJ, Giaquinto RO, Gross P, Cline HE, Zhu Y, et al. Toward single breath-hold whole-heart coverage coronary MRA using highly accelerated parallel imaging with a 32-channel MR system. Magn Reson Med. 2006;56(1):167–76.
63. Wielopolski PA, van Geuns RJ, de Feyter PJ, Oudkerk M. Breath-hold coronary MR angiography with volume-targeted imaging. Radiology. 1998;209(1):209–19.
64. Akcakaya M, Basha TA, Chan RH, Manning WJ, Nezafat R. Accelerated isotropic sub-millimeter whole-heart coronary MRI: compressed sensing versus parallel imaging. Magn Reson Med. 2014;71(2):815–22.
65. Lustig M, Donoho D, Pauly JM. Sparse MRI: the application of compressed sensing for rapid MR imaging. Magn Reson Med. 2007;58(6):1182–95.
66. Pang J, Bhat H, Sharif B, Fan Z, Thomson LE, Labounty T, et al. Whole-heart coronary MRA with 100% respiratory gating efficiency: self-navigated three-dimensional retrospective image-based motion correction (TRIM). Magn Reson Med. 2014;71(1):67–74. doi:10.1002/mrm.24628. Epub 2013 Feb 7.
67. Aitken AP, Henningsson M, Botnar RM, Schaeffter T, Prieto C. 100% efficient three-dimensional coronary MR angiography with two-dimensional beat-to-beat translational and bin-to-bin affine motion correction. Magn Reson Med. 2015;74(3):756–64.
68. Cruz G, Atkinson D, Henningsson M, Botnar RM, Prieto C. Highly efficient nonrigid motion-corrected 3D whole-heart coronary vessel wall imaging. Magn Reson Med. 2016. doi: 10.1002/mrm.26274. [Epub ahead of print].
69. Henningsson M, Prieto C, Chiribiri A, Vaillant G, Razavi R, Botnar RM. Whole-heart coronary MRA with 3D affine motion correction using 3D image-based navigation. Magn Reson Med. 2014;71(1):173–81.
70. Prieto C, Doneva M, Usman M, Henningsson M, Greil G, Schaeffter T, et al. Highly efficient respiratory motion compensated free-breathing coronary mra using golden-step Cartesian acquisition. J Magn Reson Imag: JMRI. 2015;41(3):738–46.
71. Ingle RR, Wu HH, Addy NO, Cheng JY, Yang PC, Hu BS, et al. Nonrigid autofocus motion correction for coronary MR angiography with a 3D cones trajectory. Magn Reson Med. 2014;72(2):347–61.
72. Edelman RR, Manning WJ, Burstein D, Paulin S. Coronary arteries: breath-hold MR angiography. Radiology. 1991;181(3):641–3.
73. Manning WJ, Li W, Boyle NG, Edelman RR. Fat-suppressed breath-hold magnetic resonance coronary angiography. Circulation. 1993;87(1):94–104.
74. Deshpande VS, Shea SM, Laub G, Simonetti OP, Finn JP, Li D. 3D magnetization-prepared true-FISP: a new technique for imaging coronary arteries. Magn Reson Med. 2001;46(3):494–502.
75. Li D, Paschal CB, Haacke EM, Adler LP. Coronary arteries: three-dimensional MR imaging with fat saturation and magnetization transfer contrast. Radiology. 1993;187(2):401–6.
76. Giorgi B, Dymarkowski S, Maes F, Kouwenhoven M, Bogaert J. Improved visualization of coronary arteries using a new three-dimensional submillimeter MR coronary angiography sequence with balanced gradients. AJR Am J Roentgenol. 2002;179(4):901–10.
77. Spuentrup E, Bornert P, Botnar RM, Groen JP, Manning WJ, Stuber M. Navigator-gated free-breathing three-dimensional balanced fast field echo (TrueFISP) coronary magnetic resonance angiography. Investig Radiol. 2002;37(11):637–42.
78. Kaul MG, Stork A, Bansmann PM, Nolte-Ernsting C, Lund GK, Weber C, et al. Evaluation of balanced steady-state free precession (TrueFISP) and K-space segmented gradient echo

sequences for 3D coronary MR angiography with navigator gating at 3 Tesla. RoFo: Fortschr auf dem Gebiete der Rontgenstrahlen und der Nuklearmedizin. 2004;176(11):1560–5.
79. Nezafat M, Henningsson M, Ripley DP, Dedieu N, Greil G, Greenwood JP, et al. Coronary MR angiography at 3 T: fat suppression versus water-fat separation. Magma. 2016.
80. Yang Q, Li K, Liu X, Du X, Bi X, Huang F, et al. 3.0T whole-heart coronary magnetic resonance angiography performed with 32-channel cardiac coils: a single-center experience. Circ Cardiovasc Imag. 2012;5(5):573–9.
81. Botnar RM, Stuber M, Danias PG, Kissinger KV, Manning WJ. Improved coronary artery definition with T2-weighted, free-breathing, three-dimensional coronary MRA. Circulation. 1999;99(24):3139–48.
82. Brittain JH, Hu BS, Wright GA, Meyer CH, Macovski A, Nishimura DG. Coronary angiography with magnetization-prepared T2 contrast. Magn Reson Med. 1995;33(5):689–96.
83. Bornert P, Koken P, Nehrke K, Eggers H, Ostendorf P. Water/fat-resolved whole-heart Dixon coronary MRA: an initial comparison. Magn Reson Med. 2014;71(1):156–63.
84. Mookadam F, Goel R, Alharthi MS, Jiamsripong P, Cha S. Epicardial fat and its association with cardiovascular risk: a cross-sectional observational study. Heart Views: Off J Gulf Heart Association. 2010;11(3):103–8.
85. Sicari R, Sironi AM, Petz R, Frassi F, Chubuchny V, De Marchi D, et al. Pericardial rather than epicardial fat is a cardiometabolic risk marker: an MRI vs echo study. J Am Soc Echocardiogr: Off Publ Am Soc Echocardiogr. 2011;24(10):1156–62.
86. Huber ME, Paetsch I, Schnackenburg B, Bornstedt A, Nagel E, Fleck E, et al. Performance of a new gadolinium-based intravascular contrast agent in free-breathing inversion-recovery 3D coronary MRA. Magn Reson Med. 2003;49(1):115–21.
87. Li D, Dolan RP, Walovitch RC, Lauffer RB. Three-dimensional MRI of coronary arteries using an intravascular contrast agent. Magn Reson Med. 1998;39(6):1014–8.
88. Liu X, Bi X, Huang J, Jerecic R, Carr J, Li D. Contrast-enhanced whole-heart coronary magnetic resonance angiography at 3.0 T: comparison with steady-state free precession technique at 1.5 T. Investig Radiol. 2008;43(9):663–8.
89. Nassenstein K, Breuckmann F, Hunold P, Barkhausen J, Schlosser T. Magnetic resonance coronary angiography: comparison between a Gd-BOPTA- and a Gd-DTPA-enhanced spoiled gradient-echo sequence and a non-contrast-enhanced steady-state free-precession sequence. Acta Radiol. 2009;50(4):406–11.
90. Regenfus M, Ropers D, Achenbach S, Kessler W, Laub G, Daniel WG, et al. Noninvasive detection of coronary artery stenosis using contrast-enhanced three-dimensional breath-hold magnetic resonance coronary angiography. J Am Coll Cardiol. 2000;36(1):44–50.
91. Tang L, Merkle N, Schar M, Korosoglou G, Solaiyappan M, Hombach V, et al. Volume-targeted and whole-heart coronary magnetic resonance angiography using an intravascular contrast agent. J Magn Reson Imaging. 2009;30(5):1191–6.
92. Yang Q, Li K, Liu X, Bi X, Liu Z, An J, et al. Contrast-enhanced whole-heart coronary magnetic resonance angiography at 3.0-T: a comparative study with X-ray angiography in a single center. J Am Coll Cardiol. 2009;54(1):69–76.
93. Laurent S, Elst LV, Muller RN. Comparative study of the physicochemical properties of six clinical low molecular weight gadolinium contrast agents. Contrast Media Mol Imag. 2006;1(3):128–37.
94. Wagner B, Drel V, Gorin Y. Pathophysiology of gadolinium-associated systemic fibrosis. Am J Physiol Ren Physiol. 2016;311(1):F1–F11.
95. Botnar RM, Stuber M, Kissinger KV, Kim WY, Spuentrup E, Manning WJ. Noninvasive coronary vessel wall and plaque imaging with magnetic resonance imaging. Circulation. 2000;102(21):2582–7.
96. Fayad ZA, Fuster V, Fallon JT, Jayasundera T, Worthley SG, Helft G, et al. Noninvasive in vivo human coronary artery lumen and wall imaging using black-blood magnetic resonance imaging. Circulation. 2000;102(5):506–10.

97. Edelman RR, Chien D, Kim D. Fast selective black blood MR imaging. Radiology. 1991;181(3):655–60.
98. Botnar RM, Stuber M, Lamerichs R, Smink J, Fischer SE, Harvey P, et al. Initial experiences with in vivo right coronary artery human MR vessel wall imaging at 3 tesla. J Cardiovasc Magn Reson: Off J Soc Cardiovasc Magn Reson. 2003;5(4):589–94.
99. Botnar RM, Kim WY, Bornert P, Stuber M, Spuentrup E, Manning WJ. 3D coronary vessel wall imaging utilizing a local inversion technique with spiral image acquisition. Magn Reson Med. 2001;46(5):848–54.
100. Katoh M, Spuentrup E, Buecker A, Manning WJ, Gunther RW, Botnar RM. MR coronary vessel wall imaging: comparison between radial and spiral k-space sampling. J Magn Reson Imag: JMRI. 2006;23(5):757–62.
101. Kim WY, Stuber M, Bornert P, Kissinger KV, Manning WJ, Botnar RM. Three-dimensional black-blood cardiac magnetic resonance coronary vessel wall imaging detects positive arterial remodeling in patients with nonsignificant coronary artery disease. Circulation. 2002;106(3):296–9.
102. Andia ME, Henningsson M, Hussain T, Phinikaridou A, Protti A, Greil G, et al. Flow-independent 3D whole-heart vessel wall imaging using an interleaved T2-preparation acquisition. Magn Reson Med. 2013;69(1):150–7.
103. Hundley WG, Bluemke DA, Finn JP, Flamm SD, Fogel MA, Friedrich MG, et al. ACCF/ACR/AHA/NASCI/SCMR 2010 expert consensus document on cardiovascular magnetic resonance: a report of the American College of Cardiology Foundation Task Force on Expert Consensus Documents. J Am Coll Cardiol. 2010;55(23):2614–62.
104. Hofman MB, Paschal CB, Li D, Haacke EM, van Rossum AC, Sprenger M. MRI of coronary arteries: 2D breath-hold vs 3D respiratory-gated acquisition. J Comput Assist Tomogr. 1995;19(1):56–62.
105. Lobbes MB, Miserus RJ, Heeneman S, Passos VL, Mutsaers PH, Debernardi N, et al. Atherosclerosis: contrast-enhanced MR imaging of vessel wall in rabbit model – comparison of gadofosveset and gadopentetate dimeglumine. Radiology. 2009;250(3):682–91.
106. Oshinski JN, Hofland L, Mukundan Jr S, Dixon WT, Parks WJ, Pettigrew RI. Two-dimensional coronary MR angiography without breath holding. Radiology. 1996;201(3):737–43.
107. Paschal CB, Haacke EM, Adler LP. Three-dimensional MR imaging of the coronary arteries: preliminary clinical experience. J Magn Reson Imag: JMRI. 1993;3(3):491–500.
108. Post JC, van Rossum AC, Hofman MB, Valk J, Visser CA. Three-dimensional respiratory-gated MR angiography of coronary arteries: comparison with conventional coronary angiography. AJR Am J Roentgenol. 1996;166(6):1399–404.
109. Stuber M, Botnar RM, Danias PG, Sodickson DK, Kissinger KV, Van Cauteren M, et al. Double-oblique free-breathing high resolution three-dimensional coronary magnetic resonance angiography. J Am Coll Cardiol. 1999;34(2):524–31.
110. Scheidegger MB, Muller R, Boesiger P. Magnetic resonance angiography: methods and its applications to the coronary arteries. Technol Health Care. 1994;2(4):255–65.
111. Pennell DJ, Bogren HG, Keegan J, Firmin DN, Underwood SR. Assessment of coronary artery stenosis by magnetic resonance imaging. Heart. 1996;75(2):127–33.
112. Bogaert J, Kuzo R, Dymarkowski S, Beckers R, Piessens J, Rademakers FE. Coronary artery imaging with real-time navigator three-dimensional turbo-field-echo MR coronary angiography: initial experience. Radiology. 2003;226(3):707–16.
113. Dewey M, Teige F, Schnapauff D, Laule M, Borges AC, Rutsch W, et al. Combination of free-breathing and breathhold steady-state free precession magnetic resonance angiography for detection of coronary artery stenoses. J Magn Reson Imag: JMRI. 2006;23(5):674–81.
114. Jahnke C, Paetsch I, Nehrke K, Schnackenburg B, Gebker R, Fleck E, et al. Rapid and complete coronary arterial tree visualization with magnetic resonance imaging: feasibility and diagnostic performance. Eur Heart J. 2005;26(21):2313–9.

115. Jahnke C, Paetsch I, Schnackenburg B, Bornstedt A, Gebker R, Fleck E, et al. Coronary MR angiography with steady-state free precession: individually adapted breath-hold technique versus free-breathing technique. Radiology. 2004;232(3):669–76.
116. Maintz D, Aepfelbacher FC, Kissinger KV, Botnar RM, Danias PG, Heindel W, et al. Coronary MR angiography: comparison of quantitative and qualitative data from four techniques. AJR Am J Roentgenol. 2004;182(2):515–21.
117. Manning WJ, Li W, Edelman RR. A preliminary report comparing magnetic resonance coronary angiography with conventional angiography. N Engl J Med. 1993;328(12):828–32.
118. Ozgun M, Hoffmeier A, Kouwenhoven M, Botnar RM, Stuber M, Scheld HH, et al. Comparison of 3D segmented gradient-echo and steady-state free precession coronary MRI sequences in patients with coronary artery disease. AJR Am J Roentgenol. 2005;185(1):103–9.
119. Sakuma H, Ichikawa Y, Chino S, Hirano T, Makino K, Takeda K. Detection of coronary artery stenosis with whole-heart coronary magnetic resonance angiography. J Am Coll Cardiol. 2006;48(10):1946–50.
120. Sakuma H, Ichikawa Y, Suzawa N, Hirano T, Makino K, Koyama N, et al. Assessment of coronary arteries with total study time of less than 30 minutes by using whole-heart coronary MR angiography. Radiology. 2005;237(1):316–21.
121. Boffano C, Chiribiri A, Cesarani F. Native whole-heart coronary imaging for the identification of anomalous origin of the coronary arteries. Int J Cardiol. 2009;137(1):e27–8.
122. Greil GF, Seeger A, Miller S, Claussen CD, Hofbeck M, Botnar RM, et al. Coronary magnetic resonance angiography and vessel wall imaging in children with Kawasaki disease. Pediatr Radiol. 2007;37(7):666–73.
123. Galjee MA, van Rossum AC, Doesburg T, van Eenige MJ, Visser CA. Value of magnetic resonance imaging in assessing patency and function of coronary artery bypass grafts. An angiographically controlled study. Circulation. 1996;93(4):660–6.
124. Jenkins JP, Love HG, Foster CJ, Isherwood I, Rowlands DJ. Detection of coronary artery bypass graft patency as assessed by magnetic resonance imaging. Br J Radiol. 1988;61(721):2–4.
125. Rubinstein RI, Askenase AD, Thickman D, Feldman MS, Agarwal JB, Helfant RH. Magnetic resonance imaging to evaluate patency of aortocoronary bypass grafts. Circulation. 1987;76(4):786–91.
126. White RD, Caputo GR, Mark AS, Modin GW, Higgins CB. Coronary artery bypass graft patency: noninvasive evaluation with MR imaging. Radiology. 1987;164(3):681–6.
127. Vrachliotis TG, Bis KG, Aliabadi D, Shetty AN, Safian R, Simonetti O. Contrast-enhanced breath-hold MR angiography for evaluating patency of coronary artery bypass grafts. AJR Am J Roentgenol. 1997;168(4):1073–80.
128. Wintersperger BJ, Engelmann MG, von Smekal A, Knez A, Penzkofer HV, Hofling B, et al. Patency of coronary bypass grafts: assessment with breath-hold contrast-enhanced MR angiography – value of a non-electrocardiographically triggered technique. Radiology. 1998;208(2):345–51.
129. Wintersperger BJ, von Smekal A, Engelmann MG, Knez A, Penzkofer HV, Laub G, et al. Contrast media enhanced magnetic resonance angiography for determining patency of a coronary bypass. A comparison with coronary angiography. RoFo: Fortschr auf dem Gebiete der Rontgenstrahlen und der Nuklearmedizin. 1997;167(6):572–8.
130. Glagov S, Weisenberg E, Zarins C, Stankunavicius R, Kolettis G. Compensatory enlargement of human atherosclerotic coronary arteries. N Engl J Med. 1987;316(22):1371–5.
131. Tuzcu EM, Kapadia SR, Tutar E, Ziada KM, Hobbs RE, McCarthy PM, et al. High prevalence of coronary atherosclerosis in asymptomatic teenagers and young adults: evidence from intravascular ultrasound. Circulation. 2001;103(22):2705–10.
132. Virmani R, Burke AP, Farb A, Kolodgie FD. Pathology of the vulnerable plaque. J Am Coll Cardiol. 2006;47(8 Suppl):C13–8.

133. Stone GW, Maehara A, Lansky AJ, de Bruyne B, Cristea E, Mintz GS, et al. A prospective natural-history study of coronary atherosclerosis. N Engl J Med. 2011;364(3):226–35.
134. Nissen SE, Tuzcu EM, Schoenhagen P, Brown BG, Ganz P, Vogel RA, et al. Effect of intensive compared with moderate lipid-lowering therapy on progression of coronary atherosclerosis: a randomized controlled trial. JAMA: J Am Med Assoc. 2004;291(9):1071–80.
135. Botnar RM, Stuber M, Kissinger KV, Kim WY, Spuentrup E, Manning WJ. Noninvasive coronary vessel wall and plaque imaging with magnetic resonance imaging. Circulation. 2000;102(11085960):2582–7.
136. He Y, Zhang Z, Dai Q, Zhou Y, Yang Y, Yu W, et al. Accuracy of MRI to identify the coronary artery plaque: a comparative study with intravascular ultrasound. J Magn Reson Imaging. 2012;35(1):72–8.
137. Gerretsen S, Kessels AG, Nelemans PJ, Dijkstra J, Reiber JH, van der Geest RJ, et al. Detection of coronary plaques using MR coronary vessel wall imaging: validation of findings with intravascular ultrasound. Eur Radiol. 2013;23(1):115–24.
138. Miao C, Chen S, Macedo R, Lai S, Liu K, Li D, et al. Positive remodeling of the coronary arteries detected by magnetic resonance imaging in an asymptomatic population: MESA (Multi-Ethnic Study of Atherosclerosis). J Am Coll Cardiol. 2009;53(18):1708–15.
139. Macedo R, Chen S, Lai S, Shea S, Malayeri AA, Szklo M, et al. MRI detects increased coronary wall thickness in asymptomatic individuals: the multi-ethnic study of atherosclerosis (MESA). J Magn Reson Imaging. 2008;28(5):1108–15.
140. Gerretsen SC, Kooi ME, Kessels AG, Schalla S, Katoh M, van der Geest RJ, et al. Visualization of coronary wall atherosclerosis in asymptomatic subjects and patients with coronary artery disease using magnetic resonance imaging. PloS one. 2010;5(9):e12998.
141. Fernandes JL, Serrano Jr CV, Blotta MH, Coelho OR, Nicolau JC, Avila LF, et al. Regression of coronary artery outward remodeling in patients with non-ST-segment acute coronary syndromes: a longitudinal study using noninvasive magnetic resonance imaging. Am Heart J. 2006;152(6):1123–32.
142. Hazirolan T, Gupta SN, Mohamed MA, Bluemke DA. Reproducibility of black-blood coronary vessel wall MR imaging. J Cardiovasc Magn Reson: Off J Soc Cardiovasc Magn Reson. 2005;7(2):409–13.
143. Desai MY, Lai S, Barmet C, Weiss RG, Stuber M. Reproducibility of 3D free-breathing magnetic resonance coronary vessel wall imaging. Eur Heart J. 2005;26(21):2320–4.
144. Anderson TJ, Meredith IT, Yeung AC, Frei B, Selwyn AP, Ganz P. The effect of cholesterol-lowering and antioxidant therapy on endothelium-dependent coronary vasomotion. N Engl J Med. 1995;332(8):488–93.
145. Terashima M, Meyer CH, Keeffe BG, Putz EJ, de la Pena-Almaguer E, Yang PC, et al. Noninvasive assessment of coronary vasodilation using magnetic resonance angiography. J Am Coll Cardiol. 2005;45(1):104–10.
146. Nguyen PK, Meyer C, Engvall J, Yang P, McConnell MV. Noninvasive assessment of coronary vasodilation using cardiovascular magnetic resonance in patients at high risk for coronary artery disease. J Cardiovasc Magn Reson: Off J Soc Cardiovasc Magn Reson. 2008;10:28.
147. Hays AG, Hirsch GA, Kelle S, Gerstenblith G, Weiss RG, Stuber M. Noninvasive visualization of coronary artery endothelial function in healthy subjects and in patients with coronary artery disease. J Am Coll Cardiol. 2010;56(20):1657–65.
148. Kelle S, Hays AG, Hirsch GA, Gerstenblith G, Miller JM, Steinberg AM, et al. Coronary artery distensibility assessed by 3.0 Tesla coronary magnetic resonance imaging in subjects with and without coronary artery disease. Am J Cardiol. 2011;108(4):491–7.
149. Moody AR, Allder S, Lennox G, Gladman J, Fentem P. Direct magnetic resonance imaging of carotid artery thrombus in acute stroke. Lancet. 1999;353(10023906):122–3.
150. Kawasaki T, Koga S, Koga N, Noguchi T, Tanaka H, Koga H, et al. Characterization of hyperintense plaque with noncontrast T1-weighted cardiac magnetic resonance coronary plaque

imaging comparison with multislice computed tomography and intravascular ultrasound. J Am Coll Cardiol Img. 2009;2(6):720–8.
151. Ehara S, Hasegawa T, Nakata S, Matsumoto K, Nishimura S, Iguchi T, et al. Hyperintense plaque identified by magnetic resonance imaging relates to intracoronary thrombus as detected by optical coherence tomography in patients with angina pectoris. Eur Heart J Cardiovasc Imag. 2012;13(5):394–9.
152. Pedersen SF, Thrysoe SA, Paaske WP, Thim T, Falk E, Ringgaard S, et al. Determination of edema in porcine coronary arteries by T2 weighted cardiovascular magnetic resonance. J Cardiovasc Magn Reson. 2011;13:52.
153. Kim WY, Christiansen EH, Thrysoe SA, Al-Mashhadi RH, Botker HE, Bottcher M, et al. First in vivo demonstration of coronary edema in culprit lesion of patient with acute coronary syndrome by cardiovascular magnetic resonance. Circ Cardiovasc Imaging. 2011;4(3):344–6.
154. Schneeweis C, Schnackenburg B, Stuber M, Berger A, Schneider U, Yu J, et al. Delayed contrast-enhanced MRI of the coronary artery wall in takayasu arteritis. PLoS One. 2012;7(12):e50655.
155. Cai J, Hatsukami TS, Ferguson MS, Kerwin WS, Saam T, Chu B, et al. In vivo quantitative measurement of intact fibrous cap and lipid-rich necrotic core size in atherosclerotic carotid plaque: comparison of high-resolution, contrast-enhanced magnetic resonance imaging and histology. Circulation. 2005;112(22):3437–44.
156. Langerak SE, Kunz P, Vliegen HW, Lamb HJ, Jukema JW, van Der Wall EE, et al. Improved MR flow mapping in coronary artery bypass grafts during adenosine-induced stress. Radiology. 2001;218(2):540–7.
157. Yuan C, Kerwin WS, Ferguson MS, Polissar N, Zhang S, Cai J, et al. Contrast-enhanced high resolution MRI for atherosclerotic carotid artery tissue characterization. J Magn Reson Imag: JMRI. 2002;15(1):62–7.
158. Kelle S, Schlendorf K, Hirsch GA, Gerstenblith G, Fleck E, Weiss RG, et al. Gadolinium enhanced MR coronary vessel wall imaging at 3.0 tesla. Cardiol Res Pract. 2010;2010:1–9.

Index

C. Constantinides (ed.), *Protocols and Methodologies in Basic Science and Clinical Cardiac MRI*, https://doi.org/10.1007/978-3-319-53001-7